Strength and Stability of locally supported cylinders

by

Cornelia Doerich

Supervisors: Professor J. Michael Rotter
Professor Jin Ooi

A thesis submitted in fulfilment of the requirements for the degree of Doctor of Philosophy

Institute for Infrastructure & Environment, The School of Engineering and Electronics,
The University of Edinburgh
William Rankine Building, The King's Buildings, Edinburgh, EH9 3JL
September 2007

Declaration

This thesis entitled “Strength and Stability of locally supported cylinders”, is submitted to the Institute for Infrastructure & Environment, The School of Engineering and Electronics, The University of Edinburgh, William Rankine Building, The King's Buildings, Edinburgh, EH9 3JL, for the Degree of Doctor of Philosophy.
The research was solely the work of the author except where otherwise acknowledged in the text and has not formed the basis of a submission for any other degree.
Publications based on this thesis:

Cornelia Doerich, J. Mark F.G. Holst and J. Michael Rotter (2005), “The behaviour of cylindrical steel shells supported on local brackets”, Proceedings of the 4th International Conference on Advances in Steel Structures, Shanghai, June 2005

J.M.F.G. Holst, **C. Doerich**, and J.M. Rotter (2005), “Accurate determination of the plastic collapse loads of shells when using finite element analyses”, Proceedings of the 4th International Conference on Advances in Steel Structures, Shanghai, June 2005

Cornelia Doerich, J. Michael Rotter (2005), “Non-linear computations of cylindrical shells on local bracket supports”, Proceedings of the 5th International Conference on Computation of Shell and Spatial Structures, Salzburg, June 2005

Cornelia Doerich, J. Michael Rotter (2007), “Buckling behaviour of cylindrical shells on local supports”, International Journal of Constructional Steel Research, accepted, not published yet

Cornelia Doerich
September, 2007

Abstract

Large quantities of particulate solids and fluids are stored in cylindrical metal shell silos and tanks with a vertical axis. Such metal silos and tanks are often required to be elevated above ground level to permit trains, trucks or conveying systems to be placed beneath a hopper from which the solid or fluid is withdrawn. Elevated silos must be supported, and access requirements often mean that the supports must be local (either on columns or supported from an elevated floor system).

The connection of a local support to an elevated cylindrical metal silo shell is a long-standing difficult problem in shell analysis, and most designs are based on simple ideas using past experiences of successes and failures. Smaller silo structures are often supported on local brackets attached to the side of the shell, but very few investigations of the behaviour or strength of such an arrangement have ever been made.

This thesis presents a comprehensive investigation into the behaviour of a cylindrical steel shell that is discretely supported on several brackets, each rigidly connected to a stiff column or floor. The study has been conducted within the framework of the European Standard for Shell Structures (EN1993-1-6, 2006), which requires that the two reference strengths of the small displacement theory plastic collapse resistance and the linear bifurcation critical elastic resistance should both be evaluated to establish the context in which more sophisticated analyses are judged, and to provide a rapid means of producing reliable but simple design information.

Therefore this thesis begins with a thorough investigation of the predictions of these two reference strengths for these structures, discovering the challenges inherent in this methodology and finally developing equations that can be used in hand calculations intended for the simple evaluation of the reference strengths for a wide variety of geometries. The influence of geometric nonlinearity is next explored, both with and without geometric imperfections. The results pose some interesting questions concerning the relative importance of geometric nonlinearity and geometric imperfections in shell buckling problems where the stress field is far from

uniform. In the final part of the investigation, analyses are conducted that include both material and geometric nonlinearity with and without geometric imperfections. The results of these analyses are presented and analysed in the context of interaction capacity curves.

Following this extensive parametric investigation using linear and nonlinear analyses of all kinds, design recommendations are formulated so that bracket supports of this type can be used on thin cylindrical shells of any thickness and with any bracket dimensions necessary to transmit the loads. Finally, proposals are made for key future research investigations.

Acknowledgement

I am deeply grateful to my supervisor Professor J. Michael Rotter for all his advice, guidance and encouragement throughout the last four years.

I would also like to thank my friends and colleagues in the university for their help and support. I am particularly thankful to Jian-Fei Chen for his encouragement and help in a difficult time.

Finally, I have to thank my partner Marios. Only with his support and most amazing patience this thesis is finished.

Contents

1 Introduction

1.1 General

Nature taught us the construction of one of the most efficient structures known. Grass stems, flowers and even parts of our bodies are constructed as thin curved shells. It is therefore no surprise that engineers copied this design in a multitude of different structures, such as silos, tanks, chimneys, pipelines, towers and masts and many more. They are also used in biodigesters and chemical plants.

Vessels to store bulk solids or fluid will be termed here silos.

Silos are used to store large quantities of particulate solids. They are usually cylindrical vessels and are used in a wide range of industries because they usually represent the most economic structural form. The materials used in the construction of silos are in general metal or concrete. While steel silos are very sensitive to vertical compression which may cause the silo to buckle, concrete silos are most commonly mainly damaged by unsymmetrical normal pressures against the silo wall causing cracks in the silo wall (Rotter, 2007).

Steel silos are very light and easy to build or dismantle structures and due to the ductility of steel they are also often able to survive damaging load situations and recover, unlike brittle concrete structures.

Very large metal silos are usually ground supported, but due to the necessity to discharge the contents into trains, trucks or conveying systems conveniently, metal silos are most frequently elevated on supports to permit a hopper to be used for gravity discharge of the contents.

Elevated silos must be supported, and access requirements often mean that the supports must be local (either on columns or supported from an elevated floor system).

The typical parts of an elevated silo (Figure 1.1) include a conical roof, a cylindrical main barrel section, a conical hopper, a stiffening ring at the junction between the conical hopper and cylinder and a skirt. The junction connection

between hopper and cylindrical part is called the transition.

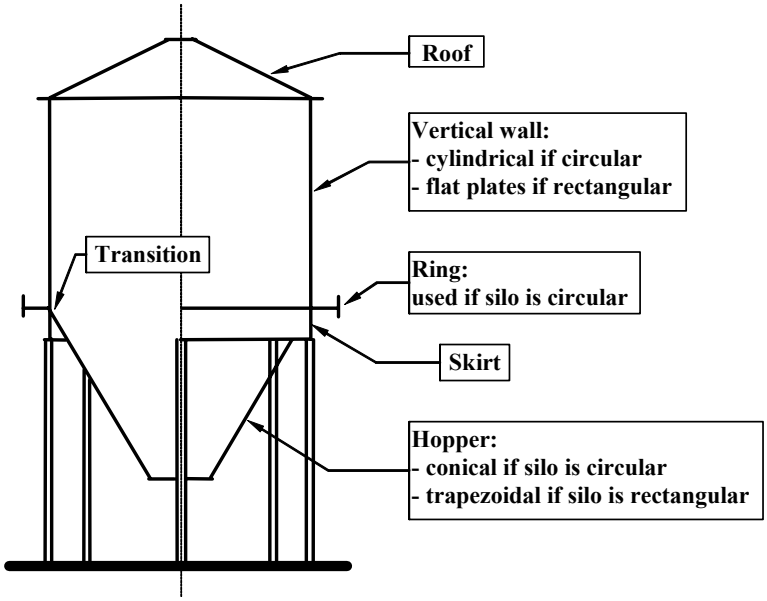

Figure 1.1: Terminology for parts of a typical silo (original picture in Rotter (2007))

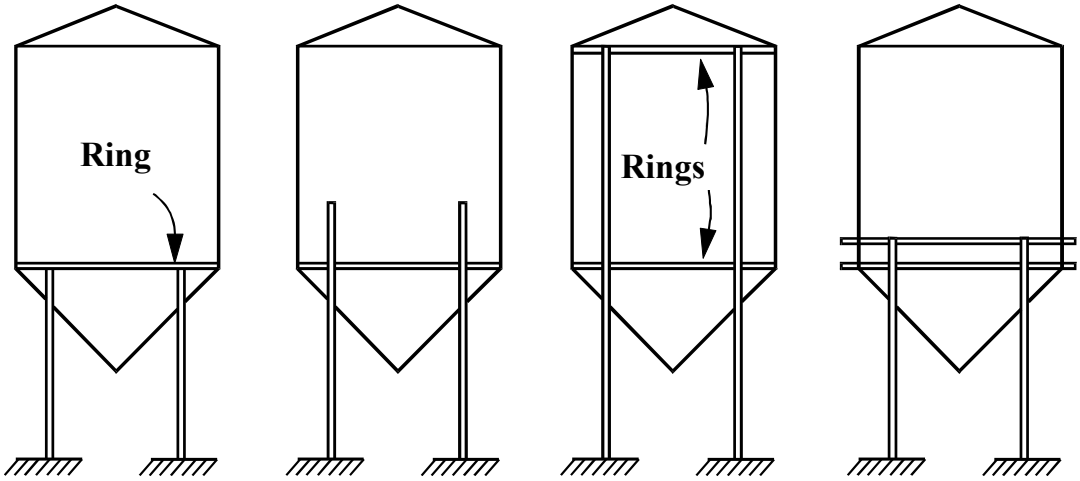

a) Very light silo: terminating columns with rings | b) Light silo: engaged columns | c) Medium and heavy silos: columns to eaves | d) Medium and heavy silos: heavy ring beam

Figure 1.2: geometries for silos or tanks on discrete supports (Original picture in Rotter (2001a))

The connection of a local support to an elevated cylindrical metal silo shell is a long-standing difficult problem in shell analysis, and most designs are based on simple ideas using past experiences of successes and failures.

The columns can be connected to the stiffening ring, to the skirt, directly on the cylindrical shell or can be connected via a bracket to the cylindrical shell.

Figure 1.3: Pictures of a bracket supported silo (photographs by J.M. Rotter)

Additional stiffening elements might be added to potentially prevent buckling (Figure 1.2)

Smaller silo structures can be supported on local brackets attached to the side of the shell (Figures 1.3 and 1.4), but very few investigations of the behaviour or strength of such an arrangement have ever been made. This support arrangement could become economically valuable for much larger storage structures since shells are very sensitive to buckling under compressive stresses, but with the bracket away from the bottom of the cylinder only part of the loading will be transferred as compression (for further information see Section 1.10). The evaluation of the strength of such a local bracket support is a very challenging task, and has evaded all attempts at hand and simple computer analysis for many decades.

Thin steel cylinders on local supports have been investigated relatively recently. Current design proposals for this kind of support are all in the form of empirical fits to a limited range of computational studies. The behaviour is reasonably well understood, but no physical mechanics model has been produced, even for the simplest types of analysis.

Overall, the case of a bracket supported silo connected to the cylinder at a place

other than at the base of the cylinder has had very limited study and only one of the extreme cases (the perfectly flexible support) has been partially explored.

Therefore the bracket supported silo is the subject of this thesis.

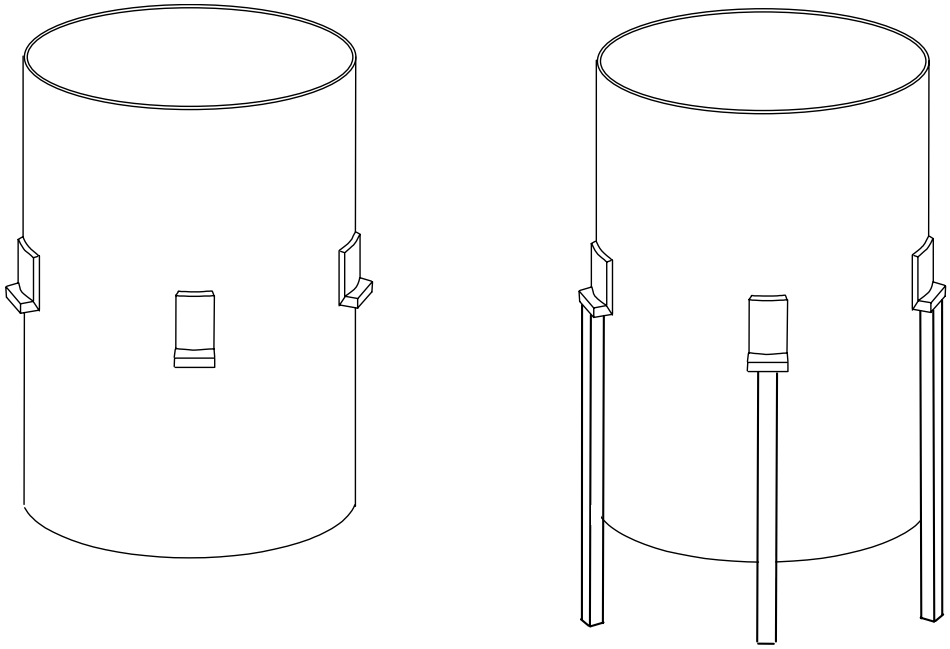

a) brackets attached to the cylinder wall b)columns attached to the bracket

Figure 1.4: schematic sketch of a bracket supported silo

Even though the term silo is used in this document to describe a cylindrical steel container for storage of bulk solids, it also applies to liquid filled liquid storage tanks. The difference between tank and silos is the way the stored material transfers stresses into the structure. Bulk solids transfer a large part of its weight as shear into the silo walls due to high friction coefficient, while fluids only have a small friction coefficient and therefore almost all of the weight is applied at the bottom of the cylinder as tension (more information can be found in Section 1.10).

1.2 An introduction to shell buckling

1.2.1 Introduction

Thin curved shells have been a long standing challenge for engineers, despite their high structural efficiency. Even though research on thin shells has been carried out for a very long time (at least since the beginning of the 20th century e.g. Lorenz, 1908; Timoshenko, 1910), shells are still the most unpredictable structural members

and fail often unexpectedly. This unpredictability is caused by the low bending stiffness in comparison to high membrane stiffness of the shell and makes a shell susceptible to a significant reduction of strength due to any small deviations from the ideal shape.

There is a rich pool of publications in shells research (Flügge (1934), Timoshenko (1936), Timoshenko and Woinowsky-Krieger (1959) Timoshenko and Gere (1961), Novozhilov and Radok (1964), Kraus (1967), Seide (1975), Brush and Almroth (1975), Calladine (1983), Kollár and Dulácska (1984), Yamaki (1984), Bushnell (1985), Teng and Rotter (2004a), Guggenberger *et al.* (2004)). This chapter aims to gives a brief outline of some of the key developments in shell analysis and shell buckling research and the current state of the art.

1.2.2 A short historical outline of buckling in shells

Any historical review of the analysis of buckling must naturally begin with Euler's analysis of the bifurcation buckling of columns. A good description of his work can be found in Timoshenko (1953). In the middle of the 18th century, Euler developed a theory to calculate the complete post-buckling behaviour of a straight pin-ended column under axial compression. As a by-product, he obtained the critical load P_E which is named after him (the Euler load) and is found as the lowest eigenvalue in a stability analysis of a straight column. The deformed state immediately after buckling is in the first eigenmode. In the case of a column with two pinned ends which are not free to translate normal to the axis, the first eigenmode is half a sine wave (Figure 1.5).

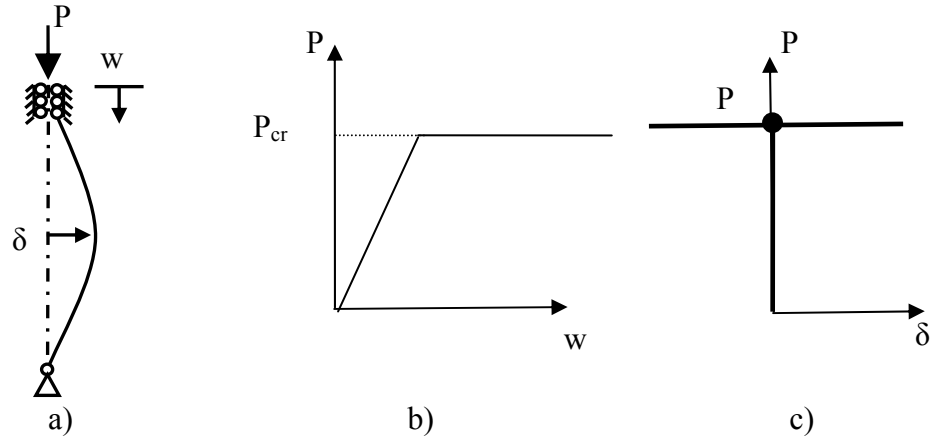

Figure 1.5: Euler buckling of a pinned column

A further development was made by Young (1807), who did not assume the column to be initially straight, but to have the shape of the first eigenmode of Euler buckling. He found that the initial imperfection caused the deflection to rise progressively with increasing load until the Euler load is approached, but that the Euler load cannot be exceeded (under small deformation theory). This same kind of theory was subsequently developed for thin plates by researchers including Timoshenko, Flügge, Lorenz and Southwell (reviewed in Flügge, 1973 and Timoshenko and Gere, 1961). It was found that flat plates display a failure load higher than the predicted classical solution, due to a stable post-buckling path (as shown in Karman *et al.*,1932) (Figure 1.6 and Figure 1.7).

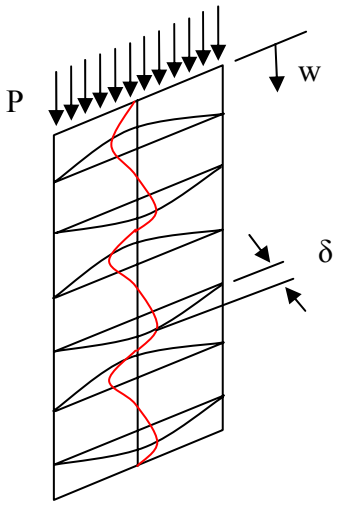

Figure 1.6: Buckles of an simply supported plate

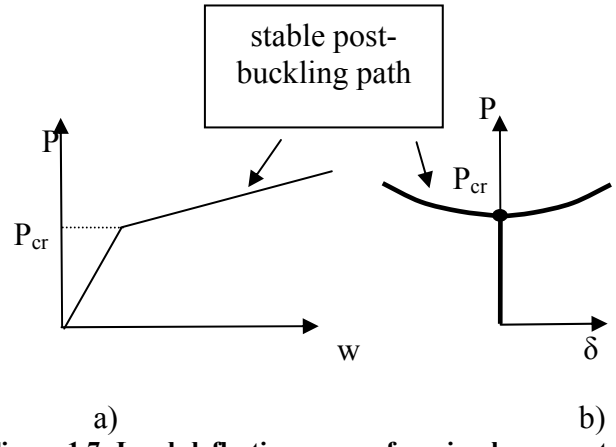

Figure 1.7: Load-deflection curve of an simply supported plate

At the beginning of the 20th century, similar analyses were developed for axially compressed cylindrical shells (Lorenz, 1908; Timoshenko, 1910: Southwell, 1914). They all found that the critical load for a perfect cylinder under a uniform compression should be given by

$$\sigma_{cl} = E\frac{t}{\sqrt{3(1-\nu^2)}R} \tag{1.1}$$

A number of assumptions were required to achieve this simple result. Notably, it was assumed that the cylinder is elastic, is moderately long, has a uniform one-dimensional membrane pre-buckling stress state, and is simply supported at its ends. The discovery of the bifurcation buckling of a perfect axially compressed cylinder (Eq. 1.1) marks the beginning of shell buckling research and despite all the above limitations, this load is still almost universally used as a reference load for more complex shell buckling problems in which axial compression plays a role.

1.2.2.1 Multiple buckling modes

Two kinds of buckling can develop: a ring buckle and several forms of "chessboard" pattern (Figure 1.8). The chessboard form can take many different shapes, since the wavelength in each direction (axial and circumferential) can vary. It was found that the buckling load was largely independent of the mode, so that Equation 1.1 is always valid within the restrictions noted above. Thus, even though the critical load is unique to the cylinder, the buckling mode is not, and several buckling modes can correspond to the same critical load.

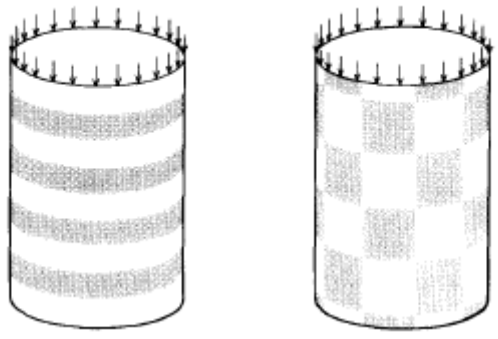

a)ring buckle b)chessboard pattern

Figure 1.8:a) ring buckles b) chessboard pattern in an axially compressed cylinder (original picture in Calladine, 1995)

This effect is due to the closeness of alternative buckling modes in the proximity

of the critical load (e.g. using modern computational methods, Limam (2004) found over 100 buckling modes within 1% of the critical load). The buckling modes usually appear in different "chessboard" patterns with waves both around the circumference and down the axis.

Koiter explored the range of different potential modes and developed a description known as the "Koiter circle" (example in Figure 1.9) which couples the wavelength in each direction with the other (Koiter, 1945: Calladine, 1983). A ring buckle (Figure 1.8a) can be found in the "Koiter circle" (Figure 1.9) when the number of circumferential wave is zero (y=0) and the number of axial waves is nonzero, while the other points of this circle represent buckling in a chessboard pattern (Figure 1.8b).

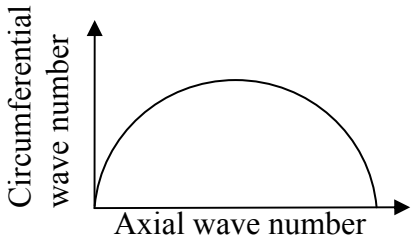

Figure 1.9: Example of a Koiter circle

In the 1930s more load cases on cylindrical shells were investigated analytically by, amongst others, Mises (1914), Donell (1933), Lundquist (1935), Flügge (1932, 1934) and Timoshenko (1936).The main load cases investigated were buckling due to external pressure and due to torsion.

1.2.2.2 Discrepancy between experiments and theory in shell buckling under axial compression

When experiments on shell buckling were conducted to test the bifurcation theories, it was expected that the same outcome would be discovered as for beam or column testing, with the results of a careful test falling within a few percent of the theoretical load. However, this was generally not the case (reported in Kollár and Dulácska, 1984; Donnell and Wan, 1950; Madsen and Hoff, 1965; Weingarten *et al.*, 1965; Wolmir, 1962; Yamaki, 1984; Teng and Rotter, 2004a) and it was found that test results for axially compressed cylinders fell far below the expected critical load

(40%-85% below) and were also very scattered.

Karman and Tsien (1941) produced an complicated nonlinear shell analysis applying an energy method using the shell bending equations developed by Donnell (1934). From the results, they concluded that a small geometrical imperfection could lead to a significant reduction in strength, taking the first step towards the explanation of the disagreement between experiment and theory. This was confirmed by Donnell and Wan (1950). At the same time, Koiter (1945) produced his PhD thesis which explored the phenomena of geometric imperfections and imperfection sensitivity more generally. He developed a much more efficient procedure for estimating determining the strengths of imperfect elastic shells. Due to the war his thesis was only translated into English much later (Koiter, 1945 in Dutch, translation 1970). It is now commonly accepted that initial geometric imperfections play the greatest role in the discrepancy between the classical theory and experiments, at least for axially compressed cylinders.

In the 1960s many different forms of initial geometric imperfections in shells were investigated and it was found that many shells, with different loads and different boundary conditions and different geometries, are sensitive to initial imperfections, but that the sensitivity is very dependent on many other factors. By the end of the 1960s the first computer programs were developed to calculate the elastic buckling failure load including nonlinear pre-buckling deformations and these became available to researchers, as described by Samuelson and Eggwertz (1992). A method of following both rising and falling nonlinear load paths was devised by Riks (1979), and is now widely used in finite element programs (e.g. ABAQUS, HKS, 2003). These programs have made it possible to investigate many more load cases and combinations with fully nonlinear theory, different boundary conditions, non-uniformities of loading and support and initial imperfections of both geometry and residual stress.

1.3 Influence of pre-buckling deformations (geometric nonlinearity)

Because the classical theories for shell buckling adopted a one-dimensional membrane stress state, they effectively assumed that the stresses associated with local bending near the boundaries would not affect the buckling strength. But Donnell (1934) found that under certain circumstances the pre-buckling deformations could be of great importance, and that there could be a significant difference in outcome if the bending was treated as linear (small displacement theory) and if it was treated accounting properly for the deformed shape (large displacement analysis) depending on the length of the cylinder and its boundary conditions. The equations he developed were however rather complicated and difficult to solve.

The influence of the geometric nonlinearity for a uniformly axially compressed shell varies with the length and end boundary conditions but normally lies between the limits 8-15% (reviewed in Yamaki (1984)).

The role of geometric nonlinearity is clearly important in these classical shell buckling problems, but it is not sufficient to account for the huge loss of strength relative to the classical solution that is seen in tests.

On the other hand, geometric nonlinearity in the pre-buckling deformations clearly plays a major role towards failure in some geometries (e.g. the open-topped, wind loaded tank investigated by Brendel and Ramm (1980)). In this case the reduction of strength due to geometric nonlinearity was more significant than the reduction of strength due to the investigated imperfections. This shows that under non-uniform loads, the effect of geometric nonlinearity may possibly be more important than geometric imperfections. This question will be seen to be important later in this thesis.

1.4 Material nonlinearity

Material nonlinearity is a deviation of the material behaviour from purely elastic behaviour. Commonly this means that apart from elastic material behaviour, elastic plastic and plastic material behaviour can be assumed in an analysis. Hence the material can yield (increase of strains without an increase of stresses). While the definition of plasticity is relatively simple when only stresses in one direction occur,

the definition becomes more complex when stresses in three dimensions occur. The basis for the solution to this problem was provided by plasticity theory of Tresca and von Mises (as reviewed in Mendelson, 1968). The plastic behaviour of plates and shells was subsequently investigated (Hopkins and Prager, 1953; Drucker, 1953, reviewed in Massonnet and Save, 1972).

The nonlinear stress-strain behaviour of the material from which the cylinder is made (material nonlinearity) is usually regarded as a minor factor in the reduction of strength. Under the reference uniform loading cases (axial compression, external pressure, uniform torsion), thin shells tend to fail by buckling before any point reaches the yield stress. As a result, it has generally been assumed that buckling studies only need to consider yielding when the shell is quite thick, or when certain special geometries such as torispherical heads are being studied (e.g. Galletly, (1980), Galletly (1982); Wunderlich *et al.*, (1982), Gotsulyak and Zhadrasinov (1985), Lu *et al.* (1995))

However, this is not the case where the load case leads to stress peaks due to other design features, as is the case with a locally supported cylinder. In these cases yielding can occur very early at low load levels and this yielding might reduce the strength of the shell.

The plastic collapse of shells has not been studied extensively, but there have been some investigations. Plastic collapse conditions in cylinders were studied extensively by Hodge and Brooklyn, 1954, Hodge and Panarelli, 1962, Hodge, 1963, 1964, and others in the 1960s. A good summary may be found in Massonnet and Save (1972). These studies were mainly concerned with pressure vessels. A later summary of this field may be found in Gerdeen (1979).

1.5 Strength reduction due to boundary conditions

Imperfections in the boundary conditions have not been found to have a strong influence on the buckling strength, so are not a satisfactory explanation for the reduction of strength. This is the case for most problems studied due to the relative short wave length of the buckling mode in comparison to the global dimensions of the shell (reviewed in Calladine, 1995), the greatest loss of strength due to the

boundary conditions was found when the edges of the shell were free to displace during buckling (reviewed in Teng and Rotter, 2004b). More information on the effects on boundary conditions can also be found in Yamaki (1984).

1.6 Snap-though and bifurcation buckling

The term buckling is often used rather loosely. In fact there are two different kinds of buckling response: bifurcation buckling and snap through buckling. Bifurcation buckling occurs when the primary equilibrium path (pre-buckling) intersects with a secondary equilibrium (post-buckling) path causing a rapid change in the deformed shape of the structure (Figure 1.10). The structure follows a stable path until bifurcation, but then rapidly transfers to the secondary path, which can be stable or unstable depending on the structure and load case. The deformations after buckling look very different from the pre-buckling deformations.

The second kind of buckling is the snap-through or limit point buckling. Snap-through is the consequence of changes of geometry, which can lead to a point of instability when the incremental change of geometry offers no stiffness with respect to the applied load set. As an example of snap-though buckling, an arch with eccentric loading is shown (Figure 1.12). The arch deflects under increasing load and has a lower stiffness in the new (deflected) shape. When it reaches the limit load, it jumps to another point on the same load deflection path (no secondary path involved) (Figure 1.13), which lead to a dramatic change of shape in the post- buckling range (Figure 1.12). In the case of snap through buckling, the deformed shape after buckling is usually similar to the inverted shape of the original configuration. This contrasts with the post-buckling deformation of a bifurcation buckle.

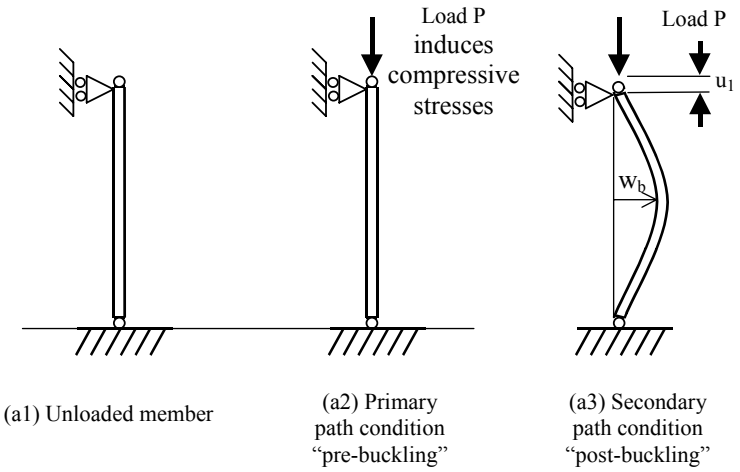

Figure 1.10: Bifurcation of a column (original pictures in ECCS, 2007)

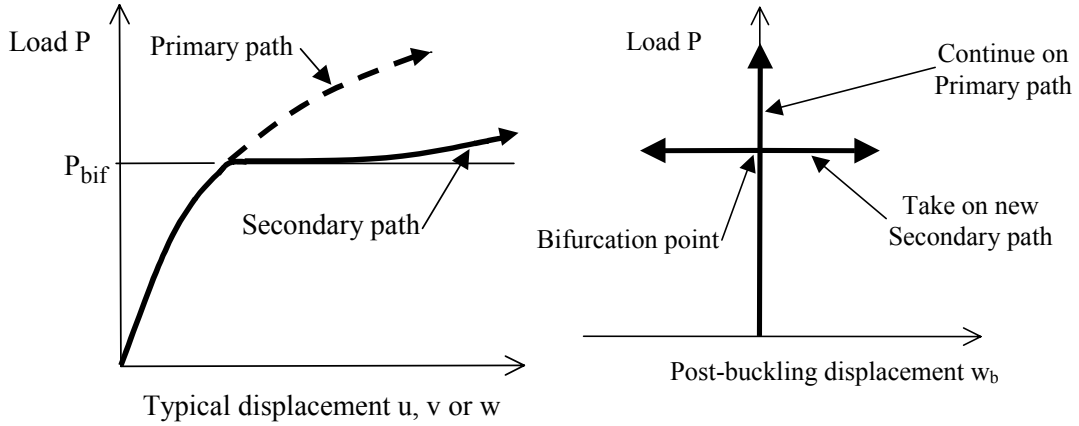

(b2) Any typical displacement in structure (b2) Displacement in buckling mode

Figure 1.11: Load deflection path of a axially compressed column (bifurcation) (original in ECCS, 2007)

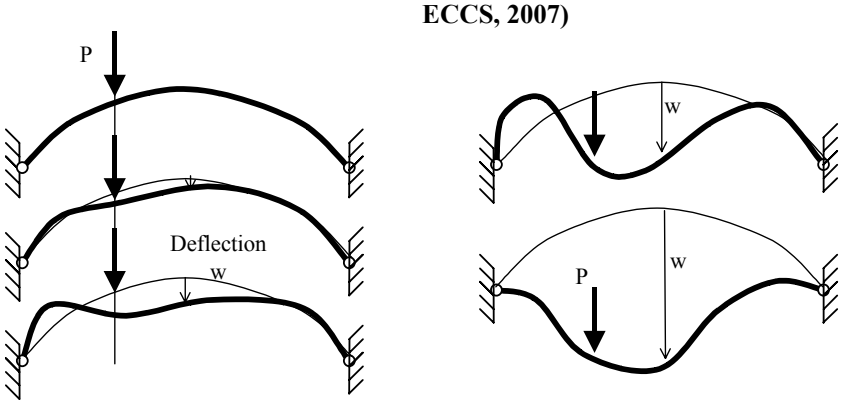

Figure 1.12: Snap though buckling of an arch(original pictures in ECCS, 2007)

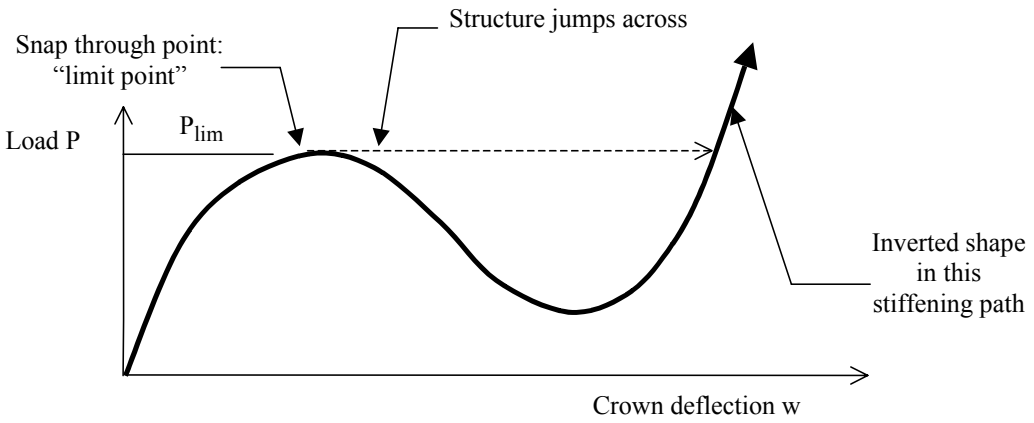

Figure 1.13: Load deflection curve of snap-through buckling (original pictures in ECCS, 2007)

1.7 Imperfection sensitivity in shells

1.7.1 Introduction

The discrepancy between the buckling strength predictions of classical theory and experiments prompted a significant amount of research. The key difficulty was that the experiments on structural members such as beams and columns, even frames and plates matched very well to the theoretical predictions of buckling strength, but this was very often not the case for shells.

One reason for the good agreement between theory and experiments for structural members such as beams and frames is that the failure mechanism usually dominated by plastic collapse due to bending. The global failure of a beam is not far from the first plastic hinge (first cross section completely yielded) and therefore the analytical solution assuming failure at the point where the section has first yielded tends to match experiments very well. When elastic buckling of beams, columns and frames is considered, the match is again quite good because the bifurcation mode is very well defined and the post-buckling behaviour is stable. These two factors cause the buckling load to be rather insensitive to minor discrepancies such as geometric imperfections and imperfections of boundary conditions.

The main reason for the difference between column buckling and shell buckling is that a perfect shell often has many different potential bifurcation modes, and many of these lead to weakening post-buckling paths. Where the post-buckling path is softening, any minor imperfection will lead to a significant reduction in achieved strength, and the structure will appear to be imperfection-sensitive. Thus for a shell

with many weakening post-buckling paths, any deviation from this state (i.e. geometric imperfections, imperfect boundary conditions and imperfect loading conditions) can lead to a significant reduction of the achieved strength below the theoretical value, even if the structure remains elastic.

1.7.2 The shape of geometric imperfections

As mentioned before the first studies of imperfect shells using geometric nonlinearity were performed by Karman and Tsien (1941), Donnell and Wan (1950), Koiter (1945 in Dutch, translation 1970), Hutchinson and Koiter (1970), Yamaki (1984). These repeatedly showed the now accepted wisdom that initial geometric imperfections are the most dominate factor causing a big difference between results obtained in experiments and classical analytical predictions. These initial studies of imperfection sensitivity led to the development of an extensive field of research.

The research changed its focus from the purely analytical approach to a numerical approach when computers became more widely available.

But the shape and amplitude of the imperfection, which should be used to produce a reasonably realistic and damaging result for the strength of the shell was still an unknown. Several different approaches were taken by different research groups to try to identify critical shapes and amplitudes for damaging imperfections.

A very popular choice of imperfection type is the idealised geometric imperfection (e.g. Brendel and Ramm, 1980; Hoehn *et al.*, 2001; Teng and Song, 2001; Cai, 2003; Pinna and Ronalds, 2003; Song *et al.*, 2004; Guggenberger *et al.*, 2004). These imperfections use an idealised shape to permit general conclusions to be reached concerning the effects of different amplitudes. Examples of idealised forms are the first eigenmode, higher order eigenmodes, and a deformed shape extracted from a linear or nonlinear analysis as the initial deformed shape of the shell. When these idealised geometric imperfections are used, the research challenge is generally seen as the task of finding the “worst” imperfection shape and amplitude.

This challenge has sometimes been addressed by searching for the “worst” imperfection shape for a given imperfection amplitude implicitly in the nonlinear finite element analysis (Deml and Wunderlich, 1997; also reviewed in Schmidt, 2000). In order to incorporate this concept, three imperfection degrees of freedom at

each of its node of the shell element were added. The resulting set of nonlinear equations at each load increment are solved for a variable geometry leading to the "definitely worst imperfection shape and therefore to the lowest buckling load possible (as reviewed in Schmidt, 2000).

However, the disadvantage of this approach is that this worst or most damaging imperfection might not be very likely to occur in practical construction. While such imperfections usually result in a significant reduction in strength, the probability that these imperfect shapes occur in a real structure are rather low. It would therefore be better to link this approach with imperfections caused by the fabrication process, which would make the calculated imperfection shape more realistic.

To incorporate more realistic imperfections into the analysis, imperfections resulting from the welding process of the shell were proposed and have been analysed extensively (e.g. Rotter and Teng, 1989; Rotter and Zhang, 1990; Teng and Rotter, 1992b; Pircher and Bridge, 2001; Huebner *et al.*, 2006). These weld imperfections were also analysed incorporating residual stress resulting from the process of welding, but were found to have usually a beneficial effect towards the failure load (Rotter, 1996; Holst *et al.*, 2000; Pircher and Bridge, 2001).

Even though weld imperfections are more realistic than, for example, an eigenmode imperfection, the real structure has many different forms of imperfection, which have naturally a somewhat random distribution due to other fabrication processes. Therefore other researchers approached the problem from a different angle. Small and full scale shells were measured and their actual shape recorded (Elishakoff *et al.* (1987), Singer and Abramovich (1995), Arbocz and Hol (1995), Arbocz (1991) and Ding *et al.* 1996a; b, also reviewed in Teng and Rotter, 2004b) and later used in nonlinear shell buckling analyses by Blachut *et al.* (1991), Chryssanthopoulos *et al.* (1991a; b), Chryssanthopoulos and Poggi (1995), Berry *et al.* (1996), Berry *et al.* (2000) and Zhao and Teng (2003). The method of construction naturally plays a very significant role in determining the form of such imperfections. Most of the above studies were of either space vehicles or pressure vessels, for which the method of fabrication is both different from each other and very different from civil engineering shells. This is consequently a difficult aspect of this methodology. A good summary of this work can be found in Teng and Rotter (2004b).

Using the measured actual shape of a cylinder, an analysis can then be conducted and should lead to an outcome closer to the experimental outcome. Clearly this is important for laboratory experiments, but the imperfections in laboratory specimens are generally different from those measured at full scale. So although this procedure might result in a closer agreement between the analysis and experiment, every single shell must still be measured before the analysis can be conducted. Thus it cannot be applied very easily to the design of full scale shells.

To address this issue in the aerospace field, imperfection databases were constructed (Arbocz, 1982), where the measurements of the imperfections for different shells were recorded. A remaining problem with these databases is that many shell structures are one-off structures, meaning that only one shell will be designed and built and therefore its measurements could not be included in the database. Imperfections also occurred randomly by nature and an imperfection measurement of the shell might not give a accurate description of the imperfections of a similar shell.

To address the difficulty of predicting strength in advance, a probabilistic modelling approach was developed (e.g. Arbocz and Hol, 1995; Schenk and Schueller, 2003; Chryssanthopoulos, 1998; Chryssanthopoulos and Poggi, 1995). A review of "the probabilistic approach to design shell structures" can be found in Arbocz and Stam (2004). In this approach random variables are used to calculate the probability of failure. But the application of this methodology still depends on having a large database of imperfection measurements. While this is possible for expensive structures or when same fabrication process is used to build a number of these structures (e.g. aerospace structures), it is unlikely to be achieved in silos and tanks, which are not as expensive as aerospace structures and are commonly one off structures.

It is natural that the amplitudes of imperfections depend on the quality of fabrication, so it was proposed by Rotter (1985) that different quality classes should be used in the design process, with a direct linkage to the tolerance control during construction. This approach does at least permit the constructed shell to be evaluated afterwards, and if necessary, down-rated for the loading it is permitted to carry.

So far no complete solution has been found to model imperfections, which are

both probable and damaging for any structure for a safe and economic design. It should be noted that even the imperfections measured on a shell do not include all the imperfections present in real structure such as material imperfections, residual stresses and imperfections of joints and boundary conditions.

Some of the well-known approaches to include the imperfection sensitivity into the analysis have been mentioned, but the research field on shell buckling is very extensive and imperfection sensitivity plays a part in most investigations. Hence this review of developments should not be seen as a complete report of the research up to date, but more an extraction of main developments.

1.7.3 Imperfection amplitudes

It is generally accepted that larger imperfection amplitude cause a greater loss of strength compared. But while some form of imperfections cause a rapid loss of strength followed by a stabilisation of the imperfection sensitivity (curve a) in Figure 1.14,other imperfection forms start with a less pronounced imperfection sensitivity, but the loss of strength continues without a stabilizing effect (curve b) in Figure 1.14 (also in e.g. Yamaki, 1984). Therefore the "worst" imperfection does not only depend on the imperfection shape, but also on a specific imperfection amplitude.

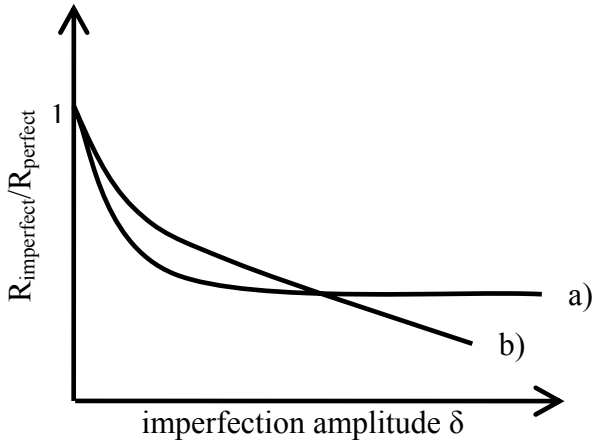

Figure 1.14: Imperfection sensitivity

An example is shown in Figure 1.15, where the linear bifurcation lowest eigenmode (LEM), non linear bifurcation lowest eigenmode (NEM), post-buckling deformed shape (PDP) and weld depression (WD) imperfection forms are all calculated for a cylinder under local axial compression (Song *et al.*., 2004).

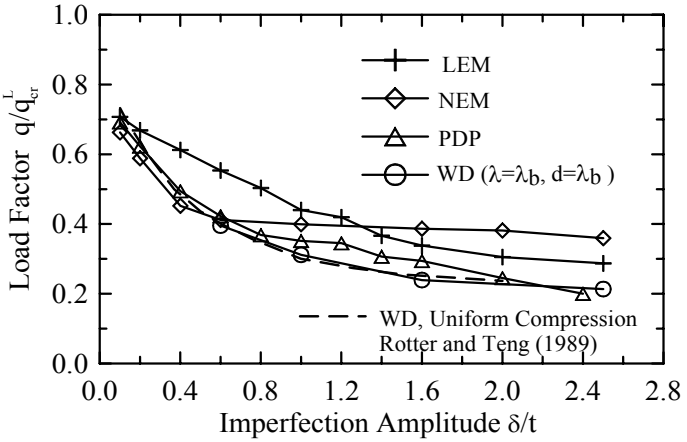

Figure 1.15: Different imperfection sensitivities for different imperfection forms (after Song et al., 2004)

Even though it is commonly accepted after extensive research (e.g. Yamaki, 1984) that larger imperfection amplitudes lead to a greater loss of strength, this is sometimes only true for very small imperfection amplitudes (Figure 1.16).

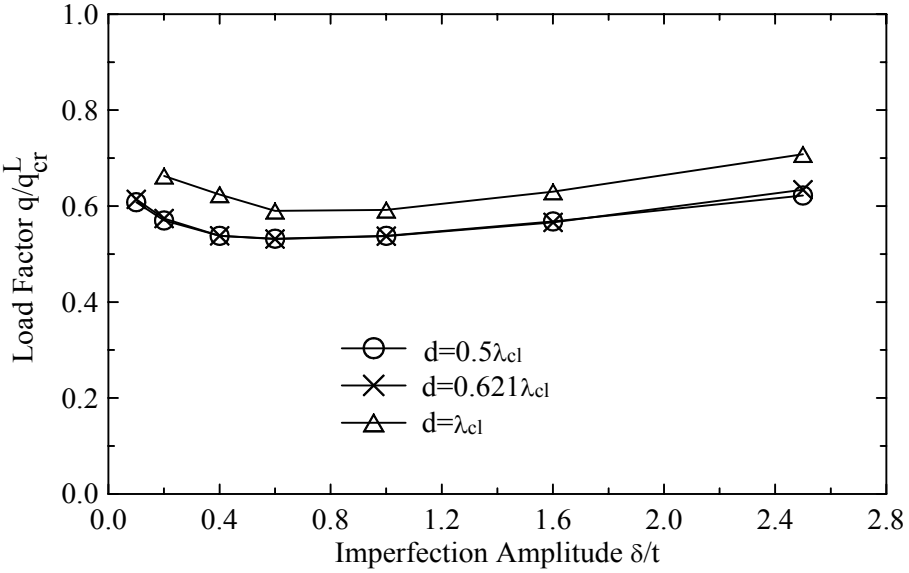

Figure 1.16: Example of descending and ascending imperfection sensitivity curves (after Song et al., 2004)

Therefore a larger imperfection amplitude does not necessarily lead to a more conservative estimate of the buckling strength (Figure 1.16). To avoid the possibility that the imperfection chosen provides a result that lays on a rising part imperfection sensitivity curve several imperfection amplitudes needs to be investigated.

It should be noted that the rules of EN1993-1-6 (2006) define only one equivalent geometric amplitude, though a warning is given in section 8.2.3.1 of the EN1993-1-6 that the calculations should verify that smaller amplitudes do not cause lower resistances.

1.8 Shells subjected to non-uniform loading and stress concentrations

1.8.1 Introduction

Studies of the buckling of shells have concentrated more on the load case of uniform compression of a cylinder than any other situation. This section will explore different loading cases and arrangement of shells, which lead to stress concentrations in the structure even though the loading is applied uniformly. Since this section will address the challenges, which are similar to the challenges found in studying the bracket supported silo, the literature will be reviewed in more detail.

1.8.2 Non-uniform loading conditions

The earliest studies of non-uniform loading conditions sought to determine the linear elastic stress distribution in the shell. An early analytical solution using the classical linear bending theory was conducted with circumferentially varying loading by Bijlaard (1955). He performed a linear analysis using a local patch load normal to the cylinder. The first studies of buckling under such loads used linear bifurcation theory and were performed by Peter (1974) and Libai and Durban (1977). These showed that a perfect shell buckles under this loading condition when the local maximum axial stress is slightly higher than the classical elastic critical stress.

The two non-uniform load cases described here in detail are a patch load normal to the shell and a vertical strip of load with finite length and width. The EN1991-1-4 (2006) specifies the use of a patch load normal to the shell to give an approximate modelling of unsymmetrical pressures on a silo wall as a consequence of eccentric filling or discharge. When the pressure normal to the wall is increased, the vertical stress is also increased because of the long wave bending response of the shell (Rotter, 2001b).

A pair of opposed strips of frictional load acting down the axis of a cylinder was investigated by Cai (2003). The purpose of this investigation was to produce a zone of high local axial stress in the middle of the shell so that the conditions under which

axial stresses cause buckling locally could be thoroughly explored, free of the additional complications of circumferential stresses and boundary conditions. The aim was to try to see what the buckling conditions might be for situations like eccentric discharge in a silo, where the axial compressive stress is locally very high but is far from the boundaries. For different widths of this partial loading, Cai (2003) found that two different kinds of buckle can develop: for narrow load strips of load a central buckle formed, but for wider strips the buckle formed at the edge of the loaded strip. A circumferential weld imperfection was placed at the zone of maximum axial stress and it was found that the imperfection sensitivity in this situation was moderate.

A similar partial load pattern was investigated by Song *et al.* (2004), who applied a local axial load on one boundary of the cylinder. This produced a slightly different stress state in the shell and buckling patterns that were affected by the proximity of the boundary. The edge of the loaded zone caused a discontinuity similar to that found by Cai et al. (2002), and they too discovered two types of buckle: one central to the loaded zone and the other associated with the discontinuity at the edge of the loaded zone. But the focus of their study became the effect of different imperfection shapes on the nonlinear bifurcation load. They studied the effects of imperfections in the form of the linear bifurcation mode, the nonlinear buckling mode, several post-buckling deformed shapes in the perfect shell, and a weld depression. One clear finding was that the linear eigenmode imperfection is far from being the worst imperfection in this case. However, the study also clearly showed that the worst imperfection form depends on the amplitude of the imperfection. For realistic amplitudes of imperfection, the weld depression led to the lowest failure load found in this investigation (Song *et al.*, 2004). However, it should be noted that the placement of this weld depression was critical, and when placed close to the boundary, it also introduced a boundary deviation which may have exacerbated the effect of the weld depression itself.

Patch loads normal to a cylinder lead to a significant loss of strength. These were first studied by Samuelson (1987, 1990) who found that quite small values of pressure acting inward on a local zone could cause very significant buckling strength deteriorations.

Walker (2001) also studied such normal loads using finite element analyses of an imperfect cylinder with a local weld depression imperfection, and found significant imperfection sensitivity.

Song and Teng (2003) studied the effects of different patch loads defined by different national silo design standards. Unfortunately the manner in which these patch loads were defined in these older standards was not very representative of true silo load cases, and the overall conclusion of their study was that such patch loads did not have a significant detrimental effect on the failure behaviour.

Gillie and Rotter (2002) performed extensive linear elastic analyses of cylinders subject to patch loads of different shapes and in different locations. They concluded that such patch loads have the potential to produce considerable von Mises stresses and axial compressive membrane stresses which could lead to either plastic failure or buckling. The response of the shell loaded with a patch load is clearly extremely complex.

1.8.3 Shells on local supports

1.8.4 Introduction

A special case of a shell subject to local loads leading to stress concentrations is the locally supported cylinder. In this case, it is not the applied loading that is non-uniform, but the supports that are discrete and lead to local stress concentrations.

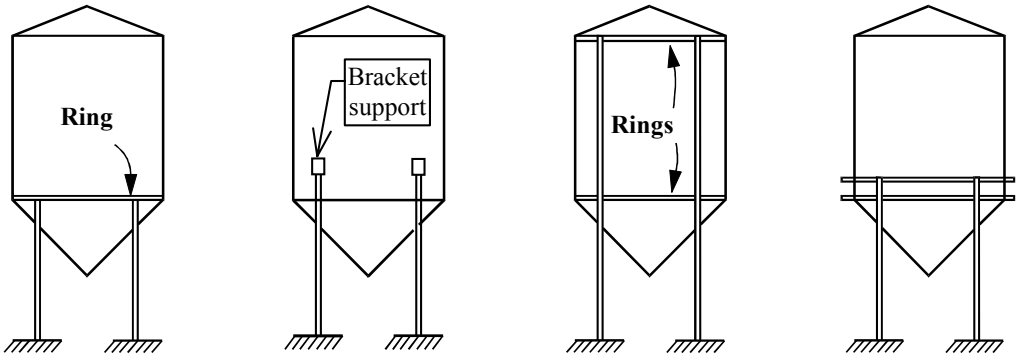

a) supports beneath cylinder | b) bracket supports | c) full length columns attached to wall | d) ring girder for large silos

Figure 1.17: Different support arrangements

In practice many shell structures, such as silos, are often supported on local supports in the form of columns to create the clearance for vehicles or conveyer belts

to be loaded directly from the silo. Even though this application is common in practice it has only been studied by researchers recently. Different support arrangements are possible (Figure 1.17). The columns are either attached to the bottom of the cylinder (Figure 1.17a), to brackets at any height on the cylinder (Figure 1.17b), where the brackets are welded onto the cylinder or the columns themselves are attached over a part or the whole length of the cylinder (engaged columns, Figure 1.17c). When the columns are positioned underneath the cylinder circumferential stiffeners (e.g. ring stiffeners or skirts for larger silos) might be necessary (Figure 1.17a d). These stiffeners are included to prevent buckling failures (Rotter, 2001a).

The first simple membrane theory calculations were probably performed in the 1930s by Flügge (1973), but the first linear shell analysis was that of Kildegaard (1969), which illustrated the complexity of the problem. This analysis covered only discrete point forces on the bottom boundary of a cylinder.

The stress patterns arising from local supports, which introduce axial forces into the bottom part of a cylinder were explored by Gould *et al.* (1976) who were mostly concerned with the complex stress patterns and load transfer from an engaged support into the shell. Later Rotter (1982) studied a similar problem of a silo with a ring girder on local supports, but the principal focus of that study was the very complex pattern of stresses that develop in such a ring. The decay of local axial compression in the cylinder was treated as secondary.

1.8.5 Computational studies of discrete supports at Edinburgh and Graz

In the past two decades, research on the behaviour of cylinders above local supports became more extensive. Comprehensive studies in Graz and Edinburgh investigated the effect of local supports underneath the cylinder, whilst experiments were conducted in both Gent and Edinburgh. The main load case investigated by the group in Graz (Figure 1.18) was uniform compression on the top boundary of a cylinder with the other boundary on a local support (Greiner and Guggenberger, 1998; Guggenberger, 1998; Guggenberger *et al.*, 2000; Guggenberger, 2006). This is a suitable load case for experimental testing, but a very approximate model for

realistic silo or tank loads (since most of the axial compression derives towards the bottom of the cylinder, or else is applied in tension at the bottom by a hopper).

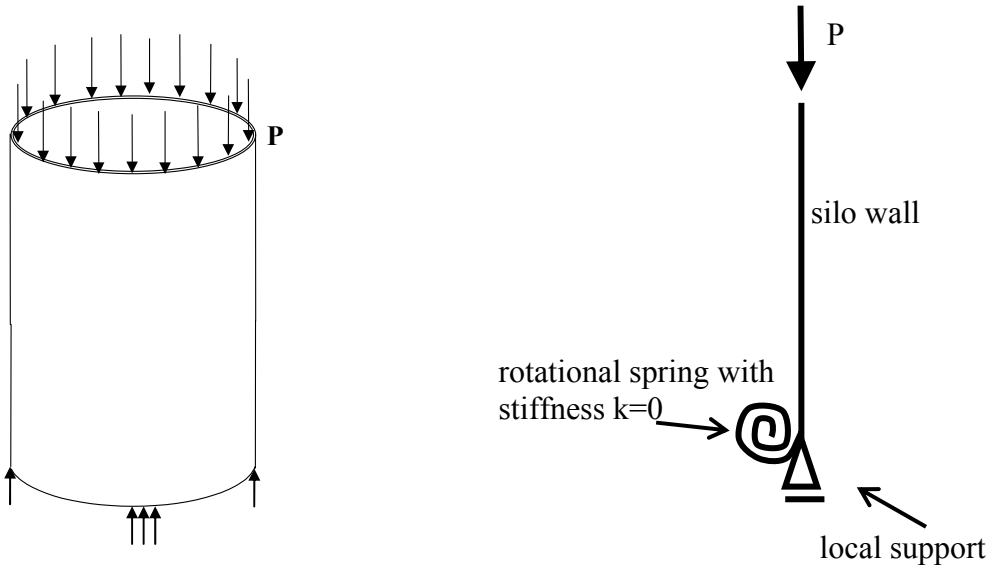

a) discretely supported silo b) rotational spring at the local support

Figure 1.18: Sketch of the discretely supported silo and rotational spring investigated in Graz

These studies assumed an unstiffened shell (i.e. no stiffening element at all on the cylinder like a ring stiffener) to explore the behaviour of this basic case before moving towards the more complex case of different stiffening elements. All the studies used only four supports which were treated as flexible (free to rotate around the circumferential axis, k=0 in Figure 1.18). A second load case in which internal pressure was included was studied by Greiner and Guggenberger (1998). In practice, internal pressure is introduced by stored solids or liquids which induce circumferential membrane stresses. These act together with the assumed compression at the shell boundary. The study found that even though the internal pressure causes a reduction in the load carrying capacity in a geometrically nonlinear elastic analysis (GNA) and in a geometrically and materially nonlinear analysis (GMNA), it had a beneficial effect on the load carrying capacity when the cylinder was treated as imperfect in a geometrically and materially nonlinear analysis with imperfections (GMNIA). This finding matches that for internally pressurised cylinders under uniform axial compression, so is perhaps less remarkable than it appears at first sight.

The imperfection chosen in this study was an approximate model of the post-

buckling mode of the perfect elastic shell. Due to the beneficial effect of the internal pressure in the most sophisticated analysis (GMNIA) it was proposed that the effect of the internal pressure should be ignored to achieve a conservative estimate of the failure load.

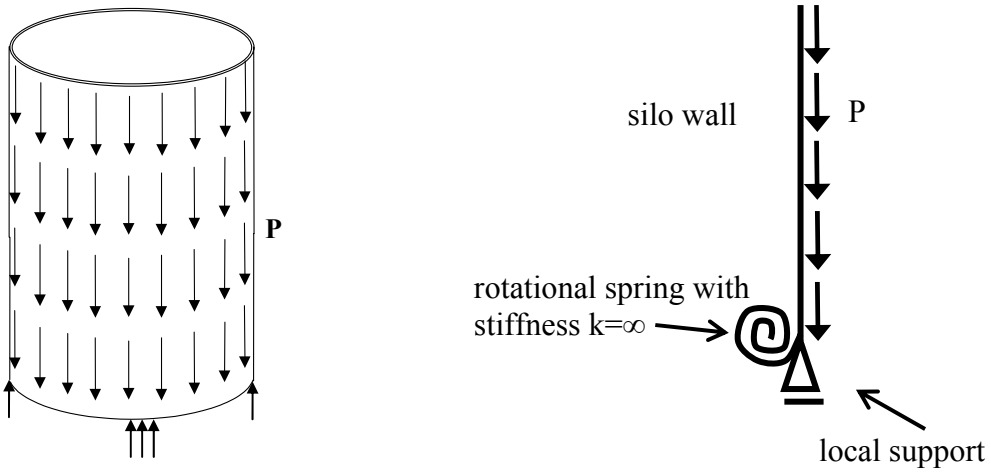

a) discretely supported silo b) rotational spring at the local support

Figure 1.19: Sketch of the discretely supported silo and rotational spring investigated in Edinburgh

At the same period as the above studies in Graz, the research group in Edinburgh produced several studies of locally supported cylinders, using both geometrically and nonlinear analysis with both elastic and materially nonlinear models (Teng and Rotter, 1990; Rotter *et al.*, 1991; Teng and Rotter, 1992a, She and Rotter, 1993; Li, 1994; Li and Rotter, 1996). The loading condition used was uniform wall friction down the shell, which induced progressively rising axial compression () , but which was still conservative relative to real silo loads. These studies examined the behaviour of cylinders with many different numbers of supports, which were all treated as rigid (k=∞, Figure 1.19), producing a rather different stress state locally in the shell. The adopted imperfection was a weld depression, which was placed a short distance above the support: this choice was influenced by the evidence from measurements on full scale silos (Rotter *et al.*, 1992; Ding *et al.*, 1996b). These studies also included the effects of internal pressure (Li, 1994), and reached the same conclusion that internal pressure is beneficial.

Teng and Rotter (1990) performed bifurcation and non-linear analyses of a silo supported on columns performed using the finite element program LUSAS. The

supports were rigid. In a rigid support, the displacement of the shell above the supports in vertical direction is constant over the width of the support, whereas the stresses of the shell above the support are constant over the width of a flexible support. The study was restricted to a single shell geometry with a varying number of column supports.

In a further study by Teng and Rotter (1992a) using the finite element program LUSAS investigated the effects of flexible supports, the effects of changing various parameters such as the silo radius to thickness ratio, the boundary conditions at the top and bottom of the silo and the number and width of the column supports. The loading was treated as a uniformly distributed axisymmetric downward meridional traction on the cylinder modelling the friction on the silo wall due to the stored bulk solid. The results showed that the number of supports has little effect on linear buckling strength within practical limits since buckling is highly localized and the stress distribution above one column does not influence the stress distribution near the next column as long as the span in between is large enough. In this investigation the first interactions between columns was found for a silo on 16 columns, which is certainly an unusual configuration.

The same reasoning applied to the height of the cylinder. As long as the cylinder is long enough to prevent interaction with the top boundary condition, the height of the cylinder does not influence the buckling strength. The bracket width was found to have a significant influence for narrow brackets, but this influences decreases with increasing width. Furthermore it was found that flexible supports reduced the strength significantly.

As part of the Edinburgh investigation, a comprehensive computational study of the locally supported silo was carried out by Li, 1994. The supports were modelled underneath the cylinder. The finite element program ABAQUS (HKS, 2003) was used for this numerical model. Three loading cases were investigated. The range of geometries used was limited, but different analyses with different levels of sophistication were used to describe the behaviour.

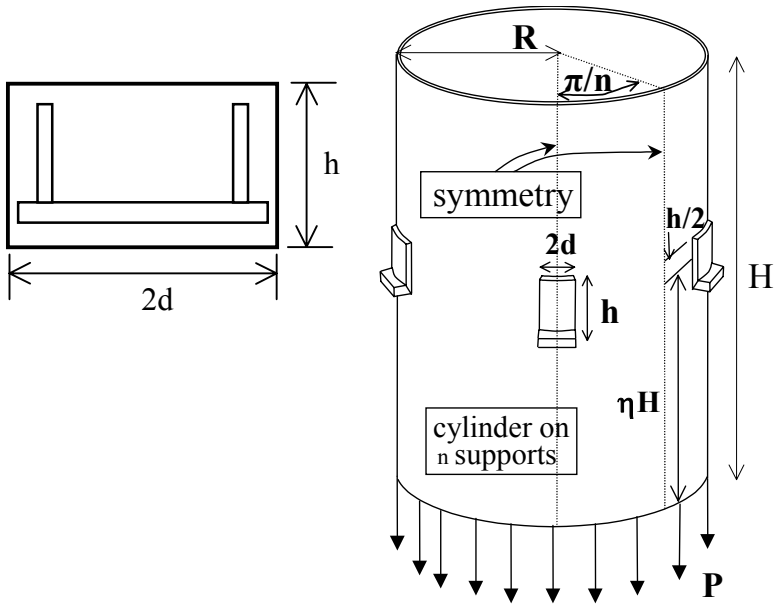

a) bracket dimensions b) shell dimensions and notation

Figure 1.20: Sketch of a bracket supported silo with the bracket located at mid-height

The research groups in Graz and Edinburgh jointly published a first proposal for design rules for axially loaded steel cylinders on local supports (Guggenberger et al. ,1998). The proposal involved substantial work in reconciling the results that the two groups had obtained (particularly because of the different load cases assumed and the different forms of imperfection studied), with different components being contributed from the two groups. These proposals included rules for both flexible and rigid supports, but they were based only on computational studies (Guggenberger et al., 1998).

In his most recent publication, Guggenberger (2006) explored the elastic stability and imperfection sensitivity of axially loaded shells on very narrow supports. An eigenvalue analysis of a cylinder with point support was investigated amongst other aspects. This is a slightly strange study, since it was established at a very early stage that narrow supports lead to predominantly plastic failures, whilst wide supports produce buckling under relatively elastic conditions. A point supported silo is a purely theoretical structure, but the outcome may provide a basis for further more practical supports. Nevertheless, in the context of what follows in this thesis, it may be said that the most useful aspect of this study is the identification of the linear bifurcation load (LBA) for a point supported cylinder.

All of the above studies focused on local supports directly underneath the middle surface of the silo wall, and no eccentricities relative to this location were explored.

1.8.6 Eccentricities at discrete supports

The first researchers to investigate the effect of the eccentricity of the support in a column supported cylinder were Gould and Sen (1974) using a linear elastic analysis. The columns in this study were not placed directly underneath the cylinder (Figure 1.17a), but were connected to the cylinder wall over a part of the height of the silo (Figure 1.17c). The moment introduced into the shell due to eccentrically placed column condition was studied by Gould and Sen, 1974, Gould *et al.*, 1976. Gould and Sen (1974) derived a simple algebraic expression for the moment transmitted to the wall of a tank by eccentric brackets when the column is assumed to be rigid, but simply supported. The distribution of radial stresses transmitted to the shell by the support was simplified to be linear over the height of the part of the column, which was attached to the silo wall.

A later study by Gould *et al.* (1976) analysed the effect of an eccentric column attached to a cylinder with conical hopper. The analyses were all linear elastic (LA). The investigation also explored the effect of ring-beam stiffeners.

The main finding of these studies was that a cylinder without ring beam transmits high localized compressive membrane stresses into a silo or tank wall in addition to the bending moments from the eccentricity of the support. By contrast, ring-stiffened cylinders have stress states that are closer to the membrane theory.

Recent studies in Edinburgh (Gillie *et al.*, 2002; Holst *et al.*, 2002; Gillie and Holst, 2003) explored another kind of silo support including eccentricity; the bracket supported silo. These researchers used the finite element program ABAQUS (HKS, 2003).

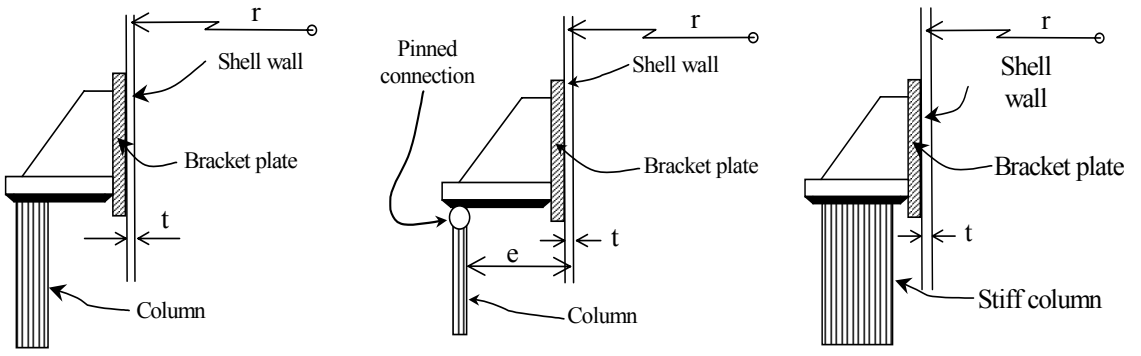

a) general arrangement b) pinned bracket c) rotationally stiff bracket

Figure 1.21: Alternative treatments of the bracket support

In this case the support is connected to the cylinder at mid-height (Figure 1.20b)

instead of being placed underneath the cylinder (Figure 1.17a). When the support, in this case a bracket, is connected to the cylinder at mid-height the stress distribution around the bracket (including tension on the bottom and shear on the side of the bracket) dominates the failure behaviour.

In these studies a pinned connection between the bracket and its supporting column was chosen (Figure 1.21b), modelling a very flexible column. This bracket support was free to rotate around the circumferential axis as well as to move in radial direction and the moment introduced by the eccentricity of the bracket plays an important part in reducing the strength and buckling load of the cylinder. As indicated in Figure 1.20a the bracket was assumed to have additional vertical stiffeners. These stiffeners were not modelled separately. Instead it was assumed that they will only provide additional stiffness to the bracket. Therefore, as a simplification, the bracket itself was modelled as infinitely stiff (Holst *et al.*, 2002; Gillie *et al.*, 2002; Gillie and Holst, 2003). The main load case in all three investigations was tension at the bottom of the silo, which is not as damaging as either compression on the top (as assumed in the Graz studies) or uniform friction down the whole cylinder (as assumed in the earlier Edinburgh studies).

This load case represents the load transmitted from a stored bulk solid onto the silo structure primarily by gravity loads on the hopper, which then produces a tensile axial membrane forces in the lower part of the silo wall.

Since different levels of sophistication can be chosen for the strength analysis, the failure criteria for each analysis must be defined. The different failure criteria to be used for shells on local supports were adopted by Holst *et al.* (2002) from the draft European Standard (ENV1993-1-6, 1999).

A major observation in Holst *et al.* (2002) is that the load deflection path extracted from material nonlinear analysis (i.e. plastic collapse of the structure) did not achieve a plateau even at relatively large deflections. Gillie *et al.* (2002) and Gillie and Holst (2003) proposed that a maximum bracket rotation should be chosen as a failure criterion for plastic collapse when no plateau could be reached. This proposal followed as a special case of the failure criterion given in ENV1993-1-6 (1999).

The eccentricity of the bracket causes a moment to be induced when the bracket

is free to rotate about the circumferential axis.

For small eccentricities, the silo fails by buckling, but at large eccentricities a plastic collapse was found by Gillie *et al.* (2002). In these investigations of Gillie *et al.* (2002) and Gillie and Holst (2003), the local support was free to rotate about the circumferential axis, but was at mid-height of the silo rather than at the bottom of the silo as in the earlier Graz and Edinburgh studies. The imperfection sensitivity studies produced some surprising findings. It was found that there was an extreme sensitivity to eigenmode imperfections and to weld depression imperfections that were relatively distant from the bracket, but weld imperfections situated just above the bracket were found to increase the strength of the silo. This outcome was perhaps not expected.

When the bracket is assumed to be rigid (Figure 1.20a) and rigidly connected to a stiff column (i.e. only free to move radially, but not to rotate about the circumferential axis) (Figure 1.21c) the effect of the eccentricity disappears, since no moment can be introduced by it (Doerich, 2002). This condition is the subject of this thesis, so the results naturally contrast with the findings of Gillie *et al.* (2002) and Gillie and Holst (2003).

A more recent development is research on engaged columns (Figure 1.17c) (Zhao and Yu, 2005). The columns are welded or bolted onto the silo wall either over the full height or over part of the height of the cylinder. This case is a logical development from the bracket supported silo. In this first simple study (Zhao and Yu, 2005), linear buckling analyses (LBA) showed that the bifurcation load increases with the width of the column as well as the length of the column, which is attached to the cylinder. The geometrically nonlinear elastic analysis (GNA) showed local dimple above the column termination for columns, which are attached to the cylinder for up to 80 % of the cylinder height. For longer columns no such dimple could be found. It might be judged from pictures provided in Zhao and Yu (2005) that buckles appear beside the engaged column as a consequence of the shear transfer, but no mention had been made about the occurrence of shear buckles or the failure mode for very long columns.

1.9 The Eurocode

The literature shows clearly that computerized numerical calculations have largely replaced analytical analyses in the study of shell buckling. The advantage of computerized numerical analyses is that more complex and sophisticated structures can be analysed. However, these analyses require the designer and the researcher to have a very good understanding of the behaviour of the structure, since only the end result of the numerical solution is available. This might lead to the misconception that every result computed by a finite element program is the correct result. More than ever before, designers and researchers need to be very aware of the dangers resulting from this misconception. Since the solution of a problem is usually not known at the beginning, it is very difficult to judge if a numerical solution is correct. Therefore very careful studies need to be undertaken before the analysis of the actual problem. The elements and meshes as well as boundary conditions and loading used in the analysis need to be checked very carefully. Moreover, checks against standard benchmark reference problems, against other existing calculations, and where possible against experimental findings, are all very necessary parts of the verification that the computer program and the numerical model of the system are both functioning as expected.

The next challenge for the designer and the researcher is to decide what kind of analysis should be used and what kinds of simplification will still produce an adequate solution.

But in the past, even when an adequate solution was achieved, sometimes it could not be incorporated into the design process because the design standards did not take numerical solutions properly into account, since these standards (e.g. DIN18800, 1990) generally took the view that their role was to define the strength of single structural members, such as columns and beams, but the determination of the stress resultants acting on them was a matter for the designer. Furthermore, these standards were all, and predominantly still are, focussed on the use of hand calculations for the design. Even so, some of the assumptions behind this methodology are not valid, as described by Rotter (2002).

Therefore a standard was needed that would regulate the use of more sophisticated analyses for special problems. Nowhere was this more necessary than

in the design of shell structures, which display a great range of behaviours and are complicated to analyse by hand. As a result of this situation, the drafting committee for the European shell structures standard (EN1993-1-6, 2006) chose to try to address all kinds of analysis and to regulate their use and the interpretation of the outcomes. This standard describes different kinds of numerical analyses and their definition of failure (Rotter, 1998b, 2005). This offers great progress for designers. It is now possible to calculate using many different kinds of finite element analysis and to use the recommendations in the standard to undertake the design of a complicated shell structure. The standard describes the complete strength of a shell with the interaction of all the effects that were individually studied before, using a capacity curve to describe the interactions between stability and plasticity (Rotter, 2002). As a result, extensive empiricism is no longer necessary when describing the strength of shells. The EN1993-1-6, 2006 is not restricted to a few specific problems, but is a generic code, where non-standard problems such as the locally supported shells can be analysed without being specifically defined as a recognised shell buckling problem (Rotter, 2002).

The Eurocode (EN1993-1-6, 2006) covers not only the use of numerical analyses: it also fully specifies the hand-calculation method for standard designs.

When the numerical approach is used, this standard also provides numerical design benchmark test for the verification of meshes and elements. Further details about the structure and philosophy of the standard can be found in Rotter (2002, 2005,).

The standard requires the calculation of the dimensionless slenderness of any structure, which is defined by

$$\bar{\lambda} = \sqrt{R_{pl} / R_{cr}} \tag{1.2}$$

where R_{cr} is the elastic critical resistance and R_{pl} is the plastic reference resistance. These two reference strengths calculate the two different idealized phenomena: pure linear elastic bifurcation buckling as the exemplar of stability failure and small displacement theory plastic collapse as material breakdown.

Different levels of analysis are described in the Eurocode at different levels of sophistication (Table 1.1).

The linear elastic analysis (LA) is based on small displacement theory and a

linear elastic material model of the perfect structure, but it includes both stretching and bending deformations. It can also be used to estimate the plastic collapse or plastic reference resistance R_{pl} using Ilyushin yield criterion (Ilyushin, 1948) at the point of first yield. The approximation of the plastic collapse load using the Ilyushin criterion is sometimes reasonably close to the true plastic collapse load if the stress field is close to uniform. When the structure has some kind of high stress concentration, the plastic collapse load is easily greatly underestimated by the use of an LA analysis, since the stress concentrations do not typically lead to a plastic failure. Instead, the development of a full plastic failure mechanism is required before failure can occur.

Type of analysis	Shell theory	Material law	Shell geometry
Membrane theory of shells	membrane equilibrium	not applicable	perfect
Linear elastic shell analysis (LA)	linear bending and stretching	linear	perfect
Linear elastic bifurcation analysis (LBA)	linear bending and stretching	linear	perfect
Geometrically non-linear elastic analysis (GNA)	non-linear	linear	perfect
Materially non-linear analysis (MNA)	linear	non-linear	perfect
Geometrically and materially non-linear analysis (GMNA)	non-linear	non-linear	perfect
Geometrically non-linear elastic analysis with imperfections (GNIA)	non-linear	linear	imperfect
Geometrically and materially non-linear analysis with imperfections (GMNIA)	non-linear	non-linear	imperfect

Table 1.1: Terminology used in EN1993-1-6 (2006) (original table in EN1993-1-6, ,2006)

The linear bifurcation analysis (LBA) is an eigenvalue analysis using small displacement theory with linear elastic material properties and without imperfections. It is based on the stresses derived from a linear elastic analysis (LA). The linear bifurcation analysis is used to determine the elastic critical resistance R_{cr} of the structure. It should be noted that this analysis cannot detect snap-through buckling and care should be taken when snap-though buckling is possible for a structure.

Snap-though and bifurcation buckling can be detected with a geometrically nonlinear elastic analysis (GNA). Pre-buckling deformations are taken into account using large displacement theory. Pure buckling behaviour without the influence of material nonlinearity or imperfections can be studied using this analysis. As most thin shell buckling problems exhibit little plastic behaviour, this analysis is often seen to be accurate enough for the strength assessment of a perfect shell. When an explicit model of imperfections is introduced into the geometrically nonlinear elastic analysis, the term used in the Eurocode changes to geometrically nonlinear analysis with imperfections (GNIA).

An accurate value for the plastic reference resistance R_{pl} can only be determined with materially nonlinear analysis (MNA). Small displacement theory and a nonlinear material model of the perfect shell are used in this analysis.

While the GNA analysis considered only the nonlinear buckling behaviour and the MNA materially nonlinear analysis considered only the plastic collapse, a geometrically and materially nonlinear analysis (GMNA) unites these two aspects of behaviour in one analysis using large deflection theory and nonlinear material properties. This analysis gives an accurate description of the perfect shell or of imperfection insensitive structures. The terminology changes to materially and geometrically analysis with imperfections (GMNIA), when explicit modelling of imperfections is introduced into the system.

The reference loads R_{cr} and R_{pl} obtained using the analyses above are used to determine the relative slenderness of the structure (Eq. 1.2). The relative slenderness can then be used to obtain the characteristic strength χ of the structure using the general capacity curve with

$$\chi = R_{GMN(I)A} \big/ R_{pl} \tag{1.3}$$

,assuming that the capacity curve parameters for the structure already exist.

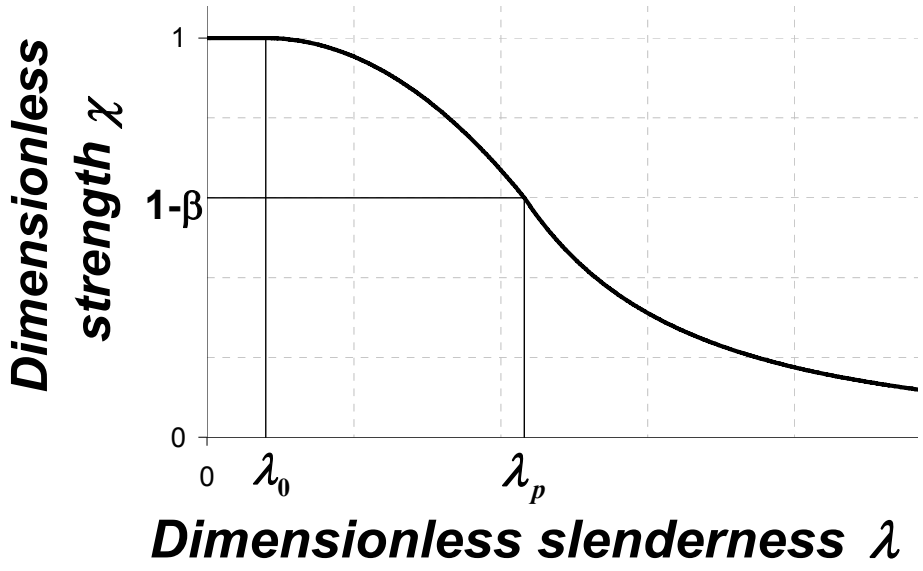

Figure 1.22: General capacity curve

If the capacity curve is not known yet for the structure, further analyses have to be performed. A fully nonlinear analysis (GMNIA) including imperfections must be performed.

When the imperfection sensitivity of the shell plays a significant role in its failure behaviour, either a GMNIA or a GNIA analysis must be performed. For these analyses an imperfection shape and amplitude have to be chosen.

The standard (EN1993-1-6, 2006) addresses the challenge of imperfection amplitudes by dividing all structures into different quality classes. For each quality class, a different maximum imperfection amplitude is defined, depending on the geometry of the structure. The following paragraph is taken from EN1993-1-6 (2006) identifying the imperfection amplitude depending on the fabrication tolerance.

(18) The amplitude of the adopted equivalent geometric imperfection form should be taken as dependent on the fabrication tolerance quality class. The maximum deviation of the geometry of the equivalent imperfection from the perfect shape $\Delta w_{0,eq}$ should be the larger of $\Delta w_{0,eq,1}$ and $\Delta w_{0,eq,2}$, where:

$$\Delta w_{0,eq,1} = \ell_g \; U_{n1} \qquad \text{... (8.29)}$$

$$\Delta w_{0,eq,2} = n_i \; t \; U_{n2} \qquad \text{... (8.30)}$$

where:

ℓ_g is all relevant gauge lengths according to 8.4.4 (2);
t is the local shell wall thickness;
n_i is a multiplier to achieve an appropriate tolerance level;
U_{n1} and U_{n2} are the dimple imperfection amplitude parameters for the relevant fabrication tolerance quality class.

Concerning the choice of imperfection form, which was discussed at some length above, the standard indicates that a number of different imperfection shapes should be considered. These include:

- out-of-roundness (deviation from circularity),

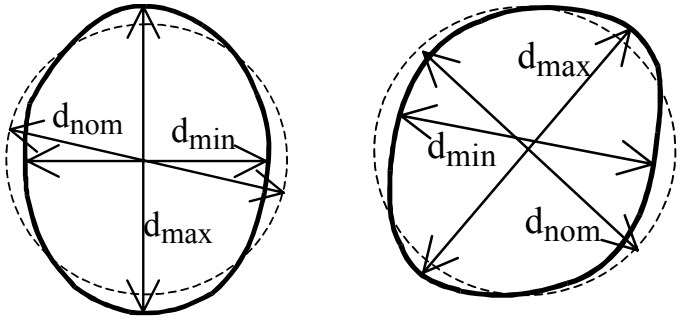

a) flattening b) unsymmetrical

Figure 1.23: Measurement of diameters for assessment of out-of-roundness (original in EN1993-1-6, 2006)

- eccentricities (deviations from a continuous middle surface in the direction normal to the shell across the junctions between plates),

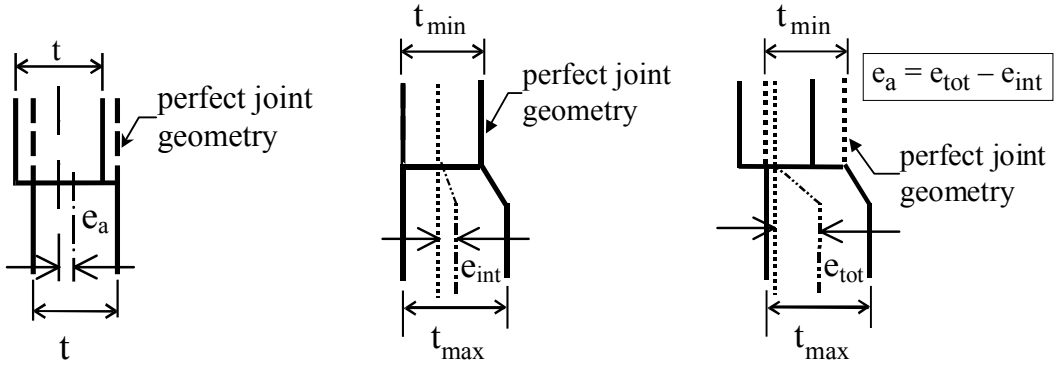

a) unintended eccentricity when there is no change of plate thickness

b) intended offset at a change of plate thickness without unintended eccentricity

c)total eccentricity (unintended plus intended) at change of plate thickness

Figure 1.24: Unintended eccentricity and intended offset at a joint (original in EN1993-1-6, 2006)

- local dimples (local normal deviations from the nominal middle surface),

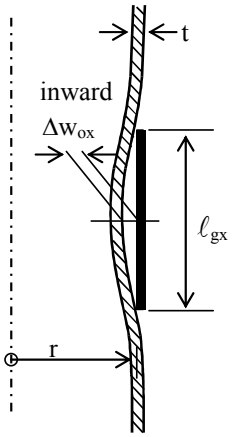

a) Measurement on a meridian
(see 8.4.4 (2) a))

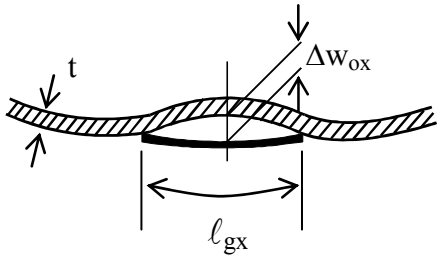

b) First measurement on a circumferential circle
(see 8.4.4 (2) a))

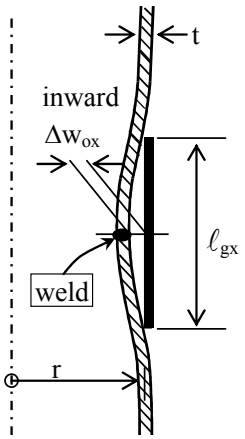

c) First measurement on a meridian across a weld
(see 8.4.4 (2) c))

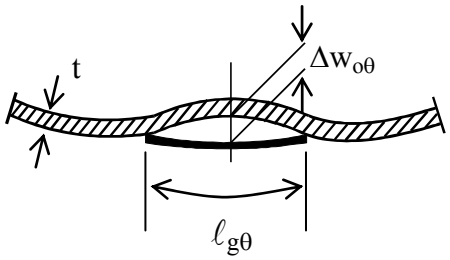

d) Second measurement on a circumferential circle
(see 8.4.4 (2) b))

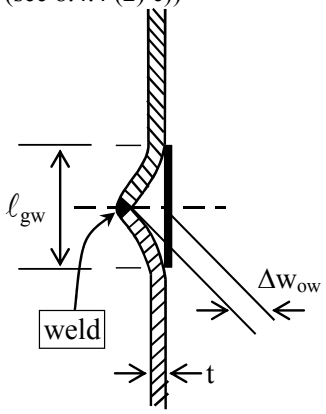

e) Second measurement on a meridian across a weld with special gauge
(see 8.4.4 (2) c))

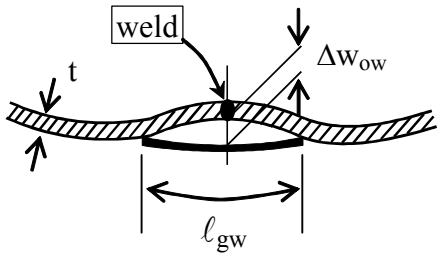

f) Measurements on a circumferential circle across a weld
(see 8.4.4 (2) c))

- material imperfections, such as: residual stresses caused by rolling, pressing, welding, straightening etc.;
- inhomogeneities and anisotropies, irregularities at and near welds (minor eccentricities, shrinkage depressions, rolling curvature errors),
- deviations from nominal thickness;
- lack of evenness of supports.

The standard also specifies that "The sign of the equivalent geometric imperfections should be chosen in such a manner that the maximum initial shape deviations are unfavourably oriented towards the centre of the shell curvature" and "The eigenmode-affine pattern should be used unless a different unfavourable pattern can be justified." These two definitions have influenced choices made in this thesis concerning the shape and direction of chosen imperfections.

In general, the framework of (EN1993-1-6, 2006) not only applies to the designer, but also to researchers. It defines a unified way of displaying the behaviour of a shell structure and studies from different researchers or different fields are made much more easily comparable and comprehensible. With only a few parameters the important aspect of the strength and stability of the shell, such as the influence of the geometric nonlinearity or the onset of plastic buckling. A more detailed discussion can be found in Chapter 6. It greatly reduces the empiricism (e. g. Guggenberger, 1998) that has been widespread in the field of shell stability

The framework of the EN1993-1-6 (2006) was applied throughout this thesis. It is believed that this thesis is one of the first studies in which the power of this framework has been put to the test to determine whether it can provide a simple methodology for exploring challenging shell buckling problems that involve many parameters.

Other structural design standards that are relevant to this thesis and are internationally acknowledged are:

Eurocode 3: Design of steel structures: Part 4.1: Steel silos: EN1993-4-1, 2007

Eurocode 3: Design of steel structures: Part 4.2: Steel tanks:EN1993-4-2, 2007

1.10 Loading condition

A silo will experience a number of different loading conditions during its lifetime. These loading conditions can be split into different categories: static loading conditions due to the bulk solid or fluid (Rotter, 2001a), loading due to operational procedures like discharging of the silo (e.g. Ooi *et al.*, 1990; Rotter, 2001a ; Rotter, 2007).

The effect of these loading conditions on a typical silo shell structure have been the subject of many individual studies: for example, studies of the structural consequences of filling and discharge (e.g. Rotter *et al.*, 1989), external sources like wind loading (e.g. Brendel *et al.*, 1981), seismic loading (e.g. Wunderlich and Seiler, 2000; Virella *et al.*, 2006; Rotter and Hull, 1989) or differential settlement of the ground underneath the silo (e.g. Godoy and Sosa, 2003; Holst and Rotter, 2004 and 2005).

Loading due to the filling and discharge of silos and due to external sources usually to non-uniform pressures (Ooi *et al.*, 1990) with consequent complicated stress patterns in the silo structure that are known to be damaging to the silo. One of most damaging conditions is eccentric discharge (Rotter, 2001a). In this case, the flow channel of the moving solids may be in contact with the silo wall creating zones of low pressure, which induce high axial membrane stresses in the silo wall (Rotter, 1986, 2001b).

Due to the highly non-uniform stress patterns in the cylindrical shell near a bracket support, the simple static loading case was chosen in this thesis to investigate the principal nature of this problem without the influence of other highly non-uniform effects like eccentric discharge.

The loading condition discussed here is the load due to a stored bulk solid within the silo. Therefore a short description of the basic theory of Janssen (1895) is given. The Janssen theory relates the vertical friction on the wall to the internal pressure due to the bulk solid and explains why pressures in silos do not increase greatly with depth below the surface.

1.10.1 Janssen silo pressure theory for vertical walls

A tall silo filled with bulk solid is shown in Figure 1.25. A small section of the bulk solid inside the silo is examined (Figure 1.25a) and the vertical equilibrium of the slice is established as a first order differential equation (Eq. 1.4), in which γ is the bulk density of the solid, τ is the frictional stress caused by the bulk solid, q is the mean vertical stress caused by the weight of the solid acting at that level and p is the horizontal pressure caused by confinement acting at that level. The section has the dimension dz as the height of the section, U is the circumference of the wall enclosing the section and the plan area is A. Shear stresses on the top and bottom of the slice are assumed to integrate to a zero resultant on each face.

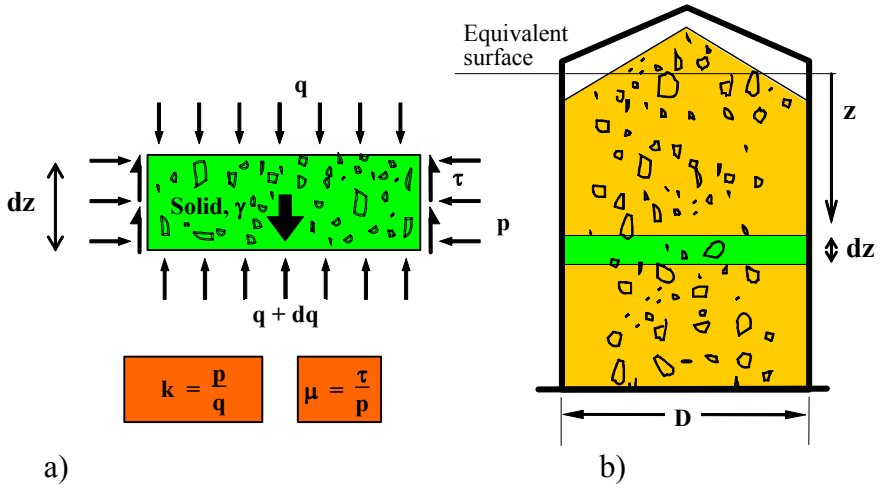

Figure 1.25: Silo contents, notation and a section of solid (original picture in Rotter (2001a))

In order to assess the mean vertical stress caused by the weight of the solid at any height of the cylinder, the vertical equilibrium of this small section (Figure 1.25a) is calculated. The solution can then be given by

$$(q+dq)\,A+U\tau\,dz=qA+A\gamma\,dz \tag{1.4}$$

or after rearranging

$$\frac{dq}{dz}A+U\tau=\gamma A \tag{1.5}$$

Two assumptions are made by the Janssen theory as described by Rotter (2001a). First, it is assumed that fully developed wall friction exists at every point on the wall and that the vertical stress q can therefore be calculated using the wall friction coefficient μ (Figure 1.25). The second assumption is that the mean horizontal pressure p on the wall is related to the mean vertical stress q by a single parameter,

known as the lateral pressure ratio K (Figure 1.25).

Inserting these assumptions into Eq. 1.5 leads to

$$\frac{\mathrm{d}q}{\mathrm{d}z} + \frac{U}{A}\mu K q = \gamma \tag{1.6}$$

After integration of Eq. 1.6 and applying a boundary condition that there is a zero mean vertical stress at z=0 (top of the silo, Figure 1.25), this leads to

$$q = q\big|_{z=0} + \frac{\gamma A}{\mu U}\left(1 - e^{-zU/(AK\mu)}\right) \tag{1.7}$$

or

$$q = q_0\left(1 - e^{-z/z_0}\right) \tag{1.8}$$

with

$$q_0 = \gamma z_0 \tag{1.9}$$

and

$$z_0 = \frac{1}{\mu K}\frac{A}{U} \tag{1.10}$$

or transformed to using Figure 1.25a

$$p = p_0\left(1 - e^{-z/z_0}\right) \tag{1.11}$$

Further information on the derivation can be found in Rotter (2001a). A typical pattern of the stress distribution can be seen in Figure 1.26.

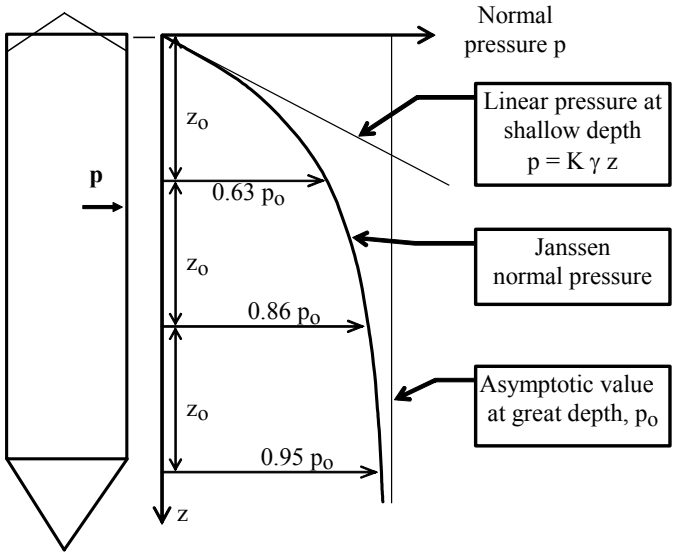

Figure 1.26: Janssen pressure pattern (original picture in Rotter (2001a))

1.10.2 Deductions from the Janssen theory to the loading conditions in the numerical model

The Janssen theory shows that the main loading components of a silo are the friction on the side of the wall and the internal pressure due to the stored bulk solid.

When the cylinder is very tall the horizontal pressure is close to uniform on a significant part of the cylinder wall and therefore the friction is also uniform due to $\tau=\mu p$, since the pressure distribution is asymptotic (Figure 1.26).

When the cylinder is moderately short or the friction coefficient is small, the greater part of the total weight of solids rests on the hopper (q is close to γz), since only a small amount is transmitted though friction into the silo walls (Figure 1.27).

In most simple descriptions, the silo is uniformly supported at the bottom of the cylinder (Rotter,2001a). When the silo is tall and the friction can be assumed to be uniform over most of the cylinder, the logical loading case for experiments and numerical analysis may be uniform friction down the silo wall is compression on the top of the silo, but for more typical large silo geometries, the dominant loading comes from the weight on the hopper.

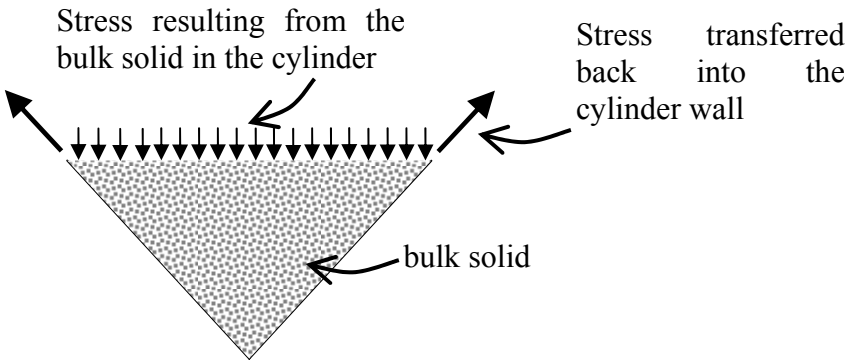

Figure 1.27: hopper load

When the silo is supported at the mid-height of the cylinder and most of the weight of solids rests on the hopper, the resulting stress condition for the cylinder is tension applied to the bottom edge of the cylinder, with a resulting shear on the sides of the bracket and compression on the top of the bracket.

When Figure 1.26 is examined again it also evident that more tension due to the friction than compression will be transmitted into the bracket and that the friction will be approximately uniform underneath the bracket.

If typical properties for bulk solid are assumed and the cylinder has a height to diameter ratio of up to 2, then most of the weight of stored solid rests on the hopper (about 70%).

If about 70% of the total weight rests on the hopper, then 30% of the weight is transferred though friction into the silo wall. But more than half of this (>15%) will be underneath the bracket and will therefore be transferred as tension into the bracket. Hence typically 85% of the weight in a silo with H/d about 2 is transferred as tension underneath the bracket.

It has also been shown (Rotter and Teng, 1989; Greiner and Guggenberger,1998; Li, 1994) that internal pressure applied by the stored material to the silo wall reduces the effect of geometric imperfections. Furthermore, the stiffness of the stored solids has a beneficial effect on the strength of the cylinder (Rotter and Zhang, 1990; Rotter *et al.*; 1989). While the wall friction will introduce compressive stresses above the bracket, which will contribute to the structures buckling sensitivity and could potentially be serious, the total amount of wall friction above the bracket is small as discussed above and is ignored for the benefit of a simple load case. The assumption of a simple load case is necessary to gain a principal understanding of the problem for the first investigation of a bracket supported silo, but needs to be expanded in future investigations.

As a result of these considerations, the chosen simple loading condition for this study of bracket supports on the side of a cylindrical shell is tension on the bottom of the cylinder without consideration of internal pressure or wall friction. This loading case applies even more clearly to fluid-storing tank structures where all the weight of the fluid rests on the hopper bottom, so all the weight of the contents comes into the cylinder as a tension on the bottom edge of the cylinder.

Standards applicable to silo loading are:

ACI313 (2004) “Standard Practice for Design and Construction of Concrete Silos and Stacking Tubes for Storing Granular Materials” ACI 313-91, with Commentary (ACI 313R-91) American Concrete Institute, Detroit, 27pp

AS3774-1996 (1996) “Loads on Bulk Solids Containers”, Australian Standard, Standards Association of Australia, Sydney, October

DIN1055-6 (2005) “Design Loads for Buildings: Loads in Silo Bins”, DIN 1055 Part 6, Deutsches Institut fuer Normung, Berlin, May.

Eurocode 1: “Basis of design and actions on structures: Part 4: Actions in silos and tanks, EN1991-1-4 (2006)

More detailed information on the effects of bulk stored solids on silo structures can be found in Rotter (2001a)

1.11 The finite element program ABAQUS

Due to the great complexity of shell structures, analytical solutions have become very difficult to perform for the kinds of practical problem that engineers must face. As a result, the analytical solutions have largely been replaced by numerical predictions. In this investigation the commercial general-purpose finite element program ABAQUS (HKS, 2003) has been used. ABAQUS standard was used in all analyses.

This program can be a powerful tool not only for standard problems, but also for the designer. It is used worldwide in a wide range of applications. The theoretical formulation is based on the finite element stiffness method.

For complex geometries, the mesh discretisation was always a challenge when it was programmed by hand, but it did have the advantage that the user knew everything about the input file including the mesh, the elements, the boundary conditions and the analysis method.

Now that the pre-processor CAE (HKS, 2003) is available and provides an easy discretisation of elements, a very complicated structure can be modelled efficiently and accurately. However the disadvantage is that the user does not know the input file intimately, which makes it much more difficult to identify and correct errors.

In this thesis, both methods have been used.

ABAQUS also provides an extensive library of shell elements including thin shell elements, thick shell elements, general purpose elements and shell elements that can address problems of heat transfer.

The facilities for material modelling are very versatile. Predefined material

models can be chosen, including different plasticity models and viscoelastic models. When more complexity is needed, user-defined material models can be implemented to model the material to specific needs.

The number of pre-defined boundary conditions is also extensive and includes symmetry boundary conditions as well as kinematic boundary conditions. More advanced boundary conditions can be implemented through user-defined subroutines.

The load incrementation in an analysis can be user-defined with a constant load increment or an automatic load incrementation exploited.

For highly nonlinear analyses, the automatic path step incrementation feature is especially useful. When the structure displays a rapid change in behaviour, as for example at bifurcation, the automatic path step incrementation responds quickly. But unfortunately this automatic path step incrementation does not always lead to an accurate result for the peak attained load (ABAQUS theory manual HKS, 2003), especially when bifurcation occurs and is followed by a falling post-buckling path. In this case the analysis must be restarted at a point shortly before buckling, using very fine used-defined incrementation (an example will be shown in Chapter 5).

For the exact calculation of the post-buckling path, the modified Riks algorithm is provided by ABAQUS. While other static method have an prescribed load and calculate the corresponding deformed shape, the modified Riks method does not only use the displacements as an unknown, but also the load magnitude. Since both, displacement and load magnitude are unknowns, ABAQUS Standard uses the “the arc length along the static equilibrium path in load displacement space”(HKS, 2003). The essence of the method is that the solution is viewed as the discovery of a single equilibrium path in a space defined by the nodal variables and the loading parameter (as described in HKS, 2003). This method has the great advantage that also equilibrium point with a negative stiffness matrix (i.e. buckling and post- buckling) can be captured.

A subspace iteration eigensolver is used for eigenvalue extraction (for further information see ABAQUS Theory manual (HKS, 2003). This eigensolver calculates the lowest eigenvalue in the system, disregarding the direction of the applied load. When for example a cylindrical shell is analysed under axial tension (instead of axial compression), the extracted eigenvalue is the absolute smallest eigenvalue and is

consequently a negative value, corresponding to a reversal of the load to produce a large zone of compression. This means that care must be taken to ensure that eigenvalues are obtained, which corresponds to the correct direction of the loading.

To resolve this problem when a reversal of loading would produce the lowest eigenvalue, a preloading must be applied in the same sense as the applied in the eigenvalue extraction analysis to ensure that the lowest eigenvalue will be in the correct sense. This preloading method is only used for linear eigenvalue analyses, where the linearity of the problem permits superposition to apply and ensures that the eigenvalue extraction will be correctly executed.

In this investigation, where a linear bifurcation analysis was performed, the eigenvalue extraction method was used. But in all other analyses, the modified Riks algorithm was used.

1.12 Problem description and numerical assumptions

The problem studied in this thesis is a bracket supported silo. The number of brackets was chosen to be four, since the support on four columns is a common arrangement. The failure behaviour is very localized around the bracket due to the stress concentrations, so the number of columns does not play a significant role as long as the failure behaviour of two adjacent brackets does not interact (Teng and Rotter ,1992a).

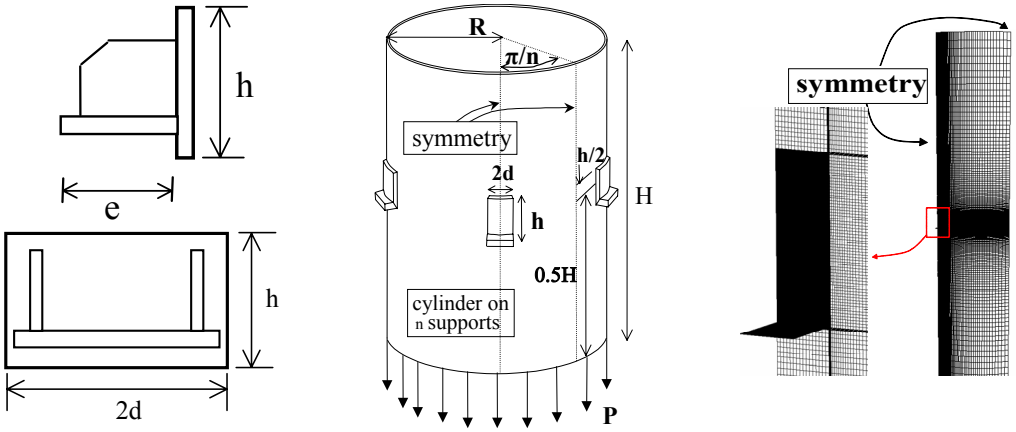

a) bracket dimensions b) shell dimensions and notation c) finite element mesh

Figure 1.28: geometry and loading of the bracket supported silo

The bracket is located at mid-height on the cylinder (Figure 1.28b) to avoid interference from the boundary conditions at the top and bottom of the silo.

The height of the cylinder has been kept constant with H/r=4 to ensure that the boundary conditions at the top and bottom of the cylinder did not affect the outcome. It is reasonable to suppose that the proximity of a boundary condition would lead to an increased predicted strength, so this assumption is conservative. For the modelling of a real structure, assumptions have to be made in the numerical analysis. Stress concentrations will appear in the bracket supported silo around the bracket. The area around the bracket was judged to be the weakest point in the structure and when it was clearly established that the failure modes did not involve points distant from the bracket, the hopper and roof were omitted in the numerical analysis and replaced by out-of-roundness constraints, modelling a stiff ring, as boundary conditions at the top and bottom edges of the silo.

The material was modelled to be either linear elastic or linear elastic-perfectly plastic depending on the analysis type, which is described in detail in later chapters. Strain hardening in the plastic region was omitted as a conservative assumption.

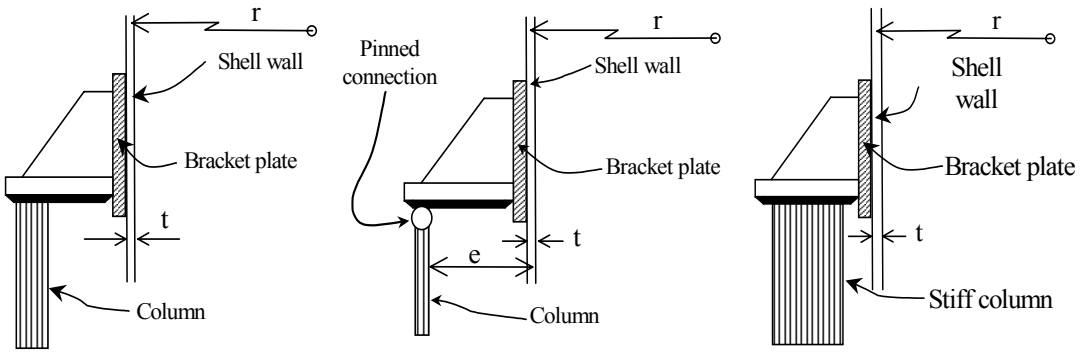

a) general arrangement b) pinned bracket c) rotationally stiff bracket

Figure 1.29: Alternative treatments of the bracket support

In a real structure, the bracket would be significantly stiffer than the cylindrical shell due to stiffening plates attached to the vertical and horizontal part of the bracket (Figure 1.29). This was achieved by increasing the thickness of the elements of the bracket to the extent that the bracket behaves rigidly compared to the shell wall.

The column was also assumed to be rigidly connected to the bracket and very stiff (Figure 1.29c), allowing for bracket movement in the radial direction only (no rotations). Following this assumption it was not necessary to model the column.

A 45 degree model of the silo was used in most analyses due to symmetry conditions. These symmetry conditions were applied at a vertical line through the middle of a bracket and at a vertical line through the midway between two bracket.

The validity of this assumption was verified for each of the nonlinear analyses list symmetry conditions.

The elements used in the final mesh were the thick shell element S8R for the bracket and for the immediate area around the bracket and the general purpose element S4R for the remainder of the structure (Figure 1.28c). The detailed reasoning behind this choice and the difficulties associated with other potential choices will be described in later chapters.

The loading was chosen as a uniformly distributed tensile ring load at the bottom of the cylindrical shell. The assumptions concerning material and geometric linearity or nonlinearity are stated in each chapter.

The shell elements used in this thesis are defined by ABAQUS (HKS, 2003) as follows:

S4R is a 4-node doubly curved general-purpose shell with reduced integration, hourglass control and finite membrane strains.

S8R is an 8-node doubly curved thick shell with reduced integration.

The thick shell element S8R is also known to display a slightly stiffer behaviour than the general purpose element S4R (ABAQUS manual (HKS, 2003))

1.13 Aims

The aim of this investigation is to obtain a good understanding of the influence of highly non-uniform stress distributions in the failure behaviour of thin curved shells. Here, the highly non-uniform stress distribution is introduced by attaching a stiff bracket onto the cylinder wall. The aim is further to provide a good description of the strength and the failure behaviour of the bracket supported silo, including a range of potential geometries for both the bracket and the cylindrical shell silo.

The study was performed purely using numerical analysis. A study of small scale experiments has been conducted (Thorburn and Patrick, 2005), but due to considerable difficulties in the experimental arrangement, no useful experimental data could be extracted for comparison with the calculations of this thesis.

Due to the lack of experimental data, benchmark tests were performed wherever possible to ensure that the results were accurate with the elements and mesh chosen.

Possible sources of error, such as boundary conditions and mesh convergence

issues, were tested for each analysis type.

Even though experimental data are vital for the verification of numerical data since they give a good insight if the assumptions in the numerical analysis, which can not be tested within the numerical analysis itself are correct, it is believed that the principal mechanisms can be captured by the numerical analysis and that this numerical study will therefore to a better understanding of the principal behaviour. Moreover, this study will permit the careful design of a limited experimental exploration to verify key findings using the knowledge gained in this study such as the relative importance of imperfections or likelihood of the structure to fail in an elastic, elastic plastic or plastic manner.

To understand the complex behaviour of a bracket supported silo it is necessary to examine the influences of geometric nonlinearity, material nonlinearity and imperfection sensitivity. The effects of geometric nonlinearity and material nonlinearity each need to be studied separately to gain knowledge of the influence and limiting conditions to which they refer. Before evaluating the influence of geometric nonlinearity, it is vital to perform a linear bifurcation analysis to give the reference condition against which bifurcations in the nonlinear analysis may be assessed.

In the next step the behaviour is studied with both geometric and material nonlinearities interacting. Finally the influence of geometric imperfections is investigated.

The whole investigation is performed within the framework of the European standard (EN1993-1-6, 2006)

To achieve the aims outlined above the following approach has been taken:

An overview of historical and current research has been given. The problem specifications and numerical assumptions were outlined and a justification has been given for the loading condition chosen in the numerical model.

The general behaviour of an example bracket supported silo will be shown in Chapter 2 to give an overview of the different possible analyses and the possible failure modes investigated in this thesis. The stress patterns found in different analyses will be compared.

Chapters 3-7 comprise an extensive parametric study of the problem.

Chapter 3 explores the outcome of linear bifurcation analysis (LBA). This analysis is not only one of the necessary reference loads required by the Eurocode, but it is vital for understanding the role of geometric nonlinearity. A good empirical approximation and a physical model to explain the linear elastic buckling failure will be presented.

The plastic collapse of the bracket supported silo is investigated in Chapter 4 and an analytical expression for the plastic failure is presented. A comparison between the strength calculated by a full materially nonlinear analysis (using small displacement theory) and several estimates using linear analysis and first yield criteria are made. Due to many difficulties in the numerical analysis, a recalculation of some previous research findings (Gillie *et al.*, 2002) will be shown and compared with their work.

Geometrically nonlinear phenomena in an elastic bracket supported silo are investigated in Chapter 5. The results are compared with the results of the linear bifurcation analysis to examine the change of strength due to pre-buckling deformations.

Chapter 6 describes the consequences of the interaction between material and geometric nonlinearity. For this purpose, capacity curves are developed which combine the new understanding and results won in the previous chapters. An empirical fit is given for the parameters of the capacity curves for the set of geometries chosen.

Chapter 7 explores the effects of geometric imperfections in the GNIA/GMNIA analysis, and demonstrates some interesting and critical aspects of imperfection sensitivity and geometric nonlinearity in unsymmetrically loaded shells.

Chapter 8 will give a summary of the conclusions drawn from the investigation and make proposals for future research.

2 Comprehensive study of the behaviour of an example shell

2.1 Introduction

This chapter presents an outline description of the behaviour of a cylindrical steel shell that is discretely supported on several brackets, each rigidly connected to a stiff column or floor. The linear, materially nonlinear, geometrically nonlinear and bifurcation behaviours of the shell under these conditions are outlined. This chapter should be seen as a short preview and overview of the analyses that are more comprehensively described in later chapters and as an introduction to the failure behaviour. The behaviour of the shell under the set of assumptions underlying each analysis is discussed further in the corresponding chapters.

2.2 Example bracket support

An example bracket support is studied here to explore the characteristics of the behaviour. This bracket was chosen as a geometry in which there is significant interaction between elastic buckling and plasticity, even though the shell is thin, placing it clearly in the elastic-plastic buckling regime for this structure. The manner in which this choice was made is shown later.

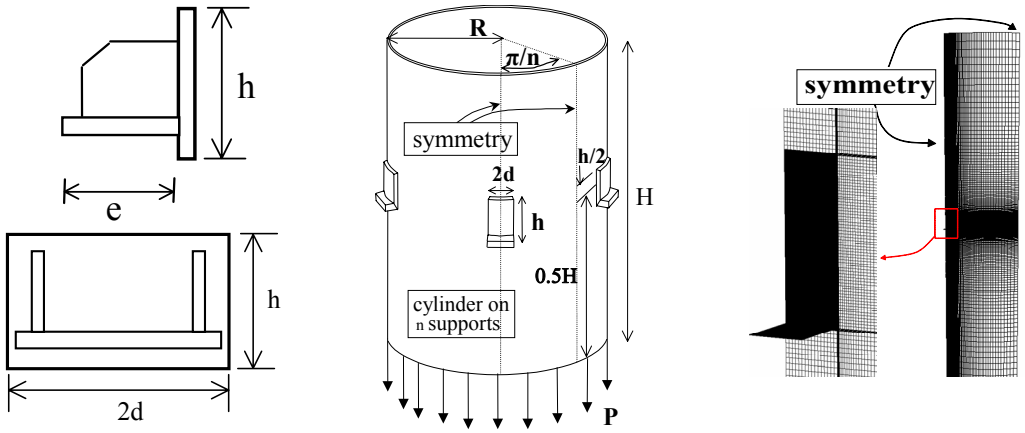

a) bracket dimensions b) shell dimensions and notation c) finite element mesh

Figure 2.1: geometry and loading of the bracket supported silo (dark lines in c) indicate very small elements)

The key parameters of this representative problem were: height of the cylinder $H/r = 4$, radius of the cylinder $r/t = 600$, height of the bracket $h/r = 0.12$, half width of the bracket $d = h/3$, thickness of the cylinder t=1 and the number of columns $n = 4$

(Figure 2.1), with the material parameters are $E = 2\times10^5$ MPa, $\nu = 0.3$ and $\sigma_Y = 250$ MPa.

Only one eighth of cylinder was model to exploiting the symmetry conditions. Two vertical symmetry lines were used, one through the middle of one bracket and another one midway between two brackets (as indicated in Figure 2.1).

In the following analyses of this chapter, all the loads are described in a dimensionless manner, using the reference force R_{REF} applied to each bracket:

$$R_{REF} = \sigma_{cl}\left(A/n\right) = \sigma_{cl}\left(2\pi rt/n\right) \tag{2.1}$$

in which the classical elastic critical buckling stress σ_{cl} for uniform axial compression is given by

$$\sigma_{cl} = 0.605\,E\,t/r \tag{2.2}$$

The force R_{REF} is used to normalise all the strength calculations. This reference load corresponds to the classical elastic critical stress for uniform axial compression being applied in tension around the full shell circumference at its lower edge. The horizontal coordinate was made dimensionless using the bending half wave length λ.

$$\lambda = \frac{\pi}{\left[3\left(1-\nu^2\right)\right]^{1/4}}\sqrt{rt} \approx 2.44\sqrt{rt} \tag{2.3}$$

The membrane stress resultants are made dimensionless using the yield stress multiplied by the thickness of the cylinder $\sigma_y t$.

The problem was studied using the commercial finite-element (FE) package ABAQUS (HKS, 2003). The analysis used two element types, both of which are rectangular doubly curved shell elements with reduced integration. Most of the model used the 4-noded general-purpose S4R element (Figure 2.2), but in the zone around the bracket and the bracket itsself the 8-noded thick shell element S8R (Figure 2.2) was used because of its superior performance in highly plastified zones. Further information on the choice of elements can be found in Chapter 4.

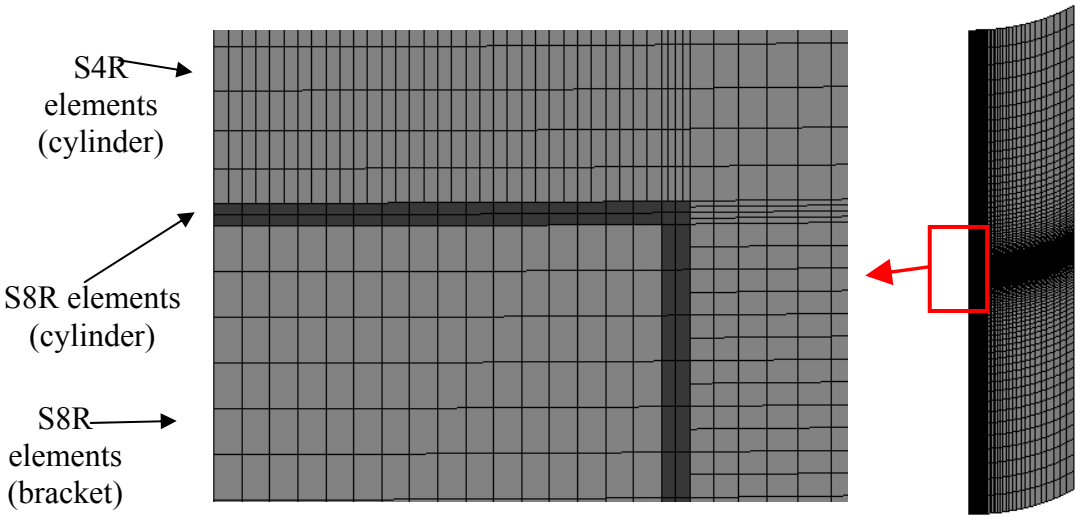

Figure 2.2: Finite element mesh using S8R (dark grey) and S4R (light grey)

In the following, the results of the different analyses defined in EN1993-1-6 (2006) are shown. These begin with the reference analyses of linear elastic analysis (LA), linear bifurcation (LBA) and the plastic reference load (MNA), and are followed by geometrically nonlinear (GNA) and geometrically and materially nonlinear (GMNA) analyses, and analyses including explicitly modelled imperfections (GMNIA). The role of each of these different analyses was described in Chapter 1.

2.3 Linear Elastic Analysis (LA)

The simplest treatment of this problem is a linear elastic stress analysis. It is useful to study the pattern of load transfer from the tension near the shell base into the bracket, in preparation for an understanding of the behaviour found later in other analyses. In simple terms, one might expect that the vertical tension from the load on the base circumference would be fed into the base of the bracket, perhaps with some shear transfer onto the sides of the bracket. The first images worthy of study are therefore the axial membrane stress pattern and the membrane shear pattern in the shell.

The bracket causes an inward deformation of the shell over a significant height above it, leading to inward bending in both the circumferential and meridional

directions (Figure 2.3a). It may be noted that the wall becomes flatter in this region, which is later seen to have a detrimental effect on the buckling strength.

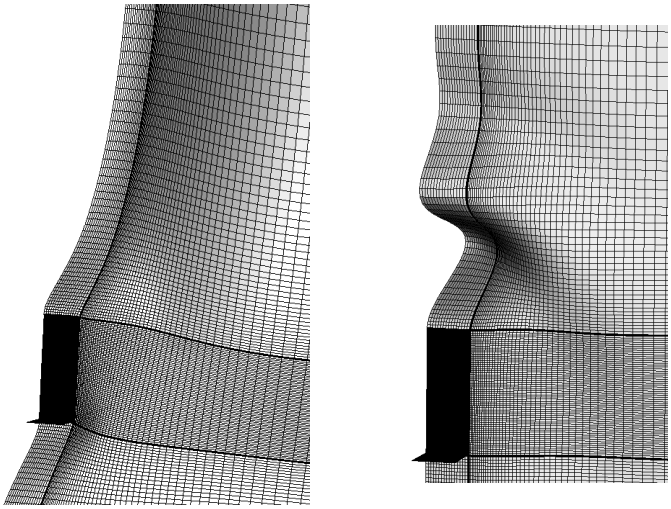

a) deformation in LA
load factor = 9.125
deformation factor = 500

b) linear bifurcation mode
(close up view)

Figure 2.3: Linear elastic deformations (LA) and linear bifurcation mode (LBA) (Note: The two dark horizontal lines and the dark vertical line correspond to very fine elements)

Figure 2.5a shows the axial membrane stress on horizontal lines at several different levels in the shell. At the bottom, the load is applied and there is the expected uniform axial tension. Half way between the base and the bracket, elevated tensile stresses develop towards the bracket meridian, with a corresponding decrease away from the bracket meridian. Just below the bracket, high tensile stresses focus into the bracket, with a distribution similar to that of a rigid footing on an elastic halfspace (Timoshenko and Goodier, 1970). A strong peak can be seen at the bracket corner, but tensile stresses also continue in the shell away from the bracket meridian, ensuring that some of the load by-passes the bracket and induces compression above it.

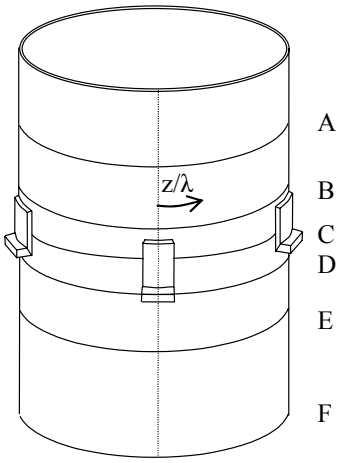

A= midway between top of the silo and bracket
B=just above the bracket
C=at the middle of the bracket
D=just below the bracket
E=midway between bracket and bottom of the silo
F=bottom of the silo

Figure 2.4: Location of the horizontal lines used in Figure 2.5

On the side of the bracket, some of the load is transferred in shear (Figure 2.5b) as can be seen in the peak in membrane shear at mid-height of the bracket. Above the bracket, load is transferred by compression into the top of the bracket (Figure 2.5a), with a similar high peak associated with the bracket corner, as was seen just below the bracket. It is clear that the corners of the bracket represent points of strong stress concentration, and that local plasticity will affect the behaviour here quite strongly. These are also points at which high shell bending stresses develop.

The circumferential membrane stresses are shown in Figure 2.5c, where it can be seen that high circumferential membrane stresses are developed near the top and bottom of the bracket through Poisson effects which arise due to the restraint of displacements by the stiff bracket. Thus this is another case where high stiffness leads to unexpected stresses and here they affect the first yield condition strongly (tensile where the axial stress is compressive, and vice versa).

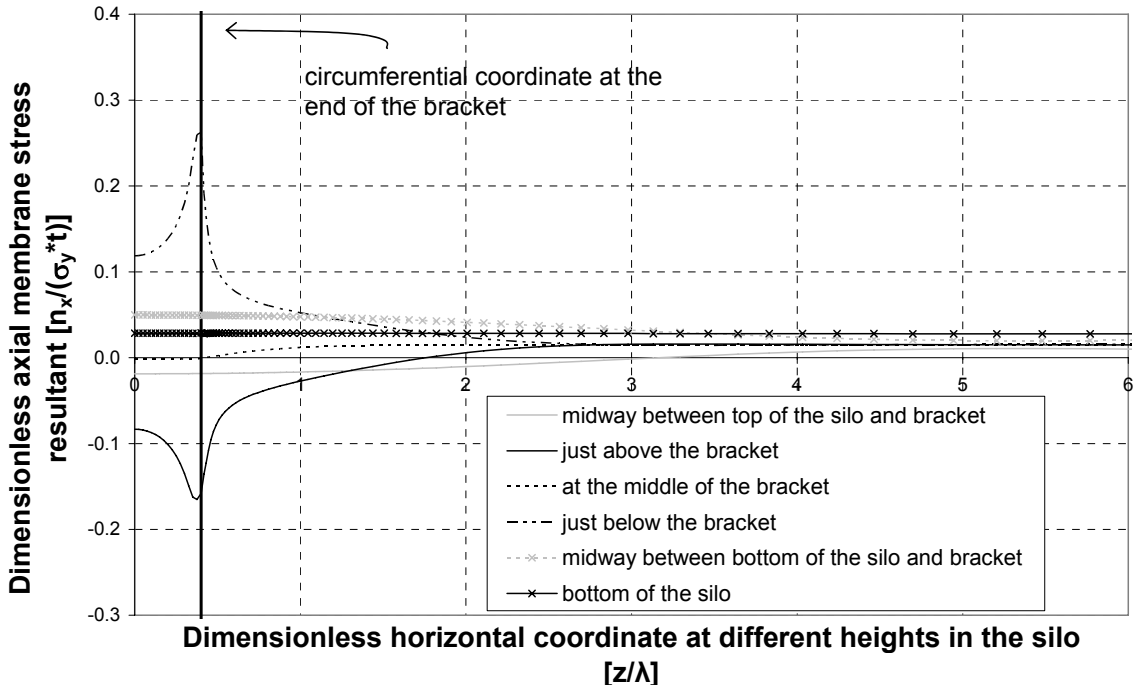

Figure 2.5a: Dimensionless axial membrane stress resultant at different heights in the silo (LA)

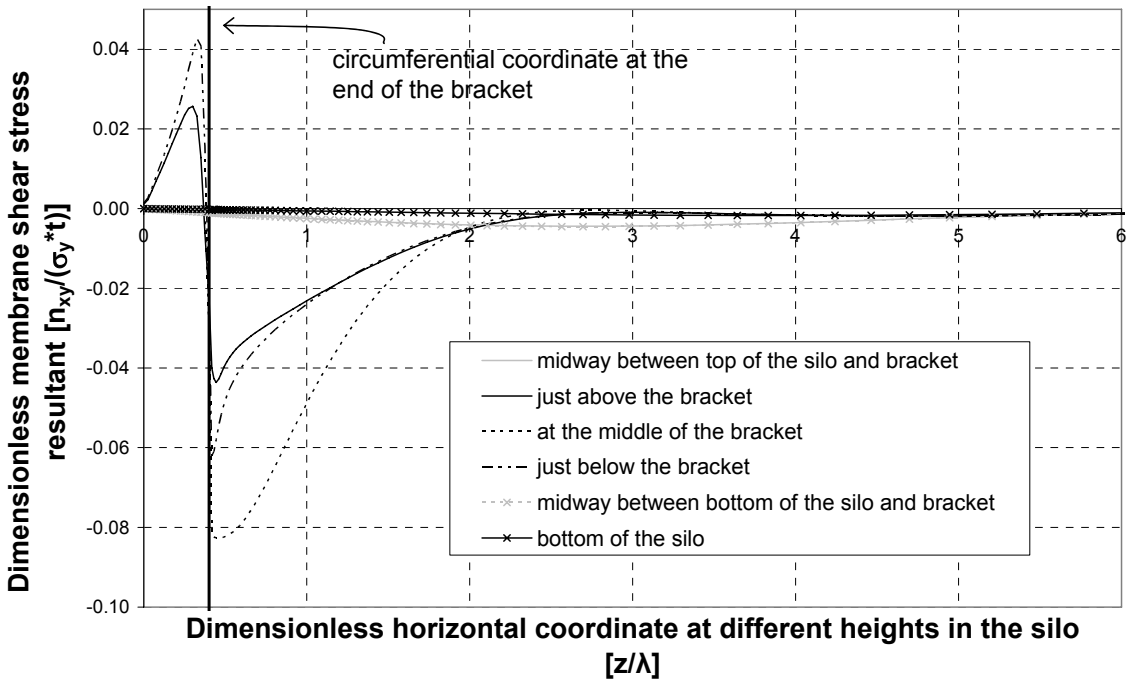

Figure 2.5b: Dimensionless membrane shear stress resultant at different heights in the silo (LA)

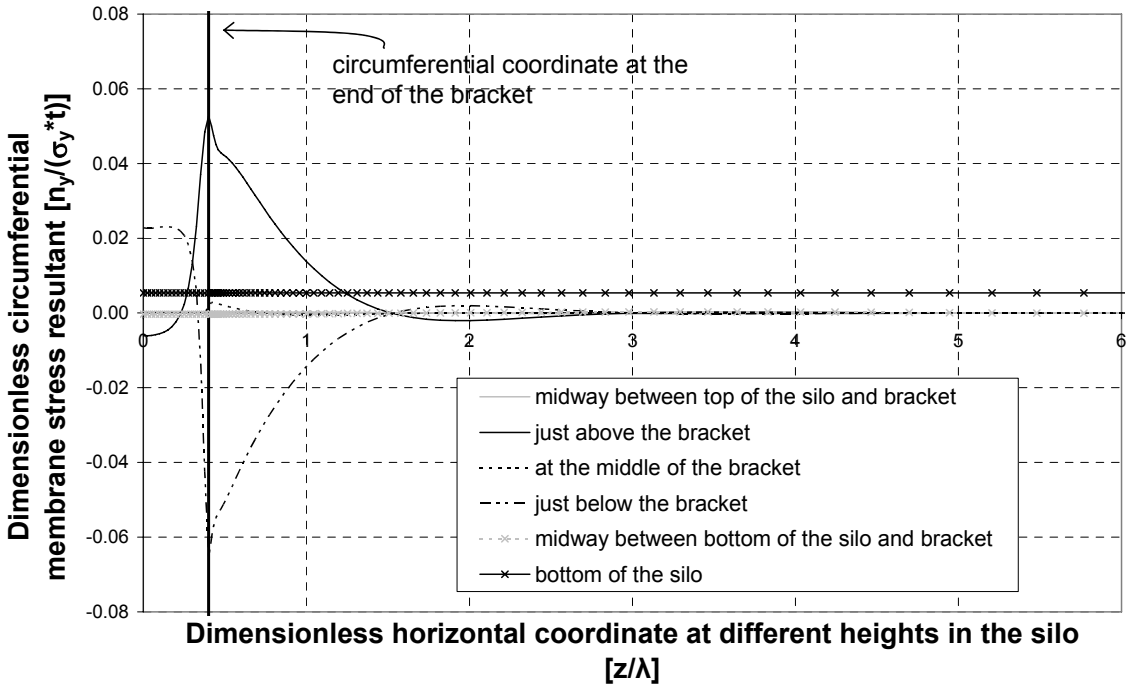

Figure 2.5c: Dimensionless circumferential membrane stress resultant at different heights in the silo (LA)

2.4 Estimating the plastic strength of the shell from linear analysis

It is not a simple task to determine the potential failure state of a shell from a linear elastic analysis. The first type of failure that might be considered here would

be a plastic collapse failure, which should strictly involve a fully developed plastic strain rate field (plastic flow mechanism) involving both bending and stretching of the shell (Massonnet and Save, 1972). But since this is quite an onerous analysis to perform, whether by hand or computationally, it is not reasonable to expect that all analysts will use a small displacement theory materially nonlinear analysis (MNA) of the structure to obtain the plastic collapse load. Consequently, the European shell standard EN1993-1-6 (2006) defines how this load can be estimated from the results of a linear elastic analysis. Since such an estimate is not easy to make, several alternative criteria were applied in the present study to see how effective they might be. The three criteria chosen for this investigation were: a) first surface yield; b) first surface yield according to the Ilyushin yield criterion, which is recommended in EN1993-1-6 (2006); and c) first membrane stress resultant yield.

Here these three estimates of the plastic collapse strength were compared with the formal limit load calculated using ABAQUS, which is described below. The results show that all three criteria lead to very conservative estimates. The first surface yield criterion predicts failure at 14.8%, the Ilyushin criterion predicts failure at 12.4%, and first membrane yield at 20.8% of the true plastic collapse load. These conservative predictions are caused by the high stress concentration at the corners of the bracket. Clearly more research is needed to find better criteria to use in estimating the plastic collapse strength from the results of linear analyses. Further discussion about the estimation can be found in Chapter 4.

2.5 Linear Bifurcation Analysis (LBA)

Following a linear elastic analysis, it is a simple matter to determine the linear bifurcation load computationally. The linear elastic bifurcation mode for the example bracket is shown in Figure 2.3b. The buckling mode is quite local and lies just above the bracket. The LBA buckling load R_{LBA} for this geometry is found to be $R_{LBA}/R_{REF} = 0.450$ even though this load is applied as a tensile force at the bottom of the shell. If it is assumed that the support force is taken only in compression above the bracket and this result is reinterpreted in terms of the mean compressive stress just above the bracket σ_{ub}, it is found that $\sigma_{ub}/\sigma_{cl} = 9.09$, so that that even if the compression is deemed to be only one third of the total load transmission, the mean vertical stress above the bracket is a poor estimate of this simplest buckling strength

measure. A Full description of the bifurcation behaviour of the bracket supported silo will be presented in Chapter 3.

2.6 Geometrically Nonlinear Analysis (GNA)

When a geometrically nonlinear analysis is used for the prebuckling calculation (GNA), the prebuckling path is close to linear and the buckling load ($R_{GNA}/R_{REF} = 0.297$) is found to be much lower than the bifurcation load of an LBA analysis. The strength reduction due to geometric nonlinearity is 36%. This shows that the local bending deformations of the prebuckling state modify the buckling resistance of the shell considerably, as was seen also in the calculations for other local stress conditions by Holst and Rotter (2005) and Cai *et al.* (2002). It may be noted that in uniformly compressed cylinders, geometric nonlinearity leads to a strength reduction of typically 15% (Yamaki, 1984), so this 36% reduction shows that geometric nonlinearity is very important: where local bending phenomena occur in a zone where a local buckle may form, the effects of geometric nonlinearity are usually very much greater than under conditions of uniform loading.

The prebuckling shape just before and the postbuckling deformed shape just after the peak load are shown in Figure 2.6. The prebuckling deformations extend far above the bracket and the postbuckling deformed shape naturally includes these deformations. The incremental change between these two forms was therefore evaluated to extract the nonlinear incremental buckling mode (Figure 2.6c). The shape and location of the GNA nonlinear buckle is significantly different from the linear bifurcation mode (Figure 2.3b). The prebuckling deformed shape (Figure 2.6a) shows an enlarged flattened zone above the bracket, which leads to lower curvature and is principally responsible for the reduction in buckling strength.

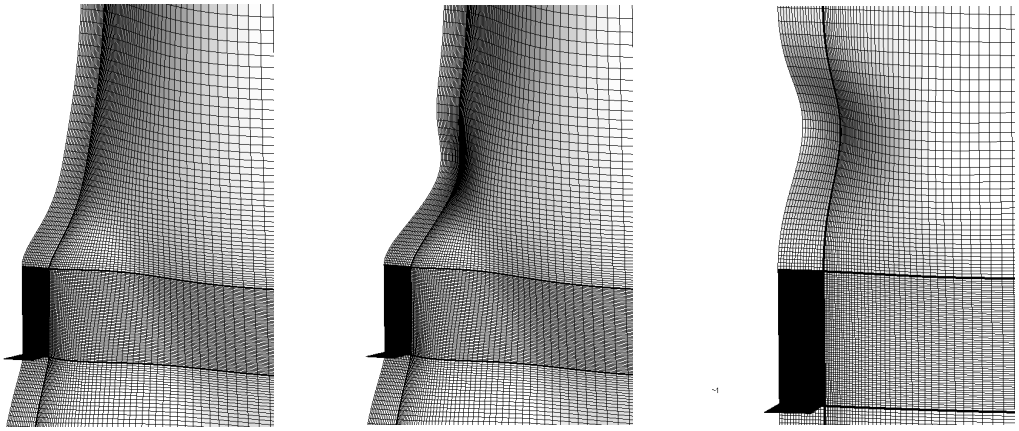

a) pre-buckling deformation, deformation factor = 35

b) post-buckling deformation, deformation factor = 35

c) nonlinear incremental bifurcation mode (close up view) deformation factor = 70

Figure 2.6: Deformation just before and just after buckling in geometrically nonlinear elastic analysis and resulting incremental buckling mode

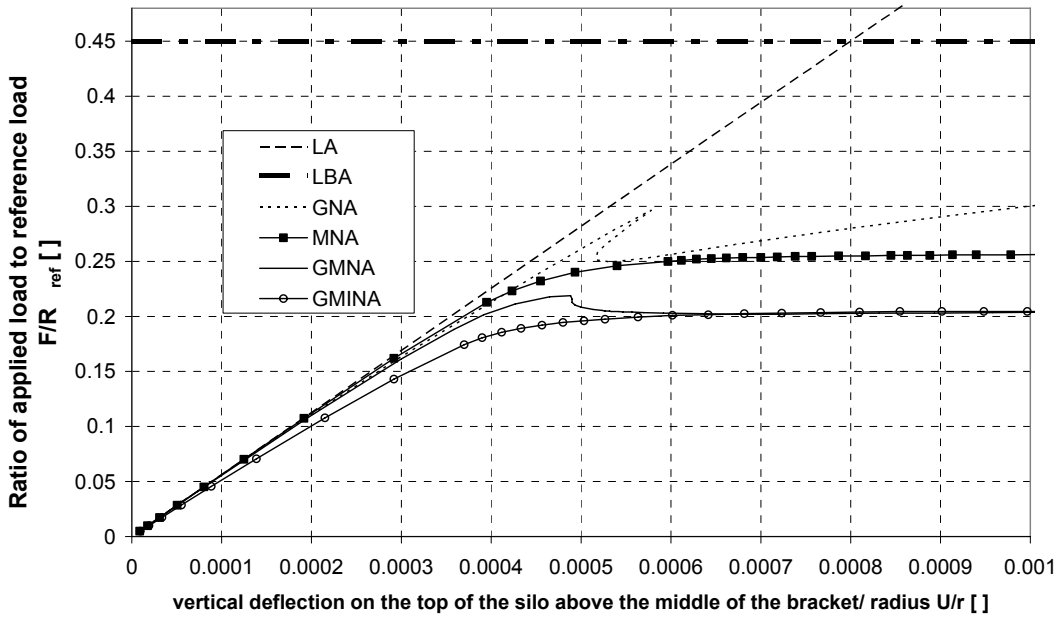

Figure 2.7: Load-displacement curves for different analysis types

The nonlinear load-deflection curve is shown in Figure 2.7 (dotted), where the nonlinear bifurcation event can be seen to cause a sudden decrease in load, as is typical in compressed shells. The membrane stress patterns seen in the geometrically nonlinear elastic analysis are shown in Figure 2.8. Three different points on the load deflection curve have been taken: one well before buckling in the elastic range, one just after buckling and one at the lowest load on the post-buckling path. The axial membrane stress resultant (Figure 2.8a) shows that the compressive peak near the

corner of the bracket is increased after buckling, as might be expected since the buckle softens the zone above the middle of the bracket. In this middle zone, the compression is highest just after buckling, but it decreases suddenly at the lowest load level and moves to be tensile deep in the post-buckling range.

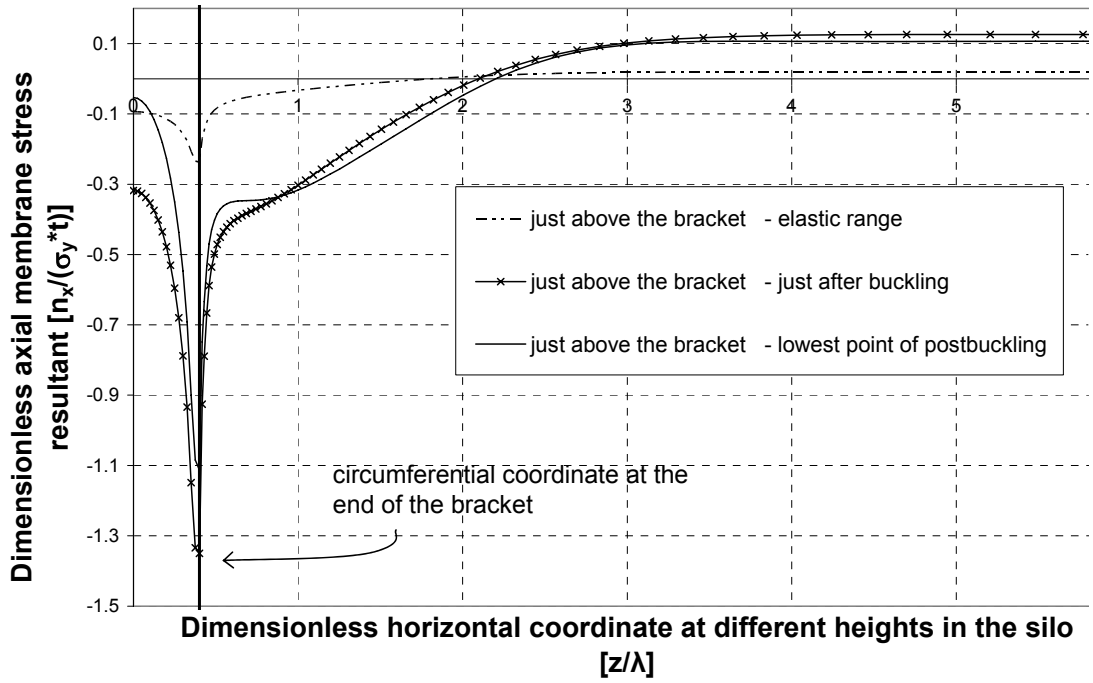

Figure 2.8a: Dimensionless axial membrane stress resultant just above the bracket at different stages (GNA)

The circumferential membrane stress resultant above the bracket (Figure 2.8b) is dominated by a high tension developing at the bracket corner, exacerbating the high local axial compression in this location and causing early yield. These stresses are sustained after buckling, making this high stress concentration susceptible to yield despite the buckling changes in geometry elsewhere. The membrane shear stresses at the mid-height of the bracket (Figure 2.8c) and circumferential membrane stresses below it (Figure 2.8d) are substantially unchanged by the buckling event above. However, it may be noted that high circumferential tensile stresses develop over the top of the bracket deep in the post-buckling regime.

The geometrically nonlinear analysis (GNA) is discussed in more detail in Chapter 5.

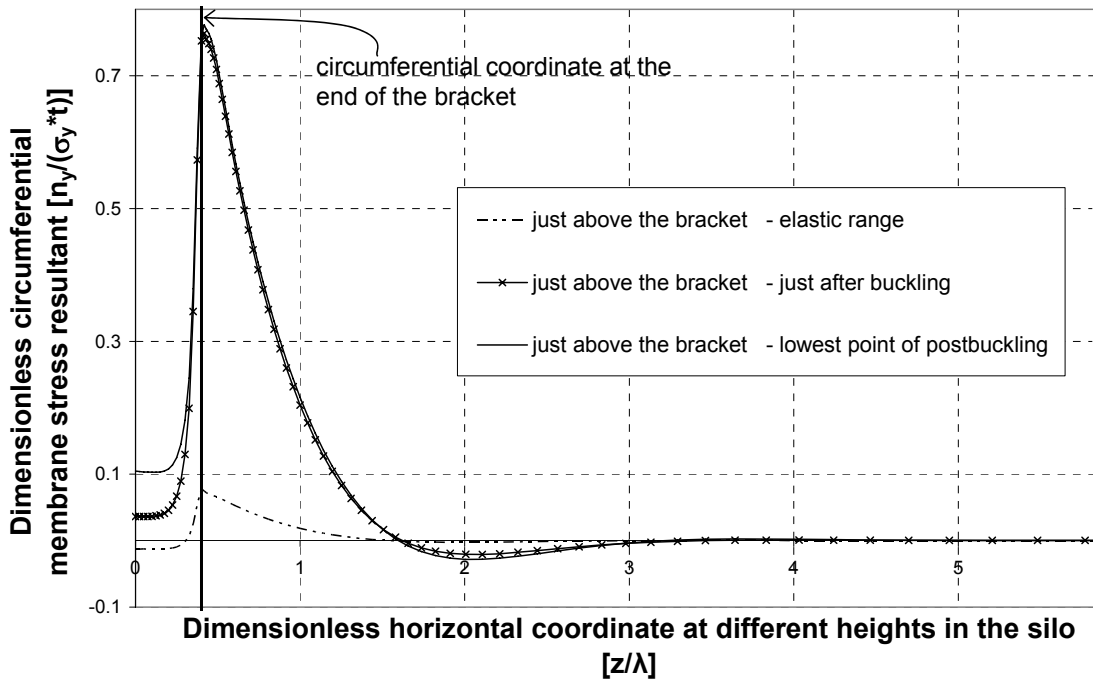

Figure 2.8b: Dimensionless circumferential membrane stress resultant just above the bracket at different stages (GNA)

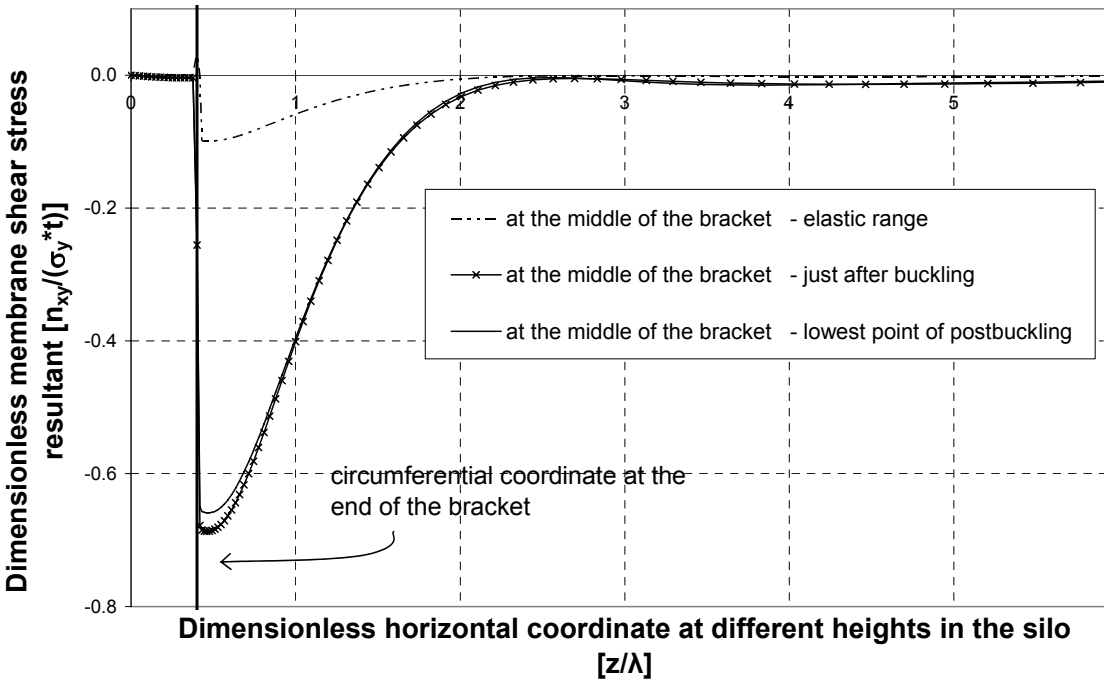

Figure 2.8c: Dimensionless membrane shear stress resultant the middle of the bracket at different stages (GNA)

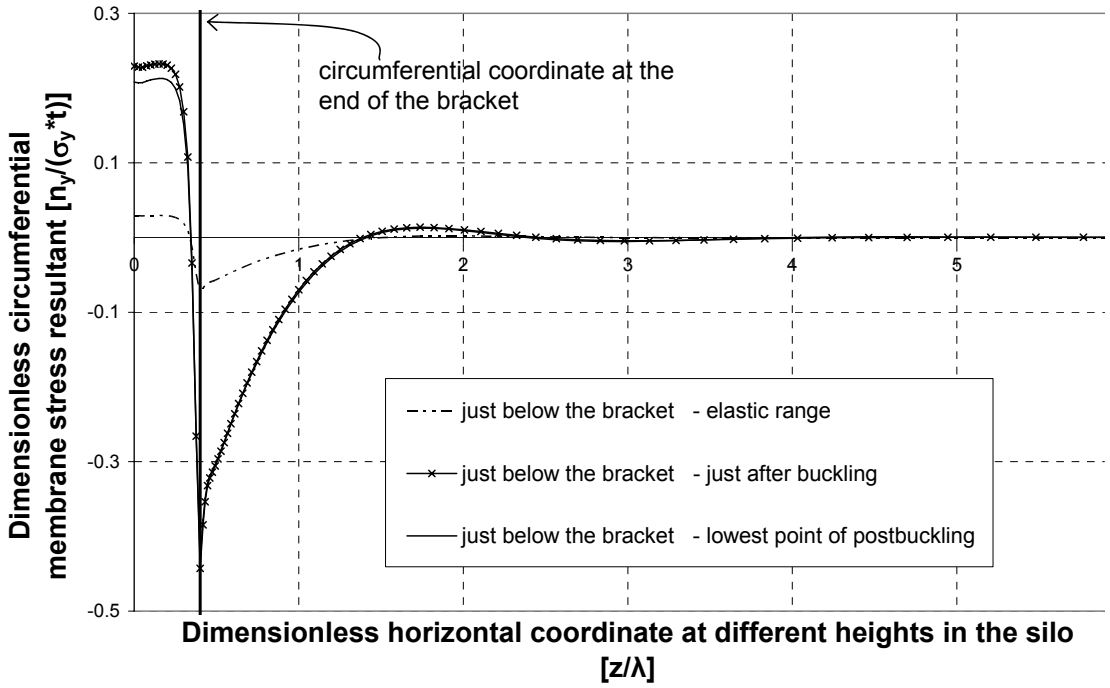

Figure 2.8d: Dimensionless circumferential membrane stress resultant just below the bracket at different stages (GNA)

2.7 Materially Nonlinear Analysis (MNA)

When ideal elastic-plastic material nonlinearity is introduced, but small displacement theory is still adopted (no change in geometry), the calculation leads to the reference MNA plastic collapse load ($R_{MNA}/R_{REF} = 0.257$). The form of the load-deflection curve is classic (Figure 2.7: black squares), with significant plastic deformations developing at loads well below the collapse load, but forming a horizontal plateau at the collapse load. The collapse load corresponds very well to a simple theoretical calculation of full plasticity around the bracket

$$R_{\text{Ref}} = 2\,2d\,t\,2/\sqrt{3}\,\sigma_y + 2h\,t\,\sigma_y/\sqrt{3} \qquad (2.4)$$

as indicated in Figure 2.9 and fully exploiting the biaxial stress state provided by the restraint of the bracket. The dimensionless membrane stress resultants around the bracket from the finite element analysis (Figure 2.10) confirm that the theoretical stress state (Figure 2.9b) is correct. The derivation of this reference load is detailed in Chapter 4. This bracket geometry was specially selected to be in the range where strong interactions are expected between plasticity and stability, so the MNA plastic collapse load is similar to the GNA buckling load (Figure 2.7).

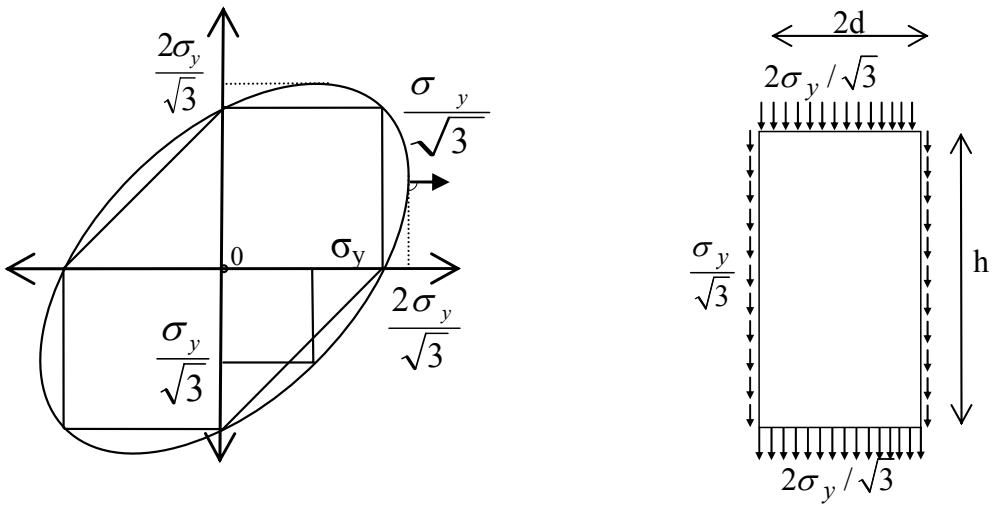

a) von Mises yield ellipse **b) stresses on different zones**

Figure 2.9: Simple membrane stress calculation of plastic collapse strength

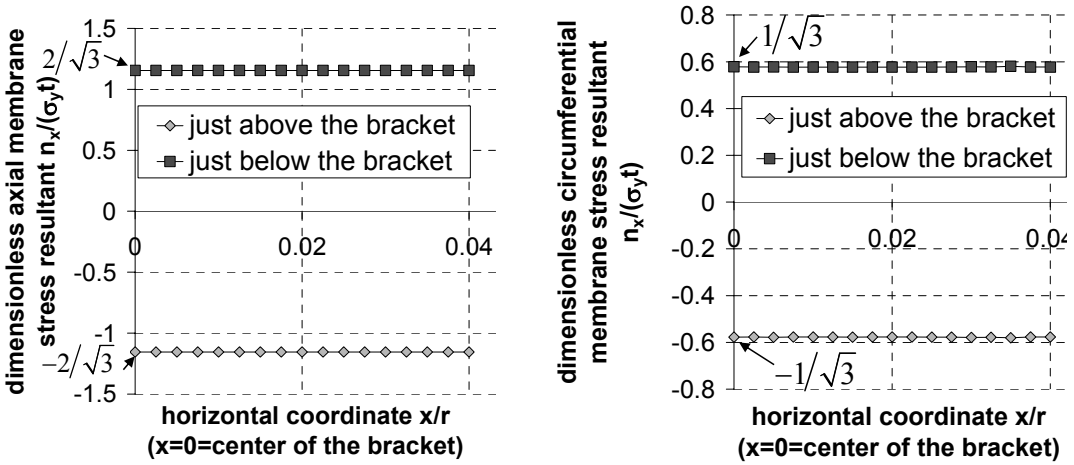

a) b)

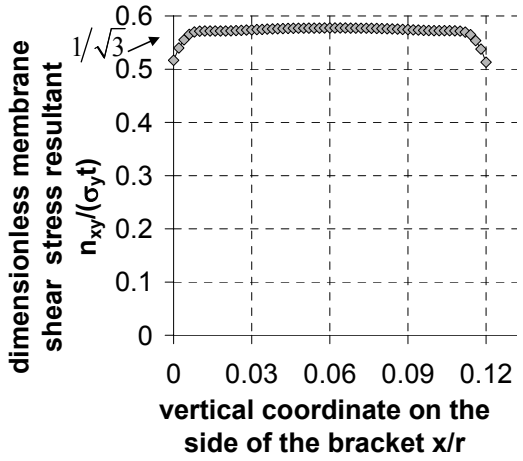

c)

Figure 2.10: Dimensionless membrane stress resultant around the bracket

The membrane stress patterns in the plastic collapse mechanism and at different heights in the silo are shown in Figure 2.11. The axial membrane stress resultant

(Figure 2.11a) reaches the limits of the von Mises envelope $\pm 2\sigma_y / \sqrt{3} \approx \pm 1.155\sigma_y$ (Figure 2.9a), above and below the bracket, but away from the bracket it decreases to the applied load per unit circumference. The circumferential membrane stress resultant (Figure 2.11b) immediately above and below the bracket reaches the corresponding reaction stress $\pm \sigma_y / \sqrt{3} \approx \pm 0.577\sigma_y$, again consistent with this point on von Mises ellipse, but away from the bracket it decreases to zero. Under fully plastic conditions, the stresses above and below the bracket are symmetrical (Figure 2.11), though under elastic conditions the axial tension below the bracket was, of course, dominant.

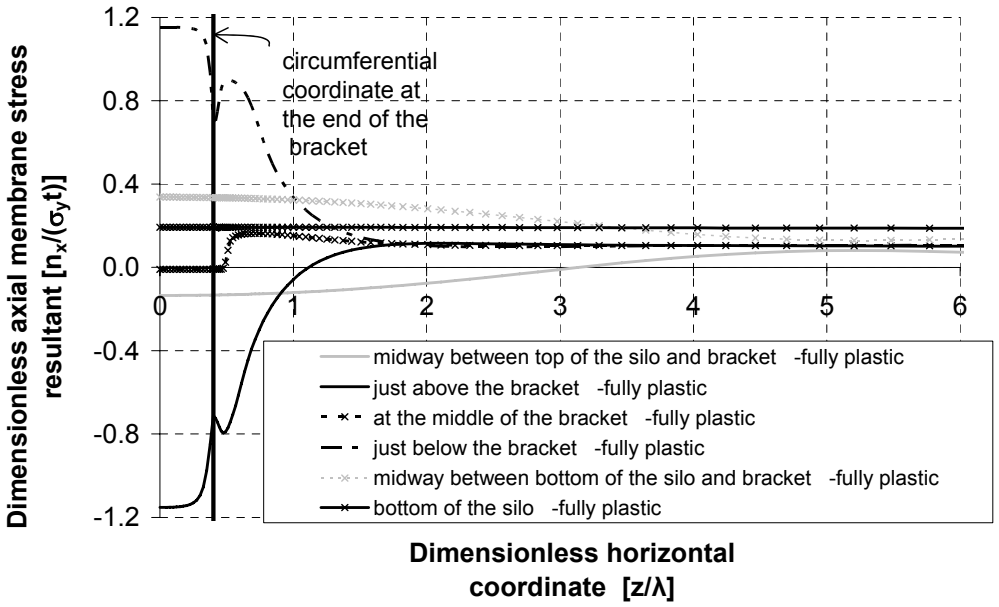

Figure 2.11a: Dimensionless axial membrane stress resultant at plastic collapse

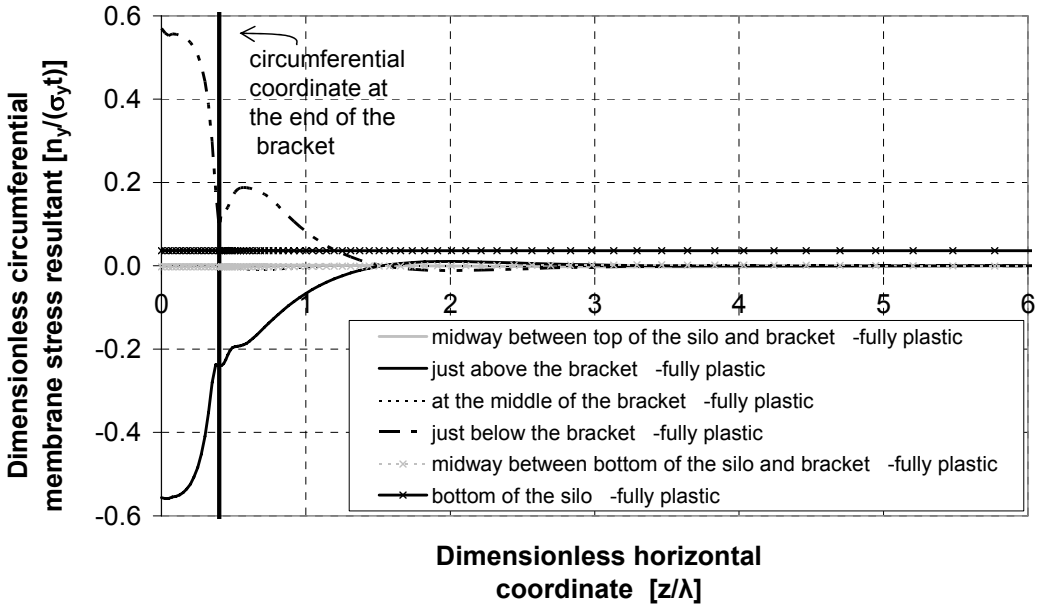

Figure 2.11b: Dimensionless circumferential membrane stress resultant at plastic collapse

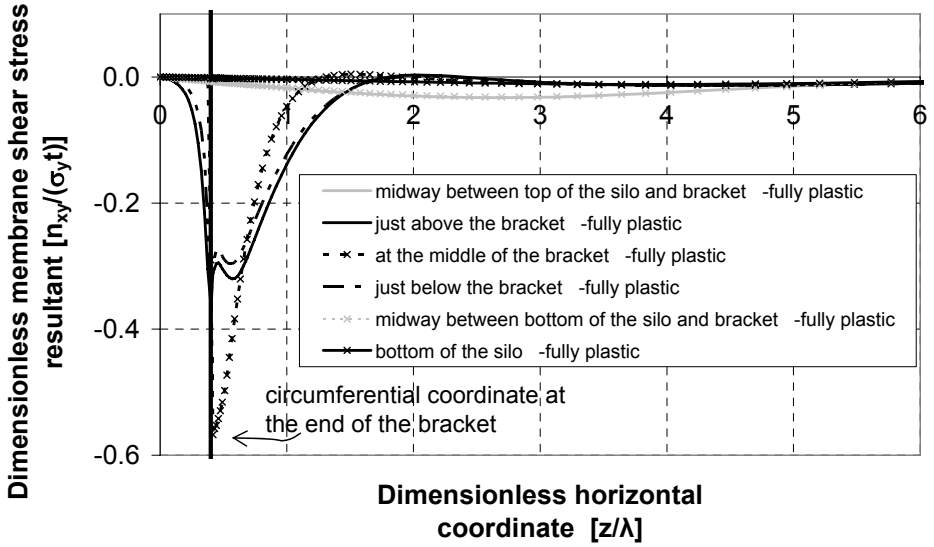

Figure 2.11c: Dimensionless membrane shear stress resultant at plastic collapse

2.8 Geometrically and Materially Nonlinear Analysis (GMNA)

When both geometrical and material nonlinearities are included (GMNA, more detailed information in Chapter 6), the limit load or bifurcation seen in the GNA analysis is, perhaps naturally, removed (Figure 2.7) and the shell moves smoothly from an unsymmetrical pre-buckling deformation pattern into a different unsymmetrical post-buckling form, passing through a limit load ($R_{GMNA}/R_{REF} = 0.219$)

as it does so. For this geometry, this limit load is slightly below the plastic collapse (MNA) and nonlinear elastic bifurcation (GNA) loads.

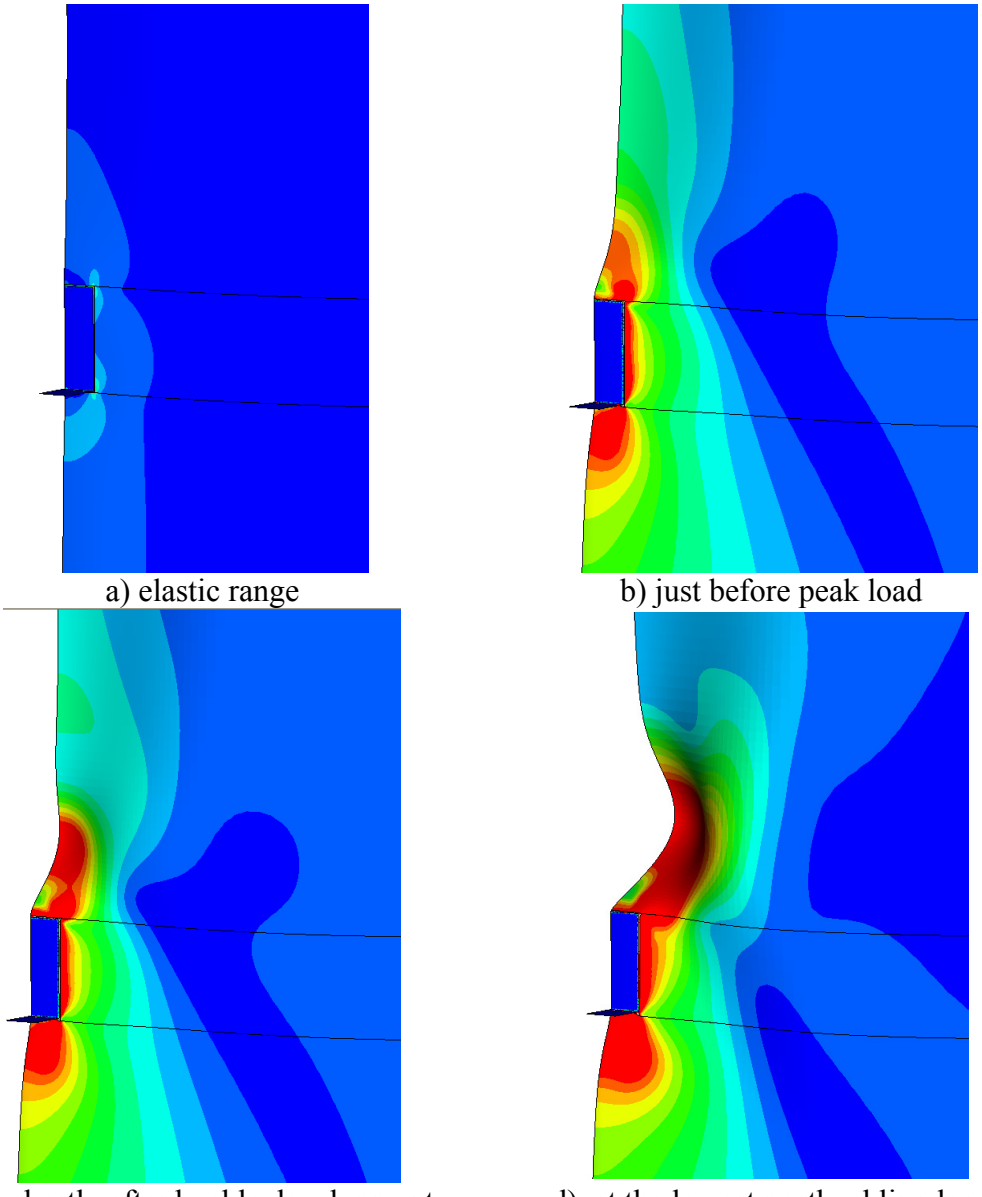

a) elastic range b) just before peak load

c) shortly after buckle development d) at the lowest postbuckling load

Figure 2.12: Von Mises stress distribution on the outer surface (GMNA analysis: deformation factor 15)

The patterns of von Mises equivalent stress on the outer surface of the silo is shown in Figure 2.12. In the elastic range (Figure 2.12a), the maximum surface equivalent stress lies beneath the corner of the bracket. Just before buckling (Figure 2.12b) yield has occurred around most of the bracket, and just after buckling (Figure 2.12c) the local inward directed buckle above the bracket has caused an extension of the yield zone. At the lowest load on the post-buckling path (Figure 2.12d), this deepening local buckle becomes extensively yielded. The images in Figure 2.12 were taken from the ABAQUS (HKS, 2003) post processor.

The distributions of the membrane stress resultants in the GMNA analysis are shown in Figure 2.13 on three horizontal lines adjacent to the bracket. The stress states at three different points on the load defection path (Figure 2.7) are shown: one in the elastic range, one just after bucking and one far into the post-buckling range. The sharp stress concentration in axial membrane stress seen in the elastic range at the bracket corner (Figure 2.8a) is rapidly smoothed by yielding after buckling (Figure 2.13a) and a rather uniform stress transfer develops at the peak attainable stress of $\pm 2\sigma_y / \sqrt{3} \approx \pm 1.155\sigma_y$ and this is sustained deep into the post-buckling range. The axial membrane stress resultant above the bracket shows a different behaviour: the elastic peak compression that developed at the corner (Figure 2.5a) moves inwards to be over the bracket after buckling, but is accompanied by a big drop in compression just beyond the corner. This drop is exacerbated in the post-buckling range. However because these stresses are strongly affected by the presence of the buckle, the uniform stress state seen in an MNA analysis (Figure 2.11a) does not develop. The circumferential membrane stress resultant (Figure 2.13c) sustains the same peak at the corner throughout, but in the post-buckling range it falls to zero above the bracket. These differences between geometrically nonlinear and materially nonlinear stress patterns illustrate the strong interactions between changes of geometry and stress smoothing due to plasticity.

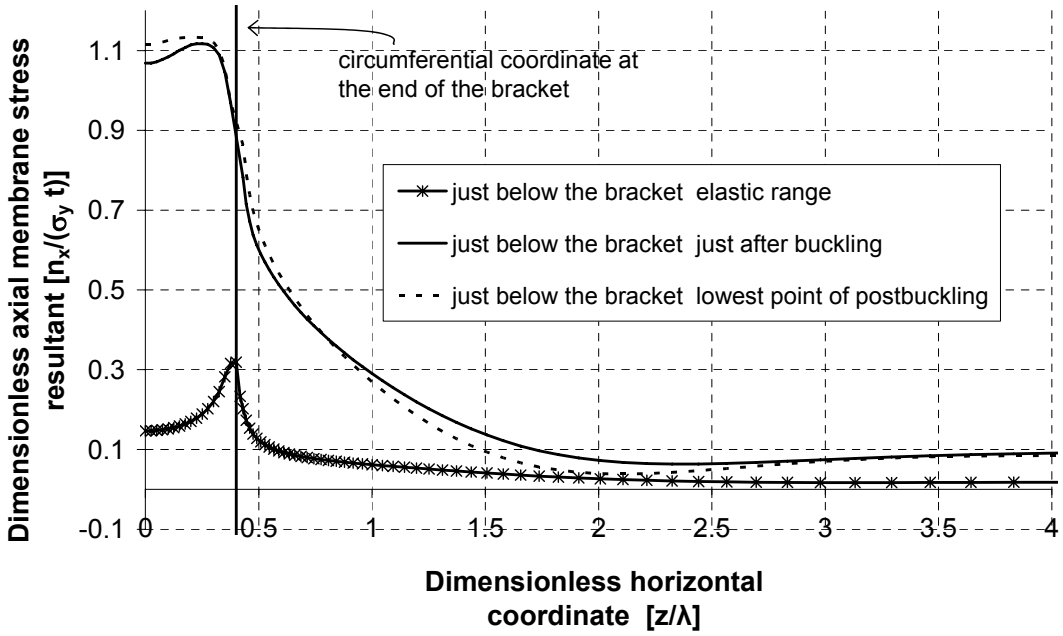

Figure 2.13a: Dimensionless axial membrane stress resultant just below the bracket at different stages (GMNA)

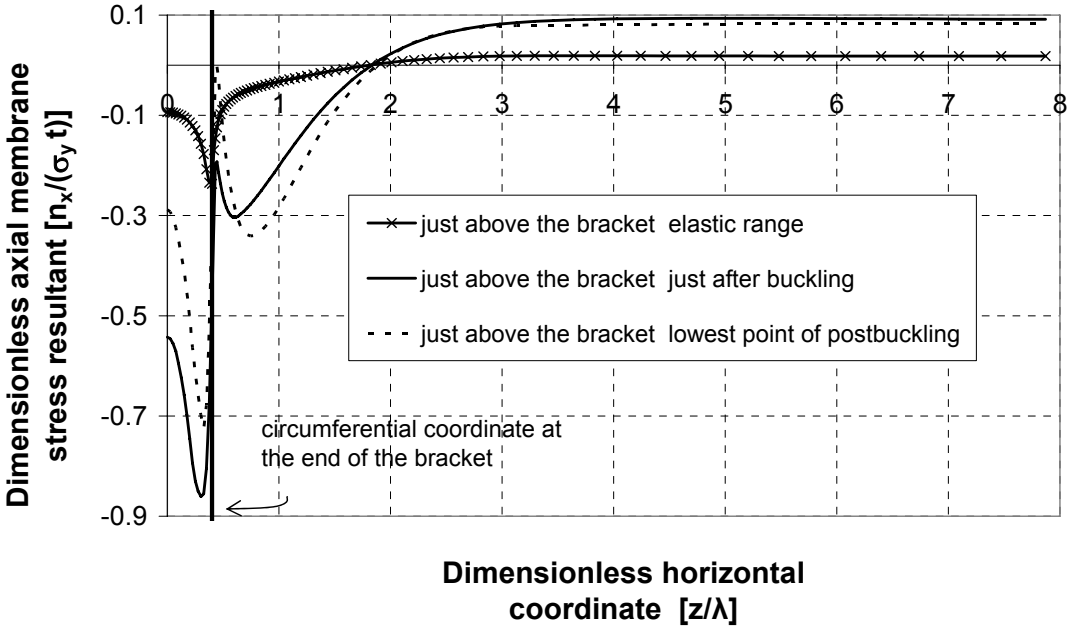

Figure 2.13b: Dimensionless axial membrane stress resultant just above the bracket at different stages (GMNA)

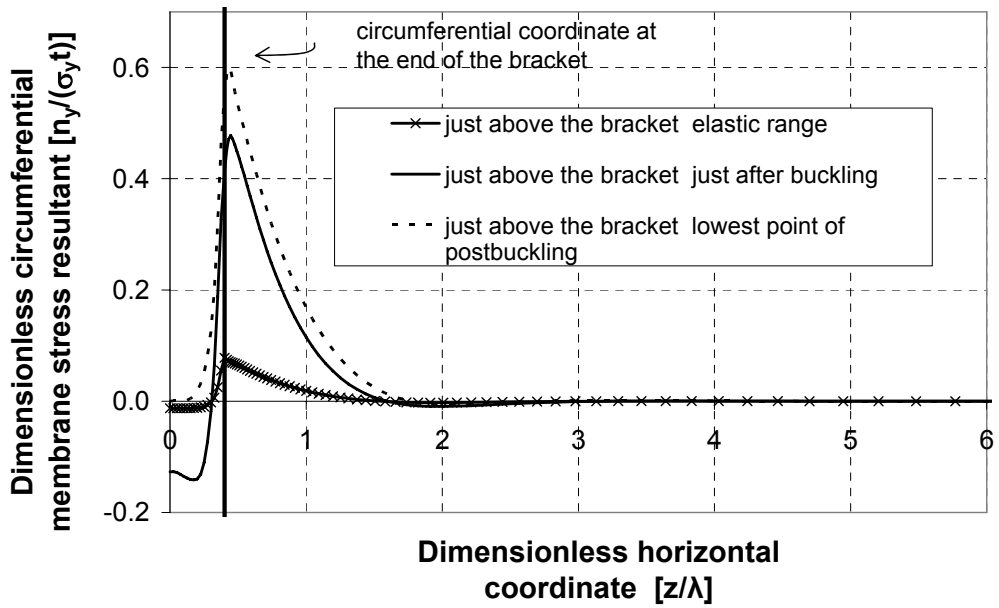

Figure 2.13c: Dimensionless circumferential membrane stress resultant just above the bracket at different stages (GMNA)

The dimensionless membrane shear resultant on a horizontal line through the middle of the bracket (Figure 2.13d) sustains the same form from pre-buckling, through buckling, and into the post-buckling range, only limited by the von Mises limit in shear $\pm\sigma_y/\sqrt{3} \approx \pm 0.577\sigma_y$ and is unaffected by the buckle above the bracket.

There is no suggestion of a plastic shear buckle here, even after extensive deformation, chiefly because the shear stress drops very quickly away from the bracket and there is not a large enough highly stressed zone for a buckle to develop. This is a common phenomenon is zones where shear stresses are locally high. It may be noted that a point-by-point assessment of buckling strength (DASt-Richtlinie-017-E, 1980; EN1993-1-6, 2006) is therefore very conservative if it depends on a high shear component.

In conclusion, the cylinder yields in shear on the side of the bracket just after buckling and in tension in the post-buckling range just below the bracket.

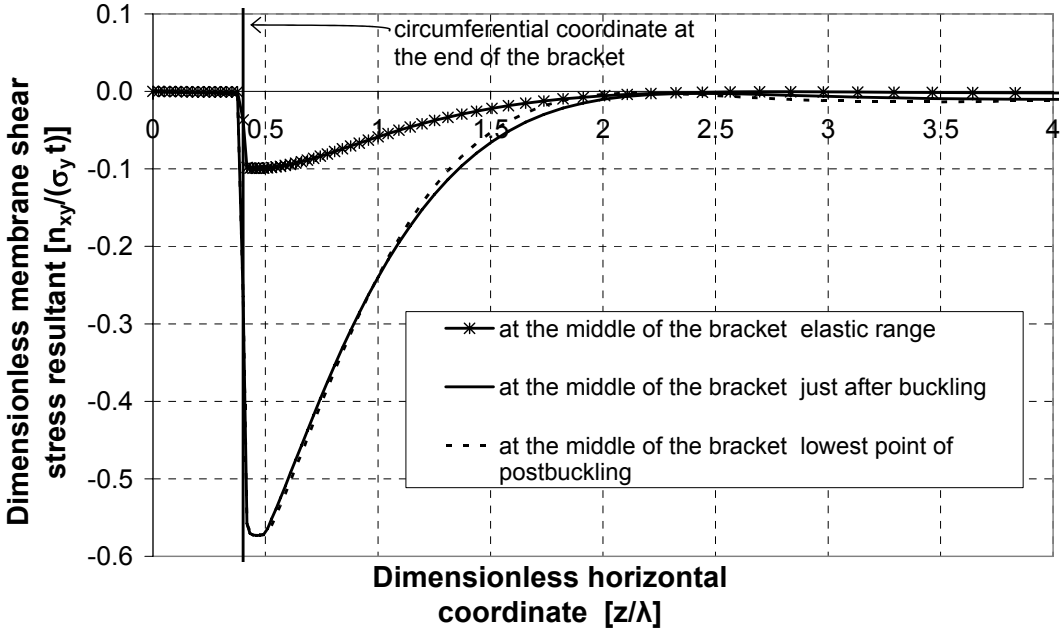

Figure 2.13d: Dimensionless membrane shear stress resultant at the mid-height of the bracket at different stages (GMNA)

2.9 Geometrically and Materially Nonlinear with explicit Imperfections Analysis (GMNIA)

Many, but not all, shell buckling configurations show considerable sensitivity to geometric imperfections. It is therefore most important to establish how imperfection sensitive the bracket-supported cylinder might be. The effect of a geometric imperfection was explored using a materially and geometrically nonlinear analysis with imperfections explicitly defined (GMNIA), and introducing a linear eigenmode

imperfection (Figure 2.3b), as proposed in EN1993-1-6 (2006), with an amplitude of one wall thickness. The resulting load deflection curve is shown in Figure 2.7 (circles), and indicates that the imperfection simply rounds off the peak seen in the GMNA analysis, producing a slight further strength reduction ($R_{GMNIA}/R_{REF} = 0.204$), together with a slightly falling post-failure curve. If the cylinder had been under uniform compression, a strength loss of perhaps 70% might have occurred due to an imperfection of this amplitude (Rotter, 2004), so this example shows that the bracket-supported cylinder is not very imperfection-sensitive. The effect of geometric nonlinearities is investigated on a wider range of geometries in Chapter 7.

2.10 Interaction between plasticity and buckling

Although the example problem gives a good insight into the details of the behaviour of this structural arrangement, it does not illustrate what changes occur as the slenderness of the system is altered, so that either buckling or plasticity might dominate. The range of possible behaviours is most easily illustrated by studying a range of geometries or material strengths that give rise to different slendernesses, using the plot proposed by Rotter (2003) to capture the full range. Here, the same shape of bracket was used, but the yield stress was modified to produce different slendernesses. This plot is shown in Figure 2.14, where the ratio of the GMNA to MNA failure loads is plotted against the ratio of the GMNA to LBA failure loads. High slenderness configurations are found at the bottom right, where elastic buckling at a knock down factor of 0.67 may be seen. When the slenderness has fallen so far that the ratio of GMNA to MNA reaches 0.4, the failure begins to be noticeably affected by yielding (though local yielding has occurred in more slender cases), and plasticity begins to dominate as the stocky conditions produce failures at which the GMNA failure load approaches the MNA value (top left). For this problem, it is clear that geometric nonlinearity plays a strong role in slender structures and that elastic-plastic buckling affects a wide range of stockier geometries. The plastic collapse load is only approached for very stocky conditions. The example problem described above was chosen, with a yield stress used of $\sigma_Y = 250$ MPa, to lie in the area where yielding and buckling phenomena would strongly interact.

A full description of the capacity curves can be found in Chapter 6.

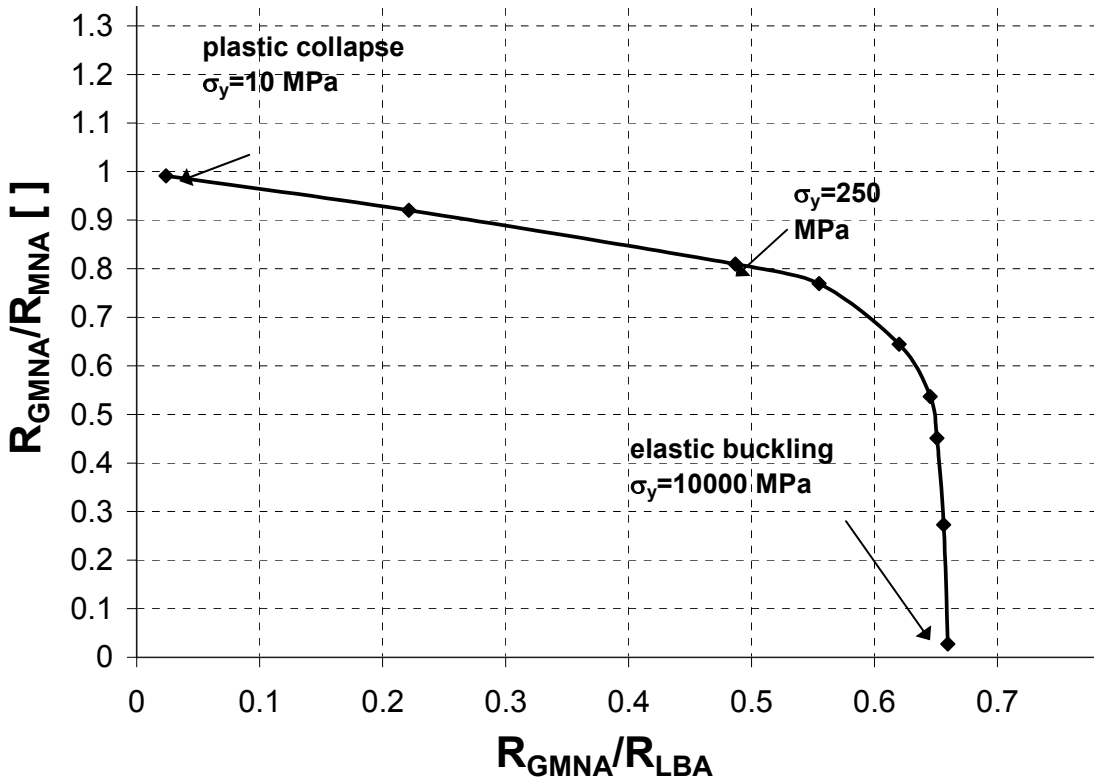

Figure 2.14: Capacity curve for shells of different slenderness

2.11 Conclusions

This chapter has presented an outline description of the behaviour of a cylindrical steel shell that is discretely supported on several brackets, each of which is rigidly connected to a stiff column. The linear, materially nonlinear, geometrically nonlinear and bifurcation behaviours of the shell have been outlined with detailed explanations of the changes in stress distribution arising from different geometrical and yield phenomena. The example shell geometry was chosen to illustrate interactions between bifurcation and plasticity in determining the failure condition. It has been shown that the behaviour is not very imperfection sensitive, at least for this geometry, so design rules should not follow the corresponding formulations for uniform axial compression too closely.

The different failure behaviours of the same geometry shell under different analyses have been explored. In the materially nonlinear analysis, plastic collapse was achieved with membrane yield all around the bracket. By contrast geometrically and materially nonlinear analysis (GMNA) showed yielding below and beside the bracket, but compressive stresses above the bracket causing buckling. The high shear stresses

on the side of the bracket did not produce buckling despite attaining the yield stress, due to their rapid decay horizontally.

This bracket problem illustrates many challenges in the interpretation of simpler computer analyses to design shells (EN1993-1-6, 2006). It is difficult to find a useful method of estimating of the plastic collapse strength when only linear analysis is used, the imperfection sensitivity of a system is not easily estimated on the basis of the principal stress direction causing buckling, and buckling is not easily predicted by taking the stress conditions at any point in the structure as representing a buckling failure stress state.

More detailed descriptions of the outcomes of the analyses described above will be presented in the following chapters of this thesis.

3 Linear Bifurcation Analysis

3.1 Introduction

The linear bifurcation analysis (LBA) is a small displacement stability analysis that assumes a perfect geometry, linear elastic material behaviour and no change in geometry (small displacement theory) before the infinitesimal displacements of the secondary path.

The parameters used to characterise the material of the shell and bracket are Young's modulus E and Poisson's ratio ν, whilst the cylinder geometry is described in terms of its radius r, thickness t and height H, and the bracket by its height h and width $2d$. Young's modulus and Poisson's ratio have been taken in all analyses as E = 200 000 MPa and $\nu = 0.30$ respectively.

The analysis is based on the assumption that a bifurcation point exists where primary and secondary load path intersect. Before this intersection point, the stresses in the structure change proportionally to the applied load, since the material is assumed to be elastic and the geometry does not change. The buckling load is then obtained by solving an eigenvalue problem (Chapter 1). An eigenvalue problem is solved when for a certain load magnitude the stiffness matrix becomes singular, which means deformations can progress without an increase of load. In Mathematical term this says that the Eq.3.1 has a nontrivial solution.

$$\lambda K v = 0 \tag{3.1}$$

Where λ=eigenvalue, v=eigenvector and K= stiffness matrix.

For structures like frames, columns and plates, this kind of analysis gives a good approximation for the elastic buckling (bifurcation) load (as discussed in Chapter 1). By contrast, for shells it loses its accuracy due to the sensitivity of shells to geometric nonlinearities and geometric imperfections, which a linear bifurcation analysis of the perfect structure ignores.

A Linear Bifurcation Analysis (LBA) is an important part of the new Eurocode (EN1993-1-6, 2006) framework, but in the past it has usually been disregarded as unimportant and not useful in interpreting the real buckling behaviour of shells. However the LBA is not only important with regard to the capacity curves of the

Eurocode (EN1993-1-6, 2006), it has a key role in itself, as noted by Rotter (2002). It is the only analysis which will always give a result for elastic buckling, and in general only requires that some compressive stresses are present. Furthermore, very few structures buckle at load levels that are as much as one order of magnitude different from the LBA state, so this load is always a good first estimate of the buckling strength. The LBA can also help with the interpretation of more sophisticated analyses in the sense that one can see how likely a structure is to fail in buckling. A closer look will be taken on this matter in the Chapters 5 and 6.

This chapter explores the behaviour of bracket supported shells under the LBA assumptions. A large number of analyses are conducted for shells and brackets of different geometries, and an attempt is made to find simple expressions that can be used to capture the evaluated strengths.

Since this analysis does not include any nonlinearity in material or geometry and is also very well researched, and since most documented analytical linear bifurcation analyses of shells begin with very complicated equations yet result in simple precise formulas, it is reasonable to expect that a simple analytical approximation to the bifurcation load should be found without difficulty. But it will be seen that when the bracket is not located at the bottom of the silo, the bifurcation load does not follow an obvious and simple pattern.

This chapter begins with general observations, and then describes the development of an empirical fit to the calculated bifurcation loads, together with a simple physical model to fit the results.

3.2 Verification

3.2.1 Convergence study and suitability of the element

To investigate the suitability of the element three different meshes with different elements were used. The first mesh used a 4- node general purpose element (S4R), whilst the second mesh consisted of 8- node thin shell elements with reduced integration (S8R5). The third mesh used a combination of elements with the general purpose element (S4R) for most of the model, but the thick shell element (S8R) around the bracket, as later described in Chapter 4. The calculated bifurcation load was about the same (within 1%) for the three investigated meshes.

To verify the mesh and the element to be used for the linear bifurcation analysis, a convergence study was performed using the third mesh with a mixture of S4R and S8R elements. The mesh converged well and was therefore suitable for use in the linear bifurcation analyses (Figure 3.1).

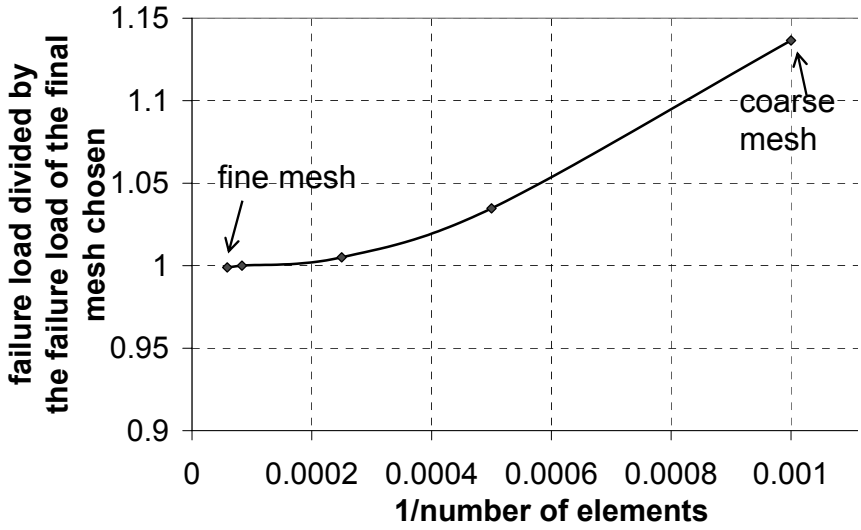

Figure 3.1: Convergence study

3.3 General observations

The Linear Bifurcation Analysis showed three modes of buckling. All of the bifurcation modes (hereafter simply referred to as buckles) occur above the bracket where the shell is in compression: no buckling modes were found corresponding to the shear stress field at the side of the bracket. In the first mode, which will be referred to as Mode A, the maximum displacement (amplitude) of the buckle appears at a height above the bracket of about $1.57 \cdot \sqrt{rt}$. In the second Mode B it appears at a height above the bracket of about $3.15 \cdot \sqrt{rt}$ (Figure 3.2). In the third Mode C, the maximum displacement occurs at a height above the bracket of about $4.90 \cdot \sqrt{rt}$, but the geometry of this bracket cannot be justified in any practical sense. In Mode A, the peak displacement in the buckling mode appears in the first wave above the bracket, but this peak moves to the second wave in Mode B (Figure 3.2). When the buckling mode is in transition from Mode A to B the first and second waves above the bracket naturally have almost the same absolute value of maximum displacement. Mode C displays then the maximum displacement in the third wave above the bracket.

A shear buckle might have been expected to be found beside the bracket for some configurations, since a strong shear field develops on either side of the bracket, but it did not occur in any of the geometries calculated The reason is possibly that, in brackets of small height, only very small zones develop high shears so the shear buckle is restrained by the small size of this zone, whilst in tall brackets, the long distance over which shear transfers can occur means that the shear stress is rather low, leading to no buckling either.

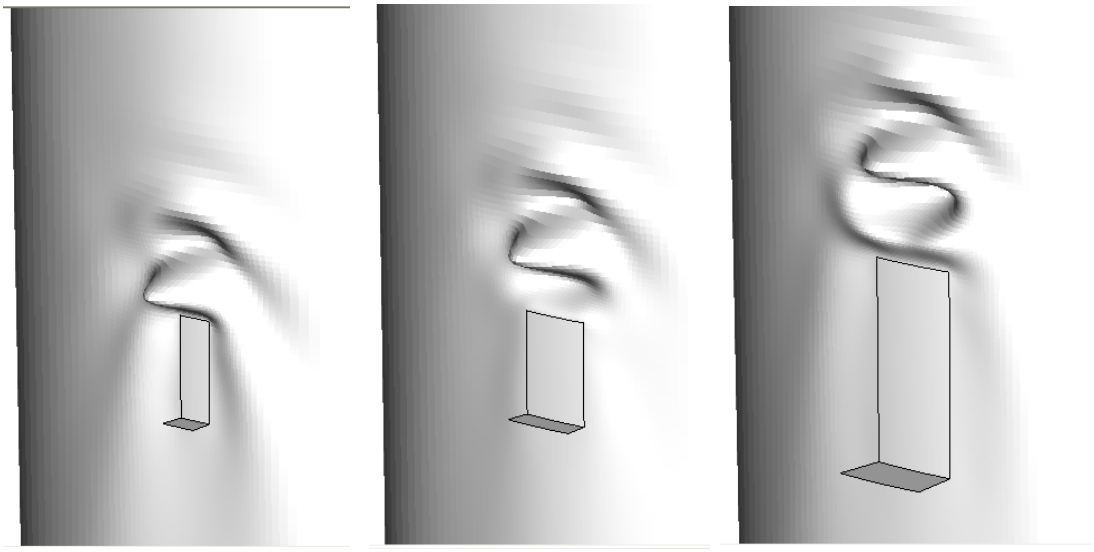

Mode A Mode B Mode C

Figure 3.2: Different eigenmodes at buckling (LBA) (deformation scale factor=70)

The different buckling eigenmodes are illustrated in Figures 3.3 to 3.5. The examples chosen for illustration of the buckling modes are all silos with a radius to thickness ratio of 600, but with different bracket geometries. For buckling Mode A the bracket geometry h/t=120, θ_o = (d/r)=0.0349 was selected (Figure 3.3), while for buckling Mode B h/t=120, θ_o = (d/r)=0.0698 (Figure 3.4) and for buckling Mode C h/t=240, θ_o = (d/r)=0.0873 (Figure 3.5). The pictures on the left hand side in these figures show the deformed shape of the first eigenmode calculated by ABAQUS (HKS, 2003). The graphs on the right hand side show the radial displacement of the eigenmode down a vertical line through the centre of one of the brackets.

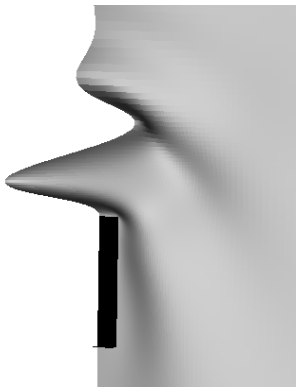

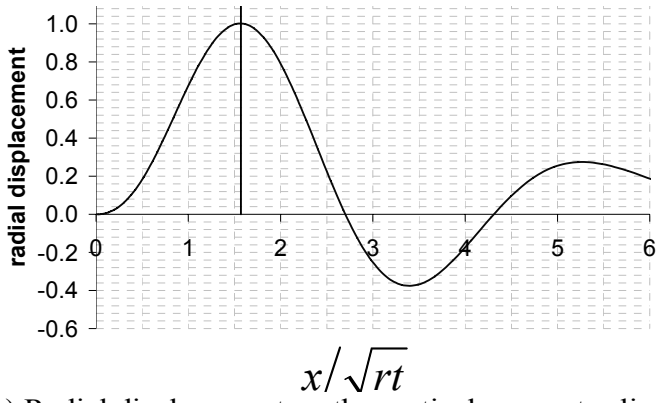

a) Picture of the finite element mesh at buckling

b) Radial displacement on the vertical symmetry line through the bracket. X=0=top of the bracket

Figure 3.3: LBA eigenmode for r/t=600, h=120, θ_o = (d/r) = 0.0349 (MODE A)

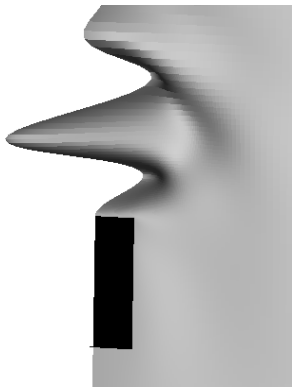

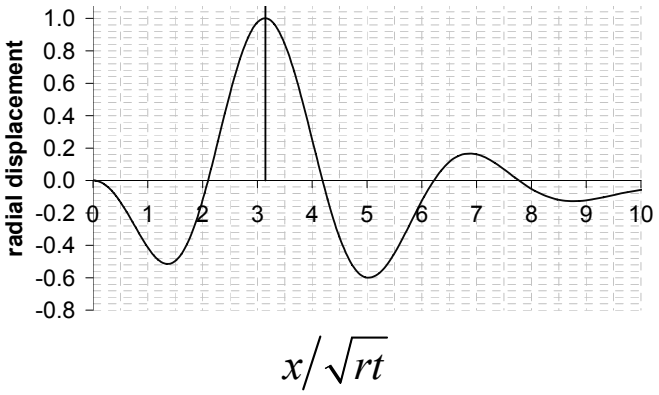

a) Picture of the finite element mesh at buckling

b) Radial displacement on the vertical symmetry line through the bracket. X=0=top of the bracket

Figure 3.4: LBA eigenmode for r/t=600, h=120, θ_o = (d/r) = 0.0698 (MODE B)

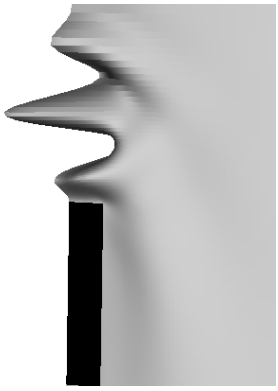

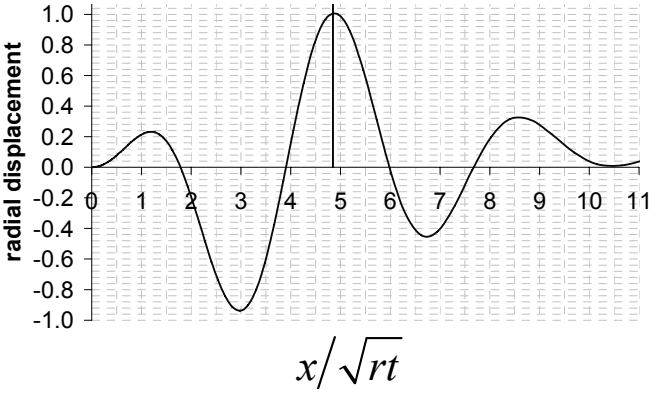

a) Picture of the finite element mesh at buckling

b) Radial displacement on the vertical symmetry line through the bracket. X=0=top of the bracket

Figure 3.5: LBA eigenmode for r/t=600, h=240, θ_o = (d/r) = 0.0873 (MODE C)

When the width of the bracket and the radius-to-thickness-ratio are kept constant, the shape of the buckle in the horizontal direction stays largely the same as shown in

Figure 3.6 for different heights of the bracket. The shape in vertical direction (Figure 3.6) does not stay exactly the same. Apart from the first half wave of the buckle a second wave or indentation can be seen at the height of about $3.5 \cdot \sqrt{rt}$ above the bracket. This second wave grows larger when the height of the bracket increases and therefore the first wave changes its shape to maintain the compatibility of the geometry. The overall shape however stays the same. When the first buckling mode (Mode A) occurs and the width of the bracket and the radius to thickness ratio of the silo are kept constant, it can be said that the buckle in a Linear Bifurcation Analysis has the same shape and appears at the same position for different heights of the bracket. The example shown in Figure 3.6 is a silo with the geometry r/t=600, θ_o = (d/r) = 0.0349, 30≤h≤300.

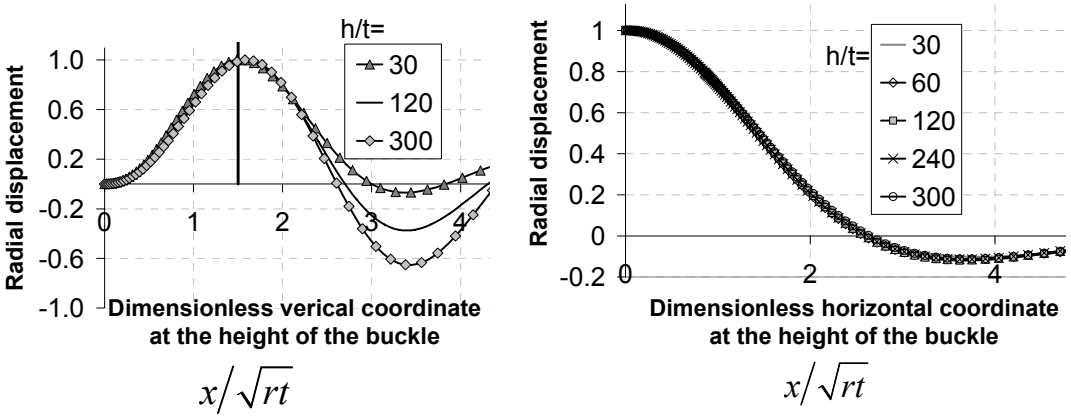

a) Radial displacement vs. vertical coordinate through the middle of the bracket

b) Displacement magnitude at buckling, λ_d above the bracket (0= above centre of the bracket

Figure 3.6 Radial displacements of the eigenmode in vertical and horizontal directions: Geometry r/t=600, θ_o = (d/r)= 0.0349

The position of the maximum displacement in the eigenmode for Mode A and Mode B is sometimes slightly higher, but for simplification the values 1.5 and 3 are adopted as fixed values in this study. Table 3.1 shows a summary of buckling modes found for a silo with a radius to thickness ratio of 600 with varying half-widths and heights of the bracket.

Λ \ θ_o=(d/r) h/t	0.01758	0.0349	0.0524	0.0698	0.0873
1.22	30	A	A	A	B	B
2.45	60	A	A	A	B	B
4.90	120	A	A	A	B	B
7.35	180	A	A	B	B	B
9.80	240	A	A	B	B	C
12.25	300	A	A	B	B	C

Table 3.1: Buckling modes for r/t=600

For brackets with a half-width θ_o=(d/r)=0.0175 and θ_o=(d/r)=0.0349 only Mode A occurs for all the bracket heights investigated (Table 3.1). When the half-width of the bracket increases to θ_o=(d/r)=0.0524, a change of buckling mode can be seen for tall brackets. Brackets with a half-width of θ_o=(d/r)=0.0698 display only Mode B. The change from Mode B to Mode C occurs then for very wide (θ_o=(d/r)=0.0873) and very tall brackets (h/t≥180). In summary the buckling mode changes from A to B or B to C mostly with increasing height, but to a lesser extent with increasing width of the bracket. Buckling Mode C only appeared for the widest and tallest brackets investigated and was considered to be outside of the practical range, though the findings here may have some important relevance to buckling above engaged columns. Therefore in this study, the buckling Modes A and B were predominantly investigated, but the buckling Mode C was taken into account for the prediction of buckling in Sections 3.4 and 3.5.

	r/t=200 θ_o=(d/r)=0.0349	r/t=400 θ_o=(d/r)= 0.0349	r/t=600 θ_o=(d/r)= 0.0349g
h/r=	width of the buckle / $\sqrt{rt}$	width of the buckle / $\sqrt{rt}$	Width of the buckle / $\sqrt{rt}$
0.05	2.83	2.90	2.69
0.1	2.79	2.85	2.58
0.2	2.70	2.65	2.59
0.3	2.65	2.65	2.59
0.4	2.66	2.65	2.60
0.5	2.65	2.65	2.64

Table 3.2: Dimensionless width of the buckle for changing bracket height (θ_o=(d/r)=0.0349)

	width of the buckle / $\sqrt{rt}$			
h/r=	θ_o=(d/r)=0.0175	θ_o=(d/r)=0.0349	θ_o=(d/r)=0.524	θ_o=(d/r)=0.0698
0.05	3.28	2.95	2.61	2.65
0.1	3.28	2.85	2.61	2.65
0.2	3.01	2.65	2.61	2.78
0.3	2.89	2.65	2.61	2.59
0.4	2.89	2.65	2.61	2.53
0.5	2.77	2.65	2.77	

Table 3.3: Change of the dimensionless width of the buckle (r/t=400)

Tables 3.2 and 3.3 show the dimensionless half width of the buckle, which was defined to be the length between the middle of the bracket and the point where the radial displacement is zero. The half width of the buckle was made dimensionless by dividing it by $\sqrt{rt}$. The parameter $\sqrt{rt}$ was chosen to make the width dimensionless, as it was expected that the width of the buckle would be a multiplier of the bending half wave length, which is a natural reference for short waves of compression buckles (Yamaki, 1984). In Table 3.2 a comparison of the half width of the buckle is made for different radius to thickness ratios for silos with *r/t*=200, 400, and 600. The height of the bracket is varied in the range $0.05 \leq h/r \leq 0.5$ and the width of the retained at bracket θ_o=(d/r)=0.0349. In Table 3.3 the radius to thickness ratio was kept at r/t=400 and the width of the bracket varied between θ_o=(d/r)=0.0175 and θ_o=(d/r)=0.698. The arithmetic average of the dimensionless half width of the bracket from Tables 3.2 and 3.3 is 2.77. No apparent trend is recognisable. Hence it can be said that the shape of the buckle in the horizontal direction is largely independent of the height of the bracket, but the width of the buckle seems to be similar for each studied width of the bracket, with only a small reduction as the bracket becomes taller.

The fact that the location of the buckle and its general shape stays approximately the same is very interesting. Since the shape of a buckle under local stress conditions is much affected by the stress distribution, it could be speculated that the same dimensionless axial stress σ/σ_{cl} at a given height above the bracket might produce a buckle with the same geometry.

As a result, a closer investigation of the stress patterns at the instant of buckling was undertaken done using a Linear Elastic Analysis (LA) to calculate the stresses.

The results of these analyses will later reveal the distributions and amplitudes of the stresses necessary for linear bifurcation of the shell. The dimensionless axial membrane stress resultant $\left\{n_x/(\sigma_{cl}\cdot t)\right\}$ from this analysis can be seen in Figure 3.7. The maximum vertical stress resultant at the height where the maximum displacement amplitude of the buckle appears ($\lambda_d=1.5\cdot\sqrt{rt}$ above the bracket) stays essentially the same. The example shown in Figure 3.7a is a cylinder with r/t=600, θ_o=(d/r)=0.0349 and varying h/r, but the bell shape and the essential behaviour stays the same for all geometries investigated. The maximum dimensionless stress resultant in Figure 3.7a is about $n_{x,max}=1.36\cdot\sigma_{cl}\cdot t$. The shape of the dimensionless vertical membrane stress resultant maintains the bell shape for all bracket heights (h/r). With growing height (h/r) the bell shape widens and the maximum stress decreases slightly. This effect is due to the increased shear field at the side of the bracket. As the bracket becomes taller more stress is transferred through the side of the bracket in shear. This shear-field allows an additional compression field to develop above and to the side of the bracket. Figure 3.7b shows the maximum axial membrane resultant for a selection of geometries. The values are very close to their average value of $n_{x,max}=1.35\cdot\sigma_{cl}\cdot t$. When the bracket becomes very wide, as in the example with r/t=400 and θ_o=(d/r)=0.0698, the maximum membrane stress resultant decreases since there is a wider stable stress field to produce a buckle.

This will be investigated further in section 3.5

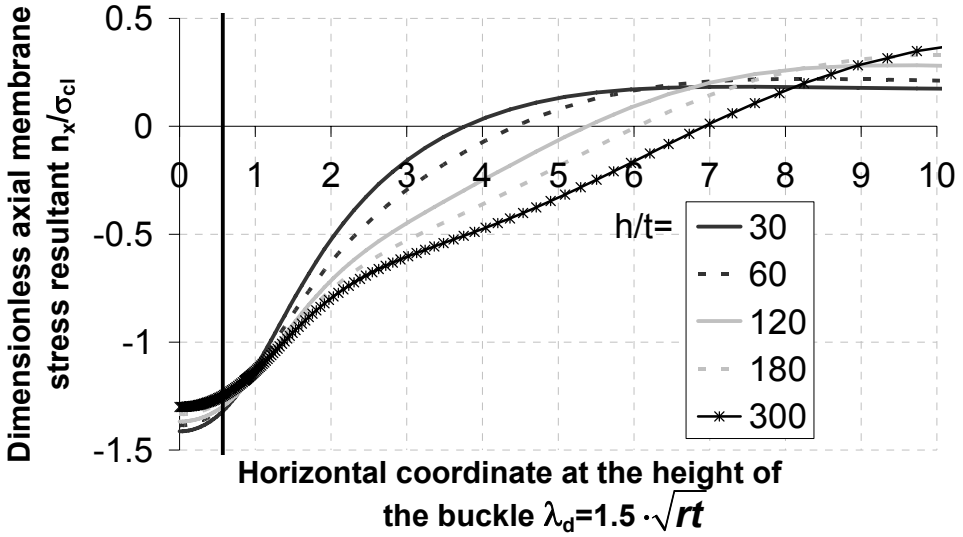

Figure 3.7a) Axial membrane stress resultant at λ_d above the bracket from a linear analysis (LA) at the linear bifurcation load, r/t=600, θ_o=(d/r)=0.0349

r/t	θ_o=d/r	Dimensionless vertical stress resultant
200	0.0349	-1.40
400	0.0175	-1.39
400	0.0349	-1.39
400	0.0524	-1.33
400	0.0698	-1.23
600	0.0349	-1.36

FFigure 3.7b) Maximum dimensionless vertical membrane stress resultant average for 0.05≤h/r≤0.5

3.4 LBA empirical fit

In this section, an attempt is made to find a simple means of predicting the LBA bifurcation strength of a shell with a local bracket at the mid-height. The parameters used are Young's modulus E and Poisson's ratio ν for the material of the shell, the radius r, thickness t and height H of the cylinder, height h and width $2d$ for the bracket geometry. The Young's modulus and the Poisson's ratio have been taken in all analyses as E = 200 000 MPa and ν = 0.30 to represent mild steel.

To normalize a dimension of the shell and bracket geometry, or a distance within the shell, the linear bending wave length λ was used as the appropriate parameter for the shell geometry (Eq. 3.2)

$$\lambda = \frac{\pi}{\left[3\left(1-\nu^2\right)\right]^{1/4}}\sqrt{rt} \approx 2.44\sqrt{rt} \tag{3.2}$$

For an easier assimilation of the results, the applied loading and the axial stresses are normalized by the classical elastic critical stress σ_{cl} for a cylinder under uniform axial compression (Eq. 3.3).

$$\sigma_{cl} = \frac{E}{\sqrt{3\left(1-\nu^2\right)}}\frac{t}{r} \tag{3.3}$$

3.4.1 Infinitesimally small bracket

At the beginning of this investigation it was decided to try to reduce the number of parameters, so the remaining parameters could be studied without difficulties. Therefore the bracket was first reduced to a point support or a bracket with zero dimensions. All other parameters were kept as described. The linear bifurcation load can then only depend on the elastic properties of the shell and its radius and thickness. The graphs in this section show the dimensionless axial support force $F_{LBA}/(\sigma_{cl}\, t^2)$ per bracket, which is calculated from the uniform tensile load applied on the bottom edge of the shell.

A convergence study was done to verify the mesh (Figure 3.8). Two different elements were used (S4R and S8R5) to confirm the suitability of the elements chosen (S4R).

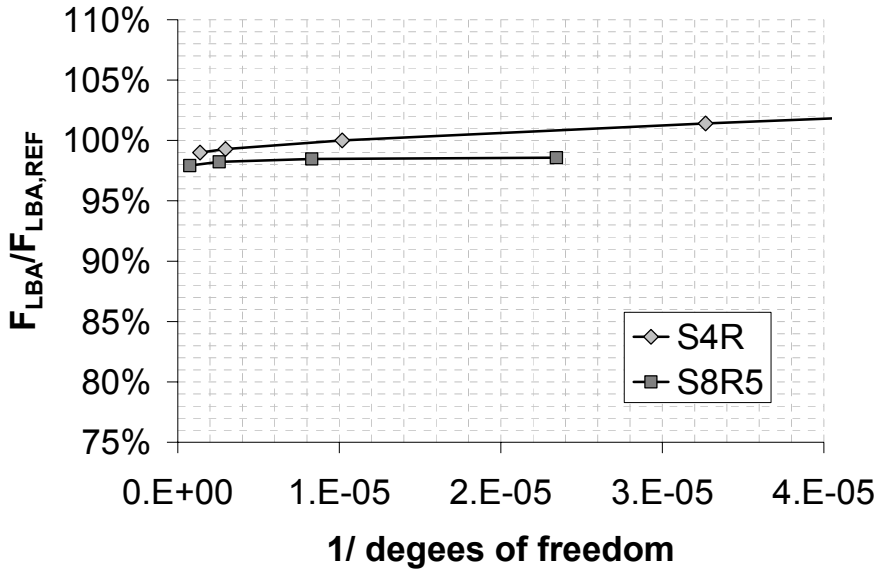

Figure 3.8: Convergence study (r/t=600)

The 8- node thin shell element (S8R5) converges faster and to a slightly lower load than the general purpose elements (S4R). The difference between the bifurcation loads of the very fine mesh with S8R5 elements and the mesh chosen using the general purpose element S4R ($F_{LBA}/F_{LBA,REF}$=100%) is about 2%, but the increase of computing power needed for the quadratic element could not justify its use. The range considered in the case of the bracket with zero dimensions was $200 \leq r/t \leq 1000$, $1 \leq t \leq 3$. In all the other analyses performed in this thesis, the dimensions were normalised relative to the thickness, for this case of the point

support only, different thicknesses were used to demonstrate conclusively that normalising all parameters relative to the thickness is always valid.

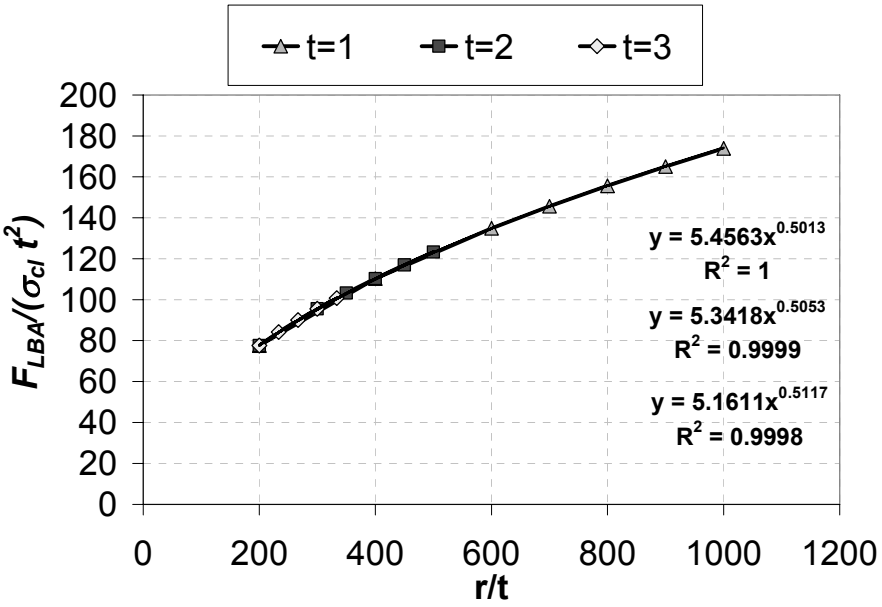

Figure 3.9: Dimensionless bifurcation load vs. r/t (h=d=0)

Figure 3.9 shows the relationship between the dimensionless bifurcation load expressed as the vertical reaction force on one bracket at buckling $F_{\mathrm{LBA}}/(\sigma_{\mathrm{cl}}\ t^2)$ and the radius-to-thickness ratio.

It is clear that the dimensionless bifurcation load is only dependent on the radius to thickness ratio of the shell (Figure 3.9). The trendlines suggest very strongly that the dimensionless support force at linear elastic bifurcation $F_{LBA}/\sigma_{cl}t^2$ follows an equation of the form

$$F_{LBA}/\sigma_{cl}t^2 = a\left(r/t\right)^b \tag{3.4}$$

Parameter *b* is very close to 0.5, while the parameter *a* is close to a constant value of about 5, for all the thicknesses chosen. When the parameter *b* is chosen to be 0.50 and the parameter *a* is chosen to take the value of 5.48 according to a best fit analysis of parameter *a* for all thicknesses investigated, the maximum difference between the between the empirical solution and the numerical results occurred for t=3 and was 0.43%, which is of the same order as the error associated with mesh refinement, so cannot be considered to be significant. The empirical solution can then be written as

$$F_{LBA}/\sigma_{cl} \cdot t^2 = 5.48 \cdot \sqrt{r/t} \tag{3.5}$$

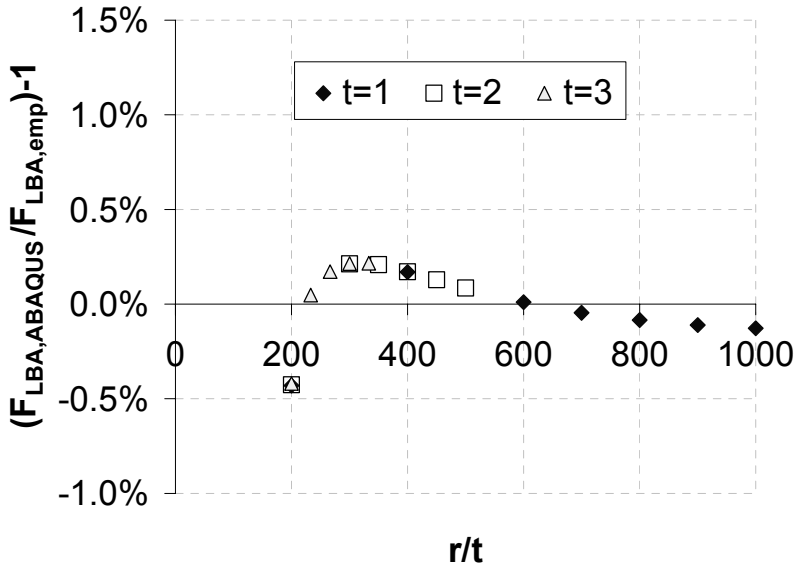

Figure 3.10: Difference between numerically calculated buckling loads and buckling loads predicted using Eq. 3.5

The differences between the prediction of Equation 3.5 the load on each bracket at bifurcation and the finite element calculations are shown in Figure 3.10. The maximum over-prediction of the support force at buckling is about 0.43%, while the greatest under-prediction is about 0.22%. The root mean square error (RMS error) is 0.22%. The largest errors appear for the smallest r/t ratio of 200. It is difficult to judge where the origin of the difference between prediction and the result of the numerical model lies. The errors are very small and not exactly the same mesh was used for the different radii of the silo. But there is always the same difference between the numerical result and the equation for each r/t ratio, irrespective of the shell thickness, despite the differences in the meshes used. These differences may lie in the precise formulation of the shell equations used in ABAQUS (HKS, 2003), which may differ slightly from the simpler versions, such as the Donnell equations (Timoshenko and Gere, 1961) which would almost certainly lead to a simple outcome.

It should be noted that Equation 3.5 has only been verified for r/t ratios in the range $200 \leq r/t \leq 1000$, but there is no reason to suppose that it is not valid for all thin shells.

3.4.2 Bracket height variation: zero width, varying the radius

Following successful identification of the bifurcation resistance of a point support in the middle of a cylindrical shell, the next step was to add one finite dimension for the bracket, to explore the effect this has on the bifurcation load. It was thought to be a good procedure to develop an understanding of the behaviour by introducing one parameter at a time into the calculation.

The height of the bracket was chosen as non-zero, but the width was still kept as zero. The hypothesis was proposed that the bifurcation load would vary in a similar manner with shell radius to that found for a point support.

The width of the bracket was chosen as small as possible within the modelling limits when using ABAQUS (HKS, 2003). The width was kept within the range $0.042 \le \Gamma = d/\sqrt{rt} \le 0.069$. It was assumed that these values would give a very close approximation for the condition $\Gamma = d/\sqrt{rt} = 0$. The range of geometries considered was 300< ≤r/t<≤1000 and 12< ≤h/t<≤100.

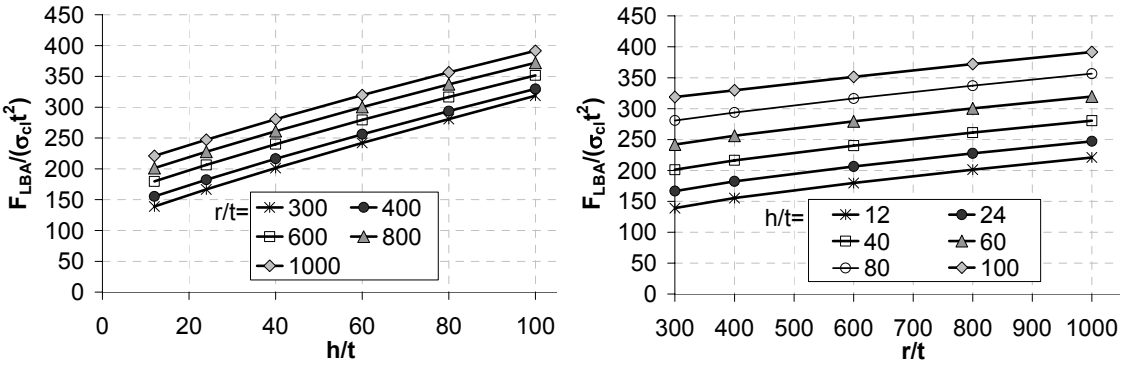

Figure 3.11: Bifurcation loads vs. r/t and h/t

The results of these linear bifurcation analyses are shown in Figure 3.11. At larger *r/t* ratios the support force at bifurcation varies almost linearly with the dimensionless height of the bracket *h/t* (Figure 3.11a), but at smaller *r/t* ratios the variation is slightly nonlinear and the behaviour is closer to a rational function in the form of Eq. 3.6.

$$\frac{F_{LBA}}{\sigma_{cl}t^2} = \frac{a_1(r/t)\cdot h/t + a_2(r/t)}{h/t + a_3(r/t)} \tag{3.6}$$

The bifurcation load was made dimensionless using the classical buckling stress

since it was expected that this reference stress will play a part in the bifurcation of a bracket supported silo.

The parameters a_1, a_2 and a_3 in Eq. 3.6 are expected to all be functions of *r/t*. Ideally the height of the bracket would have been made dimensionless by a shell length parameter like the linear bending half wave length, but these early analyses were done using the dimensional parameter *h/t*.

This function seemed to be appropriate because a rational function of this kind approaches a plateau at very large *h/t* and can also be fitted to match the point support of the previous section. A polynomial function could have been chosen to fit the bifurcation loads, but it has the disadvantage that the values of a polynomial function increase to a maximum at large *h/t* and decrease after the maximum. This would have given a poor representation beyond the certain height for the bracket.

When the values of the bifurcation load are fitted to Eq. 3.6, the parameters a_1, a_2 and a_3 are found to vary with r/t as shown in Figures 3.12 and 1.13.

A best fit for these parameters was obtained by minimizing the sum of the squares of all errors between the approximate equation and the numerical result. The outcome was then confirmed with an overall best fit using a linear regression analysis. The maximum error was 0.17% and the RMS error was only 0.08%.

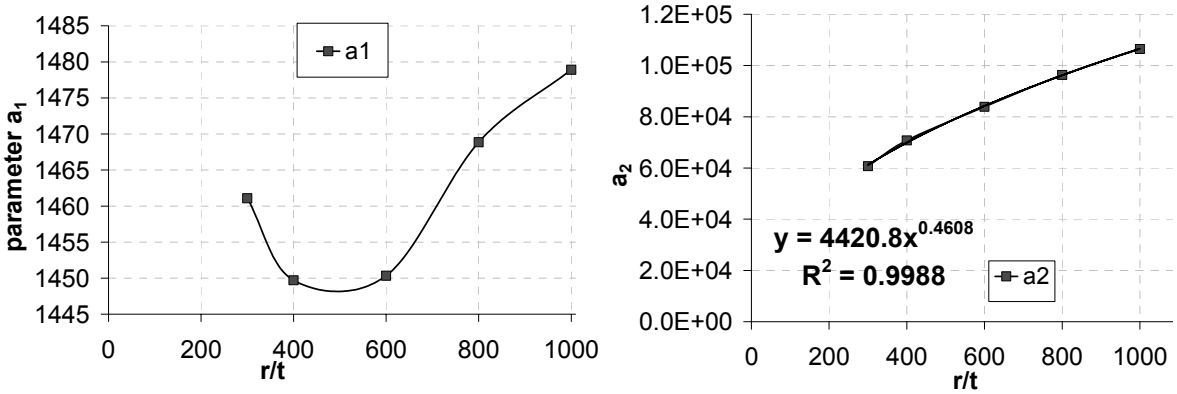

a) Variation of the parameter a_1 with r/t **b) Variation of the parameter a_2 with r/t**

Figure 3.12: Variation of the parameters a_1 and a_2 with r/t

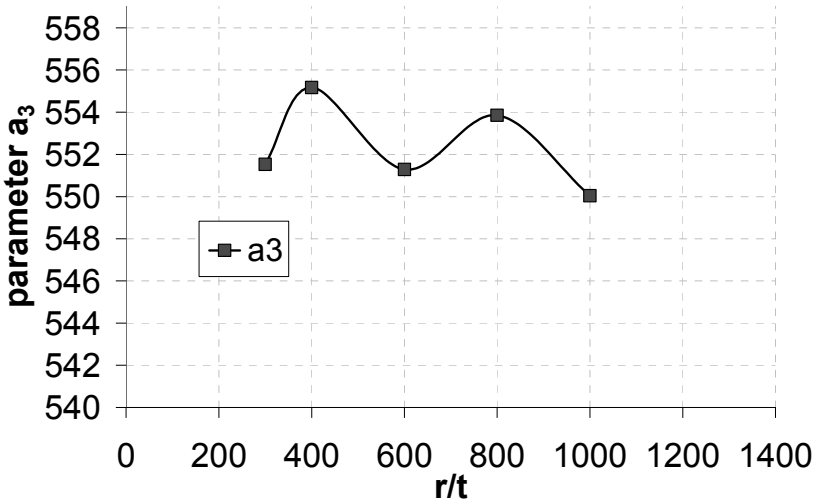

Figure 3.13: Variation of the parameter a_3 with r/t

The parameter a_3 (Figure 3.13) shows a close approximation to a constant value

$$a_3 = \text{constant} \tag{3.7}$$

Equation 3.6 can be written with a constant the parameter a_3 as

$$\frac{F_{LBA}}{\sigma_{cl} t^2} = \frac{a_1 (r/t) \cdot h/t + a_2 (r/t)}{h/t + a_3} \tag{3.8}$$

When Equation 3.8 is used to perform a new best fit to the numerical solution, the maximum discrepancy between the numerically calculated bifurcation load and the empirical solution with a constant parameter a_3 for all r/t ratios is 0.29%, while the RMS is only 0.1%.

After this best fit analysis, the parameter a_1 is almost constant over r/t with a maximum discrepancy from its average for any r/t value of only 1.33% (Figure 3.14), while parameter a_2 follows closely a function of the form

$$a_2 = a_4 (r/t)^{0.5} \tag{3.9}$$

and

$$a_1 = \text{constant} \tag{3.10}$$

The maximum difference between the parameter a_2 calculated using Eq. 3.9 and the value calculated by the previous best fit analysis is only 1.98%.

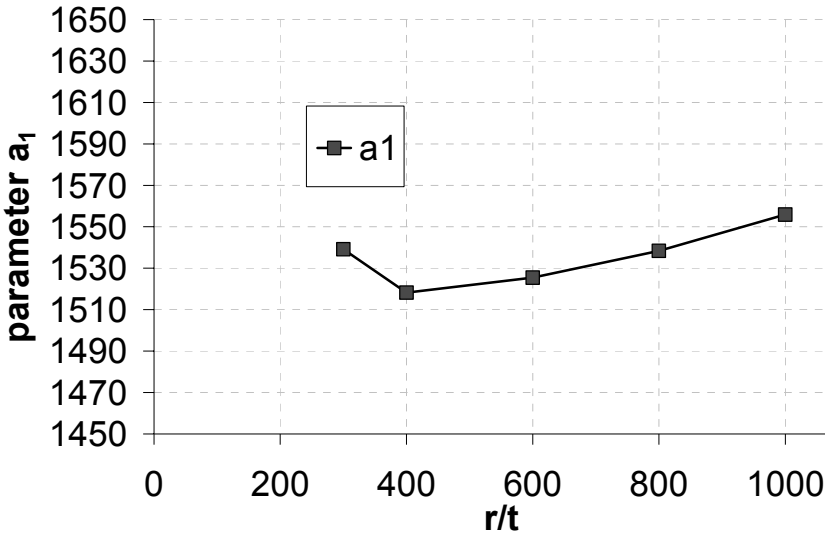

Figure 3.14: Variation of the parameter a_1 with r/t using Eq. 3.8

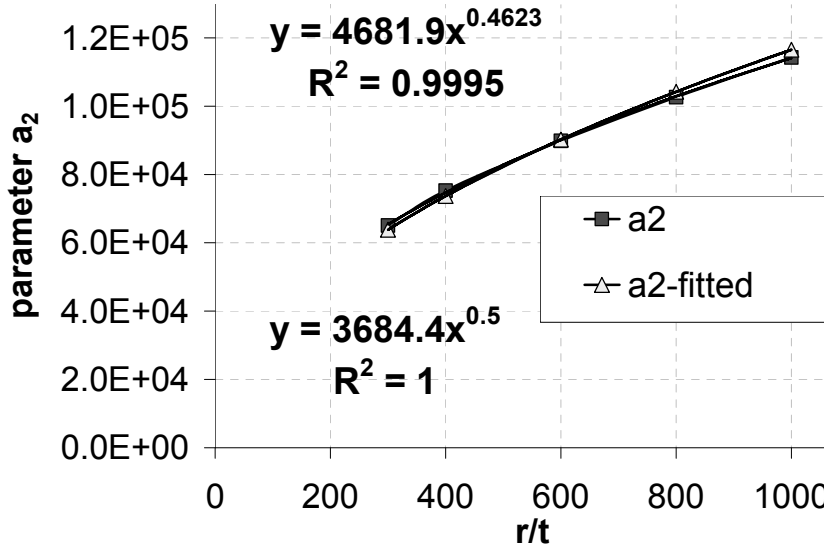

Figure 3.15: Variation of the parameter a_2 with r/t using Eq. 3.8

The equation which governs the whole system can then be described using Eq. 3.8 - 3.10 as

$$\frac{F_{LBA}}{\sigma_{cl}t^2} = \frac{a_1 \cdot h/t + a_4\sqrt{r/t}}{h/t + a_3} \tag{3.11}$$

with a_1= 2047, a_4= 5140 and a_3= 837. This equation was also used as basis for the further empirical fit with $d \neq 0$. The maximum discrepancy between the numerical results and the empirical fit using Eq. 3.11 was 3.98%, while the RMS was only 1.8 %.

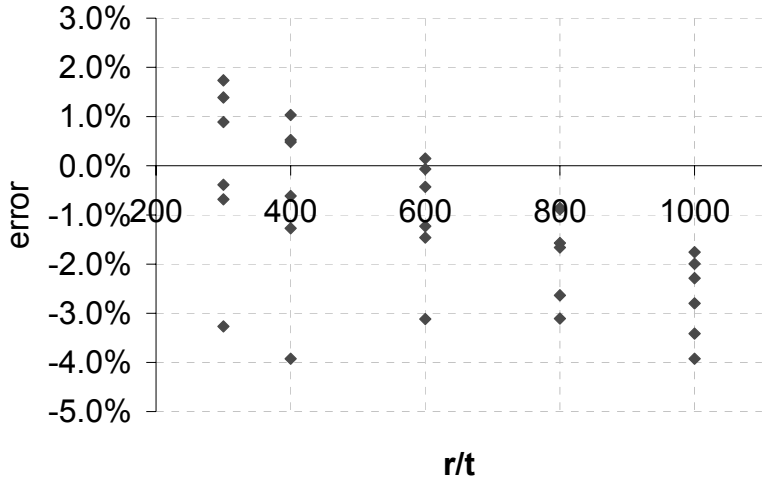

Figure 3.16: Errors in Equation 3.11 relative to the ABAQUS (HKS, 2003) result

To match the equation found for the point support (Eq. 3.5) the ratio of the parameters a_4/a_3 in Eq. 3.11 would have to be 5.48, but the ratio found in Eq. 3.11 is $a_4/a_3 = 6.14$. This difference might have its source in the modelling of bracket. The bracket was assumed to have no width, but due to modelling restriction a very small width had to be modelled. Therefore it is possible that the 12% difference (6.14/5.48=1.12) arises from there, though it seems a large difference for such a small modelling error. A further discussion about this difference can be found in Section 3.4.4.

3.4.3 Empirical fit to the bifurcation load for the cylinder with a bracket of finite dimensions

The true purpose target of this work was to explore the bifurcation loads of bracket supported cylinders with brackets of finite height and width. As above, the height of the bracket h and its half width d were made dimensionless using the characteristic length $\sqrt{rt}$. In what follows, the new dimensionless parameters $\Lambda = h/\sqrt{rt}$ and $\Gamma = d/\sqrt{rt}$ will be used to define the bracket geometry to make the description less complicated.

The aim was to derive a good empirical fit from a moderately large set of bifurcation loads (150 geometries) relating to practical geometries, and to verify this fit independently with another set of calculated bifurcation loads (a second set of 160 different geometries).

The following set of bifurcation loads calculated in ABAQUS (HKS, 2003) was

used to derive the empirical fit: the range consisted of geometries from 200≤r/t≤1000, $1 \le \Lambda = h/\sqrt{rt} \le 7$, $0.25 \le \Gamma = d/\sqrt{rt} \le 1.25$. This set contained 150 different geometries.

The heuristic procedure used to find a suitable fit to the numerically calculated bifurcation loads had the following structure:

1. Choose an appropriate function for each variable (in this case Λ, Γ and r/t);
2. Choose a function F1 for fitting the data to one of the variables (in this case Λ);
3. Fit the parameters of F1 to the data using the least squares of the error to the numerically calculated bifurcation loads;
4. Plot the parameters against another variable (in this case Γ);
5. Choose an appropriate function F2 for one of the parameters found in F1;
6. Implement this function F2 into F1 and fit the new parameters using the least squares of the error to the numerically calculated bifurcation loads;
7. Plot the parameters again. They will be slightly different now since F2 was chosen for one the parameters;
8. Choose an appropriate function F3 for one of the other parameters;
9. Implement F3 into F1 and fit it again to the least squares of the error;
10. Plot the parameters and repeat the procedure until a function for each parameter has been chosen, implemented and fitted;
11. Then compare the function derived with the original function chosen in Step 1. If they are in agreement go to next step, otherwise start the procedure again;
12. Plot the all the parameters found against the next variable (in this case r/t);
13. Repeat the entire procedure.

For the first step from the procedure discussed above it is important to find a suitable approximation for each of the variables. Therefore the bifurcation loads calculated by ABAQUS (HKS, 2003) will be shown first in their raw format to give an indication of the variation of the bifurcation loads with different variables. The variation of the bifurcation load with the radius to thickness ratio is shown in Figures 3.17 and 3.18. The shortest and the longest brackets (Figure 3.17) have been chosen, followed by the narrowest and widest bracket (Figure 3.18). The aim was to give a good general overview of the behaviour. The dimensionless bifurcation load

increases in a nonlinear manner when the radius to thickness ratio is increased. It is not easy to determine what kind of function would fit the relationship between the dimensionless support force per bracket at bifurcation $F_{LBA}/(\sigma_{cl}t^2)$ and the r/t ratio. Either a rational function of the form

$$\frac{F_{LBA}}{\sigma_{cl}t^2} = (r/t + a)/(b \cdot r/t + c) \tag{3.12}$$

or an exponential function of the form

$$\frac{F_{LBA}}{\sigma_{cl}t^2} = (r/t)^a + b \tag{3.13}$$

might seem appropriate, in which the parameters *a*, *b* and *c* are functions of Λ and Γ. The equations developed for the point support (Eq. 3.5) and the zero-width support (Eq. 3.11) do not give a coherent picture of the influence of radius to thickness ratio, so it was decided not to start seeking an empirical fit by using this variable.

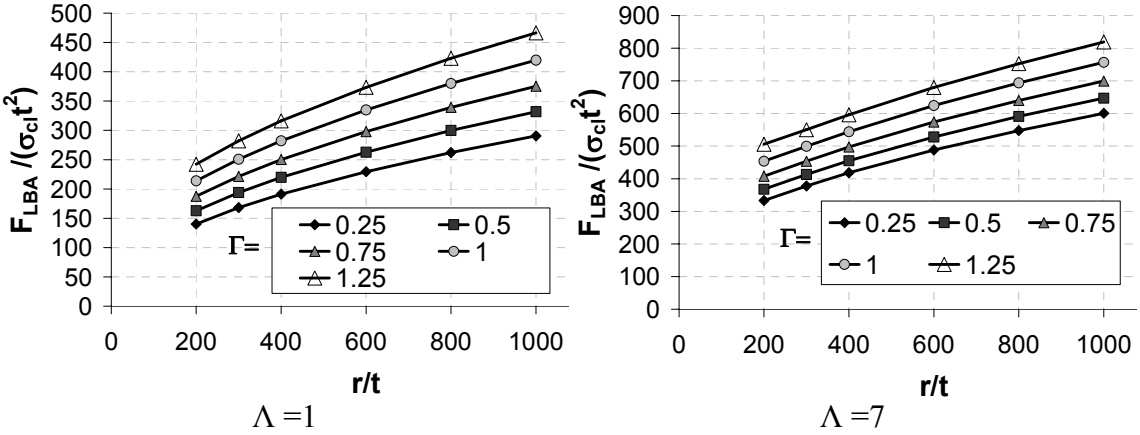

Figure 3.17: Dimensionless bifurcation load (shown as support force on one bracket) for Λ=1 and 7

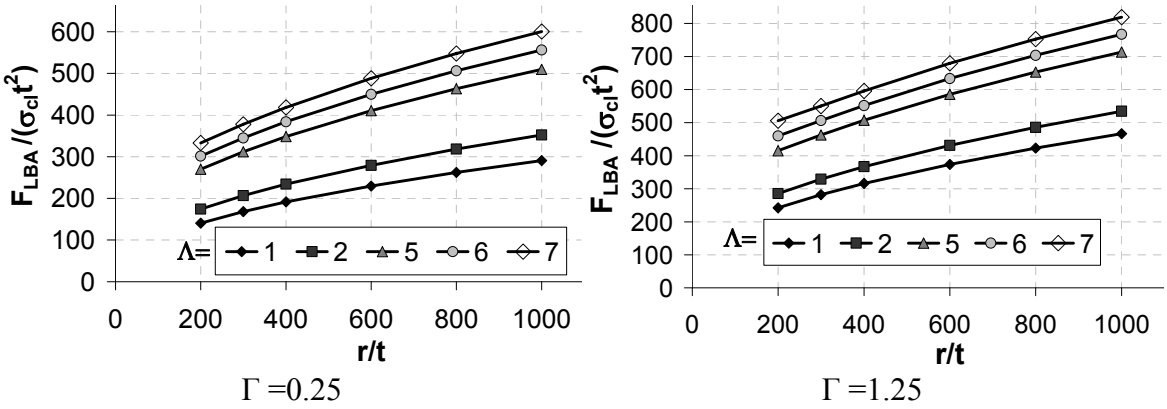

Figure 3.18: Dimensionless bifurcation load (shown as support force on one bracket) for Γ =0.25 and 1.25

The second study explored the variation of the dimensionless bifurcation load with the dimensionless width of the bracket (Figures 3.19 and 3.20). Again the two extremes were examined. Figure 3.19 shows the results for the thickest and the thinnest silos and Figure 3.20 shows the shortest and the tallest brackets. The dimensionless bifurcation load increases nonlinearly with the dimensionless width of the bracket Γ. The variation of the dimensionless bifurcation load with the dimensionless width of the bracket can be closely represented by a polynomial function or else a rational function of the form shown in Equation 3.14, in which *a*, *b* and *c* are function of *r/t* and Λ

$$\frac{F_{LBA}}{\sigma_{cl}t^2} = \frac{d/\sqrt{rt}+a}{bd/\sqrt{rt}+c} \tag{3.14}$$

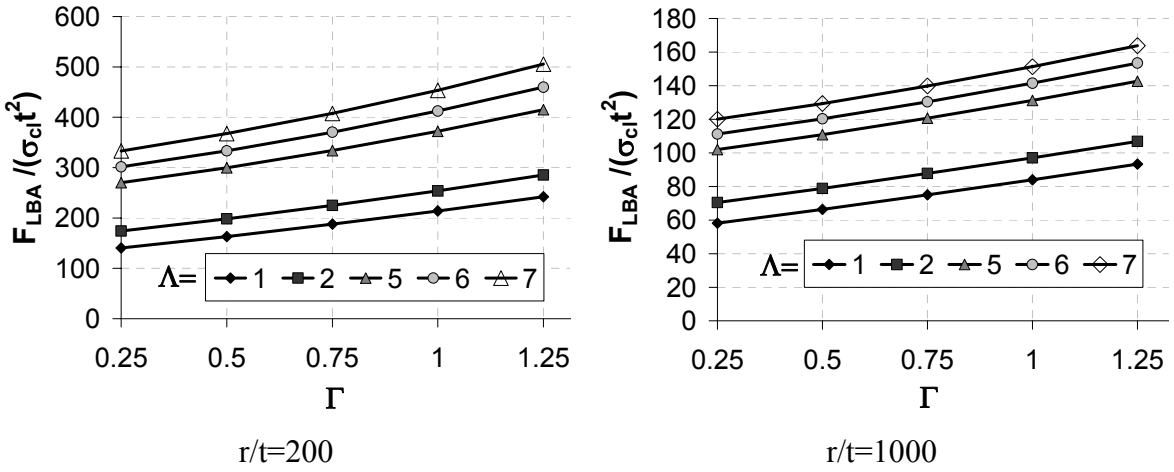

r/t=200 r/t=1000

Figure 3.19: Dimensionless bifurcation load (shown as support force on one bracket) for r/t=200 and 1000

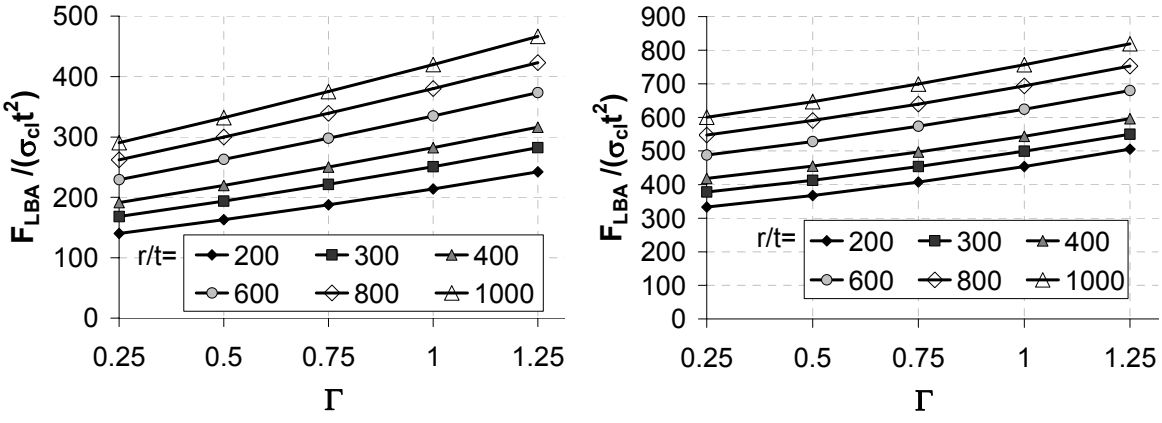

Λ =1 Λ=7

Figure 3.20: Dimensionless bifurcation load (shown as support force on one bracket) for Λ =1 and 7

The third short study examined the variation of the bifurcation load with the

dimensionless height of the bracket $\Lambda = h/\sqrt{rt}$ (Figures 3.21 and 3.22). The bifurcation load increases with the height of the bracket, because a substantial amount of the applied load is transferred directly as tension into the bottom of the bracket, and as shear into the side of the bracket. As the height of the bracket increase more of the applied load is transferred as shear into the side of the bracket, reducing therefore the percentage of load which is transferred as compression into the top of the bracket to cause bifurcation.

The bifurcation load increases almost linearly for the thickest silo with r/t=200 (Figure 3.21a), but for the thinnest silo with r/t=1000 (Figure 3.21b) the behaviour becomes increasingly nonlinear. This effect was also seen in the bifurcation loads when the bracket had zero width (Figure 3.11a).

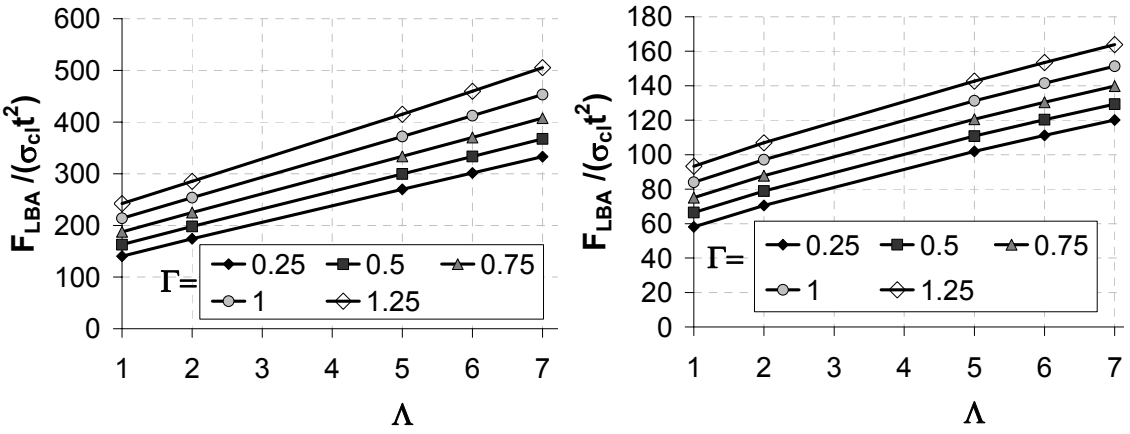

a) r/t=200 b) r/t=1000

Figure 3.21: Dimensionless bifurcation load (shown as support force on one bracket) for r/t=200 and 1000

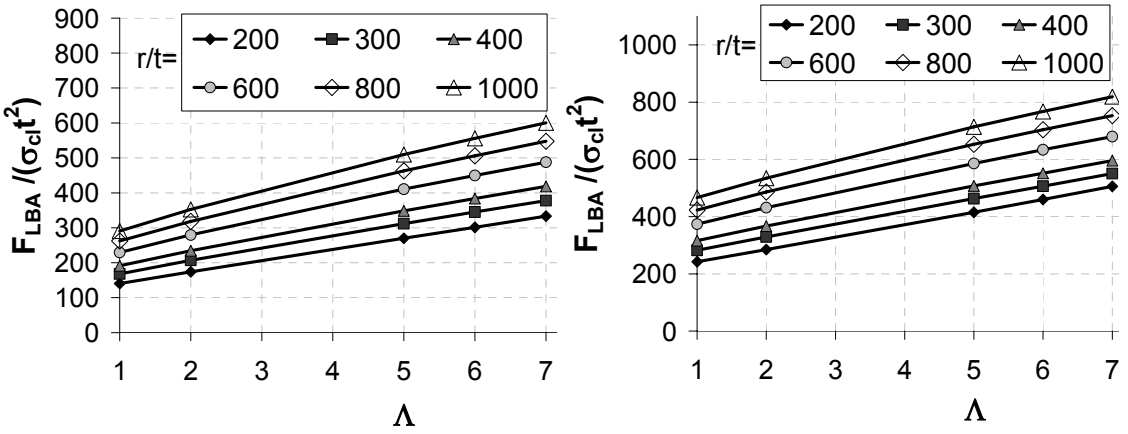

Γ =0.25 Γ =1.25

Figure 3.22: Dimensionless bifurcation load (shown as support force on one bracket) for Γ=0.25 and 1.25

Since the bifurcation load also increases nonlinearly for the narrowest and widest bracket (Figure 3.22) and to retain compatibility with the empirical equation previously found for the bracket of zero width, the function chosen to fit the bifurcation loads was chosen to depend on the dimensionless height of the bracket Λ in the form of Equation 3.15.

$$\frac{F_{LBA}}{\sigma_{cl} t^2} = \frac{h/\sqrt{rt} + a}{bh/\sqrt{rt} + c} \tag{3.15}$$

When Equation 3.15 was fitted to the numerically calculated bifurcation loads, the maximum error was ±0.4%. The parameters *a*, *b* and *c* are each expected to be functions the variables Γ and *r/t*.

After fitting the calculated bifurcation loads using Equation 3.15, a set of values of the parameters *a*, *b* and *c* were obtained for each width and radius to thickness ratio.

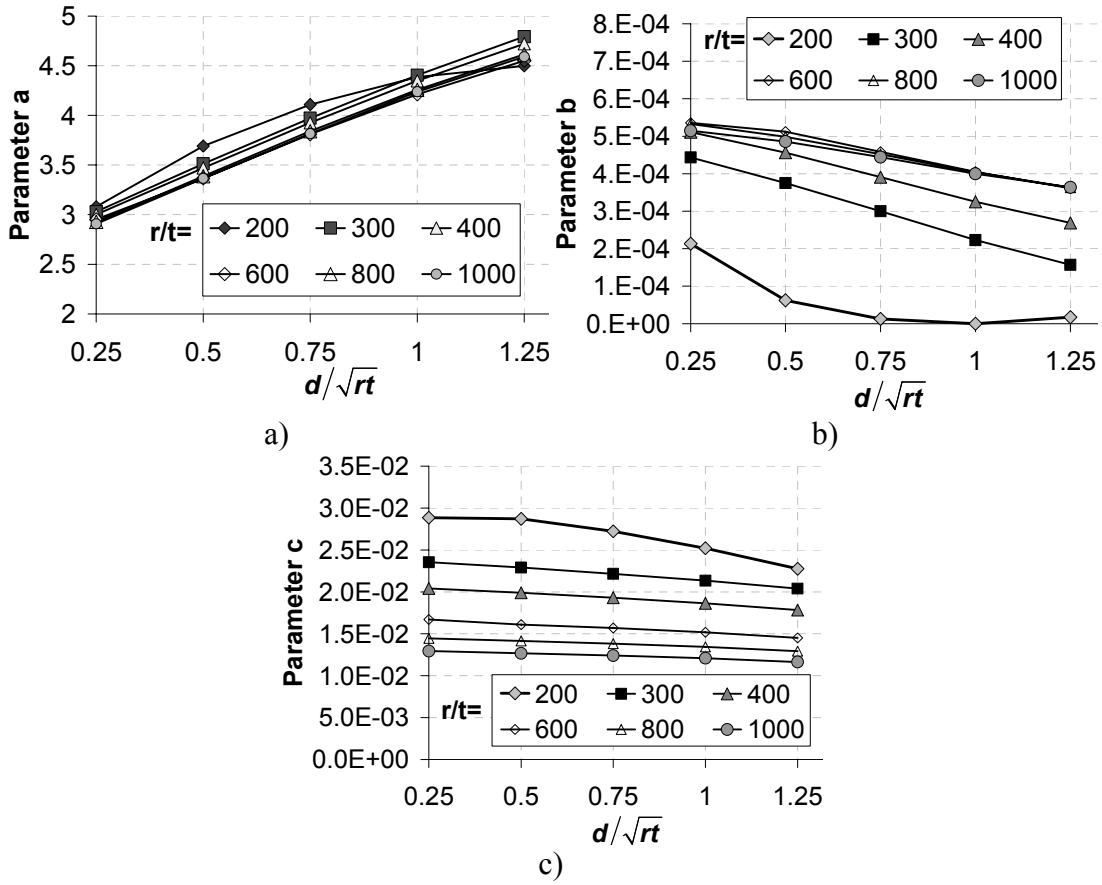

Figure 3.23: Trend of the parameters from Eq. 3.15

These best fit values of the parameters *a*, *b* and *c* are shown in Figure 3.23

plotted against the dimensionless width of the bracket $\Gamma = d/\sqrt{rt}$. It can be seen that for r/t=300 to 1000 the variation of all parameters is reasonably linear. For the thickest silo with r/t=200 the parameters differ greatly from the other r/t ratios and also display a rather nonlinear variation. A decision was therefore made to ignore the nonlinearity of these parameters and to take the general form of the parameter variations for the remaining r/t ratios. When the parameter *a* was examined more carefully, it was found to take unchanging values when r/t is large (r/t > 600). If the variation of the parameter *a* with the dimensionless width of the bracket is indeed linear, this would match the general behaviour described by Equation 3.14. In the first step, the parameter *a* was treated as varying linearly with $\Gamma = d/\sqrt{rt}$. This was done to observe the effect on the other two parameters *b* and *c*. The effect can be seen in Figure 3.24.

$$\frac{F_{LBA}}{\sigma_{cl} t^2} = \frac{\Lambda + a_1 \Gamma + a_2}{b\Lambda + c} \tag{3.16}$$

When Equation 3.16 was used to obtain the best fit, the maximum error was ±0.24% and the parameter *c* shows now a clearly linear behaviour (Figure 3.24). Therefore it was assumed in the next step that *c* varies linearly with $\Gamma = d/\sqrt{rt}$.

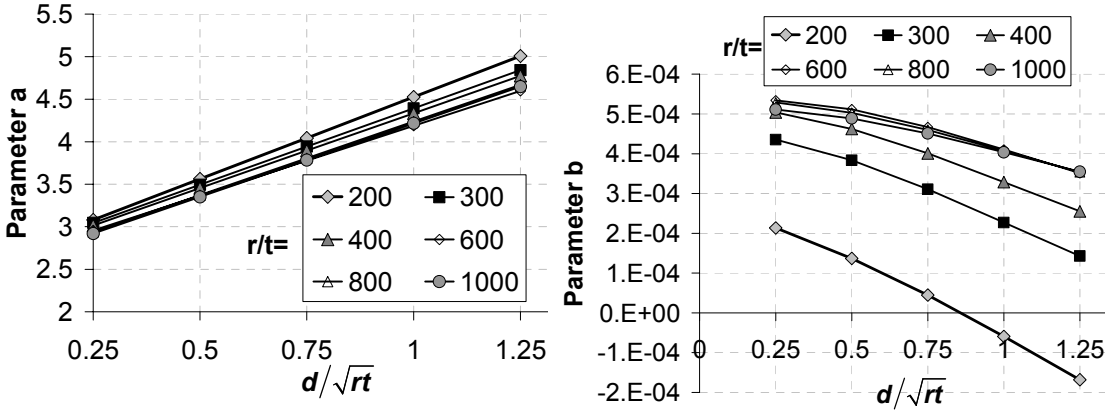

a) b)

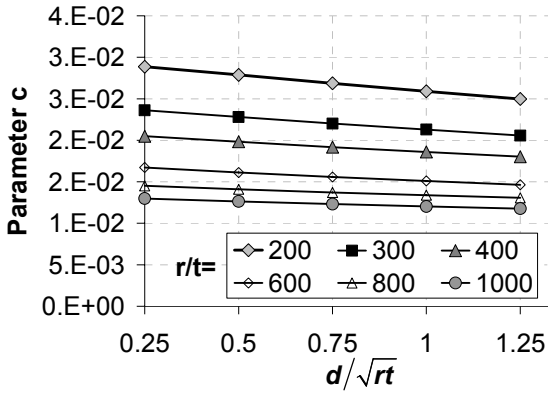

c)

Figure 3.24: Parameter variations in Equation 3.15. Parameter a_1 assumed to be linear in Γ

The parameter *a* is almost identical for all r/t, especially for large r/t (Figure 3.24), which indicates that parameter *a* is independent of r/t. And therefore also a_1 and a_2 are independent of r/t. The empirical fit can then be expressed as

$$\frac{F_{LBA}}{\sigma_{cl} t^2} = \frac{h/\sqrt{rt} + a_1 d/\sqrt{rt} + a_2}{b\, h/\sqrt{rt} + c_1 d/\sqrt{rt} + c_2} \tag{3.17}$$

where *b* is still dependent on r/t and $\Gamma = d/\sqrt{rt}$, c_1 and c_2 are only dependent now on r/t and a_1 and a_2 are constants.

When the results from Equation 3.17 were compared the bifurcation load calculated by ABAQUS (HKS, 2003) using a least squares procedure, the maximum error was ±0.29%.

Parameter *b* in Figure 3.24 does not show the clear linear behaviour seen for parameter *a* and *c*, but apart from the smallest width $\Gamma = d/\sqrt{rt}$ =0.25 it does follow a linear path.

Therefore it was also decided to adopt the assumption of a linear variation with $\Gamma = d/\sqrt{rt}$. When *a*, *b* and *c* are taken to vary linearly with $\Gamma = d/\sqrt{rt}$, and a_1 and a_2 are taken to be independent of r/t the empirical fit can then be expressed as

$$\frac{F_{LBA}}{\sigma_{cl} t^2} = \frac{h/\sqrt{rt} + a_1 d/\sqrt{rt} + a_2}{\left(b_1 d/\sqrt{rt} + b_2\right) \cdot h/\sqrt{rt} + c_1 d/\sqrt{rt} + c_2} \tag{3.18}$$

and the maximum error is ±0.44%.

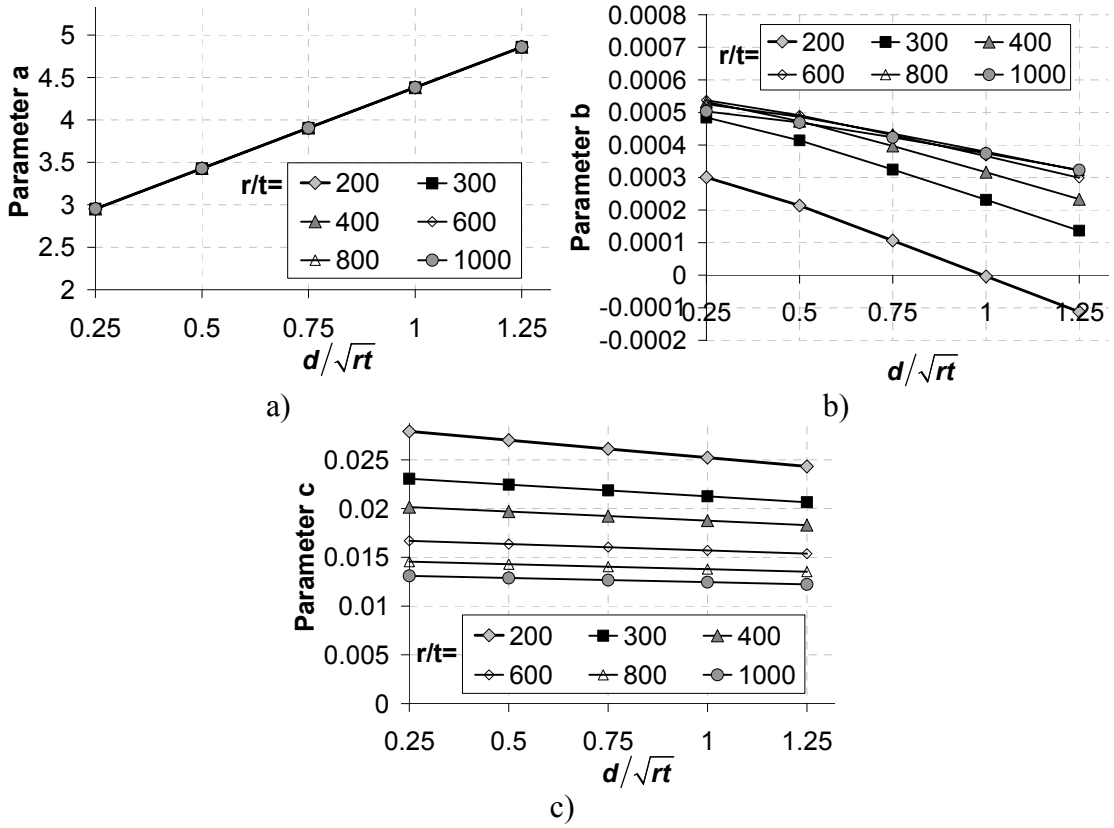

Figure 3.25: Trend of the parameters from Equation 3.15. Parameter a_3, b_3 and c_3 assumed to be linear

The only unknown parameters are now b_1, b_2, c_1 and c_2 (Equation 3.18) and they only depend on r/t. Hence these parameters were plotted against r/t (Figure 3.26).

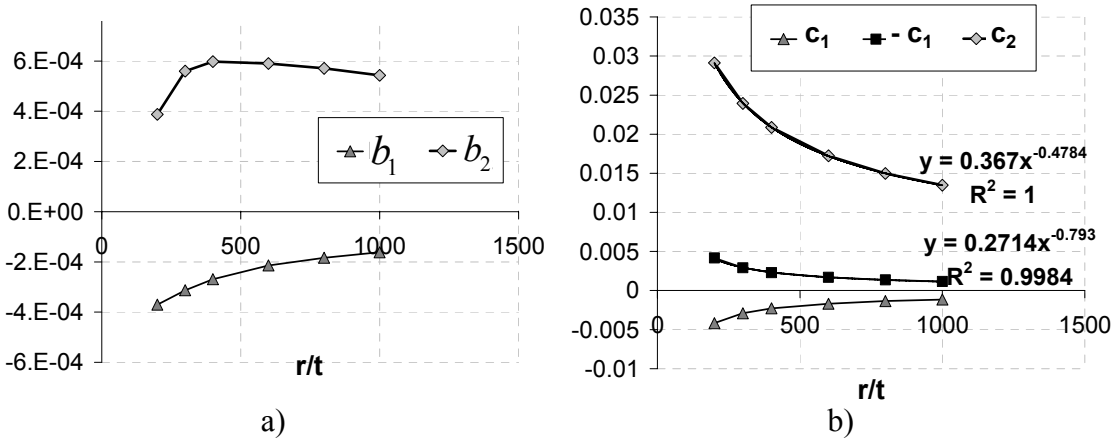

Figure 3.26: Parameters b_{11}, b_{12}, c_1 and c_2 vs. r/t

For these parameters there are no linear relationships that can be found and it is unclear what kind of equation would fit the behaviour well. The only simple variation is for parameter c_2 (Figure 3.26b), which seems to take the form

$$c_2 = c_3 / \sqrt{r/t} \tag{3.19}$$

The approximation to the numerically calculated bifurcation loads can then be expressed as buckling

$$\frac{F_{LBA}}{\sigma_{cl}t^2}=\frac{\Lambda+a_1\Gamma+a_2}{\left(b_1\Gamma+b_2\right)\Lambda+c_1\Gamma+c_3\Big/\sqrt{r/t}} \tag{3.20}$$

When this equation is implemented the maximum error was then ±1.16%.

The variation of the remaining parameters is shown Figure 3.27. The parameters still dependent on r/t are now only b_1, b_2 and c_1.

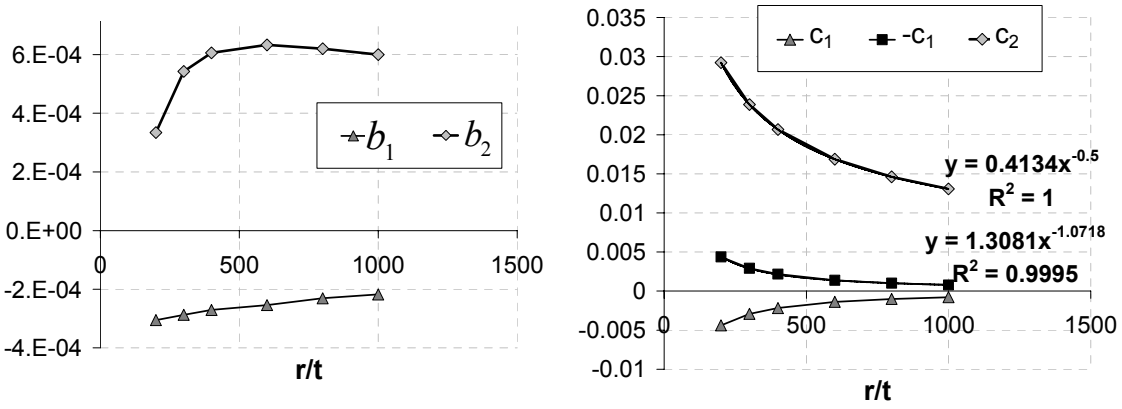

a) b)

Figure 3.27: Parameters b_1, b_1, c_1 and c_2 vs. r/t

The parameter ($-c_1$) displays a close approximation to (Figure 3.27)

$$-c_1=c_4\Big/\left(r/t\right) \tag{3.21}$$

but the parameters b_1 and b_2 still vary in the same nonlinear manner as seen in Figure 3.27.

When the empirical fit is expressed as

$$\frac{F_{LBA}}{\sigma_{cl}t^2}=\frac{\Lambda+a_1\Gamma+a_2}{\left(b_1\Gamma+b_2\right)\Lambda-\dfrac{c_4}{r/t}\Gamma+c_3\Big/\sqrt{r/t}} \tag{3.22}$$

the maximum error after fitting to the least square of the error is ±1.3%. The two remaining unknown parameters are only b_1 and b_2, which display the following behaviour after being fitted to Equation 3.22 (Figure 3.28). It is still not easy to choose a good function to capture the variation. It was decided that b_1 could be a constant, even though a linear function might seem more precise, because a linear function of b_1 does not result in any better fit and does not change the overall behaviour of b_2. Therefore b_1 was treated as constant for the benefit of eliminating

another parameter in the final equation. The parameter b_2 was represented by

$$b_2 = \frac{b_3\, r/t + b_4}{r/t + b_5} \tag{3.23}$$

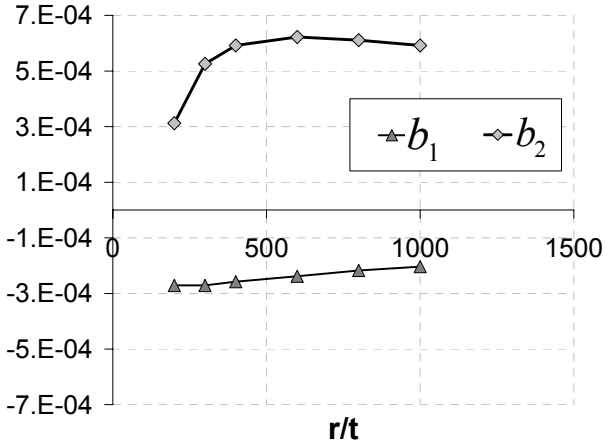

Figure 3.28: Parameters b_1, b_2 vs. r/t

The final empirical equation to represent the linear bifurcation load of bracket supported cylinders took the form

$$F_{LBA}/\sigma_{cl}t^2 = \frac{\Lambda + \left(k_1\Gamma + k_2\right)}{\left(k_3\Gamma + \dfrac{k_4\, r/t + k_5}{r/t + k_6}\right)\Lambda + \dfrac{k_7}{r/t}\Gamma + \dfrac{k_8}{\sqrt{r/t}}} \tag{3.24}$$

or rewritten

$$\frac{F_{LBA}}{\sigma_{cl}\sqrt{rt}} = \frac{k_2}{k_8}\frac{\Lambda/k_2 + \left(k_1/k_2\,\Gamma + 1\right)}{\left(k_3/k_8\,\Gamma\sqrt{r/t} + \dfrac{k_4/k_8\, r/t + k_5/k_8}{\sqrt{r/t} + k_6/\sqrt{r/t}}\right)\Lambda + \dfrac{k_7/k_8}{\sqrt{r/t}}\Gamma + 1} \tag{3.25}$$

and the maximum error was ±1.6% for the chosen data set.

3.4.4 Verification of the empirical fit to represent linear bifurcation loads

The above search for an appropriate functional form to represent linear bifurcation loads used only a limited range of parameter variations. Having found a functional form that seemed appropriate, the full set of about 300 LBA calculations [using the ranges 200≤r/t≤1000, $0.7 \le h/\sqrt{rt} \le 15.8$, $0.12 \le d/\sqrt{rt} \le 2.52$] was used

to verify the empirical fit (Equation 3.24) and to obtain optimized values for all parameters.

If the values for the parameters k_1 to k_8 from Equation 3.24 were used to approximate the bifurcation load using the full set of data, the maximum error was ±3.5%. But improved values for the parameters were found reducing the maximum error to ±1.96%

The error plot for the improved values seen in Figure 3.29 seems to be reasonably randomly distributed.

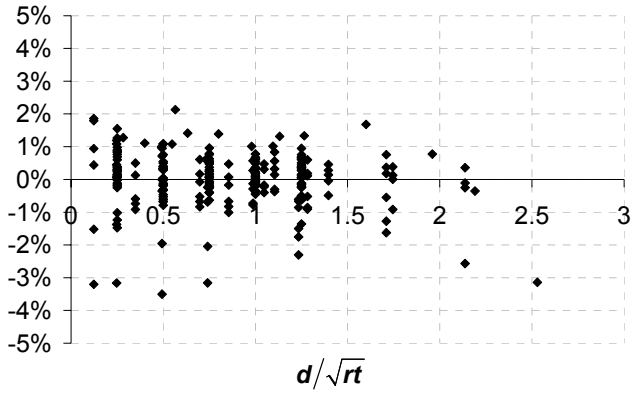

Figure 3.29: Errors in the empirical fit of Equation 3.24 using improved values

Another confirmation of the suitability of Eq. 3.24 is that when $d/\sqrt{rt}$ =0 and $h/\sqrt{rt}$ =0 Equation 3.24 reduces to Equation 3.26, which has the same form as was found for a point support in Section 3.4.1.

$$\frac{F_{LBA}}{\sigma_{cl}\sqrt{rt}} = \frac{k_2}{k_8} \tag{3.26}$$

Even though the form of this equation is the same, when the bifurcation loads calculated by ABAQUS (HKS, 2003) and therefore the empirical fit for the point support (Eq. 3.5) are compared to the result obtained from Eq. 3.26, Eq. 3.26 over-predicts all of the results by a constant error of 12%. The same over-prediction for the bracket of zero dimensions was seen in the empirical fit a bracket with zero width and finite height in Section 3.4.2 (Eq. 3.11). Then it was suggested that this error might have occurred because the width of the bracket was small but not zero, due to modelling difficulties. However, in this case, even though the correct width was used to predict the bifurcation, the same error as for brackets with zero dimensions

appears.

This may be due to a numerical error when supporting the whole silo on just four nodes (one for each bracket). This could introduce an error in the bifurcation mode for a point support. But since the bracket with zero dimensions is a purely theoretical case and the empirical fit achieves very good results for very short and very narrow brackets, the functional form of this fit is still very appropriate.

$$\frac{F_{LBA}}{\sigma_{cl}\sqrt{rt}} = \frac{k_2}{k_8}\frac{\Lambda/k_2 + 1}{\left(\frac{k_4/k_8\, r/t + k_5/k_8}{\sqrt{r/t} + k_6/\sqrt{r/t}}\right)\Lambda + 1} \tag{3.27}$$

When the dimensionless width of the bracket is taken as zero Equation 3.24 is reduced to Equation 3.27. This equation has almost the same form as the equation found in section 3.4.2 and when compared to the ABAQUS (HKS, 2003) results the maximum is 3.25% over-prediction and 3% under-prediction of the bifurcation load calculated by ABAQUS (HKS, 2003), whereas the RMS is only 1.19%.Therefore this empirical fit is considered to be a very good approximation for a very wide range of silo and bracket geometries and can be used for the prediction of linear bifurcation loads of these structures.

3.5 A simple physical model to represent the linear bifurcation load

3.5.1 Introduction

This section sets out to derive a simple physical representational model for the linear bifurcation. The empirical fit found in the previous section is good, but does not give an insight into the buckling condition. A well-planned physical model, chosen to relate the buckling condition to the location of the buckle, the stress pattern around the bracket and the local stress required to cause a buckle can provide a good insight. This chapter will first discuss the theoretical case of a bracket with zero dimensions and will then widen the range to a finite bracket.

3.5.2 Mechanical model for silos with brackets of the geometry d=h=0

A simple mechanical model was derived to obtain an alternative method of representing the linear bifurcation load.

A classical conceptual model for linear bifurcation might suggest that the load applied can be converted to a uniformly distributed load which is equal to the classical buckling stress multiplied by the thickness of the shell applied over a line of a certain length at a certain distance above the bracket.

The assumption that the whole of the load applied to the bracket will produce a buckle is correct when the bracket is positioned at the bottom edge of the shell. However, here the bracket is positioned at mid-height. Due to this positioning some of the applied load will be transmitted as tension into the bottom of the bracket, some as shear into the side of the bracket and finally some as compression into the top of the bracket. Since the height of the bracket and its width is zero for the case of a point support, the applied load will simply be divided as tension on the bottom of the bracket and compression on the top. In this case it can be assumed due to symmetry that the applied load will be transmitted equally to top and bottom of the bracket.

When half of the applied load at bifurcation is transmitted as compression above the bracket to cause the buckle, half of the support force causes compression, so this part of the force which is associated with the buckle may be written as $F_{c,LBA}=0.5F_{LBA.}$ It is supposed that $F_{c,LBA}$ produces a uniformly distributed stress equal to the classical elastic critical stress σ_{cl} at some height $a\cdot\sqrt{rt}$ above the bracket, with this assumed uniform stress acting on a length Δ (see Figure 3.30), and it is assumed that this condition causes a buckle to form, then the only unknowns in this system are the length Δ over which the classical buckling stress is sustained and the distance of this location above the bracket $a\sqrt{rt}$. Some distance is necessary to ensure that a large enough compression field is present for a full buckle to form.

The distance was made dimensionless by dividing it by $\sqrt{rt}$. The length $\sqrt{rt}$ was chosen because it is a characteristic length for shell buckling and it was shown in Section 3.3 that the buckles in the case of a bracket supported shell appear in distinct and well defined locations, which are also defined in terms of $\sqrt{rt}$. The range of

parameters chosen for this study was $200 \leq r/t \leq 1000$ and $1 \leq t \leq 3$.

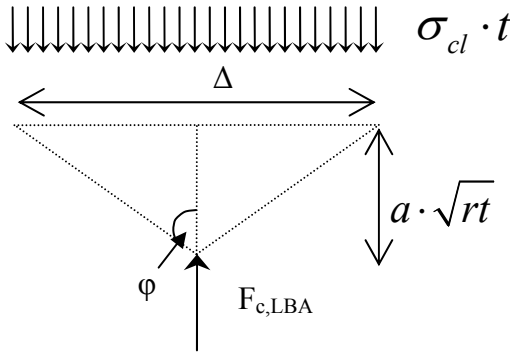

Figure 3.30: A simple physical model for bifurcation

Then

$$F_{c,LBA} = \sigma_{cl} \cdot t \cdot \Delta \tag{3.28}$$

and

$$F_{c,LBA} / \sigma_{cl} \cdot t = \Delta = 2 \cdot \tan\varphi \cdot a \cdot \sqrt{rt} \tag{3.29}$$

Using Eq. 3.29 on the linear bifurcation forces for a bracket of zero dimensions (point support) it was found that

$$2 \cdot a \cdot \tan\varphi = const = 2.74 \tag{3.30}$$

Therefore

$$F_{c,LBA} = \frac{E}{\sqrt{3\left(1-\nu^2\right)}} \frac{t}{r} \cdot t \cdot 2 \cdot \tan\varphi \cdot a \cdot \sqrt{rt} = \frac{2 \cdot \tan\varphi \cdot a \cdot E \cdot t^2}{\sqrt{3\left(1-\nu^2\right)}} \cdot \sqrt{\frac{t}{r}} \tag{3.31}$$

and with $F_{c,LBA} = 0.5 \cdot F_{LBA}$,

$$F_{LBA} = \frac{4 \cdot \tan\varphi \cdot a \cdot E \cdot t^2}{\sqrt{3\left(1-\nu^2\right)}} \cdot \sqrt{\frac{t}{r}} \tag{3.32}$$

or

$$F_{LBA} = \frac{5.48 \cdot E \cdot t^2}{\sqrt{3\left(1-\nu^2\right)}} \cdot \sqrt{\frac{t}{r}} \tag{3.33}$$

or

$$F_{LBA} = 4 \cdot \tan\varphi \cdot a \cdot \sqrt{rt} \cdot \sigma_{cl} \cdot t = 5.48 \cdot \sqrt{rt} \cdot \sigma_{cl} \cdot t \tag{3.34}$$

These equations correspond very well with the empirical model discussed before and confirm Equation 3.5 (re-printed below) which was found in a direct empirical

fit. The maximum error found is 0.43% and the RMS was 0.22%. Since the finite element calculations on which this model is based are only accurate to within a couple of percent, it is inappropriate to seek a closer fit here.

$$F_{LBA} = a \cdot t^2 \cdot \sqrt{\frac{t}{r}} \tag{3.5}$$

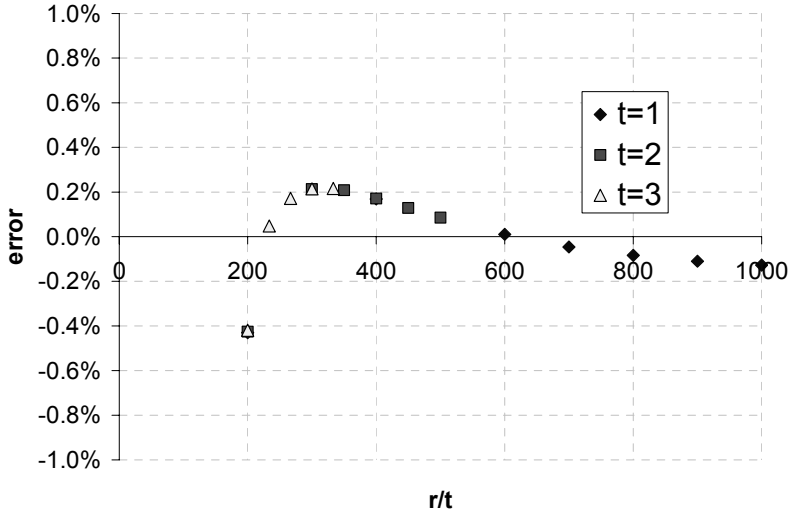

Figure 3.31: Error of the equation for a bracket with zero dimensions

3.5.3 A simple physical model for cylinders with brackets of finite dimensions

The challenge to find a physical model for a bracket with finite dimensions at mid-height of the cylinder is not an easy task. Two questions had to be answered. The first one must address the size and magnitude of the compressive stress field and the conditions required to induce a buckle. This stress field is largely controlled by the force transmitted through the top of the bracket, so this question must be answered on the basis that this is already known. In this context, one must ask what physical model could be chosen to represent these effects well?

The second question which needs to be addressed is how much compression is transmitted through the top of the bracket, and how does this vary with the bracket geometry? Does the shear field which develops on the side of the bracket influence the buckling condition?

3.5.3.1 The physical model: criterion at buckling

The first question concerns the form of the stress field and the conditions under which a buckle might form above the bracket. This was addressed as follows.

It was shown in the observations in the beginning of this chapter (Figure 3.6a) that the maximum displacement in the buckle always remains at about the same height above the bracket relative to $\sqrt{rt}$, independent of the dimensions of the bracket. Moreover, it has the same shape in horizontal direction largely independent of the height and width of the bracket with an average width of the buckle of $5.35\sqrt{rt}$ (Tables 3.2 and 3.3). The maximum dimensionless axial stress σ/σ_{cl} at this height is very similar for all bracket geometries (Figure 3.7a and b). The shape of the stress field varies slightly with the height and the width of the bracket, but always retains the same bell shape. The maximum axial stress decreases slightly for very tall bracket and the bell shape widens (Figure 3.7a and b). This is due to the shear field on the side of the bracket, which allows the axial stress to distribute more uniformly and therefore reduces the maximum dimensionless stress needed. The maximum dimensionless axial stress also decreases for wide brackets due to more uniformly distributed larger compression field at the position of the maximum displacement of the buckle.

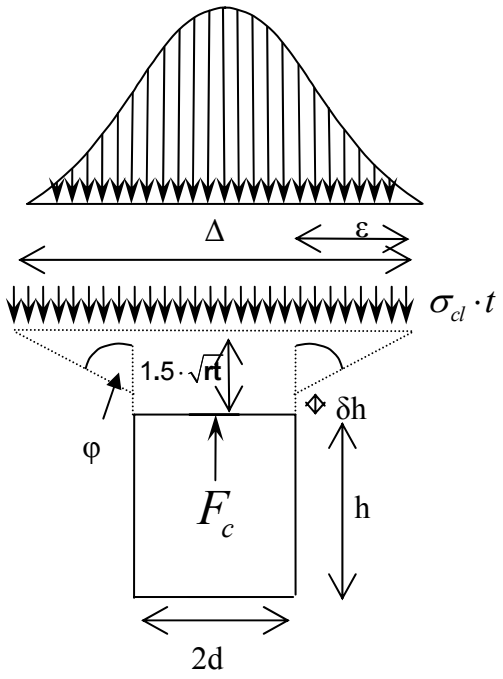

Figure 3.32: Simple model for a bracket with finite dimensions

It was therefore evident that nearly the same dimensionless stress at the same dimensionless height above the bracket was required for buckling, irrespective of the bracket size and silo geometry. However, it must be noted that the force emerging from the top of the bracket was different for each geometry. The reason is that the applied load on the bracket is transmitted into the shell as tension through the bottom of the bracket, as shear through the side of the bracket and as compression through the top of the bracket. The percentage of the applied load which is transmitted as compression through the top of the bracket and shear transmitted through the side of the bracket is different for each geometry. This is very different from the situation of a support beneath the bottom of a silo, where all of the applied load is transmitted through a well-defined short length of shell as compression.

Therefore a physical model (Figure 3.32) was chosen in which the compressive force F_c transmitted through the top of the bracket at bifurcation was interpreted as a uniform stress at a certain height above the bracket. This force F_c is the integral of the axial stress resultant on the top surface of the bracket integrated over the width of the bracket, and here it was set equal to an assumed uniformly distributed stress at the height chosen in terms of the identified location of the buckles, extending over a horizontal length Δ (Figure 3.32) and multiplied by the silo thickness. The uniformly distributed stress was assumed to be equal to the classical elastic buckling stress under uniform compression σ_{cl}, since this stress does appear to be closely correlated with buckling events provided a moderate zone of shell is compressed. The chosen height above the bracket was taken from the observations corresponding to Mode A as $\lambda_d = 1.5\sqrt{rt}$.

$$F_c = \sigma_{cl} \cdot t \cdot \Delta \tag{3.35}$$

$$F_c = 2 \cdot \sigma_{cl} \cdot t \cdot \left(\tan\varphi \cdot \lambda_d + \tan\varphi \cdot \delta \cdot h + d \right) \tag{3.36}$$

The length Δ was taken as unknown, but it is certain that the width $2d$ of the bracket must play a role in the length Δ. Here it was assumed that the stress field could be simply assumed to spread out linearly from the top surface of the bracket, spreading at each side at an angle φ (Figure 3.32). This choice makes it possible to calculate the total length simply using trigonometry. The angle φ is used not only to

account for the spread of the axial stress from the top of the bracket between the top and the chosen height, but also to account for differences in the axial stress pattern arising from different widths of bracket and different stresses arising from shear transmission on the bracket side (Figure 3.32 and Equation 3.36).

The compressive force transmitted through the top of the bracket and the height at which the maximum displacement occurs in the buckling mode are the dominant factors in this case. But the shear field that develops beside the bracket must be recognised too since a strong shear field will allow the compressive stresses above the bracket to have a more uniform distribution which will lead to a less localised stress peak and consequently earlier buckling.

The shear field was taken into account by introducing another variable δ. The spread of the stress field was deemed to be delayed if a strong shear force was being transmitted through the side of the bracket. This was represented by raising the origin of the spreading stress field by the distance δh (Figure 3.32) since it was assumed that the influence of the shear field was best expressed in terms of a percentage of the height of the bracket. Thus it was tacitly assumed that, as the bracket height was increased, the shear field next to the bracket would become more pronounced. With a more pronounced shear field the compression at the height of the maximum displacement in the buckle mode would become more uniformly distributed and therefore the force required for buckling (which is here set equal to the product of the classical buckling stress, the shell thickness and the length Δ) would decrease.

There were thus two free variables φ and δ within this model which could be adjusted to try to fit the results of precise finite element calculations. In addition, the value of the compressive force transmitted through the top of the bracket was needed as a proportion of the total force acting on the bracket. The compressive force F_c was determined by extracting the axial stress resultants at the point of buckling on the top of the bracket from a linear elastic analysis (LA) and integrating them over the width of the bracket. The axial stress resultants were extracted for 54 different geometries covering the range of geometries $200 \leq r/t \leq 1000$, $0.05 \leq h/r \leq 0.5$, $\theta_o=(d/r)=0.0349$, and additionally for $r/t=200$, $0.05 \leq h/r \leq 0.5$, $0.0175 \leq \theta_o=(d/r) \leq 0.0873$.

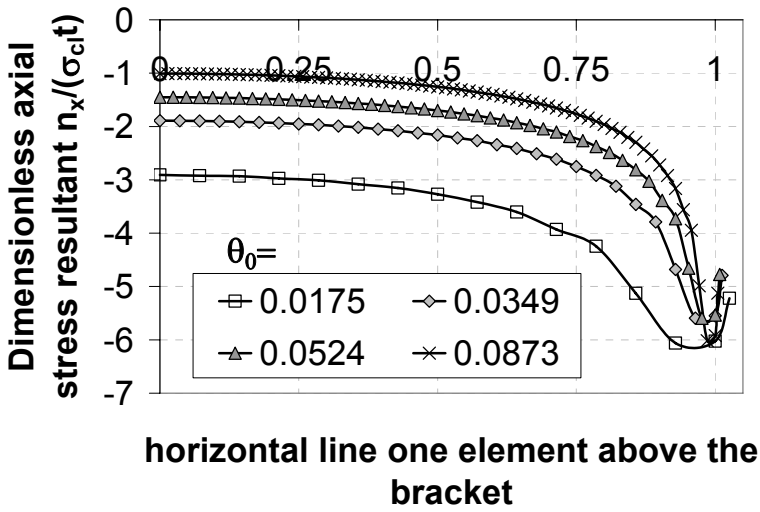

Figure 3.33: Distribution of the axial stress resultant at the top of the bracket (r/t=200, h/r=0.2)

An example of the axial stress resultant distribution just above the bracket for three different geometries is shown in Figure 3.33. Half the bracket is shown only since symmetry determines that the other side will be identical. The axial stress is seen to be almost constant over the middle part of the bracket (from x=0 to x=d/2), but this stress increases strongly towards a peak at the corner of the bracket. The narrowest bracket displays a wide peak at the corner, but this becomes narrower as the bracket width is increased.

The stress resultants were integrated over the width of the bracket using

$$F_c = \sum_{i=2}^{i=n} \frac{n_{x,i-1} + n_{x,i}}{2} \cdot \left(x_i - x_{i-1} \right) \tag{3.37}$$

where n is number of nodes on the top boundary of the bracket, $n_{x,i}$ is axial stress resultant at node i and x_i is the distance from the middle of the bracket to node i.

Best fit values for the variables φ and δ were then calculated using Equation 3.36 and least squares regression analysis. The result was found to give φ=32° and δ=0.056. Despite the simplicity of this model, with only fixed values for both φ and δ, the maximum differences between the values extracted from the finite element numerical calculation and the model are ±10%, but the RMS error is only 4.12% (Figure 3.34).

The maximum over-prediction was found to occur for very narrow brackets, whereas the maximum under-prediction was found for wide but very short brackets.

The reason for these differences lies in the simplicity of the chosen model, with some errors arising from the procedure used.

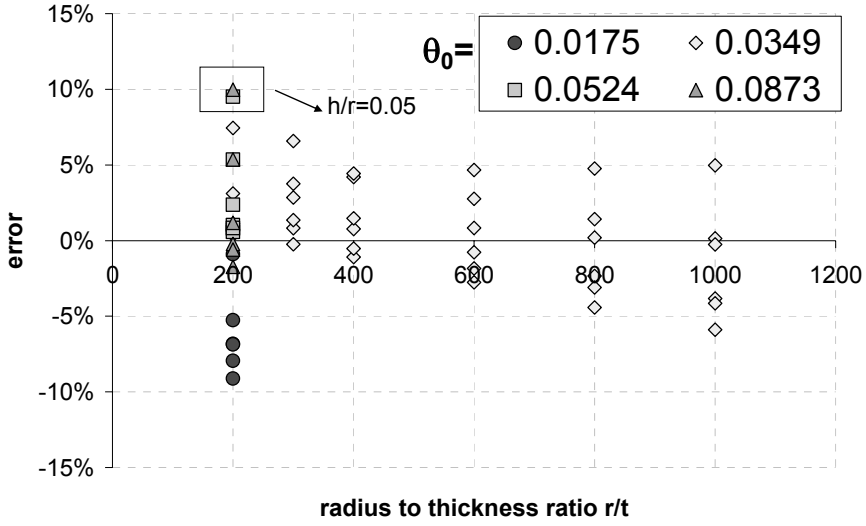

Figure 3.34: Error of the equation

When the membrane stress resultants around the bracket were extracted, they could not be extracted exactly at the edge of the bracket since the bracket and silo were connected there using a multiple point constraint in ABAQUS (HKS, 2003). This causes inaccurate values of stress at this point. Consequently it was decided to extract the stress resultants at the nodes that were one element above the bracket (at the grey line Figure 3.35). The maximum height of the first element was 1.36% of the height of the bracket for the shortest bracket, but decreasing for taller brackets to 0.12% of the bracket height. This introduced a small error that was related to the bracket height.

The over-prediction for very narrow brackets was caused by the integration of the stress resultants (Eq. 3.37). The stress resultants are the only available output at the nodes of the mesh and no values between nodes could be obtained. For a very narrow bracket, the axial stress resultant starts to increase steeply at about 75% of the bracket half-width, rising towards the stress peak at the corner of the bracket (Figure 3.33). At the corner of the bracket the peak is very wide because the element width is significant and the stresses are obtained one element above the boundary. Due to this "wide" peak and the integration method chosen the integration failed to capture the complete peak and since the stress resultants are largest at buckling for very narrow brackets, this naturally led to a small under-estimation of the compressive force and

therefore an over-prediction in Equation 3.36 for very narrow brackets (Figure 3.34).

For very wide and short brackets the model under-predicts the force. The source of this error is a combination of the simplicity of the model chosen and the restrictions in extracting the compressive force from the numerical output.

The above development used a simple physical model and there is clearly scope for improvement. The model could be improved by choosing a stress distribution that is closer to the real stress distribution as shown in Figure 3.32 and a better criterion than the uniformly distributed classical elastic buckling stress. Another improvement would be to choose a nonlinear function for the spread of the load, instead of the linear function chosen in this model. Although there are some small errors introduced here, it is reasonable to decide that these errors are relatively small and that this model is suitable for further development.

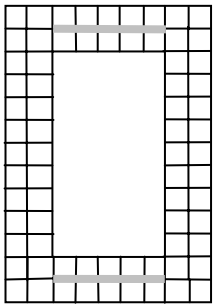

Figure 3.35: Sketch of the mesh close to the bracket

3.5.3.2 The physical model: proportion transmitted through the bracket top

The second part of this model development required the force transmitted through the top of the bracket to be expressed as a proportion of the total force on the bracket. Expressing the compressive force transmitted through the top of the bracket as F_c and the total load on the bracket at bifurcation as F_{LBA}, this proportion was expressed as the new variable ζ

$$\zeta = F_c / F_{LBA} \tag{3.38}$$

Equation 3.36 was then transformed to

$$\zeta \cdot F_{LBA} = 2 \cdot \sigma_{cl} \cdot t \cdot \left(\tan\varphi \cdot \lambda_d + \tan\varphi \cdot \delta \cdot h + d \right) \tag{3.39}$$

The next challenge was to find a suitable approximation for ζ as a function of the geometric parameters of the system. Chang and Conway (1969) found an analytical solution for the stress distribution in an infinite flat plate with an elastic inclusion.

This problem is similar to the bracket supported shell studied, but the analytical solution for the plate is quite involved, and its extension to the case of a curved shell was deemed to be outside the scope of this thesis. An empirical approximation was therefore developed.

3.5.3.3 Empirical approximation for the parameter ζ

The compressive force F_c and therefore ζ (Equation 3.38) was extracted for 54 different geometries, but due to procedural problems it was not possible to extract the compressive forces for all the geometries studied. Therefore a more unconventional path was taken.

The variable ζ was calculated using Equation 3.39 and the numerically calculated bifurcation load to fit the physical model found. An empirical fit was found to approximate the variable ζ and the approximation was then compared with new samples of the compressive force extracted from ABAQUS (HKS, 2003). For this comparison, extreme geometries like shortest and longest, narrowest and widest bracket were chosen.

The first step to find a suitable approximation for the variable ζ obtained from Equation 3.39 was to study the general behaviour more closely.

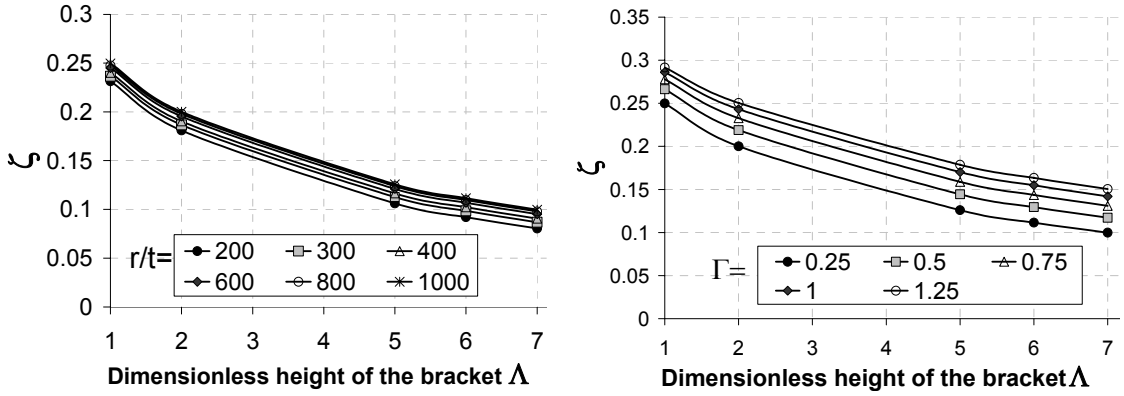

a) Γ=0.25 b) r/t=1000

Figure 3.36: Variation of the compression at the top of the bracket with Λ

The first short investigation examined the variation of ζ with the dimensionless height of the bracket. In Figure 3.36 the value of ζ is seen to decrease in a nonlinear manner since more of the load is transmitted in shear on the sides of the bracket when the bracket is tall. Therefore the compressive force transmitted through the top

of the bracket is decreases. A rational function was chosen to approximate this variation of ζ

(Equation 3.40), where the parameters a_1, a_2 and a_3 are functions of r/t and Γ ($\Gamma = d/\sqrt{rt}$).

$$\zeta = \frac{a_1\Lambda + a_2}{\Lambda + a_3} \tag{3.40}$$

Other functions such as a polynomial and exponential function were also considered. The polynomial function was not chosen because it leads to a minimum followed by an increase for larger $\Lambda = h/\sqrt{rt}$. The exponential function might have provided as good a fit as the rational function, but Equation 3.40 is simpler.

The second short study investigated the variation of ζ with the dimensionless half- width of the bracket (Figure 3.37). The percentage of the applied load transmitted as compression through the top of the bracket naturally increases as the bracket becomes wider, but the relationship is clearly nonlinear.

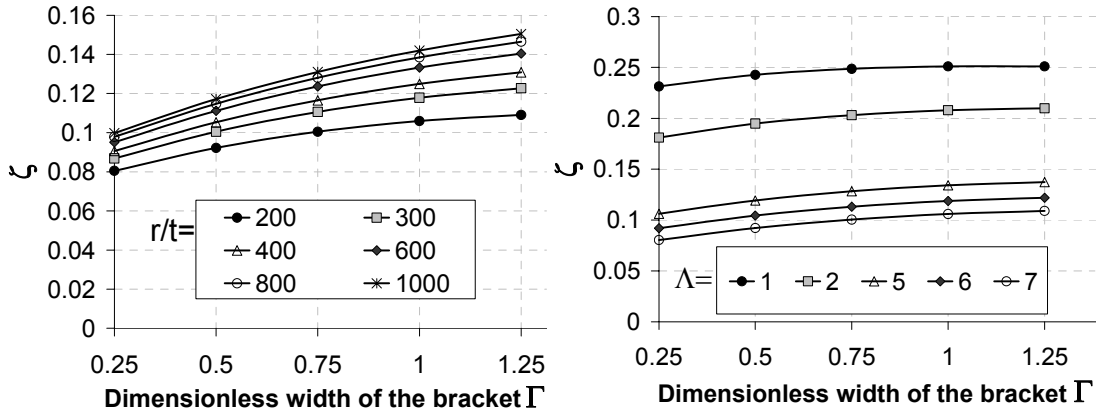

a) Λ=7 b) r/t=200

Figure 3.37: Variation of the compression at the top of the bracket with Γ

Different forms of function were found to provide a moderately good fit for the variation of ζ with $\Gamma = d/\sqrt{rt}$: polynomial, exponential and rational functions were used. The polynomial function was discarded due to the appearance of a maximum value of ζ for a large Γ followed by a decrease of ζ, which was considered unsatisfactory and not representative of the real behaviour.

The exponential function does not reach a maximum, but the best fits to the data indicated that the asymptotic value could be greater than unity. This would means

that the compressive force could be greater than the applied load for a very wide bracket, which is clearly unsatisfactory.

For the variation of ζ with $\Gamma = d/\sqrt{rt}$ a rational function Equation 3.41 was chosen as the most suitable fit, where the parameters b_1, b_2 and b_3 are functions of r/t and Λ ($\Lambda = h/\sqrt{rt}$).

$$\zeta = \frac{b_1\Gamma + b_2}{\Gamma + b_3} \tag{3.41}$$

The third investigation explored the variation of ζ with radius to thickness ratio r/t of the silo (Figure 3.38). The percentage of the applied load which is transmitted by compression through the top of the bracket increases in a nonlinear manner with r/t for a given $\Lambda = h/\sqrt{rt}$ or $\Gamma = d/\sqrt{rt}$. The function chosen to represent this pattern was again chosen to be a rational function (Equation 3.42), for the same reasons as above. The parameters c_1, c_2 and c_3 are all functions of Λ and Γ.

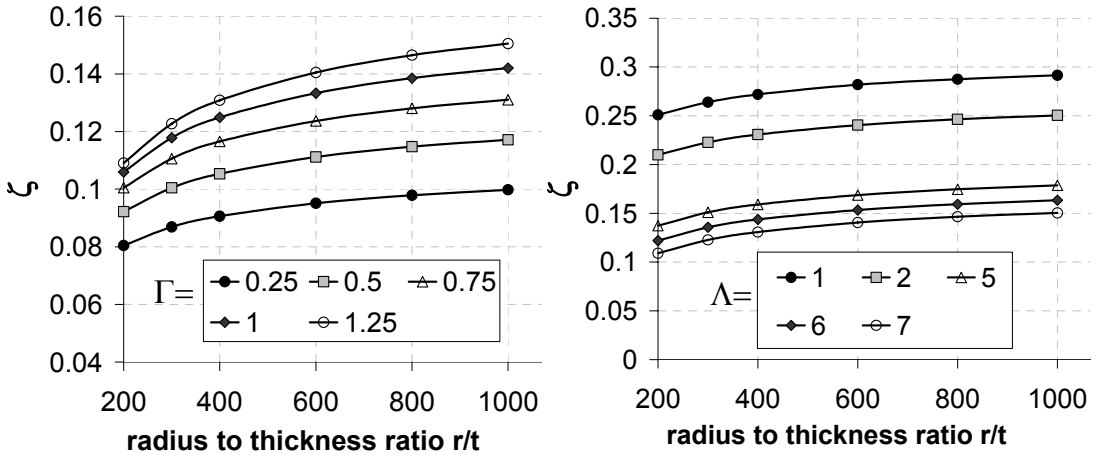

a) Λ=7 b) Γ=1.25

Figure 3.38: Variation of the proportion of force transmitted through the top of the bracket with r/t

$$\zeta = \frac{c_1 \cdot r/t + c_2}{r/t + c_3} \tag{3.42}$$

When Equation 3.42 was applied for every set of $\Lambda = h/\sqrt{rt}$ or $\Gamma = d/\sqrt{rt}$ and the parameters were fitted using least squares error minimisation, the maximum error was found to be only 0.25%. This excellent fit indicates that the form of Equation 3.42 is appropriate to the overall variation with r/t, but naturally the different parameters c_1, c_2, and c_3 all vary with both Λ and Γ. These parameters are individually studied next.

Parameter c_3 obtained from this fit seems to be effectively independent of the geometry of the bracket (Figure 3.39c). The parameter c_1 (Figure 3.39a) increases nonlinearly with Γ and can be approximated very well with another rational function

$$c_1 = \frac{c_{1,1}\Gamma + c_{1,2}}{\Gamma + c_{1,3}} \tag{3.43}$$

The parameter c_2 (Figure 3.39b) is not so easy to determine, but it was chosen to be a similar rational function of the form

$$c_2 = \frac{c_{2,1}\Gamma + c_{2,2}}{\Gamma + c_{2,3}} \tag{3.44}$$

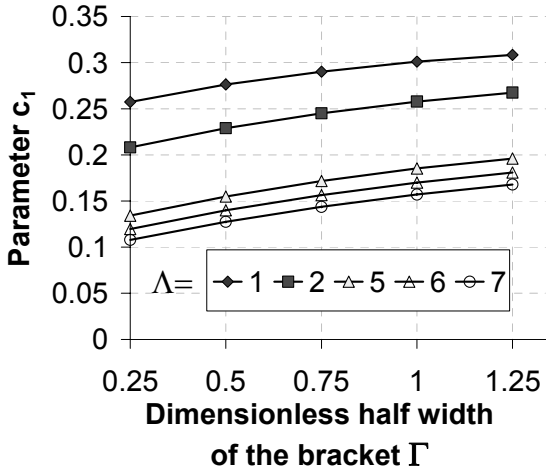

a) c_1 extracted from Equation 3.42

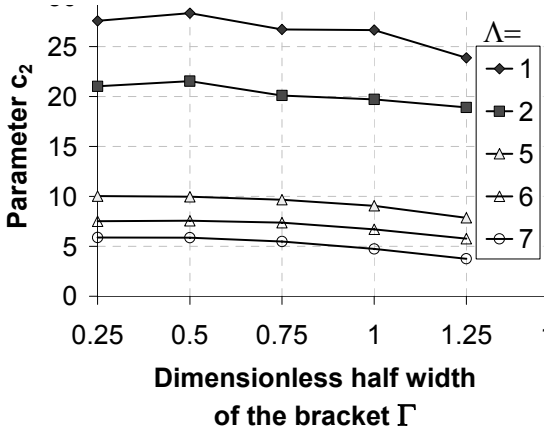

b) c_2 extracted from Equation 3.42

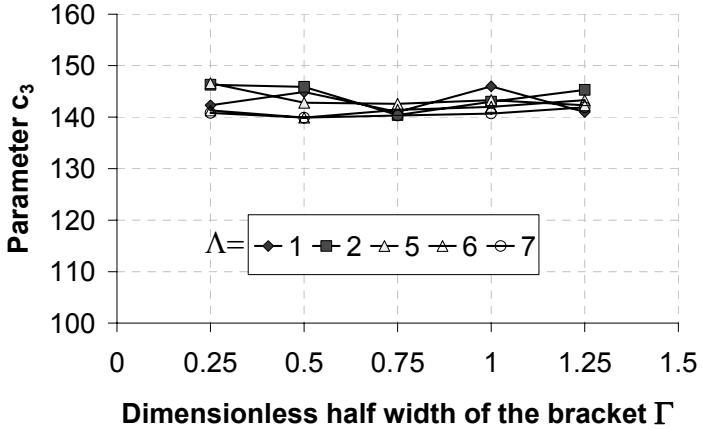

c) c_3 extracted from Equation 3.42

Figure 3.39: Variation of the parameters c_1, c_2 and c_3

Equation 3.42 has now the complete form

$$\zeta = \frac{\left(\frac{c_{1,1}\Gamma + c_{1,2}}{\Gamma + c_{1,3}}\right)\cdot\frac{r}{t} + \frac{c_{2,1}\Gamma + c_{2,2}}{\Gamma + c_{2,3}}}{r/t + c_3} \tag{3.45}$$

The maximum error after obtaining the best fit using least squares error minimisation is ±0.67% and the RMS error 0.3%. Furthermore it was found that $c_{1,3} \cong c_{2,3}$. This was implemented into Equation 3.45. By using least squares error minimisation, best fits for the parameters $c_{1,1}$, $c_{1,2}$, $c_{2,1}$ and $c_{2,2}$ were again found. The approximation then has the form

$$\zeta = \frac{\left(c_{1,1}\Gamma + c_{1,2}\right)\cdot\frac{r}{t} + c_{2,1}\Gamma + c_{2,2}}{\left(r/t + c_3\right)\left(\Gamma + c_{1,3}\right)} \tag{3.46}$$

The maximum error was ±0.94% and the RMS 0.42%.

The parameters $c_{1,1}$, $c_{1,2}$, $c_{1,3}$, $c_{2,1}$ and $c_{2,2}$ are now only dependent on $\Lambda = h/\sqrt{rt}$.

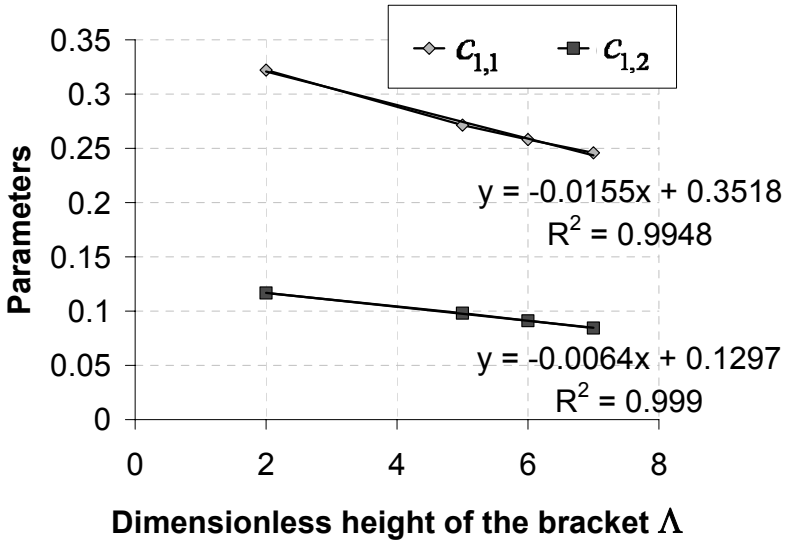

Figure 3.40: Variation of the parameters $c_{1,1}$ and $c_{2,1}$ with the dimensionless height of the bracket

When the parameters $c_{1,1}$ and $c_{1,2}$ are plotted against $\Lambda = h/\sqrt{rt}$ (Figure 3.40), a linear function is obtained for each of these parameters and the approximation then has the form

$$\zeta = \frac{\left(\left(k_1\Lambda + k_2\right)\Gamma + k_3\Lambda + k_4\right)\cdot\frac{r}{t} + c_{2,1}\Gamma + c_{2,2}}{\left(r/t + c_3\right)\left(\Gamma + c_{1,3}\right)} \tag{3.47}$$

where k_1, k_2, k_3, k_4 and c_3 are constants and parameters $c_{2,1}$, $c_{2,2}$ and $c_{1,3}$ are

dependent only on $\Lambda = h/\sqrt{rt}$. When the best fit was obtained for Equation 3.47 the maximum error was ±0.96% and the RMS error was 0.46%.

The parameter $c_{2,2}$ after fitting Equation 3.47 by least squares error minimisation shows a linear variation with Λ (Figure 3.41). This changes Equation 3.47 into

$$\Gamma = \frac{\left(\left(k_1\Lambda + k_2\right)\Gamma + k_3\Lambda + k_4\right)\cdot\dfrac{r}{t} + c_{2,1}\Gamma + k_5\Lambda + k_6}{\left(r/t + c_3\right)\left(\Gamma + c_{1,3}\right)} \tag{3.48}$$

where k_i with i=1-6 and c_3 are constants and only $c_{1,2}$ and $c_{1,3}$ depend on $\Lambda = h/\sqrt{rt}$.

The maximum error in Equation 3.48 after obtaining the best fit was ±1.01% and the RMS was 0.46%.

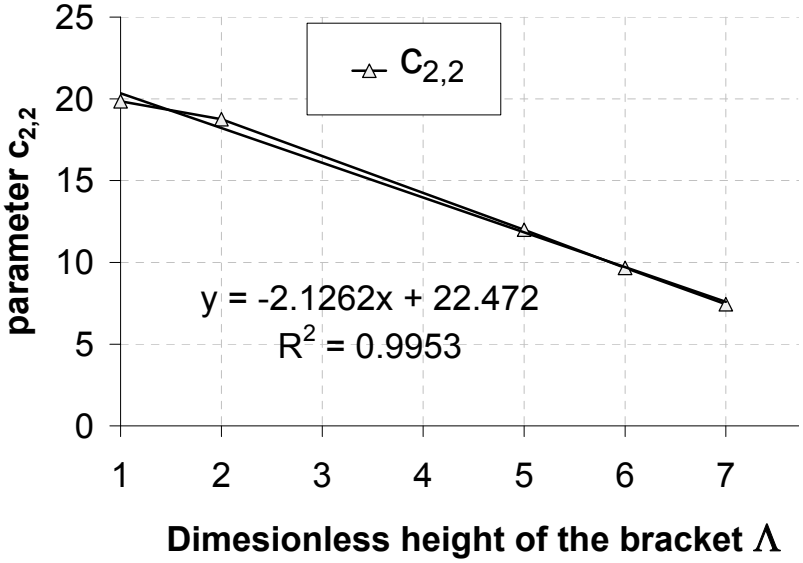

Figure 3.41: Variation of parameter $c_{2,2}$ with the dimensionless height of the bracket

The remaining two parameters $c_{2,1}$ and $c_{1,3}$ obtained after the best fit do show a rather nonlinear behaviour and no satisfying fit could be obtained using different nonlinear functions to approximate these parameters. When both of these parameters were fitted with linear functions the maximum error was ±2.14% and the RMS error was 0.96%. This fit was judged to be good enough for the purposes of approximating the bifurcation load.

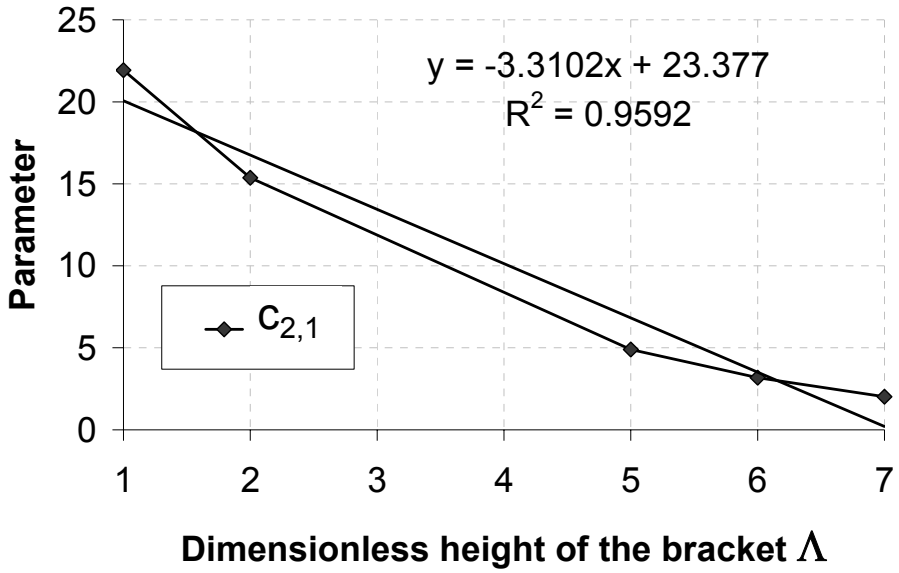

Figure 3.42: Variation of parameter $c_{2,1}$ with the dimensionless height of the bracket

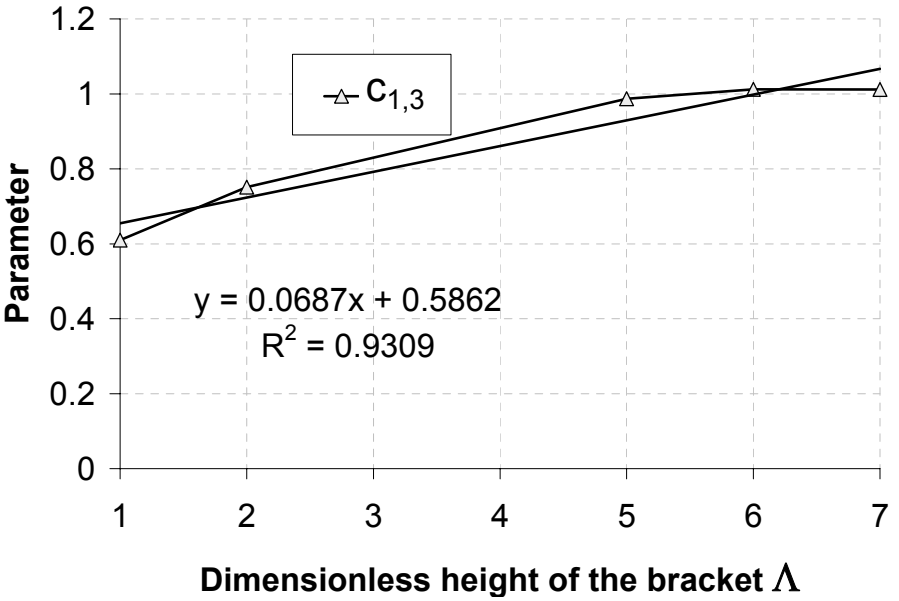

Figure 3.43: Variation of parameter $c_{1,3}$ with the dimensionless height of the bracket

The complete approximation for the percentage of compression transmitted through the top of the bracket is finally

$$\zeta = \frac{\left(\left(k_1\Lambda + k_2\right)\Gamma + k_3\Lambda + k_4\right)\cdot\Xi + \left(k_7\Lambda + k_8\right)\Gamma + k_5\Lambda + k_6}{\left(\Xi + k_{11}\right)\left(\Gamma + \left(k_9\Lambda + k_{10}\right)\right)} \tag{3.49}$$

where $\Lambda = h/\sqrt{rt}$, $\Gamma = d/\sqrt{rt}$ and $\Xi = r/t$. The maximum error of this rather complicated approximation is 2.63%, but the RMS error is only 0.86%.

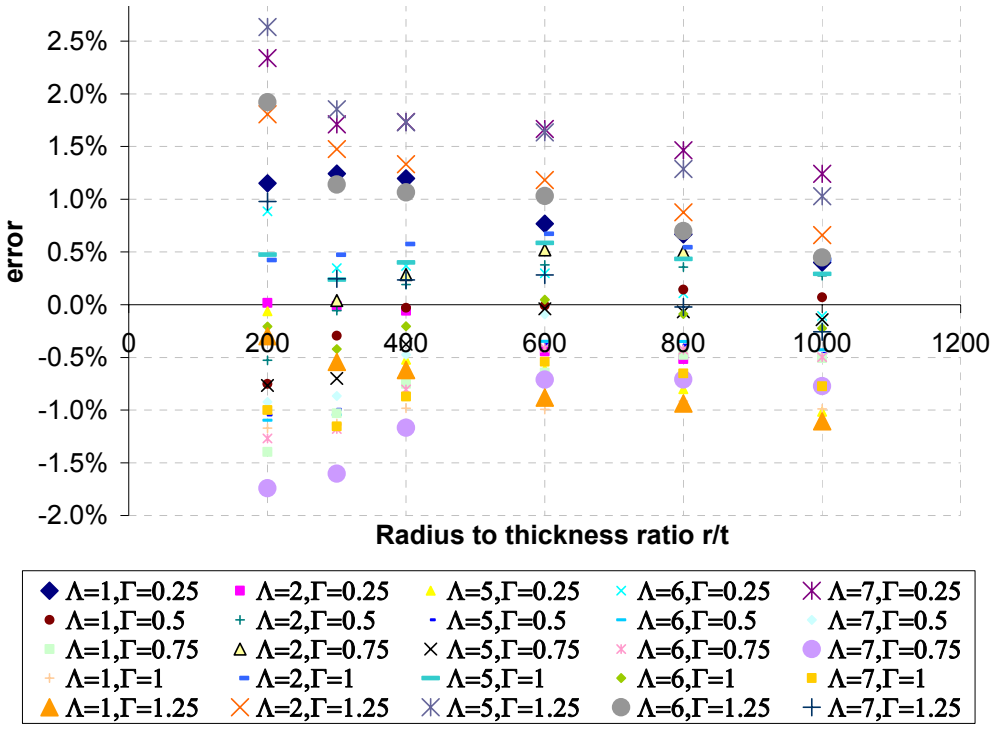

Figure 3.44: Error of Equation 3.49 to calculated results

Equation 3.49 can also be transformed in the form

$$\zeta = \frac{\left(\left(k_1\Lambda + k_2\right)\Gamma + k_3\Lambda + \zeta_0 k_{10}\right)\cdot\Xi + \left(k_7\Lambda + k_8\right)\Gamma + k_5\Lambda + \zeta_0 k_{10} k_{11}}{\left(\Xi + k_{11}\right)\left(\Gamma + \left(k_9\Lambda + k_{10}\right)\right)} \tag{3.50}$$

This transformation was chosen to achieve a single value of ζ for brackets with zero dimensions, which was necessary to stay in accordance with the physical model found for an infinitesimally small bracket, which was a natural clear reference case. For the transformed equation the maximum error was 2.66%, but the RMS error was only 0.87%.

3.5.3.4 Comparison between the empirical equation developed and the values extracted from the numerical analysis

The empirical equation developed above is rather complicated, but this arose because the behaviour that the analysis was trying to capture is rather complicated. It is unfortunate that a simpler formulation was not easily obtained, but it seems unlikely that simple functions will be found if formal algebraic analyses are undertaken. Equation 3.50 was developed to capture the values of ζ that would permit the physical model of Figure 3.32 to represent the buckling condition.

To verify that this procedure to use ζ taken from the mechanical model of Figure

3.32 for the approximation, a new set of numerical results with different geometries was devised and tested against the above development. The comparison is shown in Figure 3.45. The maximum error between the above empirical fit and the newly calculated values for geometries not included in the development of the empirical fit was ±8.7% and the RMS error was 5.3%. These errors are quite large, but acceptable, as ζ is susceptible to two sources of the error, which cannot be separated. One source of error is the lack of accuracy, when ζ obtained form ABAQUS (HKS, 2003) as mentioned before and the second source of error is the simplicity of the physical model.

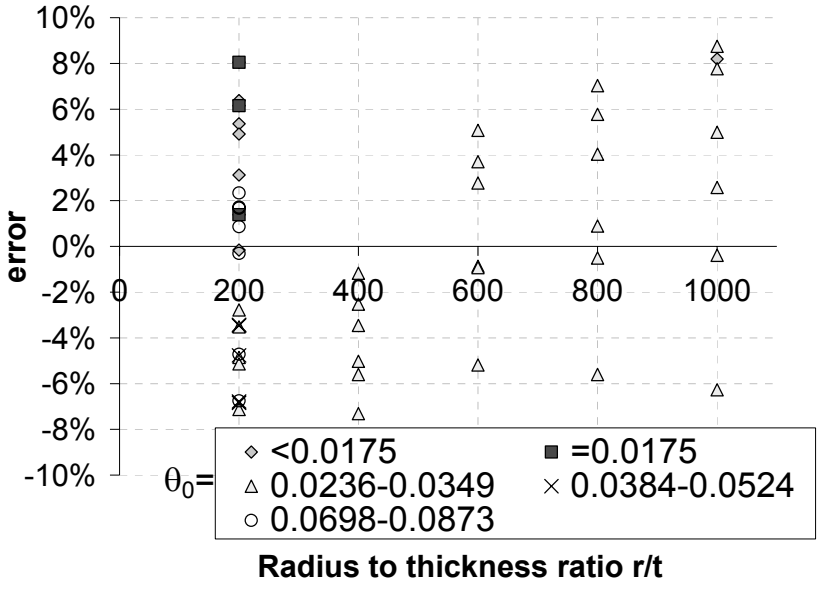

Figure 3.45: Comparison of the percentages calculated and the percentages extracted from ABAQUS (HKS, 2003).

3.5.3.5 Independent verification of the approximation with additional results

The approximation for ζ expressed by Equation 3.50 was developed from about 150 geometries covering the ranges of $200 \le r/t \le 1000$, $1 \le \Lambda = h/\sqrt{rt} \le 7$ and $0.25 \le \Gamma = d/\sqrt{rt} \le 1.25$.

To verify this empirical fit further, the linear bifurcation loads were then calculated for 150 geometries that were all different from those used to develop the expression. The range of geometries used for this independent verification was

$200 \le \text{r/t} \le 1000,\ 0 \le \Lambda = h/\sqrt{rt} \le 15.8,\ 0 \le \Gamma = d/\sqrt{rt} \le 2.52$.

When the empirically fitted value of ζ and the mechanical model (Eq. 3.35 and 3.36) was used to calculate the bifurcation load for the new set of geometries and the empirically calculated bifurcation loads showed a maximum difference to the numerically calculated bifurcation load compared of 6.7%, but the RMS was only 1.68%.

Figure 3.46: Error plot of the Bifurcation load derived fro m the mechanical model and the bifurcation load calculated in ABAQUS (HKS, 2003)

In section 3.5.2, an infinitesimally small bracket was studied. It was assumed that 50% of the applied load is transmitted as compression through the top of the support. This assumption was based on symmetry considerations. But when Equation 3.50 is applied to an infinitesimally small bracket, the equation reduces to

$$\eta\zeta = \frac{\left(\zeta_0 k_{10}\right)\cdot\Xi + \zeta_0 k_{10} k_{11}}{\left(\Xi + k_{11}\right)k_{10}} = \zeta_0 \qquad (3.51)$$

where $\zeta_0 \cong 0.33$. Thus, Equation 3.50 suggests that an infinitesimally small bracket should transmit just one third of the force in compression, whilst the original assumption took this as one half. The source of this difference is difficult to trace using the output of the numerical calculation because of the method by which the value of ζ was derived above. When the values of ζ for $\text{r/t} = 200$ and $\Gamma = d/\sqrt{rt} = 0.25 - 1.23$ are plotted (Figure 3.47), it can be seen that the value of ζ at

$\Lambda = h/\sqrt{rt} = 0$ increases as $\Gamma = d/\sqrt{rt}$ increases (the bracket becomes wider).

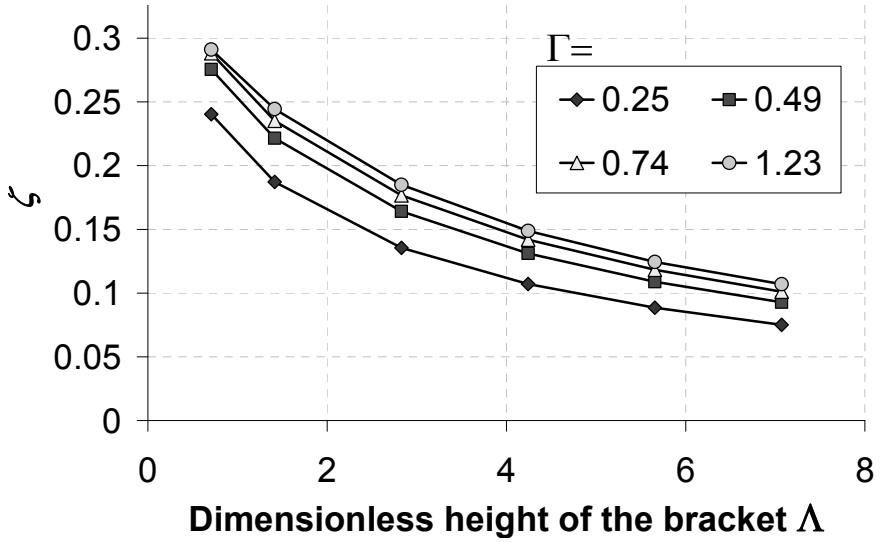

Figure 3.47: ζ extracted from ABAQUS (r/t=200)

For $\Lambda = h/\sqrt{rt} = 0$, the value of ζ from Equation 3.50 is in the region of 0.31 for the narrowest bracket and 0.35 for the widest bracket. It is reasonable to extrapolate and conclude that for $\Gamma = d/\sqrt{rt} = 0$ the value of ζ for $\Lambda = h/\sqrt{rt} = 0$ is in the same region and slightly smaller than the value for $\Gamma = d/\sqrt{rt} = 0.25$ since this was the narrowest bracket investigated. The value of ζ given by Equation 3.51 is slightly higher than the values seen in Figure 3.47, but is still a reasonable value.

Based on the above discussion, the physical model developed for an infinitesimally small bracket is still valid (Equation 3.33), but Equation 3.30 should be changed to read

$$2 \cdot a \cdot \tan\varphi = const = 1.81 \tag{3.52}$$

for $F_{c,LBA}=0.33F_{LBA}$

with

$$F_{LBA} = \frac{5.48 \cdot E \cdot t^2}{\sqrt{3\left(1-\nu^2\right)}} \cdot \sqrt{\frac{t}{r}} \tag{3.33}$$

3.6 Conclusions

This chapter has studied the behaviour of a cylindrical shell in the neighbourhood of a rectangular stiff bracket, examining the linear bifurcation behaviour. The location and form of the buckling modes were explored and it was found that three modes exist, depending on the geometry of the rectangular bracket. For brackets of typically practical geometry, the first mode dominates, consisting of a buckle a short distance above the top surface of the bracket. The location and dimensions of this buckle were explored, as the size and shape of the bracket were varied.

A very large number of linear bifurcation calculations were performed to explore the variation of the buckling load with the geometric and material parameters. Most other shell buckling problems resolve into relatively simple algebraic expressions for the linear bifurcation load, despite the complicated mathematics which precedes the outcome. It was therefore expected that this problem might yield some similar simple relationships, but this expectation was found to be far from reality. As a result, a very considerable effort was put into trying to find a suitable simple physical model to represent the buckling condition, and into obtaining a good set of empirical relationships that could be used to represent the complicated variations with the different parameters.

The idea that the linear bifurcation load would be easily represented by some simple expressions was naturally encouraged by the studies of the apparently similar problem of a support beneath the bottom of the shell wall (Guggenberger, 1991; Li, 1994; Guggenberger *et al.*, 2000; Guggenberger, 2006). However, the calculations presented in this chapter have shown that the outcome of linear bifurcation analyses for the shell supported by a bracket at mid-height is a far more complex problem than that of a shell supported on its lower edge.

It has been found that the complexity of this problem derives mainly from the position of the bracket. When the bracket is positioned on the side of the silo at mid-height, only a part of the applied load is transmitted as compression into the top of the bracket, since stresses are also transmitted as shear and tension into the side and the bottom of the bracket. The compressive force transmitted through the top of the bracket was found to be almost solely responsible for the buckling phenomena. This

is very different from a support positioned on the bottom boundary, where the compressive force introduced is easily calculated as the applied load divided by the number of supports. In addition, for a bracket positioned away from the bottom edge, the shear on the side of the bracket adds to the complexity of the problem, since the shear field next to the bracket allows the compression field above the bracket to become more uniform and this leads to buckling at lower loads.

The physical model developed and presented in this chapter is a simple one, but seems adequate for the purpose. It was assumed that the buckling load could be predicted by using a criterion of a calculated stress at the location where the buckle really forms. The calculated compressive stress was assumed to be equal to the classical elastic buckling stress for uniform compression. It was postulated that this stress could be regarded as acting uniformly over a horizontal length of shell Δ. This led to a very simple model, but the outcome appears to have been satisfactory because the simple empirical predictions are quite accurate.

Even though the model is simple, it provides a good approximation to the bifurcation load. It also provides some part of the explanation for the physical background of the buckling behaviour. The empirical approximation to the bifurcation load provides a better fit than the physical model in all cases, except for the special case of an infinitesimally small bracket, which was studied as a simple reference case. For this simple but impractical problem the empirical fit over-predicts the bifurcation load for all silos by 12%. Since the case of a bracket with zero dimensions is a purely theoretical case and the empirical equation provides a very good fit for all other cases, even the cases where the width of the bracket was chosen to be zero and the height of the bracket finite, the derived equation is judged to be suitable to use for the prediction of all bifurcation loads of the problem investigated in this work.

4 Materially Nonlinear Analysis (MNA)

4.1 Introduction

Materially nonlinear analysis describes the plastic collapse of a structure using a nonlinear description of the constitutive behaviour of the material, coupled with the assumption of small displacements and perfect structural geometry to obtain the nonlinear response of the structure. Where the stress-strain response is treated as ideally elastic-plastic, this analysis is able to identify the classical plastic collapse load of a structure. This classical plastic collapse load arises because realistic algebraic estimates of the failure load of a wide range of ductile structures can only be achieved by making these assumptions. It carries the added benefit that the classical plastic collapse load is always obtainable, unlike failure loads obtained using other analyses (Rotter, 2005).

This materially nonlinear analysis is an essential part of understanding the failure behaviour of a shell structure, since the plastic collapse load generally gives an upper bound for the remaining, more sophisticated analyses, depending on the failure behaviour of the specific geometry considered. It may be noted in passing that the plastic collapse load may be exceeded when strain hardening of the material is included, or when changes in geometry lead to increases in the loads supported.

For most shell structures, the plastic collapse state has not been studied extensively, even though there was considerable research in this area in the 1960's (Massonnet and Save, 1972). Here, this materially nonlinear, but geometrically linear, analysis is used to describe the plastic collapse of a structure by using small displacement theory and elastic-perfectly plastic material with the von Mises yield condition.

This analysis is far more sophisticated than the simple eigenvalue analysis described in Chapter 3. In computational formulations, a sequence of successively increasing load increments is required to obtain the elastic-plastic and the fully plastic states. In this study, the modified Riks algorithm was used (see also Chapter 1).

This chapter will describe first the choice and verification of the element and

mesh chosen, including benchmark calculations. This is followed by a study of the bracket supported shell and closes with the development of a simple formula to calculate the plastic collapse load.

4.2 Verification of the computational model

4.2.1 Element choice

The finite element package ABAQUS (HKS, 2003) provides several alternative shell elements for the numerical analysis. A short description of the elements considered is given here.

The first element considered was the S4R shell element, which is a 4-node doubly curved general-purpose shell, with reduced integration with hourglass control, and permitting finite membrane strains (ABAQUS manual (HKS, 2003)). ABAQUS recommends this element for thick and thin shell analysis, and claims that is gives "robust and accurate solutions for most applications" (ABAQUS analysis user's manual (HKS, 2003)). Other elements were also considered, notably the S8R thick shell element, which is defined as an "8-node doubly curved thick shell, with reduced integration" and the thin shell element S8R5 with the description "8-node doubly curved thin shell with reduced integration, using five degrees of freedom per node".

When the elements were tested for their suitability for different analyses, both of the 8 node elements displayed difficulties to achieve a solution.

The numerical analysis did not converge to a solution for some bracket geometries in the materially nonlinear analysis when the thin shell element S8R5 was used. Unfortunately, this convergence problem could not be solved.

When the thick shell element S8R was used, the analysis did not converge to a solution for the first load increment, using the modified Riks method, when used in a geometrically nonlinear, elastic buckling analysis (GNA). A test was also made using an example silo shell and bracket with the dimensions r/t=600, h/r=0.12 and h/d=3. A serious difficulty exhibited by this element was its failure to satisfy the von Mises yield criterion (Figure 4.1). The values displayed at some nodes in the ABAQUS output file (Figure 4.1) for the thick shell element S8R were much higher (e.g. $\sigma_y = 565.6\text{MPa}$) than the input yield stress given as $\sigma_y = 250\text{MPa}$. Therefore

the element was considered as not suitable.

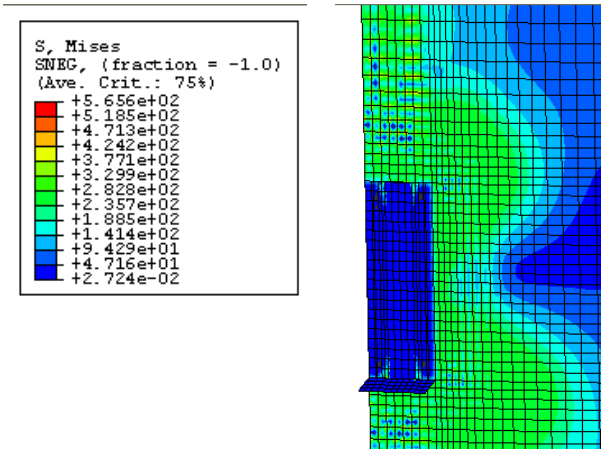

Figure 4.1: Contour plot of a shell with h/r=600, h/r=0.12, h/d=3 after a MN-analysis with S8R elements

Since it was desirable to choose an element which would give an accurate solution for all the analyses performed in this thesis and only the 4-node general purpose element fulfilled this criterion, this element was chosen in for the analysis.

4.2.2 Convergence study

A convergence study with the 4-node, general purpose element S4R was performed to verify the mesh. An example silo shell and bracket with a geometry of r/t=600, h/r=0.12 and h/d=3 (Figure 4.2) is described here. For this purpose, the plastic collapse load was calculated for the example geometry using meshes with a progressively increasing number of elements. As the number of elements was increased the collapse load should decrease towards the real collapse load, which would be reached if an infinite number of elements were used. The result should decrease because the finite element has a constrained displacement field which should always lead to an upper bound to the correct answer. One way to show the convergence of the mesh is to plot the plastic collapse load against the number of elements used in the mesh or the number of degrees of freedom in the system. The real collapse load can then be found as an extrapolation of the number of elements used towards infinity. Extrapolating the number of elements towards infinity to find the real collapse load is not an easy task. The plot does not necessarily follow a known function and has to be estimated by eye. For a better and more rigorous extrapolation a different approach was used (Figure 4.3). Instead of plotting the collapse load against the number of degrees of freedom in the system, the collapse

load was plotted against the inverse of the number of degrees of freedom in the system. The clear advantage is that the extrapolation to find the real collapse load is towards the axis. This not only allows a more accurate extrapolation but permits a first order estimate of the accuracy of the result for a particular mesh to be made.

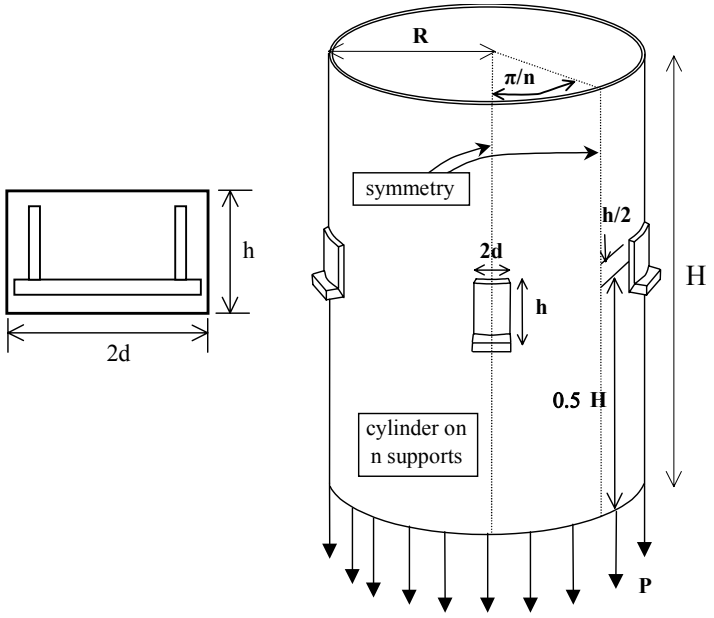

a) bracket dimensions b) shell dimensions and notation

Figure 4.2: Shell and bracket dimensions

The study shows a good convergence of the mesh. In this case the plastic collapse load for an infinite number of degrees of freedom (x=0, Figure 4.3) is ca 57.54 MPa. The collapse load produced by the mesh chosen for this study is 59.71 MPa.

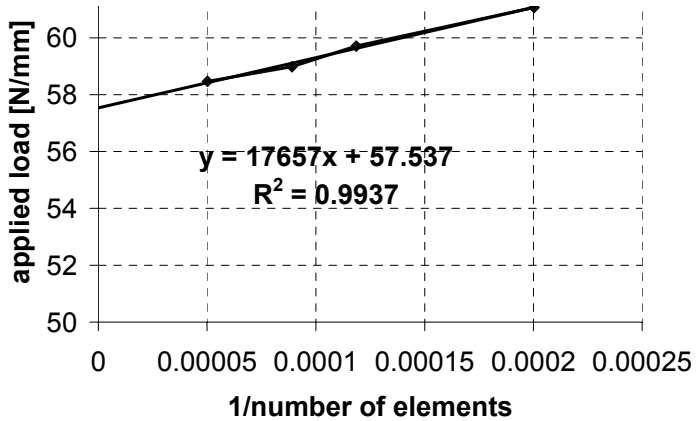

Figure 4.3: Convergence study for a shell with the dimensions r/t=600, h/r=0.12, h/d=3

The difference in collapse loads between the finest mesh and the extrapolated value from the convergence study was 3.8%, while the computing time is still within reasonable limits. Thus the mesh adopted for later calculations was deemed adequate,

but it should be noted that the numerical results should not be regarded as more precise than perhaps 4%, and should be taken as upper bounds on the correct answer.

4.2.3 Benchmark validation tests

To ensure the suitability of the element chosen, problems with a known solution were studied. These included the plastic collapse of a simply supported plate, the plastic collapse of a cylinder under a ring load normal to the shell and the plastic collapse of a silo-hopper transition junction. For all these analyses, the material model was ideal elastic plastic with Young's modulus E=200 000 MPa, Poisson's ratio ν=0.3 and a yield stress of σ_y=250 MPa.

4.2.3.1 Plastic collapse of a simply supported plate

The first benchmark test was performed on a simply supported rectangular plate loaded by a uniformly distributed transverse pressure. The dimensions of the example plate were 100x200 mm with a thickness of 1mm and a yield stress of 250 MPa.

Since the failure mechanism of the simple supported plate under small displacement theory involves only bending, this appears to be a very simple test. Different analytical solutions are available for this standard problem. An analytical solution was obtained using the yield line theory with the result given by Equation 4.1. The yield line theory uses the Tresca yield criterion to obtain an upper bound limit load (Figure 4.4a). Further information on the use of yield line theory for metal plates can be found in Massonnet and Save (1972).

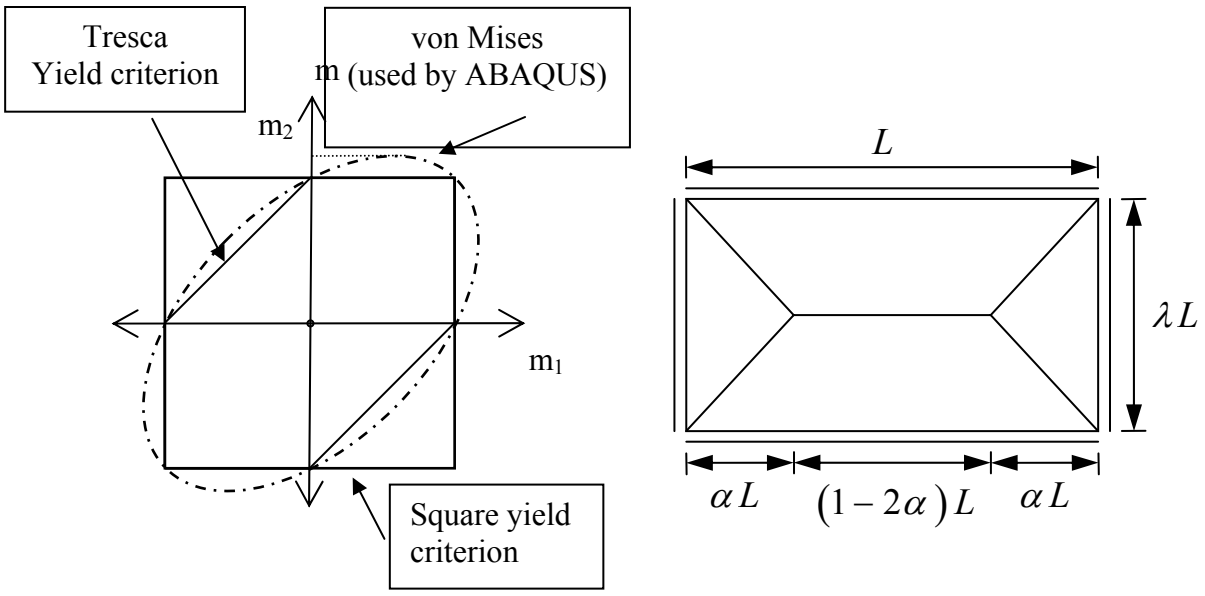

a) b)

Figure 4.4: Sketch of different yield criteria and the yield line analysis

For the example of a simply supported isotropic rectangular plate the upper bound yield line theory collapse load is

$$q_{REF} = \frac{12 \cdot m_{pl}}{\lambda^2 \cdot L^2} \cdot \frac{\lambda^2 + 2\alpha}{3\alpha - 2\alpha^2} = 56.56 \cdot \frac{m_{pl}}{L^2} \tag{4.1}$$

where (Figure 4.4)

$$\alpha_{1,2} = 1 \Big/ 2 \cdot \left(-\lambda^2 \pm \lambda \cdot \sqrt{\lambda^2 + 3} \right) \tag{4.2}$$

$$m_{pl} = \frac{\sigma_y \cdot t^2}{4} \tag{4.3}$$

For the example case (λ=0.5), and α=0.3257 (Equation 4.2) the plastic collapse load is found as

$$q_{REF} = 0.0884\, N/mm^2 \tag{4.4}$$

Another approach to this problem can be found in the text by Massonnet and Save (1972). There both upper and lower bounds to the collapse load are described using the Tresca yield criterion. Using these two limits, the bounds on the exact plastic collapse load for this example are

$$0.0625\, N/mm \le q_{REF} \le 0.0884\, N/mm \tag{4.5}$$

Even though the simply supported plate seemed to be a fairly simple test, no exact solution could be found and the lower and upper bound limit loads show a

difference of 41.4%. This shows that the exact plastic collapse load is not easy to obtain, even for apparently simple problems.

To verify the ability of ABAQUS to calculate the plastic collapse accurately using the 4-node element S4R, the numerical solution is compared to these analytical predictions.

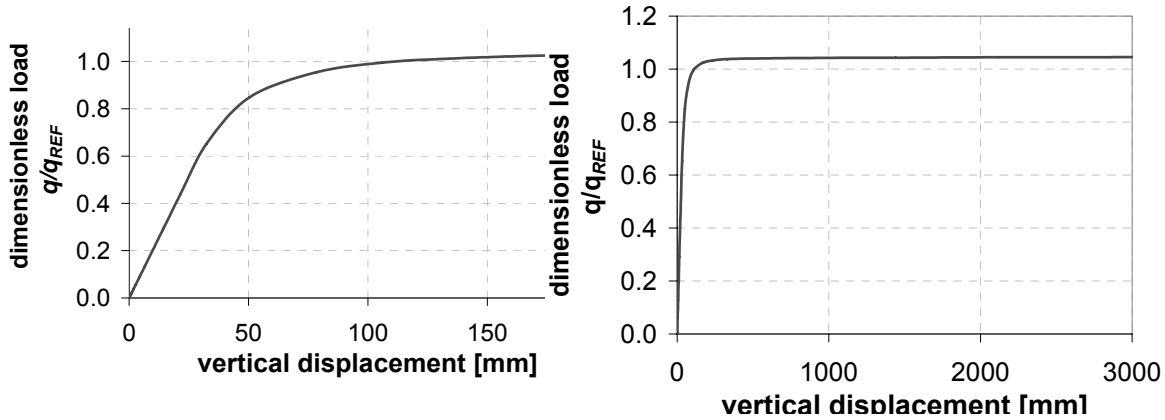

a) showing extensive plasticity b) at huge displacements

Figure 4.5: Load deflection path of a simply supported plate under uniformly distributed pressure (MNA)

To calculate the numerical solution, a materially nonlinear analysis with small displacement theory was performed in ABAQUS (HKS, 2003) using the von Mises yield criterion. The load deflection path extracted from the ABAQUS output is shown in Figure 4.5. It shows a plateau very close to the yield line solution, but over-predicts this load by about 4%. The deflections shown in Figure 4.5 are very large indeed: too large to be reasonable, but these simply arise from the attempt to determine the precise position of the plastic plateau, and to show how slow this plateau may be to be properly developed.

The analytical solution is an upper bound limit load and should therefore normally be larger then the numerical value, but the analytical solution uses the Tresca yield condition (Figure 4.4a), whereas the numerical model has used the von Mises yield condition and may therefore be larger. The 4% difference between the numerical result and the yield line theory solution is a natural result out of different yield criteria used. It may also be noted that the finite element mesh may lead to a slight over-prediction too. The difference in the predicted collapse loads caused by using different yield criteria may have been partly reduced the fact that the yield line solution is an upper bound and so potentially lies above the value that would be found for an upper bound using von Mises criterion.

4.2.3.2 Cylinder with a radial ring load

The next investigation was a thin cylinder subjected to a ring load (Figure 4.6). This example was chosen because it involves a cylindrical shell and there is an exact analytical solution using the von Mises yield criterion obtained by Sawczuk and Hodge (1960).

$$P_{REF}=1.949\cdot\sigma_y\cdot t\cdot\sqrt{t/r} \tag{4.6}$$

This solution, being exact, satisfies both the upper and the lower bound theorems and is therefore a very good test of the numerical calculation of ABAQUS (HKS, 2003). It also has the advantage that it tests the analysis in a situation involving an interaction between bending and stretching.

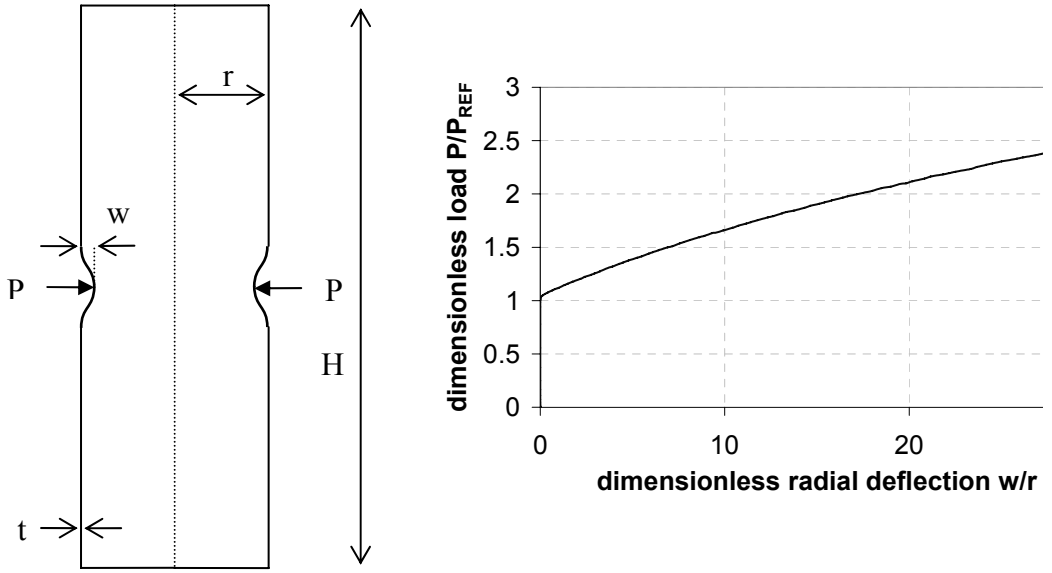

a) b) r/t=600, t=1 H=2400

Figure 4.6: Sketch and load deflection path of the cylinder with ring load

The failure mechanism for a ring loaded cylinder is a combination of plastic deformations involving both stretching and bending at different points in the shell. Under the radially inward applied load the cylinder displays deflections in the radial direction with the maximum deflection at the point where the load is applied. This introduces a high circumferential compression at this point. The plastic strain field near the load is dominated by yielding due to stretching (negative). Due to the radial displacement, the cylinder must bend in the axial direction to maintain compatibility. This introduces high bending plastic strains in the axial direction. In addition, a reaction circumferential bending moment develops throughout the mechanism.

Since a perfect elastic-plastic material was used in the numerical analysis it was

expected that the load deflection path would be in the classical form with a well developed plateau in the plastic range. Unfortunately this was not the case (Figure 4.12). Instead of the development of a plateau, the load deflection path continued to rise at large displacements. The plastic collapse load therefore could not be easily obtained directly from the load deflection path.

Much thought went into the problem of extracting an accurate plastic collapse load from a load deflection curve of this type. Here the extracted plastic collapse load is to be compared with an analytical solution to a well-known problem. But the remainder of this thesis is concerned with brackets attached to a cylindrical shell, for which there are no analytical solutions. It was therefore necessary to find a reliable method of deducing the plastic collapse load in a manner that is not arbitrary.

The work of Gerdeen (1979) on the extraction of plastic collapse loads for pressure vessels with very nonlinear load- deflection curve paths illustrates the difficulty very well: he was only able to offer a rather arbitrary criterion which relied on the load achieved when the maximum displacement of the structure was a chosen multiple of the value corresponding to elastic displacement alone. He also proposed the use of volume change as the measure of displacement. Such a criterion is clearly not of general applicability and cannot lead to satisfactory determinations in all cases. In response to this situation, a modification of the Southwell plot (Holst et al., 2005) was devised. This idea was first proposed by Holst *et al.* (2002) , but has been extended here.

The Southwell plot was originally conceived (Southwell,1932) to obtain an accurate estimate of the elastic buckling load P_{cr} in an experiment on an imperfect column (Equation 4.7).

$$w = \frac{w}{P} P_{cr} - w_0 \tag{4.7}$$

where P is the applied load, w is the measured deflection, and w_0 is the initial imperfection amplitude in the fundamental buckling mode.

This plot is valuable whenever a load displacement curve has a hyperbolic form, as the hyperbolic data are transformed into a linear plot from which the key parameters can be extracted. The difficulty with this plot is that the critical load is expressed as the slope of the function and cannot be directly extracted (Figure 4.7).

Since the load deflection curves did not develop a plateau but continued to rise (Figure 4.6), the Southwell plot did not show a straight line close to the plastic collapse load (as would be expected), but developed a highly nonlinear behaviour.

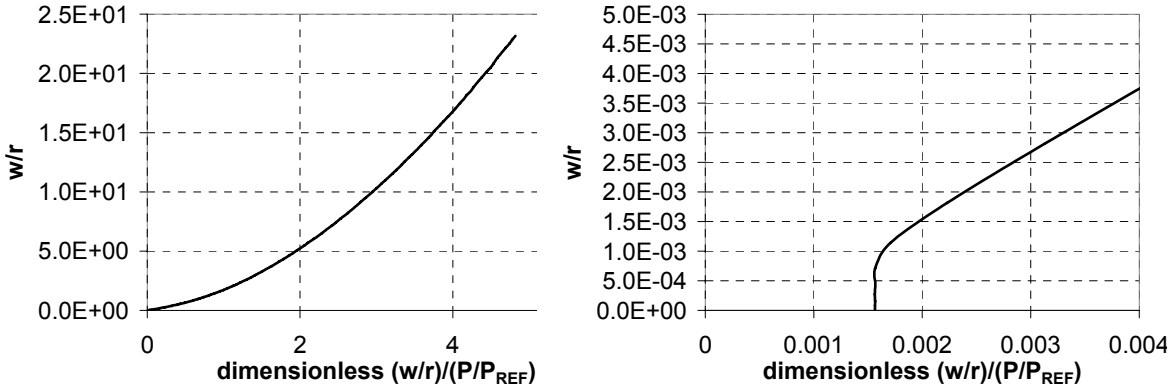

a) showing extensive plasticity b) at small displacements

Figure 4.7: Southwell plot of the cylinder with ring load (Figure 4.6)

The modified Southwell plot (Horne and Merchant, 1965) presents the data in a slightly different form

$$P = P_{cr} - w_0 \frac{P}{w} \tag{4.8}$$

where P is the applied load, w is the measured deflection, and w_0 is the initial imperfection amplitude in the fundamental buckling mode. A plot of P against P/w gives the asymptotic load as the intercept on the ordinate axis. By choosing this form, observations that are progressively closer to the desired load level give points that are progressively closer to the target intercept. The application of Southwell-type plots to other structures and in other circumstances has been discussed, for example, by Mandal and Calladine (2002) for the lateral-torsional buckling of beams. As noted above, the key feature of the Southwell plot is that it transforms a hyperbolic function into a linear one: where a phenomenon is exactly hyperbolic, it transforms into an exactly linear plot. In the analysis of metal shells, the material properties are often assumed to be elastic-perfectly plastic. However, the kink in the bilinear material law is radically smoothed by the need to develop a complete plastic mechanism, and in shells the interaction between bending and stretching in two directions exacerbates it. Thus an MNA analysis produces a load-displacement curve that approaches the hyperbolic form, particularly when close to the asymptotic load. The modified Southwell plot then provides a good means of obtaining the required

reference load.

When the modified Southwell plot is applied to the results of the ABAQUS analysis (Figure 4.8), the curve is initially vertical, because the behaviour is linear elastic. At higher loads the slope of the modified Southwell plot is close to linear over a large range before a significant increase in slope is observed towards the end of the curve (Figure 4.8). A tangent drawn to the second linear portion of the curve at the point of minimum slope intercepts the load axis at the plateau load 1.0307, which is a 3.07% higher than the classical solution.

At very large displacements the linear path turns into a vertical line (Figure 4.8). This pattern of behaviour caused much delay whilst a cause was sought. Initially it was thought that ABAQUS might introduce some artificial strain hardening into the material model to ensure convergence of the solution at high plastic strains, but no evidence could be found in the manuals to support this proposition. Instead, the ABAQUS manual proposes a "work-around" technique to deal with such effects in Section 4.4.3.4. In view of the fact that the load deflection curve continually rises and finally produces a vertical line in the modified Southwell plot in the range where very high plasticity occurs, it was thought that a better method was needed to extract the collapse load. The modified Southwell plot appears to produce a consistent, mesh independent (Figure 4.9) and repeatable method of finding this load accurately.

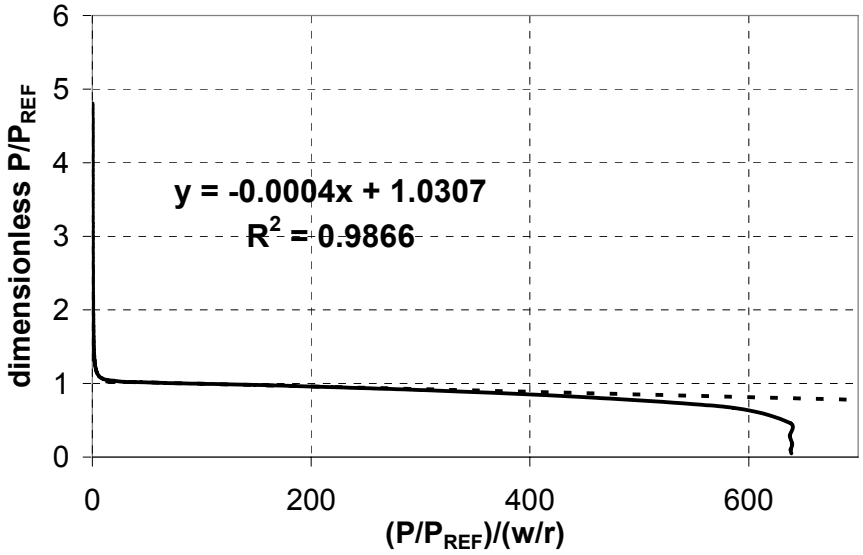

Figure 4.8: Modified Southwell plot of the cylinder with ring load (Figure 4.6)

As can be clearly seen from Figure 4.6b and Figure 4.8, the transformation of the load deflection curve into the Southwell plot enables an accurate evaluation of the

plastic collapse load to be made. There is just a slight over-prediction of the failure of 3.07%.

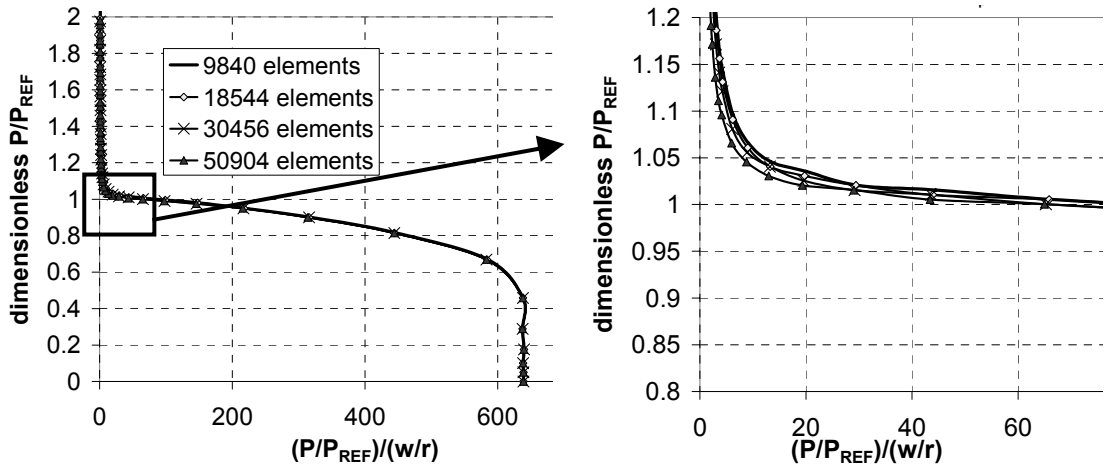

Figure 4.9: Modified Southwell plot of the ring loaded silo with different numbers of elements

4.2.3.3 Plastic collapse of a silo- hopper transition junction

The third benchmark test undertaken was the plastic collapse of a silo-hopper transition junction (Figure 4.10a). The analytical solution (Figure 4.10b) for this problem was developed by Teng and Rotter (1991). This solution can also be found as an benchmark test in the European shell standard (EN1993-1-6, 2006). The material used was linear elastic–perfect plastic using the von Mises yield criterion.

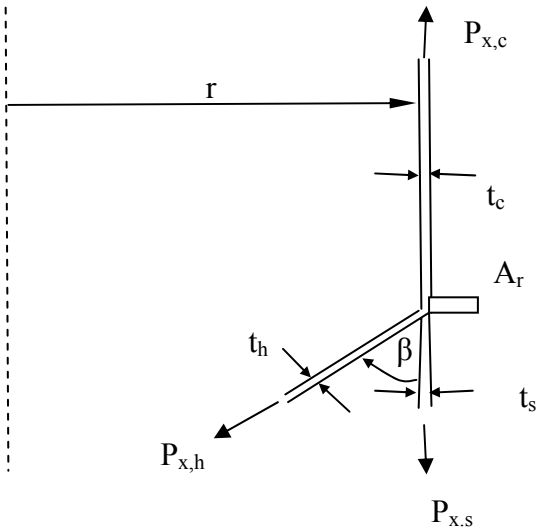

$$t_c^2 \le t_s^2 + t_h^2$$

$$|P_{xs}| << t_s f_{y,} \; |P_{xh}| << t_h f_{y,} \; |P_{xc}| << t_c f_{y,}$$

$$\eta = \sqrt{\frac{t_c^2}{t_s^2 + t_h^2}}$$

$$\psi_s = \psi_h = 0.7 + 0.6\eta^2 - 0.3\eta^3$$

$$l_{oc} = 0.975\sqrt{rt_c}$$

$$l_{os} = 0.975\psi_s\sqrt{rt_s}$$

$$l_{oh} = 0.975\psi_h\sqrt{\frac{rt_h}{\cos\beta}}$$

$$P_{xhR} \cdot r \cdot \sin\beta = f_y(A_r + l_{oc}t_c + l_{os}t_s + l_{oh}t_h)$$

Figure 4.10: Sketch and calculation of the plastic collapse of a hopper silo junction (EN1993-1-6, 2006)

The silo - hopper transition junction was chosen as a benchmark test due to its more complex failure behaviour than the benchmark tests performed above.

The overall collapse mechanism of the junction is caused by axial tension in the hopper causing circumferential compression at the transition junction, with extensive meridional bending in all shell segments. The stiffener at the transition fails under pure circumferential compression. The upper cylindrical shell and the bottom conical shell both suffer circumferential compression, but the yielding of the outer surfaces is dominated by meridional bending in a ring zone around the circumferential axis.

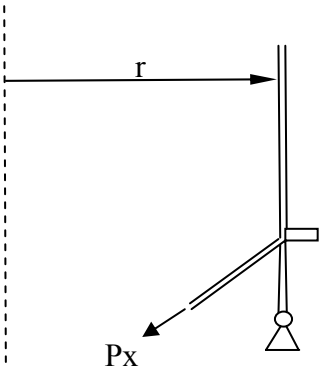

Figure 4.11: Loading and boundary condition of the silo hopper transition junction

The load is applied to the hopper as a meridional tension (Figure 4.11). The bottom of the cylindrical wall of the silo is simply supported whilst the top is free. One example is illustrated here (Table 4.1), but several different geometries were tested.

f_y=	250 MPa	A_r=	5000 mm
β=	45°	η=	0.7071
r=	5000 mm	$\psi_s=\psi_h$=	0.89393
t_c=	10 mm	l_{oc}=	218.016 mm
t_s=	10 mm	l_{os}=	194.892 mm
t_h	10 mm	l_{oh}=	231.767 mm
t_p=	50 mm	P_{xhR}=	809.408 MPa
b=	100 mm		

Table 4.1: Geometry chosen and constants required for the calculation of the plastic collapse load

The applied load and the deflections obtained from the numerical calculation have been made dimensionless in the following calculation to illustrate the ratio between numerical solution and analytical solution. The applied load is divided by

the analytical solution for plastic collapse and the deflections obtained from the numerical solution are divided by the radius of the junction.

The numerically calculated load deflection path (Figure 4.12) does not display, as seen in the previous benchmark test, a plateau. The deflections illustrated in the load deflection path (Figure 4.12) are very large and purely theoretical, but the very large values are used here to show that no plateau develops. When the same load deflection path is shown over a range of smaller deflections, it appears to develop a plateau, but it is not easy to decide at what load the "plastic collapse" may be said to have been reached, since the load continues to rise.

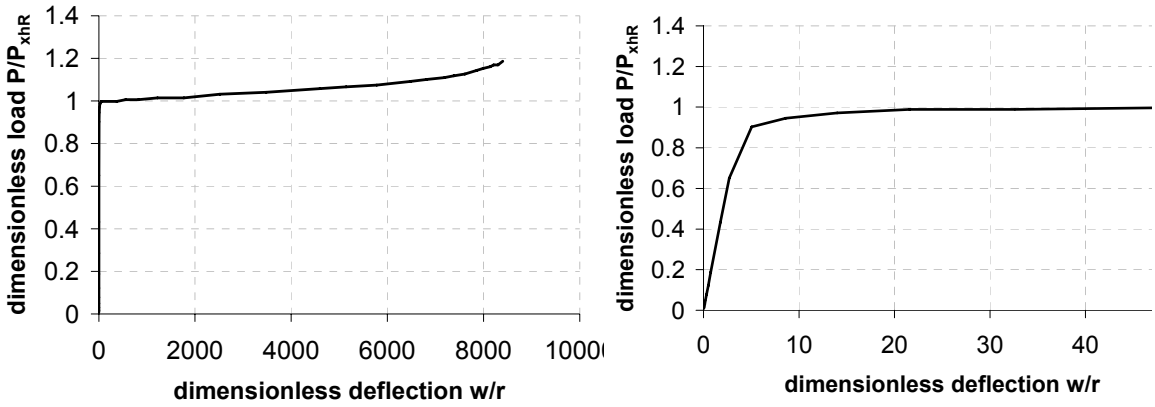

a) showing extensive plasticity b) at smaller displacements

Figure 4.12: Load deflection path of a junction

The modified Southwell plot was used once more to try to obtain a systematic method of extracting the desired collapse load. The result is shown in Figure 4.13 where the plastic collapse can be easily obtained from the modified Southwell plot. The intersection with the y-axis, which is the ratio between the load obtained from the numerical calculation and the analytical solution is very close to unity (~1.007). Therefore the numerical result of this example agreed very well with the analytical result. The other tested geometries displayed the same good agreement with the analytical solution.

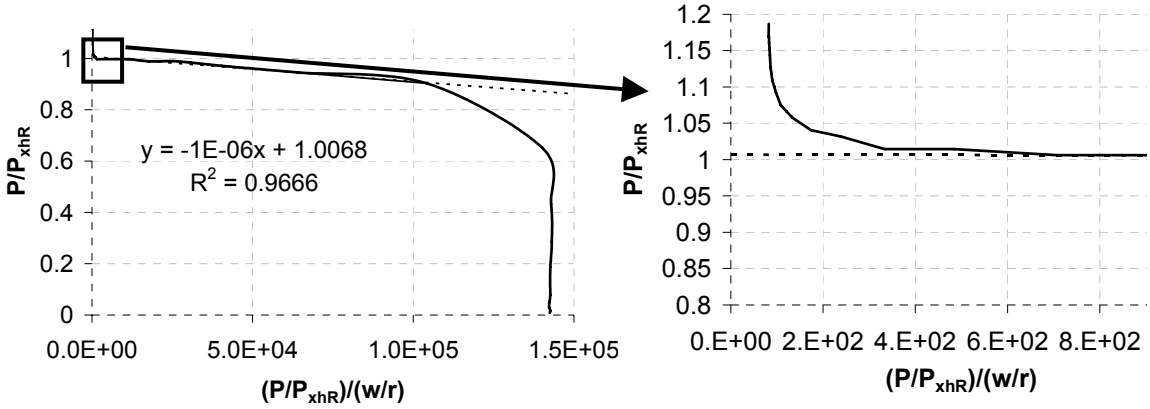

Figure 4.13: Modified Southwell plot of the hopper-silo-junction

4.2.4 Summary the verification of element and mesh

The chosen mesh converged well for the materially nonlinear analysis with small displacement theory and the element passed the benchmark tests without difficulties. Therefore it was assumed that both mesh and element are suitable for this analysis.

4.3 The bracket supported shell

4.3.1 Example geometry of a bracket supported shell

After verification of the mesh and element, the focus was moved to the problem of the bracket supported shell.

Based on the performed benchmark tests (plate, cylinder under a ring load and silo junction), it was natural to suppose that the structure would have a yield line collapse mechanism including bending and stretching. When the ABAQUS output files of the materially nonlinear analysis (MNA) were analysed, no such mechanism could be found and the loads achieved in the numerical analysis were very high.

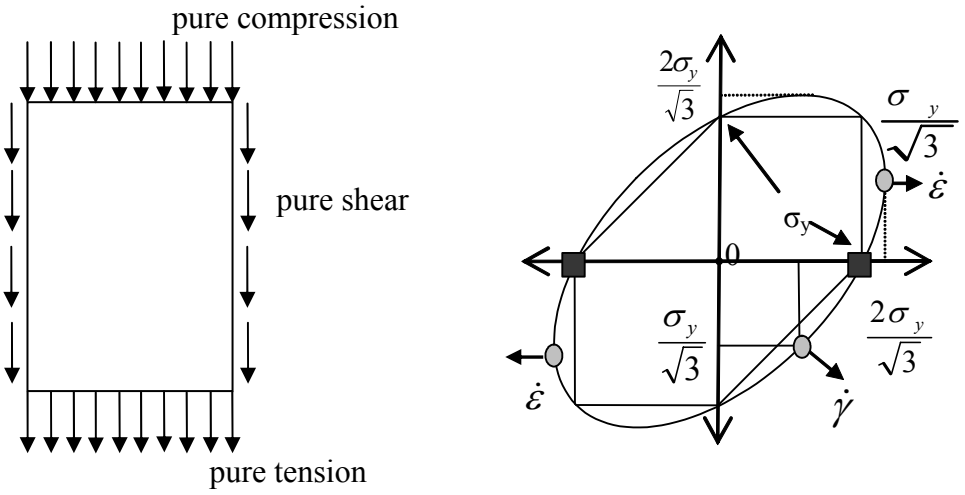

a) Stresses around the bracket b) Von Misses yield ellipse

Figure 4.14: pure tension, shear and compression around the bracket

Therefore consideration was given to the absolute maximum load that the bracket could possibly sustain. The simplest model is to assume pure uniform membrane compression on the upper boundary, pure membrane uniform shear on the sides and pure uniform membrane tension on the bottom of the bracket (Figure 4.14). These three stresses were all assumed to be at full membrane yield. But the calculated collapse load was found to be still higher than this reference load.

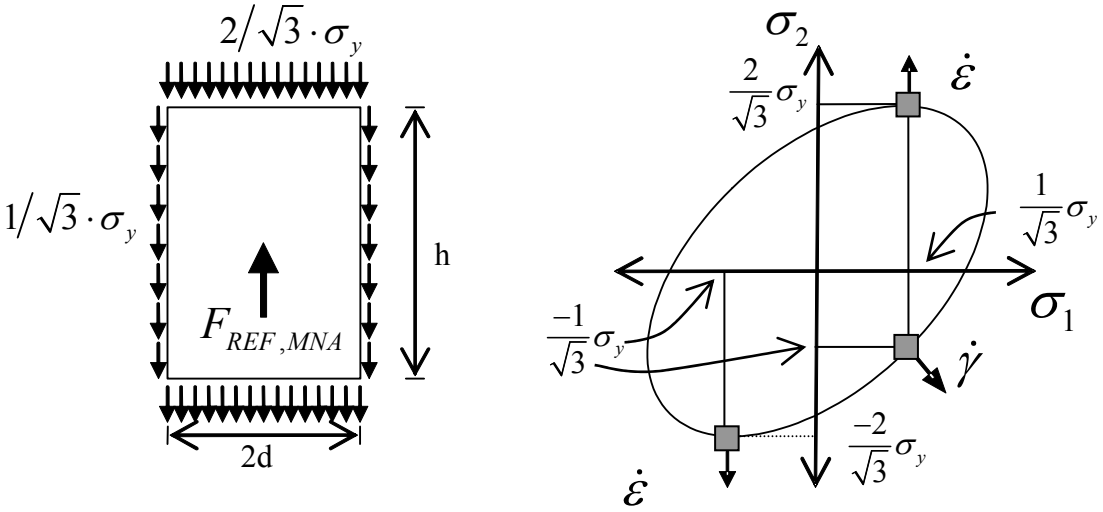

a) Stresses around the bracket b) Von Misses yield ellipse

Figure 4.15: Absolute maximum stress amplitude to be sustained by the bracket

A closer look at the von Mises yield ellipse shows that the stress state for the top and bottom can be higher than the uniaxial yield stress in both tension and compression, and this was also in accordance with the numerical output (Figure 4.15).

But the resulting reference load is clearly the absolute maximum load that the structure could possibly sustain.The maximum value for the membrane compressive and tensile stress is $2\sigma_y/\sqrt{3} = 1.15\sigma_y$ (Figure 4.15), whilst the maximum value obtained from the von Mises yield ellipse for yielding in pure shear is $\sigma_y/\sqrt{3} = 0.577\sigma_y$. These values multiplied by dimensions of the bracket then give the ultimate plastic collapse load as the maximum support force the bracket can possibly support if made of purely elastic-perfectly plastic material (Equation 4.9).

$$F_{REF,MNA} = \sigma_y \cdot t \cdot 2d \cdot 2/\sqrt{3} + \sigma_y \cdot t \cdot 2d \cdot 2/\sqrt{3} + \sigma_y \cdot t \cdot 2 \cdot h \cdot 1/\sqrt{3} \tag{4.9}$$

$$F_{REF,MNA} = \sigma_y \cdot t \cdot \left(2 \cdot 2d \cdot 2/\sqrt{3} + 2 \cdot h \cdot 1/\sqrt{3}\right) \tag{4.10}$$

where σ_y is the yield stress, t is the thickness of the shell, $2d$ is the whole width of the bracket, and h the height of the bracket.

It was shown in the benchmark test that the load deflection path in a materially nonlinear analysis does not necessarily develop a plateau. This is also the case for the problem of the bracket supported silo (Figure 15). The example cylinder and bracket used to calculate this load deflection path had the dimensions r/t=600, h/r=0.12, h/d=3 and t=1.

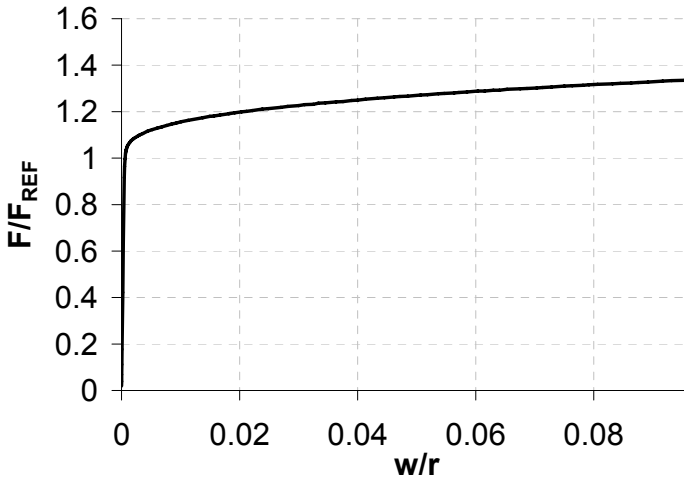

Figure 4.16: Typical Load deflection path of a silo with the geometry of r/t=600, h/r=0.12, h/d=3

The typical load deflection path obtained from the numerical analysis (Figure 4.16) displays the expected straight line in the elastic range, becomes then nonlinear in the elastic-plastic transition zone, but continues to rise instead of developing a plateau. It should be noted that the deflections in the load deflection diagram (Figure

4.16) are not as large as they were in the benchmark tests. Different possibilities have been considered to define the failure load, as illustrated in Gillie *et al.* (2002).

In Gillie *et al.* (2002) the authors proposed the use of a maximum rotation of the bracket to define failure, following the recommendation of the draft Eurocode for shells ENV 1993-1-6 (1999). But in the investigation described here the bracket was constrained against rotation, so this failure criteria was not directly applicable. Another possibility would have been to use a maximum deflection somewhere on the shell to define failure, but this would necessarily be an arbitrary value. The difficulty here would be to define what value would give an appropriate allowable maximum deflection. Both of these methods seemed ad hoc and quite inappropriate.

The modified Southwell plot was used here, since it has been shown that the plastic collapse load can be extracted accurately.

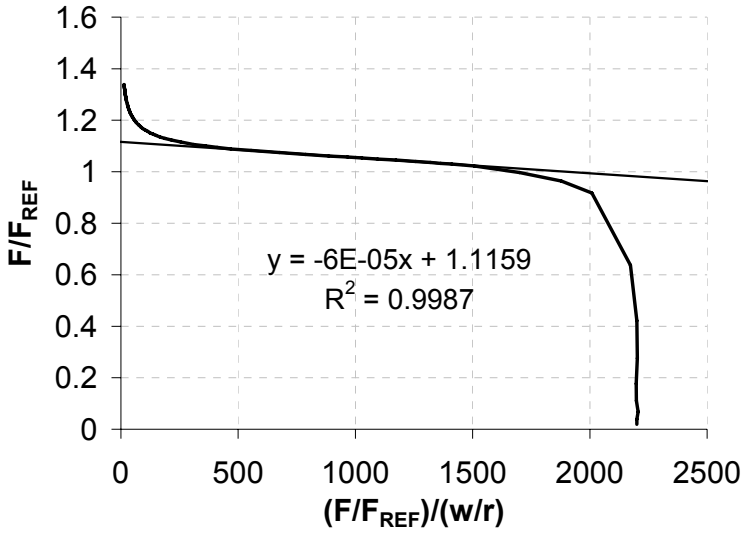

Figure 4.17: Modified Southwell plot. Shell geometry r/t=600, h/r=0.12, h/d=3

But when this reference load was compared to the numerically calculated collapse load (Figure 4.17), it was evident that the numerically calculated load was still higher (about 11%) than the reference load. It was therefore necessary to find a reason for this discrepancy, which clearly must have its origin in some error in the numerical calculation.

The phenomenon seen here was not an isolated case. All of the materially nonlinear analyses of bracket supported shells showed an over-prediction of the collapse load, with different extents (up to 26%) of over-prediction.

4.4 Investigation into the problem

4.4.1 Introduction

Due to the apparently clear over-prediction of the collapse load by the numerical simulation, a new investigation was performed to try to find the source of this discrepancy. All the investigations were performed with the cylinder and bracket geometry mentioned in the previous section (r/t=600, h/r=0.12, h/d=3, H=4r and t=1).

To investigate the problem the following factors were investigated:

- Stress distribution around the bracket
- Material (Young's modulus, Poisson's ratio and yield stress, elastic-perfectly plastic material model, number of section points, Ramberg-Osgood material model
- Geometry of cylinder (Thickness of the shell, influence of the curvature of the shell
- Bracket properties and connection to the shell
- Loading
- The symmetry boundary conditions
- The singularities at the corners of the bracket
- The suitability of the element (Shear locking, finite membrane strain, a new mesh using a mixture of elements)

4.4.2 Stress distribution around the bracket

To confirm that the internal stress state does comply with the external equilibrium, the membrane stress resultants around the bracket were extracted and integrated over the relevant lengths and then compared to the applied load in the corresponding load increment.

In a fully plastic state (yielding in both of the outer and the inner surface all around the bracket) the membrane stress resultants (Figure 4.18) correspond very well with the theoretical model, which assumed full plasticity around the bracket. This stress distribution can be found at a load increment just above the reference load, which indicates that the simple theoretical model is correct. Since there is now a

fully plastic state all around the bracket, the load applied to the cylinder bracket model should not rise further, but should display a plateau. As it was noted before, this is not the case. Therefore the internal stress resultants and the external loads are not in equilibrium.

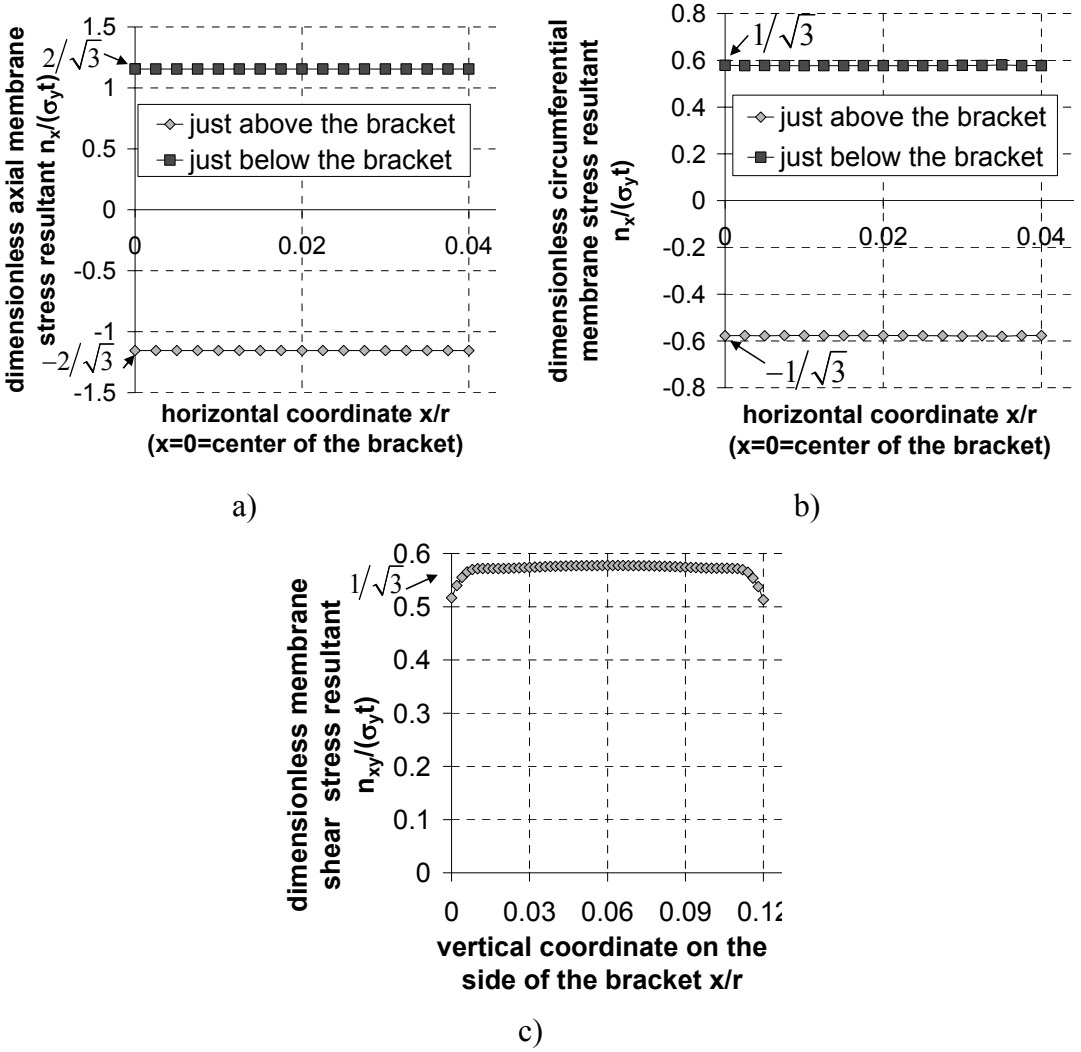

Figure 4.18: Distribution of the membrane stress resultants around the bracket in fully plastic

4.4.3 Material

4.4.3.1 Young's modulus, Poisson's ratio and yield stress

Next the element property definitions were tested. For the elastic material the Young's modulus and the Poisson ratio were tested. The Young's modulus should only make a difference in the elastic and the elastic-plastic-transition range, but an increase in the Young's modulus does reduce the absolute values of the total strain

and might therefore lead to a different result if the computer program contains a hidden algorithm that introduces an artificial strain hardening at large plastic strains. This technique has also been suggested in Rotter (2005). Different Young's moduli, higher and lower than the original Young's modulus, were chosen to investigate any changes in behaviour. The Young's modulus chosen for the original calculation was E=2.0E+05 MPa, modelling mild steel. For an easy comparison of the different Young's moduli, the x-axis (load divided by deflection) was made dimensionless by dividing the values by the constant value $P/w_{elastic}$ (Figure 4.19), since the value $P/w_{elastic}$ naturally varies linearly with the Young's modulus.

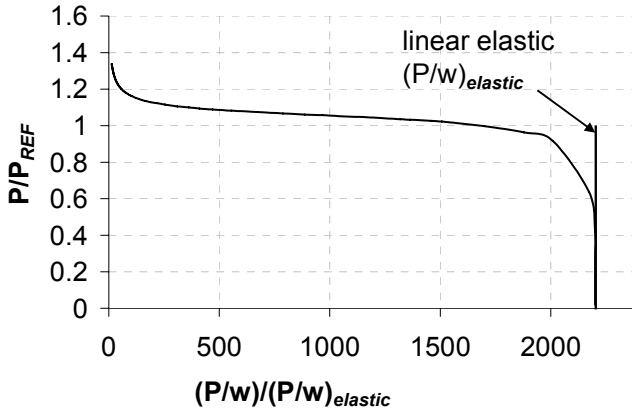

Figure 4.19: Modified Southwell plot with E=2.0E+05 MPa

For the calculation with a very high Young's modulus, the numerical calculation did not complete (Figure 4.20) due to convergence problems during the analysis. But the dimensionless modified Southwell plot is identical for all Young's moduli tested.

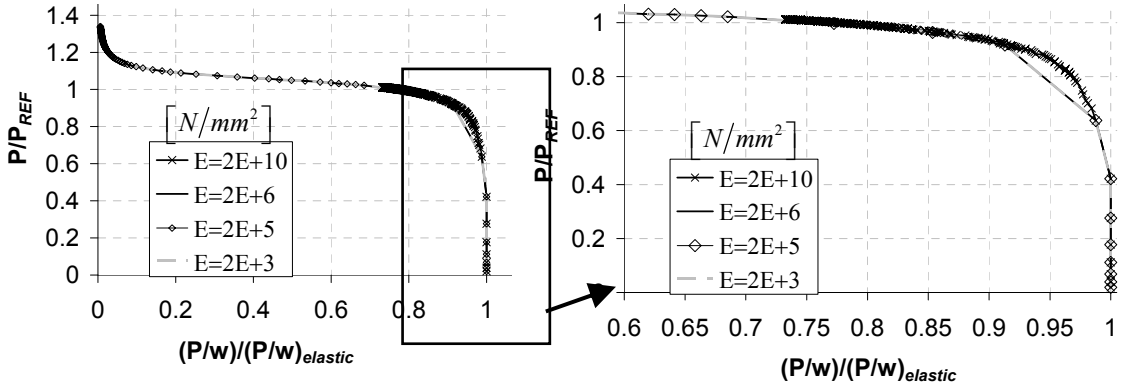

Figure 4.20: Modified Southwell plot with varying Young's modulus

Not all Young's moduli that were used in this investigation are shown here, since there would be a loss of clarity. However, the result was the same for all values of Young's modulus tested. Therefore a change in the Young's modulus does not change the outcome of the numerical analysis (Figure 4.20), contrary to the

proposal of Rotter (2005).

It was next thought that the Poisson's ratio would only change the outcome in the elastic range of the materially nonlinear, geometric linear analysis, but to ensure that the thinning or widening of structure was not included in the element formulation for highly plastic behaviour, a little study was carried out.

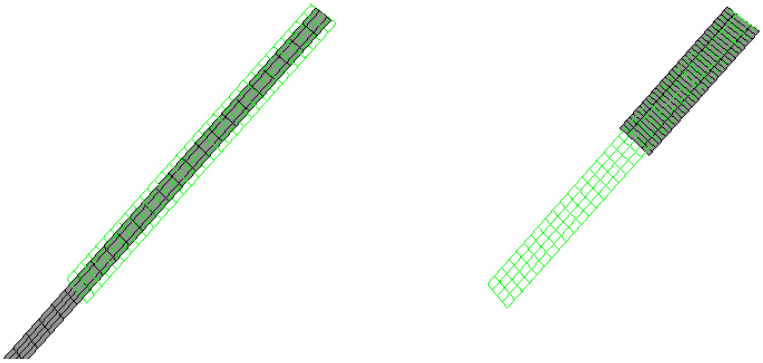

a)tension b) compression

Figure 4.21: Deformed shape of the bar in tension and compression (superimposed undeformed shape)

A bar under pure tension and under pure compression was considered (Figure 4.21). The material was elastic-perfectly plastic and small displacement theory was used. The bar was simply supported at one end and loaded in tension at the other end. If the Poisson's ratio cross-sectional area reduction is included in the element formulation, the bar in tension would thin considerably and the load would be reduced drop.

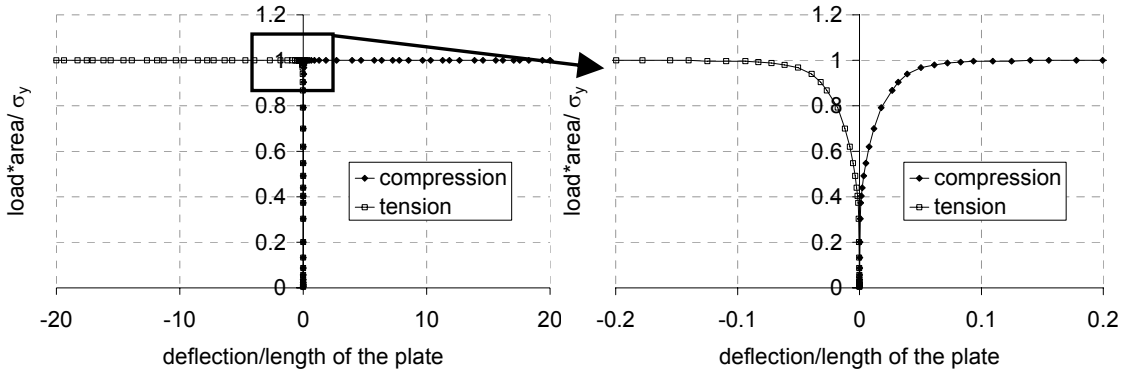

Figure 4.22: Load deflection curve for the plate under tension and compression

By contrast, when the bar is in compression, the cross-sectional area should rise and the load would increase. The bar was modelled in such a manner that it could change its width over the whole length of the bar. The results showed that this change of cross-sectional area effect is not included in the element formulation, since both the load deflection curves developed a plateau and were also identical for

tension and compression (Figure 4.22) even at very large strains (many hundreds of percent strain!).Even though it has been shown (Figure 4.22), that the Poisson's ratio does not affect the outcome of the plastic collapse load of this tension/compression test, it was also tested on the bracket supported shell. However, as expected, the value of Poisson's ratio had almost no influence on the plastic collapse load (Figure 4.23).

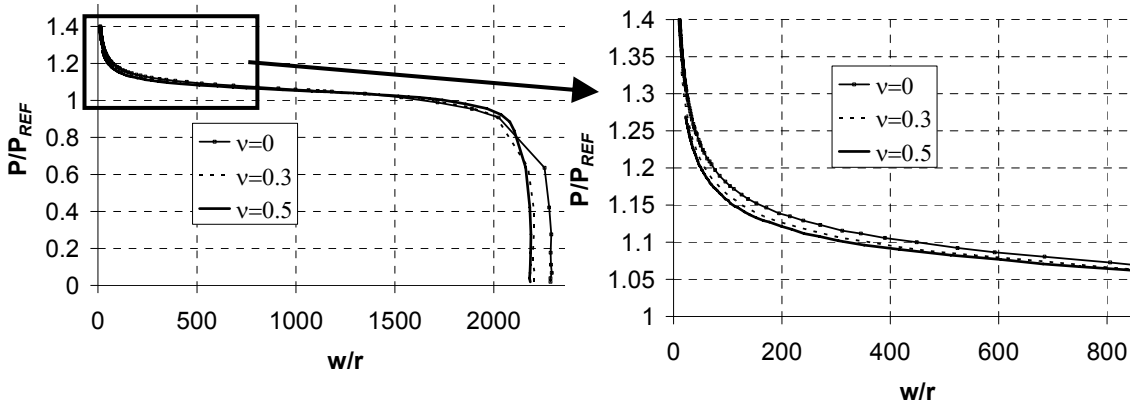

Figure 4.23: Modified Southwell plot with varying Poisson's ratio

The next parameter to be investigated was the yield stress to ensure that it had been implemented correctly. The hypothesis to be tested was that the collapse load should vary roughly linearly with the yield stress, since the analysis is small displacements (no change of geometry) and the shell-bracket system has therefore always the same stress pattern when yielding starts, though at different load levels. Hence the collapse mechanism should be the same, but at different loads, depending on the yield stress.

The results of the numerical analysis confirmed this hypothesis. For clarity the collapse load was made dimensionless by dividing by $\sigma_y t$ and is plotted against the yield stress in Figure 4.24, where the result should be a constant value. Slight differences occur in the dimensionless collapse load (Figure 4.24), but these arise from the process of extraction of the collapse load and are very small indeed. Therefore it can be said that the yield stress is not a source of the over-prediction of the collapse load.

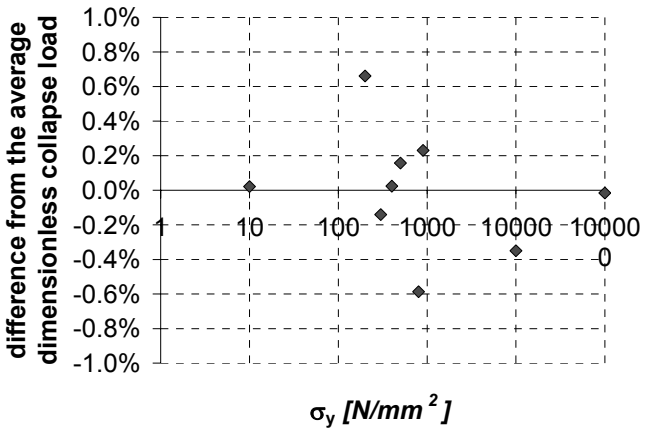

Figure 4.24: Variation of the collapse load with the yield stress

4.4.3.2 Elastic- perfect plastic material model

The next proposition considered was that the elastic-perfectly plastic material model in ABAQUS could be at fault and might cause difficulties in the finite element calculation. Therefore a very small amount of strain hardening was introduced. This change in the material model only made an insignificant difference to the end result.

4.4.3.3 Number of section points

The quality of the through-thickness representation of the stress distribution was also questioned. To explore this issue, the number of section points through the thickness of the element was varied to ensure that enough section points were being used for this kind of analysis.

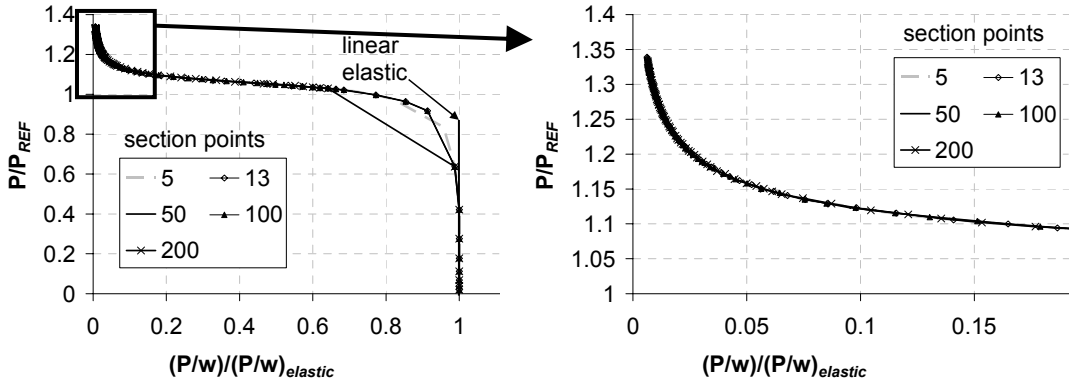

Figure 4.25: Modified Southwell plot with varying the number of section points though the thickness of the shell

The number of section points was varied from 5 to 200, but the number of section points did not make any significant difference to the end result (Figure 24).

4.4.3.4 Ramberg-Osgood material model

To ensure that the plasticity model was not the cause of the constantly rising load at plastic collapse, the Ramberg-Osgood material model was used instead. The following description is taken from ABAQUS Analysis User's Manual section 11.2.13 (HKS, 2003). In one dimension, the model is

$$E \cdot \varepsilon = \sigma + \alpha \left(\frac{|\sigma|}{\sigma^0} \right)^{n-1} \cdot \sigma \tag{4.11}$$

where σ is the stress; ε is the strain; E is Young's modulus (defined as the tangent to the stress-strain curve at zero stress); α is the "yield" offset; σ^0 is the yield stress, in the sense that, when $\sigma = \sigma^0$, $\varepsilon = \sigma^0 \cdot (1+\alpha)/E$; and n is the hardening exponent for the "plastic" (nonlinear) term: $n > 1$.

The manuals also states: "The deformation theory Ramberg-Osgood plasticity model is primarily intended for use in developing fully plastic solutions for fracture mechanics applications in ductile metals". Thus the developers of ABAQUS did not intend this use of the deformation theory of plasticity to be used in an application of the kind studied in this thesis.

The purpose of this study was to ensure that an elastic-perfectly plastic material model can capture the yield state around the bracket accurately and reflect this in a plateau at peak load, corresponding to the plastic collapse load of the system. The Ramberg-Osgood plasticity model, as coded into ABAQUS (HKS, 2003), permits use of the command "fully plastic", which terminates the analysis when a specified element suffers plastic strains in excess of 10 times the offset yield strain.

Since it was thought that ABAQUS might introduce some hardening into the von Mises the perfectly plastic model (as a potential cause of the steadily increasing load deflection path), the concept used here was that the Ramberg-Osgood model analysis could be stopped when the plastic strain becomes too large. To achieve a good comparison, the Ramberg-Osgood model was made very similar (with α=1.01, n=300, ν=0.3, E=200000MPa) to the elastic-perfectly (ν=0.3, E=200000MPa) plastic model with only a very small hardening introduced (Figure 4.26).

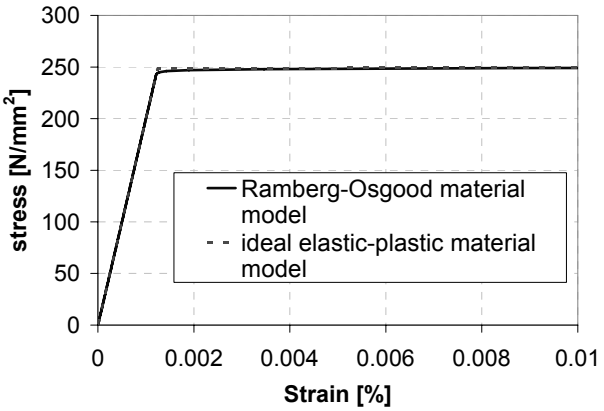

Figure 4.26: Stress-strain diagram of the elastic –perfectly plastic and the Ramberg-Osgood material model

The effect of using the Ramberg-Osgood plasticity model may be seen in the comparison with the perfectly plastic model shown in Figure 4.27. The Ramberg-Osgood model does not change the plastic collapse load, but the analysis stops well before the perfectly plastic model in the modified Southwell plot starts to curl up (that is, as P/w approaches zero). But it is evident that this adoption of the Ramberg-Osgood model is not a satisfactory solution to the problem of the very high loads observed in the analysis at large displacements.

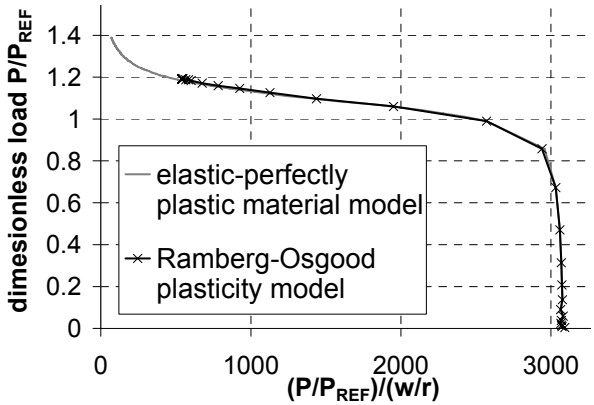

Figure 4.27: Modified Southwell plot of the same shell geometry with different plasticity models

4.4.4 Geometry of cylinder

4.4.4.1 Thickness of the shell

The element chosen for this study (S4R) is a general purpose element. It uses thick shell theory when the shell thickness is large but becomes a discrete Kirchhoff thin shell element for small thicknesses (HKS, 2003). Since the thickness of the cylinder was chosen to be a value of unity throughout this work (making all

dimensions dimensionless relative to the thickness *t*), the next investigation explored the question of the relative thickness of the element, and the consequent change in the shell theory used. The exploration was designed to see if this could be the source of the difference between numerical behaviour and the reference load.

The thickness of the elements was changed in the range $1 < t < 1000$. The resulting modified Southwell plots (Figure 4.28) show that the change of thickness of the cylinder does have a small effect on the load deflection path, but the overall behaviour is not changed.

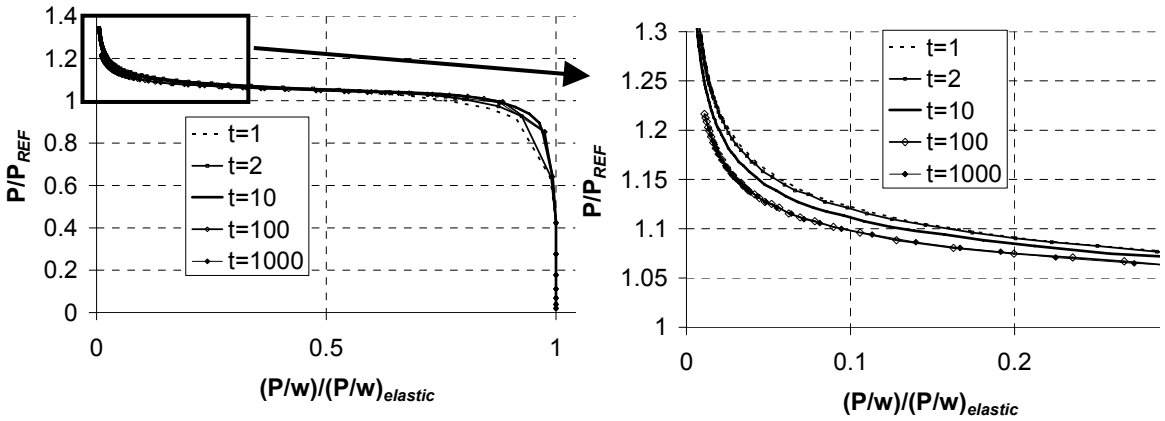

Figure 4.28: Modified Southwell plot with varying the thickness of the cylinder

The extrapolated value for the collapse load does appear to decrease slightly as the thickness of the cylinder increases. The reduction of the collapse load is 3.11% when the thickness of the shell is increased from 1 to 100 units. This is not a significant effect.

Therefore the thickness of the shell and the different shell theory used with different thicknesses of the shell (relative to its fixed radius of curvature) is not the source of the error.

4.4.4.2 Influence of the curvature of the shell

The next possibility considered was that the curvature of the shell was, in some way, the cause of this unexpected phenomenon. To explore this question, a numerical analysis was performed of a flat plate loaded by a rigid flat bracket: this simulated a shell of infinite radius.

The plate displayed the same behaviour problems as the cylindrical shell, by over predicting the load at high deformations. Therefore the curvature of the shell

has no influence on the discrepancy between theoretical model and numerical prediction.

4.4.5 Bracket properties and connection

4.4.5.1 Material properties and thickness of the bracket

In the earliest studies, the rectangular bracket and the cylindrical shell were assigned the same material properties, but the thickness of the bracket was chosen to be to significantly bigger than the thickness of the shell to simulate a rigid bracket. The next hypothesis to be tested was that the big difference in thickness of these adjacent elements was somehow causing this effect.

To study this question, the thicknesses of the bracket and the shell were made the same, but the Young's modulus of the bracket was increased. It was again found that this could not be the cause of the problem.

4.4.5.2 Connection between bracket and shell

The next hypothesis for a cause of the anomalous behaviour lay in the connection between the shell and the bracket. Initially the bracket was connected to the shell only by its edges, since a real bracket would be welded onto the shell around its boundary. The connection was now made using a multiple point constraint. A multiple point constraint connects a master surface to a slave surface, making all degrees of freedom from the slave nodes the same as those of the master nodes, melding two nodes into one. The master surface was chosen to be the bracket since it is advised in the ABAQUS manual (HKS, 2003) that the stiffer surface should be the master surface. To chose the shell as the master surface was found to make no difference to the end result.

To confirm that the connection around the edges of the bracket did not introduce an error into the calculation, the multiple point constraint of the bracket was chosen to cover the whole area of the bracket instead of just its edges. This change had no influence on the numerical solution.

The only parameter regarding the bracket-shell-connection left to check for the connection between bracket and shell was the multiple point connection itself. This check was performed by removing the connection completely. Instead of modelling

the bracket as a separate part, the entire computational model was made from a single shell and the area where the bracket would have been on the shell was given different material properties and/or a different thickness to the rest of the shell. Therefore the multiple point connection was removed, but the stiffness of the bracket and geometry was retained. It was found that the connection was not the source of the error and the load deflection path stayed exactly the same.

4.4.6 Loading

An investigation was next undertaken to see if the manner in which the load is applied can make a difference. A shell edge load and a body load applied to a section of height equal to the thickness were applied to the shell. It was found that the change in the pattern of load application made no difference to the result.

4.4.7 The symmetry boundary conditions

The above explorations used only one eighth of the shell, exploiting the symmetry of the structure to save computing time, but the symmetry boundary through the middle of the bracket also lies in the zone of very high plasticity in a materially nonlinear analysis. Therefore the symmetry condition was questioned as a possible cause of the problem. The whole shell was modelled with four brackets around the circumference. The load deflection path stayed exactly the same for the 45º and the 360 º models (Figure 4.29). Therefore it can be said that the symmetry condition did not introduce an error into the numerical calculation.

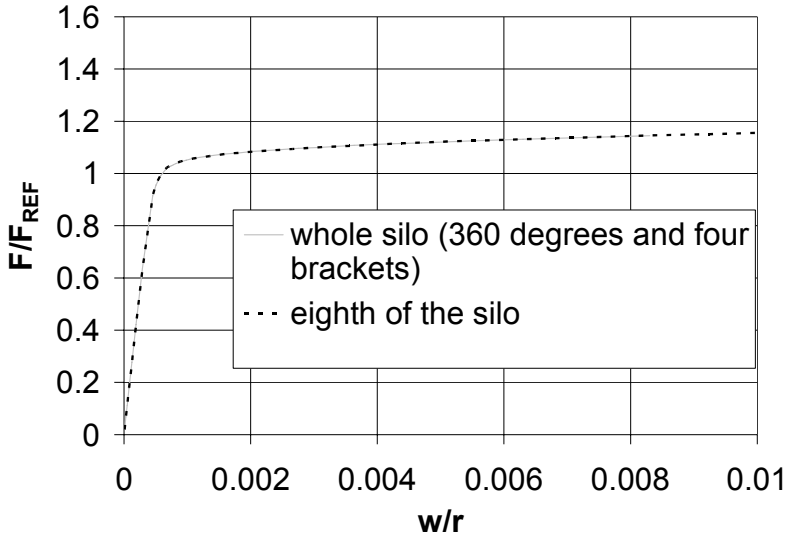

Figure 4.29: Load deflection curves for a whole shell (360°) and one eighth of a shell (45°)

4.4.8 The singularities at the corners of the bracket

The corners of the bracket represent points of high stress concentration and possible singularity. These were next examined as the cause of the errors seen above. To explore the numerical treatment of these corner areas, the elements in the shell immediately adjacent to the corners were deleted from the finite element mesh. When these elements (Figure 4.30) were removed from the analysis, the extrapolated collapse load was reduced by about 1%, but the behaviour remained the same (Figure 30).

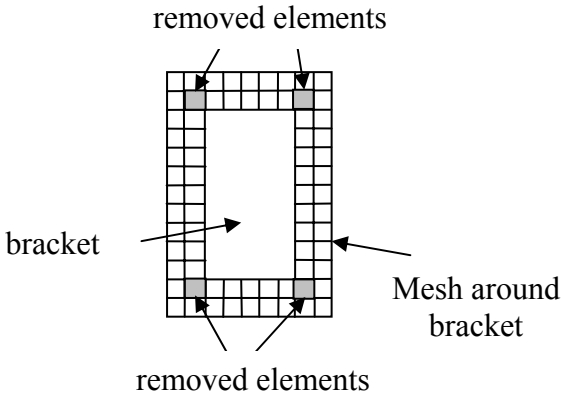

Figure 4.30: Location of the removed elements

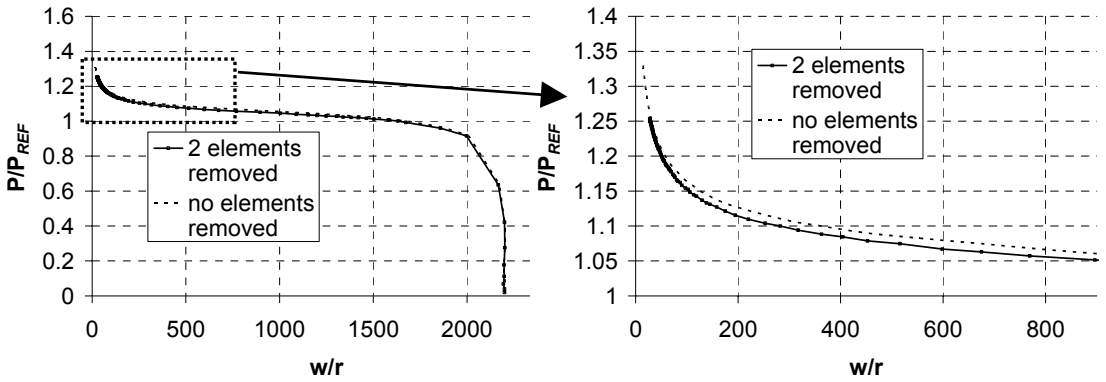

Figure 4.31: Modified Southwell plot, showing the effect of the singularity

4.4.9 The suitability of the element

4.4.9.1 Shear locking of the general purpose element S4R

Shear locking can be a problem for shell elements, resulting in very slow convergence and very stiff bending behaviour. Extensive studies have been performed to validate the shell elements offered in ABAQUS. The ABAQUS

manual (HKS, 2003) recommends elements with reduced integration, like the general purpose element S4R and the thick shell element S8R, since they are considered to be free of shear locking. The S4R and S4 element were extensively verified using different benchmarks in Bauchau *et al.* (2006).

Therefore no separate investigation of this question was undertaken here.

4.4.9.2 Finite membrane strain

The general purpose shell element S4R includes the facility to use the assumption of finite membrane strain theory, in place of small strains. When finite strain is taken into account, the thickness of the shell element increases when the element is in compression and decreases when it is in tension. In the case of the bracket supported shell, the thickness of the cylinder would increase above the bracket and decrease below the bracket, which could lead to a slightly different numerical solution from that identified in the above reference load. It was thought very unlikely that the finite strain was incorporated in the formulation of the geometrically linear analysis since the membrane stress resultants correspond very well with the theoretical model proposed and the stress resultants are calculated by integrating the corresponding stresses over the thickness and hence would have taken any change in thickness already into account.

Since the ABAQUS manual did not provide a satisfying answer to the question of inclusion of finite strain when the geometric nonlinearity is not considered, a bar in tension and compression was investigated similar to the bar tested for the Poisson's ratio. The bar was simply supported at one end and loaded at the other end. To ensure that only the effects of the change of thickness would be considered, the bar was also constraint so no change in the width could occur.

For this problem the only possible deformation is the lengthening/shortening of the bar and a change in thickness. If a change in thickness occurs and the width of the bar stays the same as the initial width throughout the analysis, the load should drop when a tensile load is applied and due to the reduced thickness of the bar and increase when a compressive load is applied.

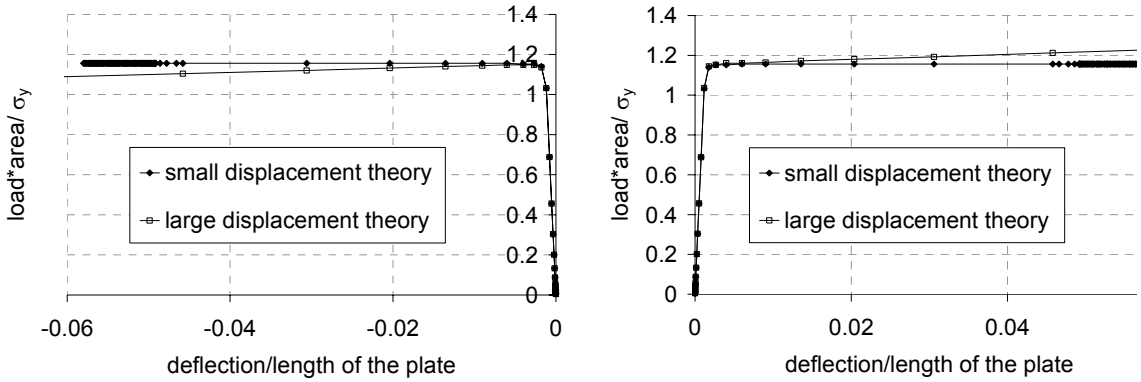

a) plate in tension b) plate in compression

Figure 4.32: Investigation into the change of thickness of the shell element

The results of this little study are shown in Figure 4.32. When small displacement theory was used, the load stayed constant in the fully plastic range, indicating that no change of thickness occurred, but when large displacement theory was used under tension the load dropped (Figure 4.32a) due to the reduced thickness of the element and under compression increased due to the larger thickness of the element.

Hence the finite strain facility of the general purpose element S4R is clearly not included in the numerical analysis when small displacement theory is used. This effect clearly cannot account for the discrepancy in the modelling of the bracket behaviour.

4.4.9.3 Investigation into a new mesh using a mixture of elements

Even though the suitability of the element S4R had been tested extensively and this element passed all of tests performed, it seemed appropriate to consider other elements again.

The 8-node thin shell element S8R5 failed to converge to a solution in some of the materially nonlinear analyses, so had been rejected earlier. And even after very extensive attempts, it was not possible to achieve convergence.

The 8-node thick shell element S8R was initially regarded as unsuitable for the analysis because, when using this element, ABAQUS displayed stress states that were far above the von Mises criterion with the input yield stress.

A further investigation into the thick shell element S8R showed that it does indeed compute the stresses that satisfy the yield criterion at the integration points,

but when it extrapolates the results to the nodes in regions with very high plasticity and high stress gradients, significant errors develop. It also produced the correct result for a materially nonlinear analysis, but still failed to converge for a geometrically nonlinear elastic analysis (GNA).

Therefore the next investigation was performed into the use of a mixture of elements in one mesh with the aim of achieving a mesh that would be suitable for all the analyses performed in thesis.

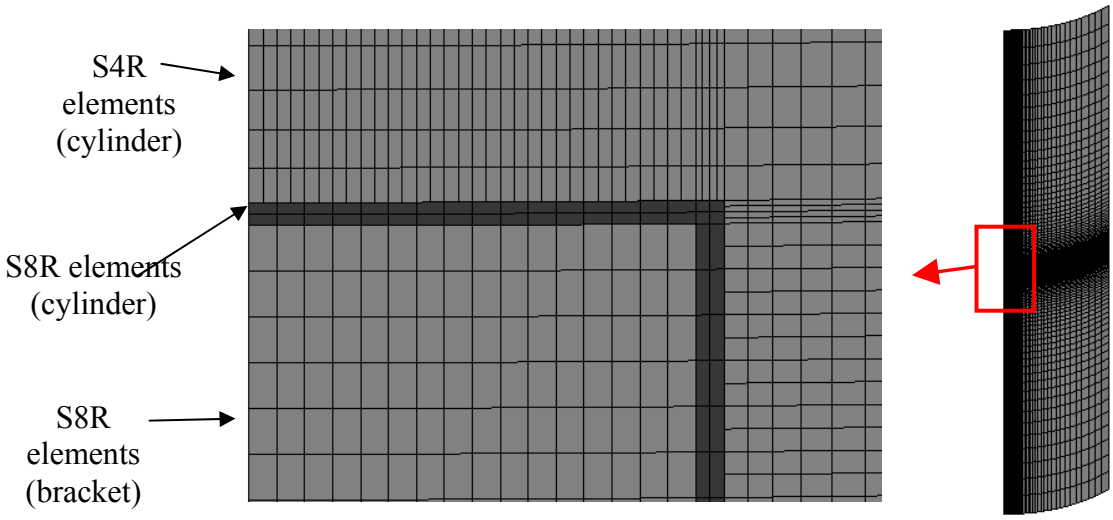

Figure 4.33: Finite element mesh using S8R (dark grey) and S4R (light grey)

Since the 4-node element S4R seemed to have problems mainly under conditions of high plastic strains but performed well in other analyses, and the 8-node thick shell element S8R performed well for high plasticity (apart from the extrapolation problem at nodes), a mesh with a mixture of these two elements was chosen. Thick shell elements were used to model the area of the cylinder directly underneath the bracket, for the bracket itself and most importantly a small ring of thick elements S8R (Figure 2.2, dark grey cylinder elements) was applied around the bracket, where the highest plasticity occurs. The remaining mesh was modelled with the general purpose element S4R (Figure 2.2, light grey cylinder elements). The connection between the different elements was made using a multiple point constraint (MPC). A multiple point constraint connects a master surface to a slave surface, making all degrees of freedom from the slave nodes the same as those of the master nodes,

melding two nodes into one. Every 8 node, thick shell element (S8R) is now connected to two 4 node, general purpose element (S4R) (Figure 2.2). The size of the element on the top and the bottom of the silo as well as the width of the element on the side of the bracket is kept constant to half a wall thickness, which correspond for the thickest silo (r/t=200) to 0.0145λ with λ being the half bending wave length (Eq. 4.12), while the height of the elements on the side of the bracket was kept constant to one wall thickness which correspond for the thickest silo (r/t=200) to 0.0290λ.

$$\lambda = \frac{\pi}{\left[3\left(1-\nu^2\right)\right]^{1/4}}\sqrt{rt} \approx 2.44\sqrt{rt} \tag{4.12}$$

Therefore a large number of elements is needed in the mesh when both element types are used due to the connections required between the 4-noded elements and 8-noded elements.

This mesh resolved the problem of the over-prediction of the reference load and produced the same result as the mesh with the thick shell element S8R only (Figure 4.34). The progressive increase in load following attainment of the full membrane yielding load was finally eliminated, and the problem extensively described above was finally resolved (Figure 4.35).

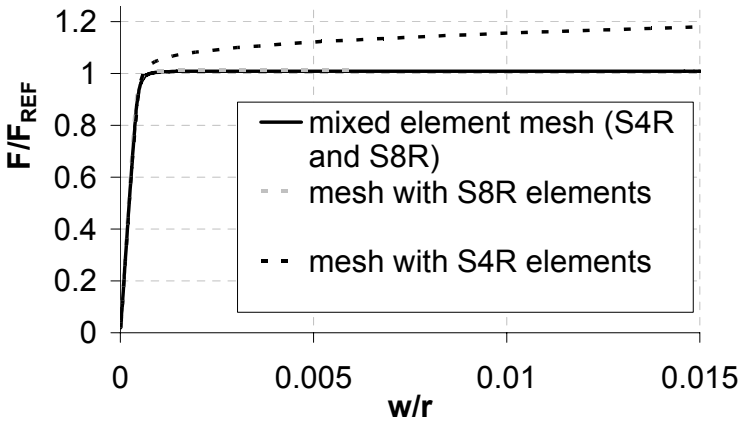

Figure 4.34: Comparison of the same mesh with same geometry but different elements

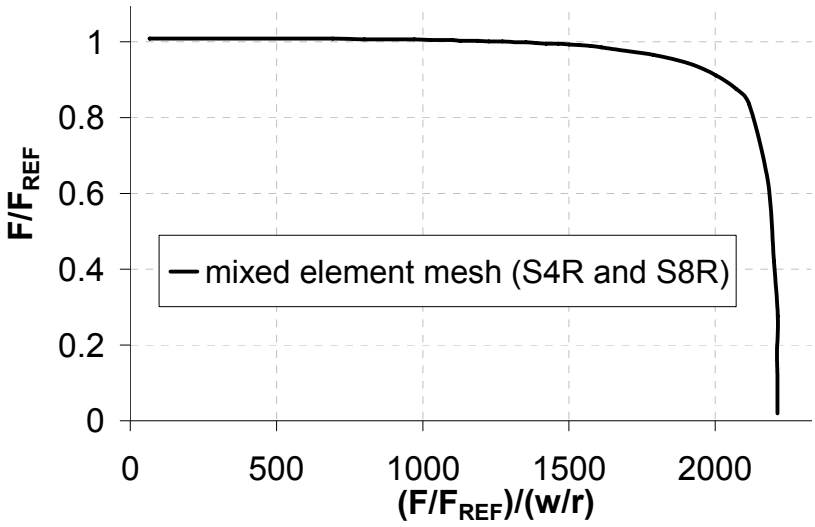

Figure 4.35: Modified Southwell plot of the example geometry using the mixed element mesh with S4R and S8R elements

This mesh was then tested extensively in other analyses and compared with the results from models for the same problem using the other elements. It was found to be suitable for all analyses: LBA, MNA, GNA and GMNA. These tests of the chosen mesh are described in the following chapters relating to the corresponding analyses.

4.5 Recalculation of published results

A similar bracket support was investigated by Gillie *et al.* (2002) and a statement was made there that no plateau could be obtained in the materially nonlinear analysis (MNA).

In the investigation of Gillie *et al.* (2002), the bracket was free to rotate about the circumferential axis, while it was constrained against circumferential rotation in this thesis, corresponding to attachment to a stiff column in place of the ideally pinned connection used by Gillie *et al.*. In both investigations, the load was applied at the bottom of the cylinder as a ring tension and a 45 degree model was used.

Here, as a verification of the outcome, one example geometry has been recalculated using a geometry used by Gillie *et al.* (2002). The cylinder of radius r=10m and height H=40m, with thickness 10mm. The height of the bracket was h=300mm with a half width d=450mm and supported at an eccentricity of e=200mm. The material was treated as linear elastic-perfectly plastic with E=200000 MPa, ν=0.3 and σ_y=250 MPa.

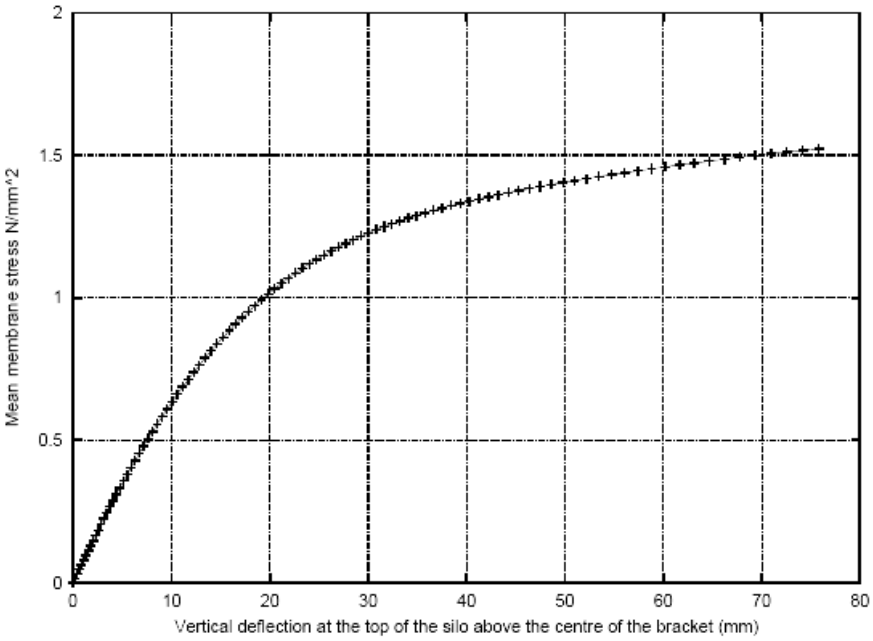

Figure 4.36: Load deflection path calculated by Gillie *et al.* (2002) for the example geometry (taken from Gillie *et al.*, 2002): note no plateau is reached

The bracket was stated to be rigid and no mention was made in Gillie *et al.* (2002) of which element was used in the calculation, but it is thought to have been S4R5 (Gillie, 2002).

Since the precise element was not known the S4R5 and S4R elements were used in an attempt to recalculate the problem. Only the results of the S4R5 element are shown here since the S4R element produced very similar results. The bracket was assumed to have several different thicknesses in different analyses since the thickness was not stated in Gillie *et al.* (2002).

The result obtained by Gillie *et al.* (2002) is shown in Figure 4.36. When this result is compared with the re-calculation of the problem (Figure 4.37), the importance of the thickness (stiffness) of the bracket is clearly visible. The horizontal scale of Figure 4.37 has been chosen to match the original (Figure 4.36)

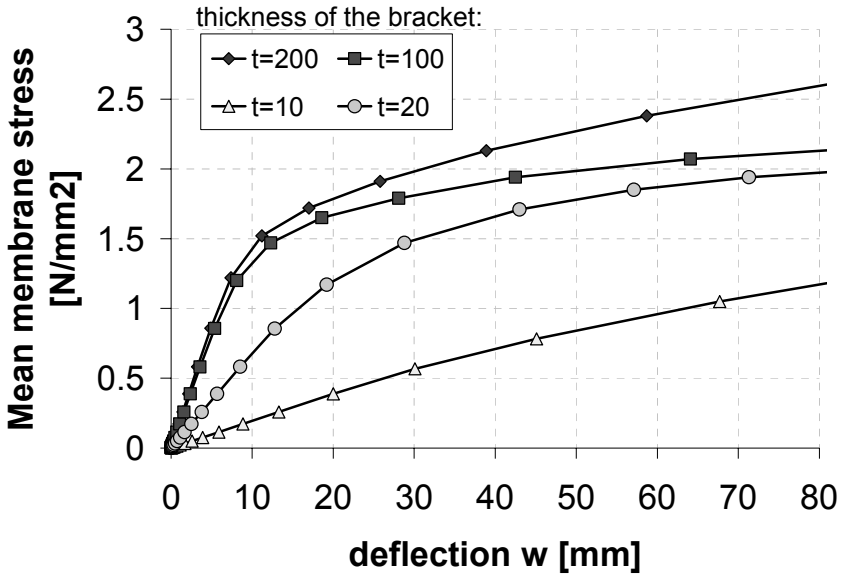

Figure 4.37: Load deflection path of the example geometry with different thicknesses for the bracket

It should be noted that the original results could not been reproduced exactly. This might be due to a different modelling assumption or possibly to the finite element mesh. But without further information about their numerical model, this cannot be verified.

When the bracket was made rigid (Figure 4.38) (as assumed in Gillie *et al.*, 2002) and the S4R/S4R5 elements were used, no plateau was obtained. When on the other hand the mesh finally achieved in Section 4.4.9.3 was used consisting of the thick shell element S8R and the general purpose element S4R in combination with the rigid bracket, a plateau does develop (Figure 4.38). Moreover a plateau can be observed with this mesh at the plastic collapse load, which is very close the reference load defined in this chapter.

A rigid bracket was achieved by increasing the thickness of the bracket to a value of t=10m. This value is clearly purely a numerical device and unreal, but it does demonstrate the effect of a truly rigid bracket.

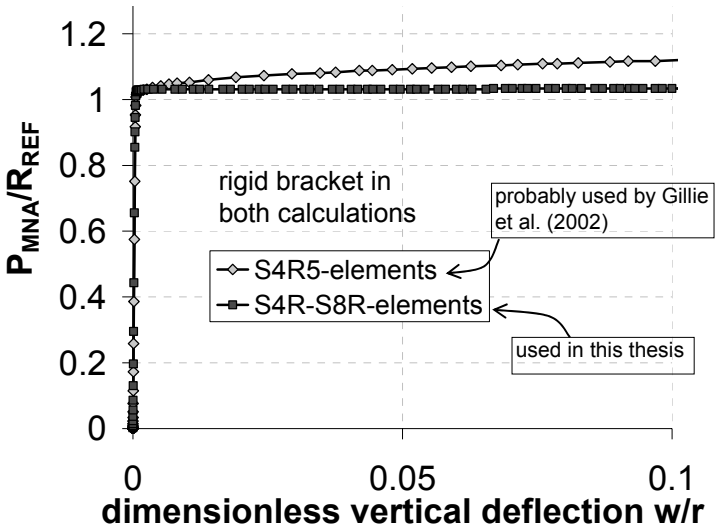

Figure 4.38: Load deflection path of the example geometry with a rigid bracket

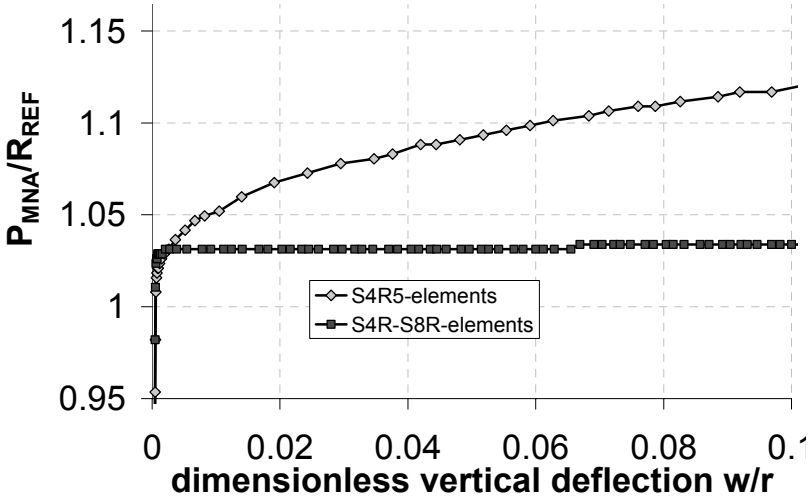

Figure 4.39: Close up view of Figure 4.38

The consequences of the poor choice of element in Gillie *et al.*, 2002 is unfortunately not confined to the materially nonlinear analysis alone. It greatly effects the geometrically and materially nonlinear analysis (GMNA). One might have expected a yield line failure mechanism, involving both stretching and bending, in this problem, but is has been shown through this example calculation that the plastic collapse is influenced by membrane yielding only for a rigid bracket.

It is clear that the results for a similar problem to that of this thesis published by Gillie *et al.*, 2002 must be treated with considerable caution. The results of the present study have a much more secure and thoroughly explored basis.

4.6 Observation using the S4R-S8R-mesh

After the above extended exploration to find an appropriate model within ABAQUS to be sure that the outcome was really secure, this mesh could now be used to explore the plastic collapse strengths of a range of bracket and shell configurations. The final mesh contained the mixture of the general purpose elements S4R and the thick shell elements S8R found above, and was used for all the subsequent studies. This mesh was used due to the inability of the S4R element to perform well in regions of highly localized plastic strains

As was shown in Section 4.4.9.3, the collapse load now corresponds well with the reference load (Equation 4.13 = Equation 4.10, repeated here for clarity), using an ideal elastic-plastic material model, the von Mises yield criterion and small displacement theory.

$$F_{REF,MNA} = \sigma_y \cdot t \cdot \left(2 \cdot 2d \cdot 2/\sqrt{3} + 2 \cdot h \cdot 1/\sqrt{3}\right) \tag{4.13}$$

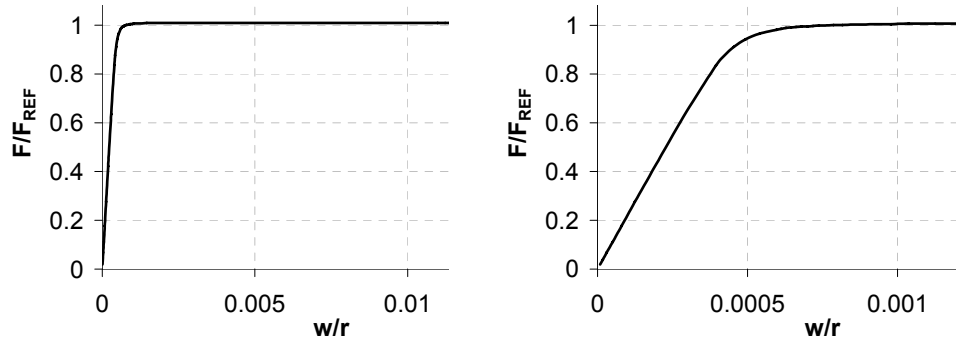

a) b)

Figure 4.40: Load deflection curve (MNA) of a shell with r/t=600, h/r=0.12, h/d=3

The load-deflection curve now finally displays the expected classical shape (Figure 4.40), with significant plastic deformations developing at loads well below the collapse load, but turning into a horizontal plateau at a well defined collapse load.

The modified Southwell plot does not need to be used any more, since the load deflection curve now finally displays a stable plateau.

To illustrate the complete behaviour of the bracket in a small displacement theory elastic perfectly plastic analysis (MNA), the stresses progressively developing in the structure are shown here, first under elastic conditions, and then at the plastic collapse load. The membrane stress resultants on a horizontal line through the shell at different heights are shown in Figure 4.41 to Figure 4.43.

First, to illustrate the elastic patterns of stress resultants, the outcome was taken from a load step in the elastic range and compares therefore to a linear elastic analysis (LA). The vertical or meridional stress resultants are shown first (Figure 38). At the bottom, the load was applied and naturally there is the expected uniform meridional axial tension. Half way between the base and the bracket, elevated tensile stresses develop towards the bracket meridian, with a corresponding decrease away from the bracket meridian. Just below the bracket, high tensile stresses focus into the bracket, with a distribution similar to that of a rigid footing on an elastic halfspace (Timoshenko and Goodier, 1970). A strong peak can be seen at the bracket corner, but tensile stresses also continue in the shell away from the bracket meridian, ensuring that some of the load by-passes the bracket and induces compression above it.

On the side of the bracket, some of the load is transferred in shear (Figure 4.43) as can be seen in the peak in membrane shear at mid-height of the bracket. Above the bracket, load is transferred by compression into the top of the bracket (Figure 4.41), with a similar high peak associated with the bracket corner, as was seen just below the bracket. It is clear that the corners of the bracket represent points of strong stress concentration, and that local plasticity will affect the behaviour here quite strongly. These are also points at which high shell bending stresses develop.

The circumferential membrane stresses are shown in Figure 4.42, where it can be seen that high circumferential membrane stresses are developed near the top and bottom of the bracket through Poisson effects which arise due to the restraint of displacements by the stiff bracket. Thus this is another case where high stiffness leads to unexpected stresses and here they affect the first yield condition strongly (tensile where the axial stress is compressive, and vice versa).

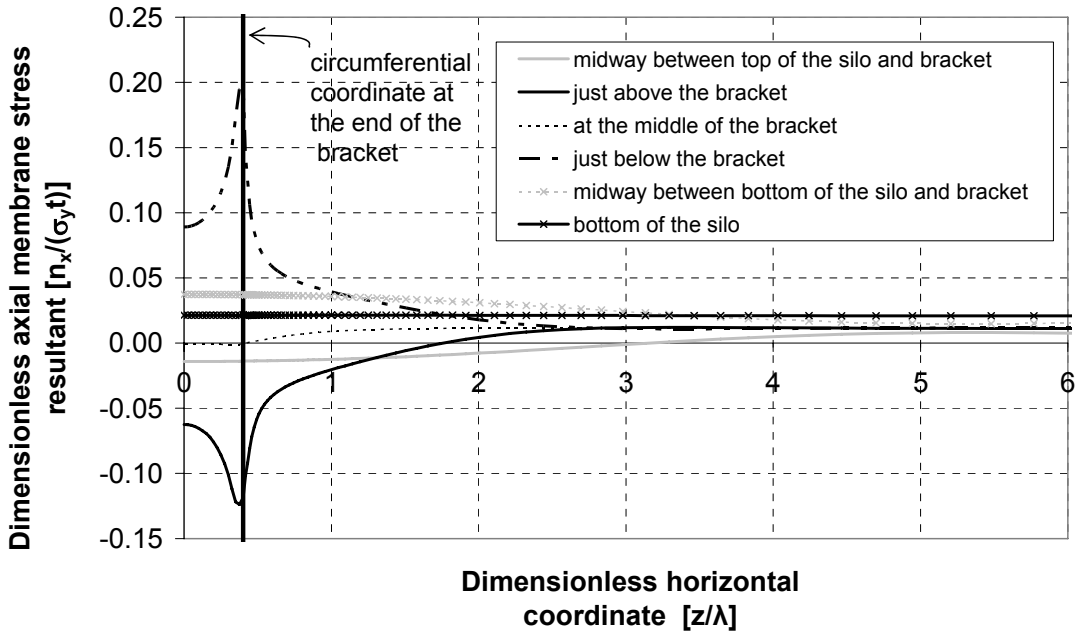

Figure 4.41: Axial membrane stress resultant in the elastic range

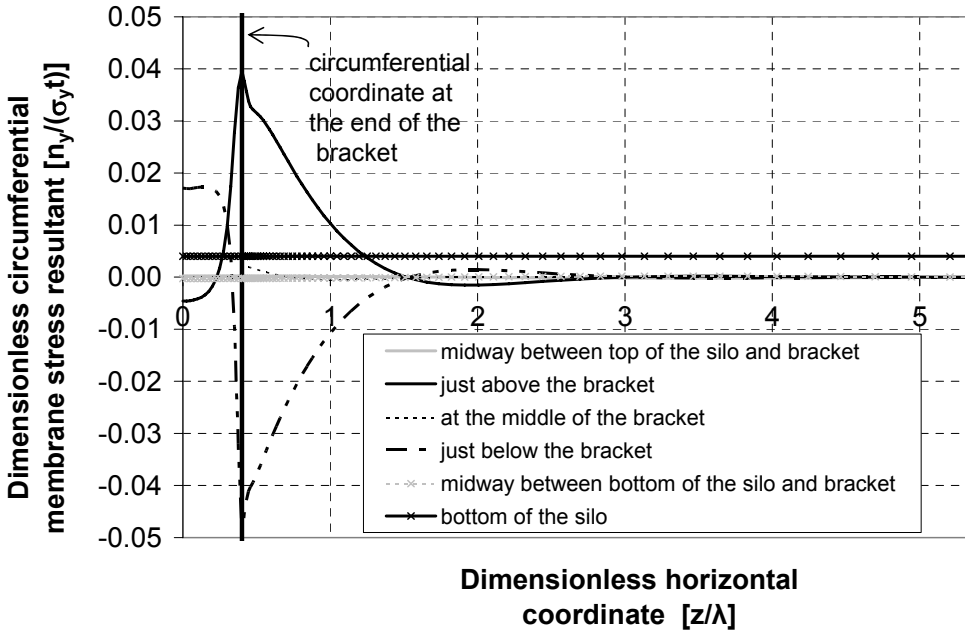

Figure 4.42: Circumferential membrane stress resultant in the elastic range

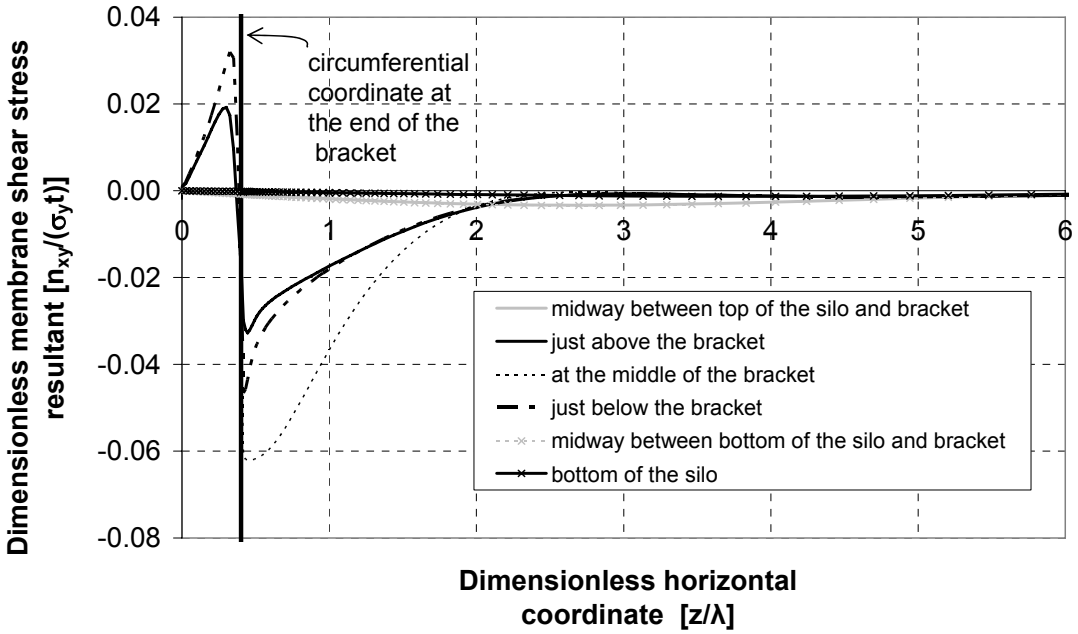

Figure 4.43: Shear stress resultant in the elastic range

In the plastic range, the different membrane stress resultants at different heights in the shell are shown in Figure 4.44, Figure 4.45 and Figure 4.46 (repeated from Chapter 2 for clarity). The axial membrane stress resultant reaches $\pm 2 \cdot \sigma_y / \sqrt{3} \approx \pm 1.1547 \cdot \sigma_y$ above and below the bracket, which are consistent with von Mises yield criterion (Figure 4.15), and which correspond to the von Mises criterion (Figure 4.15). Further away from the bracket this stress resultant decreases to the value of the overall load divided by the circumference of the shell. The circumferential membrane stress resultant reaches the value of $\pm \sigma_y / \sqrt{3} \approx \pm 0.5774 \cdot \sigma_y$ above and below the bracket, which are also consistent with von Mises yield criterion (Figure 4.15) and a plastic strain field in which the normal flow rule is satisfied by strains in only the axial direction. Further away from the bracket this stress resultant decreases to zero.

The stresses above and below the bracket are symmetrical when the area around the bracket reaches a fully plastic state (Figure 4.44 and Figure 4.45), where the axial tension below the bracket naturally dominates.

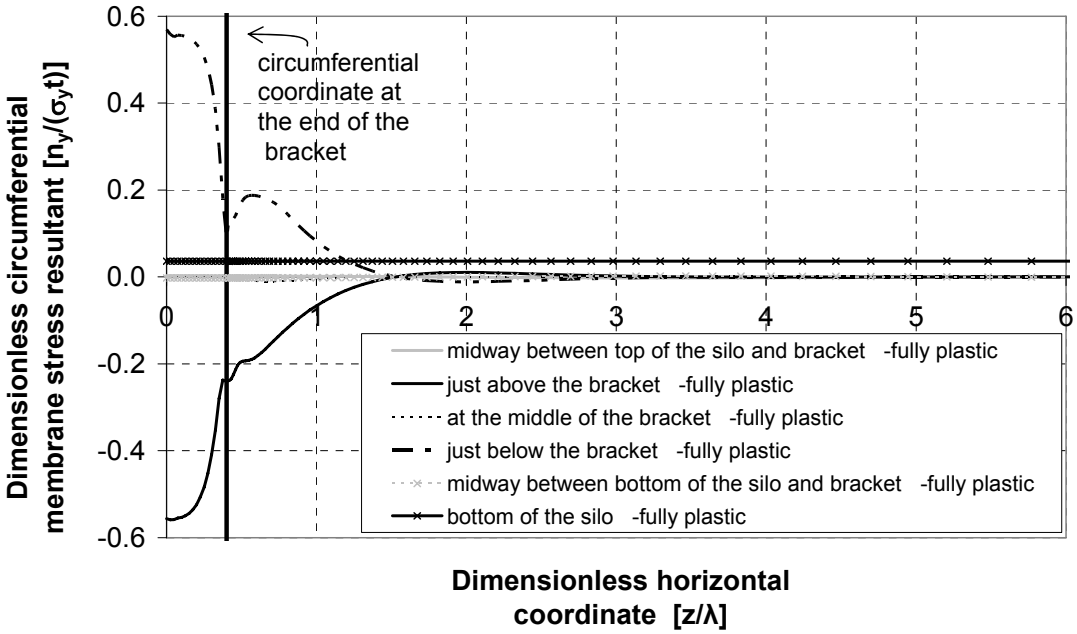

Figure 4.44: Dimensionless circumferential membrane stress resultant from a materially nonlinear analysis in the fully plastic range

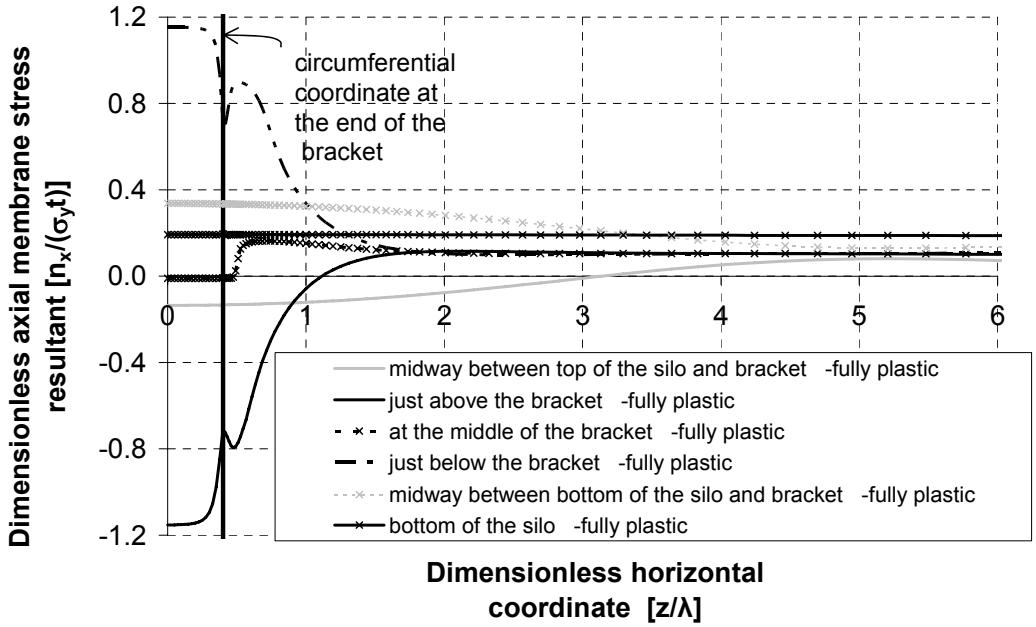

Figure 4.45: Dimensionless axial membrane stress resultant from a materially nonlinear analysis in the fully plastic range in the fully plastic range

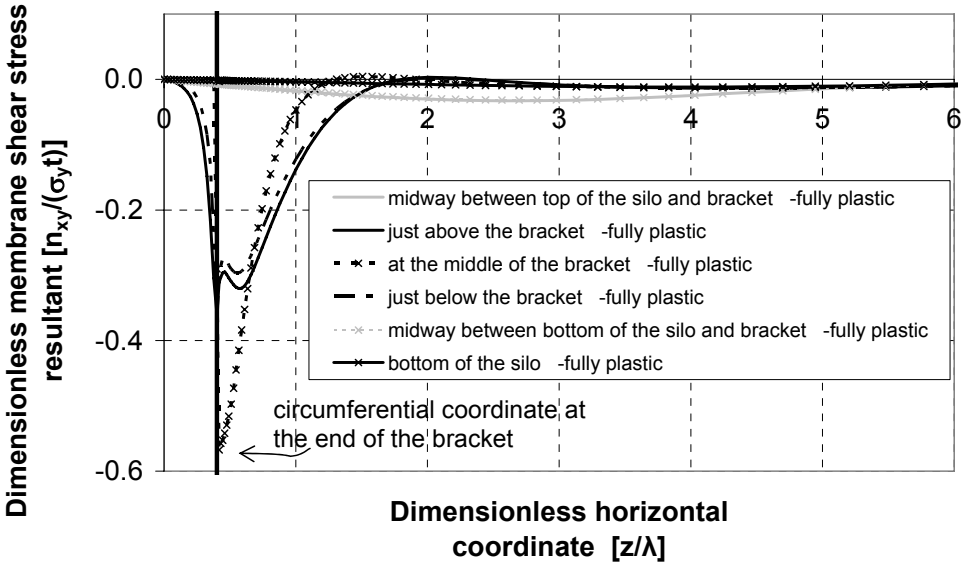

Figure 4.46: Dimensionless membrane shear stress resultant from a materially nonlinear analysis in the fully plastic range

4.7 Numerical plastic collapse values and the simple reference load

In all the calculations described above, it was clear that the plastic collapse load that was being determined should really be close to the reference load defined by Equation 4.10 and illustrated in Figure 4.15. A study was conducted to verify that this was the case. To ensure that the conclusion was secure, two extreme radius to thickness ratios were selected, being the thickest and thinnest shells explored here (r/t=200 and r/t=1000). The heights of the brackets were varied between $1 < h/\sqrt{rt} < 7$, and two extreme widths were used ($d/\sqrt{rt} = 0.25$ and $d/\sqrt{rt} = 1.25$). By using these extreme values for the radius to thickness ratio and the bracket width, together with a large range of bracket heights, the outcome could be confidently applied to all geometries of both cylinder and bracket.

The results are shown in Figure 4.47. The ratio of the numerically evaluated plastic collapse load to the simple reference load (Eq. 4.10) is plotted against bracket height for a large range of geometries. It is clear that the simple reference load is a robust measure of the true plastic collapse load for this bracket-supported shell problem.

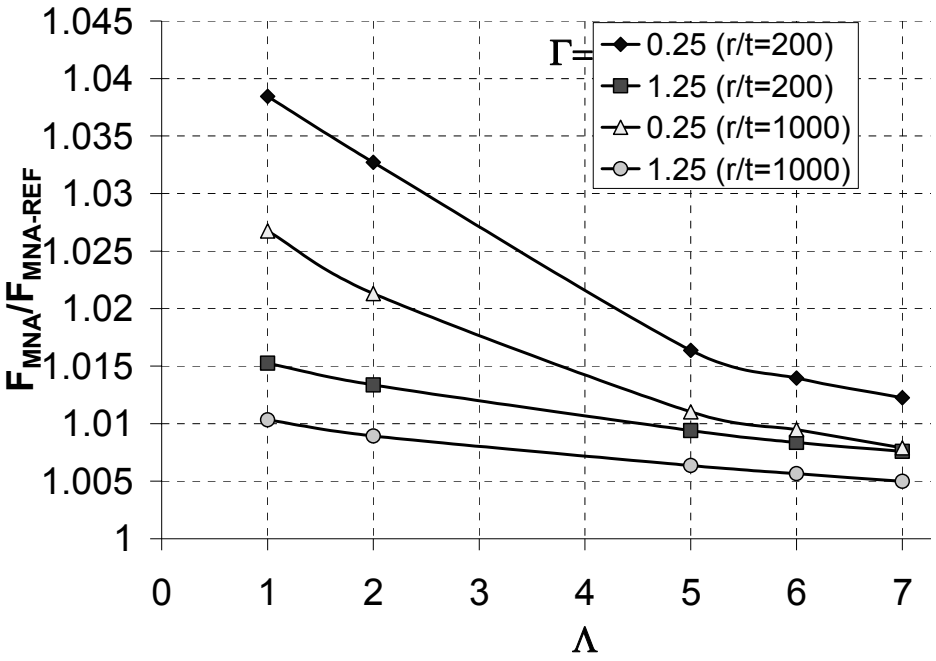

Figure 4.47: Difference between the numerically calculated plastic collapse load and the reference load (Eq. 4.10)

4.8 Numerical plastic collapse and estimates of the plastic collapse using a linear elastic analysis (LA)

The extensive difficulties described above in achieving a reliable plastic analysis of this problem illustrates one of the major challenges set by the framework of shell behaviour used in the Eurocode for shell structures (EN 1993-1-6, 2007). The plastic collapse load is one of the key reference loads to be found for the shell. It is not always easy for the analyst to use the MNA analysis, so various propositions have been put forward for ways in which the plastic collapse load may be conservatively found using only a linear elastic analysis (Rotter, 2005). The Eurocode adopts only one of these, in an attempt to be conservative for all cases. However, this leads to a very conservative treatment of many problems, so further investigations are needed to see whether a less conservative criterion can be found that remains uniformly safe for a wide range of problems.

As stated above, several different methods are available to estimate the plastic collapse load using a linear elastic analysis. The aim of this little study is to show how conservative these estimates are for the bracket supported shell.

Three different criteria were considered: first yield at the surface of the shell,

first attainment of a membrane stress resultant set that satisfy the von Mises yield criterion and the Ilyushin yield criterion. The Ilyushin criterion (Eqs 14-19) is given in the Eurocode (EN1993-1-6, 2006) for the estimation of the plastic collapse load, since the drafting committee thought it to be universally conservative for this purpose.

$$\sigma_{eq,ED} = \sqrt{\sigma_{x,d}^2 + \sigma_{\theta,d}^2 - \sigma_{x,d}\sigma_{\theta,d} + 3\left(\tau_{x\theta,d}^2 + \tau_{xn,d}^2 + \tau_{\theta n,d}^2\right)} \tag{4.14}$$

$$\sigma_{\theta,d} = \frac{n_\theta}{t} \pm \frac{m_\theta}{t^2/4} \tag{4.15}$$

$$\sigma_{x,d} = \frac{n_x}{t} \pm \frac{m_x}{t^2/4} \tag{4.16}$$

$$\tau_{x\theta,d} = \frac{n_{x\theta}}{t} \pm \frac{m_{x\theta}}{t^2/4} \tag{4.17}$$

$$\tau_{\theta n,d} = \frac{q_{\theta n}}{t} \tag{4.18}$$

$$\tau_{xn,d} = \frac{q_{xn}}{t} \tag{4.19}$$

A linear elastic analysis (LA) was performed at a fixed load level. The stresses at the outer surfaces and at the middle surface of all elements were calculated to find the locations where the highest stresses could be found. These highest stresses were extracted and used to deduce the load levels at which first yield and first membrane yield would occur using the von Mises yield criterion. To use the Ilyushin yield criterion (Equations 14-19), the membrane stress and bending stress resultants in the elements with the highest coupled resultants were extracted. The Ilyushin yield criterion was then used to deduce the load at which the equivalent stress would be equal the yield stress.

Due the high stress concentration at the corner of the bracket, these elastic estimates of the collapse load (like the first yield criterion and the Ilyushin criterion) all tend to greatly under-predict the collapse load, since these criteria do not permit any re-distribution of stresses. But it was still surprising to discover by how much the collapse load was under-predicted.

To present a general overview of this effect a selection of cylinder and bracket geometries is presented. Two different radius to thickness ratios were selected, the

thickest shell investigated in this thesis (r/t=200) and the thinnest shell (r/t=1000). The height of the brackets in this example varied between $1 < h/\sqrt{rt} < 7$, while only the narrowest ($d/\sqrt{rt} = 0.25$) and the widest ($d/\sqrt{rt} = 1.25$) brackets were investigated.

Both the thick and thin shells display an almost identical ratio between the elastically-based estimate of the plastic collapse load and the numerical MNA evaluation of the true plastic collapse load (Figure 4.48 to Figure 4.51). The under-prediction becomes worse as a wider or taller bracket is used (Figure 4.48 to Figure 4.51). The closest estimate of the plastic collapse load found from an elastic analysis was therefore found to be that for the smallest bracket.

But even the best estimation still predicts failure at 47.4% of the true plastic collapse load. In the geometry showing the worst estimate, the failure was as estimated to be as low as 9.58% of the true failure load!

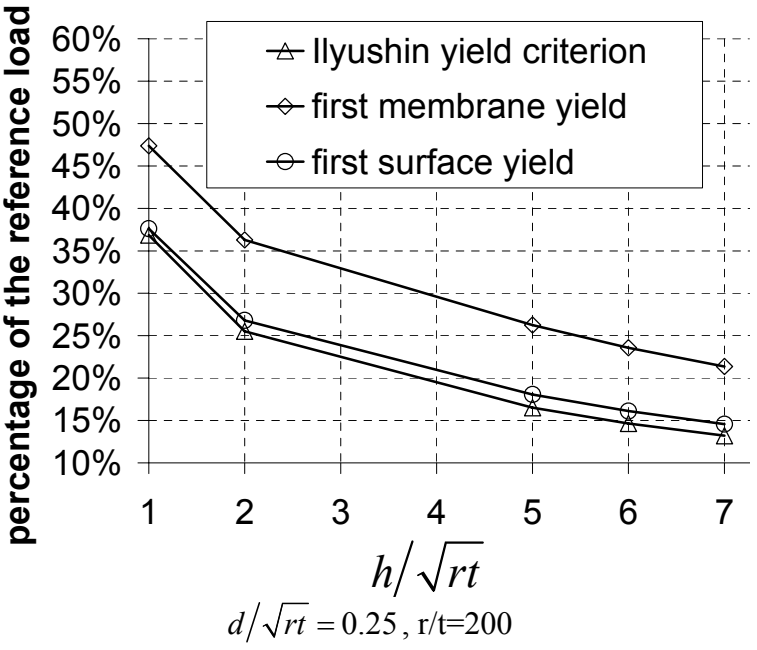

Figure 4.48: Percentage of the collapse load for different yield estimates

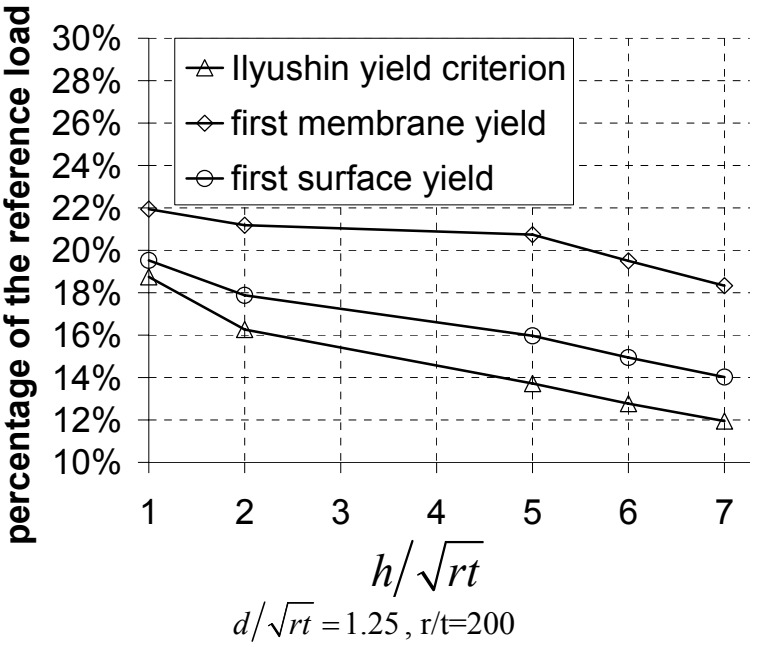

$d/\sqrt{rt} = 1.25$, r/t=200

Figure 4.49: Percentage of the collapse load for different yield estimates

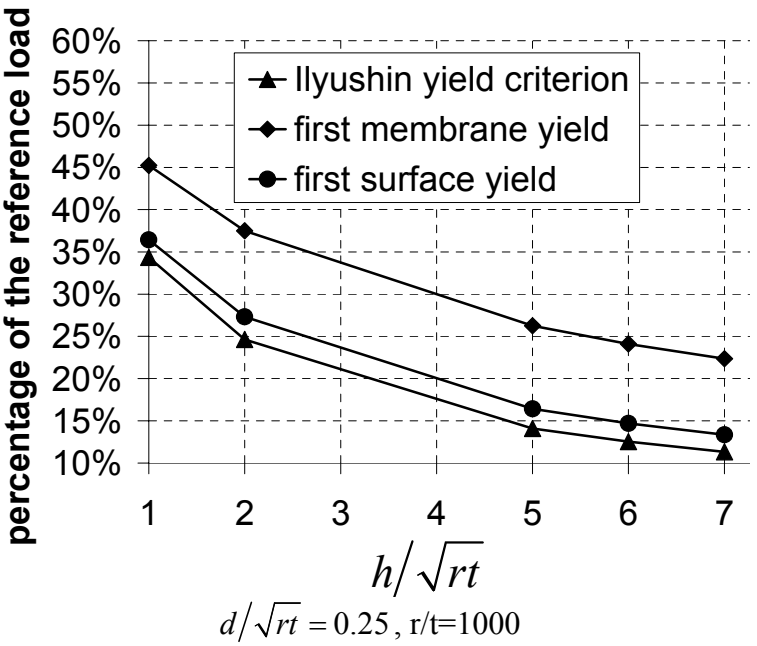

$d/\sqrt{rt} = 0.25$, r/t=1000

Figure 4.50: Percentage of the collapse load for different yield estimates

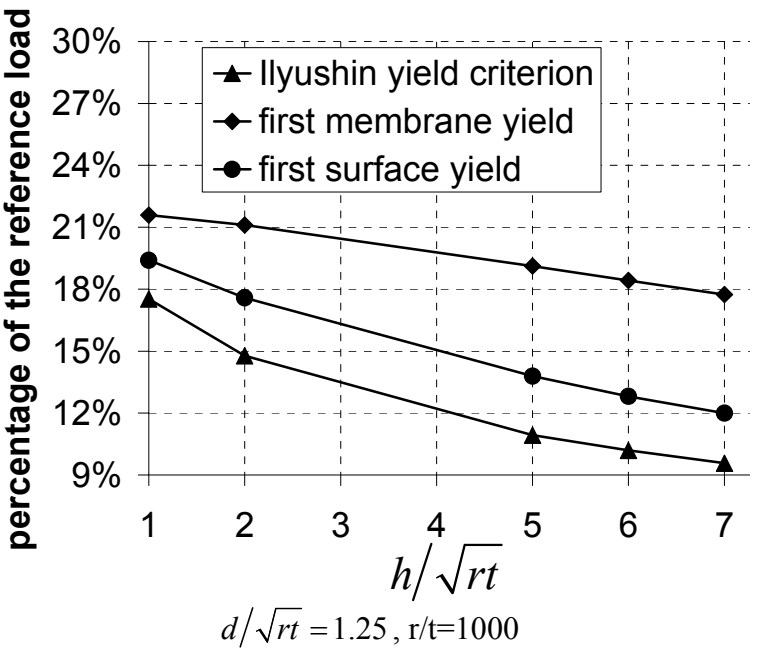

Figure 4.51: Percentage of the collapse load for different yield estimates

As might have been expected, the Ilyushin criterion and the first surface yield predict a similar failure load, since both take into account bending of the shell, which is often severe at points of discontinuity or stress concentration. The first membrane yield criterion estimates a higher plastic collapse load, but this is often still very far below the true plastic collapse load. The cause of these under-predictions is the high stress concentration at the corners of the bracket.

Whilst it was well known that these estimates of the plastic collapse load are conservative, it is slightly unfortunate that the true plastic collapse load can be under-predicted by tenfold. A simple method of finding the true plastic collapse load is therefore essential for an economic design of a shell that has any high stress concentrations or singularities. Hence the materially nonlinear analysis is really an essential part of the design of a shell structure, especially under conditions where high local stresses may develop, causing a severe under-predictions of the plastic collapse as found here for the bracket supported shell.

4.9 Conclusion

The element chosen initially (S4R) passed all of the benchmark tests conducted and therefore it was initially concluded that the S4R element would be suitable for the materially nonlinear analysis.

But it has been shown that this choice of element is the reason why the collapse load is not correctly calculated for the bracket supported shell. The other two elements (S8R, S8R5) that were tested both had difficulties in converging in many analyses.

An extensive investigation was undertaken to try to find the cause of load levels considerably in excess of the plastic collapse load developing in these shells. This investigation explored a large number of different questions, some of which might have been thought of as unlikely causes of the problem. Nevertheless this exploration demonstrates the manner in which trial problems may be devised to explore detailed questions to identify the real cause of errors in finite element analyses.

The final mesh sought here was one that could be used in all of the different analysis types (LBA, MNA, GNA, GMNA) so that an accurate comparison could be made between the analyses. Since the S8R element was known to capture yielding well it was used in a small zone around the bracket, whilst the remaining mesh was composed of S4R elements. This mesh captures the failure load of all analyses well. In the materially nonlinear analysis (MNA) the result was compared to a mesh with just S8R elements and the results were identical. For the Linear Bifurcation Analysis and Geometrically Nonlinear Analysis the mesh was compared to one with S8R5 elements with a good result. The disadvantage of this mesh is that, due to the small band of S8R elements around the bracket, there are some elements with very large height to width ratios, which are not desirable. This disadvantage was considered to be minor, since these elements are far away from the bracket.

The reason why the 4-node general purpose element S4R does not perform well in regions of highly localized plastic stresses could not be found.

A bracket support from a previous study was recalculated and it was found that also in this case the general purpose element did not produce the correct answer,

whilst the mesh with the combination of elements (S4R and S8R), in calculating the same problem, does produce a good load deflection curve with a plateau. Moreover the plastic collapse load was found to be very similar to the simple reference load identified in this chapter as the correct plastic collapse load for all bracket geometries.

Even though the materially nonlinear analysis was the most difficult to "get right", the end result was found to be very simple. The failure load can be calculated very easily by using the simple reference load (Eq. 4.10), which assumes a fully plastic membrane behaviour satisfying von Mises criterion all around the bracket.

A further study explored the use of elastic analysis to obtain a conservative estimate of the plastic collapse load. Three different criteria were used as possible ways of estimating plastic collapse. It was found that, for this problem, all three criteria led to very conservative (it may be suggested that these are unacceptably conservative) estimates of the true plastic collapse load.

5 Geometrically nonlinear analysis

5.1 Introduction

The analyses described in the previous chapters have focused on linear elastic bifurcation and plastic collapse. These two types of analysis are extreme cases of the failure load – the linear elastic bifurcation load and the plastic limit load usually provide an envelope within which the more sophisticated analyses should lie.

In this chapter the effects of geometric nonlinearity and imperfection sensitivity are explored. To explore the effect of geometric nonlinearity, the material was kept elastic (with E=200,000 N/mm^2 and ν=0.3), but large displacement theory was used. For the studies of imperfection sensitivity, different forms of geometric imperfection are investigated.

This kind of analysis, involving large displacement theory, leads to complicated equations and the behaviour is very difficult to explore analytically, so established numerical solutions were used to verify the finite element discretisation.

The definition and the challenges in identifying what is to be regarded as buckling and when this occurs will be described. In particular there is a considerable challenge in deciding what to define as failure, in conditions where neither a bifurcation nor a limit load is reached as a consequence of pre-buckling deformations.

It is commonly assumed that geometric nonlinearity does not have a very significant effect on the buckling load of most perfect shell structures in causing strength reductions below the linear bifurcation analysis, save in conditions where snap-through may be expected. Thus, nonlinear geometric effects account for a reduction in the bifurcation buckling strength of typical axially compressed perfect cylinders of the order of 15% (Yamaki, 1984), but these effects are very important in the snap-through buckling of very shallow spherical caps (Kaplan, 1974)

On the other hand, it is commonly presumed that where geometric imperfections occur in an imperfection sensitive shell structure such as a cylinder under axial compression, they will lower the buckling load significantly. It will be shown here that these common assumptions do not provide an accurate or correct picture of the failure condition for the bracket supported cylinder, and the conclusions drawn from

this study may well be relevant to many other shell structures that are subject to relatively local loading or local membrane stress concentrations.

The first part of this chapter describes geometrically nonlinear buckling without imperfections, to study the effect of the geometric nonlinearity alone. An extensive verification of the chosen element was undertaken, as it had been found in the Chapter 4 that not all elements provided by ABAQUS (HKS, 2003) are suitable for every analysis. The boundary conditions were examined carefully to ensure that the choice of an eighth of the silo with symmetry conditions is still valid. For the verification of the mesh a well established numerical solution for a cylindrical shell with a weld imperfection Type A was used (Rotter and Teng, 1989). An overview is given of the shape and the location of the buckle for different geometries and the change with geometry. The load deflection paths are described and a close look is taken into the contribution of geometric nonlinearity to the buckling load, by making a comparison with the linear bifurcation load.

In the second part of this chapter, geometric imperfections are explicitly modelled using different imperfection shapes and amplitudes for one example geometry of the target problem.

5.2 Verification of the numerical model

5.2.1 Choice of element

As the choice of element was a challenge in the materially nonlinear analysis, all suitable elements were tested first. The meshes were all constructed in exactly the same way and had the same number of elements.

The first mesh tested was formed from 8- node thin shell elements (S8R5) for the shell and 8-node thick shell elements (S8R) for the bracket.

The second mesh was constructed from 4-node general purpose elements (S4R), whilst the third mesh tested was formed only from thick shell elements (S8R). This third mesh, consisting of only thick shell elements S8R, failed to converge at any load level in the geometrically nonlinear analysis.

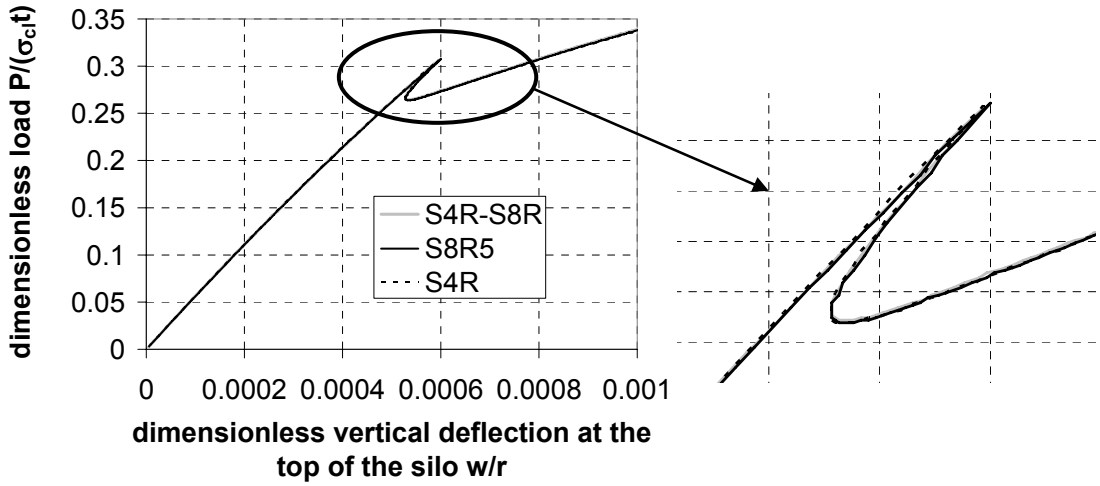

Figure 5.1: Load deflection path for different elements

The fourth and final mesh was formed from a combination of 4- node general purpose elements (S4R) and 8- node thick shell elements (S8R). This mesh was the same as the mesh used and verified for the materially nonlinear analysis (MNA).

By contrast with the materially nonlinear analysis, where the correct choice of element was vital, the choice of element does not make a significant difference to the outcome of a geometrically nonlinear analysis (Figure 5.1). Since all the meshes with different elements resulted in the same load deflection path and the same buckling load, the most suitable elements can be adopted.

The mesh with the 8-node thin shell element (S8R5) was ruled out because it required extensive computing time and the result produced by this mesh could not be compared directly with the result of the materially nonlinear analysis since this thin shell element (S8R5) had convergence difficulties in the materially nonlinear analysis.

The mesh devised using the general purpose element S4R provided a fast and accurate result for the geometrically nonlinear elastic analysis, but as described in Chapter 4, it did not produce an accurate result for the materially nonlinear analysis. Therefore the same mesh as in the materially nonlinear analysis, formed using a mixture of general purpose elements (S4R) and thick shell elements (S8R) was chosen for this investigation. This choice had the great advantage that it could also be relied on for the combined GMNA analysis, where the results of both GNA and MNA would be special cases.

5.2.2 Convergence study

The convergence study was performed with the mesh consisting of S4R and S8R elements.

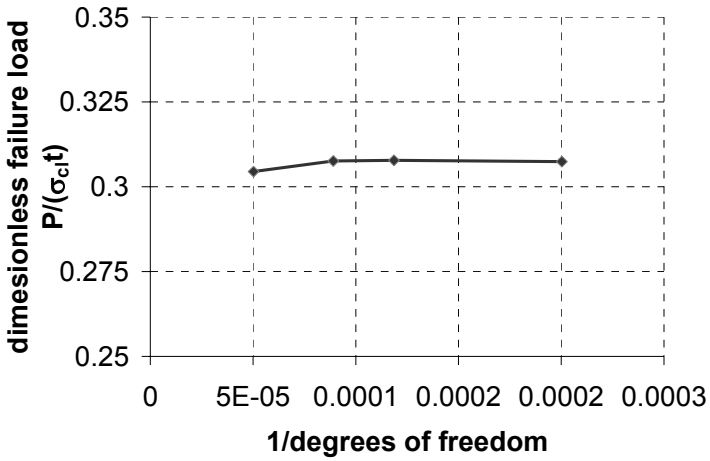

Figure 5.2: Convergence study

The difference in the predicted bifurcation load from the coarsest to the finest mesh was about 1%, and convergence was therefore very well established.

5.2.3 Refined arc length control

For geometrically nonlinear analysis, the modified Riks algorithm was used (further information can be found in Chapter 1). The automated arc–length control implemented in the Riks algorithm is usually chosen to be calculated automatically in ABAQUS (HKS, 2003). This algorithm is automatically invoked because, for most problems that are highly nonlinear, it reduces the computing time significantly while still providing accurate solutions.

But when a load deflection path changes direction very sharply, as is commonly the case for a bifurcating shell under axial compression, the automated arc length control can easily miss the peak of the curve, which is the desired buckling load (Figure 5.3). This problem can be overcome by replacing the automated (and ABAQUS recommended) arc-length control with a user defined restricted arc-length control, where the maximum load increment is restricted to a very small value. In this thesis, this restricted arc-length control has been used in combination with the restart option, as follows.

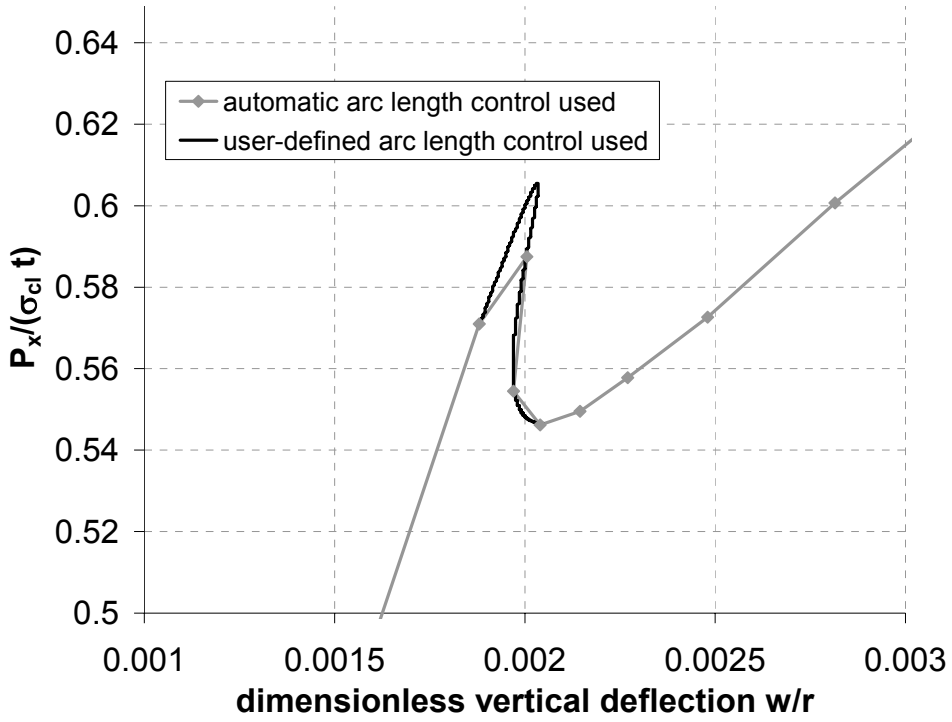

Figure 5.3: close up view of load deflection path showing poor estimate when automatic arc length control is used

The analysis is first calculated with automated arc-length control and the "complete" load displacement curve determined. The curve is examined and the approximate position of any bifurcation event determined. The analysis is then restarted at a point well before the expected buckling event using the "restart" command, and this second analysis is conducted using restricted arc-length control. Another analysis is then performed to read the results out of the restarted file and start the analysis from the point where the other analysis stopped with restricted arc-length control. This is an extremely time consuming task, because very small load increments must be chosen to capture the very sharp change in direction that often occurs in the load deflection path for bifurcating cylinders.

It has been suggested (Teng and Song, 2001) that the use of restricted arc-length control can lead to significant changes in the calculated buckling behaviour. The conclusion of this publication was that a bifurcation point might be missed when the automated arc-length control is used. This phenomenon has not been found in this investigation, but careful checks were performed to ensure that no bifurcation point was missed during the analysis.

On the contrary, throughout this study it was found that restricted arc-length

control was needed in the case of geometrically nonlinear analysis to obtain an accurate estimate of the bifurcation buckling load.

5.2.4 Boundary conditions

To ensure that the assumption of symmetry is still valid for a geometrically nonlinear analysis, the whole shell (360º and 4 bracket) was compared to an eighth of the shell (45º and half of one bracket). In both analyses almost the same buckling load was obtained (Figure 5.4).

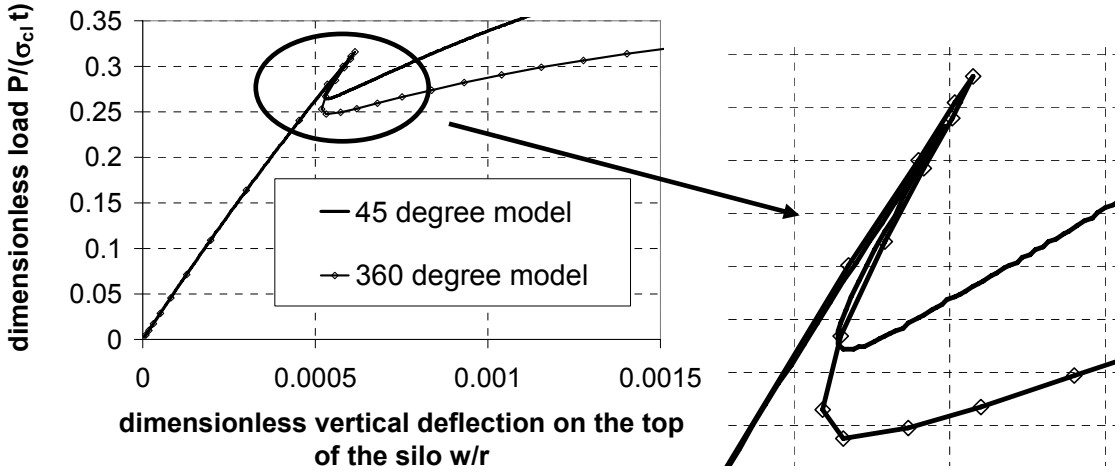

a) b) close up of a)

Figure 5.4: Comparison of the load deflection with different elements

But while the unstable post-buckling path coincides for the two models until the post-buckling minimum of the one eighth model of the shell, the whole shell model continues on the unstable post-buckling path for longer and moves then to a different stable path again. This difference was not considered to be critical in this investigation, since the divergence of these post-buckling paths is notoriously sensitive to small perturbations (Yamaki, 1984) and the target information is the bifurcation load itself.

5.2.5 Benchmark test

A geometrically nonlinear analysis is difficult to calculate analytically, so an established numerical problem was used as a benchmark test. The benchmark test chosen was a shell with weld imperfection Type A as described in Rotter and Teng (1989), which has been used by many other investigators to benchmark their

calculations (e.g. Berry, 1997; Li, 1994; Walker and Wilson, 2001).

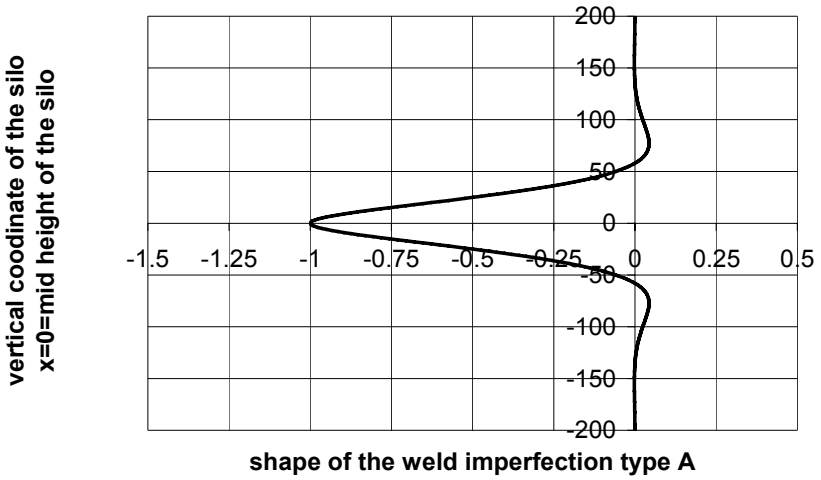

Figure 5.5: Shape of the weld imperfection

The shell with weld imperfection analyzed for the benchmark test had a thickness t=1, radius to thickness ratio of r/t=1000 and a height of H/r=3. The amplitude of the weld imperfection chosen was δ/t=1 (Figure 5.5).

The 4- node general purpose element was used in this benchmark test, since it is the element which produced an inaccurate result in the materially nonlinear analysis. Furthermore it has been shown that different elements provide exactly the same result for the bracket supported shell for the geometrically nonlinear, elastic analysis.

The numerical analyses of the shell showed the same buckling deformations as described in the work of Rotter and Teng (1989) with 18 waves around the circumference (Figure 5.6) and a meridional buckle length as described by Rotter (2004) for the imperfection amplitude δ/t=1.

The dimensionless failure load was calculated to be $P_x/(\sigma_{cl}t) = 0.318$, which compares to the result of Rotter and Teng (1989) of $P_x/(\sigma_{cl}t) = 0.306$.

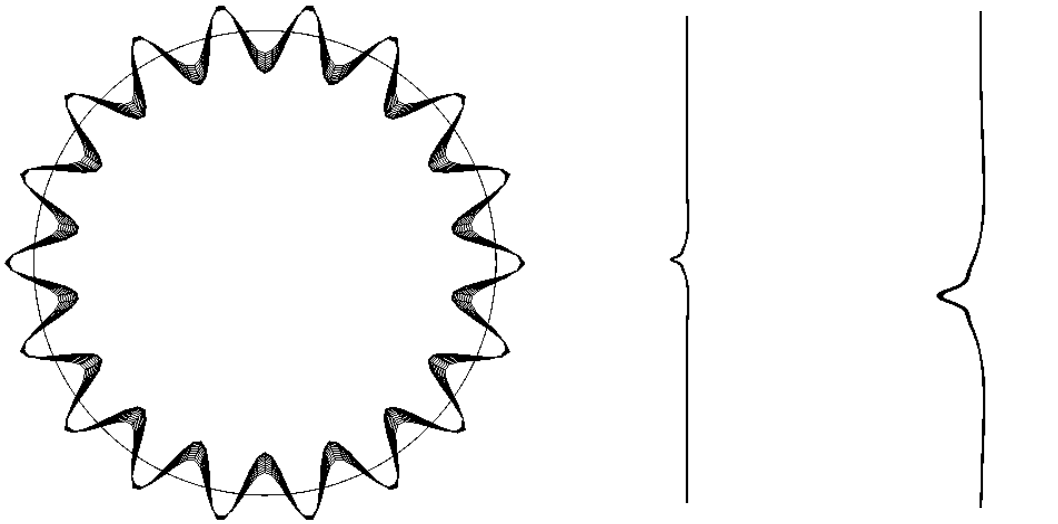

a) circumferential waves b) axial wave c) axial wave close up view

Figure 5.6: Deformed shape of the cylinder with weld-depression after buckling

The failure load calculated in this investigation using the finite element program ABAQUS is 3.8% higher than Teng and Rotter's result. This can be regarded as only a slight deviation since a different program and different elements were used to calculate the shell with weld imperfection numerically. Therefore the element has adequately performed in this benchmark test.

5.3 Geometrically nonlinear analysis without imperfections (GNA)

5.3.1 Introduction

The geometrically nonlinear analysis (GNA) is a complicated analysis, using large displacement theory and elastic material. The pre-buckling deformations and stresses play a significant role in the buckling behaviour and will, by contrast with the linear bifurcation analysis, not necessarily give a failure load (Rotter, 2002). Therefore, depending on the geometry, the buckling mode might change completely and unexpectedly.

Another challenge is the identification of the buckling mode, since it cannot be obtained as easily as in the linear bifurcation analysis, since pre-buckling deformations are present. This leads to the need to make a clear distinction between three deformation modes: the bifurcation mode, the nonlinear incremental buckling

mode and the deformed shape at buckling.

The range of geometries investigated consisted of three different radius to thickness ratios to capture the behaviour pattern for thin, medium and thick shells (r/t=1000, 600 and 400). The dimensionless height of the brackets ranged from $1 < \Lambda = h/\sqrt{rt} < 7$ and the dimensionless width from $0.25 < \Gamma = d/\sqrt{rt} < 1.25$.

5.3.2 Deformations and buckling modes

5.3.2.1 Deformed shape vs. buckling mode (linear and nonlinear)

After confirming that the mesh and element are suitable for geometrically nonlinear elastic analysis, a closer look into the behaviour of the bracket supported shell in this analysis is undertaken here. In a geometrically nonlinear analysis, the pre-buckling deformations can be of great significance to the buckling behaviour. In the case of the bracket supported shell, the most important pre-buckling deformations can be found in the compression zone above the bracket. The cylinder flattens there (Figure 5.7a) due to the compression above of the bracket. These pre-buckling deformations extend far above the bracket. The deformed shape after buckling naturally includes these pre-buckling deformations and therefore great care must be taken in describing the buckling mode.

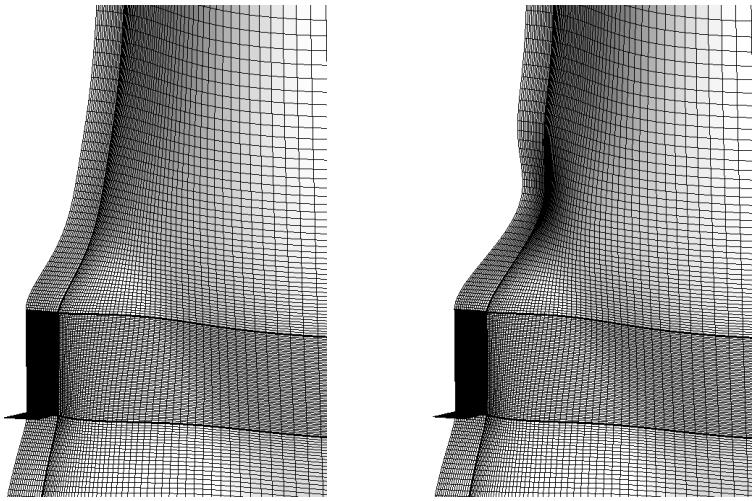

a) pre-buckling deformation, deformation factor = 35

b) post-buckling deformation, deformation factor = 35

Figure 5.7: Deformation just before and just after buckling in geometrically nonlinear elastic analysis and resulting incremental buckling mode

Therefore three different deformation modes will be shown: pre-buckling deformations, post-buckling deformations and the incremental buckling mode, which does not include pre-buckling deformations.

The pre-buckling deformed shape (Figure 5.7a) shows an enlarged flattened zone above the bracket, which leads to a lower curvature which is principally responsible for the reduction in buckling strength. It should be noted that the bifurcation buckling strength of an axially compressed shell varies approximately linearly with the shell curvature.

When the linear bifurcation mode (Figure 5.7d) is compared with the post-buckling deformed shape (Figure 5.7b), it is clear that both shapes feature a dimple just above the bracket. But the post-buckling deformed shape (Figure 5.7b) naturally shows the flattening above the bracket due to the pre-buckling deformations (Figure 5.7a). To see what changes are occurring at the instant of bifurcation from the nonlinear deformed shape it is necessary to exclude the pre-buckling deformations and determine what small changes occur at the bifurcation load. This leads to the incremental buckling mode (Figure 5.7c). The nonlinear incremental buckling mode is the change of shape of the deformation in a small deformation step at the bifurcation point.

This mode has not been widely discussed for cylinders because most studies have focussed on uniformly loaded shells in which the pre-buckling deformations are symmetric to the shell axis, making a strong contrast with the unsymmetrical bifurcation deformations (Yamaki, 1984). However, under local loads and local stress concentrations, the incremental mode defines the manner of the bifurcation departure from the primary path, even though components of the bifurcation mode are present in the primary path deformation mode.

To extract the nonlinear incremental buckling mode (Figure 5.7c), the pre-buckling (Figure 5.7a) deformations just before buckling must be subtracted from the post-buckling deformations (Figure 5.7b) just after buckling.

The shape and location of the GNA nonlinear buckle (Figure 5.7c) is significantly different from the linear bifurcation mode (Figure 5.7d).

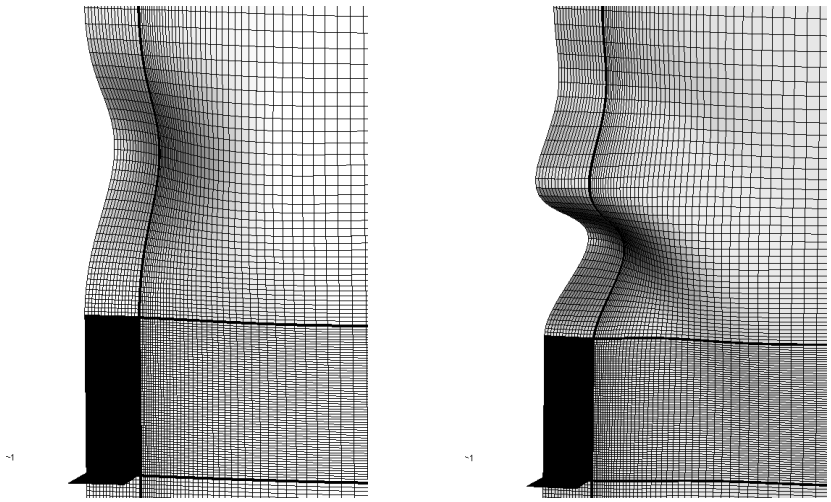

c) nonlinear incremental bifurcation mode deformation factor = 70

d) linear bifurcation mode

Figure 5.7: Nonlinear and linear buckling mode (close up view)

5.3.2.2 Location of the buckle

In the linear bifurcation analysis (LBA) (Chapter 3) it was found that the location of the buckle stayed at almost the same distance above the bracket for a fixed r/t-ratio for most bracket dimensions. Therefore a closer look was taken at the location of the incremental buckling mode in a geometrically nonlinear analysis. The location of the buckle did not stay the same, but moved further away from the bracket as the bracket width increased (Figure 5.8) and as the bracket height increased (Figure 5.9). This set of geometries is representative of all the tested geometries.

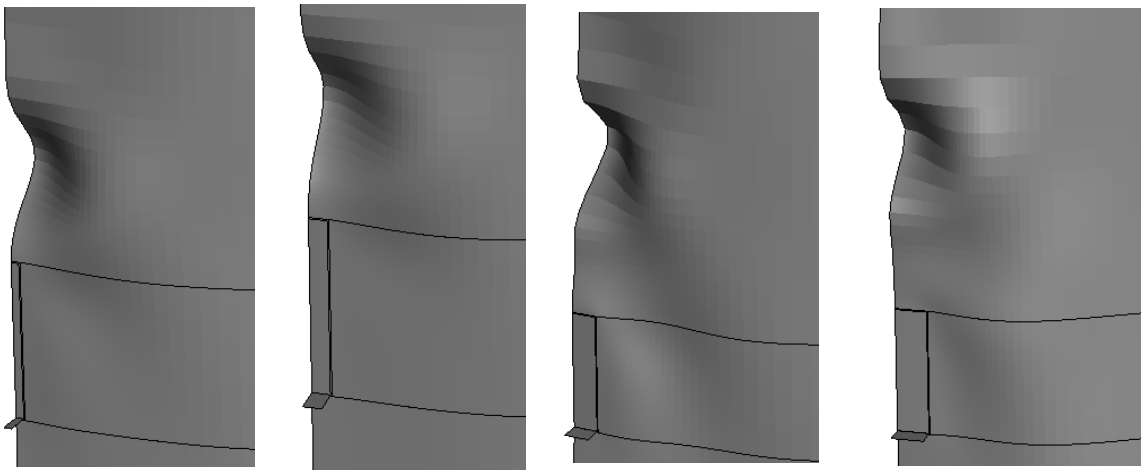

Γ=0.25 Γ=0.50 Γ=1.00 Γ=1.25

Figure 5.8: Location of the incremental nonlinear buckling mode (Λ=5, r/t=600)

The trend for the buckle to move further away from the bracket with increasing height and width of the bracket might be caused by two factors. When the bracket

becomes bigger, it acts in a manner similar to a fixed support of a column under axial compression. The similarity becomes more pronounced as the bracket is made bigger.

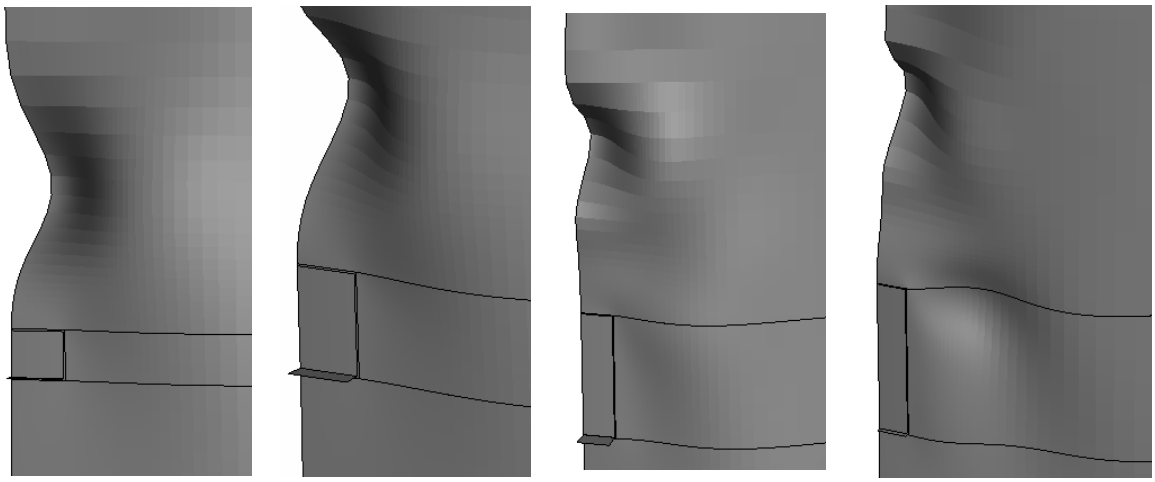

Figure 5.9: Location of the incremental nonlinear buckling mode (Γ=1.25, r/t=600)

The second reason is the flattening of the cylinder above the bracket (Figure 5.10). When the pre-buckling deformed shape just before buckling is examined (Figure 5.10) in the context of the location where the incremental buckle will form (red dots in Figure 5.10), it becomes clear that the incremental buckling mode will form at the location where the bending around the circumferential and vertical axis loses its influence and the cylinder becomes very flat (low curvature).

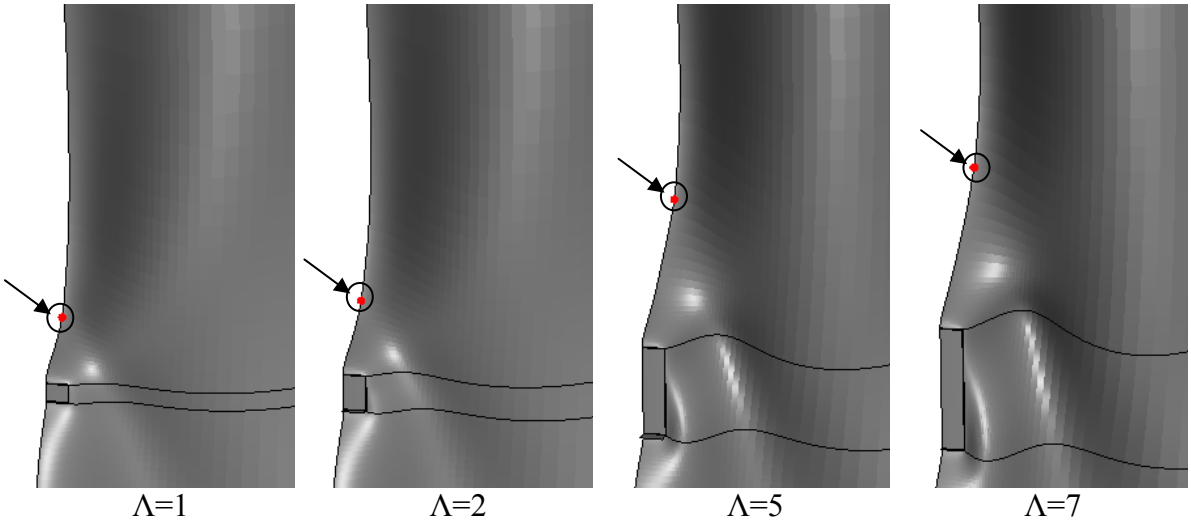

Figure 5.10: Pre-buckling deformed shape and indication of the location of the incremental buckle (Γ=1.25, r/t=600)

5.3.3 Load deflection curves and failure loads

5.3.3.1 Definition of buckling

The term buckling is commonly used rather loosely. In principal, there are really two types of buckling response: bifurcation buckling and limit point buckling. Bifurcation buckling occurs when the primary equilibrium path intersects with a secondary equilibrium path causing a rapid change of shape of the structure (Figure 5.11). When limit-load (or snap-through) buckling occurs, the buckling load is taken as the maximum load achieved before the load carrying capacity decreases (Figure 5.11). It is also possible that both a limit load and a bifurcation buckle can occur on the same path (Figure 5.11). Failure is then defined as the first critical point: either a limit load or a bifurcation. Therefore the load deflection path was monitored to find the limit load, but it was also checked at every load increment to see if any negative eigenvalues appeared, since the presence of a negative eigenvalue is an indication that a critical point (bifurcation point or limit point) has been passed.

In the case of the geometrically nonlinear analysis and within the scope of the geometries investigated in this section, only limit point buckling was encountered.

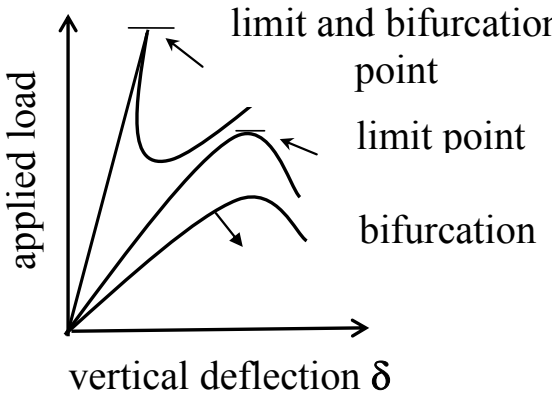

Figure 5.11: Failure criteria used for the geometrically nonlinear elastic analysis

Problems in identifying the buckling load arise when no limit point or bifurcation point can be detected (tangent stiffness matrix stays positive throughout the analysis). Within the scope of this investigation, this phenomenon occurred only for shells with very small brackets (both in height and in width) (Figure 5.12, r/t=400, $d/\sqrt{rt} = 0.25$).

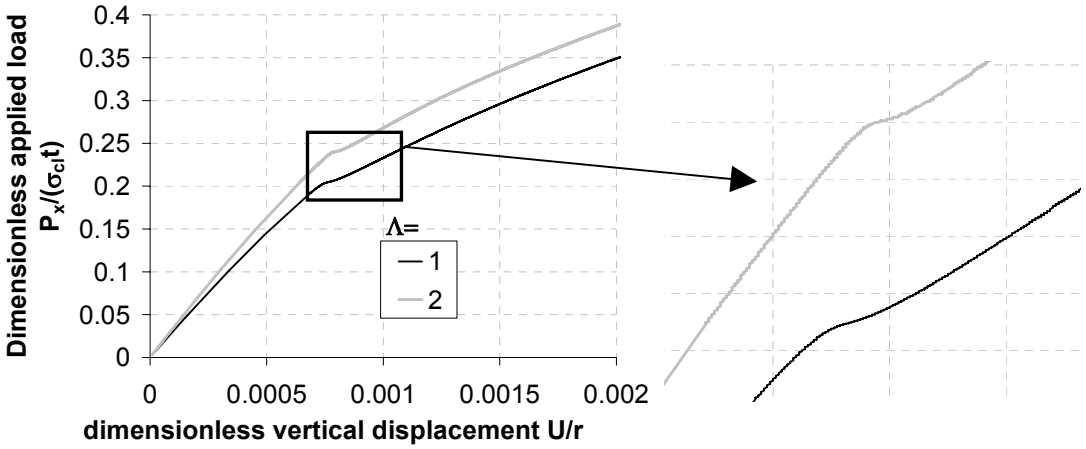

Figure 5.12: Load deflection curves without bifurcation or limit points

For these very narrow and short brackets, the slope of the equilibrium path (Figure 5.12) slowly decreases, but there is a clear, abrupt change from the pre-buckling path to the post-buckling path where a "buckling" event might have occurred (Figure 5.12). But the tangent stiffness matrix stays positive and therefore the equilibrium path always continues to rise.

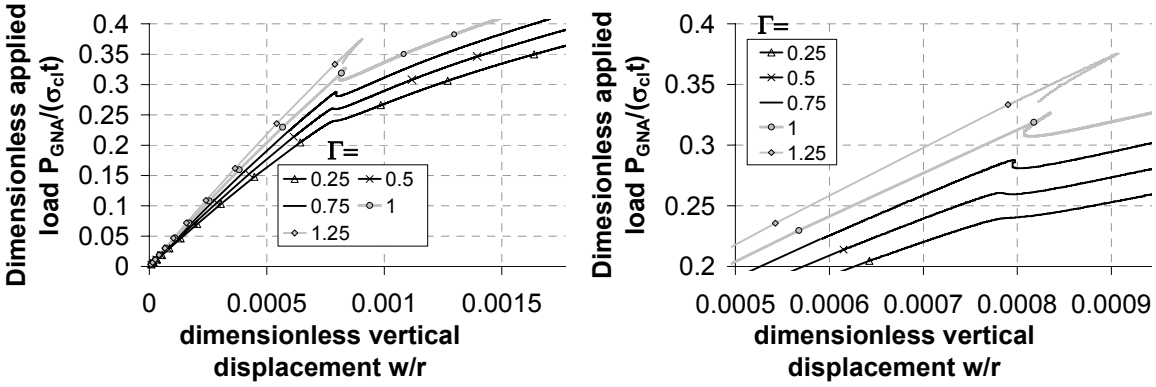

Figure 5.13: Load deflection curves (r/t=400, Λ=2)

When the equilibrium path ($\Lambda = h/\sqrt{rt} = 2$, Figure 5.12) is set into context with load deflection curves belonging to geometries with the same radius and height, but varying widths (Figure 5.13), the point in the load deflection curve where the previously shown equilibrium path has a decreasing slope is also the point where a buckle would have been expected. A very careful analysis was performed for these geometries using very small increments in the modified Riks algorithm to ensure that no bifurcation point or limit point could have been missed due to large load increments.

When no buckling can be located, a maximum permitted deflection could be used as a failure criterion. The maximum allowed displacement is recommended as a

failure criterion in the Eurocode (EN1993-1-6, 2006), which defines the maximum displacement as the maximum allowed local rotation of 0.1 radians, where the maximum rotation can occur anywhere in the shell. Gillie *et al.* (2002) on the other hand proposed to use a maximum allowable rotation of the bracket, but the bracket in the present study has been constrained against rotation and therefore the rotation of another point is required.

But since the failure load in a geometrically nonlinear analysis (GNA) will be needed in order to calculate the necessary value of the elastic imperfection sensitivity factor α (Chapter 6), a technique was developed to approximate this failure load by introducing a small disturbance in the material using the geometrically and materially nonlinear analysis (GMNA) with increasing yield stress. With increasing yield stress the material nonlinearity will lose influence in the geometrically and materially nonlinear analysis and the geometric nonlinearity will dominate and will therefore approach the result of a geometrically nonlinear elastic analysis, but it may still produce enough of an imperfection to provoke buckling. Another advantage of using this technique is that the variation of yield stress is later required to obtain capacity curves (Chapter 6) and therefore no additional work is involved as long as a capacity curve is desired.

For illustration purposes, an example with the dimensions of r/t=400, $\Lambda = h/\sqrt{rt} = 1$ and $\Gamma = d/\sqrt{rt}$ =0.25 has been chosen, since for this geometry no buckling occurred during the GNA analysis (Figure 5.12). When the inverse of the yield stress is plotted against the failure load for this example geometry from a geometrically and materially nonlinear analysis (GMNA) (Figure 5.14a), the failure load approaches a plateau (Figure 5.14b).

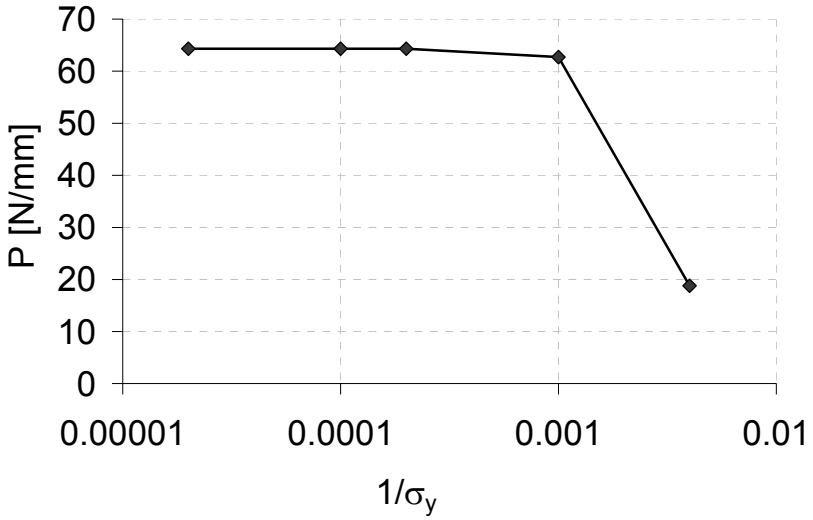

Figure 5.14: GMNA analysis with increasing yield stress

Hence when the plateau occurs the material nonlinearity has lost its influence to such an extent that the global failure is not influenced by it anymore. There is still yielding at the corners of the bracket, but it is very localized and does not influence the global behaviour.

The failure load extracted from Figure 5.14 can then be considered to be a good approximation to the geometrically elastic nonlinear analysis (GNA).

This is a more satisfying way of defining the failure for these structures since the change from bifurcation to a rather arbitrary limiting surface rotation can lead to a big change in the assessed strength for a very small change of geometry, which is clearly an unsatisfactory situation in practical terms.

5.3.3.2 Load deflection curves and failure loads

Within the scope of this study, three different radius to thickness ratios were investigated (r/t=400, 600 and 1000) to cover the whole spectrum from thick to thin shells. The thickest shell previously analysed (r/t=200) was excluded from this study since the geometrically nonlinear analysis (GNA) did not show buckling phenomena (neither limit point or bifurcation buckling) for many of bracket geometries.

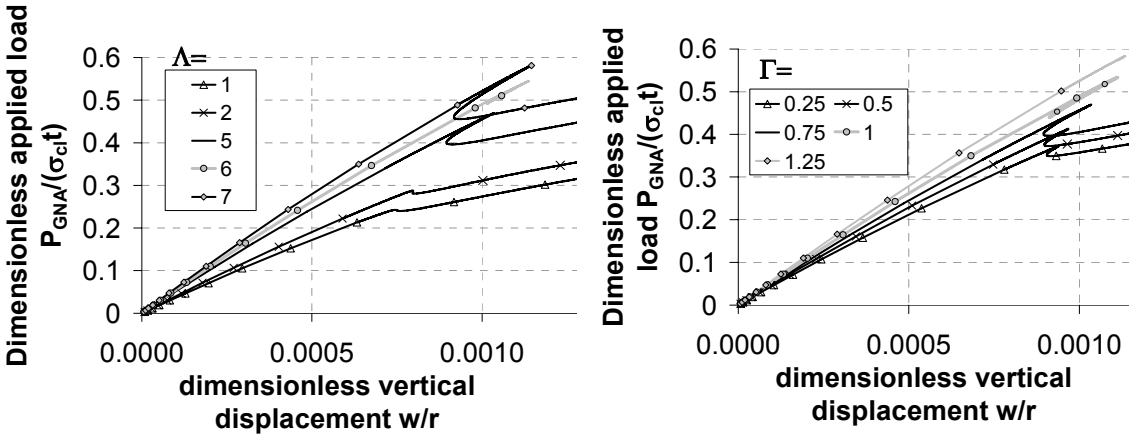

a) $\Gamma = d/\sqrt{rt} = 0.75$ b) $\Lambda = h/\sqrt{rt} = 5$

Figure 5.15: Load deflection curves for(r/t=400)

An example set of load deflection curves (Figure 5.15) gives an overview of the general behaviour found. This example has a radius to thickness ratio of r/t=400. The other geometries with larger radius to thickness ratios (r/t=600, 1000) showed very similar behaviour.

For both a narrow bracket (Fig. 15a) and a short bracket (Fig. 15b) the load displacement path shows a strong bifurcation followed by a steeply descending path, as is commonly found for uniformly compressed cylinders. As the height or width are decreased, the failure load decreases (Figure 5.15a and b), but the steeply descending post-buckling path is steadily weakened until it becomes a mere blip, and finally disappears altogether.

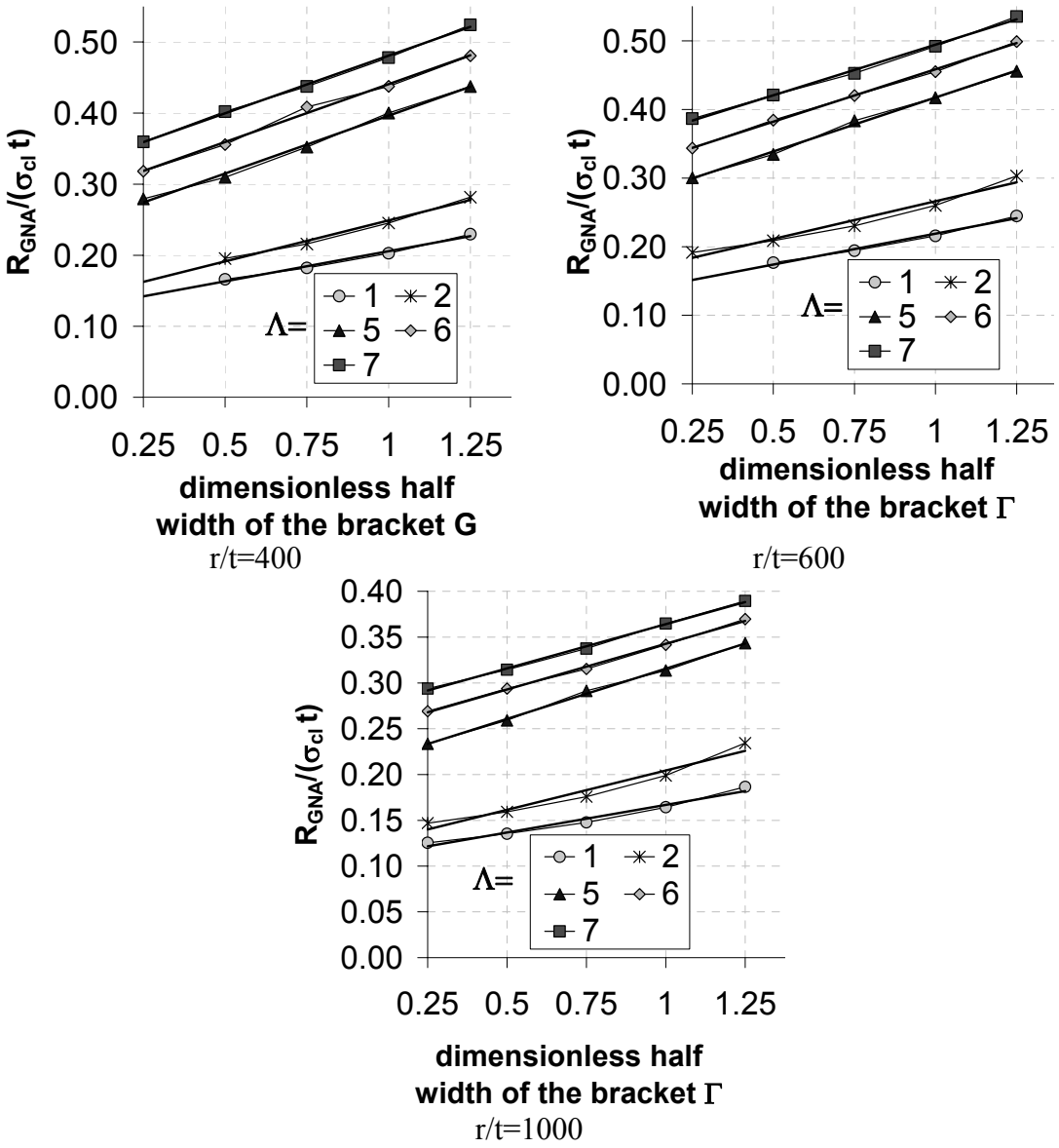

Figure 5.16: Variation of the dimensionless failure loads RGNA/(σcl t) with the dimensionless half width of the bracket Γ

When the height of bracket rises, the proportion of the applied load transferred as compression above the bracket is reduced. This compression causes the cylinder to buckle. Therefore a higher load on the bracket is needed to cause the cylinder to buckle when the height rises. The dimensionless failure loads (Figure 5.16) vary almost linearly with the dimensionless width of the bracket. The best approximation to a linear function can be made for a tall bracket ($\Lambda = h/\sqrt{rt}$ =5, 6 and 7), but the approximation loses it accuracy when the height of the bracket decreases. It should be noted that the variation of the dimensionless failure load ($R_{GNA}/(\sigma_{cl}\, t)$) has very similar pattern for all radius to thickness ratios.

A simple approximation could be given for the variation of the dimensionless nonlinear bifurcation load $R_{GNA}/(\sigma_{cl}\ t)$ with the dimensionless bracket half width Γ and the dimensionless bracket height Λ. However, this would be based on a limited range of geometries and does not fit with the philosophy of EN1993-1-6 (2006)

When the dimensionless failure loads are varied with the height of the bracket a linear approximation can be achieved within reasonable limits. An example of the stress pattern developing in the shell can be found in (Chapter 2).

5.3.4 Influence of the geometric nonlinearity

To explore the effect of geometric nonlinearity in detail, the buckling load obtained from the geometrically nonlinear analysis was compared to the linear elastic bifurcation load (LBA) in terms of the elastic imperfection sensitivity factor α, even though there is no imperfection present here.

$$\alpha = R_{GNA} / R_{LBA} \tag{5.1}$$

The cylinders investigated had radius to thickness ratios of r/t=400, 600 and 1000 and a thickness of one unit. These were chosen to include both thin shells and thick shells. The dimensionless height of the bracket varied as $1 < \Lambda = h/\sqrt{rt} < 7$ and the dimensionless half width of the bracket varied as $0.25 < \Gamma = d/\sqrt{rt} < 1.25$.

It may be noted that in uniformly compressed cylinders, geometric nonlinearity leads to a strength reduction of typically 8 to 15% (Yamaki, 1984). However in the case of a bracket supported shell, the geometrically nonlinear effect reduces the buckling load significantly, especially for small (short and narrow) brackets (Figure 5.17). The reduction of the bifurcation load due to geometrically nonlinear effects ranges from about 20 to 40%. The larger magnitude of this reduction can be explained by the highly nonlinear stress distribution during pre-buckling and the consequent flattening effect of the cylinder above the bracket. The largest reduction can be seen for very narrow and short brackets as the flattening above the bracket is more pronounced in this case.

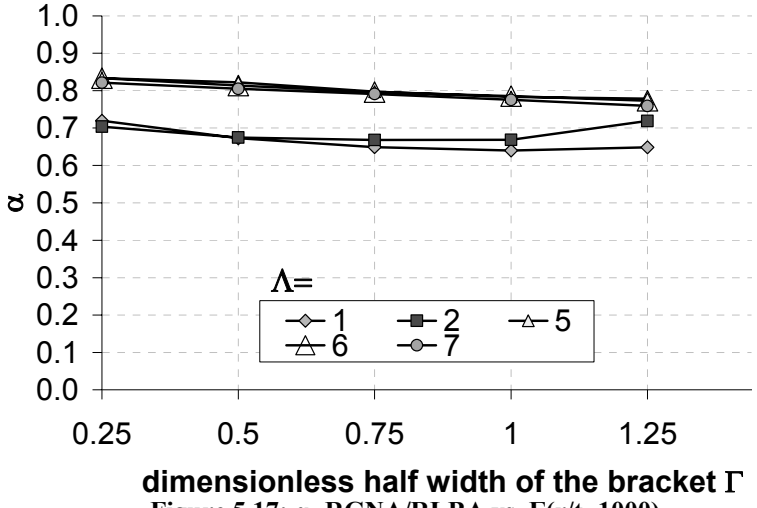

Figure 5.17: α=RGNA/RLBA vs. Γ(r/t=1000)

The ratio α of the nonlinear elastic buckling load (R_{GNA}) to the linear elastic buckling load (R_{LBA}) does not follow an obvious pattern as the geometry of the shell and bracket are changed. For all the geometries investigated, this ratio α varies between 0.604 and 0.833 (Table 5.1). The value of α (Figure 5.17) does not change significantly with the width of the bracket. In fact the maximum difference encountered for all the geometries in this investigation between the highest and the lowest value of α for any fixed r/t ratio and fixed height is only 15.5%. Therefore the influence of geometric nonlinearity does not appear to change significantly when the width of the bracket is varied.

In general it can be said that as the bracket becomes taller, the ratio α becomes higher. But this is not true for all the geometries (Figure 5.18). For very small brackets (both in height and in width), the taller bracket has a lower ratio α. This was only encountered for very small brackets. On the other hand the value of α stays almost constant for tall brackets ($h/\sqrt{rt}$ = 5, 6 and 7). This leads to the conclusion that the influence of geometric nonlinearity does not change for tall brackets and that the width does not significantly influence α for tall brackets.

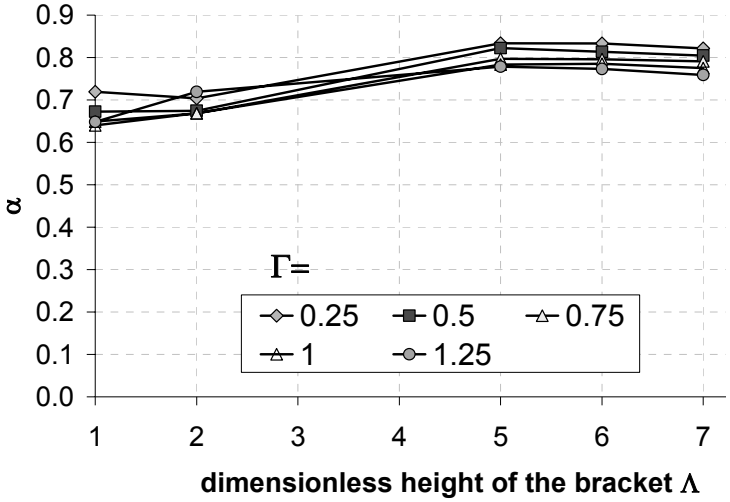

Figure 5.18: α=RGNA/RLBA vs. Λ (r/t=1000)

The influence of geometric nonlinearity decreases as the radius to thickness ratio increases (Figure 5.19), because the flattening of the shell above the bracket becomes less significant before buckling. That is to say, buckling occurs when the pre-buckling deformations are still small, so their influence is less significant.

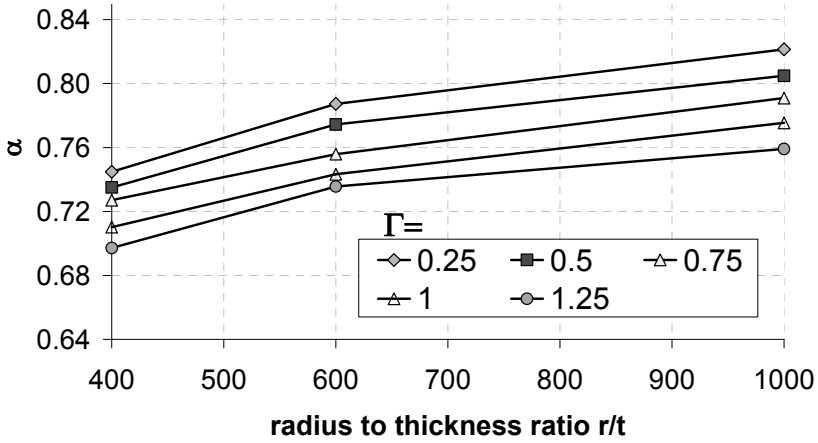

Figure 5.19: α=RGNA/RLBA vs. r/t (Λ=7)

	Λ \ Γ	0.25	0.50	0.75	1.00	1.25
r/t=400	1	0.698	0.653	0.623	0.607	0.604
	2	0.668	0.638	0.622	0.620	0.634
	5	0.704	0.691	0.698	0.720	0.700
	6	0.725	0.714	0.729	0.714	0.700
	7	0.745	0.735	0.727	0.710	0.697
r/t=600	1	0.709	0.665	0.637	0.623	0.624
	2	0.686	0.656	0.643	0.644	0.669
	5	0.754	0.752	0.777	0.737	0.734
	6	0.784	0.794	0.761	0.744	0.736
	7	0.787	0.774	0.756	0.743	0.736
r/t=1000	1	0.719	0.673	0.649	0.640	0.648
	2	0.704	0.675	0.668	0.669	0.719
	5	0.833	0.822	0.797	0.783	0.779
	6	0.833	0.814	0.796	0.785	0.773
	7	0.821	0.805	0.791	0.775	0.759

Table 5.1: Summary of all α- values

5.3.5 Summary

Geometrically nonlinear effects, as found using a geometrically nonlinear elastic analysis (GNA) lead to significantly reduced buckling loads in bracket supported shells. This is caused by the flattening of the shell above the bracket, causing a larger effective radius of curvature at the buckle location which leads to reduced buckling strengths. The strength reductions for brackets range between 16.7% and 39.6% and are much larger than those for uniformly stressed cylinders of about 15% (Yamaki, 1984). In general the reduction is roughly constant as the dimensionless width of the bracket is changed. It increases with decreasing dimensionless bracket height and with decreasing radius to thickness ratio for the range of geometries investigated. This statement is not precisely accurate for all of the geometries investigated, but is the dominant trend.

The most significant loss of strength can be found for thick shells and small brackets (both in height and in width). Therefore one might think that very small brackets and very thick shells would show the greatest loss of strength. But these are exactly the geometries which do not display buckling any more, but instead have a positive tangent stiffness matrix throughout.

This leads to the major question of how to define failure in a geometrically nonlinear elastic analysis (GNA) when no buckling occurs any more, but a geometrically and materially nonlinear analysis (GMNA) might display buckling for exactly the same geometry. The concept adopted here is to use a geometrically and materially nonlinear analysis (GMNA) to determine failure, but instead of using a realistic yield stress, a very much higher yield stress should be used. This procedure will approach the geometrically nonlinear elastic analysis when the yield stress is high enough. The result of the analysis with the highest yield stress, where buckling still occurs, may usefully be taken as the failure load of the geometrically nonlinear elastic analysis.

The uniformly compressed cylinder is a commonly used example of shell buckling, but in reality shells are quite rarely just uniformly compressed. Instead the shell will have regions of highly non-uniform stresses (e.g. where the supports of the shell are placed) and will therefore perform very differently from a uniformly compressed cylinder.

For exactly this reason, the bracket supported shell provides a very good example for many other shell problems in which local loads cause a flattening of the wall in the zone where the buckle will form, since they are prone to behave in the same manner. This makes the geometrically nonlinear elastic analysis (GNA) a more important analysis here than it is for uniformly stressed cylinders.

5.4 Geometrically nonlinear analysis with imperfections (GNIA)

5.4.1 Introduction

The buckling strengths of shells are known to be very imperfection sensitive under many circumstances. In the case of a uniformly compressed cylinder, the introduction of a small local geometric imperfection can lead to a reduction of the buckling load by up to 80% (Rotter, 2004) and contributes much more to the reduction of the buckling load than geometric nonlinearity, which only leads to a reduction of around 15% (Yamaki, 1984)

The literature (e.g. Yamaki, 1984; Rotter, 2004) provides many different

proposals for serious forms of imperfections. The imperfections can be of a geometric or material nature (EN1993-1-6, 2006).

Geometric imperfections recommended by different authors for use in design calculations may include the first eigenmode from a linear bifurcation analysis, the deformed shape from a geometrically nonlinear elastic analysis and different types of weld-imperfection (Rotter, 2004). Material nonlinearity was omitted in this part of the study to explore the effect of combined geometric nonlinearity and geometric imperfections.

The greatest challenge for any analysis that includes geometric imperfections is to decide which imperfection might be the appropriate imperfection for a certain problem. The "worst" imperfection (i.e. imperfection which leads to the lowest failure load) is usually considered to be the appropriate one. While this assumption is always on the safe side, it always holds the uncertainty that another imperfection may exist that could lead to a worse outcome, and the possibility that this worse imperfection could possibly arise in the fabrication process. On the other hand the "worst" imperfection of all might well be quite unrealistic, leading to very uneconomic designs if implemented (Rotter, 2004). At the same time the "worst" imperfection consists out of one specific imperfection shape and the corresponding imperfection amplitude, which means that a certain imperfection shape might only produce low failure loads for certain amplitudes and another imperfection shape could take over as the "worst" imperfection shape for other amplitudes.

In the case of a bracket supported shell, it is clear that a serious imperfection will be in the compression zone above the bracket, since high compressive stress concentrations only appear there. In general the first eigenmode imperfection is recommended (EN1993-1-6, 2006). As shown in Chapter 3, the first eigenmode produces a buckle just above the bracket and was therefore the first geometric imperfection investigated here. On the other hand, the imperfection should also introduce flattening of the shell above the bracket since it was shown that this is the dominant factor in the reduction in strength below the linear bifurcation load. Consequently imperfections which already introduce flattening above the bracket might have a greater effect.

After the decision is made on which form of imperfection to use, it is necessary

to decide what amplitude to use. For most shell buckling problems, the buckling load decreases with the amplitude of the imperfection. This idea was used as a basis for the investigation of the imperfection sensitivity in a geometrically nonlinear elastic analysis.

This section describes only an example geometry, but a greater range of geometries are investigated in Chapter 7. The example shell has the geometry r/t=600, h/r=0.12, h/d=3 and t=1.

5.4.2 Imperfection sensitivity of the example geometry

5.4.2.1 Shapes of the imperfections introduced

To explore the influence of imperfections on the buckling behaviour of the bracket-supported shell, five different shapes of imperfection were analysed.

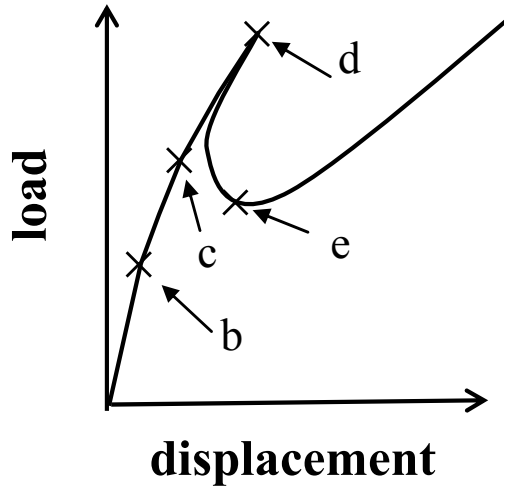

Figure 5.20: Load stages for corresponding imperfection shapes in Figure 5.21

The shape of the first eigenmode from a linear elastic analysis (Figure 5.21a) (LBA) was investigated since it is commonly recommended in the literature (see Chapter 1). From a geometrically nonlinear elastic analysis, four different deformed shapes were employed at different stages of the load deflection path as imperfection forms.

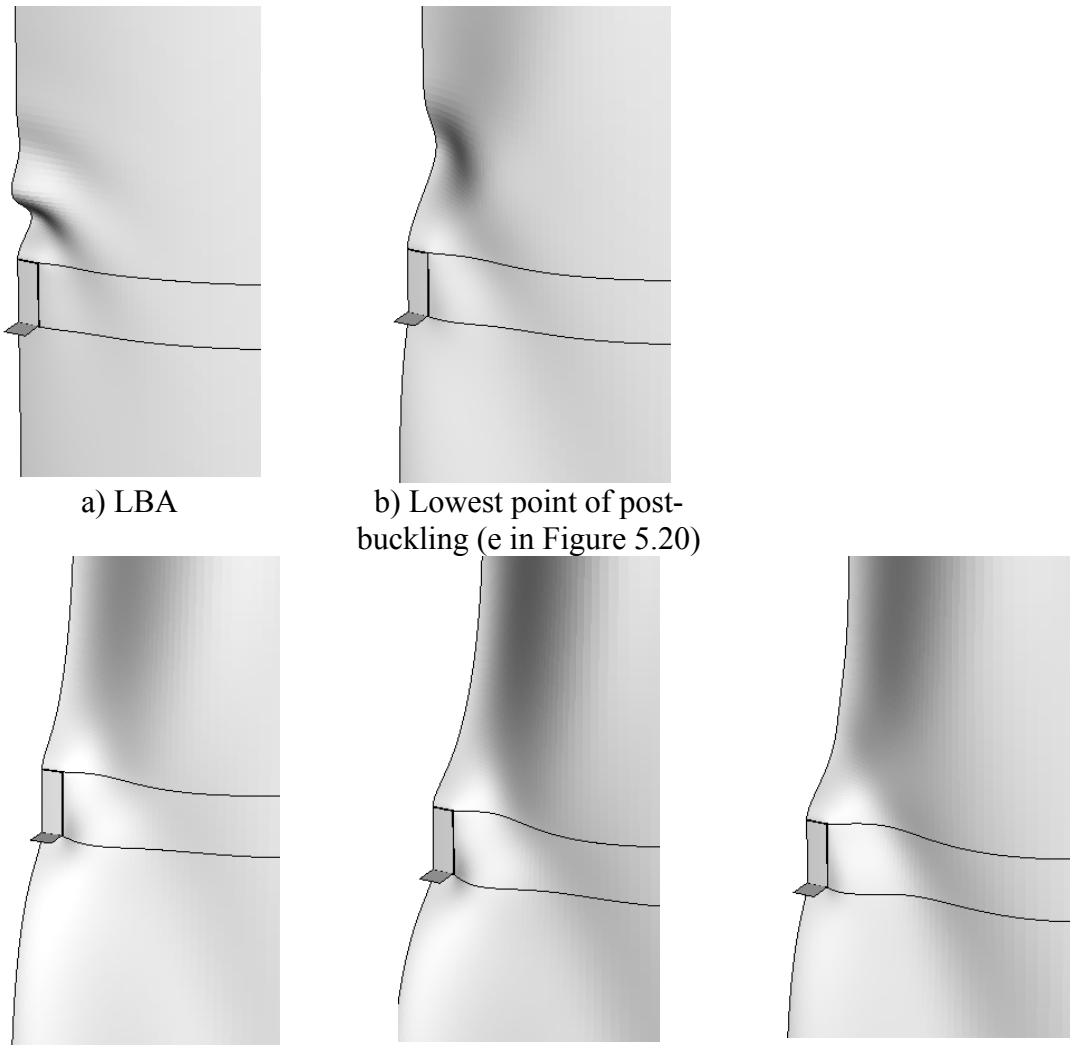

a) LBA

b) Lowest point of post-buckling (e in Figure 5.20)

c) Low load level (b in Figure 5.20)

d)Well before buckling (c in Figure 5.20)

e)At buckling (d in Figure 5.20)

Figure 5.21: Different shapes of geometric imperfections

Two deformed shapes were taken well before buckling (b and c in Figure 5.20), another shape was taken just at the point of buckling (d in Figure 5.20) and the fourth deformed shape was taken at the lowest point of the post-buckling curve (e in Figure 5.20). The different imperfection forms are shown in Figure 5.21.

The shape of the first eigenmode (LBA) and the deformed shape at the lowest point on the post buckling path (Figure 5.21 a and b) both display a clear dent, but with different shapes and position above the bracket. The deformed shapes well before buckling (Figure 5.21c and d) and at buckling (Figure 5.21e) display a flattening of the cylinder above the bracket. The flattening is more pronounced for the deformed shape at buckling.

5.4.2.2 Influence of the imperfection to the buckling load

The results of geometrically nonlinear elastic analyses, including explicit geometric imperfections in the five forms identified above (GNIA) are shown in Figure 5.22 for a substantial range of imperfection amplitudes.

It is commonly assumed that a geometric imperfection lowers the buckling load considerably relative to the strength of the perfect shell. In this case, the buckling load of an imperfect shell shows a different behaviour.

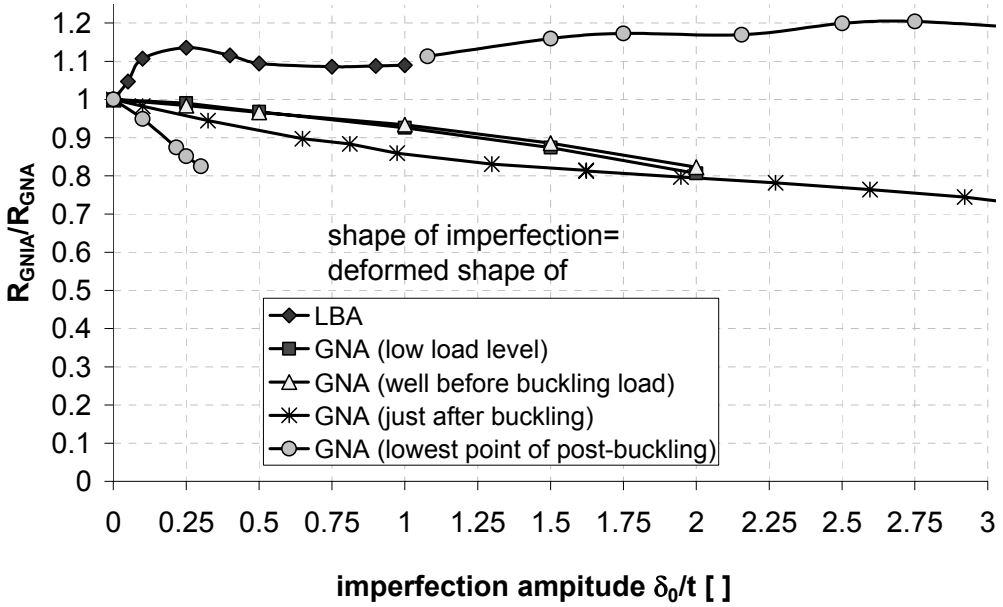

Figure 5.22: Imperfection sensitivity for different imperfections

Using the first eigenmode from a linear analysis, the buckling load is not reduced, but increases instead. No amplitude achieves a lower buckling load than is seen for the perfect shell in the case of the linear eigenmode imperfection. The failure load rises until an imperfection amplitude of $\delta_0/t=0.25$, but decreases then to a level at about 9% higher than the bifurcation load of the perfect shell. While buckling could be obtained for this imperfection shape up to an imperfection amplitude of $\delta_0/t=1$, no buckling could be found for an amplitude of $\delta_0/t=1.5$.

The imperfection in the from of the deformed shape of lowest post-buckling point initially also shows a decrease in the buckling load up to a imperfection amplitude of $\delta_0/t=0.3$ to 81% of the strength of the perfect shell (Figure 5.23), but from a imperfection amplitude $\delta_0/t=0.4$-1 no buckling could be detected anymore. While the strength of the structure steadily decreases up to $\delta_0/t=0.3$, the pre- buckling path becomes even more nonlinear and the difference between limit point and post-

buckling minimum decreases with increasing imperfection amplitude. As a consequence, for an imperfection amplitude of $\delta_0/t=0.4$, no buckling can be detected anymore, but a clearly defined change in the curvature of the load deflection curve can be observed (Figure 5.23). From an imperfection amplitude of $\delta_0/t=1.078$ a new buckling mode develops and the strength of the silo is increased above the strength of the perfect cylinder (Figure 5.24)

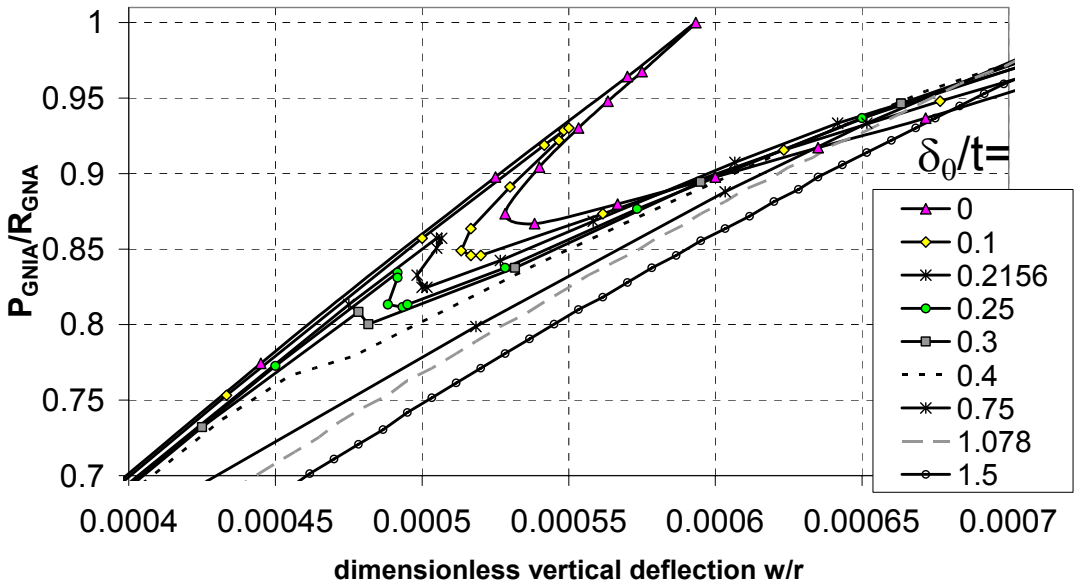

Figure 5.23: Close up of load deflection path of GNIA (imperfection shape=deformed shape at the post- buckling minimum of GNA analysis, r/t=600, h/r=0.12,h/d=3)

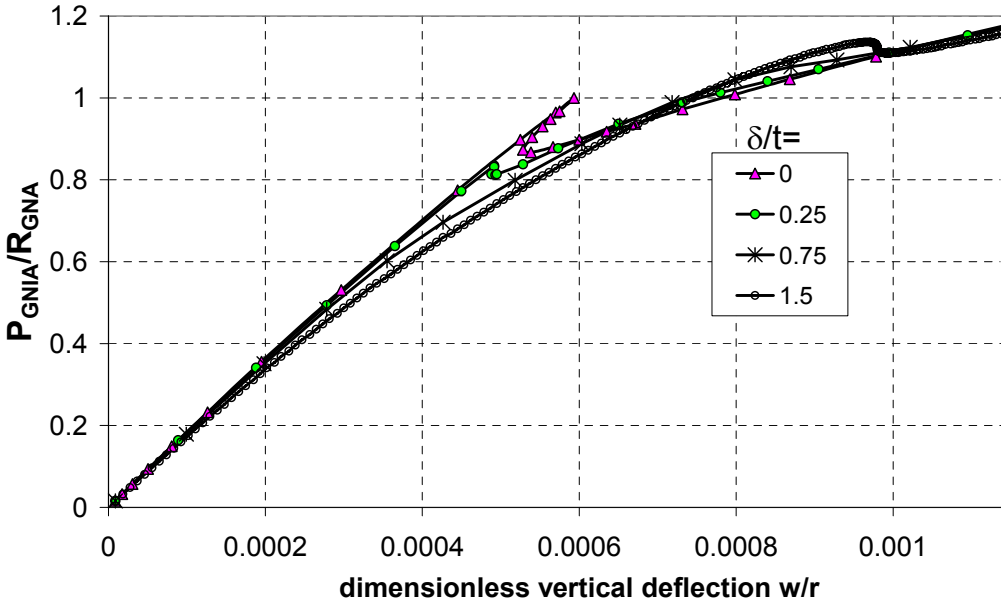

Figure 5.24: Load deflection path of GNIA (imperfection shape=deformed shape at the post- buckling minimum of GNA analysis, r/t=600, h/r=0.12,h/d=3)

The imperfections which cause flattening above the bracket do have the expected effect of reducing the failure load of the perfect shell.

The failure load was reduced in this case by 15.5% at $\delta_0/t=1$ and the decrease continued up to a value of 28.5% for an imperfection amplitude of 3.25. After this amplitude no buckling could be observed anymore.

The other two imperfection forms that used the deformed shape well before buckling and at a low load level show similar, but not such pronounced results.

The rise in the failure load for an imperfection in the form the linear eigenmode seem to be very odd at first glance, since imperfections are supposed to lower the buckling load of a perfect shell. But in this case these imperfections hinder the development of pre-buckling deformations seen in the perfect shell. In particular these imperfections hinder the flattening of the shell above the bracket, which leads to a reduction of curvature of the cylinder. Consequently the failure load is increased.

The imperfection form of the deformed shape of a GNA analysis at the post-buckling minimum includes extensive flattening (Figure 5.21b) as well as the buckle. The flattening of the shell is dominating the strength of the imperfect shell for small imperfections until no buckling can be detected anymore due to the extensive pre-buckling deformations and the load deflection path is steadily rising. A second limit point appears for larger imperfection amplitudes which leads to an increase of strength compared to the perfect structure.

The initial drop followed by a rise in the imperfect nonlinear buckling load leads to another problem, since the change of buckling mode occurs at a relatively small imperfection amplitude compared with the imperfection amplitude recommended in the Eurocode (EN1993-1-6, 2006) of $\delta_0/t=0.98$ for Fabrication Quality Class A (the best fabrication quality)A, no buckling would be found, but for Class B and C with $\delta_0/t=1.57$ and 2.46 respectively the strength of the silo would appear to be increased.

All the imperfection shapes shown above have their maximum deviation (imperfection amplitude) directed towards the central axis of the cylinder. It has been recently proposed (Schneider *et al.*, 2005) that outward imperfections might cause more serious reductions of strength. They were therefore tested, but they always showed a higher failure load than the imperfections that were inwardly directed. The tested amplitudes for the outward imperfections were $\delta/t=0.1$ and $\delta/t=1$.

These results show very clearly that great care has to be taken in the choice of imperfection shape and amplitude. Furthermore a good understanding of the perfect structure is required to assess which imperfection forms could possibly be the most serious.

5.4.3 Summary

It has been shown for an example geometry that the buckling strength of a bracket supported cylinder is not very imperfection sensitive. The most severe imperfection is the deformed shape found in a geometrically nonlinear analysis, but also this shape of imperfection only leads to a reduction of strength compared to the perfect shell of about 30% for large imperfection amplitudes, after which a further increase in imperfection amplitude causes the buckling phenomenon to disappear. This compares with a reduction of strength of about 80% for a uniformly compressed cylinder (Yamaki, 1984).

The general assumption of the Eurocode (EN1993-1-6, 2006) that the failure load generally decreases with an increase in imperfection amplitude was not verified in these calculations. The reason for the relative insensitivity of the buckling load to geometric imperfections is that when a shell is symmetrical and the pre-buckling stresses are symmetrical in the perfect shell, an imperfection changes the symmetrical pattern of the perfect shell to an unsymmetrical pattern in the imperfect shell, leading to a reduction of the bifurcation load that can be massive. But in the case of a bracket supported cylinder, or any cylinder in which the peak compressive stresses are rather local, pre-buckling stresses are already highly unsymmetrical and therefore lead to big reductions in the nonlinear buckling load when geometric nonlinearity is used in the perfect shell, but it makes the shell less imperfection sensitive. This result is probably not only valid for the example of the bracket supported shell, but may be valid for all shells in which highly non-uniform pre-buckling stresses occur.

Not only was the bracket-supported cylinder not very imperfection sensitive, but for the most common imperfection shape (the first eigenmode imperfection) it displayed the reverse effect. Instead of lowering the buckling load, this imperfection

increased the buckling load. This phenomenon is due to the way that pre-buckling deformations influence the buckling behaviour in a geometrically nonlinear analysis. As mentioned before, the flattening of the cylinder or reduction of the curvature of the cylinder is the dominant factor in the reduction of the buckling load due to geometric nonlinearity. When the linear eigenmode is introduced as a geometric imperfection, the flattening of the shell is hindered by the imperfection, causing an increase in the buckling load. The imperfection shape of the deformed shape at post-buckling minimum showed an decrease of strength for very small imperfections (19%), but no buckling could be detected for amplitudes in the range of δ_0/t=0.4-1. The load deflection path still showed a change in curvature at this point, but no bifurcation could be detected. From an imperfection amplitude of δ_0/t=1.078 a new buckling mode appeared, which lead to an increase of strength.

5.5 Conclusions

The reduction of strength due to geometric nonlinearity and imperfections have similar magnitudes. The maximum strength reduction encountered in the example silo due to geometric nonlinearity was about 36% and the maximum reduction due to imperfections was about 30%. This is very different from the uniformly compressed cylinder, where the strength reduction due to geometric nonlinearity is about 15% and due to imperfections up to 80%.

The difference between the uniformly compressed cylinder and the bracket supported shell arises because of differences in the pre-buckling stress and deformation states. The uniformly compressed cylinder has a uniform symmetrical pre-buckling condition, but the bracket supported shell is already in a highly non-uniform and unsymmetrical pre-buckling state. When the symmetrical pattern is disturbed due to imperfections, the reduction of strength is very significant. Whereas the highly non-uniform pre-buckling state of the bracket supported cylinder makes it insensitive to imperfections. Nevertheless the nonlinear flattening of the cylinder above the bracket does reduce the strength significantly compared to the linear eigenvalue analysis.

A bracket supported shell with a linear eigenmode imperfection was found to have a higher strength than the perfect shell. From the design point of view, this is a

disadvantage, since the linear eigenmode imperfection is frequently recommended as the imperfection to use if no other imperfection can be justified (e.g. EN1993-1-6, 2006). The search of the "worst" imperfection is very much a topic for research and not for the designer.

The question therefore arises: how many imperfections should a designer consider before deciding which is the worst one, if the recommended imperfection leads to a higher strength than that of the perfect shell?

It has been shown that the imperfection sensitivity does not always comply with the ideas about imperfections widely found in the shell buckling literature and used in the Eurocode, which indicates a lower strength for deeper imperfections. The analysis of an imperfect structure is very time-consuming and a designer cannot therefore be expected to explore the imperfection sensitivity in detail, but the designer could also over-estimate the strength of the structure by rigidly following the current code.

It is currently therefore a significant research challenge to develop safe definitions for imperfection sensitivity, with respect to shape and amplitude of the imperfection, for shells that have highly non-symmetric or local loads. Unfortunately, there are many practical shell structures in this category.

6 Geometrically and materially nonlinear analysis

6.1 Introduction

All the analyses described in the previous chapters have been confined by special restrictions in order to explore individual features of the problem. In the beginning the linear bifurcation analysis (LBA) was performed, which excluded both the geometrical and material nonlinearity and was used to study the pure bifurcation behaviour of the structure. The geometrically nonlinear analysis (GNA) explored the purely elastic buckling behaviour. The materially nonlinear analysis (MNA) omitted the geometrical nonlinearity to investigate pure plastic collapse. Here, geometrically and materially nonlinear analysis is used to explore the strength of the perfect structure in the light of these earlier individual and simpler estimates of different types of failure.

Bracket supported cylinders display a wide range of failure modes in geometrically and materially nonlinear analysis. This ranges from failure similar to the plastic collapse seen in the materially nonlinear analysis to almost perfectly elastic buckling.

These different kinds of failure behaviour are all here set into one framework corresponding to EN1993-1-6 (2006) and the capacity curves for individual structures will be calculated and analysed.

The second aim of this chapter is to find a suitable design approximation for the capacity curves for each radius to thickness ratio, allowing for the two dimensions that characterise the bracket.

The range of geometries investigated consisted of three different radius to thickness ratios to capture the behaviour pattern for thin, medium and thick shells (r/t=1000, 600 and 400). The dimensionless height of the brackets ranged from very short to tall ($1 < \Lambda = h/\sqrt{rt} < 7$) and the dimensionless width from very narrow to wide ($0.25 < \Gamma = d/\sqrt{rt} < 1.25$.)

The material behaviour is modelled by an elastic, perfectly plastic von Mises model and corresponds to the material model used in the previous analyses (with σ_y=250 MPa, E=200 000 MPa and ν=0.3).

6.2 Verification of the mesh and the element

6.2.1 Choice of element

The elements chosen for the geometrically and materially nonlinear analysis were the general purpose element S4R coupled with the thick shell element S8R, since this combination was found to achieve an accurate description of the failure behaviour in all the different analyses, whilst other elements failed at one challenge or another.

The outcome of a comparison of different elements is known from the previous chapters. The general purpose element S4R performs well as long as plasticity plays no role in the failure behaviour. The thin shell element S8R5 displays convergence problems when the failure is dominated by the material nonlinearity. Only the thick shell element S8R can give a good treatment for highly plastified zones, but it cannot model bifurcation.

6.2.2 Convergence study

It was shown that the mesh converged well for all analyses performed in this work.

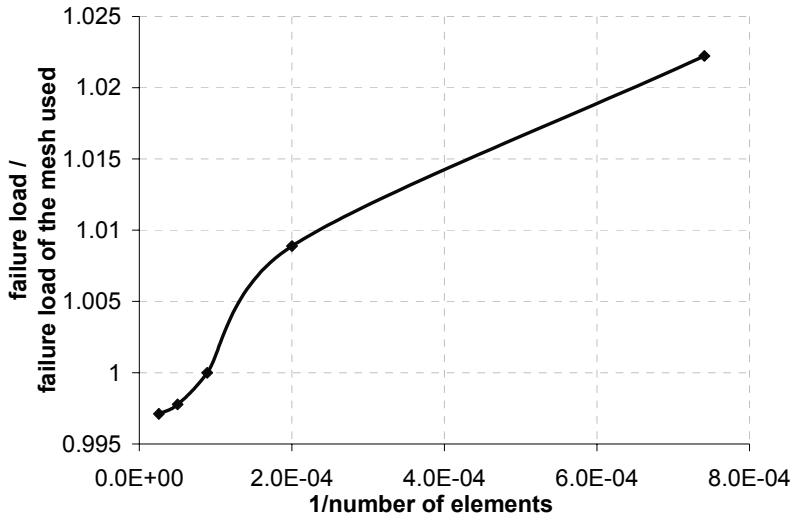

Figure 6.1: Convergence study

The geometrically and materially nonlinear analysis is a combination of the materially nonlinear analysis and the geometrically nonlinear analysis and is

therefore expected to converge well too. The convergence study was performed on an example problem that involved both plasticity and stability effects (r/t=600, Λ=3, Γ=1). The result is shown in Figure 6.1.

The failure load of a mesh with an infinite number of elements can be extracted from the graph by extrapolating the graph towards zero. Even though a very good convergence was achieved, the mesh chosen had to have a high number of elements due to the connection between the 8-noded and the 4-noded elements close to the bracket and the necessity to keep the aspect ratio of the elements at a reasonable level (Chapter 4). The extrapolated result for an infinite number of elements gives a result that is only 0.3% below that found with the chosen mesh, which had 11 200 elements.

6.2.3 Boundary conditions

A model of one eighth of the shell and half of one bracket was used once more in this analysis. Previous analyses (Chapter 4 and 5) showed that the use of symmetry boundary conditions to simulate the whole shell with four brackets does not affect the behaviour of the structure or its failure load. This is demonstrated here again for completeness.

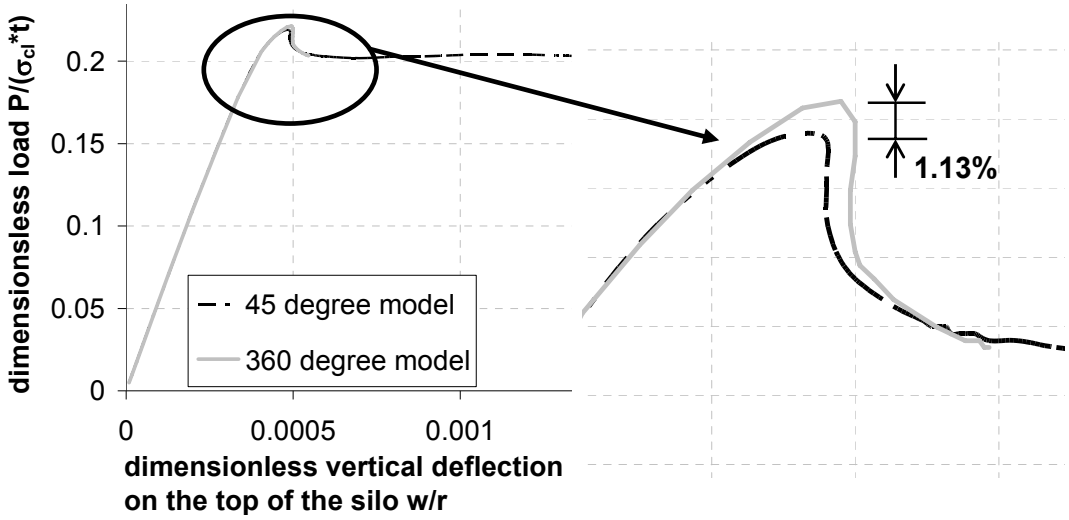

a) b) close up of a)

Figure 6.2: Comparison of the load deflection between the eighth model and the 360 degree model

6.3 Definition of failure

6.3.1 General

The possible failure modes in the geometrically and materially nonlinear analysis (GMNA) are essentially the same failure modes described in Chapter 5 with the addition of the plastic collapse load as one failure mode (Figure 5.11). In summary, failure is defined by the first bifurcation point or the first limit point, whichever occurs first or the plastic collapse plateau when no buckling occurs.

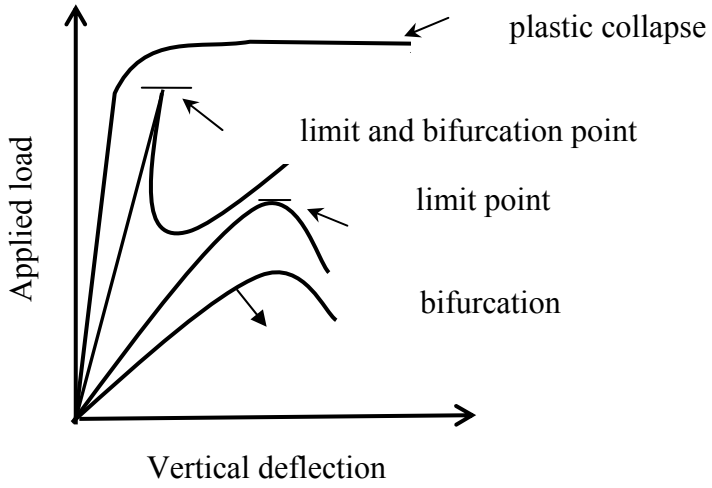

Figure 6.3: Failure criteria used for the geometrically nonlinear elastic analysis

6.4 Behaviour of the bracket supported shell using the GMNA- analysis

6.4.1 Incremental buckling modes

Three different geometries have been chosen here to illustrate the deformations and buckling modes. They were chosen to cover the whole spectrum of possible behaviour. The thickest cylinder with the smaller bracket is most likely to fail close to plastic collapse (r/t=400, Λ=1, Γ=0.25), whereas the thinnest cylinder with the largest bracket (both in height and in width) is more likely to fail close to the failure load seen in the geometrically nonlinear elastic analysis (R_{GNA}) (r/t=1000, Λ=7,

Γ=1.25). The failure behaviour of an intermediate cylinder with intermediate sized bracket will lie between these extremes (r/t=600, Λ=5, Γ=0.75). The incremental buckling modes of these three geometries show great differences (Figure 6.4). The incremental buckling mode is defined as the deformed shape just before buckling subtracted from the deformed shape just after buckling. This incremental deformation is then due to the buckling phenomenon only without the pre-buckling deformations.

The incremental buckling mode of the thickest shell with the smallest bracket (both in height and in width) (Figure 6.4a) is difficult to show since the deformations are dominated by plastic deformations around the bracket. Despite the dominant plastic deformations, the buckling mode can be seen above the bracket (black contour). For the intermediate and the thin cylinders the incremental buckling modes can be easily identified, since no very large plastic deformations occur in the increment just before and just after buckling. The contour plot was therefore omitted. The intermediate cylinder (Figure 6.4b) shows an incremental buckle just above the bracket, whereas the incremental buckle of the thin cylinder is located further away from the bracket (Figure 6.4b). This phenomenon was also seen in the linear bifurcation analysis (LBA).

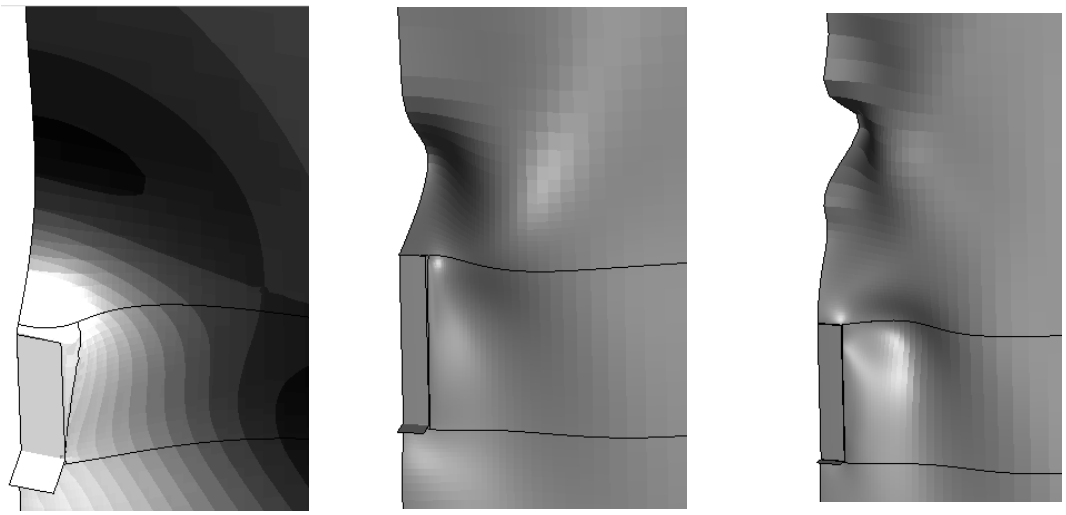

a) Thick cylinder with small bracket (both in height and in width) (r/t=400,Λ=1, Γ=0.25)

b) Medium cylinder with typical bracket (r/t=600,Λ=5, Γ=0.75)

c) Thin cylinder with large bracket (both in height and in width) (r/t=1000,Λ=7, Γ=1.25)

Figure 6.4: Incremental buckling modes for three different geometries

The von Mises stress at a load stage just before buckling shows the relative

importance of plasticity for the different geometries very clearly (Figure 6.5). The cylinder with the r/t-ratio of 400, which is the thickest shell investigated in this chapter (Figure 6.5a), displays yielding in a large area all around the bracket. The extent of the yielded area is less for the cylinder with r/t=600 (Figure 6.5b), especially above the bracket. The thinnest cylinder (r/t=1000) shows yielding just on the corners of the bracket (Figure 6.5c) due to the stress concentration there and underneath the bracket in tension.

The reason for these different yield patterns is that the first points to yield lie at the corners of the bracket due to the stress concentrations there. Even though there are stress concentrations at all four corners of the bracket, the areas around the corners of the bracket do not start to yield at the same time. The bottom corners are the first ones to yield, since the tensile stresses at the bottom are always higher than the compressive stresses on the top of the bracket due to the tensile loading at the bottom of the cylinder. By the same reasoning, the area at the bottom of the bracket starts to yield in tension after the corners, followed by yield in shear at the side of the bracket. The last area around the bracket to yield is the top in compression.

Hence for the thinnest shell (Figure 6.5c), the compressive stress which is required for buckling was reached well before yielding could progress very far.

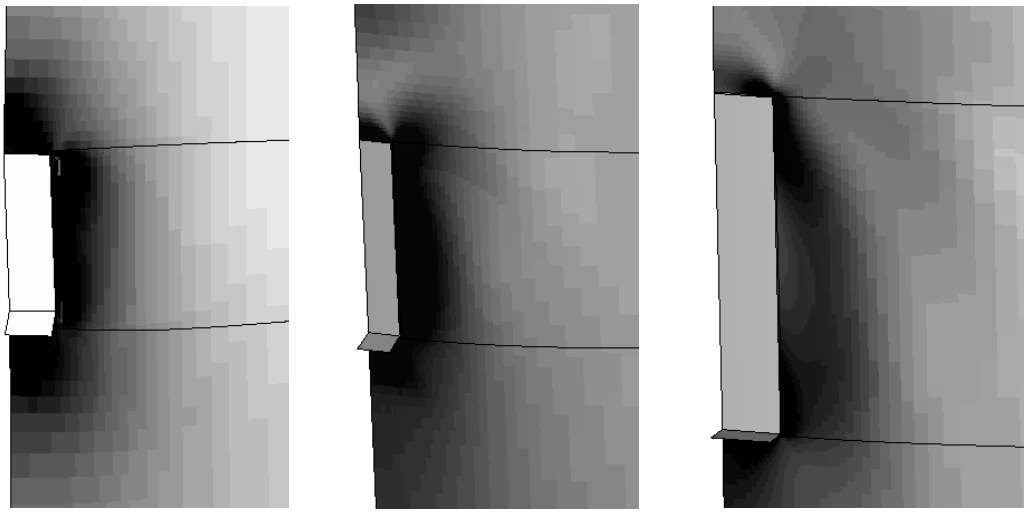

a) Thick cylinder with small bracket (r/t=400,Λ=1, Γ=0.25)

b) Medium cylinder with typical bracket (r/t=600,Λ=5, Γ=0.75)

c) Thin cylinder with large bracket (r/t=1000,Λ=7, Γ=1.25)

Figure 6.5: Von Mises stress distribution at buckling (black contour=yielding)

6.4.2 Load deflection curves and failure loads

Within the scope of this study, three different radius to thickness ratios were investigated (r/t=400, 600 and 1000) to cover the whole spectrum from thick to thin shells.

It was expected that thick shells will tend to fail in a mainly plastic manner (like a stocky column) and thin shells will fail close to elastic nonlinear buckling (like a slender column).

A few representative examples of load deflection curves are shown here, starting with geometries which display a failure load close to the plastic collapse load (Figure 6.18). The applied load is made dimensionless by using the corresponding plastic collapse load MNA) of the same geometry. For all dimensionless heights Λ and the dimensionless width Γ=0.25 of the bracket (Figure 6.6), the thickest shell (r/t=400) reaches its maximum strength very close to the plastic collapse load. By contrast with the materially nonlinear analysis (MNA), the load deflection path does not display an extensive plateau, but exhibits a limit point. When the plastic limit relative slenderness λ_p (described in Section 6.5.2) is compared to the dimensionless slenderness for each geometry (Figure 6.6) it can be seen that all geometries are well within the elastic plastic interaction range, where geometric and material nonlinearity both influence the failure behaviour, even though the failure load is close to the plastic collapse load.

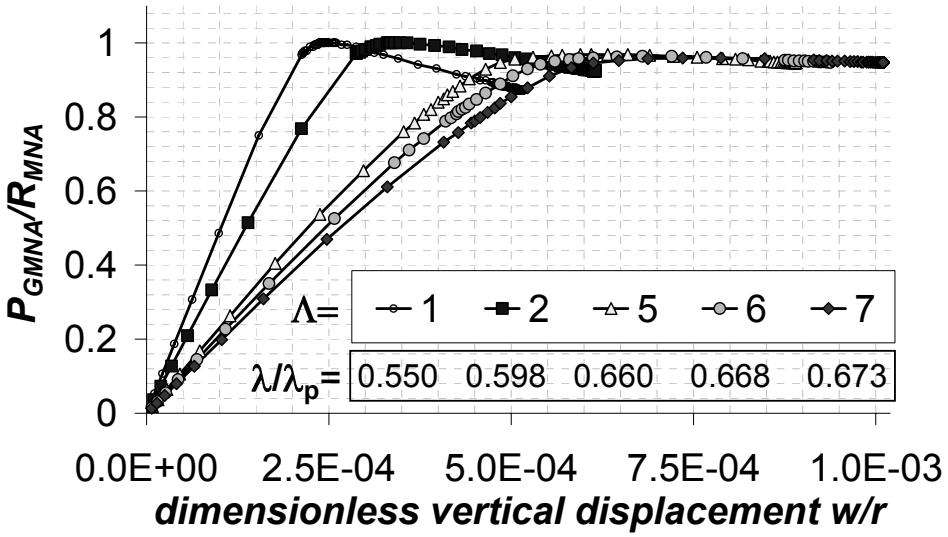

Figure 6.6: GMNA r/t=400, Γ=0.25

For thin shells with a tall bracket (Figure 6.7), the applied load is made dimensionless by dividing it by the failure load from a geometrically nonlinear analysis (GNA). For these cylinders the failure load is very close to the elastic, but nonlinear, buckling load for all the dimensionless widths of the bracket Γ. This is confirmed when the dimensionless slenderness is compared to the plastic limit slenderness λ_p. The slenderness ratio λ/λ_p for these geometries is always around 1.1, which places them clearly in the elastic buckling range.

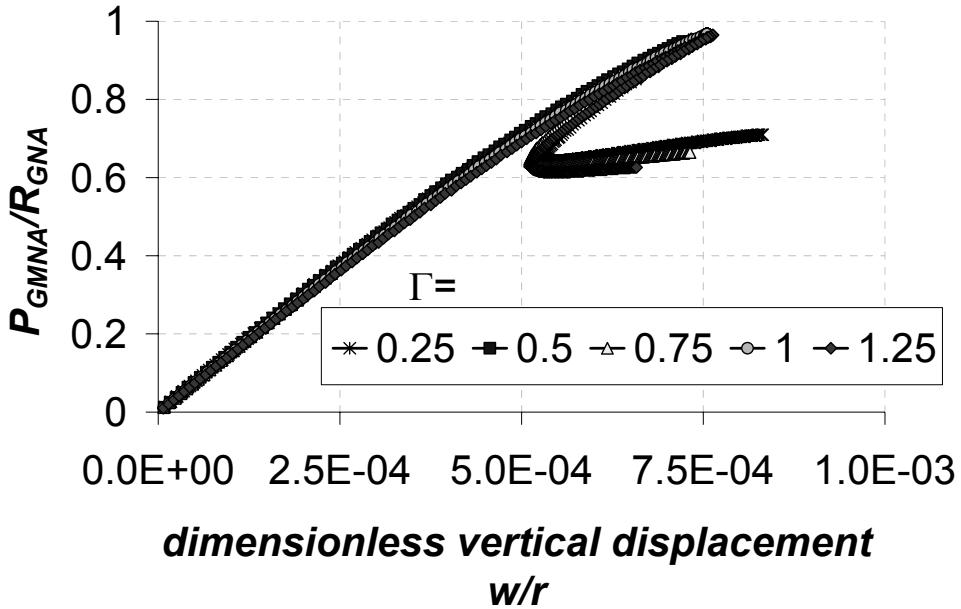

Figure 6.7: r/t=1000, Λ=7

The two cases shown (Figures 6.6 and 6.7) were the two extreme cases in this investigation. The thick shell with a small bracket (both in height and in width) (Figure 6.6) had a failure load close to plastic collapse and the thin shell with a large bracket (both in height and in width) had a failure load close the elastic buckling load (Figure 6.7). The remaining geometries lay between these boundaries.

As an example of the intermediate range, the radius to thickness ratio of 600 was chosen (Figure 6.8).

For the thin and the thick cylinder it was easy to decide what would be the appropriate reference load to make the applied load dimensionless. The decision is not so easy for the intermediate shell, since both plasticity and geometric nonlinearity will play a role in the failure behaviour. Therefore the reference load was here chosen to be

$$R_{REF} = R_{MNA}\left(1-\beta\right) \tag{6.1}$$

where R_{MNA} is the plastic collapse load and β is the plastic range factor. Choosing this reference load has the great advantage that it displays the closeness of the failure behaviour to elastic buckling as well as to plastic collapse. The reference load stands for the load in the interaction curve when elastic buckling stops and plasticity starts to influence the failure behaviour. The value of the plastic range factor β used in this representation is obtained from the interaction curve studies of Section 6.5. Therefore, GMNA failure is in context of the capacity curves in the elastic plastic interaction range if the ratio of the failure load of the GMNA analysis to the reference load is smaller than 1 and in the elastic buckling range if it is larger than 1. For intermediate cylinders, the information on how close they are to elastic buckling is much more useful, especially when also set into context with the plastic limit slenderness λ_p.

The two capacity parameters, plastic range factor β and plastic limit relative slenderness λ_p, are taken from Section 6.5, which has not been shown yet. This sequence has been chosen for a better understanding of the behaviour being shown.

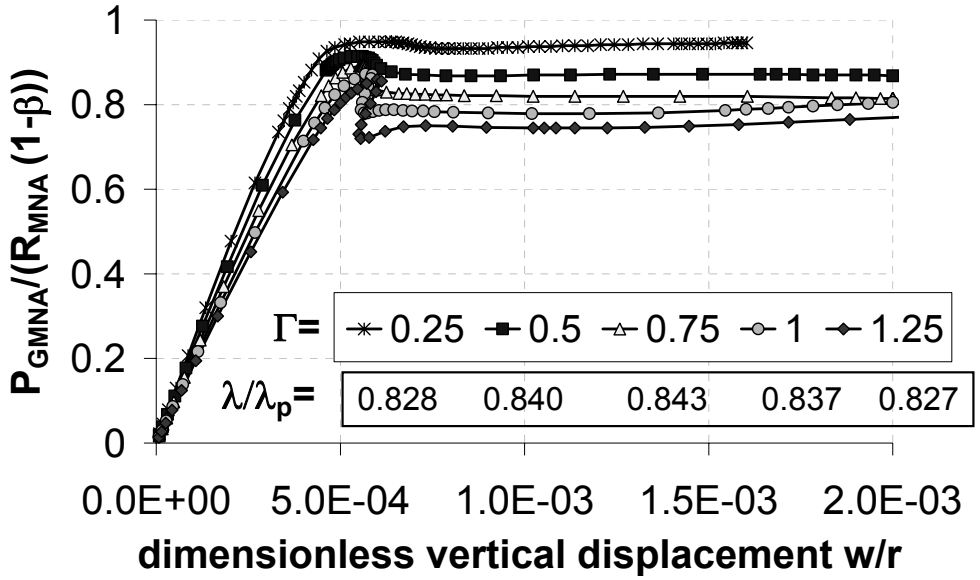

Figure 6.8: GMNA r/t=600, Λ=5

The example geometries in Figure 6.8 all fail by plastic instability at a limit point. The loss of strength after buckling becomes more significant as the bracket becomes wider. It should be noted that the load deflection path becomes very nonlinear and rounded just before buckling, which indicates that plasticity plays a significant role in the behaviour. After buckling a sharp change in the direction of the load deflection path can be observed. This contrasts with the load deflection curves

observed in the geometrically nonlinear elastic analysis (GNA) of Chapter 5

The investigated cylinder and bracket geometries show the same overall behaviour. The failure load increases with the width and the height of the bracket.

This increase can be explained by the larger area of the shell that must be yielded before the limit point is reached when material nonlinearity is dominant.

The reason for the increase in the failure load with the width and the height of the bracket is different when the failure behaviour is dominated by geometric nonlinearity. Part of the load is transferred as shear through the side of the bracket and hence a greater load is needed to achieve sufficient compressive stress above the bracket, which is the cause of buckling for a longer bracket. With increasing width, more load needs to be applied to produce the same compressive stress above the bracket, and hence the buckling load increases.

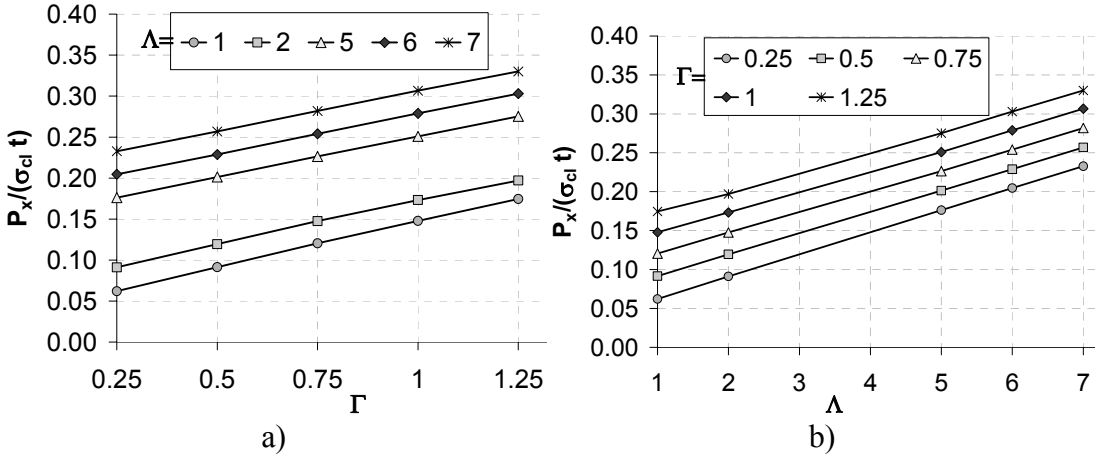

Figure 6.9: Dimensionless failure loads of GMNA analysis (r/t=400)

The failure load of the thickest shell (Figure 6.9) displays an almost linear variation with both the width and the height of the bracket. This is caused by the close similarity to the failure load of the materially nonlinear analysis, which displays a linear relationship over the width as well as the height of the bracket as shown.

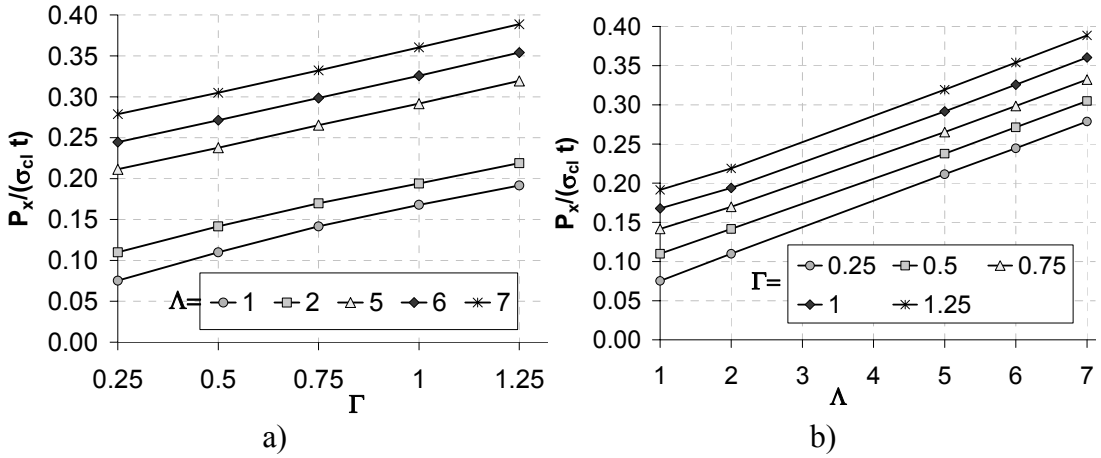

Figure 6.10: Dimensionless failure loads of GMNA analysis (r/t=600)

The variation of the failure load with bracket width becomes more nonlinear for shells with an r/t-ratio of 600 (Figure 6.10). In this case the material and geometrical nonlinearity both strongly affect the failure behaviour.

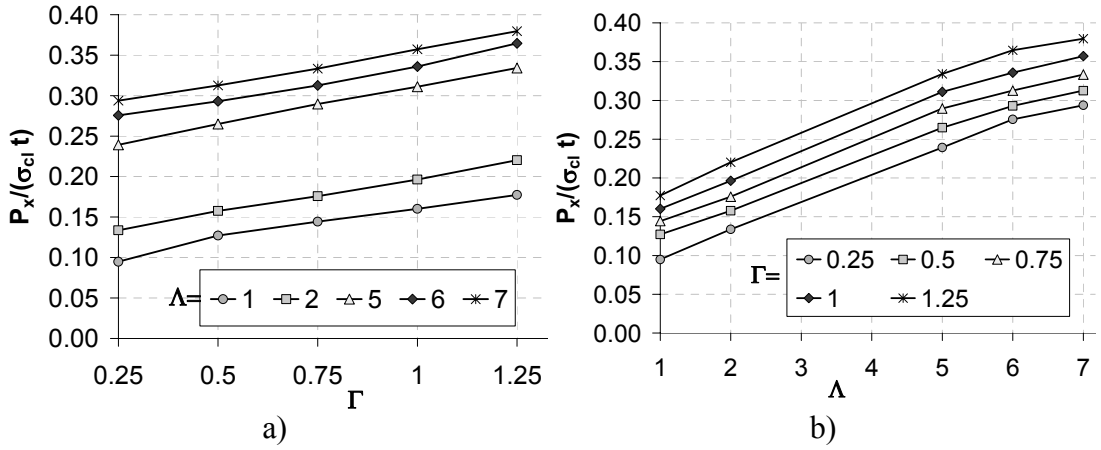

Figure 6.11: Dimensionless failure loads of GMNA analysis (r/t=1000)

The failure load of the thinnest shell (Figure 6.11) shows a nonlinear variation with the bracket width as well as with the height of the bracket since its behaviour is dominated by geometric rather than material nonlinearity.

6.5 Capacity curves of the perfect shell

6.5.1 Introduction

Traditionally a geometrically and materially nonlinear analysis (GMNA) has been seen to give a result close to the "right answer" for a perfect shell. But when the only analysis performed is the geometrically and materially nonlinear analysis

(GMNA) the analysis loses its context within the other analyses, which can define appropriate reference loads. This statement is like saying that the buckling strength of a column should be seen in the context of the yield stress and the Euler buckling stress, and that if it is not, we have difficulty assessing its meaning. Thus other analyses, like the materially nonlinear analysis (MNA), the geometrically nonlinear analysis (GNA) and the linear bifurcation analysis (LBA) are very necessary. The buckling stress of a column loses its usefulness when the yield stress and the slenderness of the column are unknown. Therefore the framework of the EN1993-1-6 (2006) is used here.

6.5.2 Description of a capacity curve

The traditional "column curve", here generalised into a "capacity curve" (Rotter, 2002) is used to set different analysis results into context. It describes the behaviour of a structure from a fully plastic collapse (low slenderness, $\lambda<\lambda_0$) to elastic buckling (high slenderness, $\lambda>\lambda_p$) using the relative slenderness λ of the structure to define where it lies within this interaction curve.

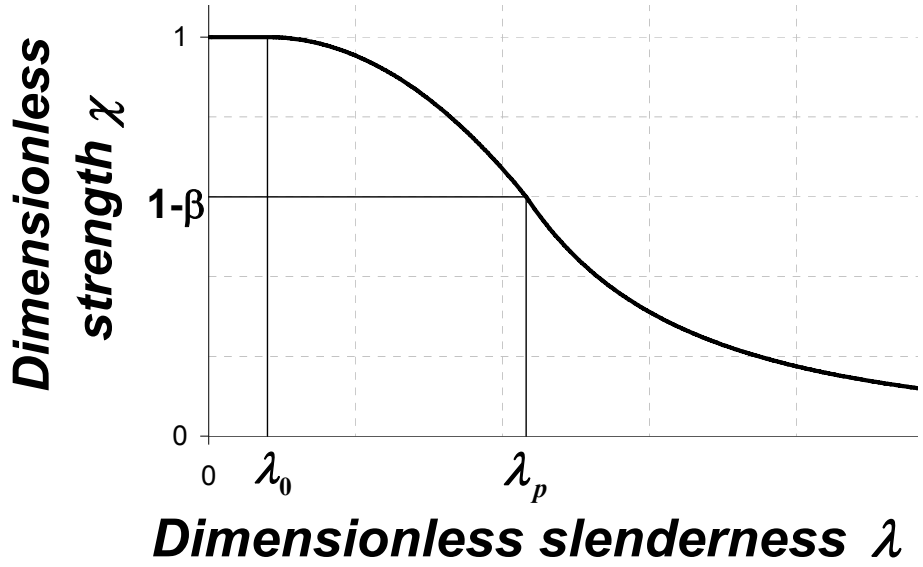

Figure 6.12: General capacity curve

The relative slenderness λ is defined as

$$\lambda = \sqrt{\frac{R_{pl}}{R_{cr}}} \tag{6.2}$$

where R_{pl} is the plastic limit resistance (R_{MNA}) and R_{cr} the elastic critical resistance (R_{LBA}).

The parameter χ is defined by

$$\chi = \frac{R}{R_{pl}} \tag{6.3}$$

Where the resistance R is the failure load calculated in a geometrically and materially nonlinear analysis with or without imperfections ($R_{GMN(I)A}$)

The shape of the capacity curve is described in EN 1993-1-6 (2006) by

$$\chi = 1 \qquad \text{when} \qquad \bar{\lambda} \le \bar{\lambda}_0 \tag{6.4}$$

$$\chi = 1 - \beta \left(\frac{\bar{\lambda} - \bar{\lambda}_0}{\bar{\lambda}_p - \bar{\lambda}_0} \right)^{\eta} \qquad \text{when} \qquad \bar{\lambda}_0 < \bar{\lambda} < \bar{\lambda}_p \tag{6.5}$$

$$\chi = \frac{\alpha}{\bar{\lambda}^2} \qquad \text{when} \qquad \bar{\lambda}_p \le \bar{\lambda} \tag{6.6}$$

with

$$\bar{\lambda}_p = \sqrt{\frac{\alpha}{1-\beta}} \tag{6.7}$$

In the plastic range (Equation 6.4) the failure load of the geometrically and materially nonlinear analysis (GMNA) is equal to the failure load of the materially nonlinear analysis (MNA) with χ=1, so the effect of the geometrical nonlinearity disappears and failure is solely due to material nonlinearity. The parameter λ_0 is the squash limit relative slenderness and defines the changeover between purely plastic behaviour and the elastic plastic interaction range. In the elastic plastic interaction range, starting at λ_0, geometric nonlinearity gains in importance more and more the closer the relative slenderness λ comes to the plastic limit relative slenderness λ_p. The parameter λ_p represents the boundary between elastic plastic buckling and elastic buckling. At this changeover the parameter χ takes the value 1- β, where β is the plastic range factor. The parameter α is the elastic imperfection reduction factor and describes the loss of strength due to geometric nonlinearity and imperfection sensitivity, when imperfections are implemented into the analysis. Since this chapter describes the behaviour of the perfect shell, the parameter α describes only the loss of strength due to geometric nonlinearity.

6.5.3 The modified capacity curve

A serious disadvantage of the traditional capacity curve (Figure 1.22) is that the exact position of the parameter 1- β and α is rather difficult to determine.

An easier extraction of these values (Rotter, 2002) can be achieved when the relative slenderness R_{MNA}/R_{LBA} (x-axis) is replaced by R_{GMNA}/R_{LBA} (Figure 6.13). R_{GMNA}/R_{LBA} can be expressed by rewriting the expression for the elastic buckling range (Equation 6.8) as

$$\chi = \frac{\alpha}{\bar{\lambda}^2} \tag{6.8}$$

with

$$\bar{\lambda}^2 = \frac{R_{MNA}}{R_{LBA}} \tag{6.9}$$

and

$$\chi = \frac{R_{GMNA}}{R_{MNA}} \tag{6.10}$$

and by rearrangement

$$\frac{R_{GMNA}}{R_{LBA}} = \alpha \tag{6.11}$$

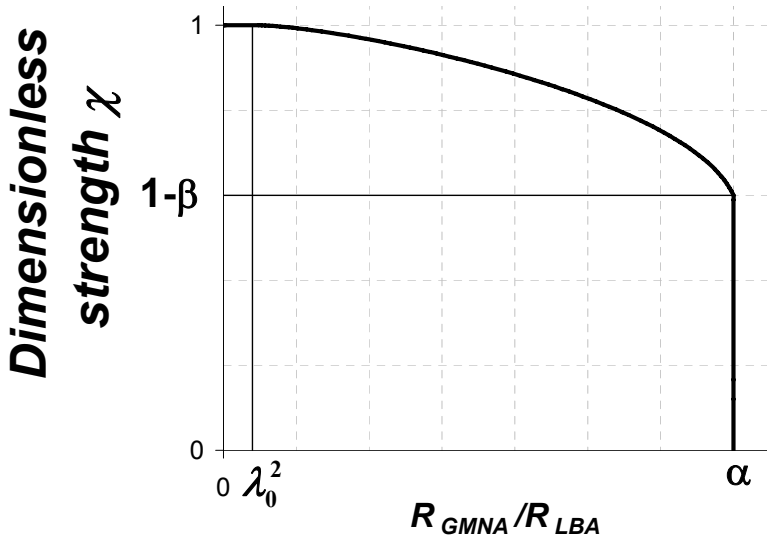

Figure 6.13: Modified capacity curve

The elastic buckling range is then transformed into a vertical line and the parameter α can be extracted easily. The position of the boundary between elastic buckling and elastic plastic interaction is now well defined (Figure 6.13) and the

parameter 1-β, which determines the point where plasticity starts to play a role in the failure behaviour can also now be extracted easily. The modification of the traditional interaction curve was first proposed by Rotter (2002).

6.5.4 Technique to change the dimensionless slenderness

To perform a series of calculations that can define an interaction curve it is necessary to change the dimensionless slenderness λ in order to plot different points in the interaction curve. In traditional structural engineering, the material was assumed to be predefined and the slenderness was changed by changing the geometry, but the dimensionless slenderness can also be varied by changing the yield stress.

When the geometry is changed in order to change the dimensionless slenderness, then it is generally true that both the effects of imperfection sensitivity and of geometric nonlinearity are altered, and therefore it may not be possible to find a unique value of α (Figure 6.14). That is to say, the value of α is likely, in general, to depend on the geometric parameters of the problem, but since it characterises elastic buckling, it cannot depend on the yield stress.

The idea to change the geometry of the structure in order to change the relative slenderness is rooted in research on columns, and for shell structures, research on uniaxially compressed cylinders, which is the most studied example of shell buckling. But this is a misleading example, because the value of α depends, for this special case, only on the slenderness, simply characterised by r/t (Yamaki, 1984). This is illustrated in Figure 14 where the slenderness of the bracket supported cylinder is changed, but clearly the value of α is not constant.

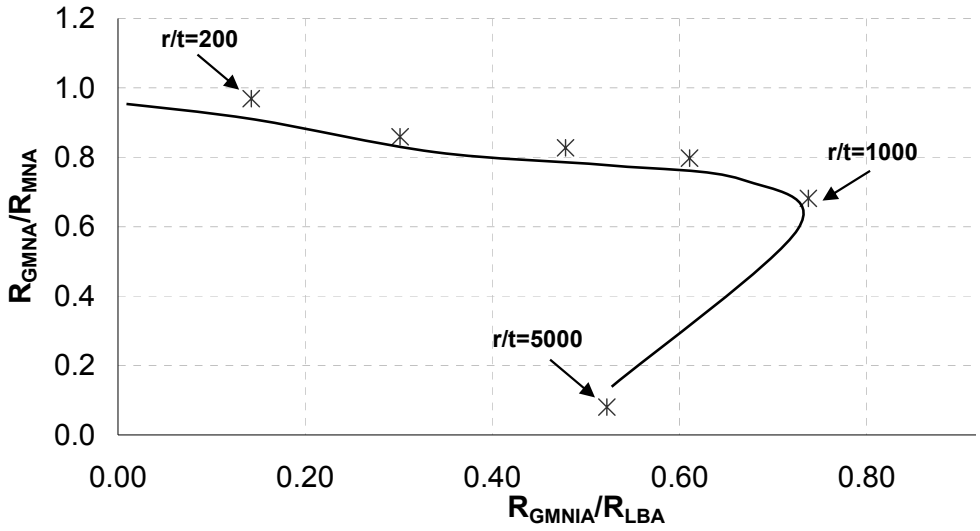

Figure 6.14: Modified capacity curve h/r=0.12, h/d=3 and inward eigenmode imperfection δ/t=2 (Doerich, 2002)

In a more general case, one can expect that the value of α will depend on all geometric parameters and therefore a reliable calculation of the capacity curve will need to keep the geometry constant in order to keep the geometric nonlinearity and imperfection sensitivity constant.

As mentioned before, the geometry can be kept constant and the dimensionless slenderness changed by changing the yield stress even though this may lead at times to a yield stress of unrealistic value. Therefore this technique, first proposed by Rotter (2003), was adopted in this investigation.

6.5.5 Extraction of the value α

The first parameter to be calculated for the use in the interaction curve is the parameter α (Figure 6.13). This parameter describes the loss of strength due to geometric nonlinearity and, where applicable, geometric imperfections. In this chapter only the perfect silo without any geometric imperfections is considered and therefore the parameter α describes the loss of strength due to geometric nonlinearity only. The modified capacity curve was used to extract the parameter and the relative slenderness was changed by changing the yield stress. When the yield stress is increased, the value on the x-axis of the modified capacity curve (R_{GMNA}/R_{LBA}) moves closer to the value α. In the extreme case, when the geometrically and materially nonlinear analysis (GMNA) with infinite yield stress is calculated, material nonlinearity loses all of its influence and only the geometric nonlinearity

remains. This analysis is then the same as the geometrically nonlinear analysis (GNA). Therefore α can be calculated as R_{GMNA}/R_{LBA} for this condition or R_{GNA}/R_{LBA}.

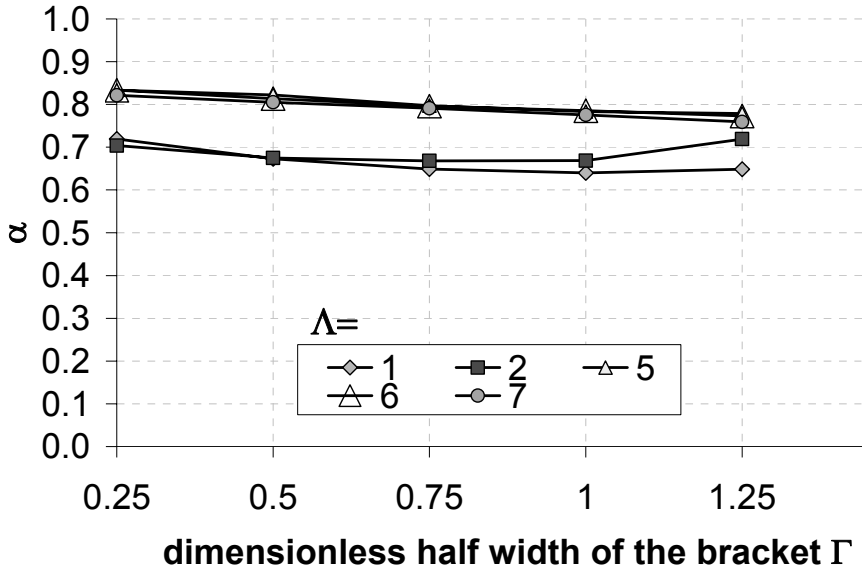

Figure 6.15: $\alpha=R_{GNA}/R_{LBA}$ vs. the dimensionless half width of the bracket Γ (r/t=1000)

For a given radius to thickness ratio, as the height and width of the bracket are changed, the parameter α does not follow any apparent trend (Figures 6.15 and 6.16). This phenomenon was seen in the previous chapter (Chapter 5, figures reprinted here).

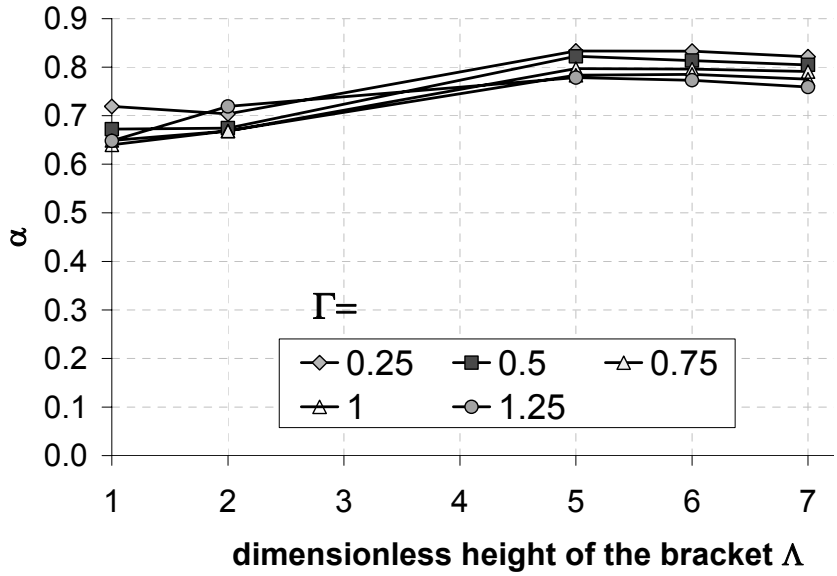

Figure 6.16: $\alpha=R_{GNA}/R_{LBA}$ vs. the dimensionless height of the bracket Λ (r/t=1000)

In the first calculations to explore the value of α for the perfect shells, the

bracket geometries were varied by keeping the ratio h/d constant whilst both h and d were changed. This set of calculations produced the results shown in Figure 6.17, where it can be seen that the value of the parameter α varies in waves.

These results cannot be compared directly with the results of later calculations, where the dimensionless width and height of the bracket were varied independently. Even though the results are not directly comparable, they still demonstrate the unusual variation of α which was seen in Figures 6.15 and 6.16.

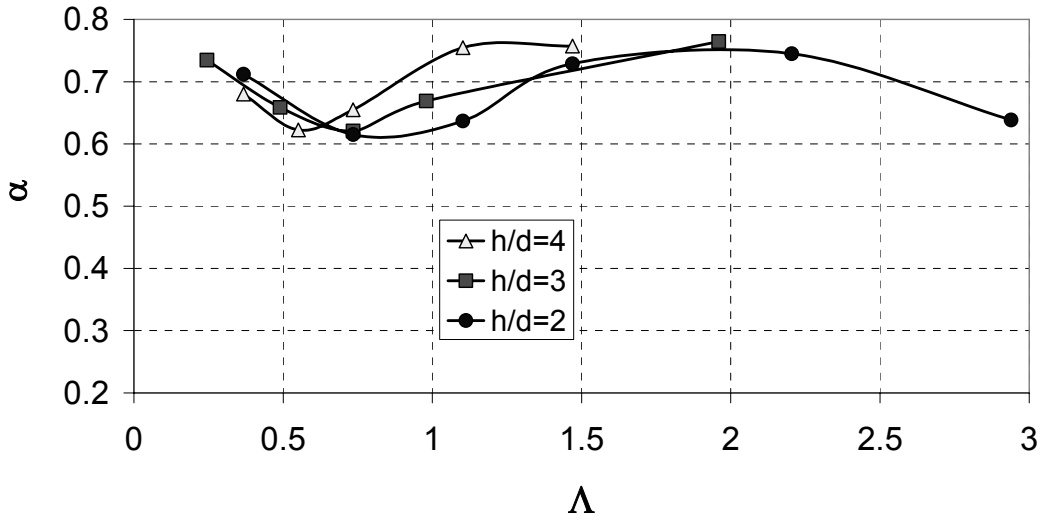

Figure 6.17: Variation of α with the dimensionless height of the bracket

To find a useful approximation for the values of α to put into the capacity curve, a safe estimate had to found. The proposed approximation was to take α as constant over the dimensionless width Γ in the investigated range (Figure 6.15), since it does not change significantly and does not follow any apparent trend. Therefore the lower bound was taken to achieve a safe value for α.

When the parameter α is plotted against the dimensionless height of the bracket Λ (Figure 5.18), the predominant behaviour is that when Λ is increased, α also increases. Therefore the variation of α with Λ was approximated with a linear function. A lower bound was again taken in this case.

This solution is rather unsatisfying, but due to changes in behaviour caused by the geometric nonlinearity, it has not been possible to identify the minimum and maximum of Figures 6.15 and 6.17. Only three r/t-ratios were considered and therefore not enough output was available to approximate any changes with the r/t ratio. It should be noted that the lower bound estimate made here is only valid in the

range of geometries explored in this investigation. Nevertheless the range is considered to cover the practical range.

A lower bound approximation for α can therefore be written as

$$\alpha = g_1 \Lambda + g_2 \tag{6.12}$$

r/t=	400	600	1000
g_1=	0.0144	0.0129	0.0167
g_2=	0.590	0.610	0.623

Table 6.1: Parameters for the approximation of α

6.5.6 Extraction of parameters η and β

6.5.6.1 Capacity curves with constant η

From its original definition (Rotter, 1998a), the parameter η was assumed by default to be constant. For example, all interactions defined in EN1993-1-6 (2006) to date are set as η=1, based on limited experimental data and simple lower bounds. This leads to a safe, but very uneconomical result for a typical bracket (Figure 6.18).

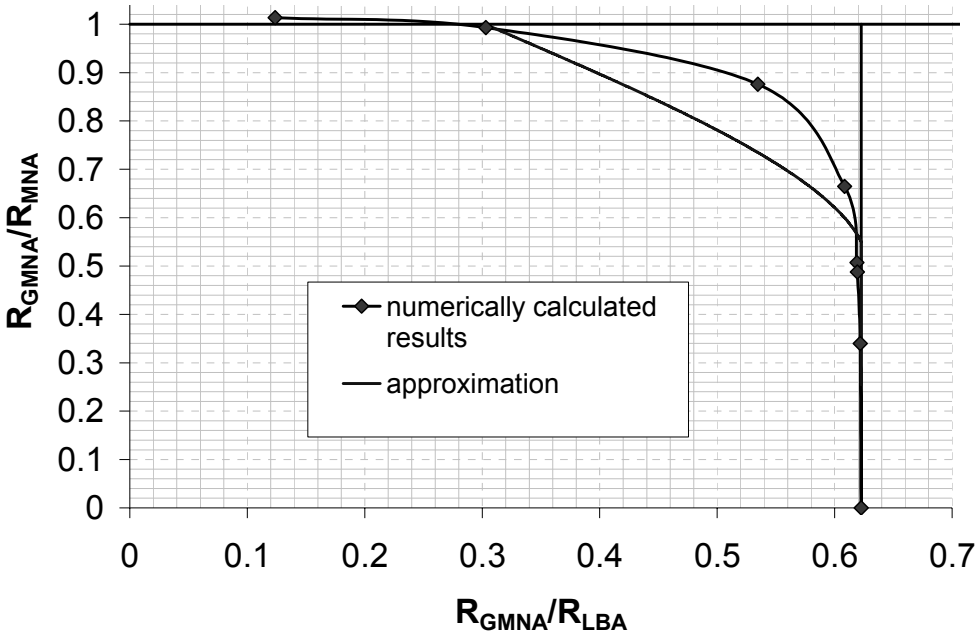

Figure 6.18: Modified capacity curve (r/t=400, Λ=1, d Γ=0.75), η=1.00

The examples shown Figures 6.18, 6.19 and 6.21 have the same geometry with a

radius to thickness ratio of r/t=400, a dimensionless height Λ=1 and a dimensionless width of Γ=0.75. In Figure 6.18, the result of using a fixed value of η=1 is shown. The result becomes more economic when η is taken to be constant but not necessarily equal to one (Figure 6.19).

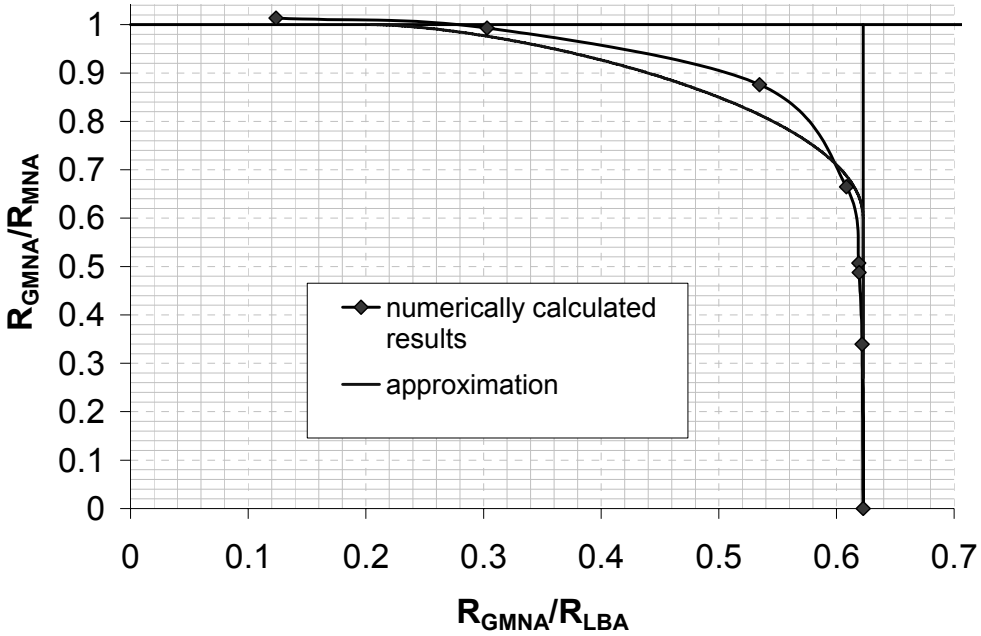

Figure 6.19: Modified capacity curve (r/t=400, Λ =1, Γ=0.75) η=1.68

Even though a constant η (η=1.68 here) results in a better approximation to the numerical results than an approximation with η=1, it will be shown later that a constant value of η also implements a restriction on the minimum value that (1-β) can achieve. This effectively restricts the stress level at which yielding can begin to affect the behaviour to stress levels that are sometimes too high for safe design.

For the constant value η=1 the lowest value for (1-β) that can be achieved may be deduced from the traditional capacity curve (Figure 6.20). The slope of the elastic plastic interaction range cannot be higher than a tangent to the elastic buckling range at λ_p. Therefore the lowest value of (1-β) (Figure 6.20) arises when the slope of the elastic plastic range (Equation 6.13) is equal to the slope of the elastic range (Equation 6.14) at λ_p (Equations 6.13-6.18).

- For η=1

$$\chi'(\lambda) = -\beta \frac{1}{\bar{\lambda}_p - \bar{\lambda}_0} \qquad \text{when} \qquad \bar{\lambda}_0 < \bar{\lambda} < \bar{\lambda}_p \quad (6.13)$$

$$\chi'(\lambda) = \frac{-2\alpha}{\bar{\lambda}^3} \qquad \text{when} \qquad \bar{\lambda}_p \le \bar{\lambda} \tag{6.14}$$

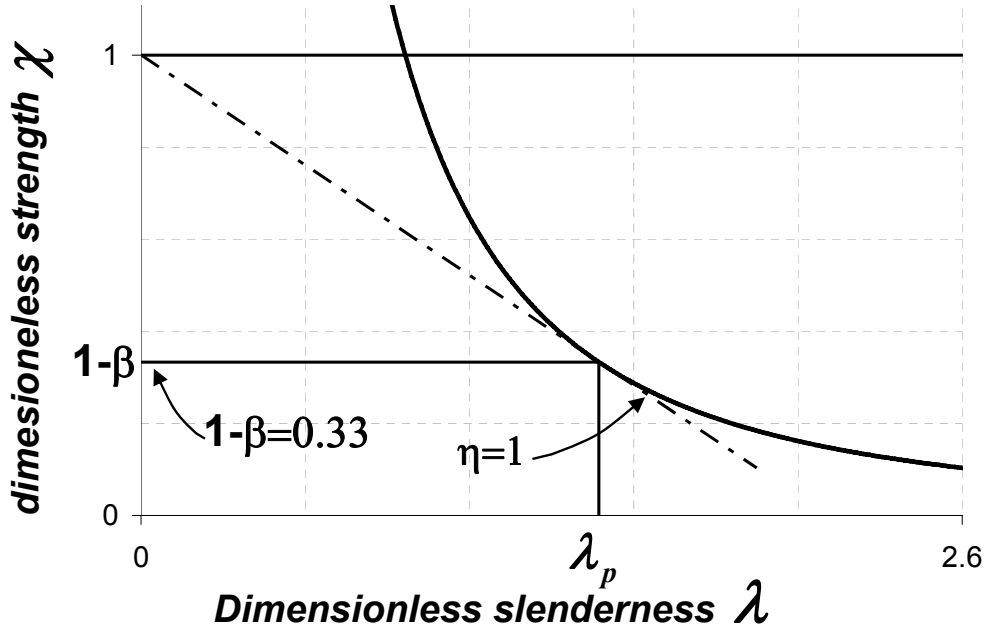

Figure 6.20: minimum 1- β, η =1, λ_0=0

- Therefore in this limiting condition

$$\chi'\left(\lambda_p\right) = -\beta\frac{1}{\bar{\lambda}_p - \bar{\lambda}_0} = \frac{-2\alpha}{\bar{\lambda}_p^3} \tag{6.15}$$

which, on rearrangement gives

$$\beta = \frac{1}{\dfrac{\bar{\lambda}_p}{2\left(\bar{\lambda}_p - \bar{\lambda}_0\right)} + 1} \tag{6.16}$$

The extreme case scenario occurs when the right hand side of the Equation 6.16 reaches its maximum value. This occurs when $\bar{\lambda}_o = 0$ then

$$\beta = \frac{2}{\dfrac{\bar{\lambda}_p}{\bar{\lambda}_p} + 2} \tag{6.17}$$

or

$$\beta = \frac{2}{3} \tag{6.18}$$

Therefore β must be less than 0.667 when $\lambda_0 > 0$ or (1-β) > 0.333 when $\lambda_0 > 0$.

This restriction does not allow for yielding at load levels below 1/3 of the plastic collapse strength of the structure, which could lead to problems when early yielding is important to the failure mechanism. This early yielding must, of course, be

significant enough to influence the collapse or buckling load, so it cannot be a tiny amount of yielding in a small and insignificant corner (like yield at a bolt hole). Most problems in shells or frame structures do not experience such extensive yielding at early stages of the load-deformation path that this restriction affects their performance, but the bracket demonstrates that this idea is not universal.

6.5.7 Capacity curves with η varying linearly with λ

To avoid this restriction on β, it is proposed here that η should be assumed to vary linearly with λ.

$$\chi = 1 - \beta \left(\frac{\bar{\lambda} - \bar{\lambda}_0}{\bar{\lambda}_p - \bar{\lambda}_0} \right)^{\eta(\bar{\lambda})} \qquad \text{when} \qquad \bar{\lambda}_o < \bar{\lambda} < \bar{\lambda}_p \qquad (6.19)$$

with

$$\eta(\lambda) = \frac{\eta_0 \left(\lambda_p - \lambda \right) + \eta_p \left(\lambda - \lambda_0 \right)}{\lambda_p - \lambda_0} \qquad (6.20)$$

The equation has an interaction exponent of η_0 at λ_0 and η_p at λ_p and permits the elastic limit interaction exponent η_p to be smaller than one if necessary. These limiting values of η are hereafter termed the "elastic limit interaction exponent" η_p found at the point where elastic behaviour ends, and the "plastic limit interaction exponent" η_0, where the plastic collapse load is reached.

This equation has the great advantage that it permits 1-β to be smaller than 1/3, corresponding to structural systems in which yield may affect the strength at mean stress levels below 1/3 of the plastic collapse strength.

It also provides a much better fit to many interaction curves for bracket supported shells, as shown in the example that was used above (Figure 6.21).

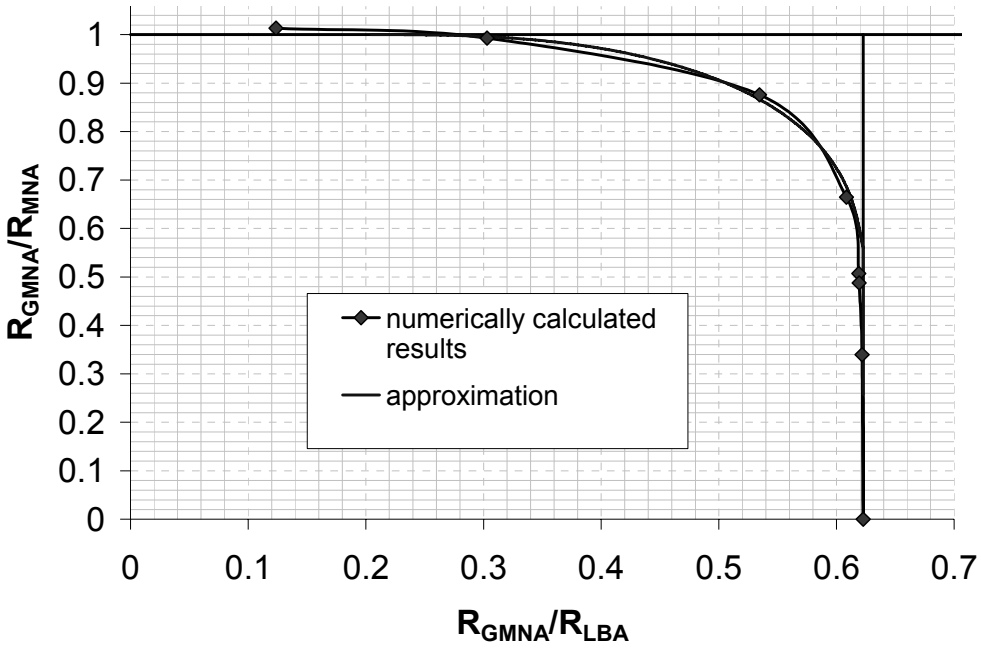

Figure 6.21: Modified capacity curve (r/t=400, Λ =1, Γ=0.75) η varies linearly with λ

However, in order to calculate the capacity curves correctly, a number of restrictions need to be carefully observed.

The slope of the traditional capacity curve in the elastic plastic interaction range has to be smaller than the slope of the elastic-buckling range at the cross-over point λ_p (Figure 6.22). There are also restrictions on the curvature of the elastic plastic interaction range. As a result the first task is to obtain the slope and the curvature of Equation 6.19, when the exponent η is also a function of the dimensionless slenderness λ.

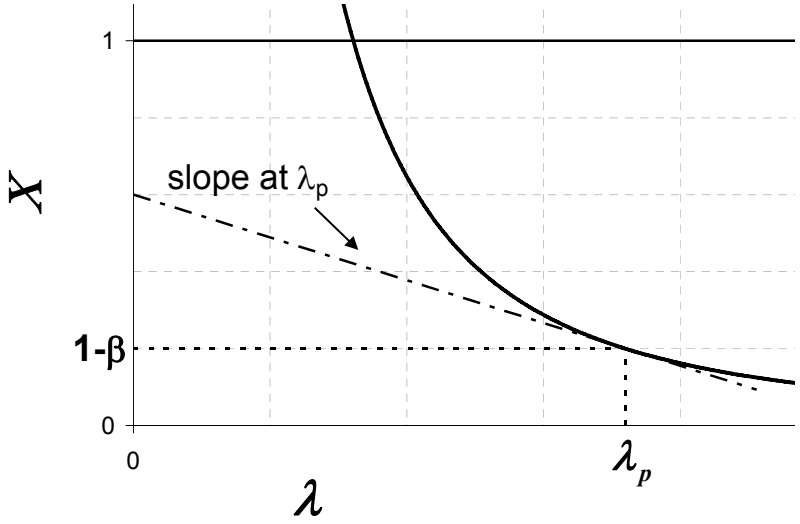

Figure 6.22: restriction of the slope of the elastic plastic interaction range

To calculate the slope and curvature of the elastic plastic interaction range Equation 6.19 is rewritten as

$$\chi(\lambda) = 1 - \beta\, u(\lambda)^{v(\lambda)} \tag{6.21}$$

with

$$u(\lambda) = \left(\frac{\lambda - \lambda_0}{\lambda_p - \lambda_0} \right) \tag{6.22}$$

$$v(\lambda) = \frac{\eta_p \left(\lambda - \lambda_0 \right) + \eta_0 \left(\lambda_p - \lambda \right)}{\left(\lambda_p - \lambda_0 \right)} \tag{6.23}$$

The slope of the elastic plastic interaction range can then be expressed as

$$-\frac{1}{\beta}\chi'(\lambda) = u(\lambda)^{v(\lambda)} \left[v'(\lambda) \ln u(\lambda) + v(\lambda) \frac{u'(\lambda)}{u(\lambda)} \right] \tag{6.24}$$

and the curvature takes the equation

$$-\frac{1}{\beta}\chi''(\lambda) = u(\lambda)^{v(\lambda)} \left[\begin{array}{l} \left(v'(\lambda) \ln u(\lambda) + v(\lambda) \dfrac{u'(\lambda)}{u(\lambda)} \right)^2 \\ + v''(\lambda) \ln u(\lambda) + v'(\lambda) \dfrac{u'(\lambda)}{u(\lambda)} \\ + \dfrac{u(\lambda)\{ v'(\lambda) u'(\lambda) + v(\lambda) u''(\lambda) \} - v(\lambda) u'(\lambda)^2}{u(\lambda)^2} \end{array} \right] \tag{6.25}$$

with

$$u(\lambda) = \left(\frac{\lambda - \lambda_0}{\lambda_p - \lambda_0} \right) \tag{6.26}$$

$$u'(\lambda) = \left(\frac{1}{\lambda_p - \lambda_0} \right) \tag{6.27}$$

$$u''(\lambda) = 0 \tag{6.28}$$

$$v(\lambda) = \frac{\eta_p \left(\lambda - \lambda_0 \right) + \eta_0 \left(\lambda_p - \lambda \right)}{\left(\lambda_p - \lambda_0 \right)} \tag{6.29}$$

$$v'(\lambda) = \frac{1}{\left(\lambda_p - \lambda_0 \right)} \left(\eta_p - \eta_0 \right) \tag{6.30}$$

$$v''(\lambda) = 0 \tag{6.31}$$

At the critical point of interest, $\lambda = \lambda_p$, Equations 6.26-6.31 take the values as

follows

$$u\left(\lambda_p\right)=\left(\frac{\lambda_p-\lambda_0}{\lambda_p-\lambda_0}\right)=1 \tag{6.32}$$

$$u'\left(\lambda_p\right)=\left(\frac{1}{\lambda_p-\lambda_0}\right) \tag{6.33}$$

$$u''\left(\lambda_p\right)=0 \tag{6.34}$$

$$v\left(\lambda_p\right)=\frac{\eta_p\left(\lambda_p-\lambda_0\right)+\eta_0\left(\lambda_p-\lambda_p\right)}{\left(\lambda_p-\lambda_0\right)}=\eta_p \tag{6.35}$$

$$v'\left(\lambda_p\right)=\frac{\eta_p-\eta_0}{\left(\lambda_p-\lambda_0\right)} \tag{6.36}$$

$$v''\left(\lambda_p\right)=0 \tag{6.37}$$

Hence the slope of the elastic plastic curve at $\lambda=\lambda_p$ is given by

$$\chi'\left(\lambda_p\right)=-\beta\left(\frac{\eta_p}{\lambda_p-\lambda_0}\right) \tag{6.38}$$

and the curvature at this point is given by

$$\chi''\left(\lambda_p\right)=\frac{-\beta}{\left(\lambda_p-\lambda_0\right)^2}\left(\eta_p^2+\eta_p-2\eta_0\right) \tag{6.39}$$

After the slope and the curvature of the elastic plastic curve are known, they can be compared with the slope and curvature of the elastic range. The slope of the elastic plastic range must be less negative than the slope of the elastic range. The limiting slope is shown in Figure 6.22, where the slope of the elastic plastic range at λ_p is equal to the slope of the elastic curve.

The slope of the elastic buckling range be written as

$$\chi'(\lambda)=\frac{-2\alpha}{\bar{\lambda}^3} \qquad \text{when} \qquad \bar{\lambda}_p\le\bar{\lambda} \tag{6.40}$$

and at λ_p this becomes

$$\chi'\left(\lambda_p\right)=\frac{-2\alpha}{\bar{\lambda}_p^3} \qquad \text{when} \qquad \bar{\lambda}_p\le\bar{\lambda} \tag{6.41}$$

Therefore the restriction for the limiting slope of the elastic plastic interaction range can be written as

$$-\beta\left(\frac{\eta_p}{\lambda_p-\lambda_0}\right)>\frac{-2\alpha}{\bar{\lambda}_p^3}=\frac{-2(1-\beta)}{\bar{\lambda}_p} \tag{6.42}$$

- or rearranged

$$2\left(\frac{1-\beta}{\beta}\right)\left(\frac{\lambda_p-\lambda_0}{\lambda_p}\right)>\eta_p \tag{6.43}$$

Equation 6.43 gives an important limitation on the highest value of η that may be used at the point of transition from elastic buckling to elastic plastic interaction.

The curvature of the elastic plastic interaction range (equation 6.39 at λ_p) must be restricted in a similar manner as illustrated in Figure 6.23 and Figure 6.24.

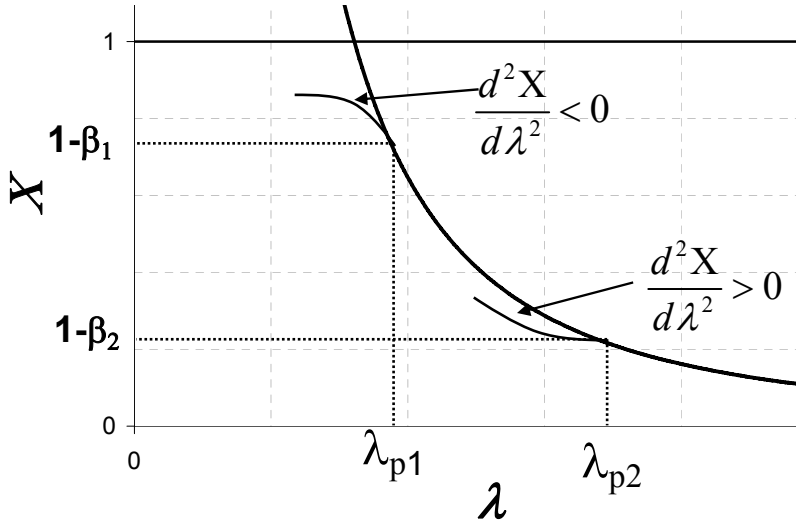

Figure 6.23: Restrictions of the curvature

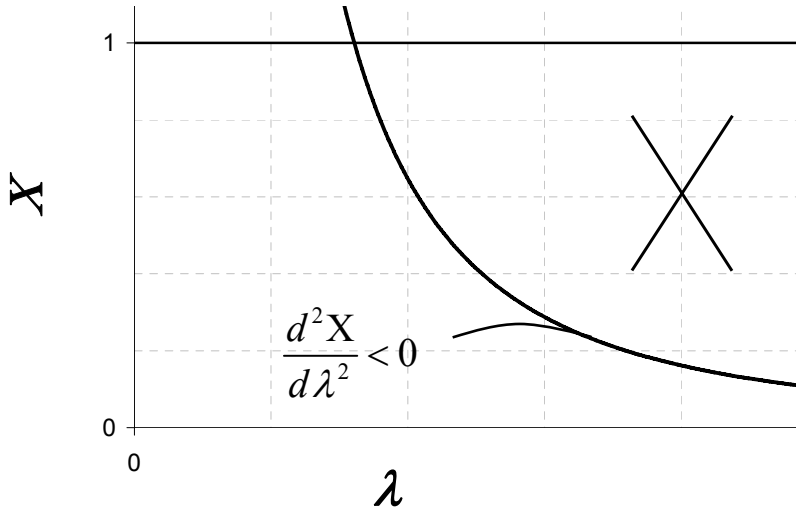

Figure 6.24: Negative curvature at a low 1-β value

The curvature of the elastic plastic interaction range needs to be positive and

smaller than the curvature of the elastic range at λ_p when early plasticity arises. Early plasticity is translated into the capacity curve as small 1-β (1-β_2 in Figure 6.23). A negative curvature at λ_p for small 1-β would lead to the case shown in Figure 6.24, which does not lead to the desired shape of a capacity curve.

For large 1-β (1-β_1 in Figure 6.23) the curvature at λ_p is desired to be negative or at most equal to the curvature of the elastic range.

Therefore since the curvature of the elastic buckling range is always positive with

$$\chi''(\lambda) = \frac{6\alpha}{\bar{\lambda}^4} \qquad \text{when} \qquad \bar{\lambda}_p \le \bar{\lambda} \qquad (6.44)$$

$$\chi''(\lambda_p) = \frac{6\alpha}{\bar{\lambda}_p^4} = \frac{6(1-\beta)}{\bar{\lambda}_p^2} \qquad \text{when} \qquad \bar{\lambda}_p \le \bar{\lambda} \qquad (6.45)$$

$$\chi''(\lambda_p) = \frac{-\beta}{(\lambda_p - \lambda_0)^2}\left(\eta_p^2 + \eta_p - 2\eta_0\right) \qquad \text{when} \qquad \bar{\lambda}_0 < \bar{\lambda} < \bar{\lambda}_p \qquad (6.46)$$

and $\lambda \geq 0$ by definition.

Hence the restriction of the curvature of elastic-plastic-interaction range can be formulated as

$$\frac{-\beta}{(\lambda_p - \lambda_0)^2}\left(\eta_p^2 + \eta_p - 2\eta_0\right) < \frac{6\alpha}{\bar{\lambda}_p^4} = \frac{6(1-\beta)}{\bar{\lambda}_p^2} \qquad (6.47)$$

or by rearrangement

$$2\eta_0 - \eta_p(1+\eta_p) - 6\left[\frac{1-\beta}{\beta}\right]\left\{1 - \frac{\lambda_0}{\lambda_p}\right\}^2 < 0 \qquad (6.48)$$

with the additional restriction that for small 1-β the curvature of the elastic plastic range should be positive at λ_p (Equation 6.49)

$$\frac{-\beta}{(\lambda_p - \lambda_0)^2}\left(\eta_p^2 + \eta_p - 2\eta_0\right) > 0 \qquad (6.49)$$

Positive curvature for small 1-β can be assured in the same manner using Equation 6.49 and the restriction can then be written as

$$2\eta_0 - \eta_p^2 - \eta_p > 0 \qquad (6.50)$$

Equation 6.50 has not been used in this investigation since the values of 1-β

were all larger than 1/3 (i.e. yielding affected the global failure load at values less than 1/3 of the plastic collapse load), but it has been included for completeness.

6.5.8 Examples of capacity curves

After identifying requirements for the general shape of a capacity curve, a closer look is taken here at the capacity curves of this investigation using examples to illustrate the general pattern. The full set of capacity curves can be found in the Appendix (Chapter 10.2-10.4)

Two distinct shapes can be observed in the capacity curves of this investigation depending on the height of the bracket.

The modified interaction curve for short brackets (Λ=1 and 2) displays a rounded shape with an extensive elastic plastic interaction zone as illustrated in the example with the geometry r/t=1000, Λ=1 Γ=1 (Figure 6.25). In this case, plasticity starts to influence the failure load at an early stage and continues to influence the failure in very smooth manner towards the plastic collapse.

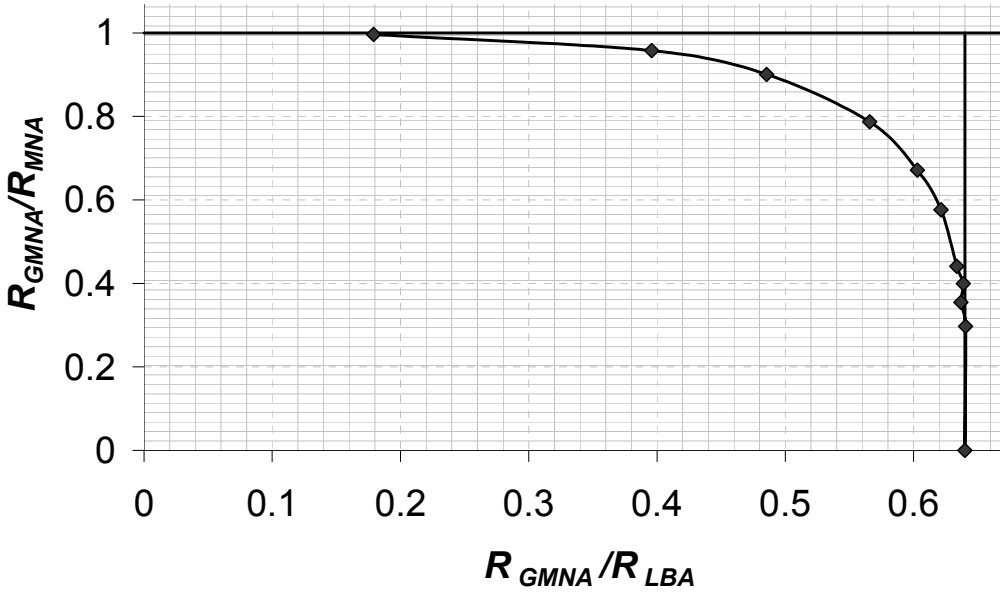

Figure 6.25: Modified capacity curve (r/t=1000, Λ =1, Γ =1)

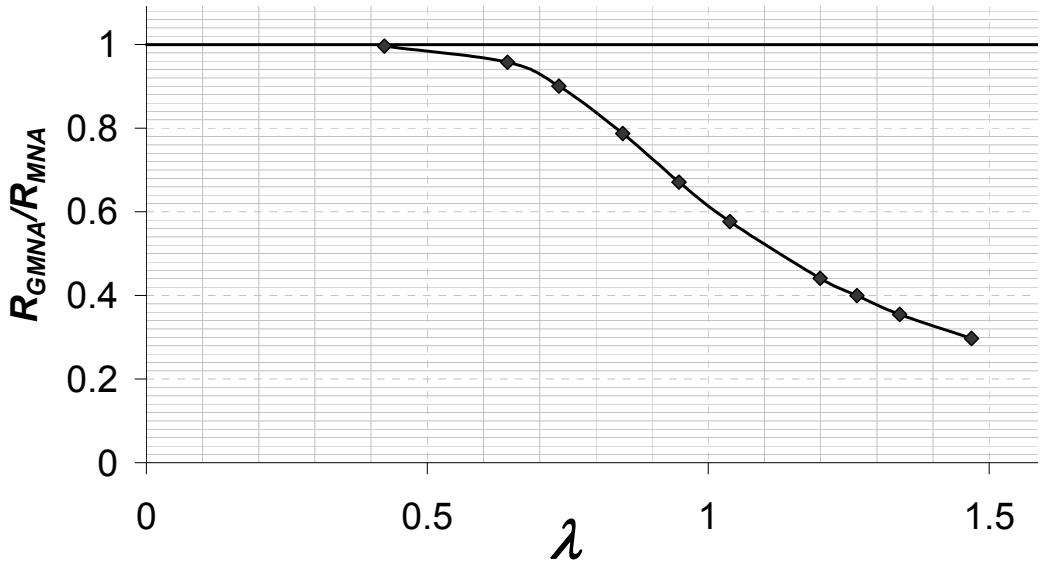

Figure 6.26: Traditional capacity curve (r/t=1000, Λ =1, Γ =1)

Taller brackets (Λ = 5, 6 and 7) display a rather different shape (Figure 6.27, example geometry: r/t=1000, Λ =7, Γ=1.25).

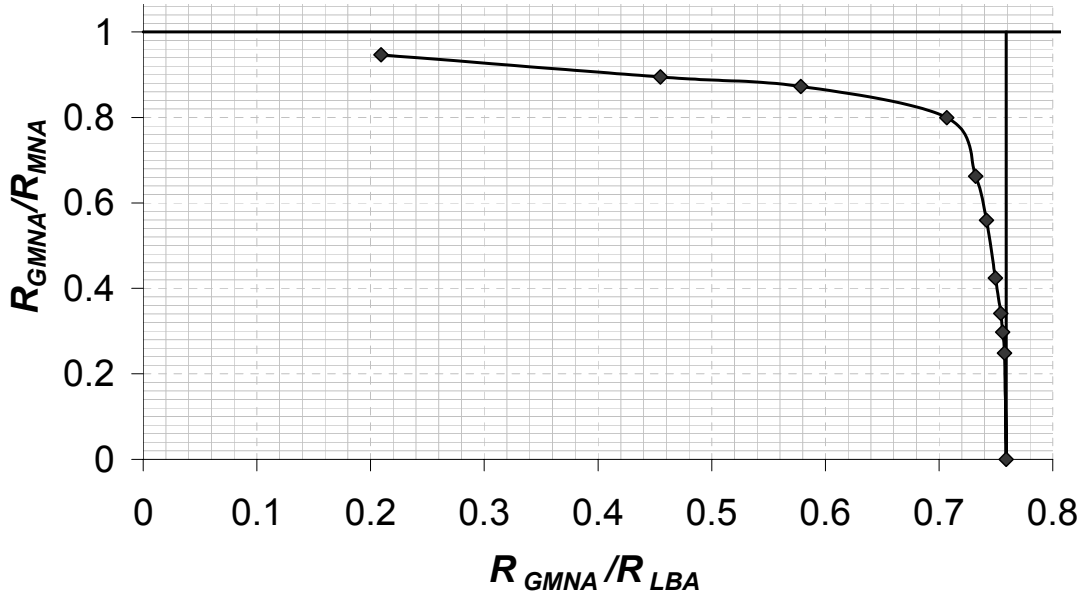

Figure 6.27: Modified capacity curve (r/t=1000, Λ =7, Γ=1.25)

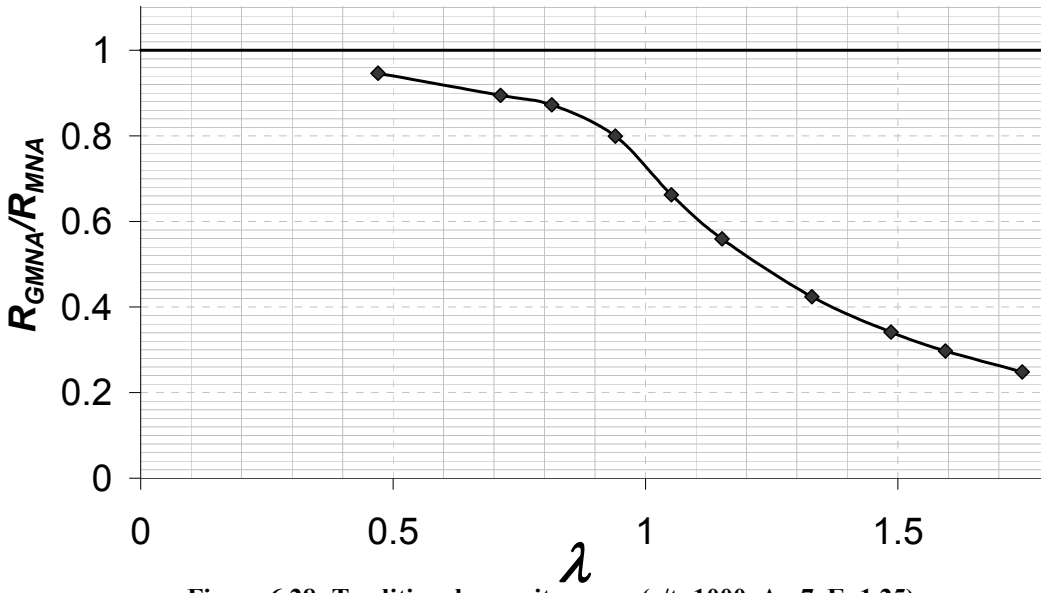

Figure 6.28: Traditional capacity curve (r/t=1000, Λ =7, Γ=1.25)

The influence of plasticity starts at a rather low value of 1-β (high plastic range factor β), but does not increase its influence in the manner seen in Figure 6.25, but stays in close proximity to the elastic buckling value (vertical line) until a value of $\chi \approx 0.7$. Then a rapid transformation of the response can be observed at around $\chi \approx 0.8$ (Figure 6.27) from an almost elastic to an almost plastic response, but the plastic collapse load is only approached very slowly ($\chi \approx 1$).

This capacity curve also shows that, at a value of strength of about 80% of the plastic collapse load ($\chi=0.8$), the failure load can still be very close to elastic buckling. This is an example where the true importance of the capacity curve can be shown. One would think that when the structure displays a strength reasonably close to the plastic collapse load, the failure mechanism would be close to a plastic collapse or at least well into the elastic plastic interaction zone, away from elastic buckling. But capacity curves reveal the true behaviour of the structure, which is here almost elastic buckling failure.

While the modified capacity curves (Figures 6.25 and 6.27) show the behaviour discussed above very clearly, the corresponding traditional capacity curves (Figures 6.26 and 6.28) look rather similar and no such description of the behaviour can be made.

6.5.9 Approximation of the parameters α, β, η_0 and η_p

To approximate the values of the parameters α, β, η_0 and η_p a best fit (using a least squares procedure) was performed for every investigated geometry. The squash limit slenderness λ_0 was considered to be zero, since no hardening was introduced into the model and therefore the failure load of the geometrically and materially nonlinear analysis (GMNA) does not rise above the plastic collapse load as this shell configuration does not exhibit geometric hardening (Rotter, 2005).

The resulting parameters were then plotted against the dimensionless width of the bracket Γ. A choice was then made for an approximating function that would result in an appropriate fit over Γ. The constants found in this approximation were then plotted against the dimensionless height of the bracket Λ and an appropriate function of Λ was sought. A short description of this approximation will be given using the radius to thickness ratio of 600 as an example. The other two r/t ratios (r/t=400 and 1000) were treated in a similar manner.

First, the best fit for each geometry (each Γ and each Λ) was performed (Figures 6.29 and 6.30).

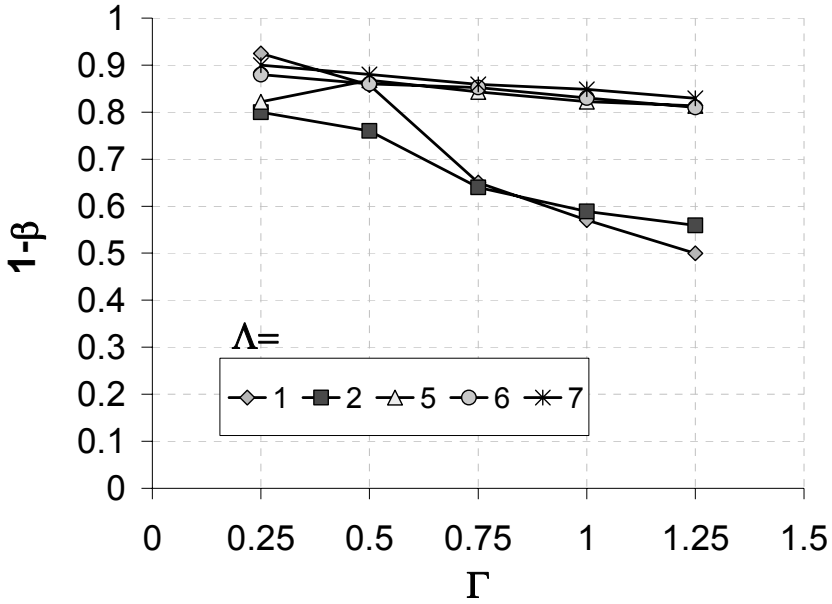

Figure 6.29: Values of 1-β for best fit for each of the geometries (r/t=600)

By inspection (Figure 6.29), the parameter 1-β follows an approximately linear variation with the dimensionless width of the bracket Γ. Hence a linear variation was used to approximate 1-β over Γ (Equation 6.51).

$$1-\beta = a\left(\Lambda, r/t\right)\Gamma + b\left(\Lambda, r/t\right) \tag{6.51}$$

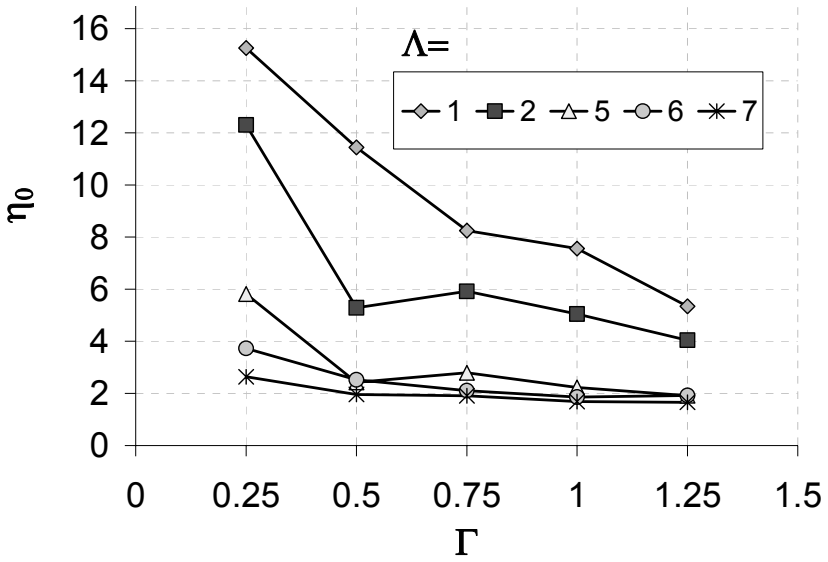

Figure 6.30: Values of η_0 for best fit for each of the geometries (r/t=600)

In a similar manner, the variation of the plastic limit interaction exponent η_0 (Figure 6.30) could also be approximated with linear function. Therefore the decision was made to use a linear function once again to describe the variation of η_0 (Equation 6.52).

$$\eta_0 = e(\Lambda, r/t)\Gamma + f(\Lambda, r/t) \tag{6.52}$$

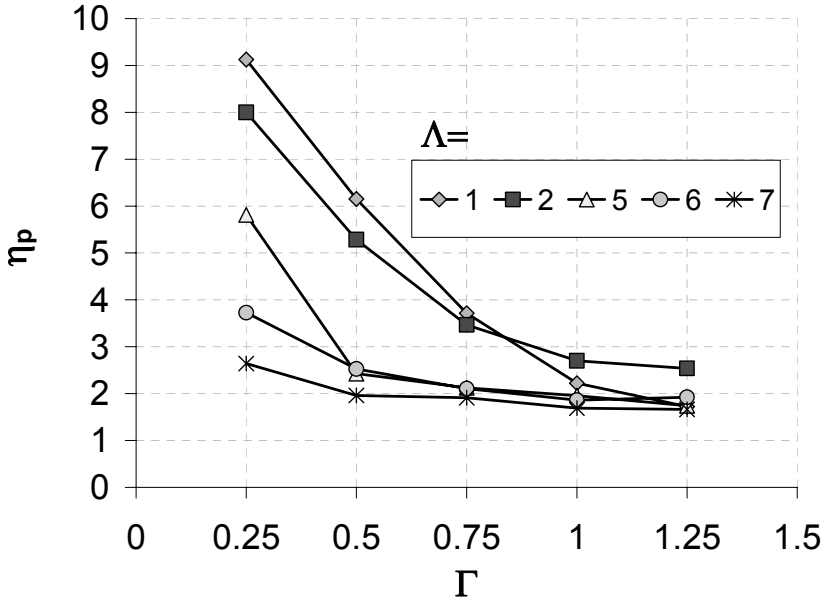

Figure 6.31: Values of η_p for best fit for each of the geometries (r/t=600)

When the best fit for each geometry was performed (Figure 6.31), it was not clear what kind of function to choose for the variation of the elastic limit buckling interaction exponent η_p with Γ, even though an exponential function might approximate the variation of η_p with Γ reasonably well (Figure 6.31). Therefore a

best fit calculation was repeated for the plastic interaction exponent η_p for each geometry, but adopting the chosen linear functions for 1-β and η_0 that describe the variation with the dimensionless width of the bracket Γ. The resulting variation of η_p with Γ (Figure 6.32) then came quite close to a linear variation (Equation 6.53).

$$\eta_p = c(\Lambda, r/t)\Gamma + d(\Lambda, r/t) \tag{6.53}$$

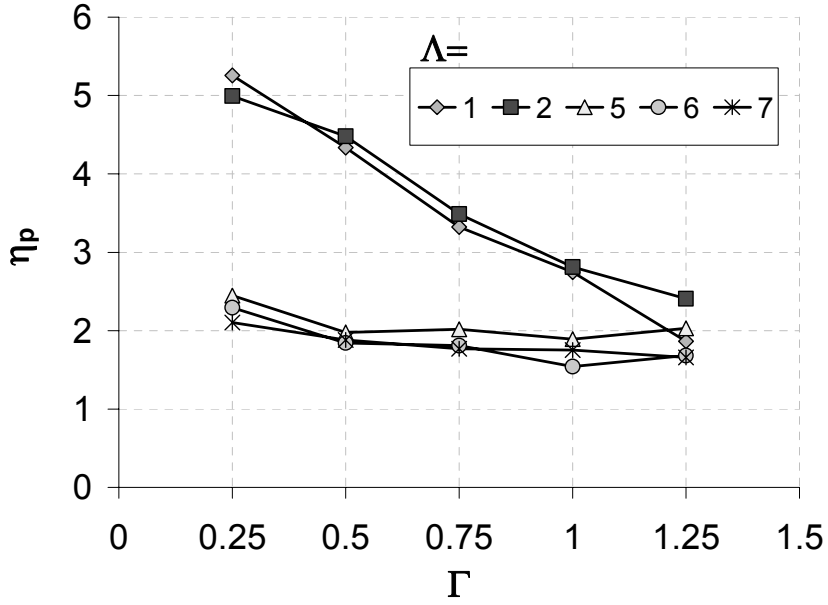

Figure 6.32: Values of η_p for best fit for each of the geometries (r/t=600) after fit of 1-βand η_0

The approximation of the parameters 1-β, η_0 and η_p with the dimensionless width of the bracket Γ can now be summarised as:

$$1-\beta = a(\Lambda, r/t)\Gamma + b(\Lambda, r/t) \tag{6.54}$$

$$\eta_p = c(\Lambda, r/t)\Gamma + d(\Lambda, r/t) \tag{6.55}$$

$$\eta_0 = e(\Lambda, r/t)\Gamma + f(\Lambda, r/t) \tag{6.56}$$

The parameters *a, b, c, d, e* and *f* depend now only the dimensionless height of the bracket Λ and the radius to thickness ratio r/t. The parameters *a-f* were then each plotted against the dimensionless height of the bracket Λ (Figures 6.33 to 6.36).

To approximate the parameters *a-f,* decisions on which functions to choose were made step by step. First, all of the parameters were inspected and the ones that follow most closely a simple pattern were chosen for the first fit. In this case these were the parameters *a* and *b* (Figures 6.33 and 6.34), which followed a linear function reasonably closely. After these functions were chosen, another least square fit on the original data was performed incorporating the linear approximation for parameters

the *a* and *b*, but the remaining parameters *c-f* were free to change.

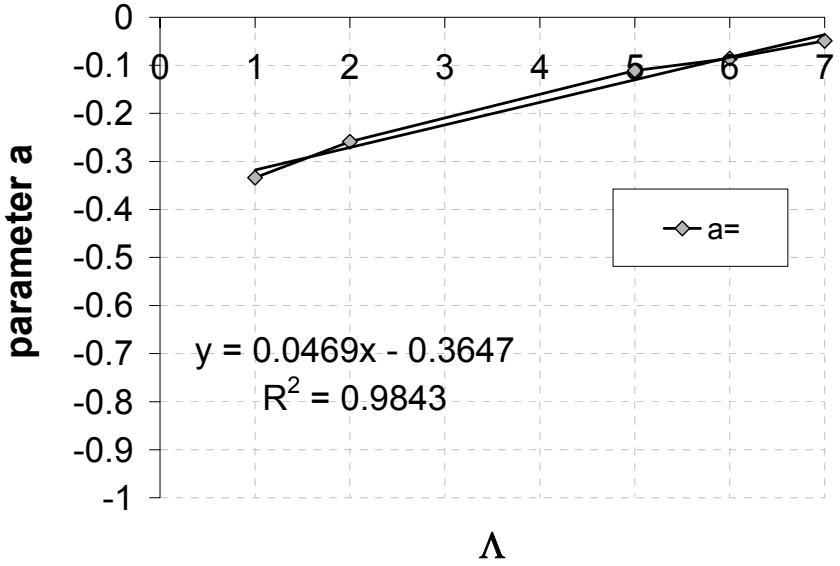

Figure 6.33: Variation of parameter *a* with Λ

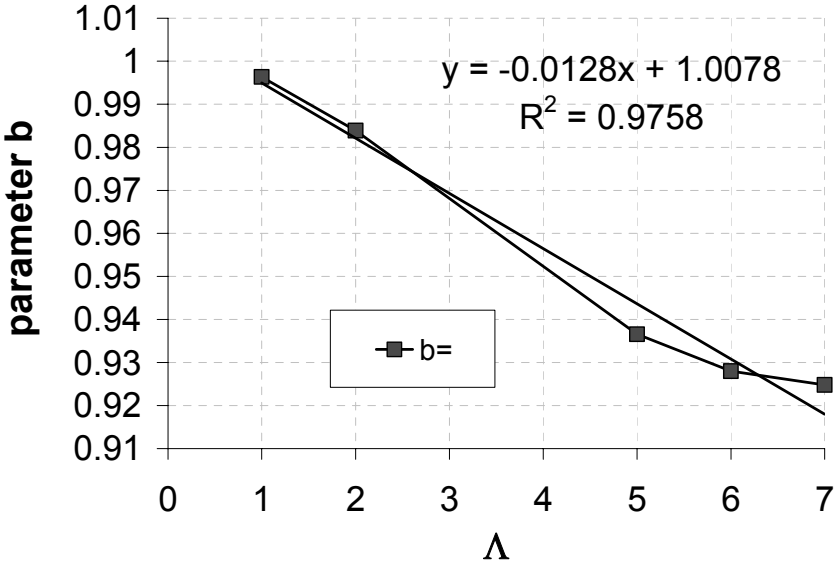

Figure 6.34: Variation of parameter *b* with Λ

After the initial fit of parameters *a* and *b* to linear functions, parameters *d* and *e* were chosen for the next fit. Both parameters followed a linear function reasonably closely and were therefore approximated to a straight line.

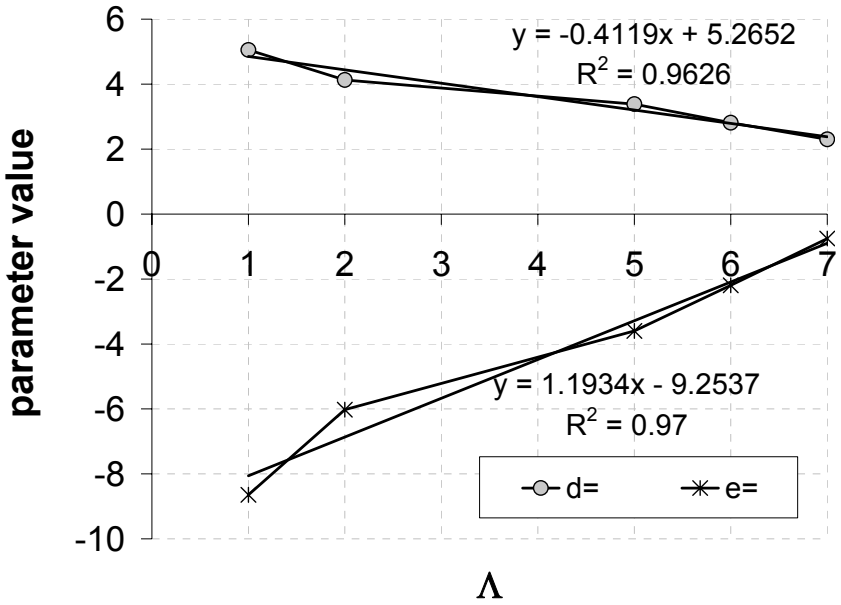

Figure 6.35: Variation of parameters *d* and *e* with Λ

The last two parameters *c* and *f* were analysed after another fit using the linear functions for *a*, *b*, *d* and *e*, but leaving the last two parameters *c* and *f* free to change. The variation of these parameters with the dimensionless height of the bracket Λ was once again very close to a linear function (Figure 6.36).

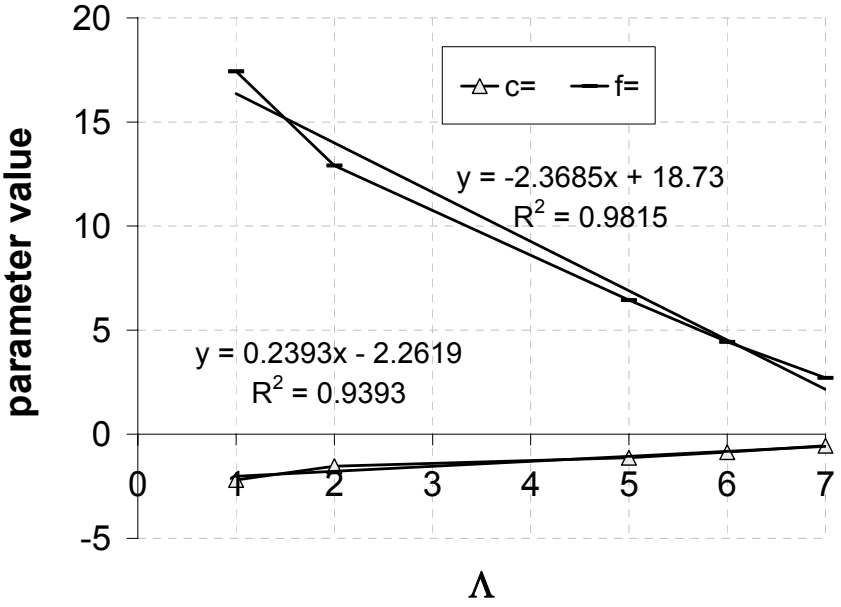

Figure 6.36: Variation of parameters *c* and *f* with Λ

The radius to thickness ratios of 400 and 1000 followed very similar behaviour to that described for r/t=600.

After all this careful fitting and choosing of functional forms, the final parameters needed for a capacity curve can be expressed as:

$$1-\beta=\left(a_1\Lambda+a_2\right)\Gamma+b_1\Lambda+1 \tag{6.57}$$

$$\eta_p=\left(c_1\Lambda+c_2\right)\Gamma+d_1\Lambda+d_2 \tag{6.58}$$

$$\eta_0=\left(e_1\Lambda+e_2\right)\Gamma+f_1\Lambda+f_2 \tag{6.59}$$

$$\alpha=g_1\Lambda+g_2 \tag{6.60}$$

r/t=	400	600	1000
a_1=	0.0365	0.0355	0.0385
a_2=	-0.301	-0.308	-0.330
b_1=	-0.0187	-0.0133	-0.0140
b_2=	1.00	1.00	1.00
c_1=	0.345	0.342	0.310
c_2	-2.94	-2.93	-2.72
d_1=	-0.443	-0.442	-0.404
d_2=	5.45	5.50	5.27
e_1=	1.38	1.37	1.53
e_2=	-10.22	-10.33	-11.26
f_1=	-2.55	-2.55	-2.76
f_2=	20.20	20.52	21.80
g_1=	0.0144	0.0129	0.0167
g_2=	0.590	0.610	0.623

Table 6.2: Parameters for the approximation of capacity curves

It should be noted that the values are very similar for all the r/t-ratios investigated (Table 6.2). With more data it may be possible to find values of the parameters which can be kept constant for any r/t-ratio, but due to the limited range of radius to thickness ratios, the conclusion here must be provisional. To achieve a reasonably accurate, but conservative, description of all the 75 capacity curves calculated (over 750 GMNA calculations), the following values are recommended for future use in design calculations:

a_1=	0.0352
a_2=	-0.308
b_1=	-0.0165
b_2=	1.026
c_1=	0.00604
$c_{2=}$	-0.401
d_1=	-0.216
d_2=	3.56
e_1=	2.348
e_2=	-17.4
f_1=	-3.55
f_2=	27.3
g_1=	0.013
g_2=	0.590

Table 6.3: Capacity curve parameters for 400<r/t<1000, 1<Λ<7, 025<Γ<1.25

The two cases of the maximum discrepancy between approximation and numerical calculation using the parameters from Table 6.3 on the safe and on the unsafe side are shown (Figures 6.38 to 6.41).

When the frequency of occurrence of each error is examined (Figure 6.37), it can be clearly seen that an error close to zero is most frequent. The maximum error on the unsafe side is a single occurrence and therefore might be safely ignored. Because a lower bound approach has been chosen for the choice of the value of α, the histogram is skewed to the safe side. Also the maximum error on the safe side, which is of the order of 23-24%, has only a few occurrences. The mean error of the distribution is 6.16% and the standard deviation is 6.82%. These seem to give remarkably good quality predictions for the strengths of this wide range of structural geometries, failing in a range of different ways from purely elastic through to perfectly plastic manners.

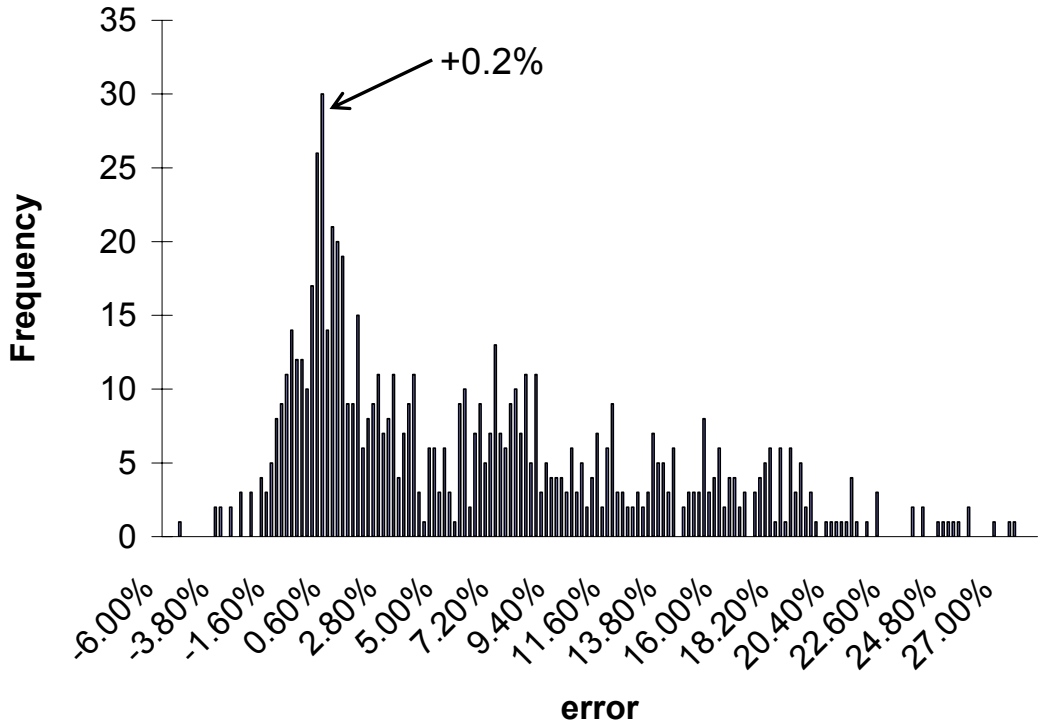

Figure 6.37: Histogram of the frequency of each error

The encountered error using this approximation is mostly on the safe side. This is a result of the lower bound approximation taken for the value of α, as discussed before, and also the lower bound approach taken to derive the parameters in Table 6.3. The maximum error for the value of α is 27.24% (Figures 6.38 and 6.39). This is a rather unsatisfying result, but due to the wave-like variation of α no better functional choice for a lower bound approximation could be found and also due to the limited range of r/t-ratios investigated, no other approximation could be chosen than a lower bound.

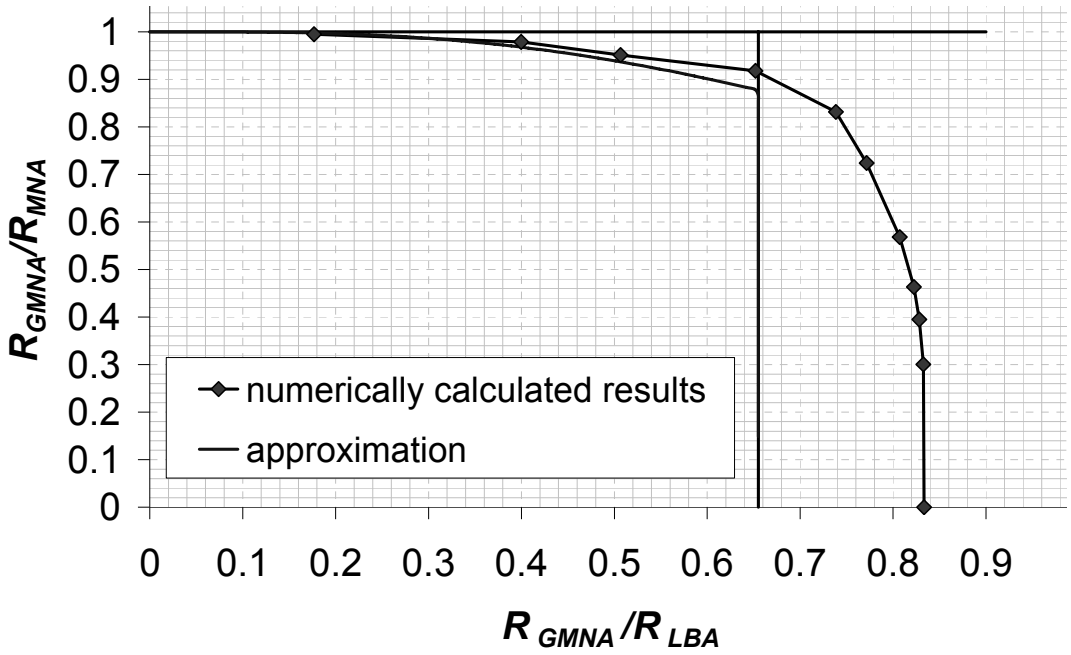

Figure 6.38: Modified capacity curve (r/t=1000, Λ =5, Γ=0.25); maximum error on the safe side

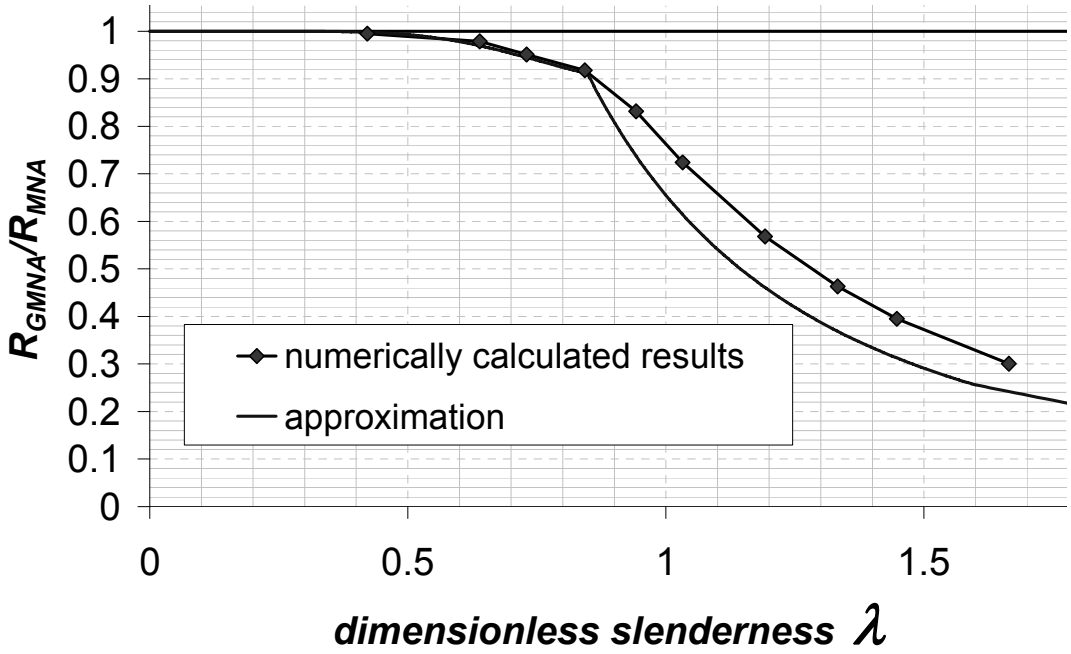

Figure 6.39: Traditional capacity curve (r/t=1000, Λ =5, Γ=0.25); maximum error on the safe side

The maximum error on the unsafe side occurs in the corner between the elastic-plastic interaction range and elastic range for a few geometries only. The maximum error on the unsafe side is 5.56% (Figures 6.40 and 6.41).

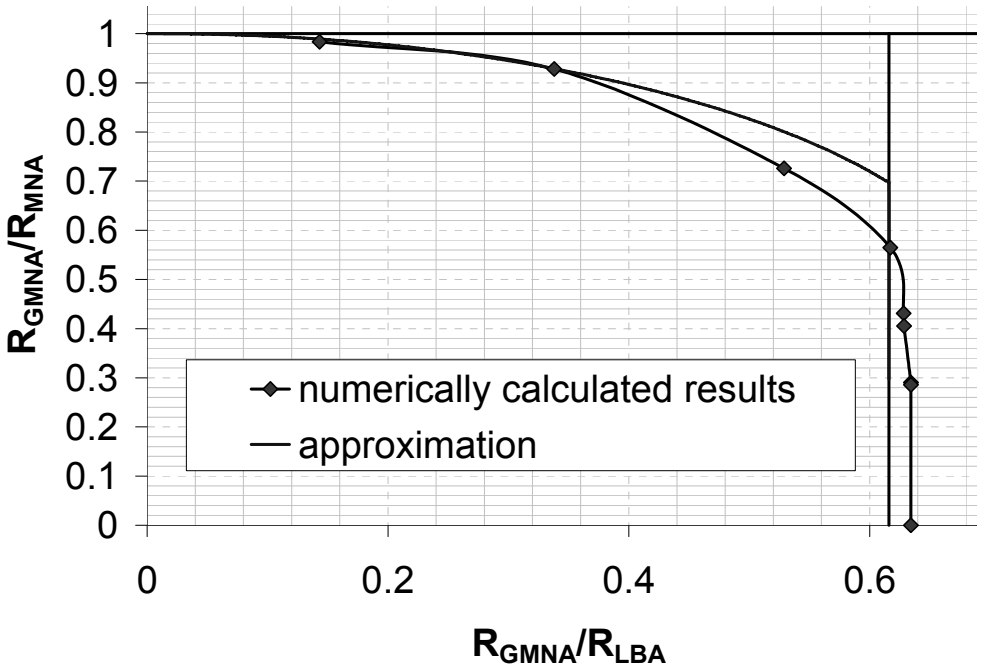

Figure 6.40: Modified capacity curve (r/t=400, Λ =7, Γ=1.25); maximum error on the unsafe side

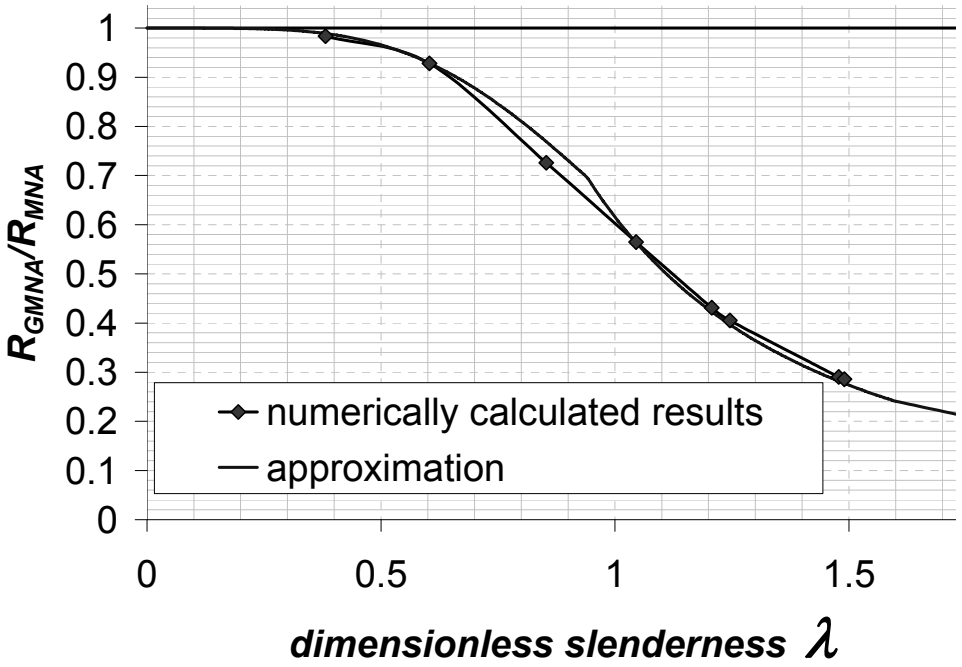

Figure 6.41: Traditional capacity curve (r/t=400, Λ =7, Γ=1.25); maximum error on the unsafe side

6.6 Summary

Geometrically and materially nonlinear analyses (GMNA) have been used in this chapter to investigate the capacity curves for perfect bracket supported shells.

The load deflection curves for a thin shell showed a shape and failure load very similar to the geometrically nonlinear elastic analysis (GNA), whereas the failure load of the thickest cylinder showed failure loads close to the plastic collapse load (MNA). When the relative slenderness was compared with the plastic limit slenderness of these cylinders, it could be seen that their location in the capacity curve is well within the elastic plastic interaction range.

The failure loads of the cylinder and bracket geometries that have been explored show the same overall behaviour: the failure load increases with the width and the height of the bracket. For a radius to thickness ratio r/t of 400, the variation of the failure load with both Λ and Γ is almost linear. This is due to the closeness of the failure load to the plastic collapse load, which varies linearly with Λ and Γ. The cylinders with a radius to thickness ratio r/t of 600 and 1000 show a more nonlinear variation with the height and the width of the bracket, since geometric nonlinearity takes on greater importance as the cylinder becomes thinner.

The general form of a capacity curve and the modified capacity curve was shown.

The modified capacity curve has the advantage over the traditional capacity curve that the elastic imperfection reduction factor α and the plastic range factor β can be extracted more accurately.

The interaction exponent η in the elastic plastic interaction range has been changed from constant to a linear function depending on the relative slenderness λ. This change opens the possibility to capture early yielding in the capacity curve, which was restricted when η was required to have a fixed value to the condition that $1-\beta<0.33$. This restriction made the original capacity curve only applicable to structures in which yield did not affect the global failure strength at loads below 1/3 of the plastic collapse loads. Although this restriction is not important for most frame structure and shell buckling problems involving relatively uniform stress fields, for the bracket and possibly similar stress concentration load conditions, it is an

unfortunate limitation.

Several restrictions must be observed when the linearly varying function of the interaction exponent is used. Three restrictions were found and their values in terms of other capacity curve parameters derived.

Two distinct shapes were found for the capacity curves when the geometries were changed. Cylinders with short brackets show an extensive elastic plastic interaction, with a rounded shape. By contrast, the capacity curves for tall brackets remained close to the elastic buckling load until very close to the plastic collapse load, and showed a rapid transition towards more plastic behaviour after that.

An empirical fit to all the capacity curves was found to capture the behaviour for each r/t ratio. The best fit parameters are very similar for all r/t ratios and therefore a conservative treatment of parameters was used to give a single approximation for all the investigated geometries

The variation of the elastic imperfection factor α with the bracket width and the height did not follow any apparent trend. Furthermore, because an early investigation showed that its variation might be wave-like in character, a lower bound approximation was used for the empirical fit of α. This lower bound approximation introduced the greatest error into the empirical fit, but since it was a lower bound approach the discrepancy is on the safe side.

6.7 Conclusions

This chapter set out to examine the behaviour of perfect bracket supported shells using the GMNA-analysis. It further developed capacity curves for the bracket supported shell including an appropriate empirical fit for a wide range of bracket and shell geometries.

The failure behaviour of the example geometries showed that thick shells with small brackets fail in a plastic collapse manner, but with a failure load very close to the plastic collapse load and yielding in an extensive area around the bracket just before buckling. By contrast, thin shells fail in an elastic buckling manner, as seen in a GNA analysis, since the buckling condition is reached well before yielding can progress to a state where it has a significant effect on the overall strength.

Each capacity curve required around 10 analyses with different yield stresses

and in total 75 capacity curves have been calculated. When these numerical analyses can achieve a reasonably accurate result with a small number of elements, more capacity curves can be calculated in a reasonable time. However, the numerical analysis currently requires a large number of elements, due to the two different elements that are necessarily used in each mesh, so the computational power required to calculate the required points numerically for a single capacity curve grows disproportionately.

The traditional capacity curve was examined next. It was shown that the modified capacity curve allows for a much easier and more accurate extraction of the elastic imperfection reduction factor α and the plastic range factor β.

It was also shown that the traditional method of changing the geometry to change the relative slenderness λ can lead to changes in geometric nonlinearity and imperfection sensitivity and may prevent a quality evaluation of the value of α. The relative slenderness can also be changed by changing the yield stress and keeping the geometry constant. This technique keeps the geometric nonlinearity and imperfection sensitivity constant leading to unique values of the parameters, and was therefore used in this thesis.

It was found that if the interaction exponent η was retained at $\eta=1$, as used throughout EN1993-1-6 (2006), it is not easy to achieve a good fit in the case of the bracket supported shell. The change to a different, but constant, value for interaction exponent η achieves a much better fit. At the same time, a constant interaction exponent of any value was shown to restrict the plastic range factor β to a maximum of 2/3 and therefore early yielding in the structure cannot be described well by a constant interaction exponent. To broaden the range of structures and structural behaviours that this capacity curve can cover, it was decided to allow η to vary linearly with the relative slenderness λ. This proposal has two great advantages: early yielding can now be considered in the capacity curve, and a much better fit to the numerical results can be achieved. This is the first investigation of a linearly varying interaction exponent and could usefully be applied to more structures to verify its suitability for a wider range of structural problems.

The variation of α with the bracket geometry was not straightforward and seemed to have a wave-like behaviour. No suitable fit could be found for this kind of

variation. Since it is known that the failure mode of the linear bifurcation analysis does not change in this range, it may be that the reason for the wave like behaviour is the change of failure mode seen the GNA analyses. If the reason for the wave-like variation of α with bracket geometry is in fact the change of failure mode, the geometries at which the change happens need to be identified by much more detailed analyses.

On the other hand, when the variation of the value of α with bracket width is examined, the change of α is minimal, but is still present. This means that even the slightest change in failure mode could make a difference. In this case it would be important to find the geometries at which the slope of the variation of α with the bracket geometries changes sign. Hence the elastic imperfection reduction factor α needs to be investigated more extensively. A lower bound approximation of α was used to achieve a safe estimate. Even with this rather inaccurate lower bound approximation of α, a high quality approximation to the 75 capacity curves has been achieved. Since only three r/t ratios were investigated, the results should be treated as provisional at the present time, though it is believed that the overall description given here is quite accurate and a great improvement on alternative methods of assessing the strength of shell buckling conditions of comparable complexity.

7 Relative importance of geometric imperfections (GMNIA/GNIA)

7.1 Introduction

The geometrically and materially nonlinear analysis with explicitly modelled imperfections is thought to be the most accurate calculation to describe the real behaviour of shell structures.

However, the challenge in this analysis is to find an appropriate imperfection shape and imperfection amplitude to achieve a conservative description for practical shell structure design. This challenge is very considerable. Therefore the recommendations in the Eurocode (EN1993-1-6, 2006) are first examined and the choice of imperfection shape is discussed. In the second part of this chapter, numerical results for the buckling strength of imperfect cylindrical shells supported on discrete brackets is studied.

7.2 Eurocode recommendations on imperfection forms

The Eurocode EN1993-1-6 (2006) very explicitly specifies the different imperfections forms and amplitudes which should be considered in any numerical analysis. The following clauses are taken directly from Eurocode 3 Part 1.6 Section 8.7.2 (EN1993-1-6, 2006).

> "(9) In formulating the GMNIA (or GNIA) analysis, appropriate allowances should be incorporated to cover the effects of imperfections that cannot be avoided in practice, including:
>
> a) geometric imperfections, such as:
>
> deviations from the nominal geometric shape of the middle surface (pre-deformations, out-of-roundness);
>
> irregularities at and near welds (minor eccentricities, shrinkage depressions, rolling curvature errors);
>
> deviations from nominal thickness;
>
> lack of evenness of supports.
>
> b) material imperfections, such as:
>
> residual stresses caused by rolling, pressing, welding, straightening etc.;

inhomogeneities and anisotropies. “

(11) The imperfections should generally be introduced by means of equivalent geometric imperfections in the form of initial shape deviations perpendicular to the middle surface of the perfect shell, unless a better technique is used. The middle surface of the geometrically imperfect shell should be obtained by superposition of the equivalent geometric imperfections on the perfect shell geometry.

(12) The pattern of the equivalent geometric imperfections should be chosen in such a form that it has the most unfavourable effect on the imperfect elastic-plastic buckling resistance ratio $r_{\mathrm{R,GMNIA}}$ of the shell. If the most unfavourable pattern cannot be readily identified beyond reasonable doubt, the analysis should be carried out for a sufficient number of different imperfection patterns, and the worst case (lowest value of $r_{\mathrm{R,GMNIA}}$) should be identified.

(13) The eigenmode-affine pattern should be used unless a different unfavourable pattern can be justified.

(14) The pattern of the equivalent geometric imperfections should, if practicable, reflect the constructional detailing and the boundary conditions in an unfavourable manner.

(15) Notwithstanding (13) and (14), patterns may be excluded from the investigation if they can be eliminated as unrealistic because of the method of fabrication, manufacture or erection.

(16) Modification of the adopted mode of geometric imperfections to include realistic structural details (such as axisymmetric weld depressions) should be explored.

(17) The sign of the equivalent geometric imperfections should be chosen in such a manner that the maximum initial shape deviations are unfavourably oriented towards the centre of the shell curvature.

(18) The amplitude of the adopted equivalent geometric imperfection form should be taken as dependent on the fabrication tolerance quality class. The maximum deviation of the geometry of the equivalent imperfection from the perfect shape $\Delta w_{0,\mathrm{eq}}$ should be the larger of $\Delta w_{0,\mathrm{eq},1}$ and $\Delta w_{0,\mathrm{eq},2}$, where

$$\Delta w_{0,eq,1} = l_g \, U_{n1} \tag{7.1}$$

$$\Delta w_{0,eq,2} = n_i \, t \, U_{n2} \tag{7.2}$$

where:

ℓ_g is all relevant gauge lengths according to 8.4.4 (2);

t is the local shell wall thickness;

n_i is a multiplier to achieve an appropriate tolerance level;

U_{n1} and U_{n2} are the dimple imperfection amplitude parameters for the relevant fabrication tolerance quality class.

NOTE 1: The National Annex may choose the value of n_i. The value $n_i = 25$ is recommended.

NOTE 2: Values for the dimple tolerance parameter U_{n1} and U_{n2} may be obtained from the National Annex. The recommended values are given in Table 8.5.

Fabrication tolerance quality class	Description	Recommended value of U_{n1}	Recommended value of U_{n2}
Class A	Excellent	0,010	0,010
Class B	High	0,016	0,016
Class C	Normal	0,025	0,025

Table 7.1: Recommended values for dimple imperfection amplitude parameters U_{n1} and U_{n2} (Table 8.5 from EN1993-1-6, 2006)

(20) Additionally, it should be verified that an analysis that adopts an imperfection whose amplitude is 10% smaller than the value $\Delta w_{0,eq}$ found in (18) does not yield a lower value for the ratio $r_{R,GMNIA}$. If a lower value is obtained, the procedure should be iterated to find the lowest value of the ratio $r_{R,GMNIA}$ as the amplitude is varied."

The following begins with a discussion of the application of these provisions to the problem of the cylinder on discrete brackets, before decisions are made concerning the imperfection forms and amplitudes to be adopted in this study.

Some of the recommendations from the Eurocode concerning imperfection shapes and amplitudes are outlined above. Possible imperfections are very explicitly outlined in this standard (Clause 9) ranging from an imperfect initial shape to imperfect material model, even though the equivalent geometric imperfection is recommended in the standard for general use. In particular the eigenmode affine imperfection shape is suggested to be used when no other more unfavourable imperfection form can be identified (Clauses 11-13). The direction of the imperfection is suggested to be towards the middle of the cylinder (Clause 17), since this represents usually the more serious imperfection form. Even though geometric equivalent imperfections are specified, it is also made clear in Clauses 14 and 16 that

imperfection shapes similar to the imperfections which might occur in practice should be used and also that structural details like weld depressions should be included, while other imperfection forms may be excluded when they are unrealistic (Clause 15).

For the bracket supported shell the recommended imperfection amplitudes for Fabrication Quality Class A (the best fabrication quality) are:

r/t=	400	600	1000
$\Delta w_{0,eq}$	0.800	0.980	1.26

Table 7.2: Recommended imperfection amplitudes for the bracket supported shell following EN1993-1-6 (2006)

The requirement is also given (Clause 20) that an imperfection amplitude 10% lower than the specified one should also be calculated. This restriction is necessary to ensure that the buckling strength does not decline when the imperfection is smaller than the value associated with the tolerance limit.

7.3 Choice of imperfection form

The "worst" imperfection is usually considered to be the appropriate one. While this assumption is always on the safe side, it always holds the uncertainty that another imperfection may exist that could lead to a worse outcome, and the possibility that this worse imperfection could possibly arise in the fabrication process. On the other hand the "worst" imperfection of all might well be quite unrealistic, leading to very uneconomic designs if implemented (Rotter, 2004).

The significance of imperfections for the buckling strength of shells has been reported frequently in the literature (as discussed in Chapter 1). In Chapter 5, it was shown, using a representative example of a bracket supported shell analysed with a geometrically nonlinear elastic analysis (GNA), that the importance of imperfections is not as significant for this structure as it is for many other shell structures. This chapter will examine the significance of geometric imperfections for a wider range of geometries.

The choice of imperfection shape and amplitude δ has always been very challenging. This is especially true for the bracket supported cylinder. The shape of

the first eigenmode imperfection is most commonly taken as the first choice (e.g. EN1993-1-6, 2006; Teng and Song, 2001), but it was shown in Chapter 5 that this imperfection increases the strength of the cylinder in the elastic range.

Therefore this imperfection shape, interesting as the result might be, is not suitable for an imperfection description to be applied in design calculations, and are also unsuitable for an imperfection sensitivity study of this problem.

Weld imperfections have been found to dramatically reduce the strength of many shell structures (e.g. Rotter and Teng, 1989; Pircher and Bridge, 2001; Song et al, 2004). The reason for the reduction of strength was explained by Rotter and Teng in terms of the circumferential compression that is locally induced by the passage of the axial compression through the imperfection, leading to a bi-axial stress field in higher compression than the axial compression alone (Rotter and Teng, 1989). This concept can be applied to other imperfection forms, and is closely related to the idea used in Chapter 3 that buckling may occur when the local axial compression reaches the value for uniform axial compression.

By contrast with the above studies, the bracket supported shell is strongly affected by the reduction in curvature of the shell above the bracket. Therefore the weld imperfection was also ruled out as not a suitable candidate for the imperfection sensitivity study since such a depression might well resist this curvature reduction.

Following from this idea, the logical imperfection shape to use is one which reduces the curvature of the shell above the bracket.

From Chapter 5 two imperfection shapes were identified as possible candidates for this study: the deformed shape of a geometrically nonlinear analysis at the post buckling minimum and the deformed shape at buckling.

The imperfections with a post-buckling shape extracted from a geometrically nonlinear analysis of the perfect structure decreased the strength for small imperfection amplitudes, but shows an increase in strength for larger imperfections. In the example structure of Chapter 5 the larger imperfection, which showed an increase in strength is very similar to recommended imperfection amplitude in the Eurocode (EN1993-1-6, 2006) for the best quality fabrication class.

The imperfection in the form of the deformed shape of a geometrically nonlinear analysis at buckling decreased the strength of the structure continuously and lead to a

similar reduction of strength for an imperfection amplitude of one wall thickness as the post buckling deformed shape with further reduction of strength for larger amplitudes (Chapter 5). Since this imperfection shape also provides a reduction of curvature above the shell, it was chosen in this investigation.

One could argue that the deformed shape of the geometrically and materially nonlinear analysis (GMNA) should be used as the most damaging imperfection shape (Schneider *et al.*, 2005), since it represents the deformed shape of the structure using exactly the same analysis.

Whereas this statement might be true, the practicality of such an imperfection is questionable. The goal here is to produce capacity curves for the imperfect structure. If the deformed shape from a geometrically and materially nonlinear analysis (GMNA) is adopted as an imperfection, then it is difficult to decide which GMNA analysis should be used to define this deformed shape, since every point of the capacity curve is calculated in a separate analysis using a different yield stress. This also leads to difficulties in determining how the fabrication tolerances should be related to these adopted imperfections. One possible solution is to take the deformed shape from an analysis calculated with a yield stress in the practical range. However, this still leaves scope for a huge range of different shapes, since the deformed shape to be adopted depends on the extent of yielding in the individual calculation.

The logic of the above indicates that a different imperfection shape should be used for every single point of the capacity curve, where the imperfection shape would change according to the deformed shape found for this particular analysis with this particular yield stress. But this would lead to incredible difficulties: at what load level should the deformed shape be chosen as an imperfection to keep it in accordance with all the other different deformed shapes used for the same capacity curve? Therefore also this possibility was discarded. Finally the deformed shape of the geometrically nonlinear elastic analysis at buckling was chosen as imperfection shape.

The range of geometries investigated consisted of three different radius to thickness ratios to capture the behaviour pattern for thin, medium and thick shells (r/t=1000, 600 and 400). The dimensionless height of the brackets ranged from $1 < \Lambda = h/\sqrt{rt} < 7$ and the dimensionless width from $0.25 < \Gamma = d/\sqrt{rt} < 1.25$. The

material properties used were σ_y=250 MPa, E=200 000 MPa and ν=0.3 to model mild steel. The definition of failure remained the same as in Chapter 6.

7.4 Geometrically and materially nonlinear analysis with imperfections (GMNIA)

7.4.1 Challenges in the definition of failure (r/t=1000, δ/t=1)

After a decision has been made to use the deformed shape of geometrically nonlinear analysis (GNA) at buckling, the next decision must concern the imperfection amplitude to be chosen. As a starting point for the discussion of imperfection sensitivity, an imperfection amplitude δ of one wall thickness is used here to explore the behaviour. This amplitude was used with the thinnest shell (r/t=1000), since this r/t ratio was expected to be the most imperfection sensitive. It should be noted that the imperfection amplitude suggested in the Eurocode (EN1993-1-6, 2006) for Fabrication Quality Class A is 1.26 times the wall thickness (Section 7.2), so the adopted value is quite close to that defined in this standard.

The result for geometries with r/t=1000 followed closely the example geometry in Chapter 5 in most cases.

The load deflection curves shown in Figures 7.1 and 7.2 compare the failure behaviour of the perfect and the imperfect structure with δ/t=1 for four different geometries (here called Geometries A1/A2 and Geometries B1/B2) for a geometrically and materially nonlinear analysis (GMNA and GMNIA).

These four geometries illustrate well the general behaviour found. For the perfect shell with high brackets (Figures 7.1a and 7.2a) the difference between buckling and post- buckling minimum is “significant”, while for shorter brackets (Figures 7.1b and 7.2b) the difference becomes smaller. These effects become even more pronounced when imperfections are introduced.

While this phenomenon does not affect the results of the imperfect cylinders with high bracket (Figures 7.1a and 7.2a, Geometries A1 and B1), it does affect the failure of imperfect cylinders with short brackets greatly (Figures 7.1b and 7.2b, Geometries A2 and B2).

Even though the curves look very similar (Figures 7.1b and 7.2b, Geometries A2 and B2) and the geometry only differs by the width of the bracket (r/t=1000, Λ=1, Γ=1.25 (A2) and 1.00 (B2)), the failure behaviour and interpretation for these geometries are quite different.

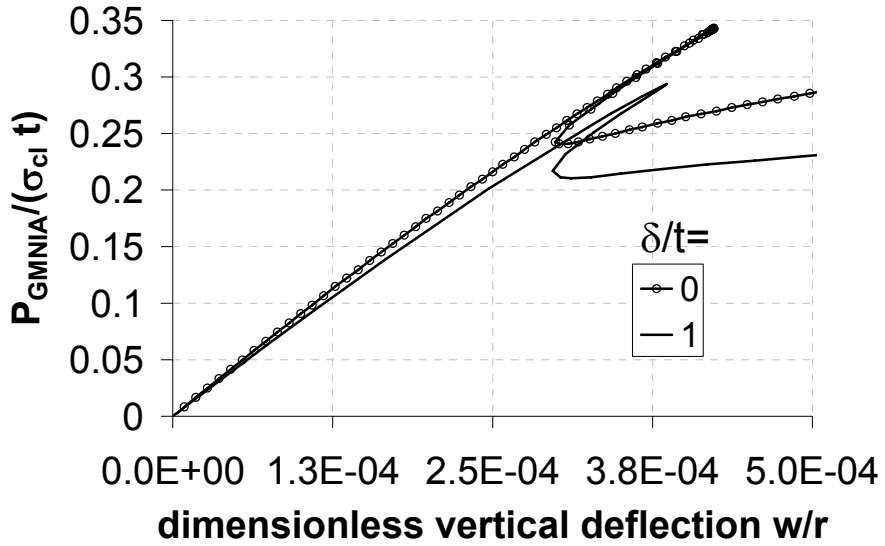

Figure 7.1a: Load deflection curves for Geometry A1 (r/t=1000, Λ=5, Γ=1.25, δ/t=1), GMNIA

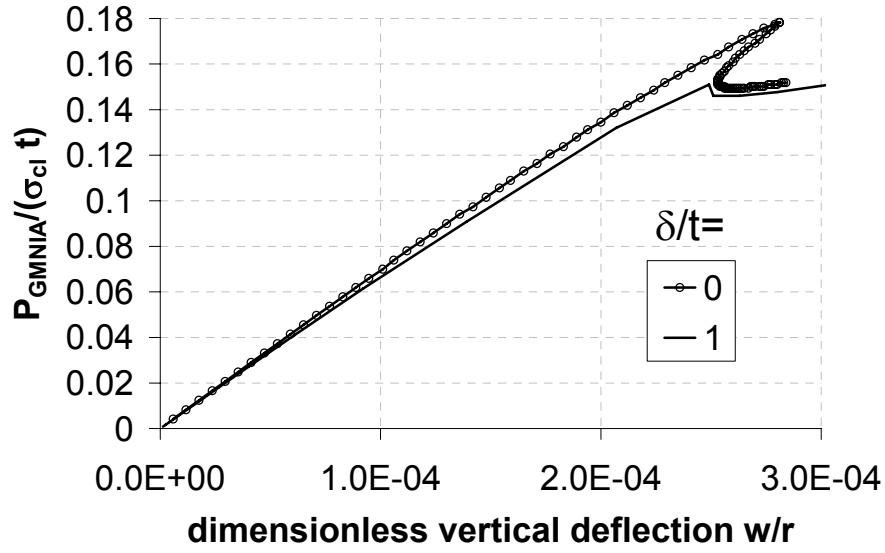

Figure 7.1b: Load deflection curves for Geometry A2 (r/t=1000, Λ=1, Γ=1.25, δ/t=1), GMNIA

Both perfect structures with short brackets (Figures 7.1b and 7.2b, Geometries A2 and B2) display a nonlinear pre-buckling path with a sharp fall in load carried after buckling. The imperfect load deflection curves also exhibit very similar features. The pre-buckling path of the imperfect structure is softer and more nonlinear than that of the perfect structure.

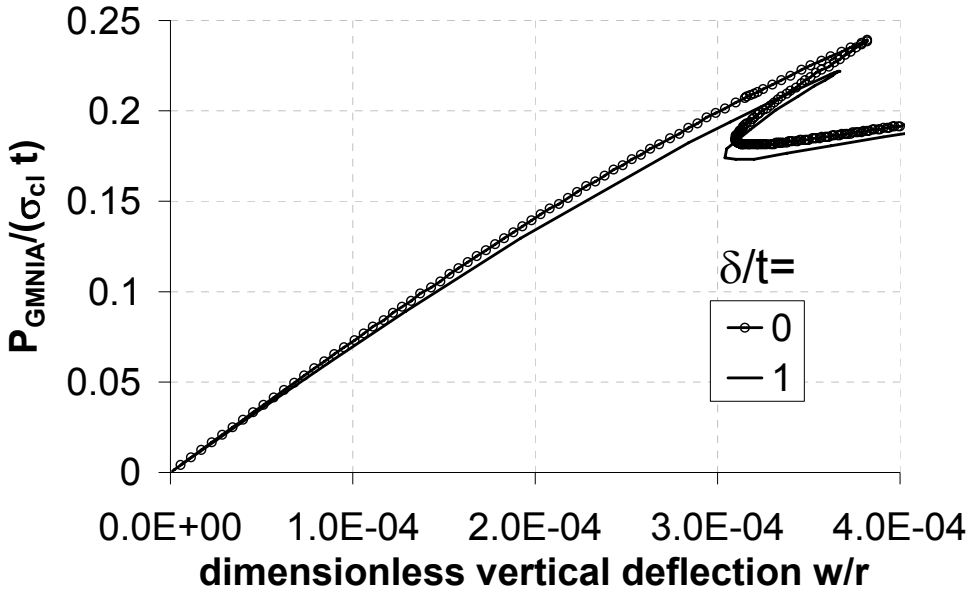

Figure 7.2a: Load deflection curves for Geometry B1 (r/t=1000, Λ =5, Γ =0.25, δ/t=1), GMNIA

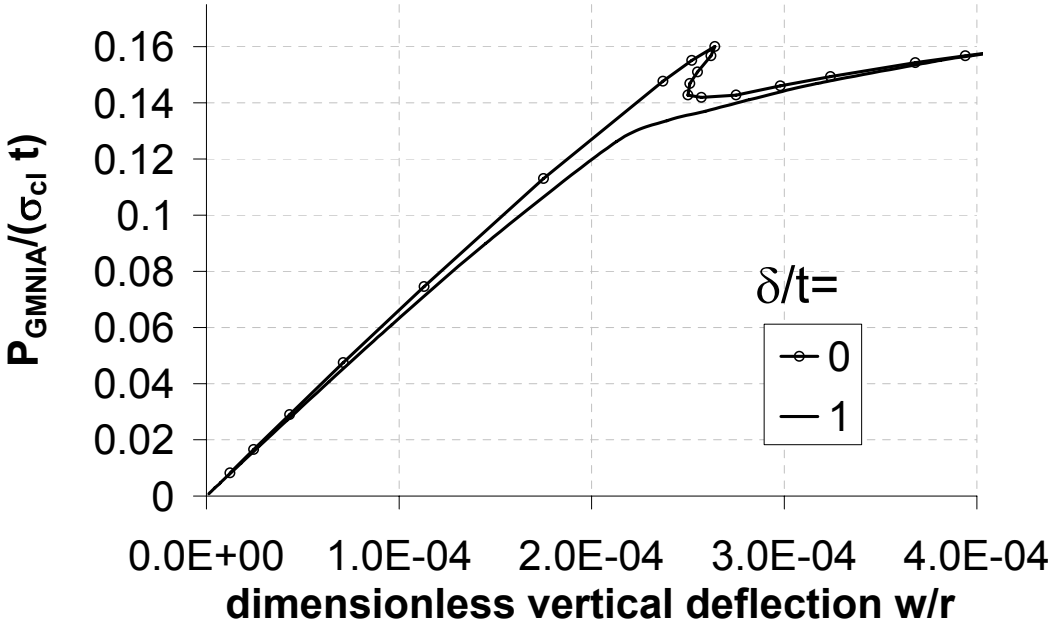

Figure 7.2b: Load deflection curves for Geometry B2 (r/t=1000, Λ=1, Γ=1.00, δ/t=1), GMNIA

But while the load deflection curve for imperfect Geometry A2 (wide bracket Γ=1.25) in Figure 7.1b still displays buckling, the load deflection curve for imperfect Geometry B1 (Γ=1.00) in Figure 7.2b does not exhibit buckling.

For both geometries, the more prominent indication that some bifurcation event has occurred is given by the change of slope of the load deflection curve rather than any fall in load carried ($w/r \approx 2.5\ 10^{-4}$).

A bifurcation event was detected in the imperfect Geometry A2 (Figure 7.1b),

but the pre-buckled shape was already locally deformed, so the bifurcation scarcely made any difference. But since the definition of failure from the EN1993-1-6 (2006) was adopted, this bifurcation point satisfies the criterion of failure.

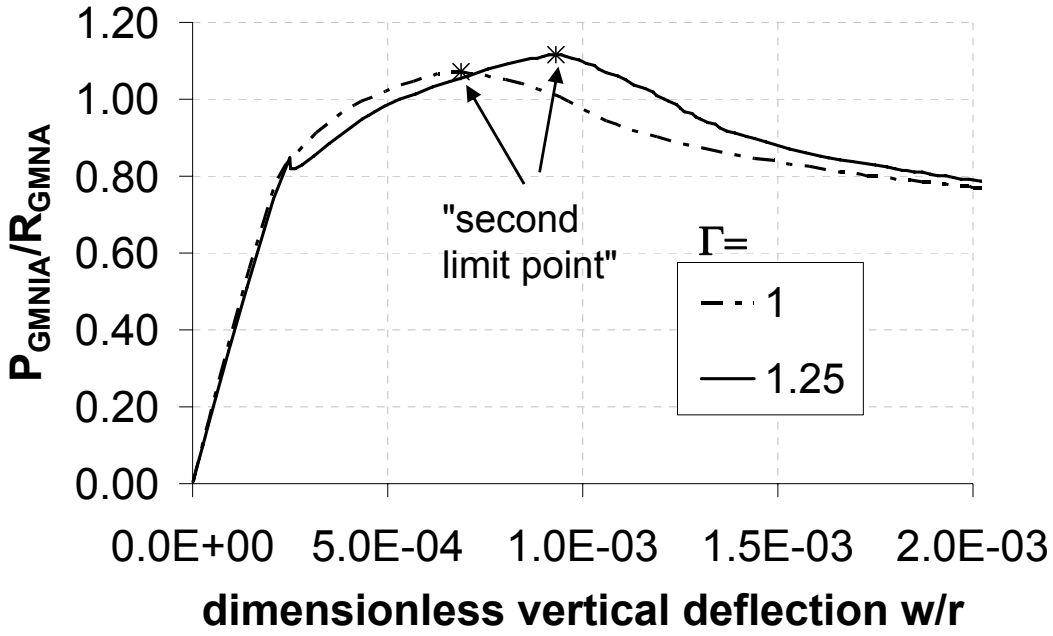

Figure 7.3: Load deflection curves (r/t=1000, Λ =1, δ/t=1), GMNIA

But when the load deflection curves for both of these example structures are followed further, a much higher and more definite limit point appears well beyond the bifurcation or "first limit point" (Figure 7.3). The term "first limit point" is used here to describe the point where the slope of the load-deflection curve decreases rapidly or negative for the first time, as seen in the above example geometries A2 and B2 at around w/r=2.5 10^{-4}. By contrast, the "second limit point", seen between w/r =0.5 10^{-3} and w/r = 1 10^{-3} (Figure 7.3), occurs well after the "first limit point".

Using the definition of EN1993-1-6 (2006), failure occurs for imperfect Geometry B2 (bracket width Γ=1.00,Figure 7.2b) at the "second limit point" (Figure 7.3) and for imperfect Geometry A2 (wide bracket Γ=1.25, Figure 7.1b) at the "first limit point".

If bifurcation at the "first limit point" is chosen to mean failure, Geometry B2 would have a slightly lower failure load than Geometry A2. If instead failure is chosen to be at the "second limit point", the strength of Geometry A is deemed to be 1.3 times that of Geometry B.

It can be argued that the "first limit point" for Geometry A2 (Figure 7.1b) should

not be considered as failure since the loss of strength after buckling is minimal and the post-buckling path is strengthening up to the "second limit" load. But this leads to another difficulty. There may be many post-buckling paths (Yamaki, 1984) and it cannot be verified that the one calculated by a numerical analysis always finds the lowest post-buckling path. If it is certain that the very lowest post-buckling minimum has been found, the definition of failure becomes uncertain. How much loss of strength would there need to be to classify this point as failure? How can we avoid an abrupt change in assessed strength for a small change in geometry if the criterion of failure depends on an arbitrary choice of how much post-buckling drop is permitted?

On the other hand one could argue that even though the load- deflection path in Figure 7.2b does not show a drop in load, the rapid reduction of the slope could be considered sufficient to classify this point as failure. This would make a safe but a very uneconomical estimate of the failure load.

The appearance of a "second limit point", well after the occurrence of the "first limit point", was observed in all investigated geometries in the geometrically and materially nonlinear analysis (GMNIA). If the second limit point is adopted as the true failure state, a further interesting situation arises.

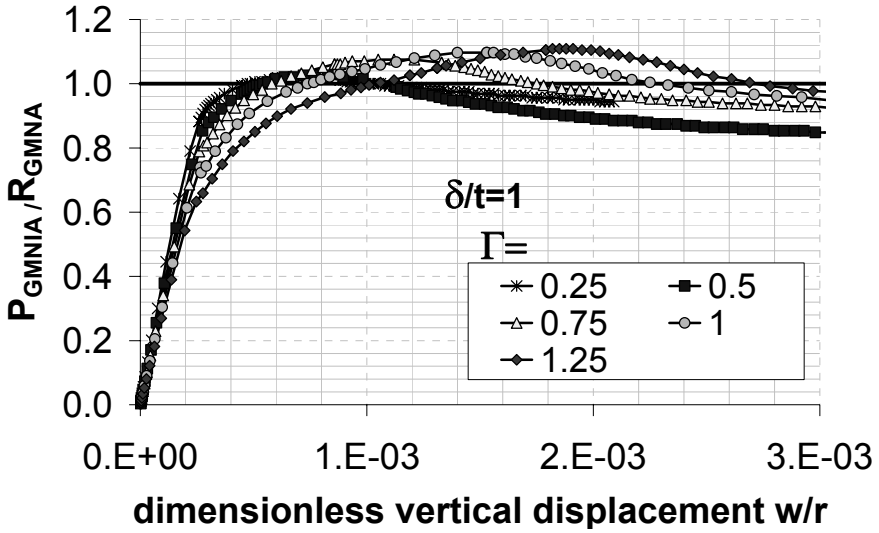

Figure 7.4: Load deflection curves (r/t=1000, Λ=2, δ/t=1), GMNIA

For an r/t-ratio of 1000, where the second limit point is chosen to define failure, the failure load for an imperfection amplitude of one wall thickness is higher than the failure load of the perfect structure. To illustrate this behaviour, five example geometries with different width brackets are shown in Figure 7.4 with r/t=1000 and a

dimensionless bracket height of Λ=2. The applied load is made dimensionless by using the failure load of the perfect structure. This choice gives a clear illustration of the strengthening of the imperfect structure (δ/t=1).

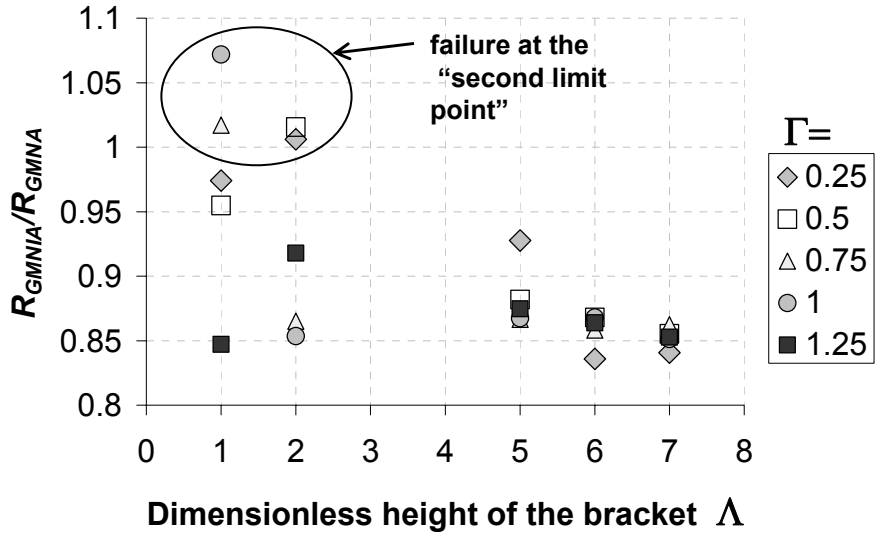

Figure 7.5: Summary of the ratio of imperfect to perfect cylinder strength (r/t=1000, δ/t=1), GMNIA

The ratio of imperfect to perfect cylinder strengths is summarised in Figure 7.5. The maximum decrease of strength due to the imperfection was found to be 16% (Figure 7.5) compared to the perfect structure and only a few occurrences of a limit point at the "second limit point" were found (Figure 7.5)

The above result suggests that an imperfection amplitude of one wall thickness is perhaps not large enough to produce a significant reduction in strength.

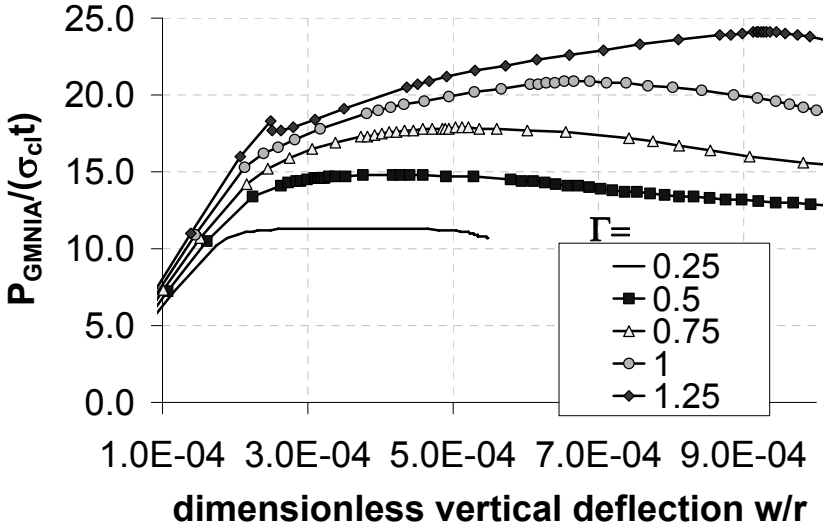

Figure 7.6: Load deflection curves from GMNIA analysis with r/t=1000 and Λ=1

The overall trend is that the imperfection sensitivity increases with increasing width and height of the bracket (Figure 7.5), but this trend is not true when the change of failure mode occurs (Figure 7.6). In this example (r/t=1000, Λ=1) the widest bracket (Γ=1.25) fails at the "first limit point", the silos with a bracket width of Γ=1.00 and 0.75 fail at the "second limit point" and appear to have an increased failure load. The failure loads for cylinders with very short brackets (Λ=1) and dimensionless widths in the range $0.25 \leq \Gamma \leq 0.50$ are all very close to the failure load of the corresponding perfect shells (Figure 7.5). This similarity occurs because the failure mechanism is dominated by material nonlinearity and the failure load of the perfect and imperfect shell are both very close to the plastic collapse load, which is controlled by yielding all around the bracket. When yielding around the bracket determines failure almost completely, it is perhaps natural to find that no significant decrease of strength can be observed due to imperfections.

7.4.2 Imperfection sensitivity in cylinders with r/t=600 and δ/t=1 (GMNIA)

The imperfection amplitude of one wall thickness was also applied to the other radius to thickness ratios (r/t = 400 and 600) to determine whether any change of behaviour would be found with increased curvature compared to the thinnest cylinder.

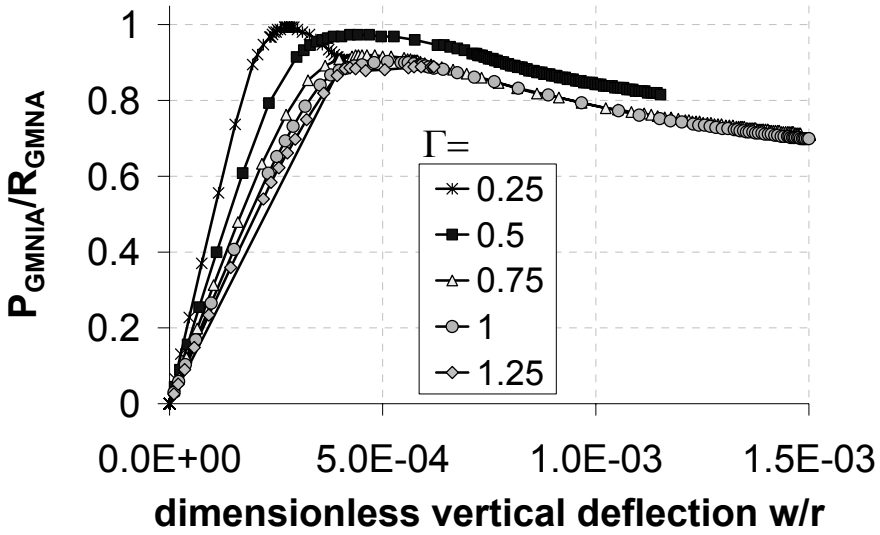

Figure 7.7: Load deflection curves (r/t=600, Λ =1, δ/t=1), GMNIA

For cylinders with short brackets Λ=1 (Figure 7.7) and Λ=2 (not shown here) and an imperfection amplitude of one wall thickness, the imperfection sensitivity is

minimal since the failure of the perfect shell is already very close to a plastic collapse as discussed before. The imperfection sensitivity becomes slightly more pronounced for wide brackets because the role of plasticity in the failure mode decreases slightly.

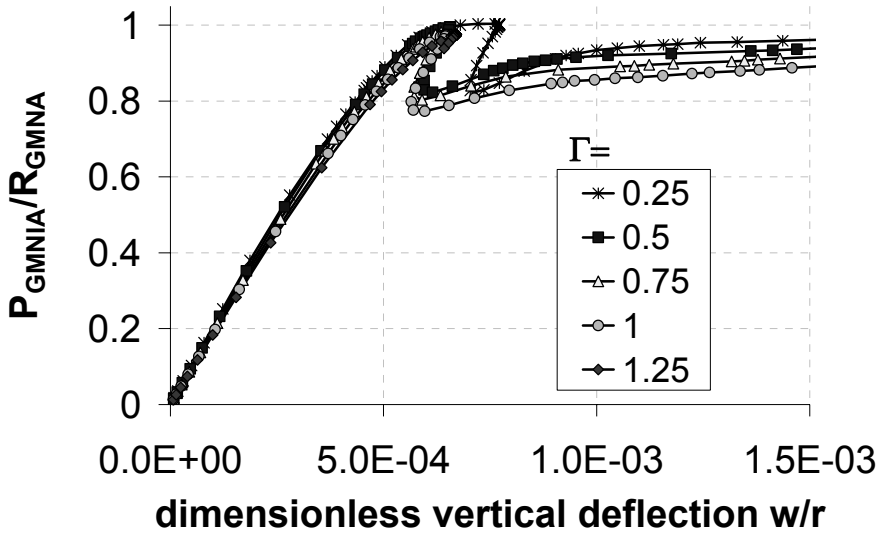

Figure 7.8: Load deflection curves (r/t=600, Λ=7, δ/t=1), GMNIA

For the other cylinders with tall brackets Λ=5, 6 and 7 (Λ=7 shown Figure 7.8), the failure load of the imperfect shells is almost the same as the failure load of the perfect shell.

The summary of failure loads (r/t=600) shows that imperfection sensitivity does not seem to be significant (Figure 7.9). The largest reduction of strength compared to the perfect shell is about 11%.

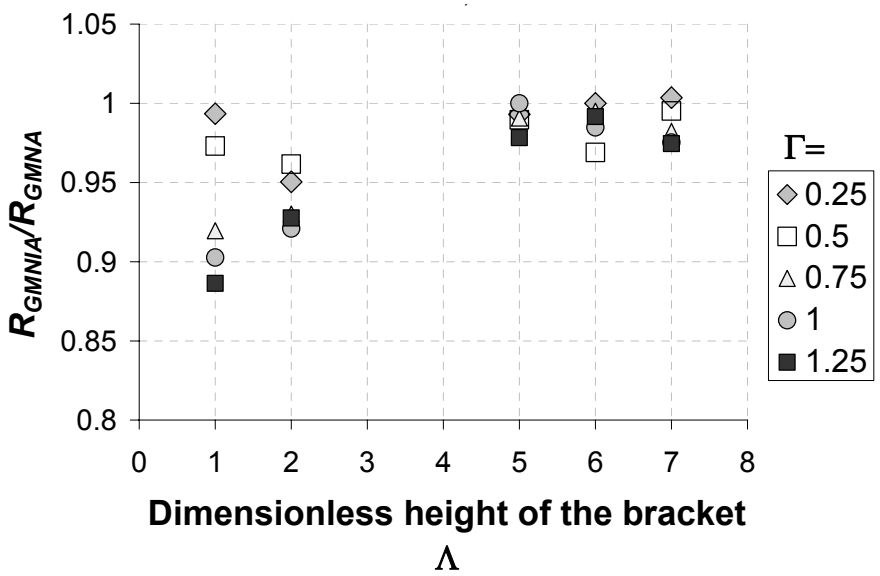

Figure 7.9: Summary of the ratio of imperfect to perfect cylinder strength (r/t=600, δ/t=1), GMNIA

7.4.3 Imperfection sensitivity in cylinders with r/t=400 and δ/t=1 (GMNIA)

The thickest of the investigated shells (r/t=400) was not expected to be imperfection sensitive, but is shown here for completeness. The behaviour is always dominated by material nonlinearity. Plastic buckling can be observed for cylinders with short brackets with Λ=1 (Figure 7.10) and Λ=2 (not shown here), which leads to a reduction in the failure load of cylinders on wide brackets Γ=0.75, 1.00 and 1.25 as discussed above.

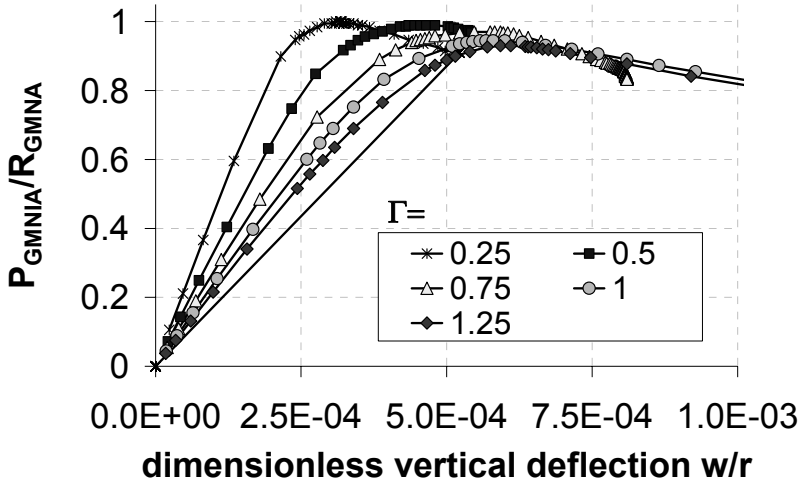

Figure 7.10: Load deflection curves (r/t=400, Λ =1, δ/t=1),GMNIA

This set of bracket supported shells with r/t=400 and Λ=5, 6 and 7 (Λ=7 shown in Figure 7.11) do not buckle at the "first limit", but all fail at the "second limit point". For all geometries the failure load of the imperfect shell has about the same value as that of the perfect shell.

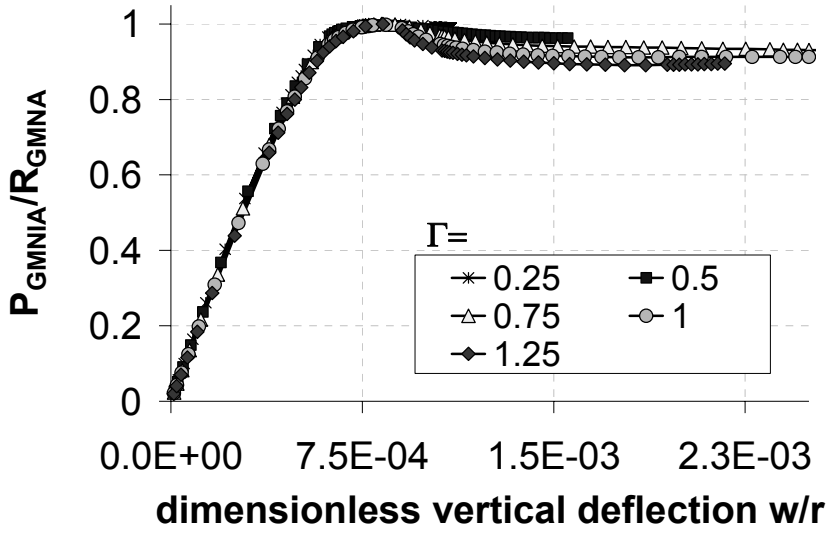

Figure 7.11: Load deflection curves (r/t=400, Λ =7, δ/t=1), GMNIA

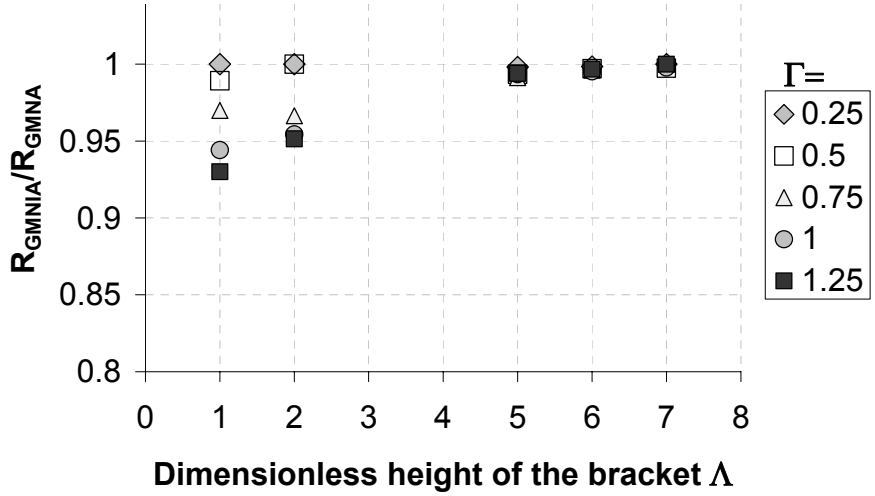

Figure 7.12: Summary of the ratio of imperfect to perfect cylinder strength (r/t=400, δ/t=1), GMNIA

The summary of failure loads (Figure 7.12) shows a slight decrease in the failure load for cylinders with short (Λ=1 and 2) and wide (Γ=5, 6 and 7) brackets, but overall the imperfection sensitivity is not significant for cylinders with r/t=400.

7.5 Geometrically nonlinear analysis with imperfections (GNIA)

7.5.1 GNIA or alpha value for capacity curves for δ/t=1

Since this investigation follows the frame work of the Eurocode (EN1993-1-6,2006), the next step was taken in order to calculated the elastic imperfection reduction factor α for each the capacity curve.

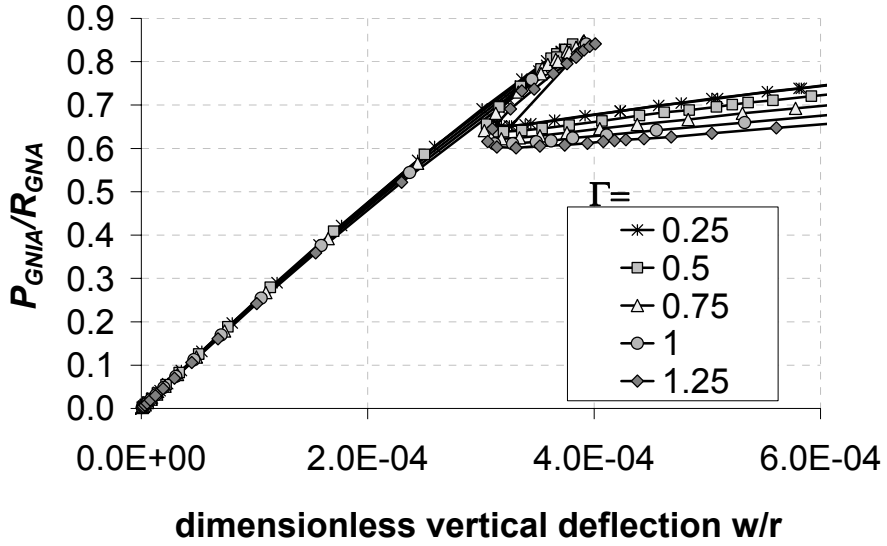

Figure 7.13: Load deflection curves (r/t=1000, Λ =7, δ/t=1), GNIA

The imperfection sensitivity remained low in the GNIA analysis as it was seen in the materially nonlinear analysis of the previous section (Figure 7.13).

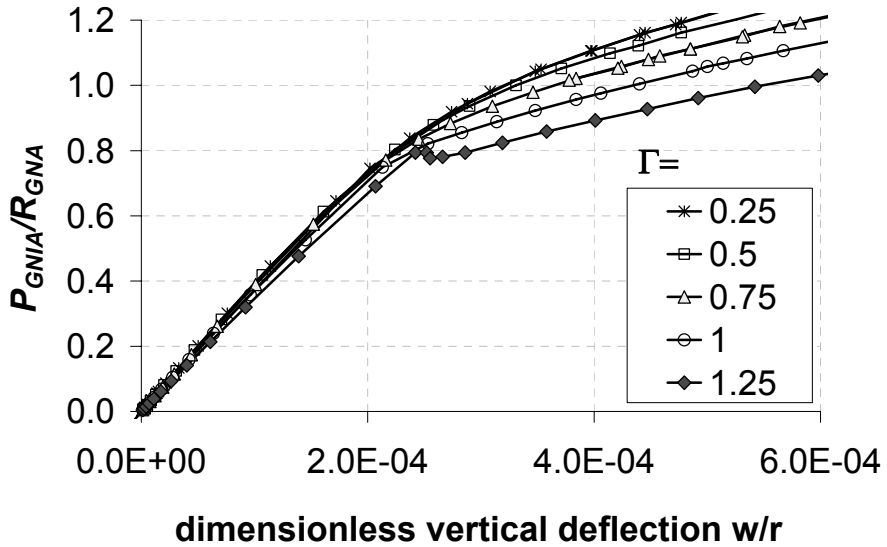

Figure 7.14: Load deflection curves (r/t=1000, Λ =1, δ/t=1), GNIA-close up

For most of the short bracket (Λ=1, 0.25≤Γ≤1, and 2, 0.25≤Γ≤0.5) buckling

could not be detected and determinate of the stiffness matrix remained positive throughout the analysis (Figure 7.14 and Figure 7.15 for Λ=1).

The load carried rises very steeply up to values of the order of 1.5 to 2.3 times the failure load of the perfect shell (Figure 7.15). For such shells, it is clearly necessary to define failure in terms of some limit of acceptable deformation.

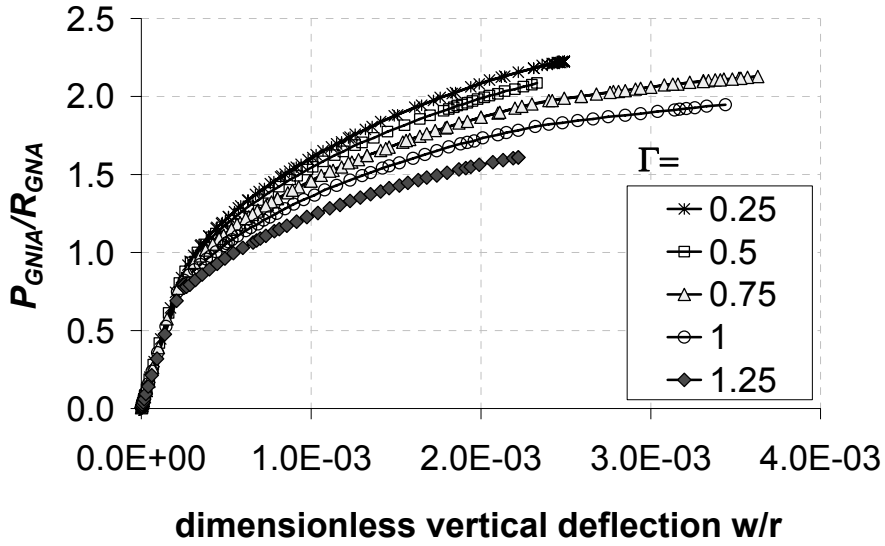

Figure 7.15 Load deflection curves (r/t=1000, Λ =1, δ/t=1), GNIA

When a buckling event was detected the reduction of strength was found in the range of 9.8% and 21% (Figure 7.16)

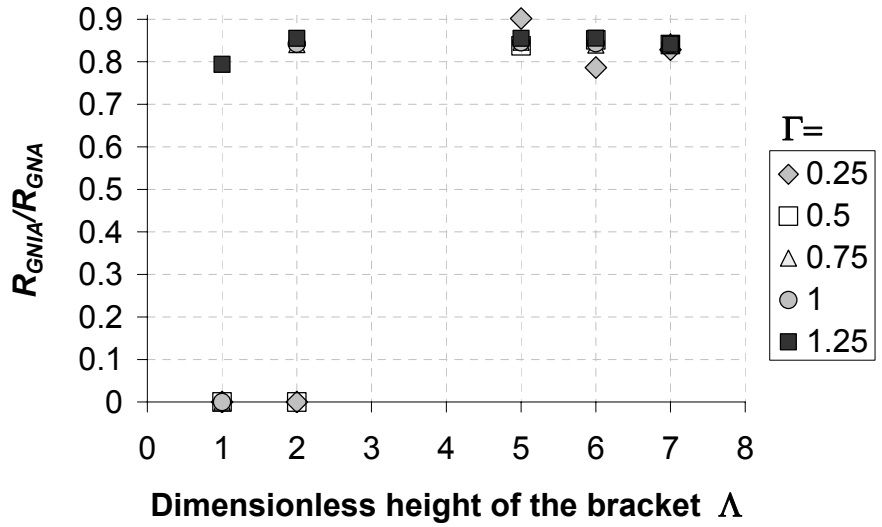

Figure 7.16: Summary of the ratio of imperfect to perfect cylinder strength (r/t=1000 δ/t=1), GNIA

The imperfection sensitivity remained low for shells with r/t ratios of 400 and 600 (Table 7.3 and Table 7.4: the letter "X" indicates that no bifurcation event could be found). For those that did bifurcate, the loss of strength due to imperfections was

between 14% and 27%.

Λ \ Γ	0.25	0.5	0.75	1	1.25
1	X	X	X	X	0.787
2	X	X	X	X	0.812
5	0.842	0.853	0.801	0.780	0.797
6	0.853	0.823	0.751	0.814	0.857
7	0.813	0.807	0.808	0.815	0.805

Table 7.3: Summary of dimensionless bifurcation load R_{GNIA}/R_{GNA} (r/t=600, δ/t=1)

Λ \ Γ	0.25	0.5	0.75	1	1.25
1	X	X	X	X	X
2	X	X	X	X	X
5	0.859	0.823	0.822	0.767	0.730
6	0.840	0.842	0.830	0.735	0.752
7	0.847	0.849	0.736	0.761	0.751

Table 7.4: Summary of dimensionless bifurcation load R_{GNIA}/R_{GNA} (r/t=400, δ/t=1)

7.5.2 Failure behaviour of imperfect cylinders with various imperfection amplitudes

The above investigation revealed that cylinders with an imperfection amplitude of one wall thickness (δ/t=1) showed a moderate imperfection sensitivity. In order to explore the behaviour larger imperfection amplitudes are shown here.

The widest and the narrowest brackets (Γ=0.25 and 1.25) were chosen as representative geometries for each r/t ratio and each value of the dimensionless height Λ.

The thinnest shell with r/t=1000 with large brackets (both in height and in width) showed the most prominent imperfection sensitivity (Figure 7.17) with reduction of strength of 54% for very large imperfection amplitudes. The reduction of strength for the imperfect shells also leads to reduction of the relative difference between the

point of buckling and the post- buckling minimum. Therefore the maximum imperfection sensitivity was found when the difference between post- buckling minimum and buckling was close to zero and the buckling event could scarcely be seen (Figure 7.17, δ/t=5.27).

The imperfections also lead to reduction of stiffness on the pre- buckling path (e.g. Figure 7.17), which is in contrast to the load deflection curves of an imperfect shell under uniform compression (Yamaki, 1984). This effect might be attributed to the very nonlinear pre- buckling deformations of the perfect shell and the resulting significant influence of geometric nonlinearity.

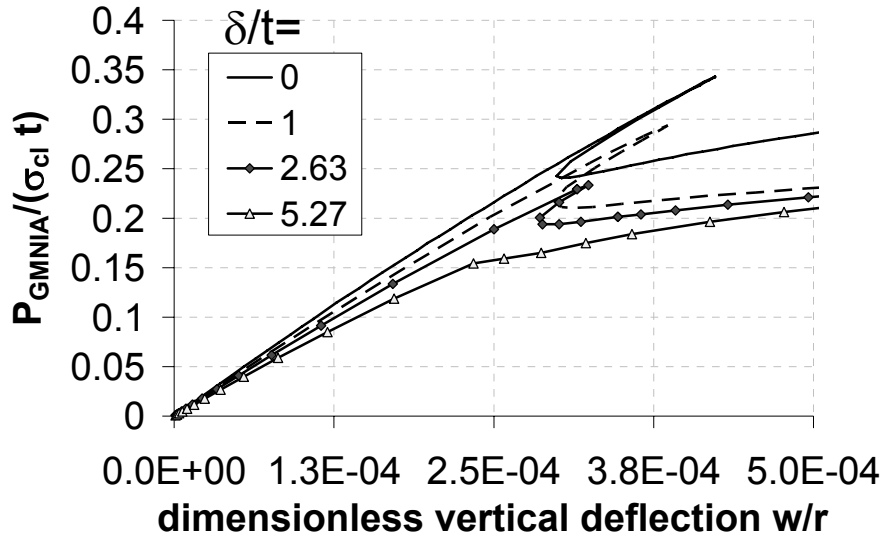

Figure 7.17: Load deflection curves (r/t=1000, Γ =1.25, Λ =5), GMNIA

For smaller bracket (both in height and in width) (Figure 7.18) the influence of material nonlinearity becomes more significant leading to more rounded and softer buckling response in the perfect structure. When imperfections are introduced the responds becomes even softer and no buckling event can be detected at the "first limit point" (Figure 7.18). The imperfect silos fail then at the "second limit point" at a failure load, which is higher than the failure load of the perfect structure.

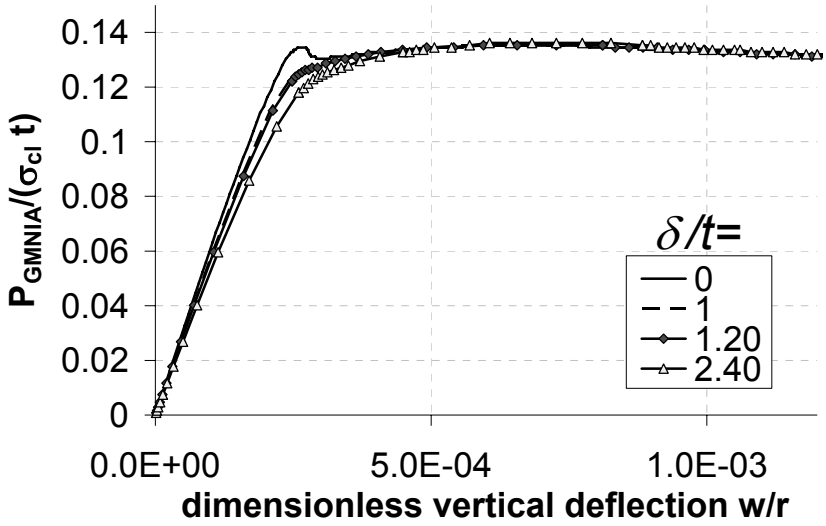

Figure 7.18: Load deflection curves (r/t=1000, Γ =0.25, Λ =2), GMNIA

	Γ=0.25				Γ=1.25		
Λ=	δ/t=	R_{GNIA}/R_{GNA}	R_{GMNIA}/R_{GMNA}		δ/t=	R_{GNIA}/R_{GNA}	R_{GMNIA}/R_{GMNA}
1	1	X	0.97		1	0.79	0.85
	1.05	X	0.99		1.46	0.77	1.13
	2.09	X	0.98		2.91	X	1.13
2	1	X	1.01		1	0.90	0.92
	1.20	X	1.01		1.87	0.77	0.85
	2.40	X	1.01		3.75	0.58	0.64
5	1	0.85	0.93		1	0.86	0.86
	2.11	0.73	0.91		2.63	0.67	0.70
	4.21	X	1.28		5.27	0.46	0.48
6	1	0.79	0.84		1	0.86	0.86
	2.28	0.66	0.69		2.73	0.65	0.67
	4.55	X	1.13		5.47	X	1.14
7	1	0.83	0.84		1	0.84	0.85
	2.38	0.66	0.66		2.82	0.63	0.67
	4.76	X	1.2		5.64	X	1.23

Table 7.5: Summary of dimensionless failure load (r/t=1000, various δ/t)

The cylinders with radius to thickness ratios of 400 and 600 do not display significant imperfection sensitivity for the investigated imperfection amplitudes. The shell with the intermediate thickness (r/t=600) showed a loss of strength of about

17% (Table 7.6), which reduced to 13% (Table 7.7) for the thickest cylinder in the geometrically and materially nonlinear analysis (GMNIA).

	Γ=0.25				Γ=1.25		
Λ=	δ/t=	R_{GNIA}/R_{GNA}	R_{GMNIA}/R_{GMNA}		δ/t=	R_{GNIA}/R_{GNA}	R_{GMNIA}/R_{GMNA}
1	0.95	X	0.99		1	0.79	0.89
	1	X	0.99		1.30	X	0.89
	1.91	X	0.99		2.59	X	0.88
2	1	X	0.98		1	0.82	0.93
	1.11	X	1.00		1.60	0.74	0.89
	2.23	X	0.99		3.21	X	0.90
5	1	0.85	0.99		1	0.79	0.98
	1.68	0.80	0.98		2.20	0.64	0.84
	3.36	X	0.91		4.39	X	0.94
6	1	0.86	1.00		1	0.86	0.99
	1.90	0.72	0.98		2.79	0.66	0.87
	3.80	X	1.00		5.59	X	0.96
7	1	0.82	1.00		1	0.83	0.97
	2.04	0.67	0.91		2.82	0.62	0.83
	4.07	X	1.01		5.64	X	0.94

Table 7.6: Summary of dimensionless failure load (r/t=600, various δ/t)

On the other hand, the elastic analysis (GNIA) showed a more significant imperfection sensitivity with a loss of strength of 38% for the cylinder with intermediate thickness (Table 7.6) and 41% (Table 7.7) for the thickest cylinder.

	Γ=0.25				Γ=1.25		
Λ=	δ/t=	R_{GNIA}/R_{GNA}	R_{GMNIA}/R_{GMNA}		δ/t=	R_{GNIA}/R_{GNA}	R_{GMNIA}/R_{GMNA}
1	0.93	X	1.00		1.00	X	0.93
	1.00	X	1.00		1.18	X	0.92
	1.86	X	0.99		2.37	X	0.87
2	1.00	X	1.00		1.00	X	0.95
	1.01	X	1.00		1.39	X	0.93
	2.02	X	1.00		2.78	X	0.89
5	1.00	0.86	1.00		1.00	0.75	0.99
	1.42	0.84	1.00		1.90	0.63	0.99
	2.83	0.73	0.99		3.79	0.69	0.94
6	1.00	0.81	1.00		1.00	0.78	1.00
	1.58	0.79	1.00		1.98	0.61	0.99
	3.15	0.65	0.99		3.96	0.59	0.94
7	1.00	0.82	1.00		1.00	0.80	1.00
	1.73	0.75	1.00		2.05	0.66	0.99
	3.47	X	0.99		4.10	X	0.94

Table 7.7: Summary of dimensionless failure load (r/t=400, various δ/t)

The load deflection curves with the same bracket geometries as shown for the cylinder with the radius to thickness ratio of 1000 (Figure 7.17and Figure 7.18) are shown in Figure 7.19 to Figure 7.22 for the two remaining r/t-ratios of 600 and 400.

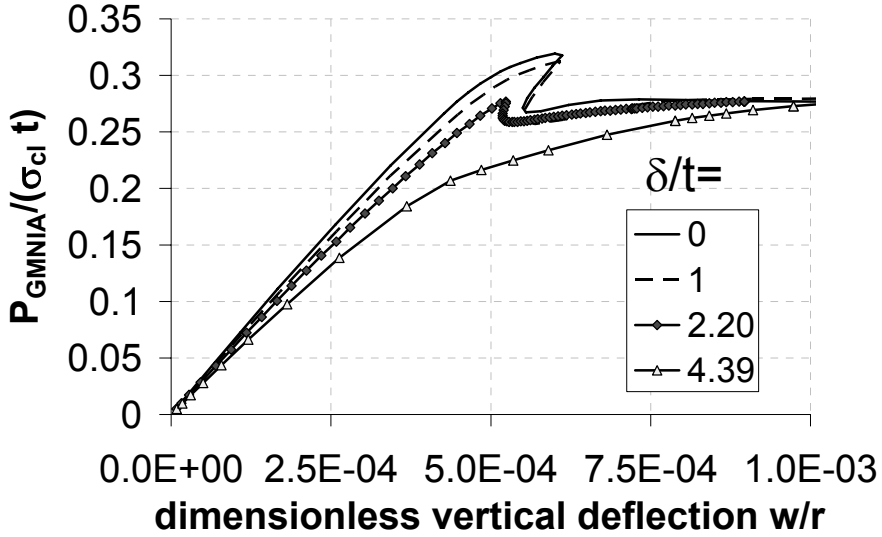

Figure 7.19: Load deflection curves (r/t=600, Γ =1.25, Λ =5), GMNIA

Silos of intermediate thickness (r/t=600) and large bracket (both in height and in width) (example in Figure 7.19) show the same principal response as the thin silos (r/t=1000).With increasing imperfection amplitude the response becomes softer and the ratio between the buckling load and the post-buckling minimum decreases (Figure 7.19) until buckling at the "first limit point" can not be detected anymore. By contrast with the thinnest cylinder (r/t=1000), plasticity influences the behaviour of the cylinders with intermediate thickness (r/t=600). For the perfect cylinder, the response is highly nonlinear near bifurcation and the post-buckling path drops rapidly (Figure 7.19).

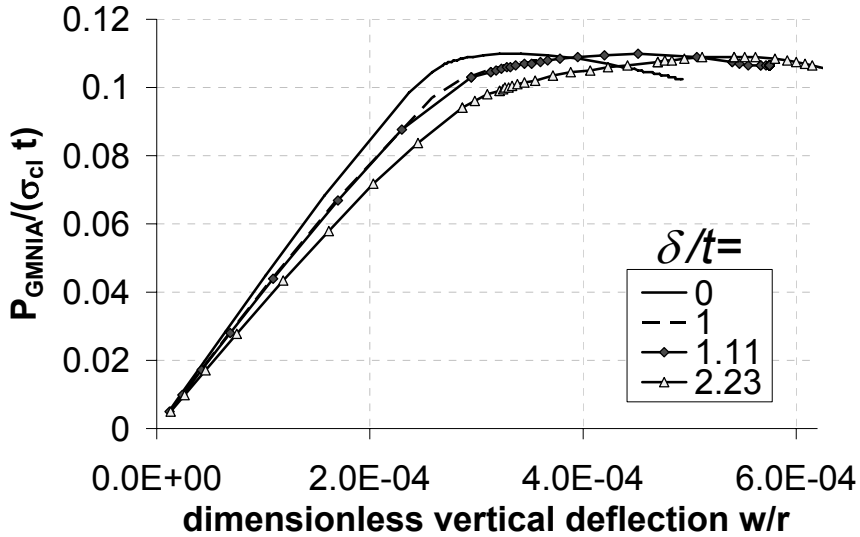

Figure 7.20: Load deflection curves (r/t=600, Γ=0.25, Λ =2), GMNIA

Shells of intermediate thickness, but small bracket (both in height and in width) (Figure 7.20) and the thickest shell (r/t=400, Figure 7.21 and Figure 7.22) do not show much imperfection sensitivity in the GMNIA analysis. This is caused by the extensive yielding in the pre-buckling path. The perfect shell already has a very soft and rounded response. With increasing imperfection amplitude, the response becomes even softer and a small bifurcation event occurs when much more plasticity is present, until the response becomes so soft that the loss of strength after buckling is minimal (Figure 7.21) and the overall response is similar to a load deflection curve for plastic collapse.

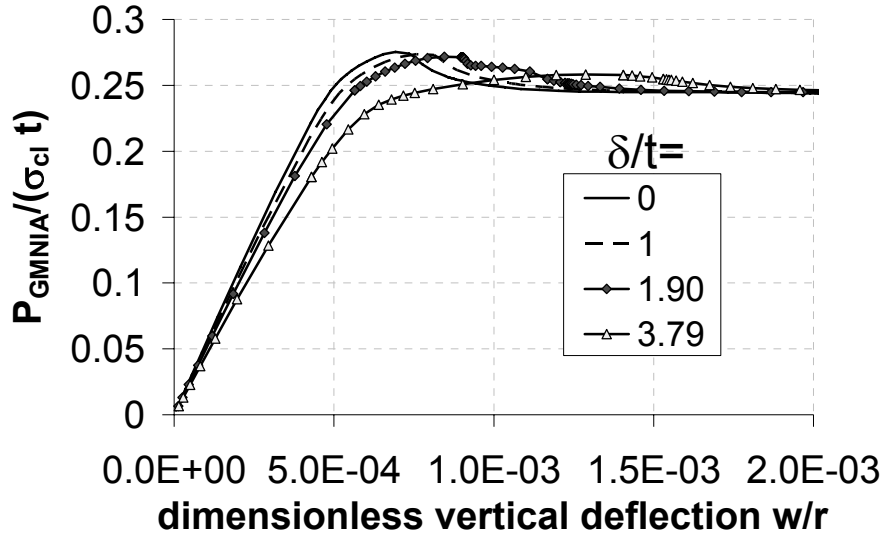

Figure 7.21: Load deflection curves (r/t=400, Γ=1.25, Λ =5), GMNIA

The thickest cylinder (r/t=400) with a narrow and short bracket (Γ=0.25, Λ=2) does not show any imperfection sensitivity (Figure 7.22) and while geometric imperfections make the elastic response softer, the very plastic peak limit load of the perfect shell disappears almost completely.

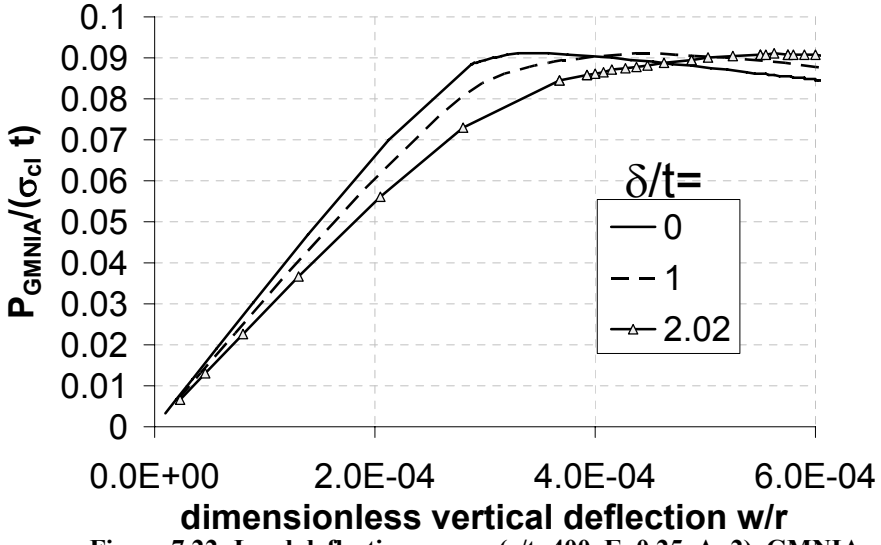

Figure 7.22: Load deflection curves (r/t=400, Γ=0.25, Λ=2), GMNIA

7.5.3 Summary

The overall behaviour of the imperfect shell is similar to that of the perfect shell. A very thin shell shows elastic buckling whilst a thick shell displays extensive yielding and the failure behaviour is similar to a plastic collapse. This pattern follows that of a very slender column failing by elastic buckling and a very stocky column experiencing plastic collapse. Cylinders with tall brackets display a higher

failure load than the same cylinder with a shorter bracket. This is due to the shear transfer of stress on the side of the bracket.

Since for any given value of the applied load the magnitude of stress is inversely proportional to the bracket width, it follows that with wide brackets (all other parameters remaining unchanged) have higher failure loads.

The imperfection sensitivity decreases when more plasticity is involved in the failure behaviour. Therefore a thin cylinder with a high and wide bracket shows the most significant imperfection sensitivity as long as failure is defined by the "first limit point.

The initially chosen imperfection amplitude of one wall thickness has shown a low imperfection sensitivity with a reduction of the failure load of up to 16% compared to the perfect shell when material nonlinearity was included and up to 27% when elastic behaviour was investigated.

A limited set of geometries with larger imperfection amplitude was analysed. The imperfection sensitivity for shell of intermediate thickness and thick shells was found to be low due to the influence of material nonlinearity for all imperfection amplitudes investigated.

The thin shell (r/t=1000) on the other hand showed a maximum decrease of strength of 54% for a very large imperfection. When such a high imperfection sensitivity was encountered the difference between the buckling load and the post-buckling minimum was almost zero and the post- buckling stiffening after the post-buckling minimum.

7.6 Conclusions

When the imperfection sensitivity of the bifurcation load was first considered in this thesis, it was expected that the bracket supported shell would be imperfection sensitive, in the same manner that most other studied cases of shell buckling have been found to be imperfection sensitive. When different shapes of imperfection were tested in the GNIA analysis, it was discovered that the imperfection in the form of the first eigenmode increased the strength of the structure instead of lowering it. While the deformed shape of the post- buckling minimum found in the geometrically nonlinear analysis (GNA) lowered the strength of the structure for very small

imperfection amplitudes, the strength was increased by larger imperfection amplitudes. The imperfection shape chosen for this study however was the deformed shape of the geometrically nonlinear analysis (GNA) at buckling, since it lowered the since this shape showed an continuous decrease of strength for all imperfection amplitudes and the decrease was also of the same magnitude as for the imperfection shape of the post- buckling minimum.

In the geometrically and materially nonlinear analysis (GMNIA) two different limit points were found. When failure at the "first limit point" was detected the strength of the structure decreased, but when the imperfection amplitude was too large the bifurcation event for the perfect shell disappeared and was replaced by failure at a "second limit point" at a much higher load in the GMNIA analysis. The failure load at the "second limit point" was as high, or higher than, the failure load of the perfect shell. When the loss of strength was significant at the "first limit point, it was also always accompanied by a progressively milder and milder bifurcation.

While the influence of an imperfection amplitude of one wall thickness found not to be significant, larger imperfections lead to a further decrease of strength (up to 54%) for the thin shells (r/t=1000) when failure at the "first limit point" was found. But the same imperfection amplitudes, which caused the greatest reduction of strength also led to a post-buckling minimum that was only very slightly smaller than the buckling load. When the difference between buckling load and post- buckling minimum is very small a slight change in geometry might lead to failure at the "second limit point" and the assessed strength of two very similar structures might differ considerably. It is therefore difficult to decide whether a minimal loss of strength after buckling should be included in design strength assessments.

The same behaviour was found in the GNIA analysis. Here too the most damaging imperfection amplitude coincided with a minimum difference between the buckling load and the post-buckling minimum.

When the buckling of a GNIA analysis using the "worst imperfection" is used to calculate the elastic imperfection reduction factor α, its value may be as low as 0.35. This should be compared with that for an externally pressurized cylinder (EN1993-1-6, 2006), where the value of alpha for the imperfect structure is around 0.7. A value below 0.7 was already produced by geometric nonlinearity in the perfect bracket

supported shell.

Also a value of α=0.35 would indicate that this structure is very imperfection sensitive, but this is a misleading result. This great imperfection sensitivity is only a result of the definition of failure.

More research needs to be done in what we define as failure, since a bifurcation with next to no loss of strength can hardly be described as damaging for a structure and is only failure by definition.

While the question of imperfection sensitivity is difficult to answer for thin shell, the thick and intermediate shells did not show any significant reduction of strength due to the investigated imperfection shape.

It is clear that this study of imperfection sensitivity is only a small part of a comprehensive study to understand the behaviour of the cylinder on discrete bracket supports completely. A more extensive investigation into other imperfection shapes and amplitudes is necessary.

However, the study has really led into a much more challenging field which requires much further research. This field demands answers to the question of what engineers should use as a criterion of failure, and whether it is acceptable for small changes in behaviour to lead to very large changes in the assessed strength.

8 Summary and conclusions

8.1 Introduction

A bracket supported silo has been investigated in this thesis within the framework of the European standard for strength and stability of shell structures EN1993-1-6 (2006). Due to a lack of experimental data and the considerable complexity of the problem, this study is entirely numerical

The computational models were all built within the program ABAQUS, which is capable of undertaking all the different analysis types defined in the Eurocode.

The bracket was treated as a rigid rectangular plate rigidly connected to a thin elastic-plastic cylindrical shell, and placed at some distance from the boundaries of the shell. The loading on the silo was characterised by a uniform tensile force acting at the lower edge of the cylinder, caused by the stored solid in the silo which was deemed to be principally carried by the hopper located beneath the cylinder. The accompanying internal pressure and frictional traction on the silo wall was omitted to produce a simplified treatment of the bracket problem.

The different kinds of numerical analysis defined in European standard for strength and stability of shell structures EN1993-1-6 (2006) have been used to investigate the different aspects of the behaviour of this cylindrical shell subject to a local load. In particular, special features were found associated with stress concentrations at the corners of the stiff bracket, and with stress transmission through the different boundaries of the bracket. The twin goals of the thesis have been to describe the structural behaviour of this system and to devise a design treatment of the problem that can capture a significant range of cylinder radius to thickness ratios and of bracket geometries. Because such a geometrical configuration needs many parameters to define it, the task of devising a satisfactory design treatment is quite substantial and involves a considerable part of the work of the thesis.

8.2 Problem description, methodology and literature review

The thesis opens with a description of the problem and the assumptions being made in the computational modelling. A brief review of the literature on shell structures, shell buckling and plastic collapse is next given with particular emphasis on the problem of a cylinder with its axis vertical and subjected to vertical local loads.

To give an overview over the different analyses and the response of the structure to each analysis, a carefully chosen example problem was fully described in Chapter 2, with exploration of the patterns of stress transfer and the outcome of each of the different kinds of analysis to be used later in the thesis.

In the following chapters, each kind of analysis was used, and the predictions of the strength of the structure given by that analysis type discussed in detail.

8.3 Linear bifurcation analysis

The first type of analysis studied was the linear bifurcation analysis (LBA). Three different eigenmodes were identified with their maximum amplitudes at different locations. It was expected that some simple relationships might be found that would capture the eigenvalues for brackets of different geometries, since many other shell buckling problems have this character, but it was found that these relationships were very complicated for the bracket-supported cylinder. As a result, a considerable effort had to be put into finding some simple relationships that could define the linear elastic bifurcation eigenvalues for this problem. An empirical fit to approximately 150 geometries was developed, and it was then independently verified using a further 150 geometries. Even though the empirical fit does match the numerical results very well, it does not lead to a good insight into the physical behaviour of the structure. To try to achieve this, a simple physical model was developed. This model still required an empirical fit to calculate the compressive force transmitted through the top of the bracket, but this empirical fit could possibly later be replaced by an analytical solution. Using these empirical fits, the linear bifurcation load can now be accurately predicted and hence the elastic critical resistance R_{cr} required in the Eurocode as one of the two reference loads.

8.4 Materially nonlinear analysis

The second basic type of analysis used aimed to determine the plastic collapse load of the bracket supported cylinder using a materially nonlinear analysis (MNA) with small displacement theory. This is the second reference load required by the Eurocode. This analysis proved to be a great challenge for the numerical analysis, as accurate reliable values for the plastic collapse load were sought, but the program ABAQUS failed to give credible results when simple choices of elements for the modelling were used. A substantial amount of work was undertaken to trace the source of these problems and three validation problems of increasing complexity were used to ensure that the computational model finally chosen was adequate for the task. These three different benchmark tests were performed to verify the element and mesh, and all tests accurately predicted the known algebraic collapse load.

The plastic collapse mechanism of a bracket supported silo was found to be confined to the area around the bracket and it was discovered that the maximum load that the cylinder could carry could be easily calculated using a very elementary analysis of the stress state at collapse using the von Mises yield criterion. Since the initial attempts to analyse the problem produced predicted failure loads much higher than was possible within the bounds of plasticity theory and the adopted assumptions, a considerable effort went into identifying the causes of this very obvious error. A thorough and extensive study of the possible source of error revealed that the commonly used S4R element is not capable of capturing very localized extensive yielding and consequently leads to a wrong result in the materially nonlinear analysis (MNA). The reason for this error in the element was not found even after many explorations using simple problem tests, but a solution to the difficulty was found by using a mixture of element types and taking advantage of the ability of each type to model plasticity and buckling. This mesh was then able to achieve the correct answer for all analyses.

The results from an existing publication treating a similar but not identical problem of a bracket supported cylinder were checked. In this previous study, the S4R element was used. Several cases were recalculated using the mesh finally chosen in this thesis, and it was shown that the plastic collapse loads presented in that study were incorrect due the unfortunate choice of element

A simple analytical expression was found to model the plastic collapse load very accurately, corresponding very well with the numerical results when the proposed mixture of elements was used. Using this simple equation, the second reference load (the plastic limit load required in the Eurocode (EN1993-1-6, 2006)) can now be calculated accurately.

8.5 Elastic geometrically nonlinear analysis

The third type of analysis used to study the bracket was an elastic geometrically nonlinear analysis (GNA). This exploration was principally concerned with the bifurcation or limit load buckling of perfect cylinders. The loss of strength due to the geometrical nonlinearity was measured by comparison of the nonlinear bifurcation load with the linear bifurcation load. For most other shell buckling problems, geometric nonlinearity plays a relatively small role, and the effects of geometric imperfections cause very large reductions in strength below the linear bifurcation load. By contrast, it was found for this problem of the bracket-supported cylinder that geometric nonlinearity plays a strong role in reducing the bifurcation buckling strength (up to 40%), but that geometric imperfections play a much smaller role. The reasons for this difference were explored and conclusions were drawn that are more widely relevant than simply to the bracket supported shell. It is evident that local loads can often cause an increase in the radius of curvature (flattening) and that this increase causes serious reductions in the shell buckling strength.

The investigation into the variation of the influence of the geometric nonlinearity with the geometry of the structure did not reveal a simple pattern, but a wave-like variation. This variation may be related to the changing location of the buckle in the linear elastic bifurcation analysis (LBA) against which the geometrically nonlinear elastic analysis (GNA) was being compared. Whilst the location of the buckle in the linear elastic bifurcation analysis (LBA) stayed in a relatively constant position with respect to the shell parameter $\sqrt{rt}$ for different geometries, the location of the buckle in the GNA did not.

It was found that the location of the maximum amplitude of the buckle in the geometrically nonlinear elastic analysis (GNA) moves away from the bracket when the height or the width of the bracket is increased. Some further investigations into

the loss of strength due to geometric nonlinearity could be usefully undertaken to gain a fuller understanding of the nonlinear buckling behaviour of the shell.

8.6 Geometrically and materially nonlinear analysis

Following the exploration of the two reference loads (linear elastic bifurcation and plastic collapse) and the knowledge gained about the elastic imperfection reduction factor (Chapter 5), the next study (Chapter 6) explored the behaviour of perfect shells in which both geometric and material nonlinearities were included. This analysis should give the "right" answer for the strength of the perfect structure.

The goal of this analysis is to identify the conditions under which elastic plastic buckling occurs. Elastic plastic buckling is conventionally represented by the capacity curve for the structure, so this curve was the goal of this study. The generalised capacity curve was taken from Eurocode 3 Part 1.6 (EN 1993-1-6, 2006), which defines the strengths of all shells in terms of the parameters α, β, η, λ_o and λ_p. These five parameters may each vary with the geometry and material properties of the structure, so a considerable amount of work is required to define them all.

To calculate the parameters of the capacity curves, 75 different geometries requiring over 750 different analyses were investigated. It was essential that geometric nonlinear effects were retained as constant in their effect as each curve was calculated, so the relative slenderness of the structure was changed by changing the yield stress of the material of the structure, rather than by changing the geometry of the structure. The latter is the commonly chosen method, since it is perfectly satisfactory for beam, column and frame structures.

The modified capacity curve was extensively used instead of the traditional capacity curve, as it affords easier and more precise extraction of the required parameters.

It was shown that a fixed choice for the value of the interaction exponent η leads to serious restriction on the form of the capacity curve in cases where early yielding needs to be considered. Therefore it was proposed that the interaction exponent η should be allowed to vary linearly with relative slenderness to eliminate this restriction. It was found that further restrictions should be placed on the values of the limiting interaction exponent to ensure that the elastic plastic strengths do not

exceed the elastic strengths. Algebraic relationships for these restrictions were determined.

Finally these calculations were used to develop expressions for the parameters of the capacity curve for a wide range of geometries of bracket and shell relative slenderness. Empirical expressions were derived which can be used in design calculations.

8.7 The effects of geometric imperfections

The imperfection sensitivity of bracket supported silos was studied using equivalent geometric imperfections in Chapter 7.

First, the recommendations of the European standard were implemented to choose different imperfection forms. A single example geometry was tested using a range of different imperfection forms and amplitudes in a geometrically nonlinear elastic analysis (GNIA), but the imperfection sensitivity did not follow the pattern expected of shells.

In particular, the commonly used eigenmode imperfection increased the failure load of the example bracket supported cylinder by up to 20% in this elastic nonlinear analysis when compared to the bifurcation load of the perfect shell. The imperfection sensitivity is commonly more pronounced for an imperfection with its maximum deviation directed towards the centre of the shell due to the biaxial compressive stress field arising from the inwards directed imperfection. Because of the uncommon imperfection sensitivity of the bracket supported silo using the first eigenmode imperfection, not only imperfections with a maximum imperfection displacement directed towards the centre of the cylinder were tested, but also imperfections directed outward for all imperfection shapes. The numerical calculation of imperfections directed away from the centre of the shell (outward) revealed a bifurcation load which was not only higher than the bifurcation load with imperfections directed towards the centre of the shell (inward), but also higher than the failure load of the perfect shell for all imperfection forms.

Of all the different imperfection shapes tested, only two reduced the failure load significantly; these shapes was the deformed shape of a geometrically nonlinear elastic analysis (GNA) at buckling and the deformed shape of a geometrically

nonlinear elastic analysis (GNA) at the post- buckling minimum. The loss of strength was similar for both imperfection shapes. While the post- buckling deformed shape leads to reduction of strength for small imperfections followed by an increase of strength for larger imperfection above the strength of the perfect shell, the deformed shape at buckling leads to a continuous decrease of strength.

The shape of the deformed shape at buckling also reduces the bifurcation load because it introduces a flattening of the cylindrical shell above the bracket, which is the main cause of the reduction in strength of the investigated bracket supported silo.

The imperfection sensitivity was then explored further using the imperfection of the deformed shape at buckling and a wide range of geometries in both geometrically and materially nonlinear analysis (GMNIA) and geometrically elastic analysis (GNIA). It was found that two different limit points exist depending on the imperfection amplitude. The first limit point is a bifurcation point lowering the strength of the shell, while the second limit point occurs when the imperfection amplitude is too large and the tangent stiffness matrix stays positive when passing the point where the "first limit point" might be expected. It was shown that when failure occurs at the "second limit point" the strength of the imperfect shell is almost the same as, or even higher than, the strength of the perfect shell.

The greatest loss of strength was found when the shell failed at the first limit point, but the difference between buckling strength and post-buckling minimum decreased very much as the limit point load fell, to such a degree that bifurcation could only be detected with great difficulty. The imperfection amplitudes for which such behaviour was detected could be called the "worst" imperfection amplitude. However, when the buckling load and the load at the post-buckling minimum are almost the same and no detectable loss of strength can be found at this point, it is questionable if this can reasonably be defined as failure or if the "second limit point" should be defined as such.

While the thick and intermediate shell did not show a significant imperfection sensitivity, it is not possible to give a simple answer to the question of the imperfection sensitivity for the thin shells. The structure is imperfection sensitive if the definition of failure is taken as the first bifurcation or limit point as suggested in the Eurocode (EN1993-1-6, 2006). If, on the other hand, bifurcation with minimal

loss of strength after bifurcation is considered not to fulfil the criteria of failure, the bracket supported silo is not imperfection sensitive. The study of the imperfection sensitivity of the bracket supported silo is far from complete, but it has been shown that the imperfection sensitivity changes greatly when a nonlinear stress pattern and significant pre-buckling deformations are present. In the most researched case of the uniformly compressed cylinder the influence of pre-buckling deformations is small compared to the imperfection sensitivity of the structure, but in the case of the bracket supported silo the influence of pre-buckling deformations is probably greater than the imperfection sensitivity of the structure.

8.8 Summary

Overall this thesis has led to a deeper understanding of the behaviour of structures with highly non-uniform stress patterns. It has been found that a bracket attached to the shell at mid-height leads to much more complicated behaviour than is found when discrete supports are placed at the bottom of the cylinder. Even though the failure response of the bracket supported silo is complex, high precision empirical expressions and a physical model have been developed to approximate the linear bifurcation load and a simple equation has been found to calculate the plastic collapse load. Further, a set of empirical equations to capture the five parameters of the capacity curve for the perfect structure have been developed.

It was shown that geometric nonlinearity is generally of greater significance than imperfection sensitivity when highly non-uniform stresses lead to pronounced pre-buckling deformations. This outcome is in opposition to the common assumption concerning the imperfection sensitivity of shells. Therefore, while the recommendation regarding imperfections in the European standard might be extensive and adequate for shells subject to relatively uniform stress conditions, much care should be exercised when more realistic stress states in shells are investigated.

This thesis has developed what is thought to be the first extensive study of capacity curves for a shell buckling problem. It was found that it was necessary to make some modifications to the simple capacity curve form to accommodate a greater range of applications.

8.9 Suggestions for further research

This thesis has presented a thorough study of the bracket supported cylinder, but some questions still need to be answered apart from those mentioned above.

The reason why the general purpose element S4R is not capable of capturing highly localized yielding could not been found. It is of the utmost importance to find the source of this error since this element is very widely used in research and design. A further benchmark test might be necessary in the European standard to ensure that the chosen elements are capable of capturing localized yielding.

A provisional proposal of an empirical fit has been given for the capacity curves, but a wider range of radius to thickness ratios needs to be investigated to verify and improve the approximation.

For the further development of understanding the behaviour of the bracket supported silo the assumptions made in this thesis should also be reviewed.

The column was assumed to very stiff and rigidly connected to the bracket. The influence of the stiffness of the column should be investigated by replacing the rigid support with elastically deformable supports.

The load case of tensile load at the bottom of the cylinder might be a simple and realistic load case (as shown in Chapter 1), but an additional friction on the cylinder wall might lead to a more imperfection sensitive behaviour and should be investigated. The bracket was placed at the mid-height of the cylinder, which allowed the study of the structure without influence of boundary conditions, but the bracket should be moved closer to the boundaries to investigate the changes in behaviour.

The imperfection sensitivity of the bracket supported silo has provided a few challenges. It is clear that more detailed study including more imperfection shapes and amplitudes is needed to understand the behaviour of the imperfect bracket supported silo.

The thesis has posed a very substantial question on how failure can be defined in a unique, but reasonably realistic way. It is critical that small changes in geometry do not lead to large jumps in the assessed strength, but it is not easy to find criteria that will produce this outcome as the criterion of failure necessarily moves from one aspect (e.g. bifurcation) to another (e.g. limiting the permitted deformation). This

question is not only of interest for the buckling of cylindrical shells, but all shell structures, and indeed to all structures in which buckling and changes of geometry lead to significantly complicated behaviour. It should be a critical topic for research for some time to come.

9 References

ACI313 (2004). "Standard Practice for Design and Construction of Concrete Silos and Stacking Tubes for Storing Antigranulocytes Materials (Aci 313) and Commentary." Aci Structural Journal **88**(1): 113-114.

Arbocz, J. (1982). The Imperfection Data Bank: A Means to Obtain Realistic Buckling Loads. Buckling of Shells. Eds: E. Ramm. Berlin, Springer Verlag**:** 535-567.

Arbocz, J. (1991). Towards an Improved Design Procedure for Buckling Critical Structures. Buckling of Shell Structures, on Land, in the Sea and in the Air. Eds**:** 270-276.

Arbocz, J. and Hol, J. M. A. M. (1995). "Collapse of Axially Compressed Cylindrical Shells with Random Imperfections." Thin-walled structures **23**(1/4): 131.

Arbocz, J. and Stam, A. R. (2004). A Probabilistic Approach to Design Shell Structures. Buckling of Thin Metal Shells. Eds: J. G. Teng and J. M. Rotter. London, Spon**:** 455-490.

AS3774-1996 (1996). " Loads on Bulk Solids Containers." Australian Standard, Standards Association of Australia.

Bauchau, O. A., Laulusa, A., Choi, J. Y., Tan, V. B. C. and Li, L. (2006). "Evaluation of Some Shear Deformable Shell Elements." International Journal of Solids and Structures **43**(17): 5033.

Berry, P. A. (1997). Buckling under Axial Compression of Cylindrical Shells with Circumferential Weld Shrinkage Depression. Department of Civil Engineering. Sydney, University of Sydney. **PhD Thesis**.

Berry, P. A., Bridge, R. Q. and Rotter, J. M. (1996). "Imperfection Measurement of Cylinders Using Automated Scanning with a Laser Displacement Meter." Strain **32**(1): 3-7.

Berry, P. A., Rotter, J. M. and Bridge, R. Q. (2000). "Compression Tests on Cylinders with Circumferential Weld Depressions." Journal of Engineering Mechanics-ASCE **126**(4): 405-413.

Bijlaard, P. P. (1955). "Stresses from Local Loading in Cylindrical Pressure Vessels." Trans. ASME **77**(August): 805-816.

Blachut, J., Galletly, G. D. and Moffat, D. G. (1991). An Experimental and Numerical Study into the Collapse Strength of Steel Domes. Buckling of Shell Structures, on Land, in the Sea and in the Air. Eds**:** 344-358.

Brendel, B. and Ramm, E. (1980). "Linear and Nonlinear Stability Analysis of Cylindrical Shells." Computers and Structures **12**(4): 549.

Brendel, B., Ramm, E., Fischer, D. F. and Rammerstorfer, F. G. (1981). "Linear and Non-Linear Stability Analysis of Thin Cylindrical Shells under Wind Loads." Journal of Structural Mechanics **9**(1): 91-113.

Brush, D. O. and Almroth, B. O. (1975). Buckling of Bars, Plates and Shells. New York, McGraw-Hill.

Bushnell, D. (1985). Computerized Buckling Analysis of Shells. Dordrecht.

Cai, M. (2003). Buckling Strength of Steel Thin Cylindrical Shells under Elevated Local Axial Compression. Institute of Infrastructure and Enviroment.

Edinburgh, University of Edinburgh. **PhD**.
Cai, M., Holst, J. M. F. G. and Rotter, J. M. (2002). Buckling Strength of Thin Cylindrical Shells under Localized Axial Compression. 15th ASCE Engineering Mechanics Conference, June 2-5, Columbia University, New York, NY:pp. 8.
Calladine, C. R. (1983). Theory of Shell Structures. Cambridge, Cambridge University Press.
Calladine, C. R. (1995). "Understanding Imperfection-Sensitivity in the Buckling of Thin-Walled Shells." Thin-Walled Structures **23**(1-4): 215-235.
Chang, C. S. and Conway, H. D. (1969). "Stress Analysis of an Infinite Plate Containing an Elastic Rectangular Inclusion." Acta Mechanica **8**(3-4): 160.
Chryssanthopoulos, M. K. (1998). "Probabilistic Buckling Analysis of Plates and Shells." Thin-Walled Structures **30**(1-4): 135.
Chryssanthopoulos, M. K., Baker, M. J. and Dowling, P. J. (1991a). "Imperfection Modeling for Buckling Analysis of Stiffened Cylinders." Journal of Structural Engineering-Asce **117**(7): 1998-2017.
Chryssanthopoulos, M. K., Baker, M. J. and Dowling, P. J. (1991b). "Statistical Analysis of Imperfections in Stiffened Cylinders." Journal of Structural Engineering **117**(7): 1979.
Chryssanthopoulos, M. K. and Poggi, C. (1995). "Stochastic Imperfection Modelling in Shell Buckling Studies." Thin-Walled Structures **23**(1-4): 179-200.
DASt-Richtlinie-017-E (1980). "Beulsicherheitsnachweise Für Schalen" Dast Richtlinie 013. Köln, Deutscher Ausschuss für Stahlbau**:** 13.
Deml, M. and Wunderlich, W. (1997). "Direct Evaluation of the `Worst' Imperfection Shape in Shell Buckling." Computer Methods in Applied Mechanics and Engineering **149**(1-4): 201.
DIN1055-6 (2005). Actions on Structures - Part 6: Design Loads for Buildings and Loads in Silo Bins. Deutsches Institute fur Normung. Berlin. **88:** 113-114.
DIN18800 (1990). Steel Structures: Stability, Buckling of Shells. Berlin, November 1990, Deutsches Institut fuer Normung. **Part4**.
Ding, X., Coleman, R. and Rotter, J. M. (1996a). "Surface Profiling System for Measurement of Engineering Structures." Journal of Surveying Engineering **122**(1): 3-13.
Ding, X., Coleman, R. and Rotter, J. M. (1996b). "Technique for Precise Measurement of Large-Scale Silos and Tanks." Journal of Surveying Engineering **122**(1): 14-25.
Doerich, C. (2002). Bracket Supported Silos. Institure fuer Stahlbau. Karlsruhe, University of Karlsruhe.
Donell, L. H. (1933). Stability of Thin-Walled Tubes under Torsion. NACA Techincal report No 479**:** 95-116.
Donnell, L. H. (1934). "A New Theory for the Buckling of Thin Cylinders under Axial Compression and Bending." Trans. ASME **56**: 795-806.
Donnell, L. H. and Wan, C. C. (1950). "Effect of Imperfections on Buckling of Thin Cylinders and Columns under Axial Compression." Journal of Applied Mechanics,ASME **17(1)**: 73-83.
Drucker, D. C. (1953). Limit Analysis of Cylindrical Shells under Axially Symmetric Loading. 1st Midwest. Conf. Solids Mech., Urbana, IL:pp. 158-163.
ECCS (2007). European Recommendations for Steel Construction: Buckling of

Shells. 5th edition, European Convention for Constructional Steelwork, Brussels.
Elishakoff, I., van Manen, S., Vermeulen, P. G. and Arbocz, J. (1987). "First-Order Second-Moment Analysis of the Buckling of Shells with Random Imperfections." AIAA Journal **25**(8): 1113.
EN1991-1-4 (2006). Eurocode 1: Actions on Structures - Part 4: Silos and Tanks. CEN. Brussels.
EN1993-1-6 (2006). " Eurocode 3: Design of Steel Structures, Part 1.6: Strength and Stability of Shell Structures." CEN.
EN1993-4-1 (2007). "Eurocode 3: Design of Steel Structures: Part 4.1: Steel Silos." CEN.
EN1993-4-2 (2007). "Eurocode 3: Design of Steel Structures: Part 4.2: Steel Tanks." CEN.
ENV1993-1-6 (1999). " Eurocode 3: Design of Steel Structures, Part 1.6: Strength and Stability of Shell Structures." CEN.
Flügge, W. (1932). "Die Stabilitaet Der Kreiszylinderschale." Ingenieur.-Archiv **Bd3**: 463.
Flügge, W. (1934). Statik Und Dynamik Der Schalen. Berlin, Springer.
Flügge, W. (1973). Stresses in Shells. 2nd ed, Berlin, Springer-Verlag.
Galletly, G. D. (1980). Elastic-Plastic Buckling and Collapse of Ellipsoidal and Torispherical Shells Subjected to Uniform Internal Pressure, Tbilisi, USSR, North-Holland:pp. 289.
Galletly, G. D. (1982). The Buckling of Fabricated Torispherical Shells under Internal Pressure. Buckling of Shells. Eds: E. Ramm. Berlin, Springer**:** 429-466.
Gerdeen, J. C. (1979). "Critical-Evaluation of Plastic Behavior Data and a United Definition of Plastic Loads for Pressure Components." Welding Research Council Bulletin(254): 1-64.
Gillie, M. (2002). Personal Communication. Edinburgh.
Gillie, M. and Holst, J. M. F. G. (2003). "Structural Behaviour of Silos Supported on Discrete, Eccentric Brackets." Journal of constructional steel research: JCSR **59**(7): 24.
Gillie, M., Holst, J. M. F. G., Münch, M. and Rotter, J. M. (2002). "Behaviour of Silos Supported on Discrete Brackets." International Journal of Structural Stability and Dynamics **2**(1): 45-62.
Gillie, M. and Rotter, J. M. (2002). "The Effects of Patch Loads on Thin-Walled Steel Silos." Thin-Walled Structures **40**(10): 835-852.
Godoy, L. A. and Sosa, E. M. (2003). "Localized Support Settlements of Thin-Walled Storage Tanks." Thin-Walled Structures **41**(10): 941-955.
Gotsulyak, E. A. and Zhadrasinov, N. T. (1985). "Stability of Torispherical and Toriconical Vessel Heads under Internal Pressure." International Applied Mechanics **21**(3): 244.
Gould, P. L. and Sen, S. K. (1974). "Column Moments in Eccentrically Supported Tanks." Journal of the Structural Division,ASCE **100**(10): 2165-2169.
Gould, P. L., Sen, S. K., Wang, R. S. C., Suryoutomo, H. and Lowrey, R. D. (1976). "Column Supported Cylindrical-Conical Tanks." Journal of the Srtuctural Division,ASCE **102**(2): 429-447.
Greiner, R. and Guggenberger, W. (1998). "Buckling Behaviour of Axially Loaded

Steel Cylinders on Local Supports - with and without Internal Pressure." Thin-Walled Structures **31**: 159-167.

Guggenberger, W. (1991). Buckling of Cylindrical Shells under Local Axial Loads. International Colloquium on Buckling of Shell Structures on Land, in the Sea and in the Air, Villeurbanne, Lyon, France, Elsevier Science Publishers B.V., Amsterdam, Neth:pp. 323-333.

Guggenberger, W. (1998). "Proposal for Design Rules of Axially Loaded Steel Cylinders on Local Supports." Thin-Walled Structures **31**(1-3): 169-185.

Guggenberger, W. (2006). "Elastic Stability and Imperfection Sensitivity of Axially Loaded Cylindrical Shells on Narrow Supports." Computational Mechanics **37**(6): 537-550.

Guggenberger, W., Greiner, R. and Rotter, J. M. (2000). "The Behaviour of Locally-Supported Cylindrical Shells: Unstiffened Shells." Journal of Constructional Steel Research **56**(2): 175-197.

Guggenberger, W., Greiner, R. and Rotter, J. M. (2004). Cylindrical Shells above Local Supports. Buckling of Thin Metal Shells. Eds: J. G. Teng and J. M. Rotter. London, Spon Press 2004**:** 88-128.

HKS (2003). Abaqus User's Manual Ver 6.4, Hibbit. Rhode Island, USA, Karlsson & Sorensen Inc.

Hodge, P. G. J. (1963). Limit Analysis of Rotationally Symmetric Plates and Shells. New Jersey, Englewood Cliffs: Prentice-Hall.

Hodge, P. G. J. (1964). "Plastic Design of a Closed Cylindrical Structure." Journal of Mechanics and Physics of Solids **12**: 1-10.

Hodge, P. G. J. and Brooklyn, N. Y. (1954). "Rigid-Plastic Analysis of Symmetrically Loaded Cylindrical Shells." Journal of Applied Mechanics **21**(December).

Hodge, P. G. J. and Panarelli, J. (1962). "Interaction Curves for Circular Cylindrical Shells According to the Mises or Tresca Yield Criterion." Journal of Applied Mechanics **29**(June).

Hoehn, K., Scheider, W. and Timmel, I. (2001). Einfluss Der Imperfektionsamplitude Auf Die Maßgebende Versagensart Stählerner Kamine. Lacer No. 6. Leibzig, Massivbau und Baustofftechnologie, Wirtschaftswissenschaftliche Fakultät, Leipzig, Federal Republic of Germany.

Holst, J. M. F. G., Doerich, C. and Rotter, J. M. (2005). Accurate Determination of the Plastic Collapse Loads of Shells When Using Finite Element Analyses. Proc. ICASS'05, Shanghai:pp.

Holst, J. M. F. G. and Rotter, J. M. (2004). Settlement beneath Cylindrical Shells. Buckling of Thin Metal Shells. Eds: J. G. Teng and J. M. Rotter. Spon, London**:** 129-153.

Holst, J. M. F. G. and Rotter, J. M. (2005). "Axially Compressed Cylindrical Shells with Local Settlement." Thin-Walled Structures **43**(5): 811.

Holst, J. M. F. G., Rotter, J. M. and Calladine, C. R. (2000). "Imperfections and Buckling in Cylindrical Shells with Consistent Residual Stresses." Journal of Constructional Steel Research **54**(2): 265-282.

Holst, J. M. F. G., Rotter, J. M., Gillie, M. and Münch, M. (2002). Failure Criteria for Shells on Local Supports. New Approaches to Structural Mechanics, Shells and Biological Structures, Celebration volume for the 60th birthday of Prof. C.R. Calladine, University of Cambridge, Kluwer Academic Publishers,

London:pp. 315-327.
Hopkins, H. G. and Prager, W. (1953). "The Load Carrying Capacities of Circular Plates." Journal of the Mechanics and Physics of Solids **2**(1): 1.
Horne, M. R. and Merchant, W. (1965). "The Stability of Frames."
Huebner, A., Teng, J. G. and Saal, H. (2006). "Buckling Behaviour of Large Steel Cylinders with Patterned Welds." International Journal of Pressure Vessels and Piping **83**(1): 13.
Hutchinson, J. W. and Koiter, W. T. (1970). Postbuckling theory. Appl. Mech. Rev.(23): 1353–1366.
Ilyushin, A. A. (1948). Plasticity (in Russian). Moscow: Gostekhizda.
Janssen, H. A. (1895). "Versuche Uber Getreidedruck in Silozellen." Zeitschrift des Vereines Deutscher Ingenieure **39**(35): 1045-1049.
Kaplan, A. (1974). Buckling of Spherical Shells. Thin Shell Structures- Theory, Experiment and Design. Eds: Y. C. Fung and E. E. Sechler. NJ, Prentice-Hall, Englewood Cliffs**:** 247-288.
Karman, T. v., Sechler, E. G. and Donnell, L. H. (1932). "The Strength of Thin Plates in Compression." Trans. Am. Soc. Mech. Engrs(54): 53–57.
Karman, T. v. and Tsien, H. S. (1941). "The Buckling of Thin Cylindrical Shells under Axial Compression." J. Aeronaut. Sci.(8): 303–312.
Kildegaard, A. (1969). Bending of a Cylindrical Shell Subjected to Axial Loading. Second Symposium on Theory of thin Shells, IUTAM, Copenhagen, Springer, Berlin:pp. 301-315.
Koiter, W. T. (1945). Over De Stabiliteit Van Het Elastisch Evenwicht. Amsterdam, Uitgeverij H. J. Paris 1945. **PhD**.
Koiter, W. T. (1970). Stability of Elastic Equilibrium: Translation, AFFDL-TR-70-25, Wright-Patterson Air Force Base.
Kollár, L. and Dulácska, E. (1984). Buckling of Shells for Engineers. Chichester, Wiley 1984.
Kraus, H. (1967). Thin Elastic Shells: An Introduction to the Theoretical Foundations and the Analysis of Their Static and Dynamic Behaviour. New York, Wiley.
Li, H. Y. (1994). Analysis of Steel Silo Structures on Discrete Supports. Department of Civil Engineering & Building Science. Edinburgh, University of Edinburgh. **PhD:** 221.
Li, H. Y. and Rotter, J. M. (1996). Algebraic Analysis of Elastic Circular Cylindrical Shells under Local Loadings (Part 1 and Part 2). International Conference on Advances in Steel Structures, ICASS '96, Hong Kong, PERGAMON PRESS LTD:pp. 801-807 and 808-814.
Libai, A. and Durban, D. (1977). "Buckling of Cylindrical Shells Subjected to Nonuniform Axial Loads." (77-WA/APM-12): 7.
Limam, A. (2004). Buckling of Shells and Behaviour under Crash Conditions of Tubular Structures: Experimental and Numerical Studies. L'Institut National des Sciences Appliquées de Lyon. Lyon, France.
Lorenz, R. (1908). "Achsensymmetrische Verzerrungen in Duennwandigen Holhlzylindern." Zeitschrift VDI **52**: 1706-1713.
Lu, Z., Obrecht, H. and Wunderlich, W. (1995). "Imperfection Sensitivity of Elastic and Elastic-Plastic Torispherical Pressure Vessel Heads." Thin-Walled Structures **23**(1-4): 21.

Lundquist, E. E. (1935). Strength Tests of Thin-Walled Duralumin Cylinders in Combined Transverse Shear and Bending, National Advisory Committee for Aeronautics, Washington, DC, United States**:** 18.

Madsen, W. A. and Hoff, N. J. (1965). The Snap-through and Postbucklingequilibrium Behavior of Circular Cylindrical Shells under Axial Load. Stanford, California, STANFORD UNIV CALIF DEPT OF AERONAUTICS AND ASTRONAUTICS.

Mandal, P. and Calladine, C. R. (2002). "Lateral-Torsional Buckling of Beams and the Southwell Plot." International Journal of Mechanical Sciences **44**(12): 2557-2571.

Massonnet, C. E. and Save, M. (1972). Plastic Analysis and Design of Plates, Shells and Disks. Amsterdam; London, North-Holland Publishing Co. 1972.

Mendelson, A. (1968). Plasticity; Theory and Application. New York, Macmillan.

Mises, R. v. (1914). "Der Kritische Aubendruck Zylindrischer Rohre." Z. d. Vereins dt. Ingenieure **58** (19): 750.

Novozhilov, V. V. and Radok, J. R. M. (1964). Thin Shell Theory. 2nd ed., Groningen, Noordhoff.

Ooi, J. Y., Pham, L. and Rotter, J. M. (1990). "Systematic and Random Features of Measured Pressures on Full-Scale Silo Walls." Engineering Structures **12**(2): 74-87.

Peter, J. (1974). Zur Stabilitat Von Kreiscylinderschalen Unter Ungleichmaessig Verteilten Axialen Randbelastungen. Hannover, Univ Hannover, Germany. **PhD**.

Pinna, R. and Ronalds, B. F. (2003). "Buckling and Postbuckling of Cylindrical Shells with One End Pinned and the Other End Free." Thin-walled structures **41**(6): 507-527.

Pircher, M. and Bridge, R. (2001). "The Influence of Circumferential Weld-Induced Imperfections on the Buckling of Silos and Tanks." Journal of Constructional Steel Research **57**(5): 569-580.

Riks, E. (1979). "An Incremental Approach to the Solution of Snapping and Buckling Problems*1." International Journal of Solids and Structures **15**(7): 529-551.

Rotter, J. M. (1982). Analysis of Ringbeams in Column-Supported Bins. ACMSM 8: Proceedings of the Eighth Australasian Conference on the Mechanics of Structures & Materials., Newcastle, Aust, Univ of Newcastle, Newcastle, Aust:pp. 33-1.

Rotter, J. M. (1985). Buckling of Ground-Supported Cylindrical Steel Bins under Vertical Compressive Wall Loads. Metal Structures Conference, Melbourne, Institution of Engineers Australia:pp. 112-127.

Rotter, J. M. (1986). The Analysis of Steel Bins Subject to Eccentric Discharge. Second International Conference on Bulk Materials Storage Handling and Transportation, Institution of Engineers, Australia, Wollongong:pp. 264-271.

Rotter, J. M. (1996). Elastic Plastic Buckling and Collapse in Internally Pressurised Axially Compressed Silo Cylinders with Measured Axisymmetric Imperfections: Interactions between Imperfections, Residual Stresses and Collapse. Proc. International Workshop on Imperfections in Metal Silos: Measurement, Characterisation and Strength Analysis, CA-Silo, Lyon, France:pp. 119-140.

Rotter, J. M. (1998a). "Development of Proposed European Design Rules for Buckling of Axially Compressed Cylinders." Advances in Structural Engineering **1**(4): 273-286.

Rotter, J. M. (1998b). "Shell Structures: The New European Standard and Current Research Needs." Thin-Walled Structures **31**(1-3): 3-23.

Rotter, J. M. (2001a). Guide for the Economic Design of Circular Metal Silos. London; New York, Spon Press.

Rotter, J. M. (2001b). "Pressures, Stresses and Buckling in Metal Silos Containing Eccentrically Discharging Solids." Festschrift Richard Greiner, Celebration volume for the 60th birthday of Prof. Richard Greiner: 85-104.

Rotter, J. M. (2002). Shell Buckling and Collapse Analysis for Structural Design. Paper for the Festschrift for Professor Chris Calladine, Cambridge:pp.

Rotter, J. M. (2003). Buckling of Shallow Conical Shell Roofs for Small Diameter Tanks and Silos. International conference on design, inspection and maintenance of cylindrical steel tanks and pipelines, Prague, Czech Republic:pp. 169-175.

Rotter, J. M. (2004). Buckling of Cylindrical Shells under Axial Compression. Buckling of Thin Metal Shells. Eds: J. G. Teng and J. M. Rotter. London, Spon**:** 42-87.

Rotter, J. M. (2005). The Practical Design of Shell Structures Exploiting Different Methods of Analysis. SSTA8: Eighth Conference on Shell Structures: Theory and Applications, Gdansk-Jurata, Taylor and Francis, London:pp. pp. 71-86.

Rotter, J. M. (2007). Silo and Hopper Design for Strength. Chapter 4 in Bulk Solids Handling Equipment Selection and Operation. Eds: E. D. McGlinchey. Oxford, Blackwell**:** 37 p.

Rotter, J. M., Coleman, R., Ding, X. L. and Teng, J. G. (1992). The Measurement of Imperfections in Cylindrical Silos for Buckling Strength Assessment. Proc., Fourth International Conference on Bulk Materials Storage Handling and Transportation, Institution of Engineers, Australia, Wollongong:pp. 473-479.

Rotter, J. M. and Hull, T. S. (1989). "Wall Loads in Squat Steel Silos During Earthquakes." Engineering Structures **11**(3): 139-147.

Rotter, J. M., Jumikis, P. T., Fleming, S. P. and Porter, S. J. (1989). "Experiments on the Buckling of Thin-Walled Model Silo Structures." Journal of Constructional Steel Research **13**(4): 271-299.

Rotter, J. M. and Teng, J.-G. (1989). "Elastic Stability of Cylindrical Shells with Weld Depressions." Journal of Structural Engineering **115**(5): 1244-1263.

Rotter, J. M., Teng, J. G. and Li, H. Y. (1991). Buckling in Thin Elastic Cylinders on Column Supports. International Colloquium on Buckling of Shell Structures on Land, in the Sea and in the Air, Villeurbanne, Lyon, France, Elsevier, London:pp. 334-343.

Rotter, J. M. and Zhang, Q. (1990). "Elastic Buckling of Imperfect Cylinders Containing Granular Solids." Journal of Structural Engineering **116**(8): 2253-2271.

Samuelson, L. A. (1987). Design of Cylindrical Shells Subjected to Local Loads in Combination with Axial or Radial Pressure. Proc. Int. Colloquium on the Stability of Plate and Shell Structures, Gent, Belgium, ECCS:pp. 589-596.

Samuelson, L. A. (1990). Effect of Local Loads on the Stability of Shells Subjected to Uniform Pressure Distribution. Proc. IUTAM Symposium on Contact

Loading and Local Effects in Thin-Walled Plated and Shell Structures, Prague, Preliminary Report 1990:pp. 34-38.
Samuelson, L. Å. and Eggwertz, S. (1992). Shell Stability Handbook.
Sawczuk, A. and Hodge, P. (1960). "Comparison of Yield Conditions for Circular Cylindrical Shells." Journal of the Franklin Institute **269(5)**: 362-374.
Schenk, C. A. and Schueller, G. I. (2003). "Buckling Analysis of Cylindrical Shells with Random Geometric Imperfections." International journal of non-linear mechanics **38**(7): 1119.
Schmidt, H. (2000). "Stability of Steel Shell Structures - General Report." Journal of Constructional Steel Research **55**(1-3): 159-181.
Schneider, W., Timmel, I. and Hohn, K. (2005). "The Conception of Quasi-Collapse-Affine Imperfections: A New Approach to Unfavourable Imperfections of Thin-Walled Shell Structures." Thin-Walled Structures **43**(8): 1202.
Seide, P. (1975). Small Elastic Deformations of Thin Shells. Leiden, Kluwer Academic Publishers.
She, K. M. and Rotter, J. M. (1993). Nonlinear and Stability Behaviour of Discretely Supported Cylinders. Research Report.93-01, Department of Civil Engineering. University of Edinburgh.
Singer, J. and Abramovich, H. (1995). "Development of Shell Imperfection Measurement Techniques." Thin-Walled Structures **23**(1-4): 379.
Song, C. Y. and Teng, J. G. (2003). "Buckling of Circular Steel Silos Subject to Code-Specified Eccentric Discharge Pressures." Engineering Structures **25**(11): 1397-1417.
Song, C. Y., Teng, J. G. and Rotter, J. M. (2004). "Imperfection Sensitivity of Thin Elastic Cylindrical Shells Subject to Partial Axial Compression." International journal of solids and structures **41**(24-25): 7155.
Southwell, R. V. (1914). "On the General Theory of Elastic Stability." Phil. Trans. Roy. Soc. **Series A 213**: 187-244.
Southwell, R. V. (1932). "On the Analysis of Experimental Observations in Problems of Elastic Stability." Proceedings of the Royal Society of London **135**(Series A): 601-616.
Teng, J. G. and Rotter, J. M. (1990). A Study of Buckling in Column-Supported Cylinders. International Union for Theoretical and Applied Mechanics Symposium, Prague, Academia Press:pp. 52-61.
Teng, J. G. and Rotter, J. M. (1991). "Collapse Behavior and Strength of Steel Silo Transition Junctions.1. Collapse Mechanics." Journal of Structural Engineering-Asce **117**(12): 3587-3604.
Teng, J. G. and Rotter, J. M. (1992a). "Linear Bifurcation of Perfect Column-Supported Cylinders - Support Modeling and Boundary-Conditions." Thin-Walled Structures **14**(3): 241-263.
Teng, J. G. and Rotter, J. M. (1992b). Strength of Circular Steel Silos: New Investigations. Simultaneus Convening of the 4th International Conference on Bulk Materials Storage, Handling and Transportation and the 7th International Symposium on Freight Pipelines, Jul 6-8 1992, Wollongong, Aust, Publ by IE Aust, Barton, Aust:pp. 459-466.
Teng, J. G. and Rotter, J. M. (2004a). Buckling of Thin Metal Shells. London, Spon.
Teng, J. G. and Rotter, J. M. (2004b). Buckling of Thin Shells: An Overview. Buckling of Thin Metal Shells. Eds: J. G. Teng and J. M. Rotter. London,

Spon**:** 1-41.
Teng, J. G. and Song, C. Y. (2001). "Numerical Models for Nonlinear Analysis of Elastic Shells with Eigenmode-Affine Imperfections." International Journal of Solids and Structures **38**(18): 3263-3280.
Thorburn, R. and Patrick, R. (2005). Experiments on Buckling of Cylindrical Shells on Local Supports. School of Engineering and Electronics. Edinburgh, University of Edinburgh. **MEng theses in Civil Engineering**.
Timoshenko, S. (1910). "Einige Stabilitaetsprobleme Der Elastizitaetstheorie." Zeitschrift Mathematik und Physik **58**: 337-385.
Timoshenko, S. (1953). History of Strength of Materials, with a Brief Account of the History of Theory of Elasticity and Theory of Structures. New York, McGraw-Hill.
Timoshenko, S. and Gere, J. M. (1961). Theory of Elastic Stability. New York, McGraw-Hill.
Timoshenko, S. P. (1936). Theory of Elastic Stability. New York, Mc Graw-Hill 1936.
Timoshenko, S. P. and Goodier, J. N. (1970). Theory of Elasticity. 3rd edn, New York, McGraw-Hill.
Timoshenko, S. P. and Woinowsky-Krieger, S. (1959). Theory of Plates and Shells. 2nd edn, New York, McGraw-Hill.
Virella, J. C., Godoy, L. A. and Suarez, L. E. (2006). "Dynamic Buckling of Anchored Steel Tanks Subjected to Horizontal Earthquake Excitation." Journal of Constructional Steel Research **62**(6): 521.
Walker, P. and Wilson, D. R. (2001). Buckling of Cylinders with Local Loads Normal to the Shell. School of Civil and Environmental Engineering. Edinburgh, University of Edinburgh. **MEng theses:** ~150.
Weingarten, V. I., Morgan, E. J. and Seide, P. (1965). "Elastic Stability of Thin-Walled Cylindrical and Conical Shells under Axial Compression." Aiaa Journal **3**(3): 500-&.
Wolmir, A. S. (1962). "Biegsame Platten Und Schalen." Verlag für Bauwesen(75): 194–195.
Wunderlich, W., Rensch, H. J. and Obrecht, H. (1982). Analysis of Elastic-Plastic Buckling and Imperfection-Sensitivity of Shells of Revolution. Buckling of Shells. Eds: E. Ramm. Berlin, Springer**:** 137-174.
Wunderlich, W. and Seiler, C. (2000). "Nonlinear Treatment of Liquid-Filled Storage Tanks under Earthquake Excitation by a Quasistatic Approach." Computers & Structures **78**(1-3): 385.
Yamaki, N. (1984). Elastic Stability of Circular Cylindrical Shells. North-Holland.
Young, T. (1807). "A Course of Lectures on Natural Philosophy and the Mechanical Arts."
Zhao, Y. and Teng, J. G. (2003). "A Stability Design Proposal for Cone-Cylinder Intersections under Internal Pressure." International Journal of Pressure Vessels and Piping **80**(5): 297.
Zhao, Y. and Yu, J. (2005). Structural Behavior of Column-Supported Steel Silos with Engaged Columns. Fourth International Conference on Advances in Steel Structures, Shanghai, Elsevier:pp. 1521-1526.

10 Appendix

10.1 Notations

The following notations are used in this thesis. All symbols are defined where they first appear in the text. In general only one meaning is assigned to each symbol, but in those cases where more than one meaning is possible, the correct one will be evident from the context in which it is used.

r	radius of the cylinder
t	thickness of the cylinder
Ξ=r/t	radius to thickness ratio of the cylinder
H	height of the cylinder
2d	width of the bracket
h	height of the bracket
$\Lambda = h/\sqrt{rt}$	dimensionless height of the bracket
$\Gamma = d/\sqrt{rt}$	dimensionless half width of the bracket
U	circumference
A	area
n	number of columns
F	vertical support force per bracket
P_x	applied load as tension on the bottom of the shell
R_x	failure load
σ_{cl}	classical buckling stress
w	vertical deflection at the top of the cylinder
σ_{ub}	mean compressive stress just above the bracket
λ	bending half wave length
σ	stress
n_x	axial membrane stress resultant
E	Young's modulus
σ_y	yield stress
ν	Poisson ratio

ζ	percentage of the applied load transferred as compression into the top of the bracket
φ	angle of spread
λ_d	location of the buckle
δ	influence of the shear field as a percentage of the height of the bracket
Δ	length on which the classical buckling stress is applied
$\theta_o = (d/r)$	dimensionless width of the bracket
δ/t	dimensionless imperfection amplitude
α	elastic imperfection reduction factor
β	plastic range factor
$\bar{\lambda}$	relative slenderness
λ_0	squash limit relative slenderness
λ_p	plastic limit slenderness
χ	characteristic strength
η	interaction exponent
η_0	plastic limit interaction exponent
η_p	elastic limit interaction exponent
R_{cr}	elastic critical resistance
R_{pl}	plastic reference resistance
γ	the bulk density of the solid
τ	frictional stress
q	mean vertical stress
μ	wall friction coefficient
p	mean horizontal pressure

10.2 Modified capacity curves (r/t=400)

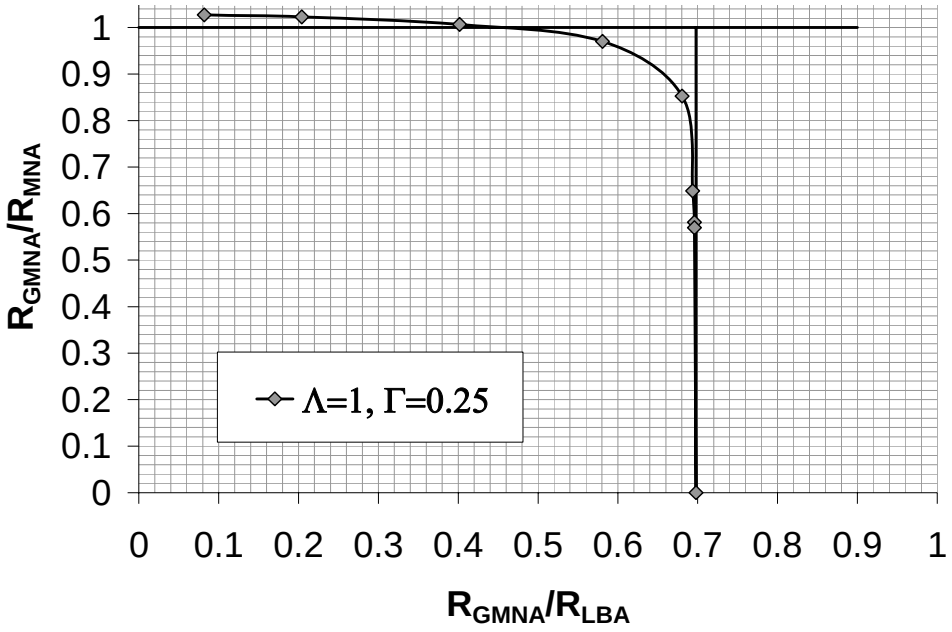

Figure 10.1: Modified capacity curve (Λ=1, Γ=0.25, r/t=400)

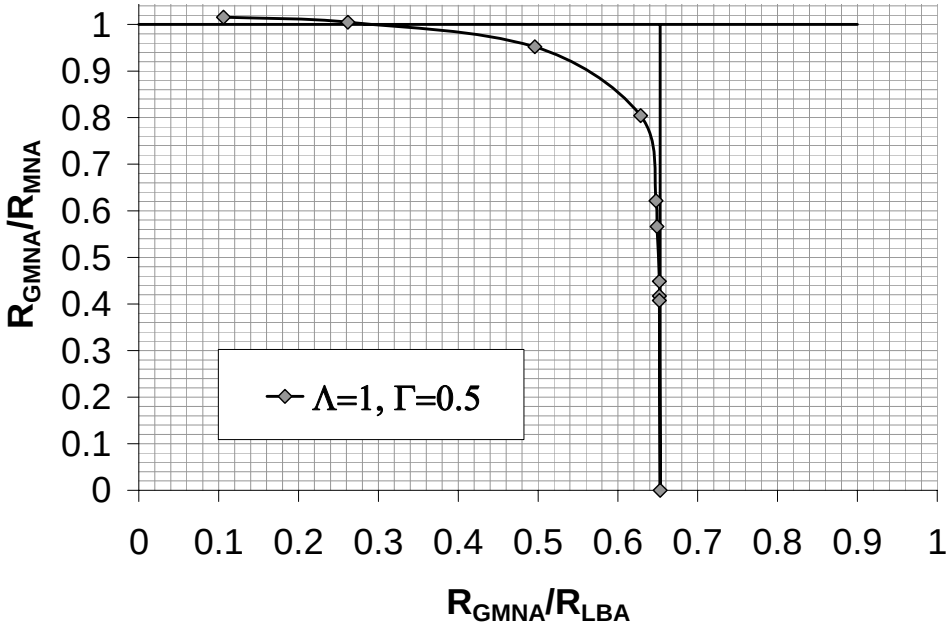

Figure 10.2: Modified capacity curve (Λ=1, Γ=0.50, r/t=400)

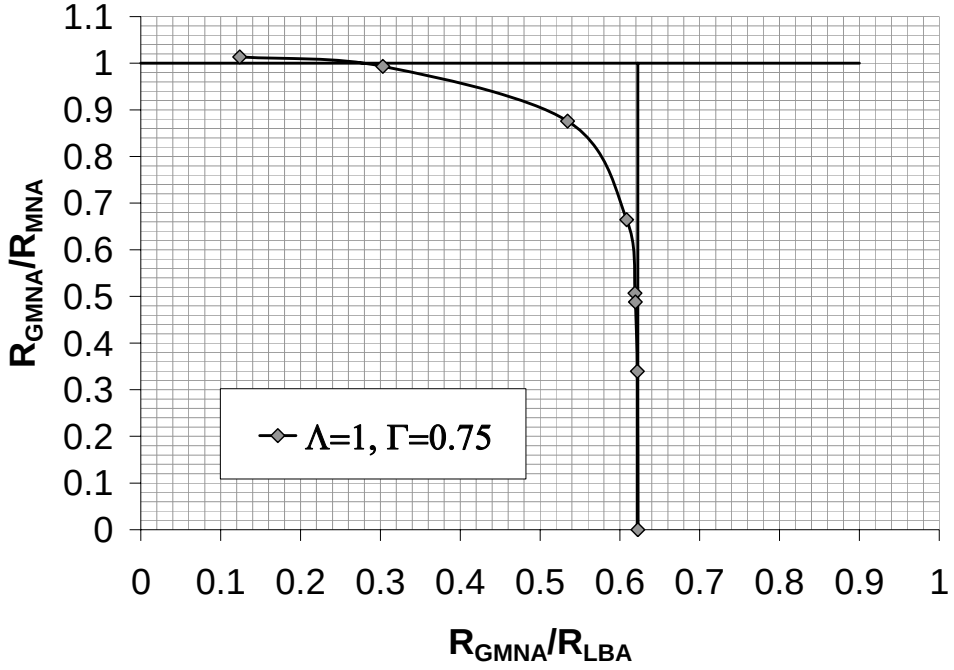

Figure 10.3: Modified capacity curve (Λ=1, Γ=0.75, r/t=400)

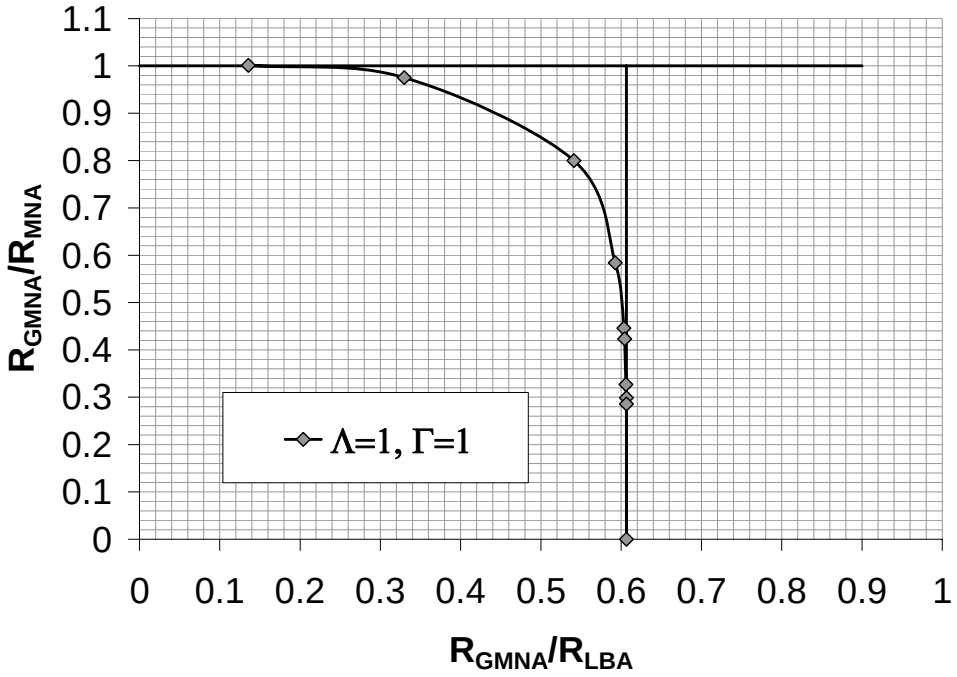

Figure 10.4: Modified capacity curve (Λ=1, Γ=1.00, r/t=400)

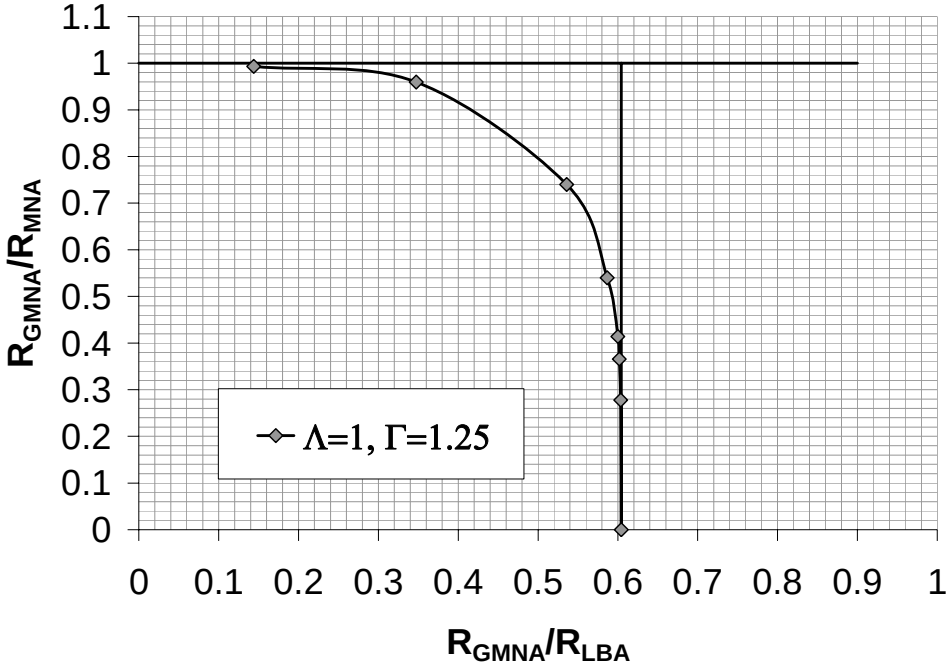

Figure 10.5: Modified capacity curve (Λ=1, Γ=1.25, r/t=400)

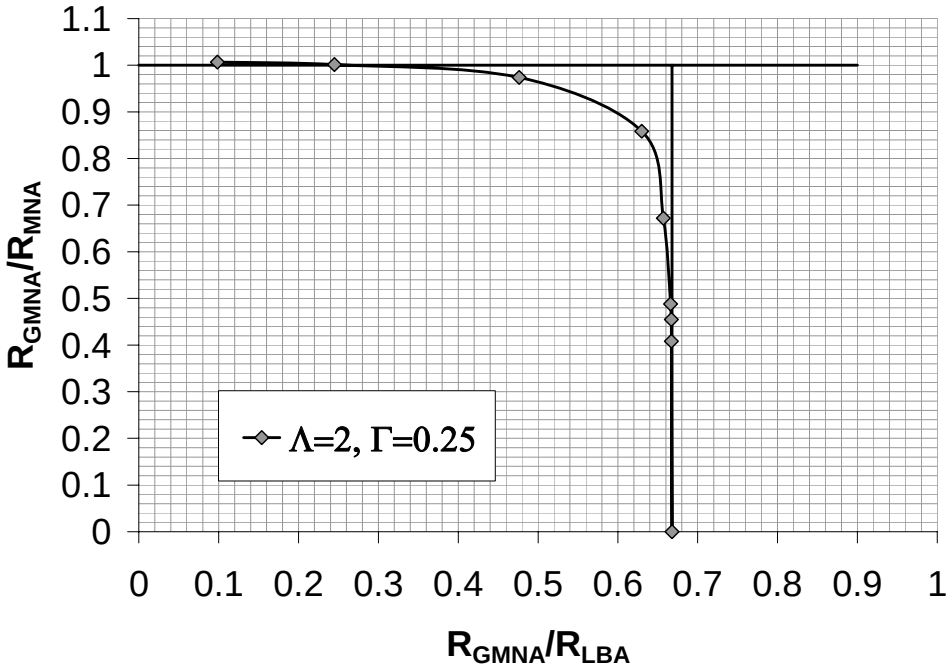

Figure 10.6: Modified capacity curve (Λ=2, Γ=0.25, r/t=400)

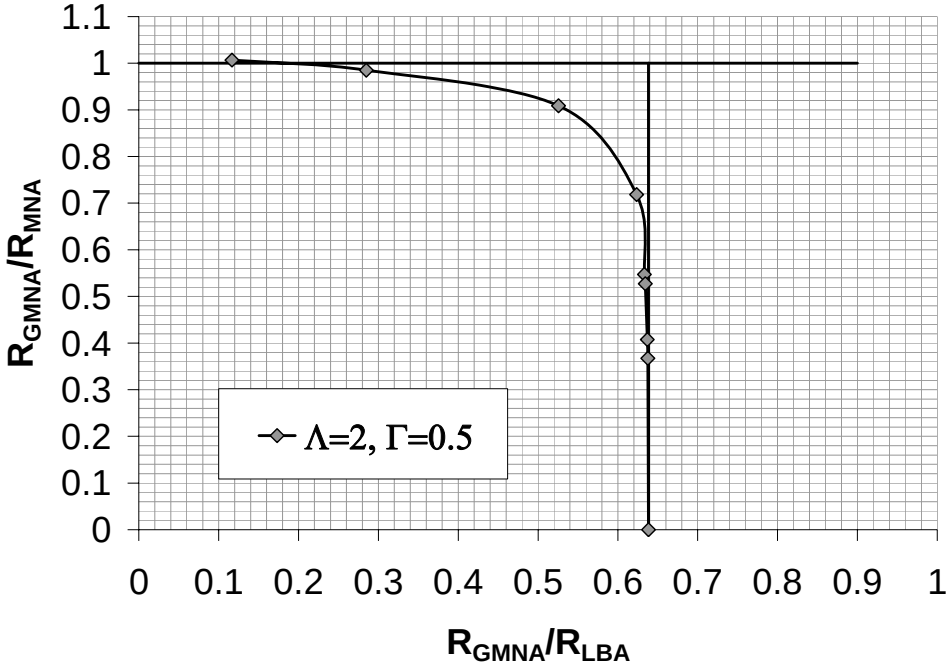

Figure 10.7: Modified capacity curve (Λ=2, Γ=0.50, r/t=400)

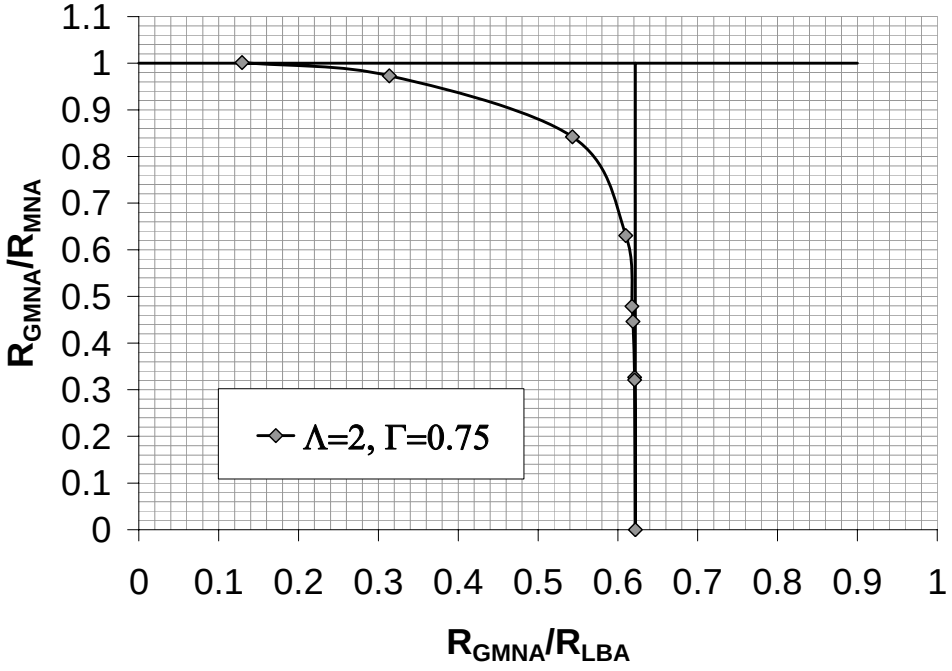

Figure 10.8: Modified capacity curve (Λ=2, Γ=0.75, r/t=400)

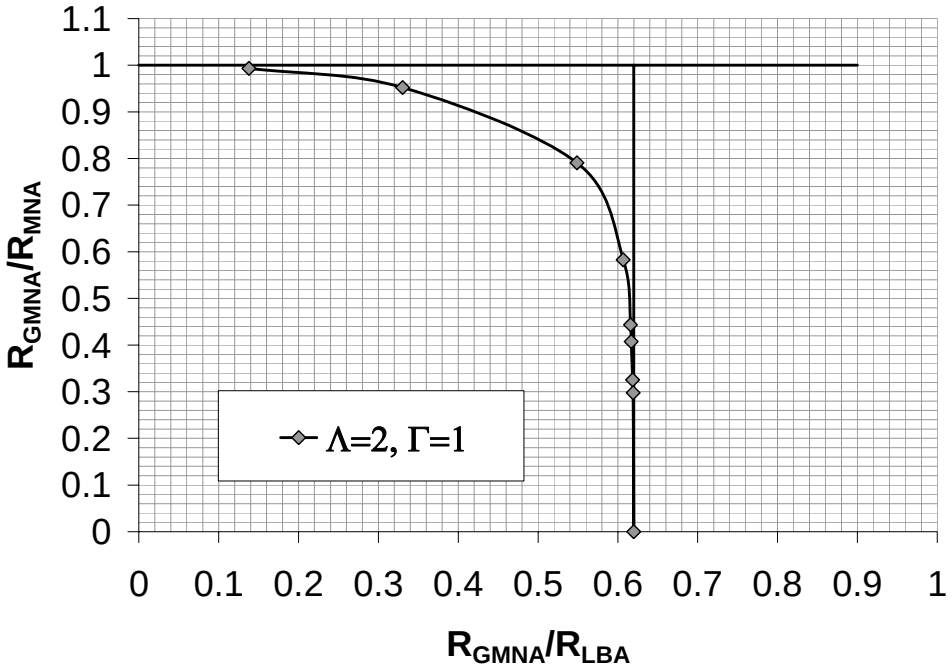

Figure 10.9: Modified capacity curve (Λ=2, Γ=1.00, r/t=400)

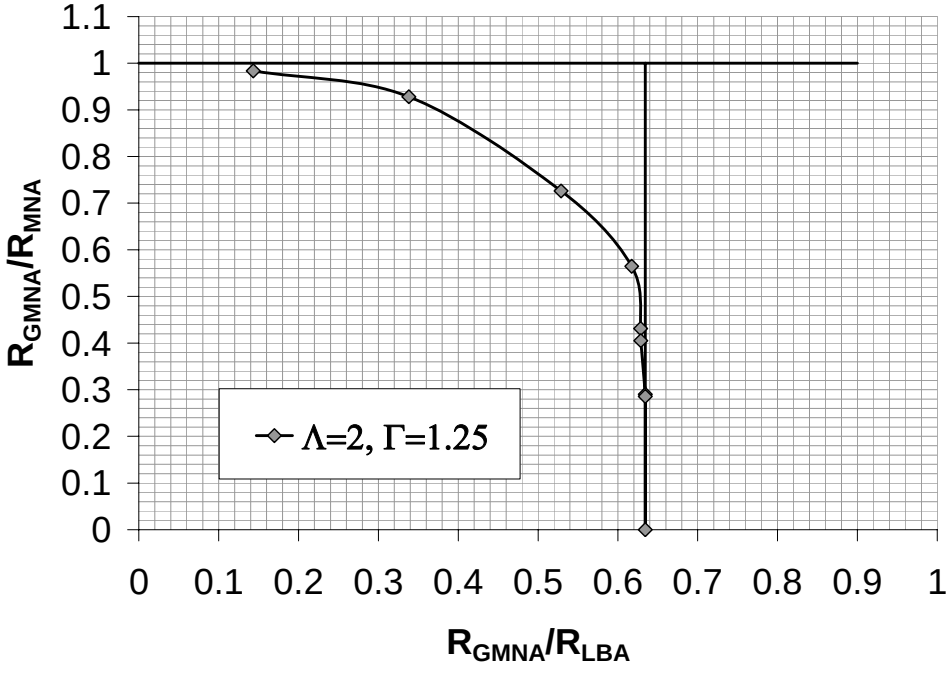

Figure 10.10: Modified capacity curve (Λ=2, Γ=1.25, r/t=400)

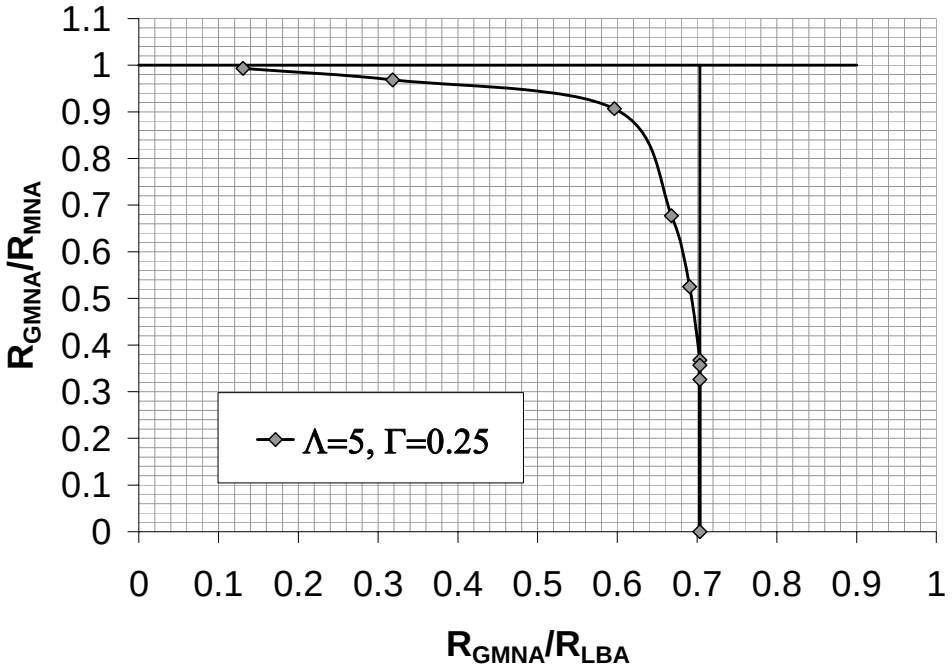

Figure 10.11: Modified capacity curve (Λ=5, Γ=0.25, r/t=400)

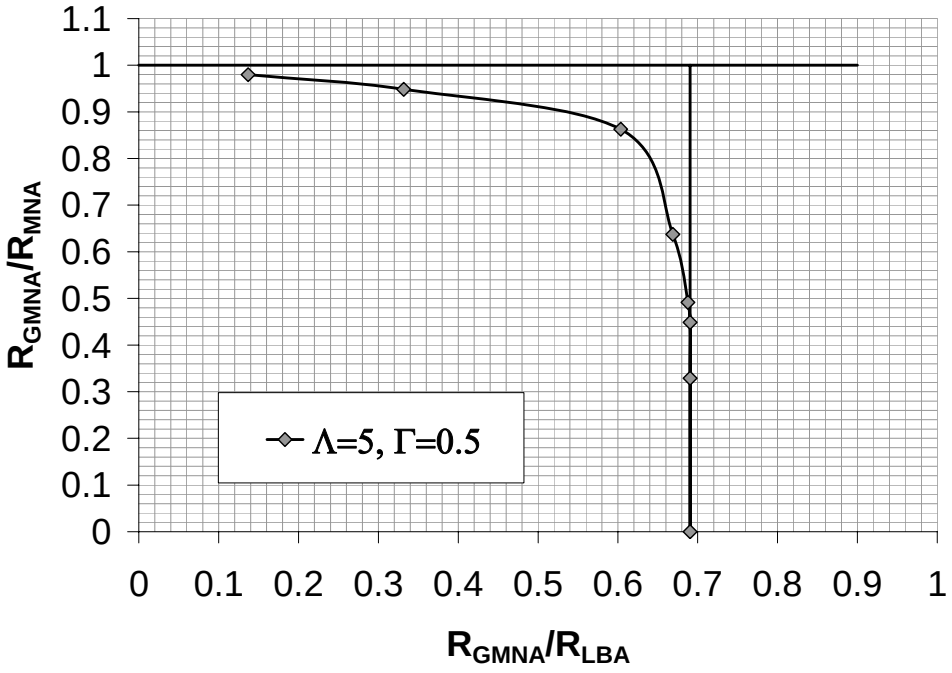

Figure 10.12: Modified capacity curve (Λ=5, Γ=0.50, r/t=400)

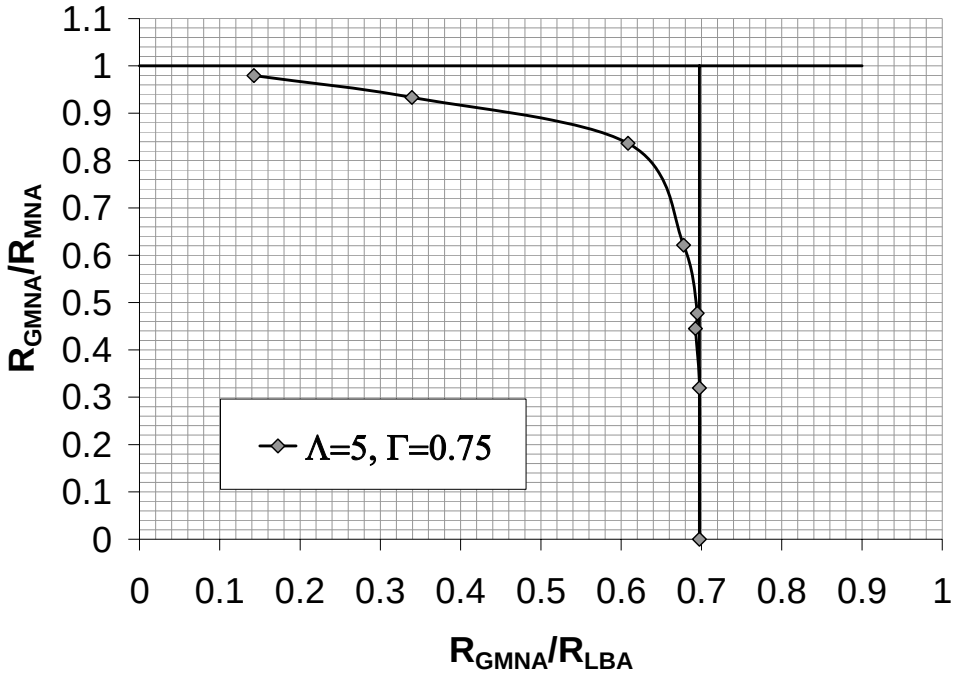

Figure 10.13: Modified capacity curve (Λ=5, Γ=0.75, r/t=400)

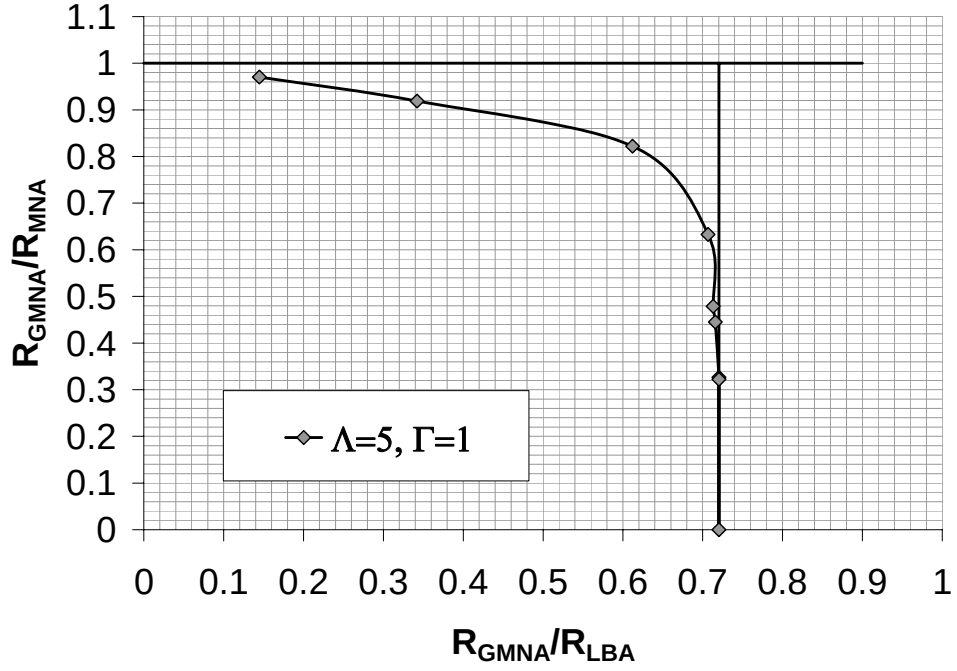

Figure 10.14: Modified capacity curve (Λ=5, Γ=1.00, r/t=400)

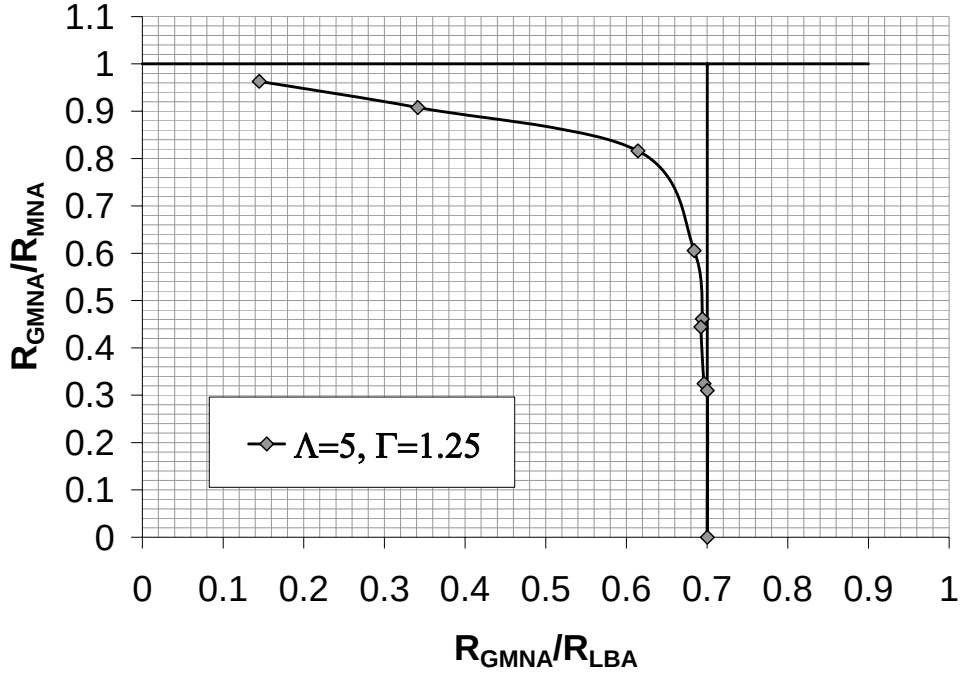

Figure 10.15: Modified capacity curve (Λ=5, Γ=1.25, r/t=400)

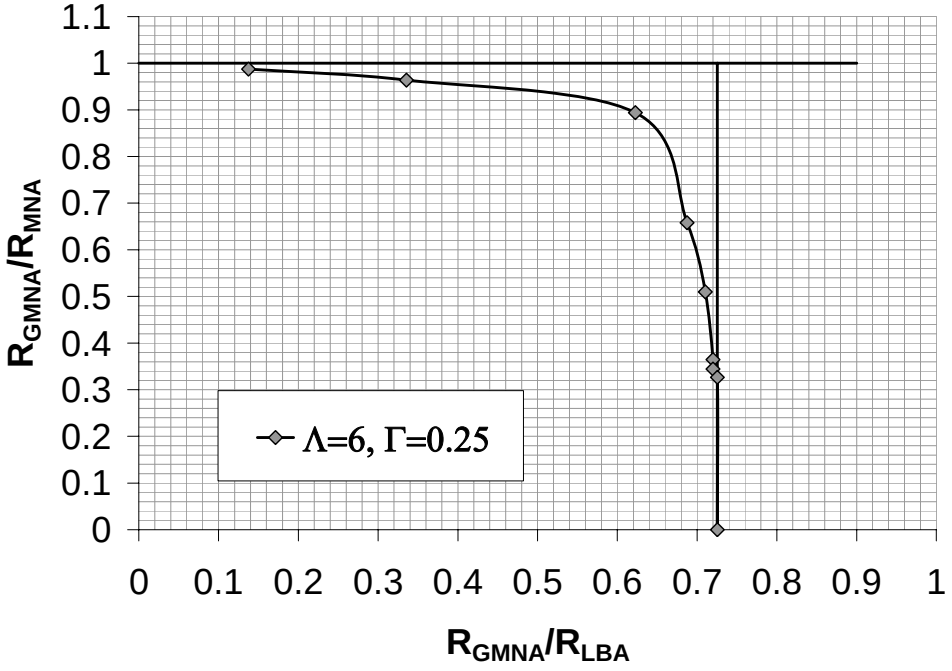

Figure 10.16: Modified capacity curve (Λ=6, Γ=0.25, r/t=400)

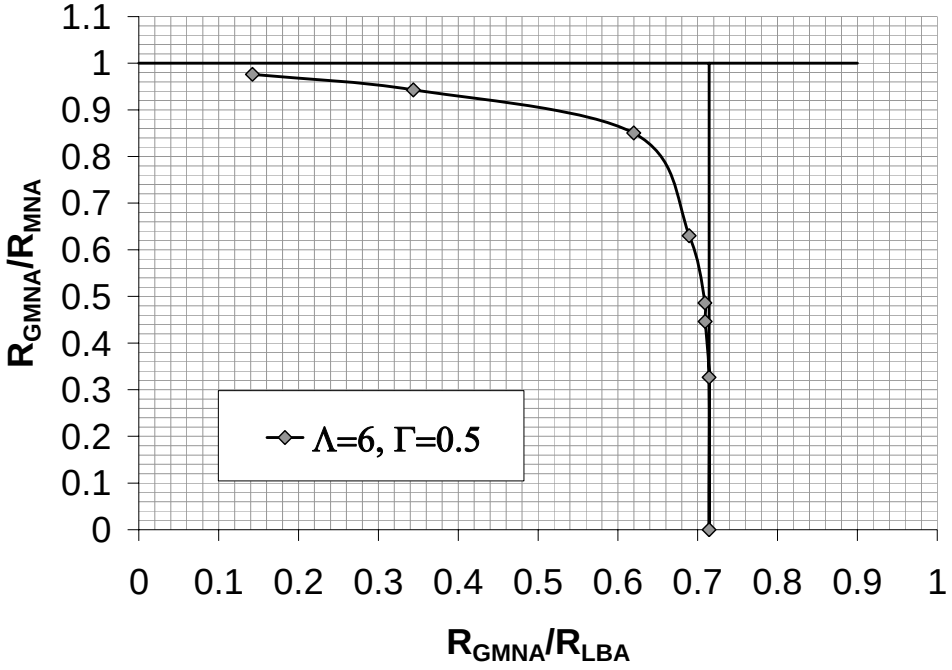

Figure 10.17: Modified capacity curve (Λ=6, Γ=0.50, r/t=400)

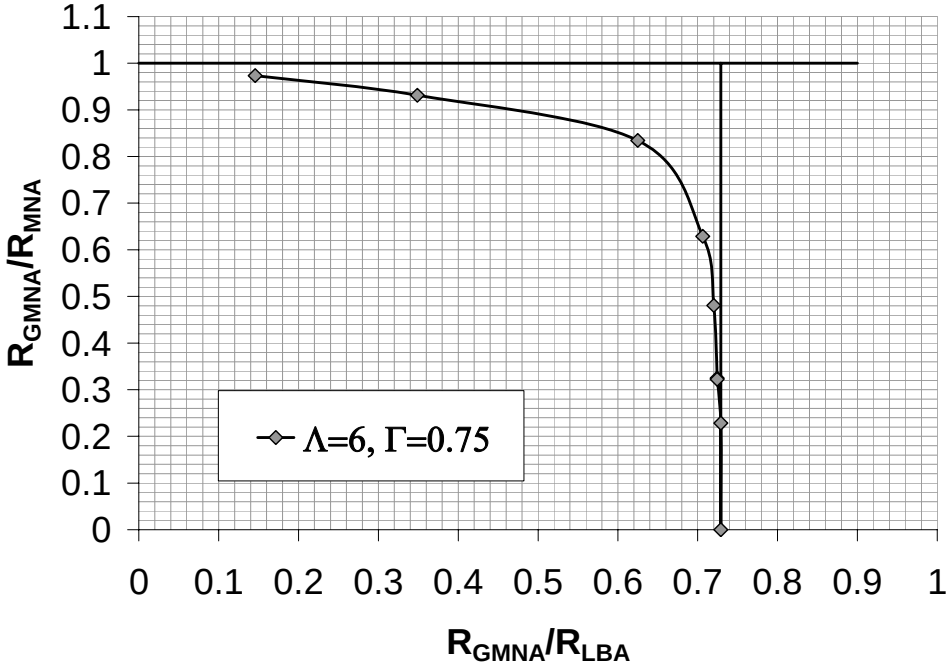

Figure 10.18: Modified capacity curve (Λ=6, Γ=0.75, r/t=400)

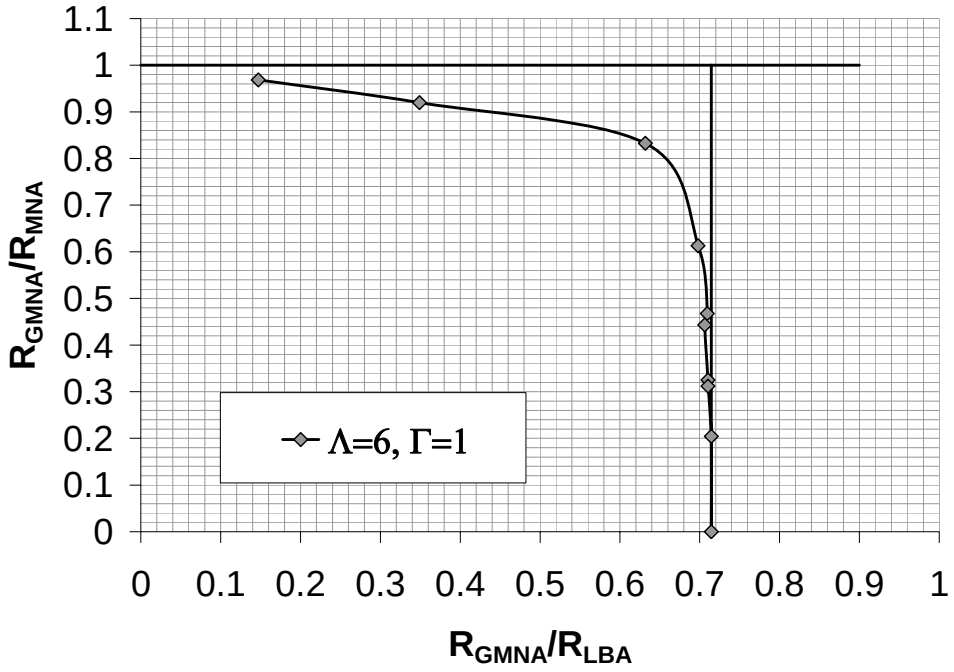

Figure 10.19: Modified capacity curve (Λ=6, Γ=1.00, r/t=400)

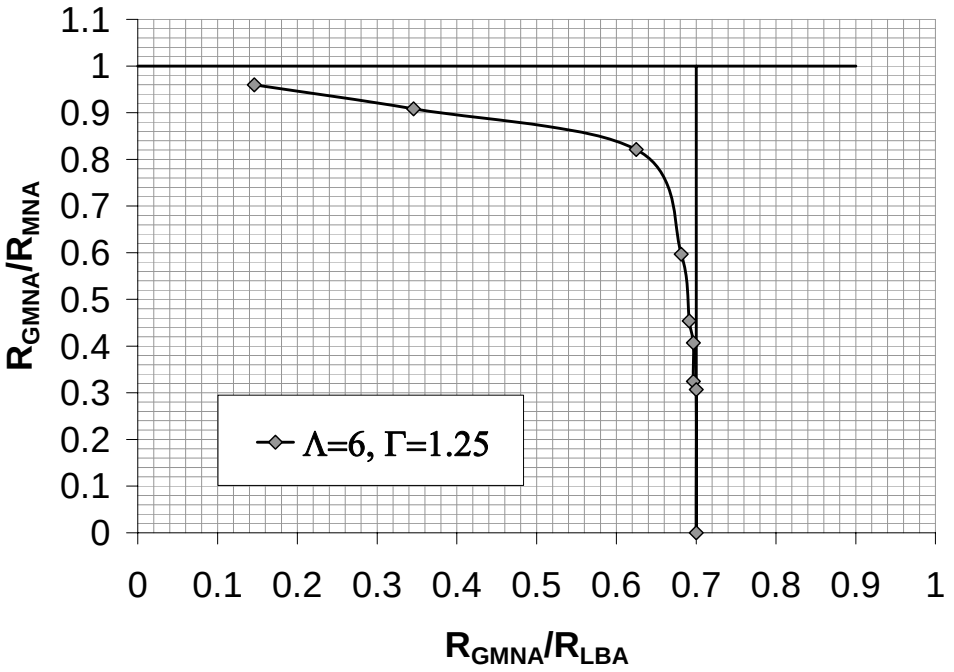

Figure 10.20: Modified capacity curve (Λ=6, Γ=1.25, r/t=400)

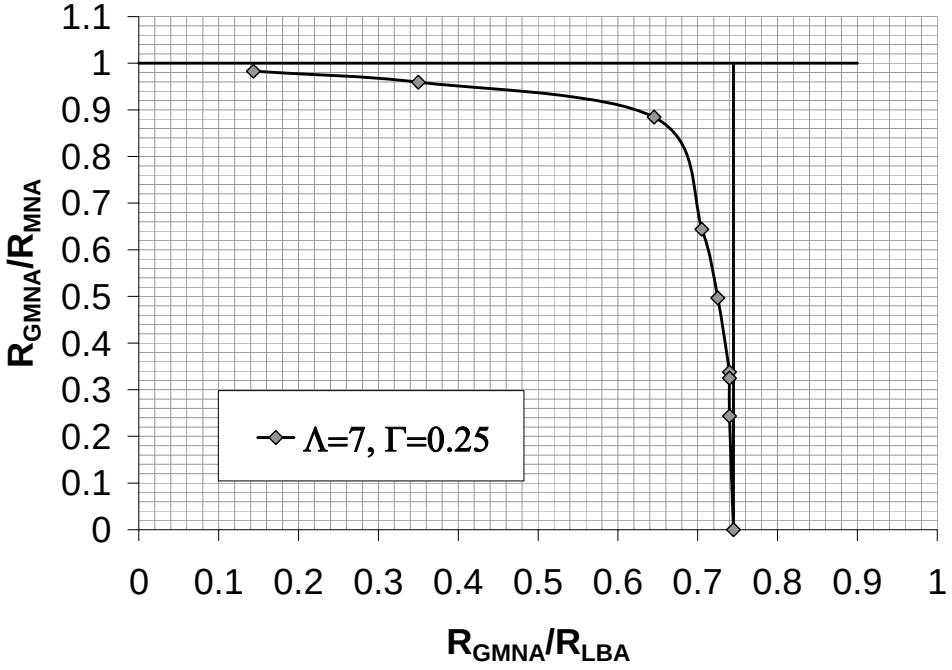

Figure 10.21: Modified capacity curve (Λ=7, Γ=0.25, r/t=400)

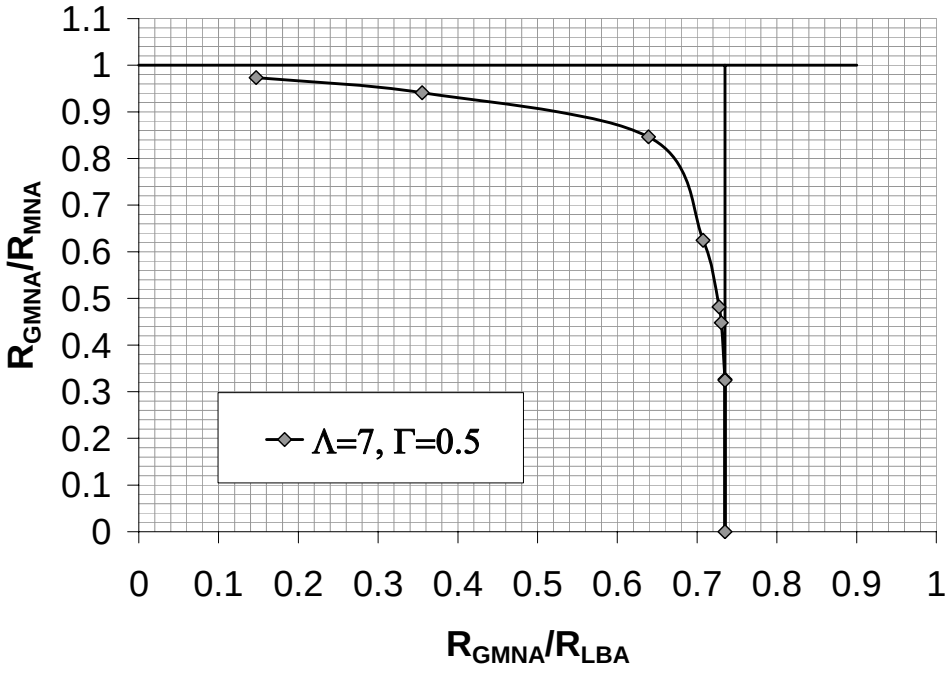

Figure 10.22: Modified capacity curve (Λ=7, Γ=0.50, r/t=400)

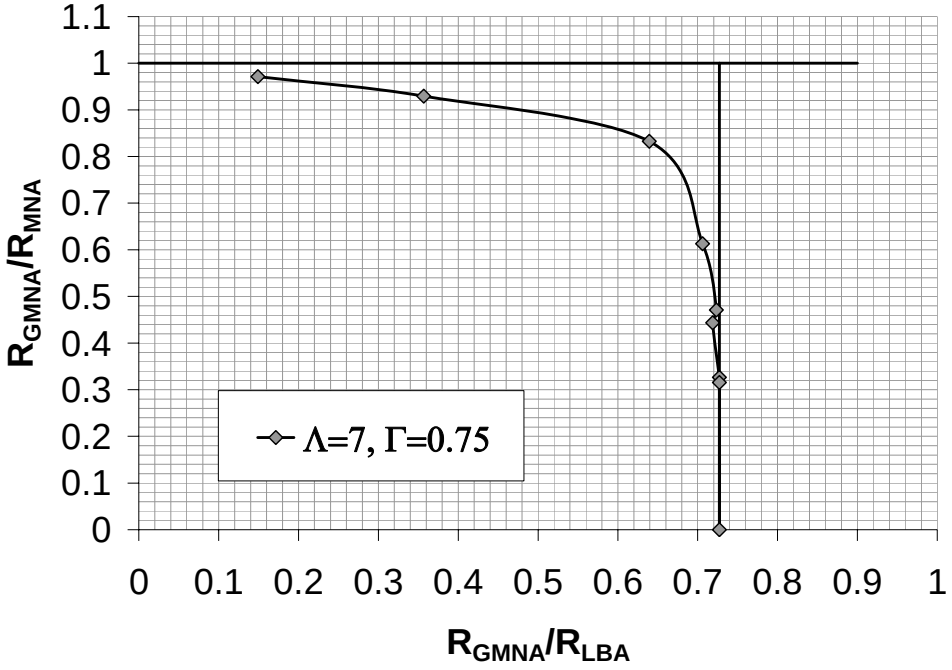

Figure 10.23: Modified capacity curve (Λ=7, Γ=0.75, r/t=400)

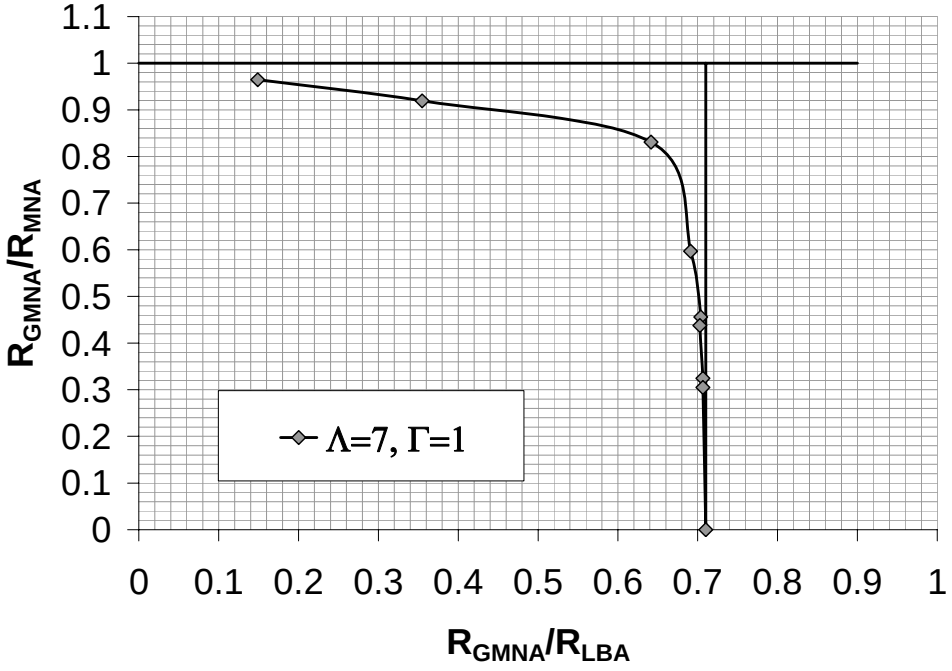

Figure 10.24: Modified capacity curve (Λ=7, Γ=1.00, r/t=400)

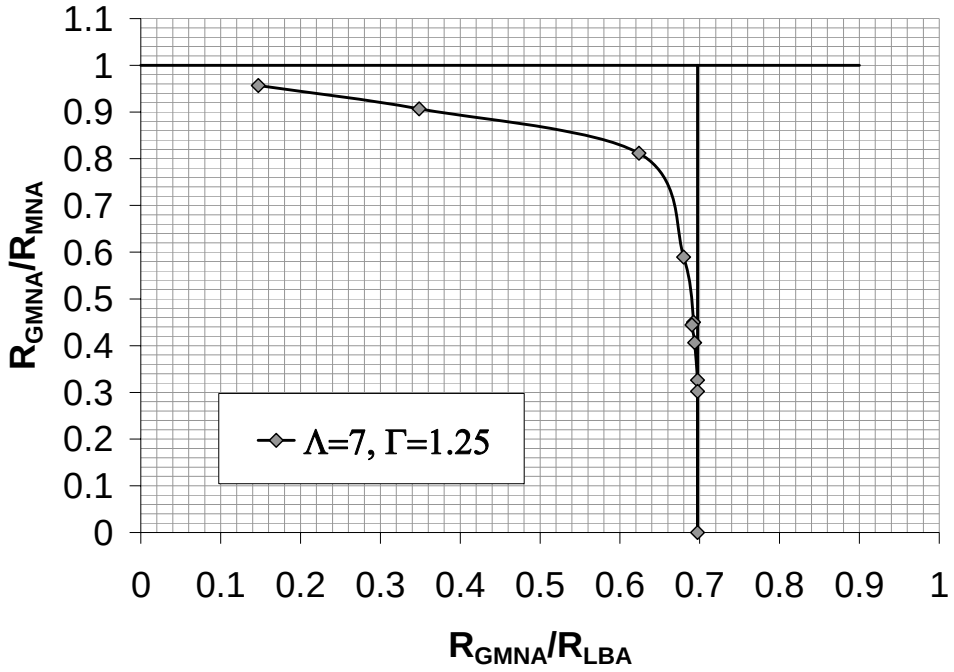

Figure 10.25: Modified capacity curve (Λ=7, Γ=1.25, r/t=400)

10.3 Modified capacity curves (r/t=600)

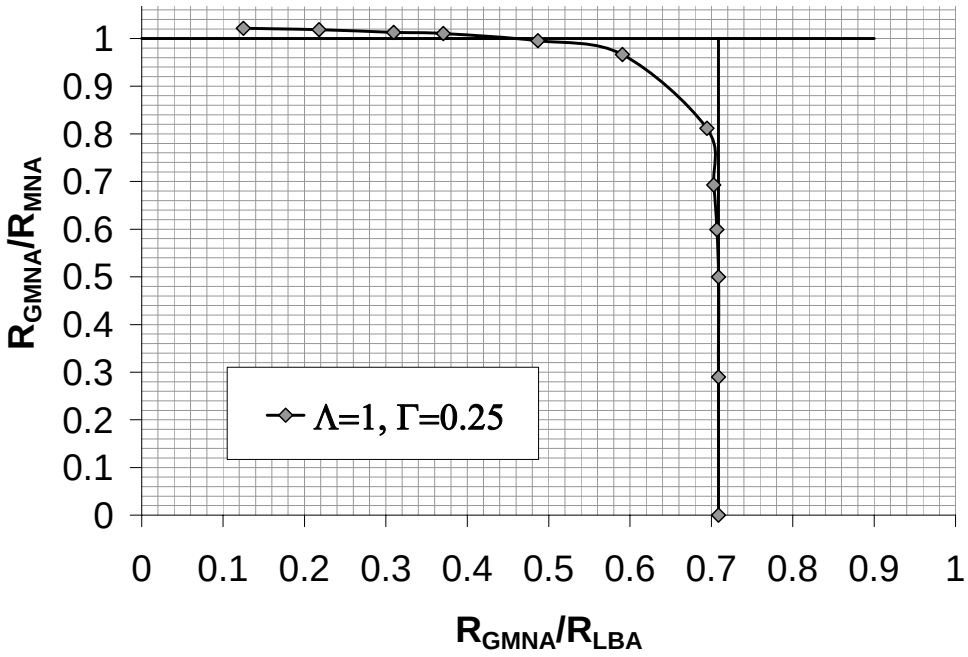

Figure 10.26: Modified capacity curve (Λ=1, Γ=0.25, r/t=600)

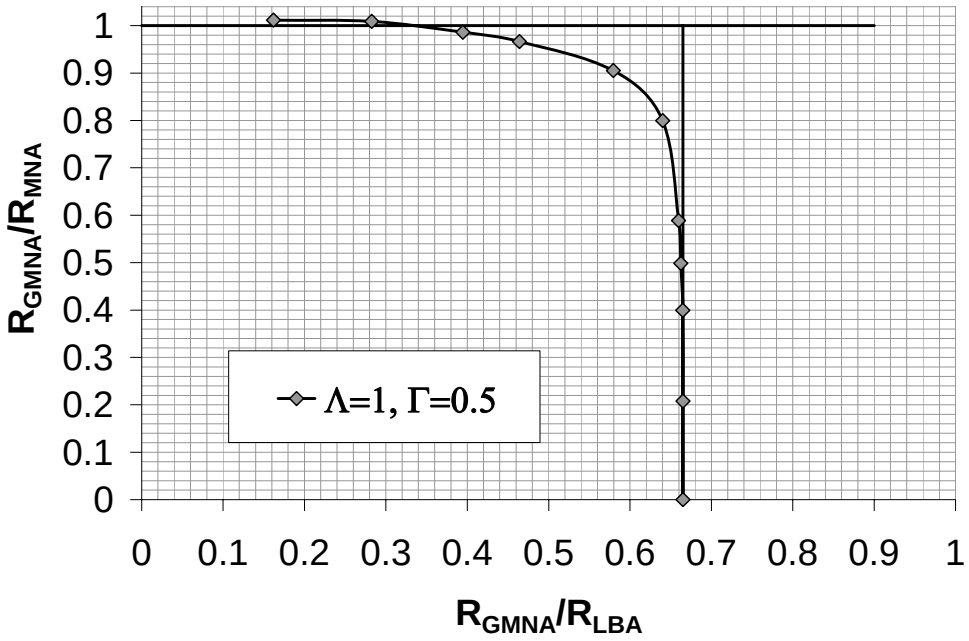

Figure 10.27: Modified capacity curve (Λ=1, Γ=0.50, r/t=600)

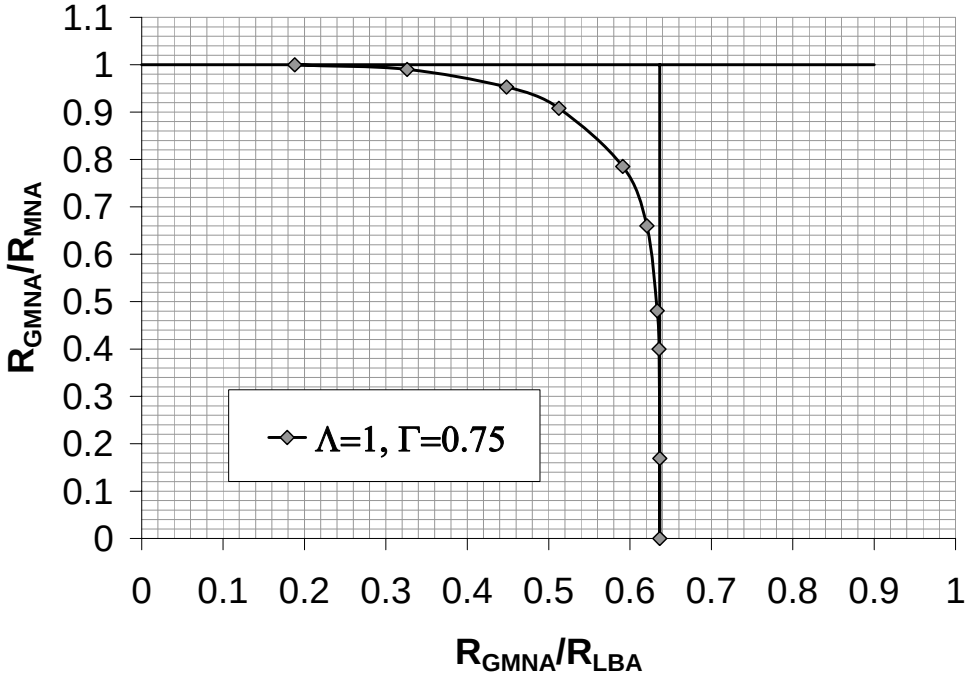

Figure 10.28: Modified capacity curve (Λ=1, Γ=0.75, r/t=600)

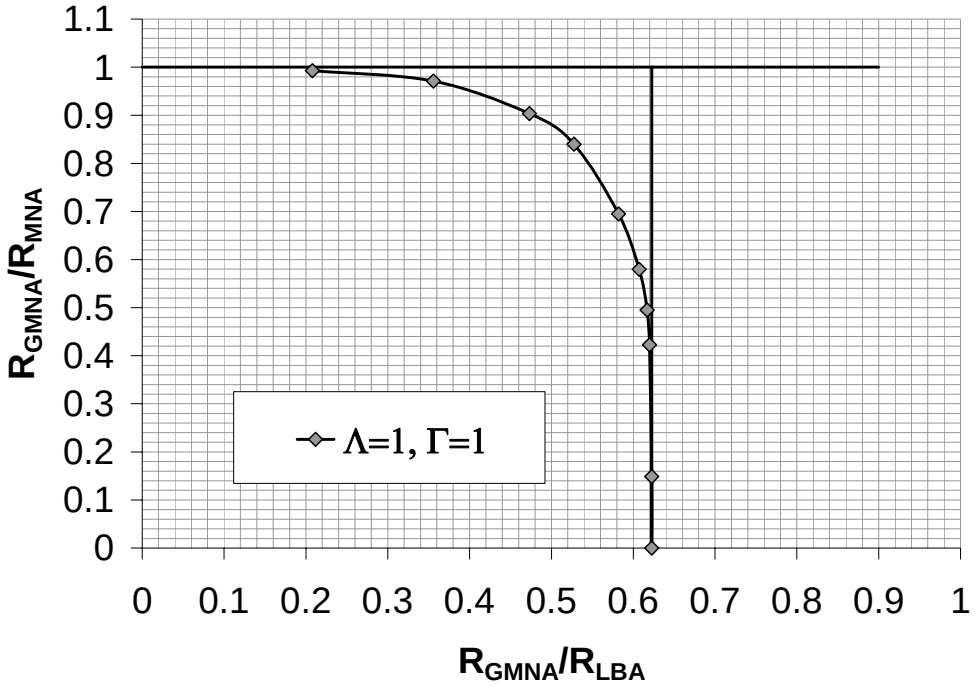

Figure 10.29: Modified capacity curve (Λ=1, Γ=1.00, r/t=600)

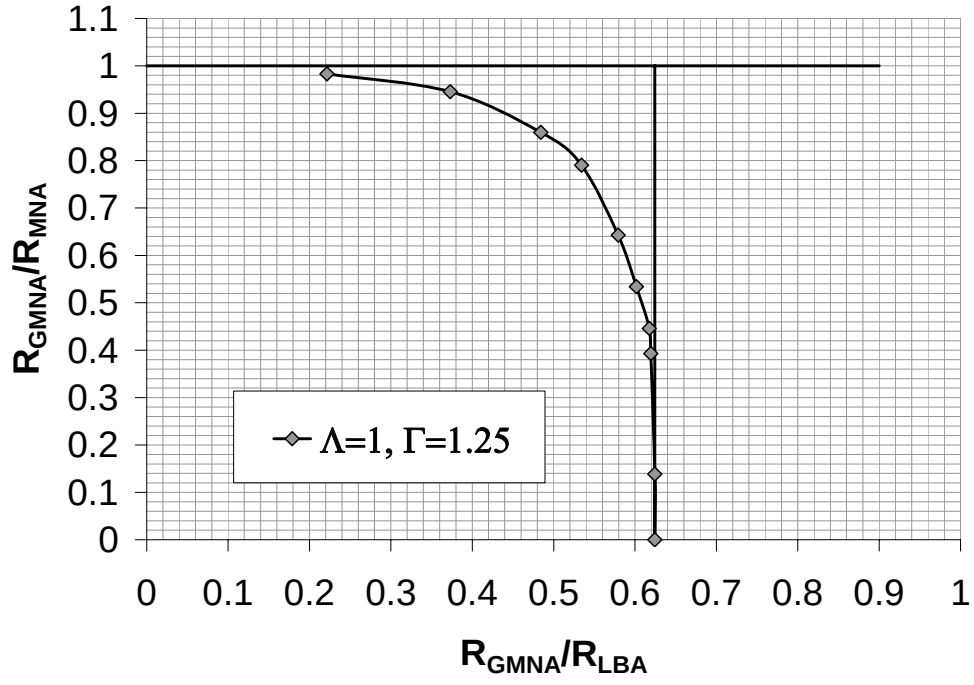

Figure 10.30: Modified capacity curve (Λ=1, Γ=1.25, r/t=600)

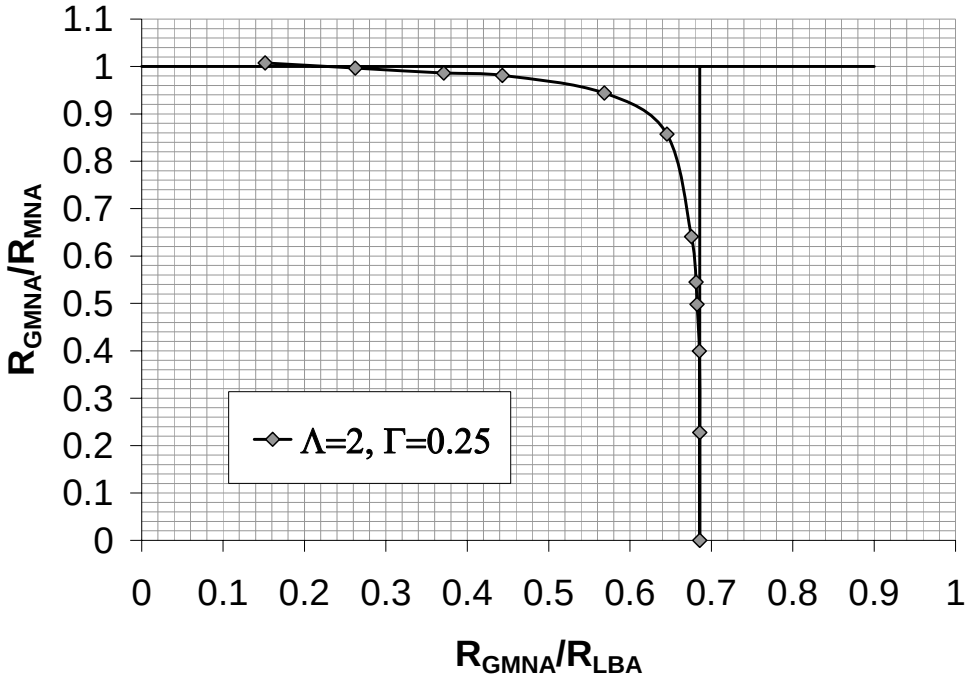

Figure 10.31: Modified capacity curve (Λ=2, Γ=0.25, r/t=600)

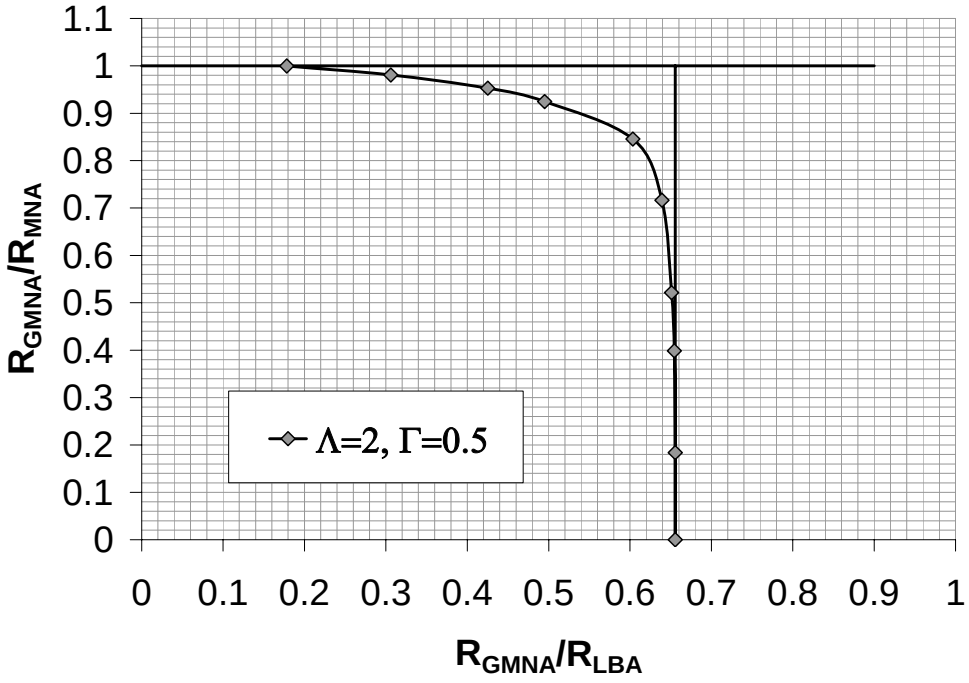

Figure 10.32: Modified capacity curve (Λ=2, Γ=0.50, r/t=600)

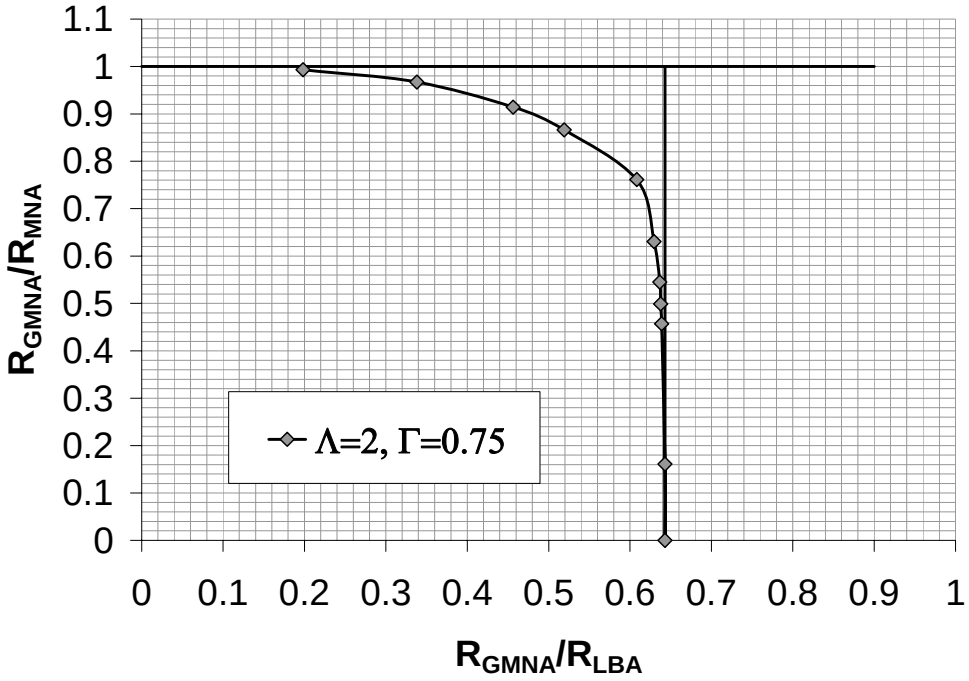

Figure 10.33: Modified capacity curve (Λ=2, Γ=0.75, r/t=600)

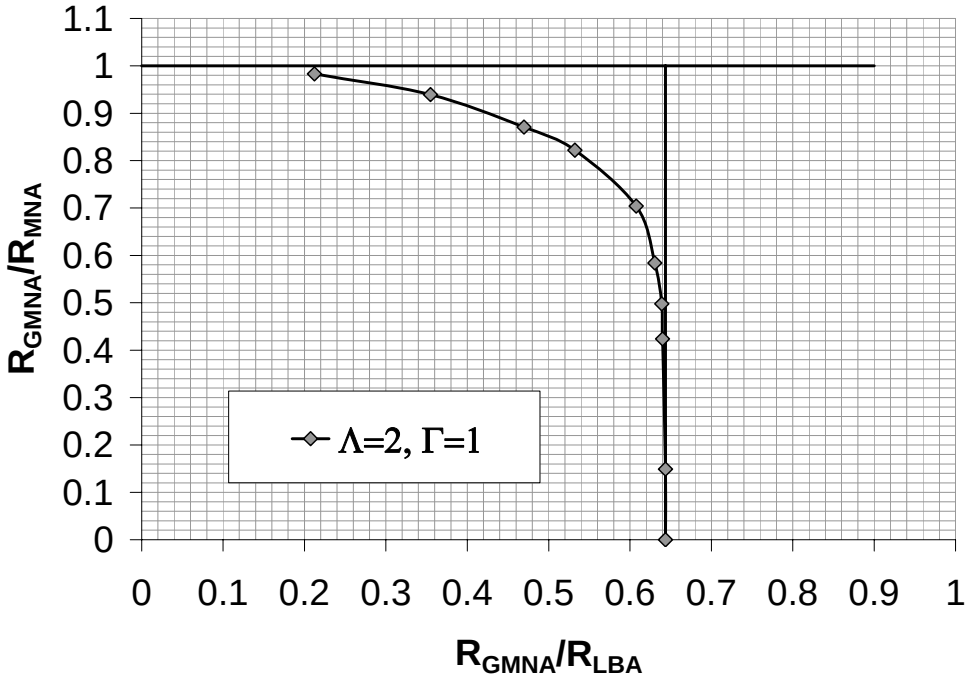

Figure 10.34: Modified capacity curve (Λ=2, Γ=1.00, r/t=600)

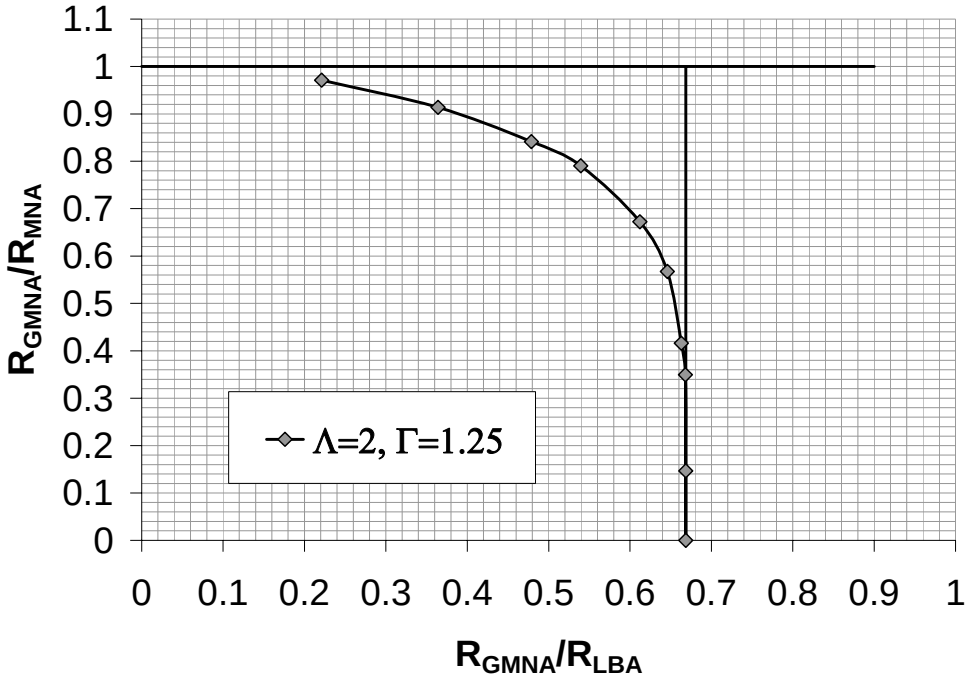

Figure 10.35: Modified capacity curve (Λ=2, Γ=1.25, r/t=600)

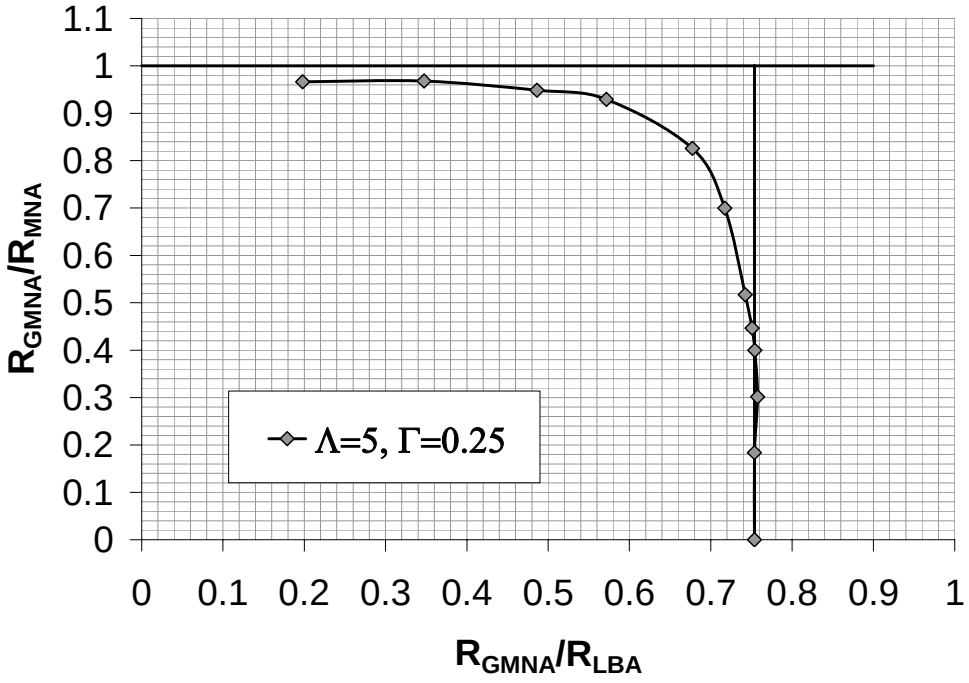

Figure 10.36: Modified capacity curve (Λ=5, Γ=0.25, r/t=600)

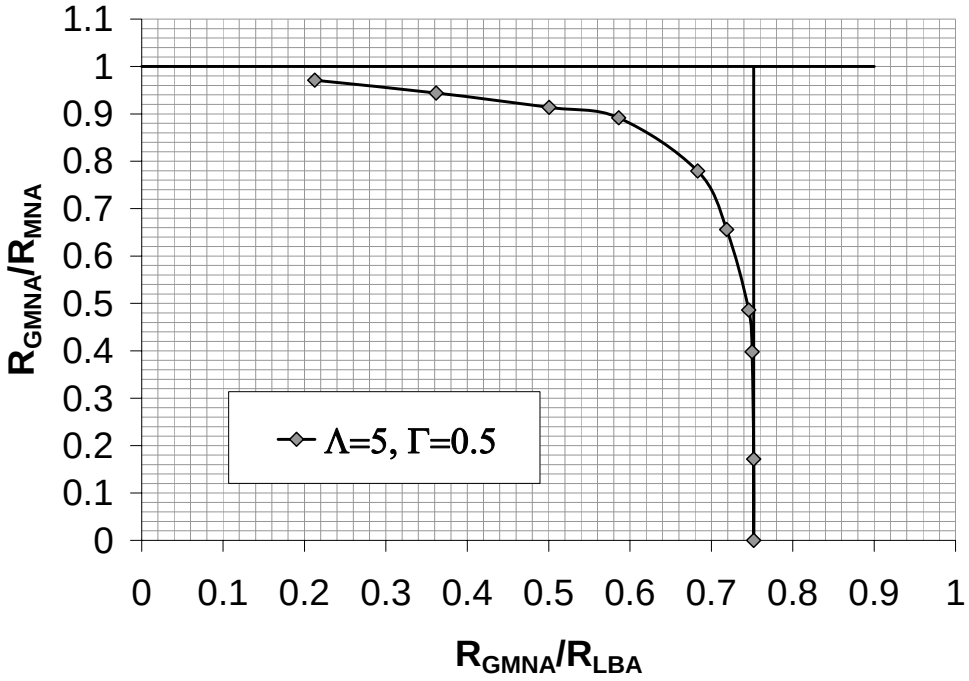

Figure 10.37: Modified capacity curve (Λ=5, Γ=0.50, r/t=600)

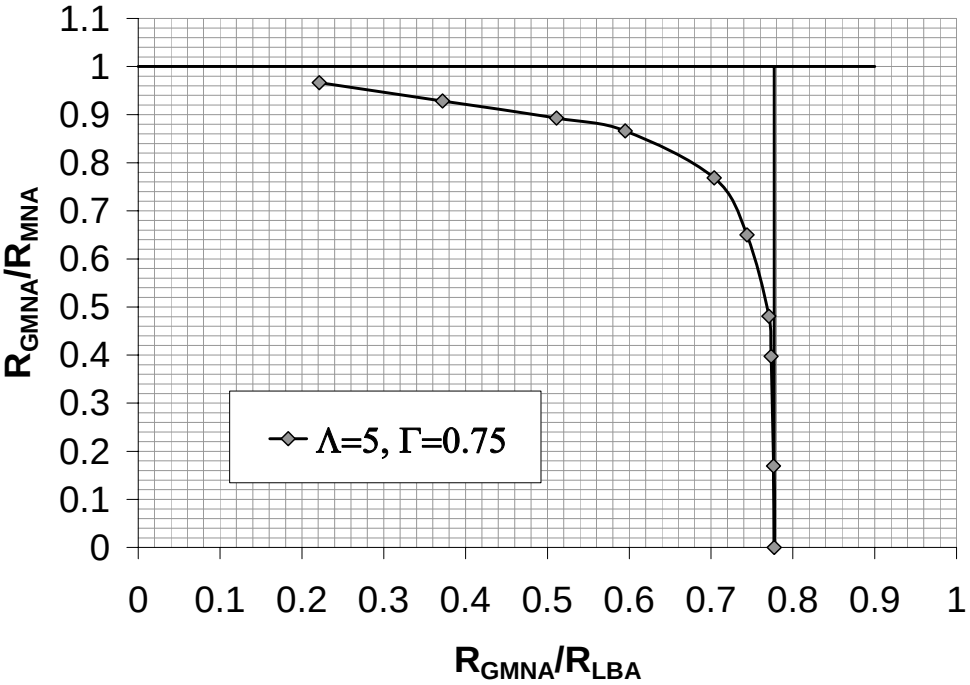

Figure 10.38: Modified capacity curve (Λ=5, Γ=0.75, r/t=600)

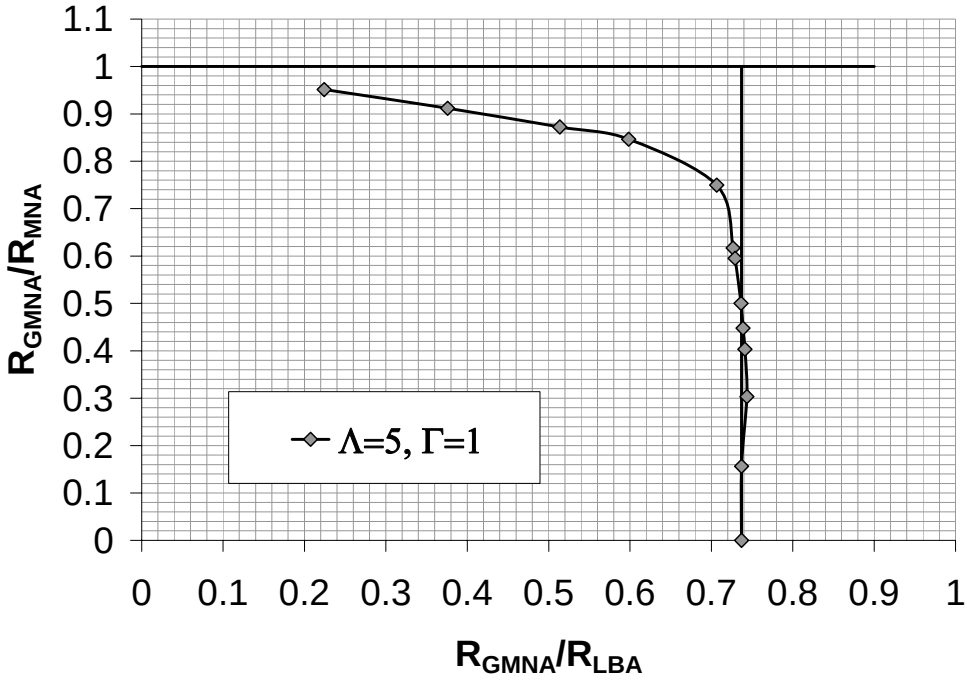

Figure 10.39: Modified capacity curve (Λ=5, Γ=1.00, r/t=600)

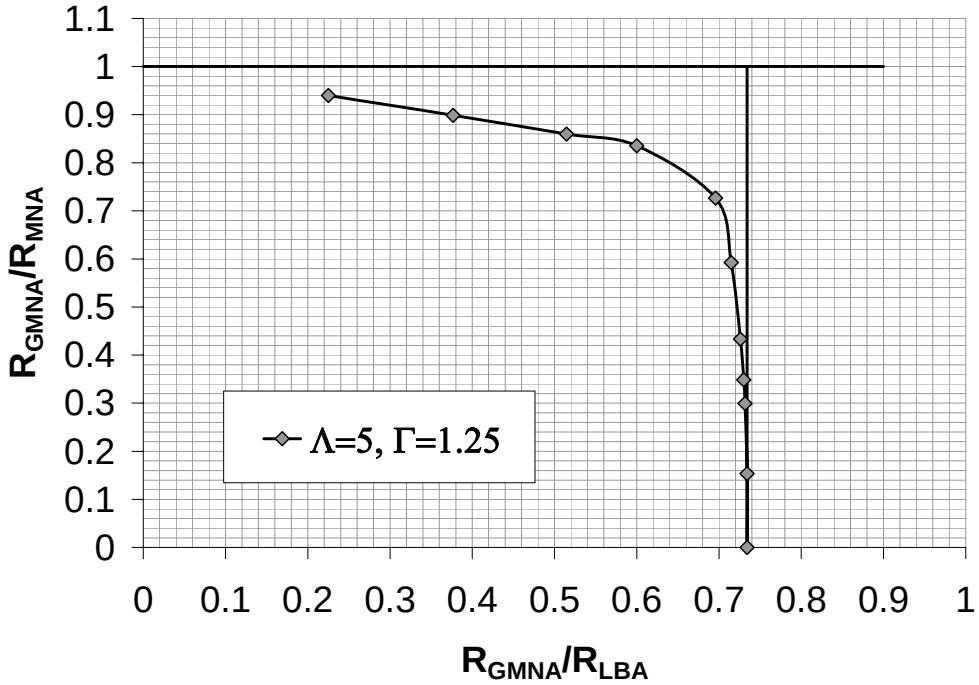

Figure 10.40: Modified capacity curve (Λ=5, Γ=1.25, r/t=600)

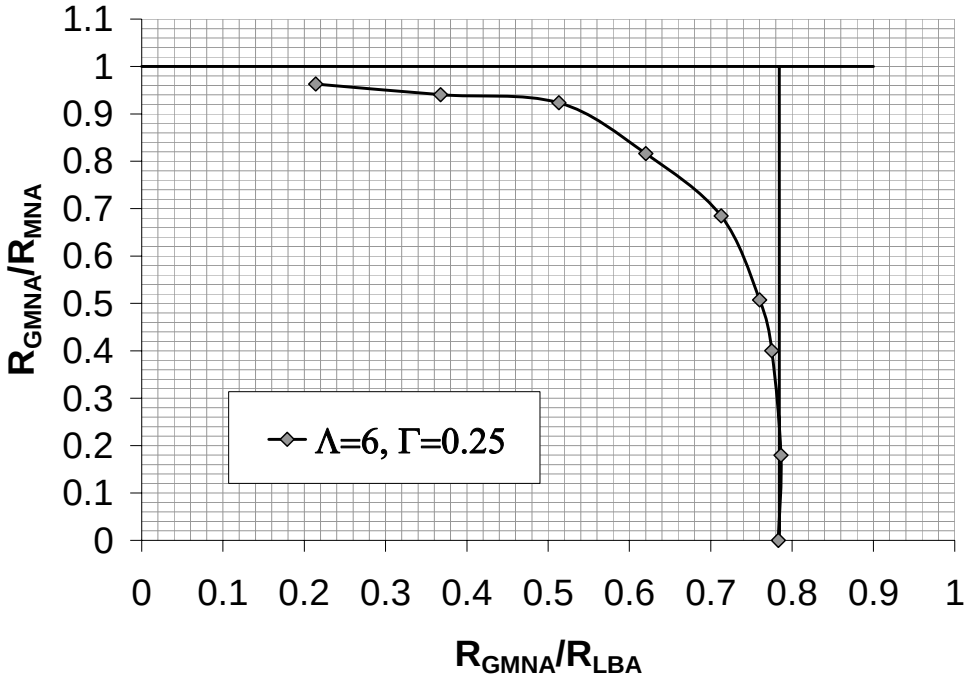

Figure 10.41: Modified capacity curve (Λ=6, Γ=0.25, r/t=600)

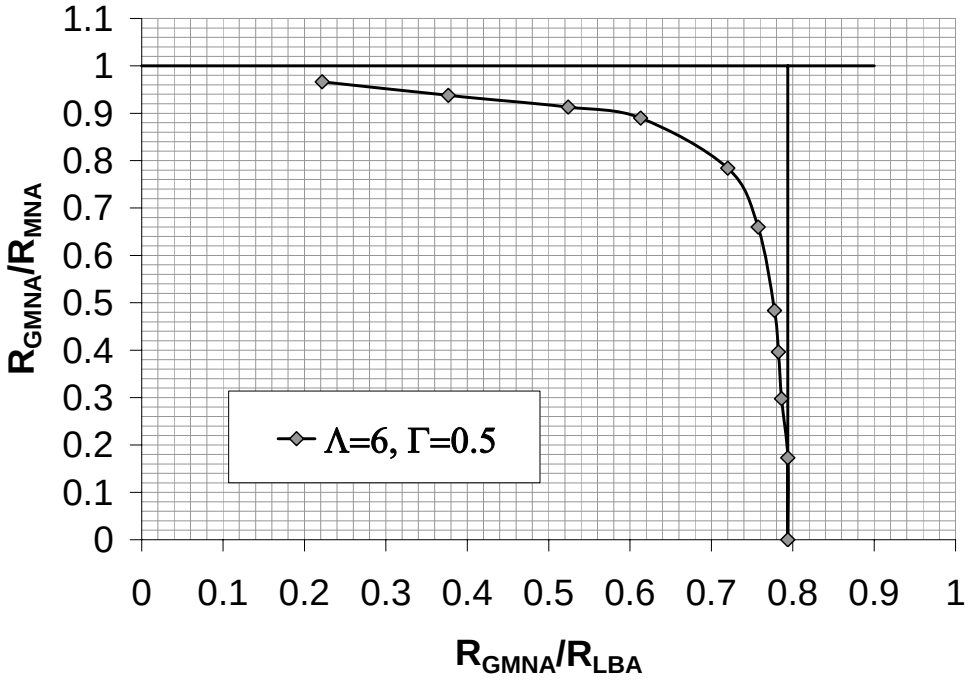

Figure 10.42: Modified capacity curve (Λ=6, Γ=0.50, r/t=600)

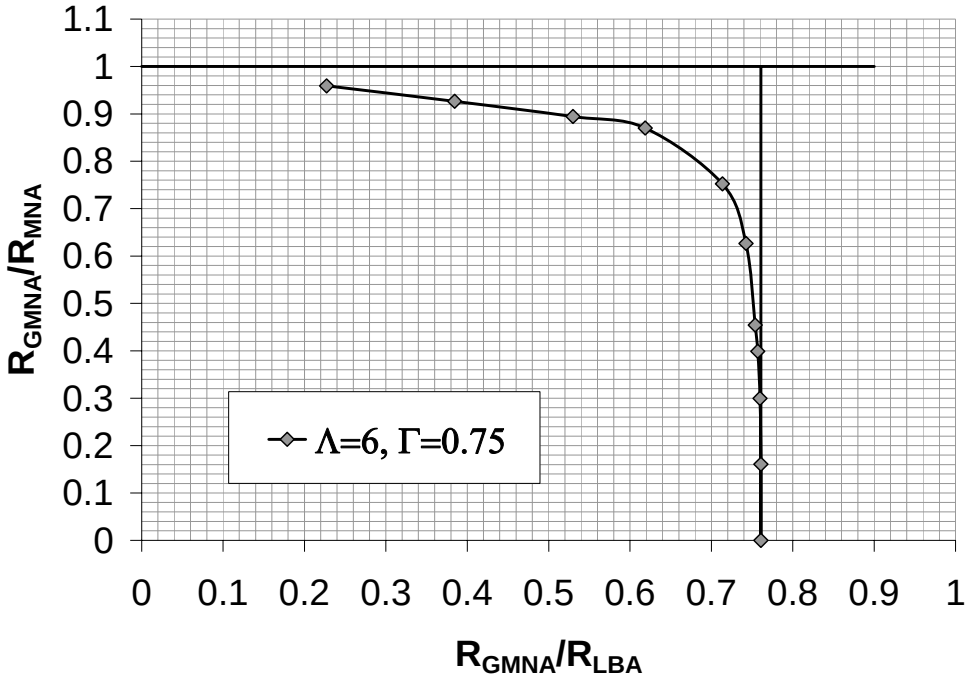

Figure 10.43: Modified capacity curve (Λ=6, Γ=0.75, r/t=600)

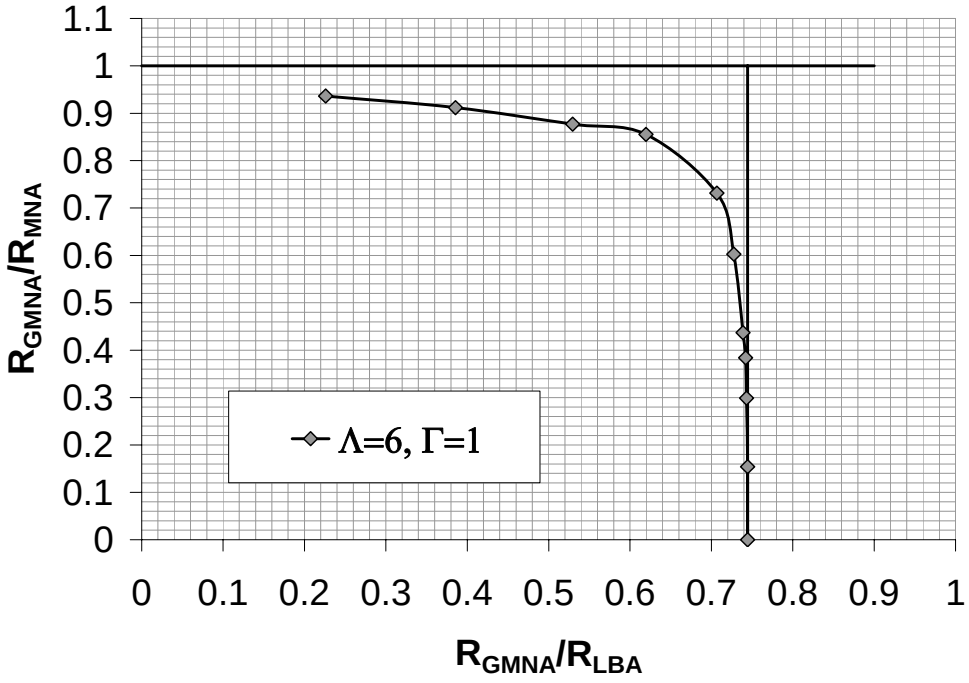

Figure 10.44: Modified capacity curve (Λ=6, Γ=1.00, r/t=600)

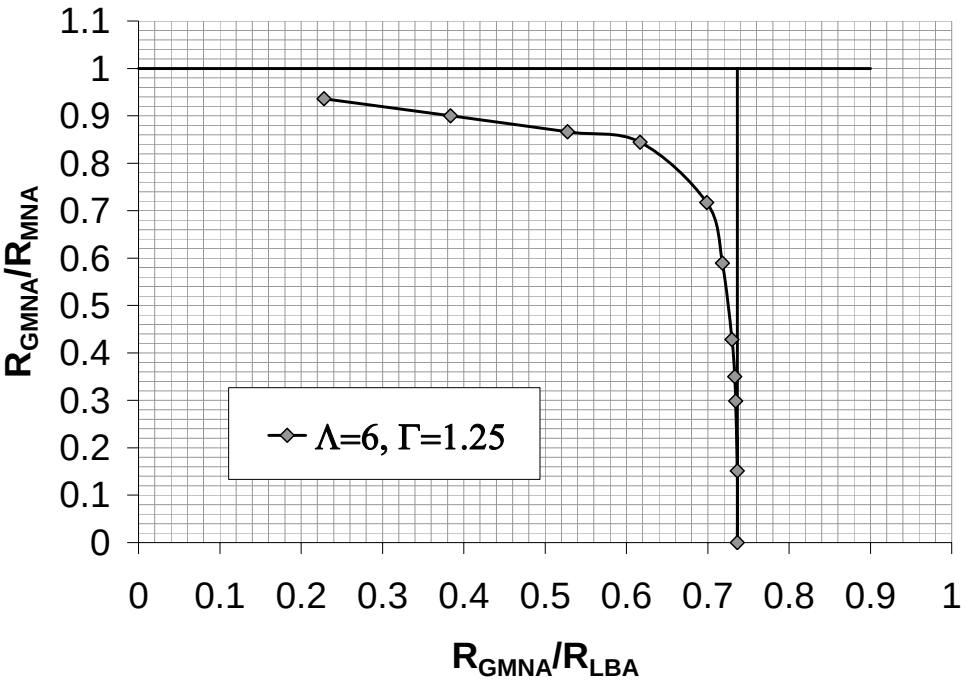

Figure 10.45: Modified capacity curve (Λ=6, Γ=1.25, r/t=600)

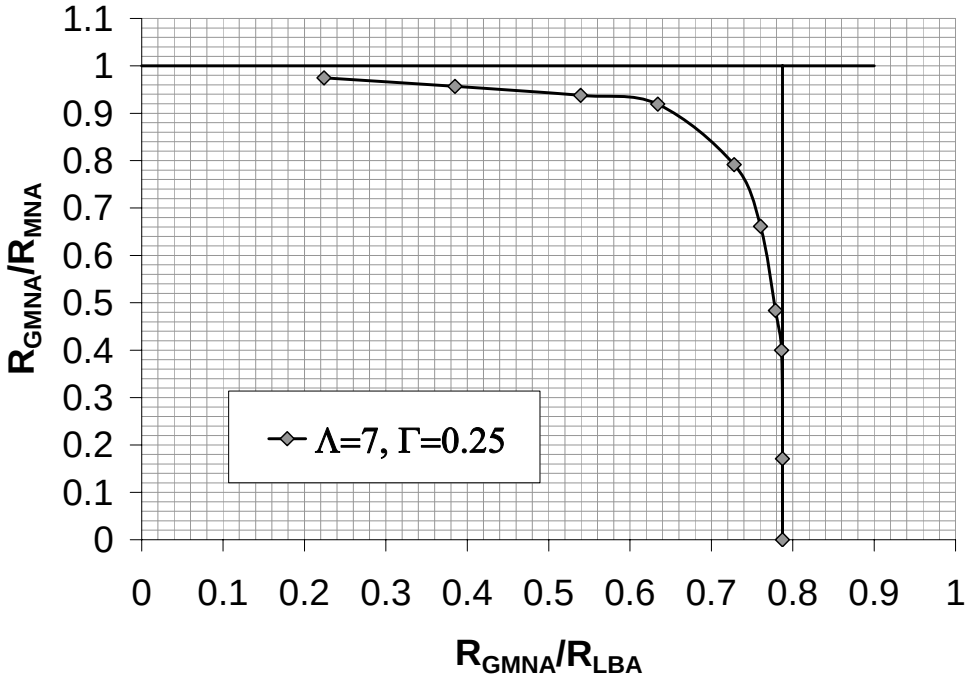

Figure 10.46: Modified capacity curve (Λ=7, Γ=0.25, r/t=600)

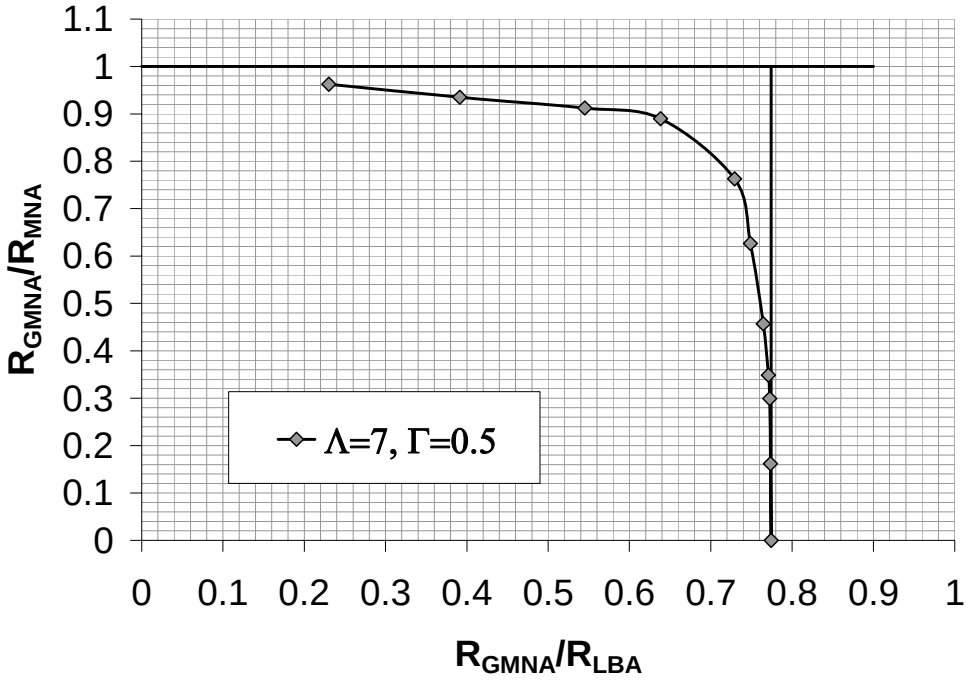

Figure 10.47: Modified capacity curve (Λ=7, Γ=0.50, r/t=600)

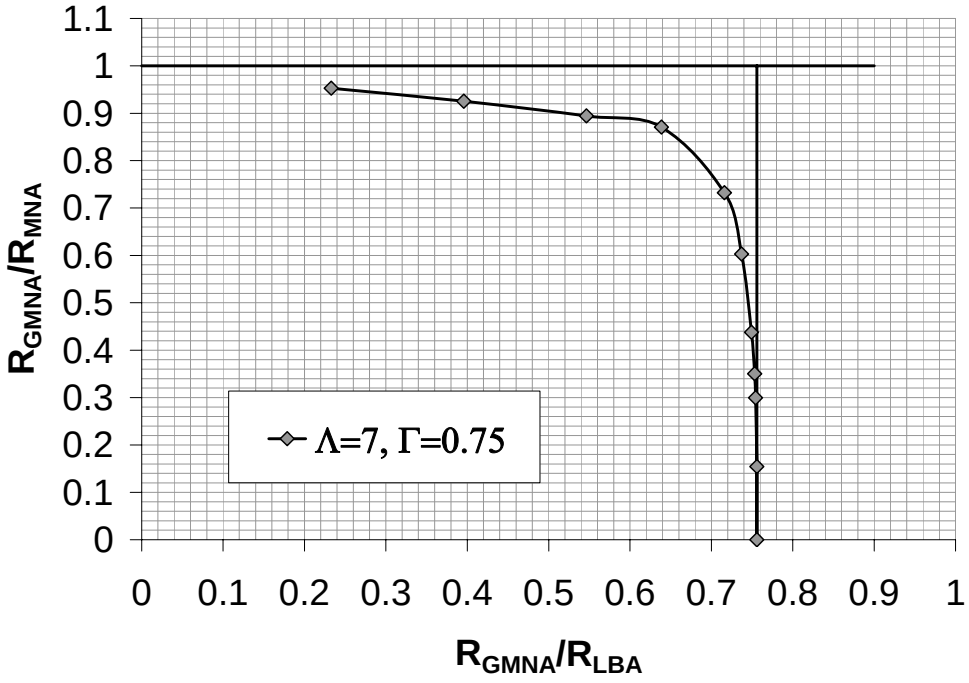

Figure 10.48: Modified capacity curve (Λ=7, Γ=0.75, r/t=600)

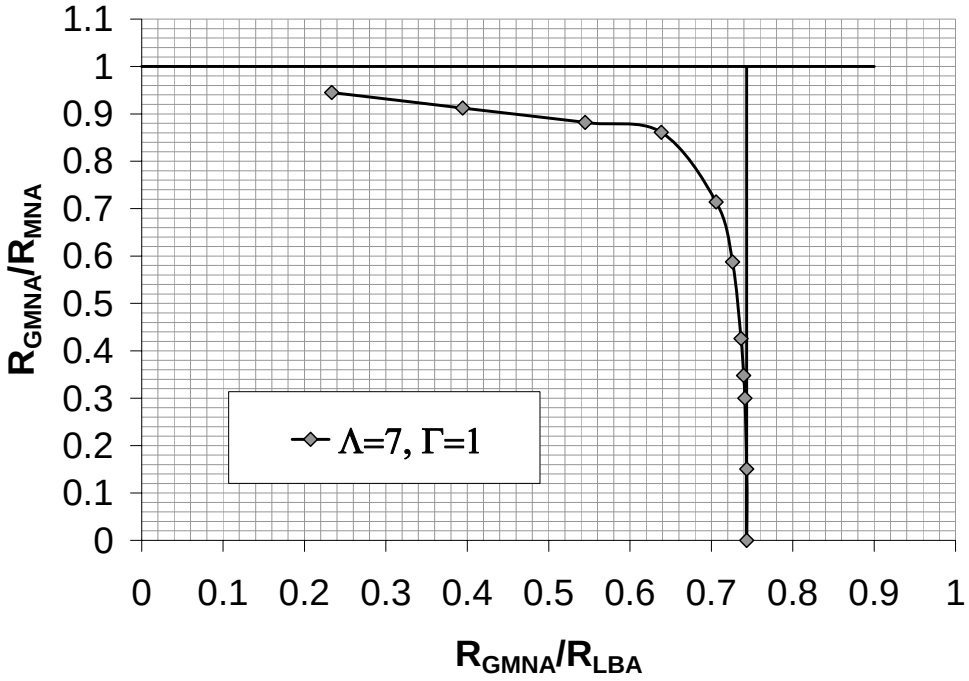

Figure 10.49: Modified capacity curve (Λ=7, Γ=1.00, r/t=600)

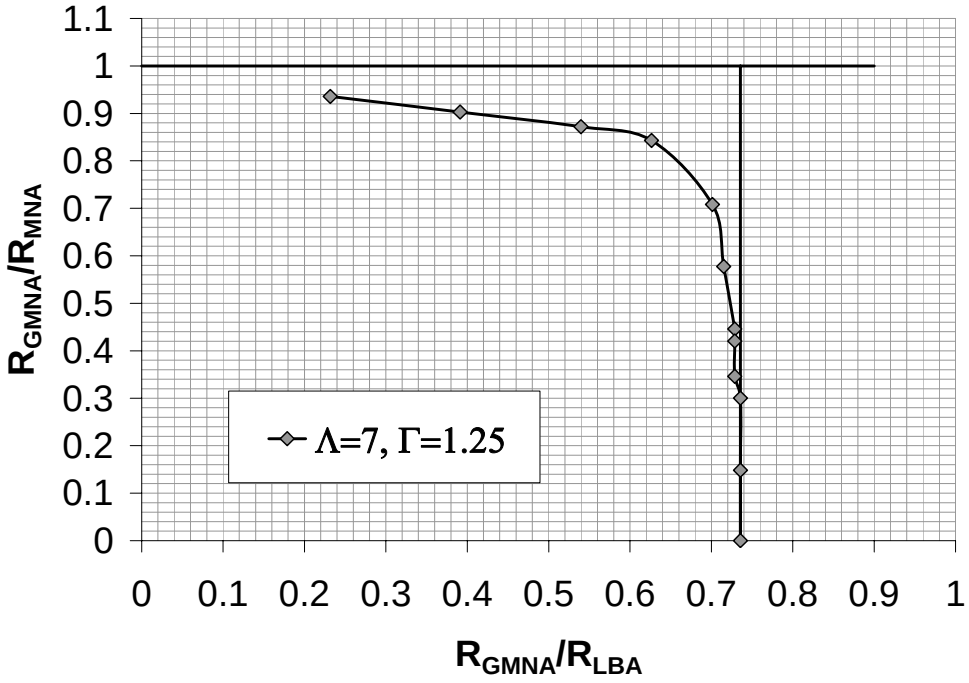

Figure 10.50: Modified capacity curve (Λ=7, Γ=1.25, r/t=600)

10.4 Modified capacity curves (r/t=1000)

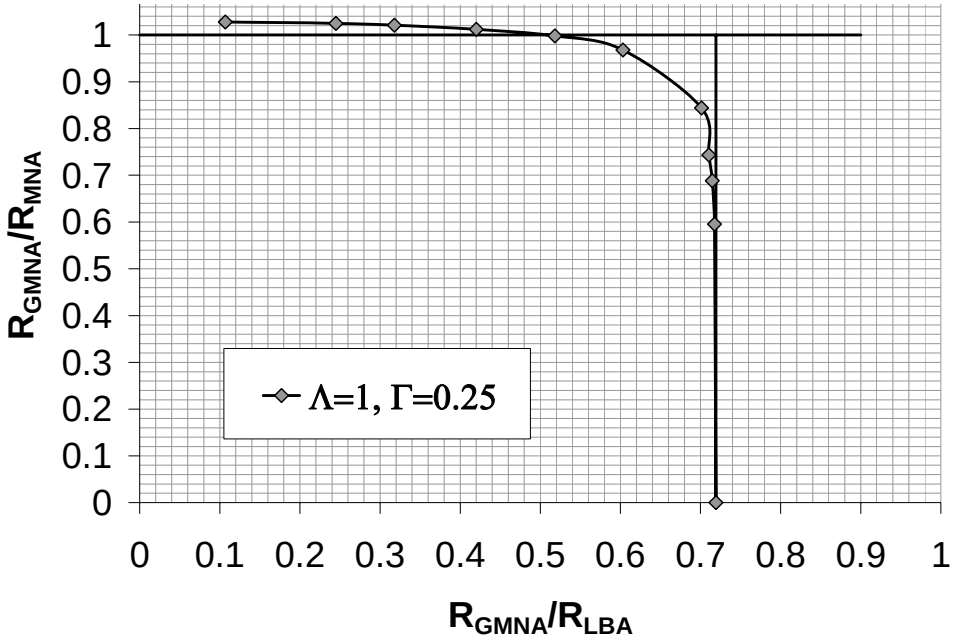

Figure 10.51: Modified capacity curve (Λ=1, Γ=0.25, r/t=1000)

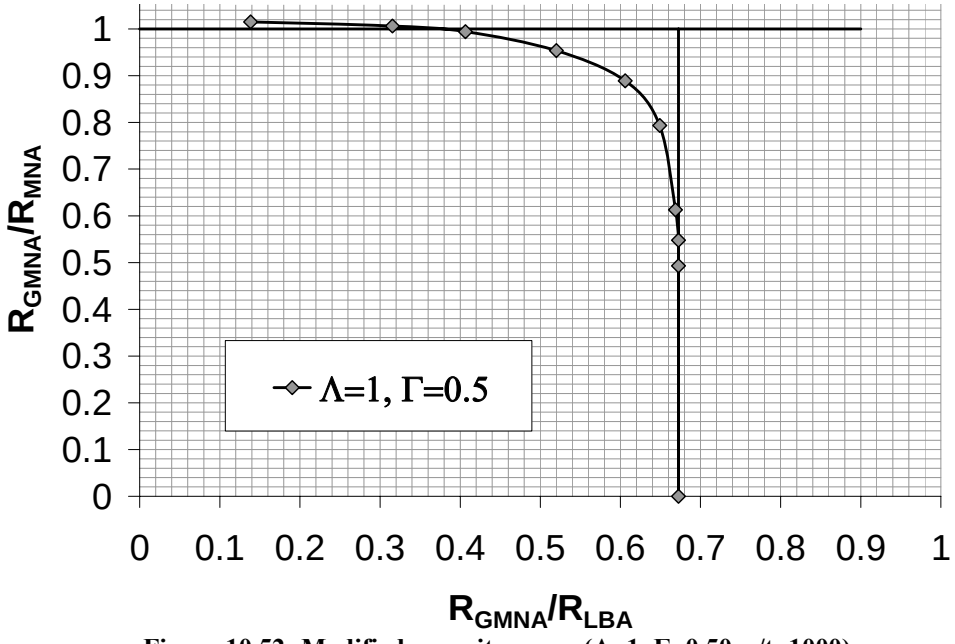

Figure 10.52: Modified capacity curve (Λ=1, Γ=0.50, r/t=1000)

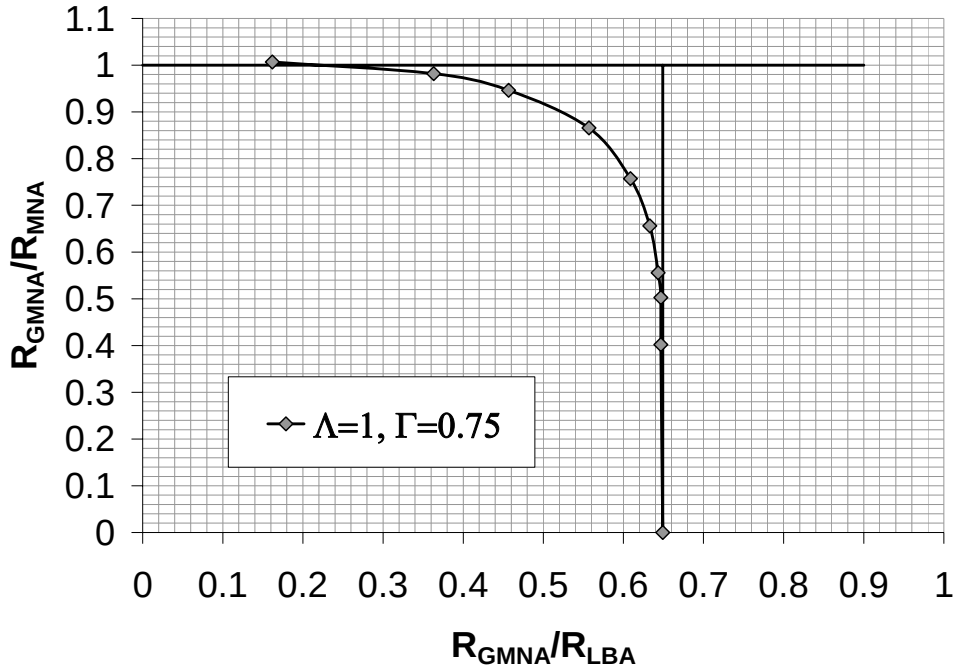

Figure 10.53: Modified capacity curve (Λ=1, Γ=0.75, r/t=1000)

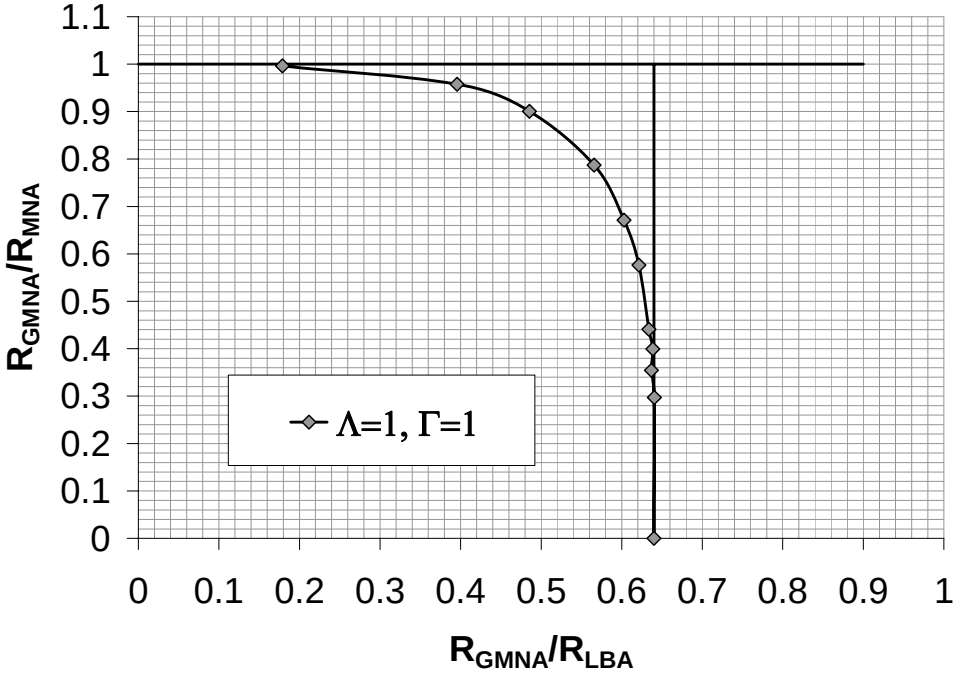

Figure 10.54: Modified capacity curve (Λ=1, Γ=1.00, r/t=1000)

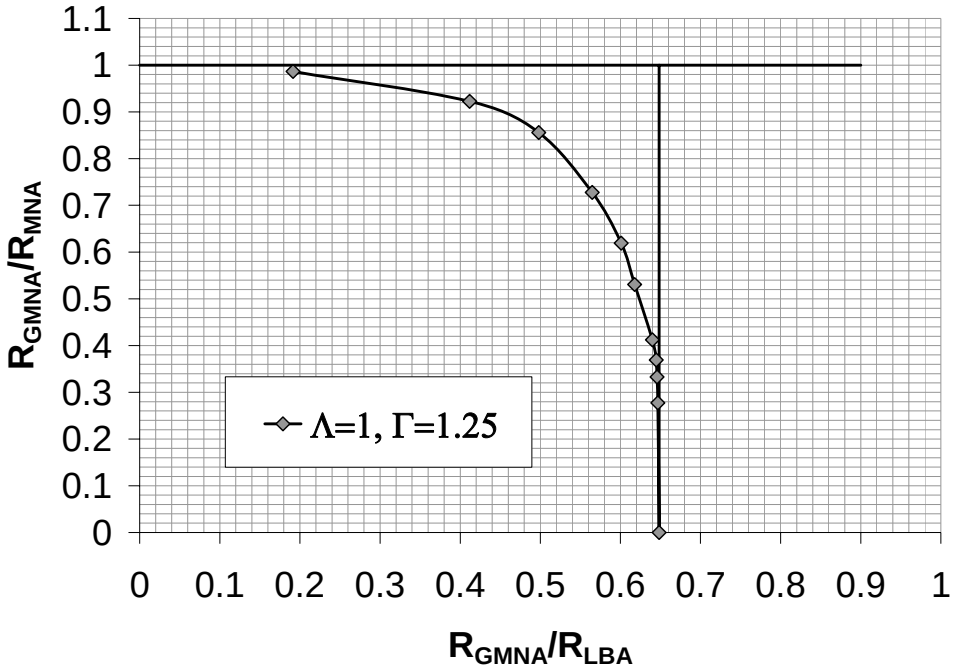

Figure 10.55: Modified capacity curve (Λ=1, Γ=1.25, r/t=1000)

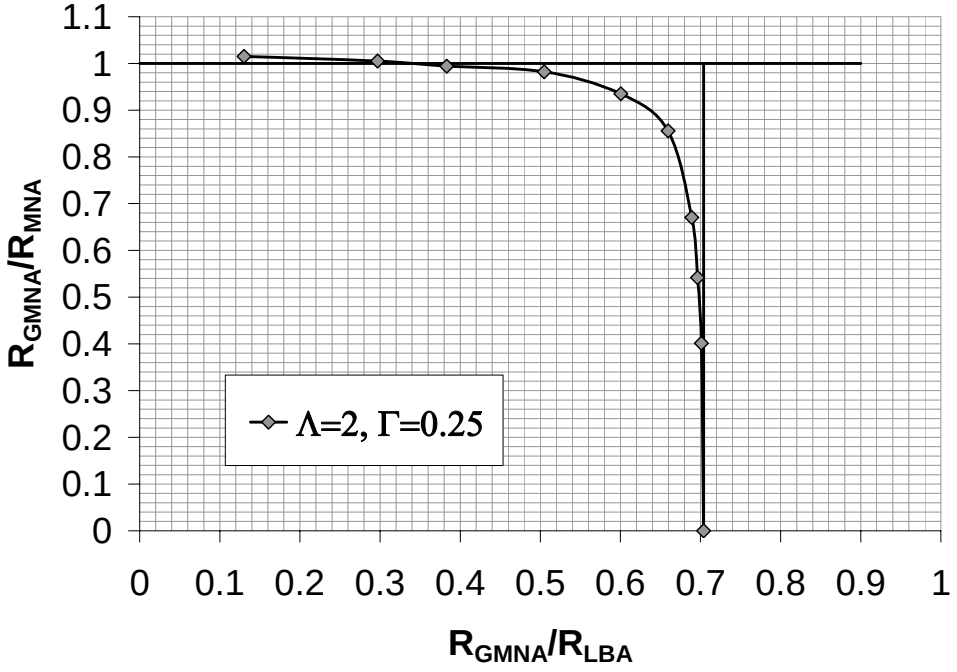

Figure 10.56: Modified capacity curve (Λ=2, Γ=0.25, r/t=1000)

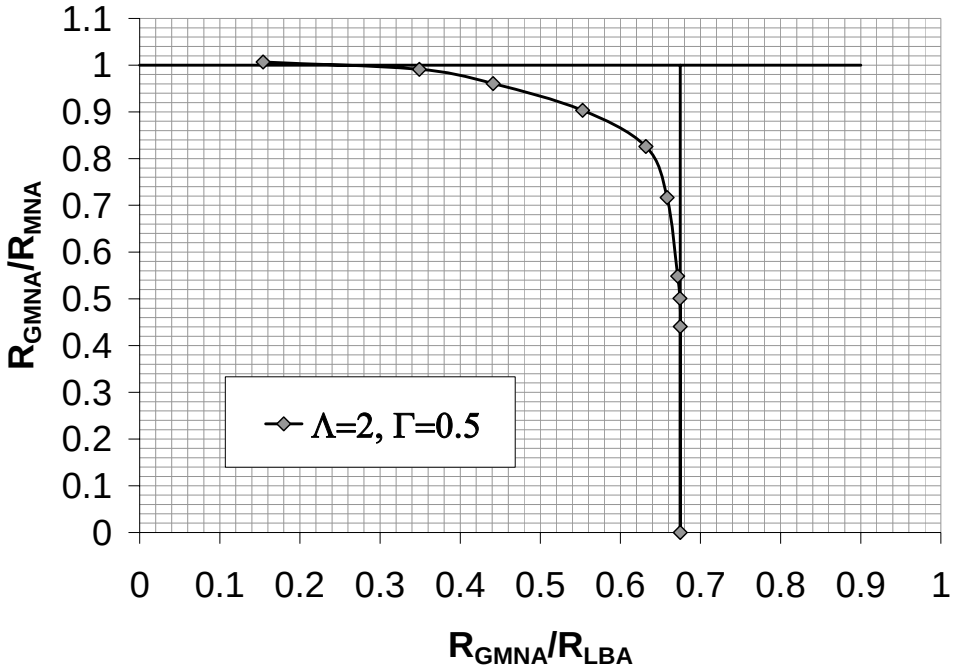

Figure 10.57: Modified capacity curve (Λ=2, Γ=0.50, r/t=1000)

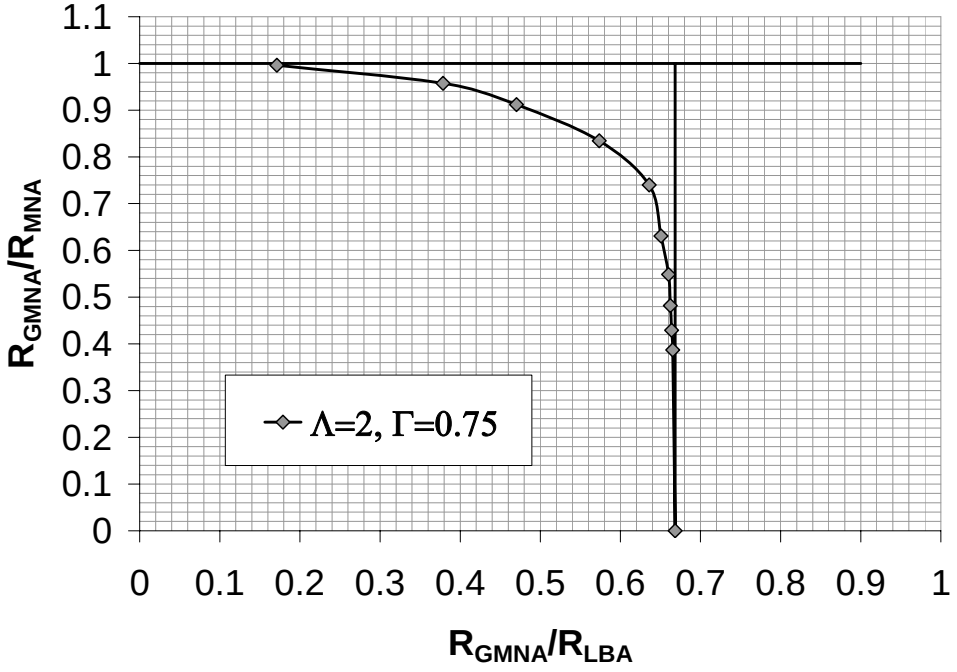

Figure 10.58: Modified capacity curve (Λ=2, Γ=0.75, r/t=1000)

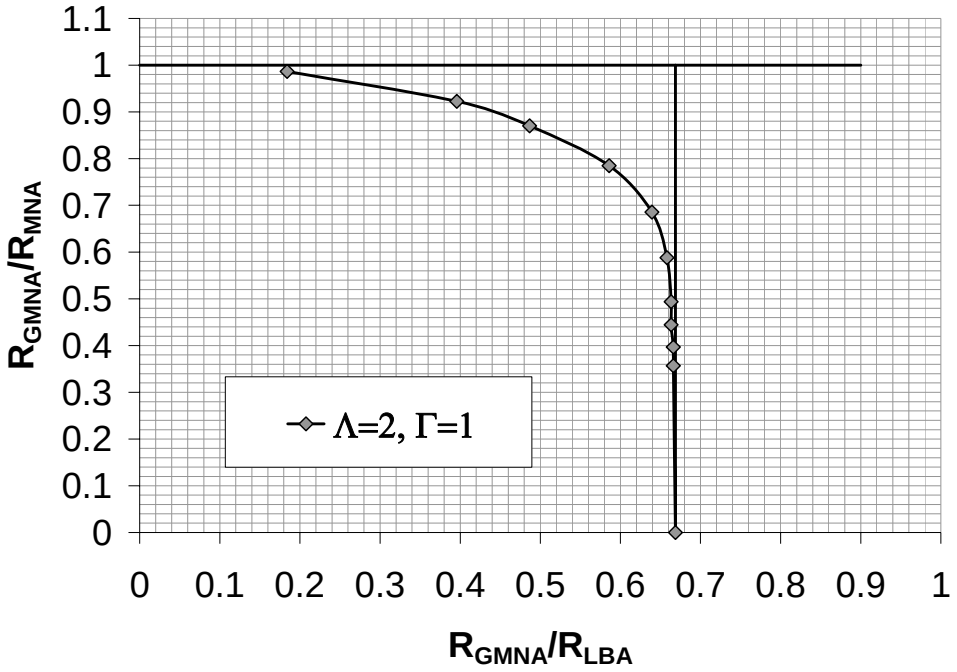

Figure 10.59: Modified capacity curve (Λ=2, Γ=1.00, r/t=1000)

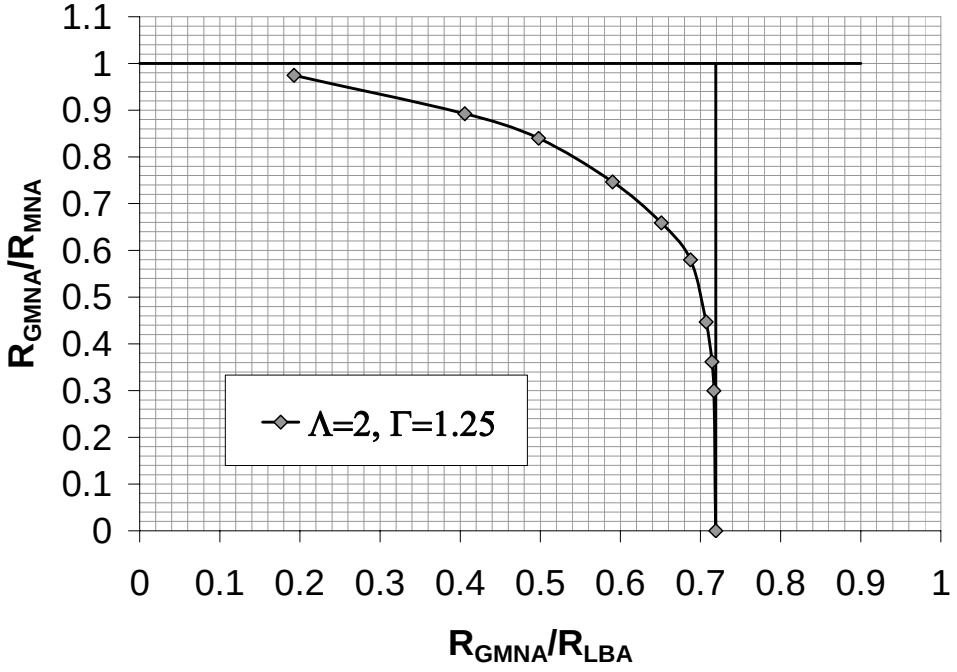

Figure 10.60: Modified capacity curve (Λ=2, Γ=1.25, r/t=1000)

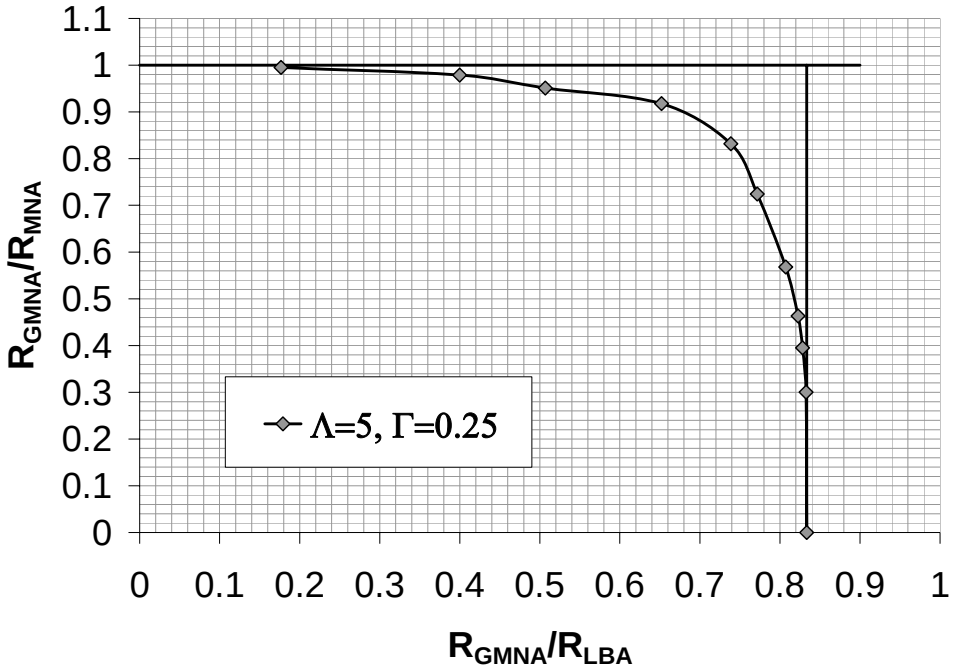

Figure 10.61: Modified capacity curve (Λ=5, Γ=0.25, r/t=1000)

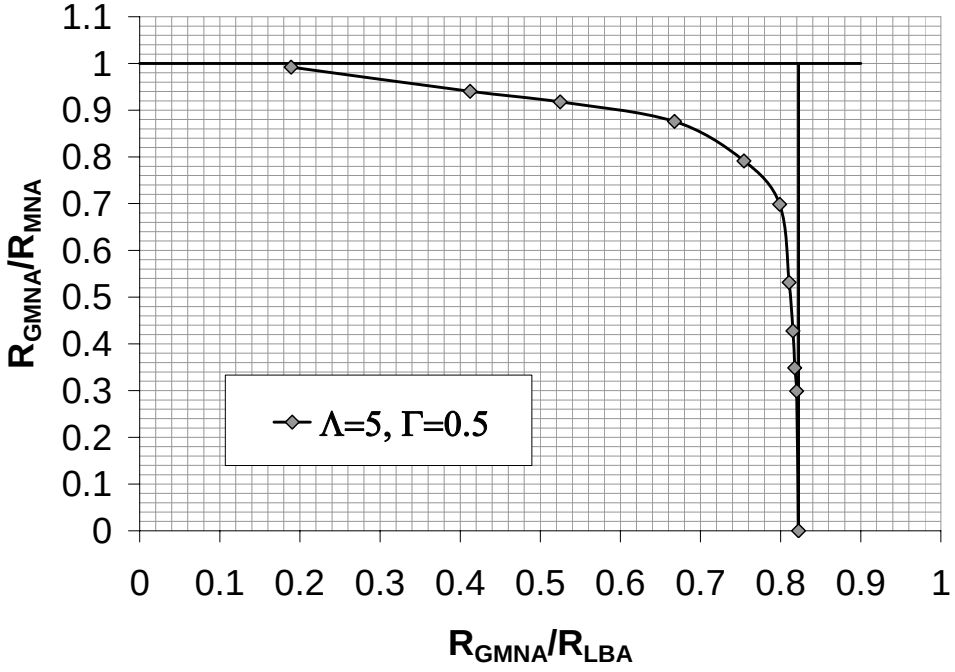

Figure 10.62: Modified capacity curve (Λ=5, Γ=0.50, r/t=1000)

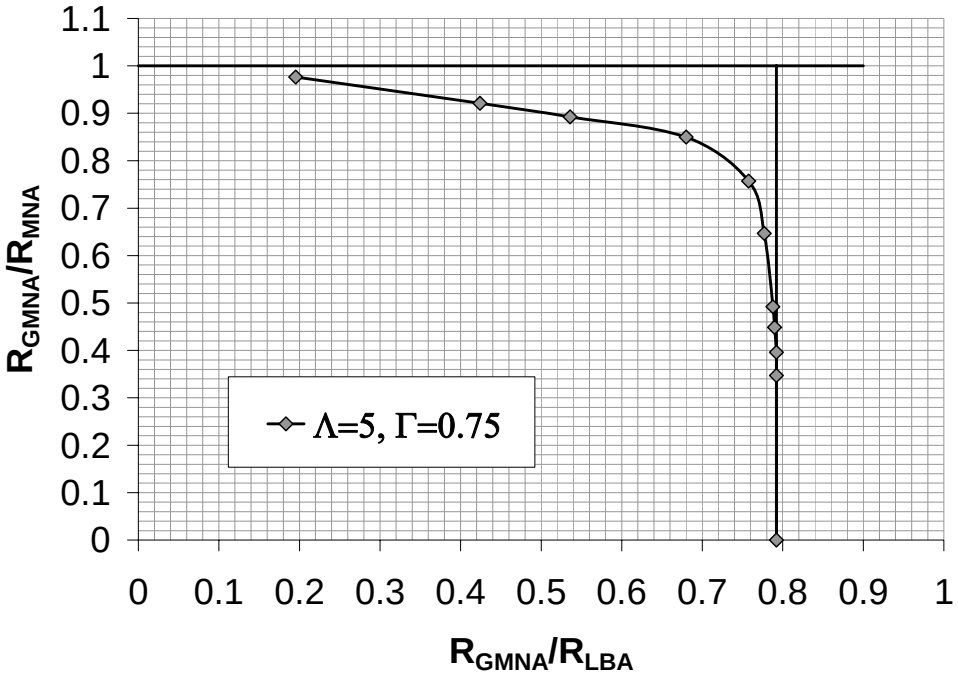

Figure 10.63: Modified capacity curve (Λ=5, Γ=0.75, r/t=1000)

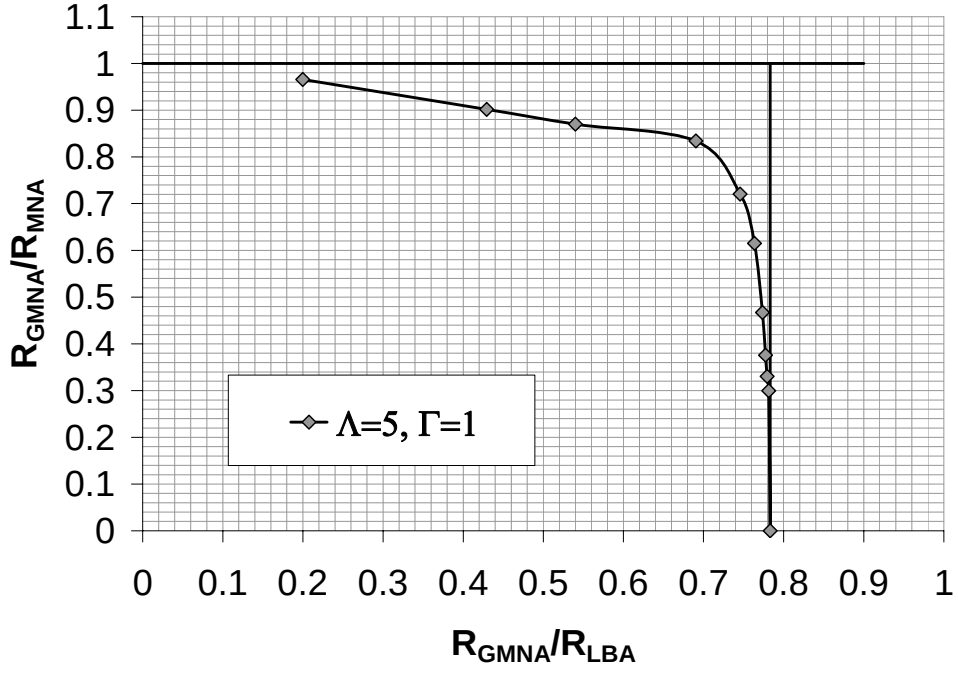

Figure 10.64: Modified capacity curve (Λ=5, Γ=1.00, r/t=1000)

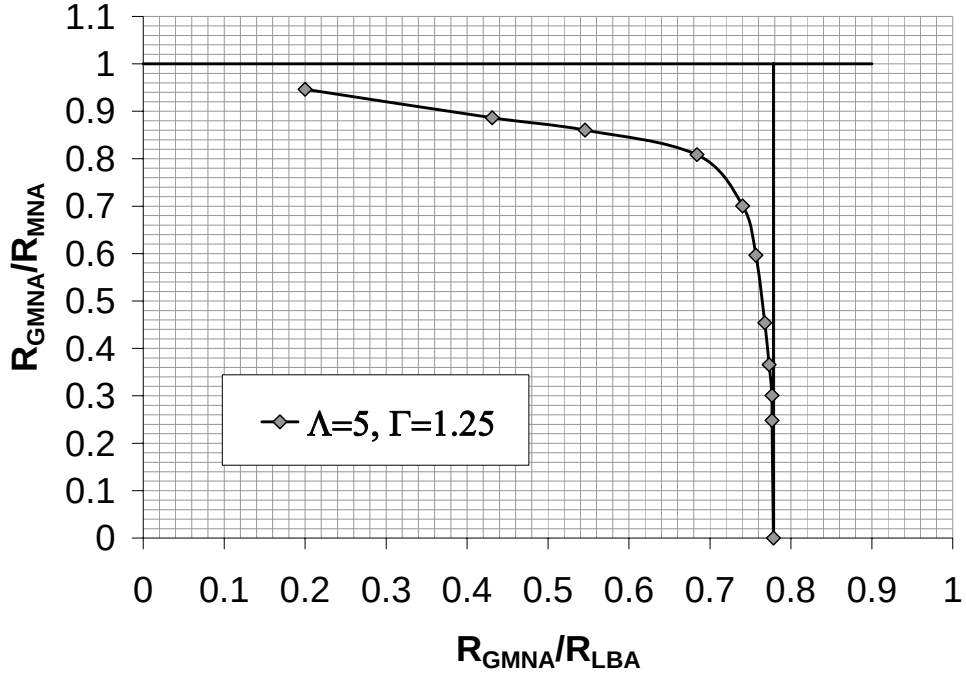

Figure 10.65: Modified capacity curve (Λ=5, Γ=1.25, r/t=1000)

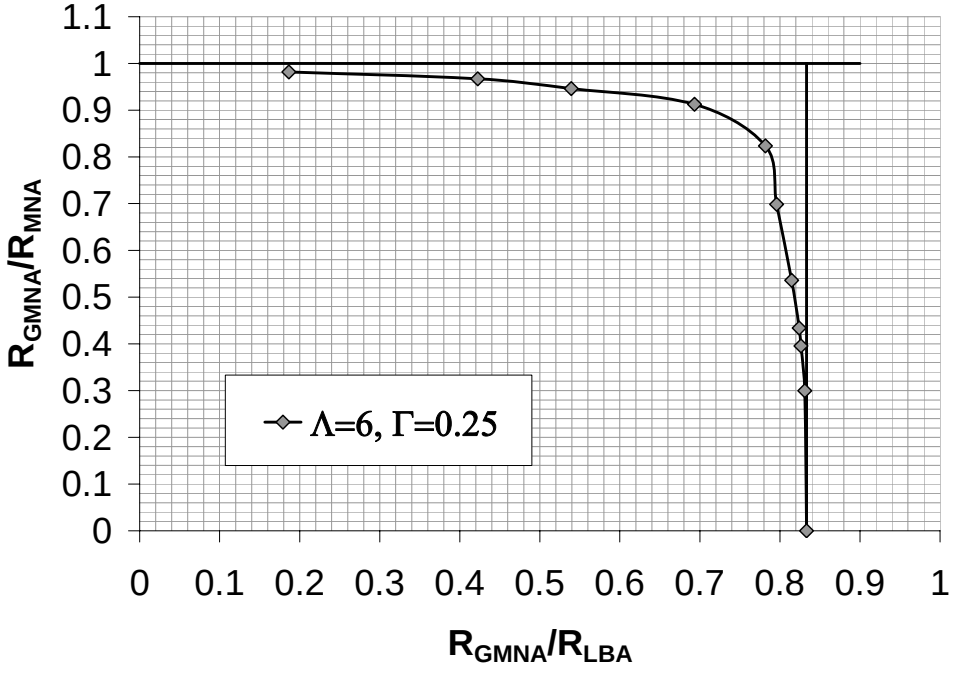

Figure 10.66: Modified capacity curve (Λ=6, Γ=0.25, r/t=1000)

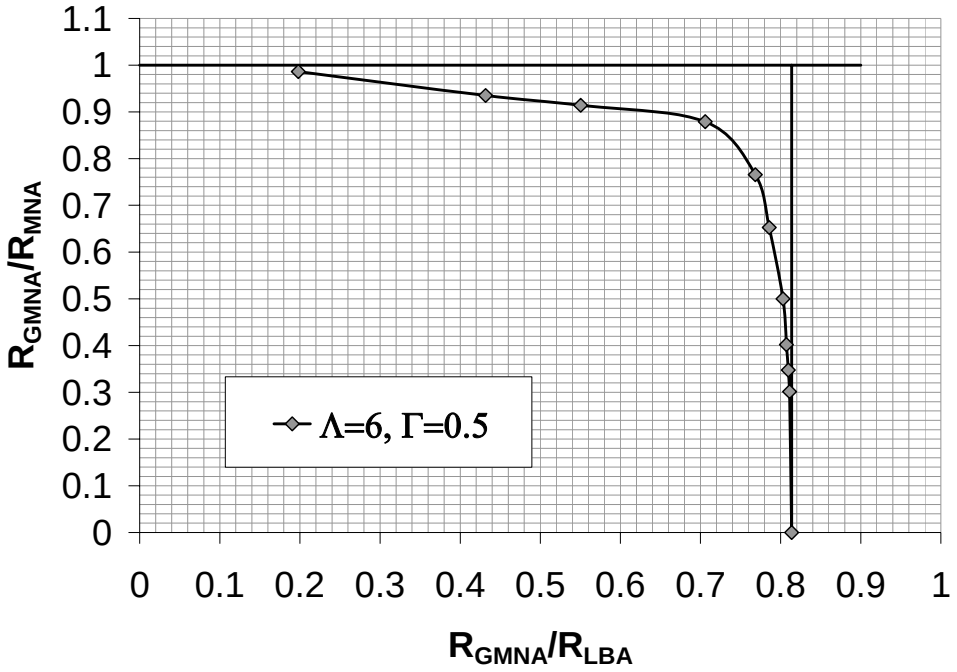

Figure 10.67: Modified capacity curve (Λ=6, Γ=0.50, r/t=1000)

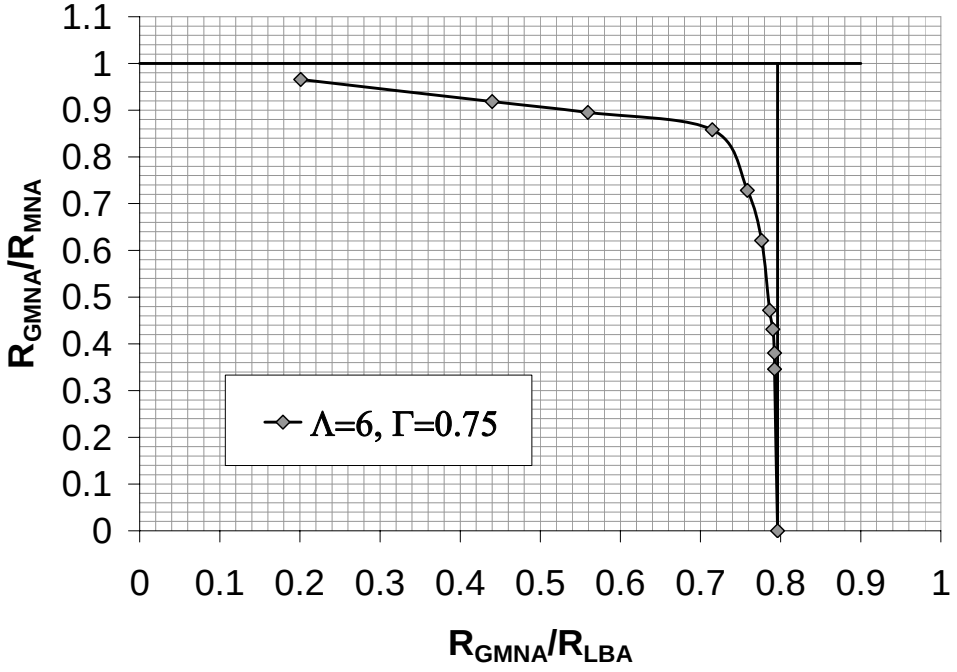

Figure 10.68: Modified capacity curve (Λ=6, Γ=0.75, r/t=1000)

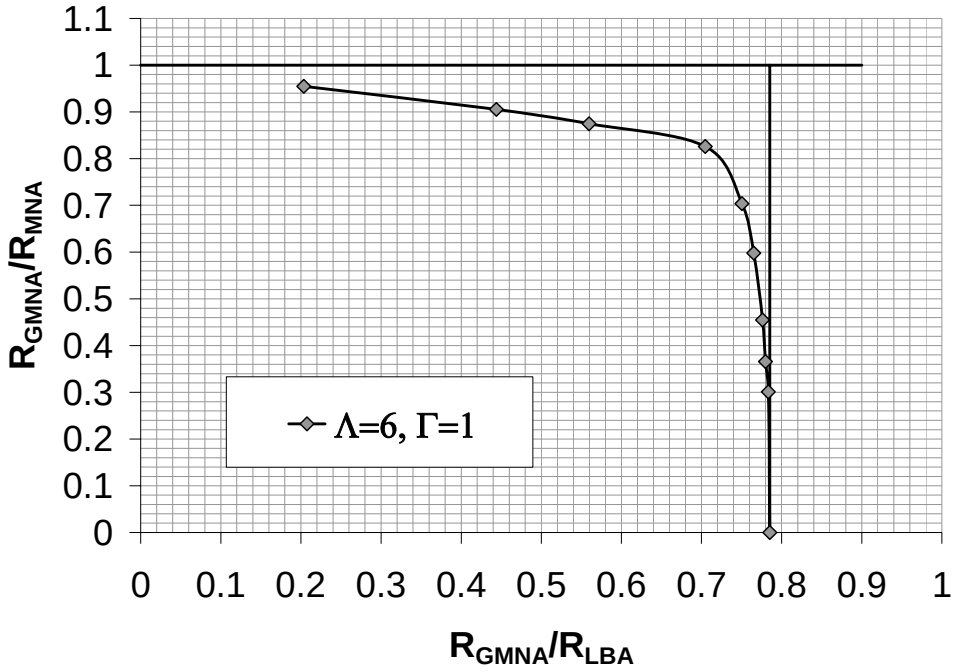

Figure 10.69: Modified capacity curve (Λ=6, Γ=1.00, r/t=1000)

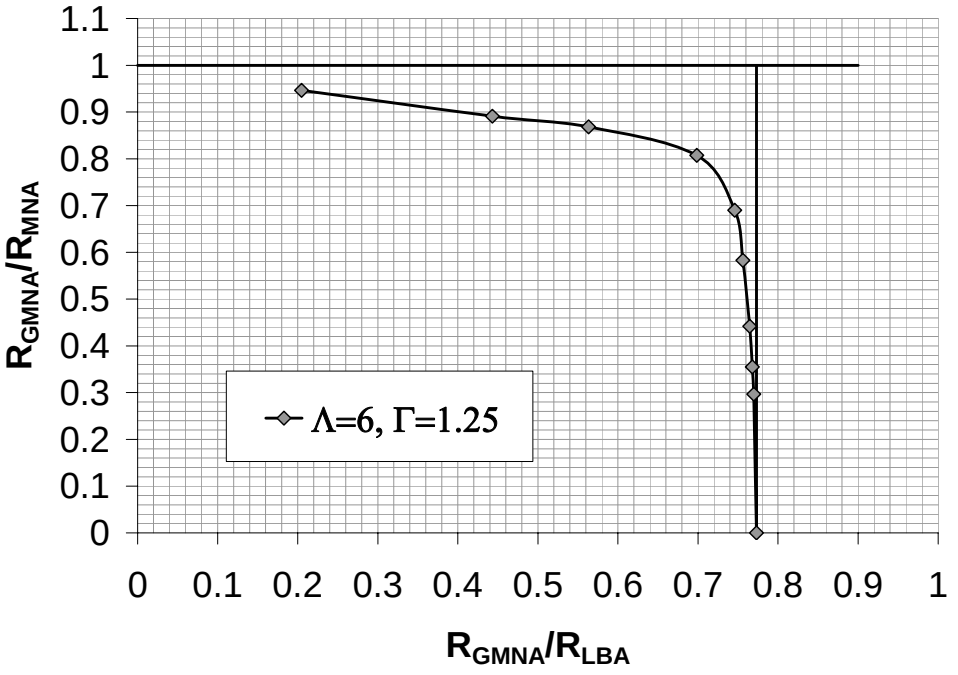

Figure 10.70: Modified capacity curve (Λ=6, Γ=1.25, r/t=1000)

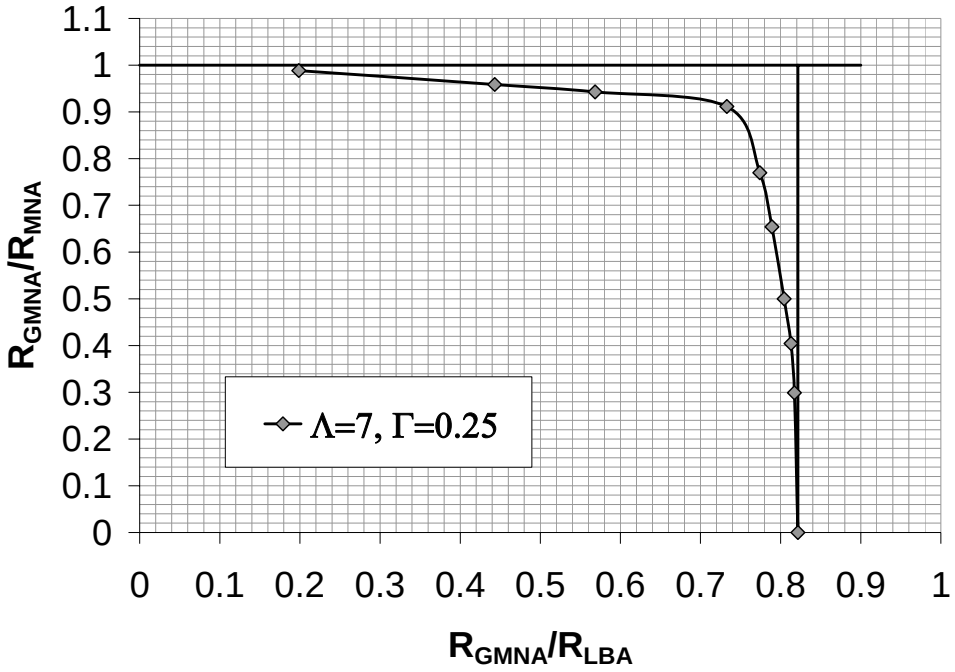

Figure 10.71: Modified capacity curve (Λ=7, Γ=0.25, r/t=1000)

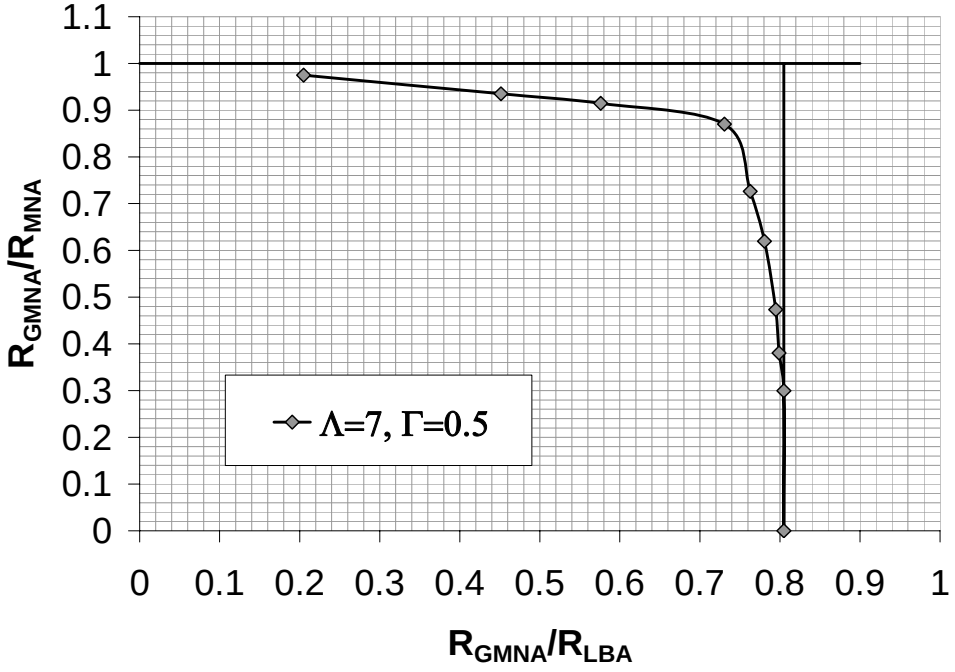

Figure 10.72: Modified capacity curve (Λ=7, Γ=0.50, r/t=1000)

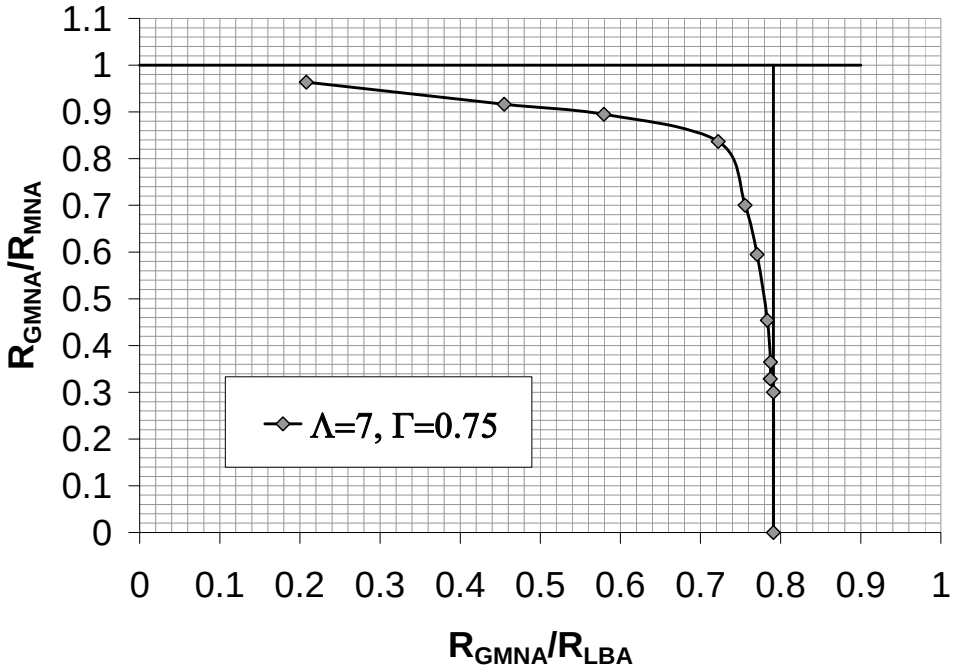

Figure 10.73: Modified capacity curve (Λ=7, Γ=0.75, r/t=1000)

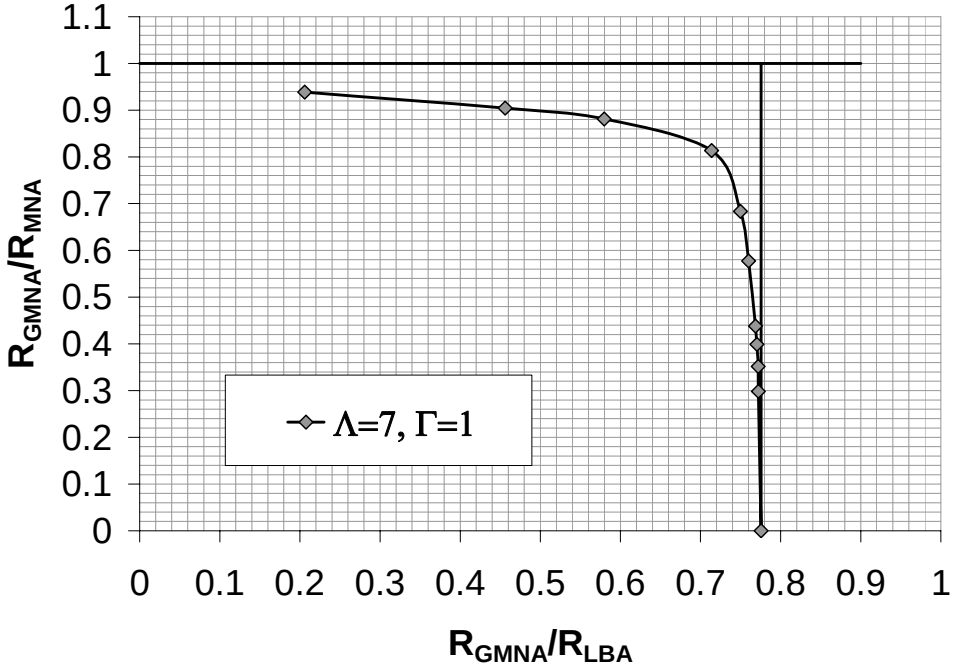

Figure 10.74: Modified capacity curve (Λ=7, Γ=1.00, r/t=1000)

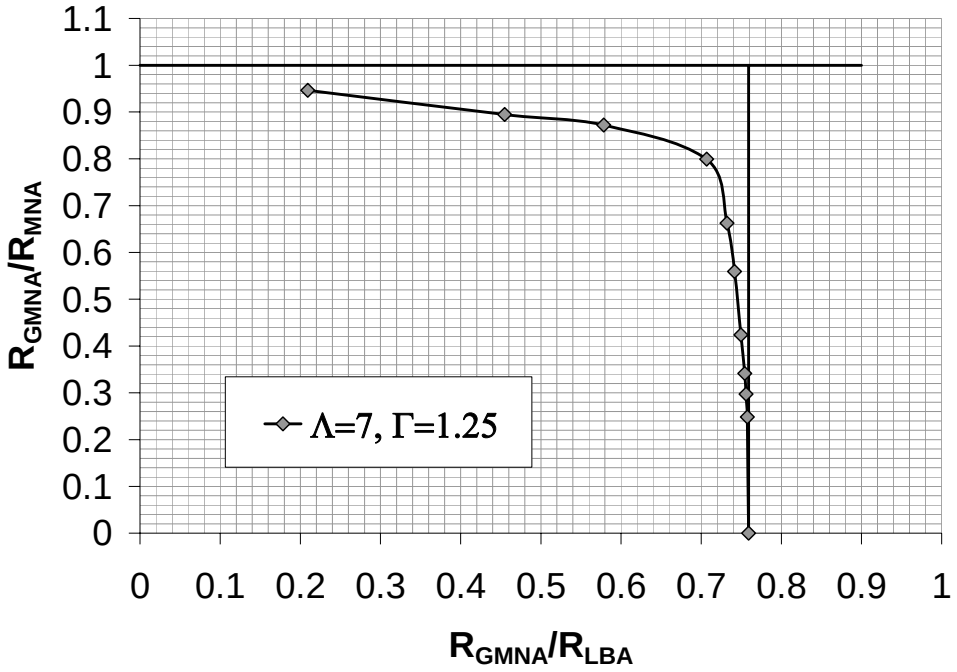

Figure 10.75: Modified capacity curve (Λ=7, Γ=1.25, r/t=1000)